/karatekinuni

https://ikstc.karatekin.edu.tr

2nd INTERNATIONAL KARATEKIN SCIENCE AND TECHNOLOGY CONFERENCE

21 - 22 DECEMBER 2023

ÇANKIRI, TÜRKİYE

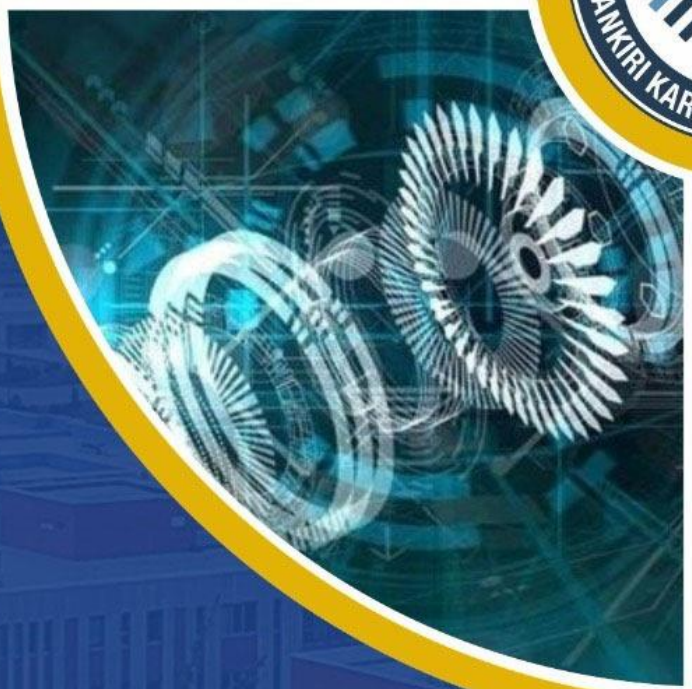

ÇANKIRI KARATEKİN ÜNİVERSİTESİ 2007

Fulltext Proceeding Book

Science from Çankırı to the World

www.karatekin.edu.tr

IKSTC2nd

2nd International Karatekin Science and Technology Conference

FULLTEXT PROCEEDING BOOK

December 21-22, 2023 – Çankırı, Turkiye

Editors

Dr. Muhammed Bora AKIN

Dr. Zehra Gülten YALÇIN

ISBN: 978-605-82910-8-9

IKSTC2nd 2023

2nd International Karatekin Science and Technology Conference

Fulltext Proceeding Book

ISBN: 978-605-82910-8-9

ÇANKIRI KARATEKİN UNIVERSITY PUBLICATION®

TURKIYE

TR: +90 376 218 95 00

https://ikstc.karatekin.edu.tr/

All rights reserved to Çankırı Karatekin University.

It cannot be copied or reproduced without permission.

Whole legal and ethical responsibilities belong to the authors.

ÇAKU Publications - 2023©

Publish Date: December 27th, 2023

ISBN: 978-605-82910-8-9

ABOUT THE CONFERENCE

CONFERENCE NAME

2nd International Karatekin Science and Technology Conference

DATE AND PLACE

December 21-22, 2023 Çankırı – Turkiye

ORGANIZING AGENCY

ÇAKU – Çankırı Karatekin University

CHAIRMAN OF THE CONFERENCE

Prof. Dr. Harun ÇİFTÇİ

GENERAL COORDINATOR

Prof. Dr. Volkan EYÜPOĞLU

OFFICIAL LANGUAGE OF THE CONFERENCE

English

PARTICIPANT COUNTRIES

Algeria, Azerbaijan, Bosnia and Herzegovina, Djibouti, Egypt, Gabon, Iran, Iraq, Jordan, Libyan Arab Jamahiriya, Morocco, Palestine, Pakistan, Saudi Arabia, Spain, Turkiye, Yemen

IKSTC2nd 2023

Conference Chairman

Prof. Dr. Harun ÇIFTÇI, Rector, Çankırı Karatekin University, Turkiye

Conference Vice Chairman

Prof. Dr. Hüseyin ODABAŞ, Vice Rector, Çankırı Karatekin University, Turkiye
Prof. Dr. İbrahim ÇIFTÇI, Vice Rector, Çankırı Karatekin University, Turkiye
Prof. Dr. Şebnem KUŞVURAN, Research Dean, Çankırı Karatekin University, Turkiye

Honorary Chair

Prof. Dr. Sadik KAKAC, TUBA Science Academy Honorary Member, Turkiye

Organization Chairman

Prof. Dr. Volkan EYÜPOĞLU, Çankırı Karatekin University, Turkiye

University Independent Representative

Prof. Dr. Sevki ADEM, Çankırı Karatekin University, Turkiye

Organization Committee

Organization Committee

Prof. Dr. Celal Tugrul ZEYREK, Cankiri Karatekin University, Türkiye
Assoc. Prof. Dr. Baris SIMSEK, Cankiri Karatekin University, Türkiye
Assoc. Prof. Dr. Beytullah EREN, Sakarya University, Türkiye
Assoc. Prof. Dr. Caner TANIS, Cankiri Karatekin University, Türkiye
Assoc. Prof. Dr. Ceyhun TURKMEN, Cankiri Karatekin University, Türkiye
Assoc. Prof. Dr. Ender BUGDAY, Cankiri Karatekin University, Türkiye
Assoc. Prof. Dr. Ercan AYDOGMUS, Firat University, Türkiye
Assoc. Prof. Dr. Faruk KARAASLAN, Cankiri Karatekin University, Türkiye
Assoc. Prof. Dr. Gonca DURMAZ GUNGOR, Cankiri Karatekin University, Türkiye
Assoc. Prof. Dr. Gulay KARAHAN, Cankiri Karatekin University, Türkiye
Assoc. Prof. Dr. Huseyin GOKCE, Cankiri Karatekin University, Türkiye
Assoc. Prof. Dr. Serap CETINKAYA, Sivas Cumhuriyet University, Türkiye
Asst. Prof. Dr. Fatih ISSI, Cankiri Karatekin University, Türkiye
Asst. Prof. Dr. Goksu GOREL, Cankiri Karatekin University, Türkiye
Asst. Prof. Dr. Gonca BUYRUKOGLU, Cankiri Karatekin University, Türkiye
Asst. Prof. Dr. Mehmet Ali BIBERCI, Cankiri Karatekin University, Türkiye
Asst. Prof. Dr. Muhammed Bora AKIN, Cankiri Karatekin University, Türkiye
Asst. Prof. Dr. Murat KONCA, Cankiri Karatekin University, Türkiye
Asst. Prof. Dr. Musa ACARTURK, Cankiri Karatekin University, Türkiye
Asst. Prof. Dr. Mustafa KARHAN, Cankiri Karatekin University, Türkiye
Asst. Prof. Dr. Pembe Merve KARABULUT, Cankiri Karatekin University, Türkiye
Asst. Prof. Dr. Sakine KIRATLI, Cankiri Karatekin University, Türkiye
Asst. Prof. Dr. Seda OZGEN, Cankiri Karatekin University, Türkiye
Asst. Prof. Dr. Selma AKCAY, Cankiri Karatekin University, Türkiye
Asst. Prof. Dr. Taha ETEM, Cankiri Karatekin University, Türkiye
Asst. Prof. Dr. Zehra Gulten YALCIN, Cankiri Karatekin University, Türkiye
Dr. Cagatay ERSIN, Cankiri Karatekin University, Türkiye
Dr. Enis SERT, Cankiri Karatekin University, Türkiye
Dr. Mustafa DAG, Cankiri Karatekin University, Türkiye
Dr. Vedat Arda KUCUK, Cankiri Karatekin University, Türkiye
Mehmet Ali Boz, Cankiri Karatekin University, Türkiye

Scientific Committee

Prof. Dr. Abdullah Emin AKAY, Bursa Technical University, Türkiye
Prof. Dr. Alkan GUNLU, Cankiri Karatekin University, Türkiye
Prof. Dr. Avni BERISHA, University of Prishtina, Kosovo
Prof. Dr. Ayhan Abdullah CEYHAN, Konya Technical University, Türkiye
Prof. Dr. Azize Serap TUNCER, Cankiri Karatekin University, Türkiye
Prof. Dr. Beytullah AFSIN, Ondokuz Mayis University, Türkiye
Prof. Dr. Bulent DEDE, Suleyman Demirel University, Türkiye
Prof. Dr. Carlos GARCÍA-GONZÁLEZ, Universidad de Santiago de Compostela, Spain
Prof. Dr. Celal Tugrul ZEYREK, Cankiri Karatekin University, Türkiye
Prof. Dr. Cigdem Yuksektepe ATAOL, Cankiri Karatekin University, Türkiye
Prof. Dr. Ender SARIFAKIOGLU, Cankiri Karatekin University, Türkiye
Prof. Dr. Esra Betul KOC OZTURK, Bolu Abant Izzet Baysal University, Türkiye
Prof. Dr. Fethiye GODE, Suleyman Demirel University, Türkiye
Prof. Dr. Hakan COLAK, Cankiri Karatekin University, Türkiye
Prof. Dr. Ilkay SISMAN, Sakarya University, Türkiye
Prof. Dr. Inanc OZGEN, Firat University, Türkiye
Prof. Dr. Ismail Sahin, Gazi University, Türkiye
Prof. Dr. Kemal SARIOGLU, Erciyes University, Türkiye
Prof. Dr. Kudret YILDIRIM, Sakarya University, Türkiye
Prof. Dr. Levent Cenk KUMRUOGLU, Iskenderun Technical University, Türkiye
Prof. Dr. M. Nuri ONER, Cankiri Karatekin University, Türkiye
Prof. Dr. Malik ČABARAVDIČ, University of Zenica, Bosnia &Herzegovina
Prof. Dr. Mahmut AKDEMIR, Sakarya University, Türkiye
Prof. Dr. Mehmet NEBIOGLU, Sakarya University, Türkiye
Prof. Dr. Mehmet CIFTCI, Bingol University, Türkiye
Prof. Dr. Meryem Nilufer YARASIR, Sakarya University, Türkiye
Prof. Dr. Metin GURU, Gazi University, Türkiye
Prof. Dr. Muhammad AKRAM, University of The Punjab, Pakistan
Prof. Dr. Muhammad RIAZ, University of The Punjab, Pakistan
Prof. Dr. Muslum KUZU, Karabuk University, Türkiye
Prof. Dr. Naim CAGMAN, Gaziosmanpasa University, Türkiye
Prof. Dr. Ramazan DEMIRDAG, Agri Ibrahim Cecen University, Türkiye
Prof. Dr. Sezgin AYAN, Kastamonu University, Türkiye
Prof. Dr. Ufuk OZTURK, Bolu Abant Izzet Baysal University, Türkiye
Prof. Dr. Ummuhan Ozmen OZDEMIR, Gazi University, Türkiye
Prof. Dr. Umut Pekin TIMUR, Cankiri Karatekin University, Türkiye
Prof. Dr. Unal AKDAG, Aksaray University, Türkiye
Prof. Dr. Veysel COMAKLI, Agri Ibrahim Cecen University, Türkiye
Prof. Dr. Yeliz PEKBEY, Ege University, Türkiye

Scientific Committee (Continued)

Prof. Dr. Zafer ERDEN, Hacettepe University, Türkiye
Assoc. Prof. Dr. Ahmet Turgut BILGICLI, Sakarya University, Türkiye
Assoc. Prof. Dr. Armagan GUNSEL, Sakarya University, Türkiye
Assoc. Prof. Dr. Baris SIMSEK, Cankiri Karatekin University, Türkiye
Assoc. Prof. Dr. Bengi OZKAHRAMAN, Hitit University, Türkiye
Assoc. Prof. Dr. Bilal NISANCI, Ataturk University, Türkiye
Assoc. Prof. Dr. Burak TUZUN, Sivas Cumhuriyet University, Türkiye
Assoc. Prof. Dr. Canan CIMSIT, Kocaeli University, Türkiye
Assoc. Prof. Dr. Caner TANIS, Cankiri Karatekin University, Türkiye
Assoc. Prof. Dr. Ceyhun KOSE, Tokat Gaziosmanpasa University, Türkiye
Assoc. Prof. Dr. Deniz BAS, Cankiri Karatekin University, Türkiye
Assoc. Prof. Dr. Ebru AKKEMIK, Siirt University, Türkiye
Assoc. Prof. Dr. Ebru KILICAY, Cankiri Karatekin University, Türkiye
Assoc. Prof. Dr. Elsir Adam OMER SALIH, Alzaeim Alazhari University, Sudan
Assoc. Prof. Dr. Emel AKYOL, Yildiz Technical University, Türkiye
Assoc. Prof. Dr. Emin BOZKURT, Cankiri Karatekin University, Türkiye
Assoc. Prof. Dr. Ender BUGDAY, Cankiri Karatekin University, Türkiye
Assoc. Prof. Dr. Fatih KORKMAZ, Cankiri Karatekin University, Türkiye
Assoc. Prof. Dr. Fatma BAYRAKCEKEN NISANCI, Ataturk University, Türkiye
Assoc. Prof. Dr. Gulay KARAHAN, Cankiri Karatekin University, Türkiye
Assoc. Prof. Dr. Harun GOKCE, Gazi University, Türkiye
Assoc. Prof. Dr. Hasan ARSLANOGLU, Canakkale Onsekiz Mart University, Türkiye
Assoc. Prof. Dr. Hudayi ERCOSKUN, Cankiri Karatekin University, Türkiye
Assoc. Prof. Dr. Huseyin GOKCE, Cankiri Karatekin University, Türkiye
Assoc. Prof. Dr. Irmak KARADUMAN ER, Cankiri Karatekin University, Türkiye
Assoc. Prof. Dr. Mehmet SEZGIN, Cankiri Karatekin University, Türkiye
Assoc. Prof. Dr. Melike Bilgi KAMAC, Cankiri Karatekin University, Türkiye
Assoc. Prof. Dr. Nadira BUSATLIC, University of East Sarajevo, Bosnia & Herzegovina
Assoc. Prof. Dr. Nesibe DILMAC, Cankiri Karatekin University, Türkiye
Assoc. Prof. Dr. Nursel ALTAN OZBEK, Duzce University, Türkiye
Assoc. Prof. Dr. Olcay GENCYILMAZ, Cankiri Karatekin University, Türkiye
Assoc. Prof. Dr. Omer Faruk DILMAC, Cankiri Karatekin University, Türkiye
Assoc. Prof. Dr. Selim BUYRUKOGLU, Cankiri Karatekin University, Türkiye
Assoc. Prof. Dr. Serhat SIREKBASAN, Cankiri Karatekin University, Türkiye
Assoc. Prof. Dr. Sertac ORUC, Cankiri Karatekin University, Türkiye
Assoc. Prof. Dr. Sezin TUTA SIMSEK, Cankiri Karatekin University, Türkiye
Assoc. Prof. Dr. Tamer CANKAYA, Bolu Abant Izzet Baysal University, Türkiye
Assoc. Prof. Dr. Telem SIMSEK, Hacettepe University, Türkiye
Assoc. Prof. Dr. Veyis KARAKOC, Cankiri Karatekin University, Türkiye

Scientific Committee (Continued)

Assoc. Prof. Dr. Zehra OZBAS, Cankiri Karatekin University, Türkiye
Asst. Prof. Dr. Cuma CAKMAK, Dicle University, Türkiye
Asst. Prof. Dr. Eda GURSU SAHIN, Cankiri Karatekin University, Türkiye
Asst. Prof. Dr. Erdi KAYABINAR, Yalova University, Türkiye
Asst. Prof. Dr. Fatih ISSI, Cankiri Karatekin University, Türkiye
Asst. Prof. Dr. Gul UGUR KAYMANLI, Cankiri Karatekin University, Türkiye
Asst. Prof. Dr. Gonca BUYRUKOGLU, Cankiri Karatekin University, Türkiye
Asst. Prof. Dr. Haluk KORUCU, Cankiri Karatekin University, Türkiye
Asst. Prof. Dr. Hasim CAPAR, Dicle University, Türkiye
Asst. Prof. Dr. Jeton HALILI, University of Prishtina,Kosovo
Asst. Prof. Dr. Kamal H. JIHAD, University of Kirkuk, Iraq
Asst. Prof. Dr. Mehmet Ali BIBERCI, Cankiri Karatekin University, Türkiye
Asst. Prof. Dr. Mehmet Burak KAYNAR, Hacettepe University, Türkiye
Asst. Prof. Dr. Mehmet GUCYETMEZ, Sivas University of Science and Technology, Türkiye
Asst. Prof. Dr. Mohammed Rashad BAKER, University of Kirkuk,Iraq
Asst. Prof. Dr. Muhammed Bora AKIN, Cankiri Karatekin University, Türkiye
Asst. Prof. Dr. Musa ACARTURK, Cankiri Karatekin University, Türkiye
Asst. Prof. Dr. Musa Faruk CAKIR, Cankiri Karatekin University, Türkiye
Asst. Prof. Dr. Mustafa KARHAN, Cankiri Karatekin University, Türkiye
Asst. Prof. Dr. Mustafa TEKE, Cankiri Karatekin University, Türkiye
Asst. Prof. Dr. Nergiz BOLAT, Suleyman Demirel University, Türkiye
Asst. Prof. Dr. Nihan Feyman GOK, Cankiri Karatekin University, Türkiye
Asst. Prof. Dr. Orhan KEKLIKCIOGLU, Erciyes University, Türkiye
Asst. Prof. Dr. Ozkan ARSLAN, Tekirdag Namik Kemal University, Türkiye
Asst. Prof. Dr. Pembe Merve KARABULUT, Cankiri Karatekin University, Türkiye
Asst. Prof. Dr. Remzi Orkun, AKGUN, Cankiri Karatekin University, Türkiye
Asst. Prof. Dr. Ruhan Altun ANAYURT, Cankiri Karatekin University, Türkiye
Asst. Prof. Dr. Sakine KIRATLI, Cankiri Karatekin University, Türkiye
Asst. Prof. Dr. Seda OZGEN, Cankiri Karatekin University, Türkiye
Asst. Prof. Dr. Seda SAHIN, Cankiri Karatekin University, Türkiye
Asst. Prof. Dr. Selma AKCAY, Cankiri Karatekin University, Türkiye
Asst. Prof. Dr. Serap KOCABIYIK CASKURLU, Istanbul University Cerrahpasa, Türkiye
Asst. Prof. Dr. Seval SELVI SARIGUL, Erzincan Binali Yildirim University, Türkiye
Asst. Prof. Dr. Sevcan Toptas KILIC, Cankiri Karatekin University, Türkiye
Asst. Prof. Dr. Sezen TEKIN, Cankiri Karatekin University, Türkiye
Asst. Prof. Dr. Sura BOYRAZ, Yozgat Bozok University, Türkiye
Asst. Prof. Dr. Taner AKARSU, Cankiri Karatekin University, Türkiye
Asst. Prof. Dr. Umit YIRTICI, Kirikkale University, Türkiye
Asst. Prof. Dr. Zehra Gulten YALCIN, Cankiri Karatekin University, Türkiye

Scientific Committee (Continued)

Dr. Berceste BEYRIBEY PRICE, UK Department for Energy Security and Net Zero, United Kingdom
Dr. Emel BOLAT YESILOVA, Cankiri Karatekin University, Türkiye
Dr. Emel EKINCI, Cankiri Karatekin University, Türkiye
Dr. Enis SERT, Cankiri Karatekin University, Türkiye
Dr. Fadime BALDEMIR, Cankiri Karatekin University, Türkiye
Dr. Ferhat BOLAT, Cankiri Karatekin University, Türkiye
Dr. Harun BALDEMIR, Cankiri Karatekin University, Türkiye
Dr. Mahmud Esad YIGIT, Cankiri Karatekin University, Türkiye
Dr. Mehmet GUNES, Cankiri Karatekin University, Türkiye
Dr. Mustafa DAG, Cankiri Karatekin University, Türkiye
Dr. Ravi RAWAT, UPES University, India
Dr. Songul SAHIN, Cankiri Karatekin University, Türkiye
Dr. Xiangling YUE, University of St Andrews, United Kingdom
Dr. Cagatay ERSIN, Cankiri Karatekin University, Türkiye
Dr. Gunseli Bobus ALKAYA, Mersin University, Türkiye
Dr. Shahla Uthman UMAR, University of Kirkuk, Iraq
Emre OZDEMIRCI, Cankiri Karatekin University, Türkiye
Furkan OZDEMIR, Cankiri Karatekin University, Türkiye
Mehmet Salih YILDIZ, Cankiri Karatekin University, Türkiye

Conference Moderators

Assoc. Prof. Dr. Ceyhun TÜRKMEN, Çankırı Karatekin University, Turkiye
Assoc. Prof. Dr. Gülay KARAHAN, Çankırı Karatekin University, Turkiye
Asst. Prof. Dr. Asuman ÜNAL, Çankırı Karatekin University, Turkiye
Asst. Prof. Dr. Gonca BUYRUKOĞLU, Çankırı Karatekin University, Turkiye
Asst. Prof. Dr. Murat KONCA, Çankırı Karatekin University, Turkiye
Dr. Adem ÇIÇEK, Çankırı Karatekin University, Turkiye
Dr. Çağatay ERSIN, Çankırı Karatekin University, Turkiye
Dr. Enis SERT, Çankırı Karatekin University, Turkiye
Dr. Mahmut Esat YİĞİT, Çankırı Karatekin University, Turkiye
Dr. Serkan KOLDAŞ, Çankırı Karatekin University, Turkiye
Dr. Vedat Arda KÜÇÜK, Çankırı Karatekin University, Turkiye
Eren YURDAKUL, Çankırı Karatekin University, Turkiye
Hüsamettin ŞERBETÇI, Çankırı Karatekin University, Turkiye
İrem ECEMIŞ, Çankırı Karatekin University, Turkiye
Simge ÇİZGEN TAN, Çankırı Karatekin University, Turkiye

Invited Speakers

Prof. Dr. Avni BERISHA, University of Prishtina, Kosovo
Prof. Dr. İdris KABALCI, Usak University, Türkiye
Prof. Dr. Malik ČABARAVDIĆ, University of Zenica, Bosnia & Herzegovina
Prof. Dr. Metin GURU, Gazi University, Turkiye
Prof. Dr. Sadık KAKAÇ, TOBB University, Turkiye
Assoc. Prof. Dr. Abdelghafour ZAABOUT, University Mohammed 6 Polytechnic, Morocco
Assoc. Prof. Dr. Abdelhafeez M. A. MOHAMMED, King Abdulaziz University, Saudi Arabia
Assoc. Prof. Dr. Emel AKYOL, Yildiz Technical University, Türkiye
Assoc. Prof. Dr. Nadira BUŠATLIĆ, University of Zenica, Bosnia & Herzegovina
Assoc. Prof. Dr. Magdy H. MOURAD MOHAMMAD, Cairo University, Egypt
Asst. Prof. Dr. Azhar RASUL, Government College University Faisalabad, Pakistan
Asst. Prof. Dr. Ravi RAWAT, UPES University, India

Conference Topics

Agricultural Science and Engineering
Biology
Chemical Engineering
Chemistry
Civil Engineering
Combustion and Fuels
Computer Engineering
Electric and Electronics Engineering
Environmental Engineering
Food Engineering
Forest Engineering
Health Sciences
Landscape Architecture
Mathematics
Material Science
Metallurgy and Materials Engineering
Mechanical Engineering
Medicinal Science
Occupational Health and Safety
Physics
Statistics

Dear Participant,

The total number of speakers at "2nd International Karatekin Science and Technology Conference" was 190 together with the invited speakers.

A total of 11 invited speakers, 8 of whom are foreign and 4 of whom are Turkish nationals, made presentations at the conference.

In addition to the invited speakers, 98 foreign speakers from various countries made presentations at the conference. 52% of the 190 speakers in total were foreigners.

Thank you to all the participants who gave generously of their time, especially the speakers who shared their studies and experiences and the institutions who assisted in.

2nd International Karatekin Science and Technology Conference Organizing Committee

T.C.
ÇANKIRI KARATEKİN ÜNİVERSİTESİ
Genel Sekreterlik

Sayı : E-52133317-051.02-163281
Konu : Görevlendirme (Akademisyen Temsilcisi)

FEN FAKÜLTESİ DEKANLIĞINA

İlgi : 15.12.2023 tarihli ve E-49144793-903-163203 sayılı yazı.

Üniversitemiz ev sahipliğinde 21-22 Aralık 2023 tarihleri arasında düzenlenecek olan "2ND INTERNATIONAL KARATEKIN SCIENCE AND TECHNOLOGY CONFERENCE" kapsamında, Fen Fakültesi Kimya Bölümü öğretim üyesi Prof. Dr. Şevki ADEM'in "Konferans Akademisyen Temsilcisi" olarak katılım sağlaması Rektörlüğümüzce uygun görülmüştür.

Bilgilerinizi ve gereğini rica ederim.

Prof. Dr. Harun ÇİFTÇİ
Rektör

Bu belge, güvenli elektronik imza ile imzalanmıştır.
Belge Doğrulama Kodu : 0JZR-KV1Z-0YDP Belge Doğrulama Adresi : https://ebyssorgu.karatekin.edu.tr

Adres: Çankırı Karatekin Üniversitesi Uluyazı Kampüsü Rektörlük Binası Merkez/ Çankırı
Telefon No : 0 376 218 95 05 Fax No : 0 376 218 95 09
e-Posta : genelsekreterlik@karatekin.edu.tr İnternet Adresi : https://www.karatekin.edu.tr/
Bilgi İçin :Nurullah CANSIZ
Şef V.
Telefon No:7212

Index

ESTIMATION OF STRESS-STRENGTH RELIABILITY FOR TRANSMUTED POWER FUNCTION DISTRIBUTION

***Caner TANIŞ*[1,*]**

[1] *Science Faculty, Statistics, Çankırı Karatekin University, Çankırı, Turkey*

Abstract

This study provides an estimation of the stress-strength reliability for the transmuted power function distribution. We analyzed the transmuted power function distribution and its properties and obtained stress-strength reliability. The maximum likelihood method was used to estimate the transmuted power function distribution parameters. Furthermore, by using the invariance property of the maximum likelihood estimator, we obtained the maximum likelihood estimator of the stress-strength reliability. We designed a comprehensive Monte Carlo simulation study to check whether the maximum likelihood estimator satisfies the estimation procedures in terms of bias and mean square error. The simulation results show that the maximum likelihood estimator of the stress-strength reliability of the transmuted power function distribution satisfies the estimation procedures.

Keywords: *Transmuted power function distribution, Maximum likelihood estimation, Stress-strength reliability, Monte Carlo simulation*

1. Introduction

Transmuted power function distribution is introduced by [1]. The cumulative distribution function (CDF) and probability density function (PDF) are

$$F(x;\alpha,\lambda)= x^{\alpha}\left[1+\lambda\left(1- x^{\alpha}\right)\right], \tag{1}$$

and

$$f(x;\alpha,\lambda)= \alpha x^{\alpha-1}\left[1+\lambda- 2\lambda x^{\alpha}\right] \tag{2}$$

respectively, where $0< x< 1$ and $\alpha> 0$ is a shape parameter and $-1\leq \lambda\leq 1$ [1]. In this study, we briefly show transmuted power function distribution by $TPF(\alpha,\lambda)$. $TPF(\alpha,\lambda)$ distribution is useful in many fields namely, engineering, agriculture, economics, biology, and chemistry. [1] examined some distributional properties such as moments, variance, quantile function, reliability function, hazard function, order statistics, and generalized TL-moments for the $TPF(\alpha,\lambda)$ distribution. Also, Tanış [2] focused on estimation methods and characterizations such as density shapes and risk measures for $TPF(\alpha,\lambda)$ distribution.

Stress-strength model describes the lifetime of a component (or a system) with strength Y and exposed to stress X, and is defined as the stress-strength reliability $R= P(X< Y)$. The stress-strength models have comprehensive application ares including medicine, biology, engineering and agriculture. The R can be written as follows:

$$R= P(X< Y)= \int_{0}^{\infty} F_X(y)\, f_Y(y)\,dy, \tag{3}$$

where $f_Y(.)$ is the PDF of *Y*, and $F_X(.)$ is the CDF of *X*. Recenlty, there are many papers about the stress-strength reliability in the literature. Some of these studies are [3-5].

* Corresponding author. *e-mail address: canertanis@karatekin.edu.tr*

This study discusses the estimation of the stress-strength reliability for the $TPF(\alpha,\lambda)$ distribution. The study is organized as follows: Section 2 presents the maximum likelihood estimation of the $TPF(\alpha,\lambda)$ distribution. In. Section 3, compherensive Monte Carlo simulation study is performed to assess the performance of the maximum likelihood estimates in terms of mean squares error (MSE) and biases.

2. Materials and Methods

In this section, we obtain the maximum likelihood estimator (MLE) of R for the $TPF(\alpha,\lambda)$ distribution.

Let *X* and *Y* independently distributed with $X: TPF(a_1,l_1)$ and $Y: TPF(a_2,l_2)$. The R is obtained as follows:

$$\begin{aligned} R &= \int_0^1 a_2 y^{a_1} y^{a_2-1}\left[1+l_1\left(1-y^{a_1}\right)\right]\left[1+l_2-2l_2 y^{a_2}\right]dy \\ &= (1+l_1+l_2+l_1l_2)a_2\int_0^1 y^{a_1+a_2-1}dy-2(l_2+l_1l_2)a_2\int_0^1 y^{a_1+2a_2-1}dy \\ &\quad -(l_1+l_1l_2)a_2\int_0^1 y^{2a_1+a_2-1}dy+2l_1l_2a_2\int_0^1 y^{2a_1+2a_2-1}dy \\ &= (1+l_1+l_2+2l_1l_2)\frac{a_2}{a_1+a_2}-2(l_2+l_1l_2)\frac{a_2}{a_1+2a_2}-(l_1+l_1l_2)\frac{a_2}{2a_1+a_2} \end{aligned} \tag{4}$$

To obtain the MLE of R, firstly we derive the MLEs the parameters of the $TPF(\alpha,\lambda)$ distribution.

Let $X_1, X_2, \cdots, X_n$ be a random sample from the $TPF(\alpha,\lambda)$ distribution. The log-likelihood function is

$$\ell(\boldsymbol{\theta}) = n\log(\alpha)+(\alpha-1)\sum_{i=1}^{n}\log\left(1+x_i^2\right)+\sum_{i=1}^{n}\log\left(1+\lambda-2\lambda x_i^{\alpha}\right), \tag{5}$$

where $\boldsymbol{\theta}=(\alpha,\lambda)$ is a parameter vector. Then, MLE of $\boldsymbol{\theta}$ is given as follows:

$$\hat{\boldsymbol{\theta}}_{MLE} = \arg\max_{\boldsymbol{\theta}}\left\{\ell(\boldsymbol{\theta})\right\}. \tag{6}$$

The MLE given in (6) can be derived by **optim ()** function in R with BFGS algorithm.

Using the invariance property of the MLE, by substituting the MLE of $\boldsymbol{\theta}$ into Eq. (4), the MLE of R is calculated as follows:

$$\hat{R}_{MLE} = \left(1+\hat{l}_1+\hat{l}_2+2\hat{l}_1\hat{l}_2\right)\frac{\hat{a}_2}{\hat{a}_1+\hat{a}_2}-2\left(\hat{l}_2+\hat{l}_1\hat{l}_2\right)\frac{\hat{a}_2}{\hat{a}_1+2\hat{a}_2}-\left(\hat{l}_1+\hat{l}_1\hat{l}_2\right)\frac{\hat{a}_2}{2\hat{a}_1+\hat{a}_2}. \tag{7}$$

3. Simulation Study

In this section, we perform an extensive Monte Carlo simulation study to evaluate the performances of the MLE of R according to MSE and bias. In the simulation study, we consider the parameter settings as follows:

Case 1: $a_1=0.2, l_1=0.3, a_2=0.4, l_2=0.3$,
Case 2: $a_1=0.3, l_1=0.2, a_2=0.3, l_2=0.4$,
Case 3: $a_1=1, l_1=-0.2, a_2=0.5, l_2=-0.5$.

We employ 5000 trials for sample sizes n=100,200,500,1000. The simulation results are given in Table 1.

Table 1. The bias and MSE values of the R

Case	R	n	$\hat{R}_{MLE}$	bias	MSE
1	0.6176	100	0.6309	0.0133	0.7836
		200	0.6190	0.0014	0.0007
		500	0.6181	0.0004	0.0003
		1000	0.6174	-0.0001	0.0001
2	0.4210	100	0.4191	-0.0018	0.1032
		200	0.4222	0.0012	0.0017
		500	0.4213	0.0003	0.0003
		1000	0.4212	0.0001	0.0001
3	0.3865	100	0.2115	-0.1749	37.9998
		200	0.3864	-0.00007	0.0065
		500	0.3847	-0.0017	0.0002
		1000	0.3846	-0.0019	0.0001

From the Table 1, it is clear that as the sample size increases decreases the bias and MSE as expected. Also, as n increases $\hat{R}_{MLE}$ approaches the R and MSE approaches the zero.

References

[1] Shahzad, M. N., & Asghar, Z. (2016) Transmuted Power Function Distribution: A More Flexible Distribution, Journal of Statistics and Management Systems 19(4), 519-539.

[2] Tanış, C. (2021). On transmuted power function distribution: characterization, risk measures, and estimation. *Journal of New Theory*, (34), 72-81.

[3] Tanış, C., Saraçoğlu, B., Asgharzadeh, A., & Mousa, A. B. D. İ. (2023). Estimation of Pr (X< Y) for Exponential Power Records. *Hacettepe Journal of Mathematics and Statistics*, 1-13.

[4] Agiwal, V. (2023). Bayesian estimation of stress strength reliability from inverse Chen distribution with application on failure time data. *Annals of Data Science*, *10*(2), 317-347.

[5] Karam, N. S., & AbdAwon, H. M. (2023). Stress-Strength Reliability Bayesian of Generalized Exponential-Poisson Distribution for Complete Data. *Mustansiriyah journal of pure and Applied Sciences*, *1*(1), 91-107.

Performance of machine learning-based network slicing methods in 5G and beyond communication

Furkan BALCI[1,*]

[1] *Faculty of Technology, Department of Electrical-Electronics Engineering, Gazi University, Ankara, Türkiye*

Abstract

In recent years, advancements in communication technologies have given rise to needs such as high transmission speed, reliability, and low latency. Improvements in these aspects are crucial in fourth-generation (4G) communication technologies. Following 4G, the Network Slicing method introduced with 5G allows the network infrastructure to be divided to meet different service requirements, enabling flexible and efficient utilization of network resources. The performance of machine learning-based 5G network slicing methods was tested by simulating 3rd Generation Partnership Project (3GPP) compliant error-prone users and base stations. Five different machine learning methods, along with their parameter spaces, were used in tests for network slicing, employing four methods (eMBB, M1oT, V2X, and URLLC). The performance of these classifier models was analyzed using both error-prone user data and ideal user data. The simulation data were used to conduct a performance analysis of machine learning methods mentioned in the literature, investigating their usability. A 96% accuracy rate was achieved using the XGBoost method with error-prone user data, and a 97% accuracy rate was achieved with ideal user data. Additionally, the relationships between the system cycle and user count, as well as the data rate reduction system, were examined in the simulation.

Keywords: *5G and Beyond Communication, Machine Learning, Network Slicing*

1. Introduction

Since ancient times, communication technologies used by humans have continually evolved as a result of increasing user numbers and emerging security needs. Various generational advancements (1G, 2G, 3G, 2.5G, 2.75G, etc.) have been attempted to meet these needs. The fifth-generation (5G) communication currently in use brings with it high expectations and significant opportunities due to the growing diversity of mobile devices, usage variations, and application diversity. The rapid diversification of different application possibilities, the increase in user demands, and the need for various technical requirements have marked a prominent era for 5G technology. Users increasingly demand various service types that align with their growing data needs. With the introduction of 5G, these dynamic demands have necessitated the evolution of existing infrastructure to enable the flexible provision of different services within the same platform and the creation of higher-capacity systems [1]. The high-performance standards set by 5G allow this evolution to manifest its impact across various sectors. For example, advancements such as making autonomous systems smarter and more reliable, enhancing the impact and accessibility of virtual reality experiences, and enabling more efficient operations of smart factories are planned based on the infrastructure and speed advantages provided by 5G. In this context, the opportunities offered by 5G technology not only meet the increasing data demands but also pave the way for significant advancements in various sectors.

In recent years, the increases in communication demands have led communication service providers to develop programmable system solutions in response to the rising technical requirements. The methods of Software-Defined Networking (SDN) and Network Functions Virtualization (NFV) used in fourth-generation (4G) communication systems, along with the solutions developed in this context, have allowed for greater control over the system [1]. The new technologies introduced with 4G have enabled higher performance compared to previous generations [1]. In the transition to 5G, many of these technologies have been retained, and necessary enhancements have been made. The most notable among these enhancements is network slicing technology. The technologies used from 1G to 5G are summarized in Table 1. Network slicing allows the creation of multiple virtual networks within the same physical infrastructure, enabling these networks to provide services to different types of users. This approach aims to utilize systems more effectively and to implement new services in a more

* Corresponding author. *e-mail address: furkanbalci@gazi.edu.tr*

controllable and rapid manner. The controllability targeted by this approach plays a crucial role in the marketability of new services [2].

Since 2014, research on 5G network slicing has been underway. Network slicing technology benefits from the performance of machine learning methods in signal classification. Machine learning methods have been applied in areas such as network slicing reservation and network slice resource status [3]. In their study, Mei et al. focused on autonomous vehicles as different users from mobile communication devices and utilized inter-vehicle communication variables (such as packet delay, packet loss, data rate) [4]. Abidi et al. achieved network slicing with 93% accuracy using neural networks and deep belief networks in a simulation environment designed in accordance with 3GPP standards [5]. In their work, Toscana et al. employed a deep learning model to classify data into temporal and time-independent categories, achieving feedback-based network slicing with 75% accuracy [6]. Sun et al. rearrange unused network portions using a deep reinforcement learning model, thus reserving unused network portions for more efficient network management [7]. Thantharate et al., in their study, simulated 65,000 different users using machine learning methods in compliance with 3GPP rules, achieving a 95% accuracy in classifying network slices [8].

Table 1. Characteristics of Communication Systems Generations

	1G	2G	3G	4G	5G
Time	1980's	1990's	2000's	2010's	2020's
Technology	FDMA	CDMA TDMA	CDMA FDMA TDMA	OFDMA MIMO SDN NFV	OFDMA mMIMO Network Slicing
Download Speed	2.4 kbits/s	64 kbits/s	2 Mbits/s	1 Gbits/s	10 Gbits/s
Latency	-	500 ms	100 ms	50 ms	<1ms

In this study, the performance of machine learning methods on 5G network slicing classification was analyzed in detail by simulating realistic 3GPP-compliant error-prone users and base stations for 5G communication technologies. The association of users and base stations was established to ensure healthy communication without service disruption. For the smooth continuation of this binary association, accurate classification of network slices is crucial. To address the common issue of base station capacity problems, a data rate management mechanism was developed within the simulation architecture. Representing the mobile communication network, the simulation environment facilitated the realization of handovers between base stations and the internal handover processes within base stations, primarily due to changes in user-to-base station connections. Thus, alongside network slices, the simulation environment incorporated data rate management and user handover mechanisms.

In this study, Section 2 provides information about the simulation environment and the general workflow created. Section 3 offers a detailed interpretation of the performance analyses of machine learning methods on the simulation and the results obtained. Section 4 encompasses the conclusions and discussions.

2. Generation of Simulation Environment and Synthetic Data

In this study, a simulation has been conducted using 3GPP documents to create a scenario suitable for 5G communication, involving users and base stations. With this simulation, a scenario has been established where users communicate using 5G communication technology over 5 base stations placed in a 1 km² area. The simulation, conducted in two different scenarios, utilized error-prone environment and ideal environment scenarios.

The data presented in this study has been obtained from a synthetic simulation. User and base station parameters conforming to 3GPP documents with different configurations have been identified. In this simulation, parameters such as the position of users, users' movement speeds, source type, packet delay, packet loss, and data rate are utilized. The network slices designated for 5G communication in the simulation are considered as advanced versions of existing mobile services, including Enhanced Mobile Broadband (eMBB), which focuses on 5G communication, Ultra-Reliable Low Latency Communications (URLLC), which emphasizes packet delay and packet loss, Massive Internet of Things (MIoT), supporting communication with a high number of devices, and Vehicle-to-Everything (V2X), supporting communication technology from vehicles to other devices.

In creating the simulation environment, both lower and upper bounds specified in 3GPP documents are utilized. To ensure equal data distribution across all classes, the number of data instances in each class has been equalized. Some examples of synthetic data obtained from the simulation environment are shared in Table 2.

Table 2. Characteristics of Communication Systems Generations

Type	Network Slice	Source Type	Packet Delay	Packet Loss	Data Rate (byte)	Movement Speed (m/s)
File sharing	eMBB	Non-GBR	245.52	3.2e-02	180674	1.95
Smart home/car	MIoT	GBR	203.83	3.4e-04	286	1.67
Healthcare	URLLC	DC-GBR	1.16	6.2e-07	367	1.45
Autodriving	V2X	GBR	61.25	6.7e-06	215378	63.74
AR/VR/Gaming	eMBB	Non-GBR	15.25	2.1e-04	2758967	0.06
Sensor Notification	V2X	GBR	21.67	9e-05	89547	0.85
Electric Distribution	URLLC	GBR	53.84	5.3e-06	567	0.02

One of the first parameters to be determined for the simulation environment is the type (macro, micro) and location of base stations. When determining the positions of base stations, care has been taken to ensure that they do not overlap in coverage areas within the simulation field. A total of 6 base stations have been positioned, with 3 being macro and 3 being micro base stations.

For the created simulation environment, the use of the correct network slice alone is not the sole objective. To obtain more realistic results, it is also crucial that users do not experience service interruptions against changing channel parameters while in motion. In the simulation environment, the user-base station relationship is initially established, utilizing channel parameters. Subsequently, a classifier for the network slice to be placed in the simulation is integrated. For users placed in the appropriate network slice, a data rate management mechanism based on the XGBoost model comes into play to address the issue of capacity reduction at the base station. Since user movements are considered as a parameter, a handover mechanism is implemented for possible user handover processes.

To associate users and base stations, path loss (PL) and shadow loss (SL) parameters are employed. To enhance the realism of the simulation environment, non-line-of-sight (NLOS) and three-dimensional distance calculations are used. Equation 1 shares the formula for this distance calculation, where hB represents the base station height, hU represents the user height, and x-y denotes the coordinates of the user and base station.

$$d_{3D} = \sqrt{(h_k - h_B)^2 + (x_k - x_B)^2 + (y_k - y_B)^2} \quad (1)$$

Using the distances obtained in Equation 1, path loss (PL) calculations can be performed for both macro and micro base stations. In Equation 2, path loss calculations for macro (PLUMa) and micro (PLUMi) base stations are provided. Here, the carrier frequency (fc) is chosen as 3.5GHz.

$$PL_{UMa} = 10^{(32.4+20log_{10}f_c+30log_{10}(d_{3D}))/10}$$
$$PL_{UMi} = 10^{(32.4+20log_{10}f_c+31.9log_{10}(d_{3D}))/10} \quad (2)$$

Using the path loss (PL) obtained in Equation 2, shadow loss (SL) calculations are demonstrated in Equation 3.

$$G(x) = \frac{1}{\sqrt{2\pi\sigma^2}} exp\, \frac{\pi^2}{2\sigma^2}$$
$$R(x) = \|G(x)G(x)\|$$
$$P(x) = \frac{R(x)}{PL.SL} \quad (3)$$

Using P(x), assignments of residual users to base stations can be carried out. In this process, base stations determine and allocate users based on which one has the stronger channel parameters. Users falling below the threshold value set in base stations cannot receive service.

To enhance the realism of the simulation environment, support is provided through auxiliary control mechanisms. These mechanisms include the data rate management system and the user handover system. The data rate management system typically comes into play when establishing a new relationship between users and a base

station or when the capacity of a base station falls below a threshold. Since usage types consist of categorical data, the Extreme Gradient Boost model (XGBoost) will be utilized here. This will extend the period during which the base station provides high-quality service. As for the user handover system, a simple handover system operates based on the threshold defined according to the calculated channel parameters, facilitating user handovers as needed to maintain service quality.

3. Simulation Results

In the scope of this study, a 5G communication environment simulation has been conducted for a 1 km² area in accordance with the 3GPP documents. Six base stations and 300 users are positioned as depicted in Figure 1. The fundamental characteristics of the employed base stations are provided in Table 3.

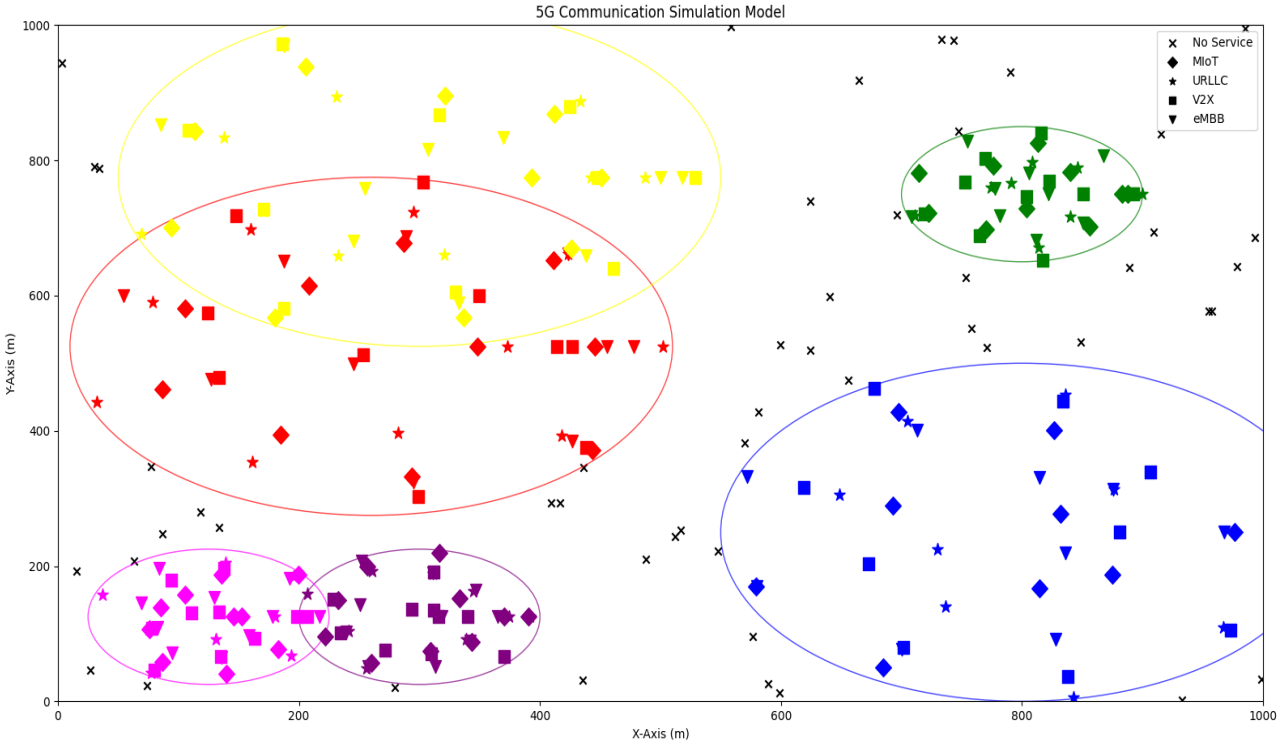

Figure 1. The users and base stations in the simulation environment.

Table 3. The data of the base stations in the simulation environment.

Type	Storage	Position	Diameter	Length
Macro	5e7 byte	(260,525)	250 m	30 m
Macro	5e7 byte	(800,250)	250 m	30 m
Macro	5e7 byte	(300,775)	250 m	30 m
Micro	1e7 byte	(800,750)	100 m	10 m
Micro	1e7 byte	(800,250)	100 m	10 m
Micro	1e7 byte	(125,125)	100 m	10 m

Data was collected from users in two different scenarios based on this configuration. The first set of data consists of communication data generated in an ideal environment, while the second scenario involves data with user error margins. Machine learning methods were retested for the two simulation environments. Precision, recall, and F1-score metrics were used for the performance analysis of the models. Weighted average, considering the number of examples for each class, and macro-average, not considering the number of examples, were employed when calculating these metrics.

Fundamental machine learning methods commonly encountered in the literature were utilized. These methods include artificial neural networks, k-nearest neighbors, support vector machines, and random forests. In the initial testing phase, simulation data without error margins was used. User data without error margins conforms to the limits specified in the 3GPP documents. Table 4 provides information about the parameter space used and the parameters with the highest accuracy.

Table 4. Machine learning algorithms parameter space.

Algorihm	Parameter	Parameter Space	Selected Parameter
kNN	k	3, 5, 7, 9, 11, 13, 15	11
	Weights	uniform, distance	uniform
	Metric	euclidean, Manhattan	manhattan
	p	2, 3	2
MLP	Hidden Layer	1, 2, 3, 4, 5	3
	Neuron (Hidden)	100, 150, 200, 250, 300	200
	Activation Function (Hidden)	ReLU, Sigmoid, Tanh	Sigmoid
	Activation Function (Output)	Softmax, Sigmoid, Linear	Softmax
	Learning Rate	0.0001, 0.001, 0.01	0.001
	Epochs	50, 100, 150	100
	Dropout Rate	0.2, 0.5, 0.7	0.2
RF	Number of Trees	50	
	Tree Depth	None, 10, 20, 30	20
XGBoost	Number of Trees	50, 100, 200	100
	Maximum Depth	3, 6, 9	9
	Learning Rate	0.01, 0.1, 0.3	0.01
	Subsample	0.8, 0.9, 1.0	0.9
	L1	0, 0.1, 1.0	0.1
	L2	0, 0.1, 1.0	0.1
SVM	Kernel	Linear, Poly, RBF, Sigmoid	Poly
	Degree of Poly	2, 3, 4	4

In tests conducted with user data without error margins, where the training data and test data exhibit similarity, the metric results generally show high performance. The results of the performance metrics for the models are shared in Table 5. The XGBoost algorithm achieved the highest performance.

Table 5. Results of data without error margins.

	Weighted Average			Macro Average		
	Sensitivity	Precision	F1-Score	Sensitivity	Precision	F1-Score
kNN	97%	97%	97%	97%	97%	97%
MLP	95%	96%	95%	95%	96%	96%
RF	94%	94%	94%	94%	94%	94%
XGBoost	98%	98%	98%	98%	97%	98%
SVM	89%	89%	89%	89%	89%	89%

Error amounts in data with error margins were calculated by taking the average of error rates mentioned in the literature. These error margins were determined as 7% for delay-critical users and 25% for non-delay-critical users. These error rates were randomly added to the test portions of the user data obtained from the simulation. User data with error margins conforms to the limits specified in the 3GPP documents.

In tests conducted with user data containing error margins, where there is a difference between training data and test data due to the added error margins, the metric results generally show high performance compared to the tests without error margins. The results of the performance metrics for the models are shared in Table 6. The XGBoost algorithm achieved the highest performance.

Table 6. Results of data containing error margins.

	Weighted Average			Macro Average		
	Sensitivity	Precision	F1-Score	Sensitivity	Precision	F1-Score
kNN	96%	96%	96%	96%	96%	96%
MLP	93%	94%	94%	93%	94%	94%
RF	92%	93%	93%	92%	93%	93%
XGBoost	97%	97%	97%	97%	97%	97%
SVM	85%	84%	85%	85%	84%	85%

When examining both tables, it is observed that XGBoost methods adapt best to this simulation, while SVM method classifies with the worst performance. The cyclic system and data rate reduction system in the simulation

also work in conjunction with the network language classifier. Parameters such as user turnover rate, data rate reduction rate, and total user connection rate are associated with the increase in the number of users. With the increase in the number of users, the data rate reduction rate is directly proportional, while the user turnover rate and data rate reduction rate show an inversely proportional change.

4. Conclusion and Discussions

In this study, a simulation environment designed based on 3GPP resources aims to classify network slicing. Various ML models have been employed in the simulation, which includes users and base stations, to place users in the most suitable network slice. The performance of these models is compared to select the most suitable one. The simulation environment is designed to resemble a real environment, so not only the network slicing architecture but also architectures like user handover and data rate regulation have been added. In the combination of these seemingly complex structures, the data rate reduction architecture and the network slicing architecture use the same training dataset. These data feed the ML models. The XGBoost model is used in the data rate reduction architecture to classify usage types. This allows customization and optimization of communication networks for specific usage types. The RF model, by detecting intensive video streams or inter-object communication, can manage network resources more efficiently. In the network slicing mechanism, the integration of various ML models aims to classify based on the majority decision of these models. These ML models are designed to classify network traffic in a more detailed and accurate way. Diversifying the selected models is important to focus on different features and understand the strengths of each. Classifying decisions based on the majority principle of the models will be crucial for stability and reliability in the system. The integration of these two mechanisms can make communication networks more flexible and scalable, responding more quickly and effectively to user demands. Additionally, the performance comparison of ML models will play a critical role in understanding the advantages and limitations of each model and creating a roadmap for future improvements. Network slicing classification in 5G technology is realized in two different scenarios: an ideal environment and a user error-prone environment. Precision, sensitivity, and F1-score metrics are used when analyzing the performance of ML models. Examining these metrics, it is observed that simulations involving error lead to a performance decrease for some models and an increase for others.

In conclusion, in future studies, developing a mechanism that can predict the required capacity for a specific network slice within a certain time frame using past user data is considered. This predictive mechanism can make simulation studies smoother and more efficient. In these future studies, using memory-based Machine Learning (ML) models and making accurate predictions will be crucial. These models, fed with past user data, can more accurately predict future capacity needs.

References

[1] Matias, J., Garay, J., Toledo, N., Unzilla, J., & Jacob, E. (2015). Toward an SDN-enable NFV architecture. *IEEE Communications Magazine*, 53(4):187-193.

[2] Gawas., A. U. (2021). An overview on evolution of mobile wireless communication network:1G-6G. *International Journal on Recent and Innovation Trends in Computing and Communication*, 3(5):3130-3133.

[3] Borcoci, E., Dragulinescu, A., Li, F., Vochin, M. C., & Kjellstadli, K. (2021). An overview of 5G slicing operational business models for internet of vehicles, maritime IoT applications and connectivity solutions. *IEEE Access.*

[4] Myung, H., Lim, J., & Goodman, D. (2006). Single carrier FDMA for uplink wireless transmission. *IEEE vehicular technology magazine, 1(3):30-38.*

[5] Nelson, R., & Kleinrock, L. (1985). Spatial TDMA: A collision-free multihop channel access protocol. *IEEE Transactions on communications*, 33(9):934–944.

[6] Foukas, X., Patounas, G., Elmokashfi, A., & Marina, M. (2017). Network slicing in 5G: Survey and challenges. *IEEE communications magazine*, 55(5):94–100.

[7] Lucena, J., Ameigeiras, P., Lopez, D., Ramos-Munoz, J., Lorca, J., & Folgueira, J. (2017) Network slicing for 5G with SDN/NFV: Concepts, architectures, and challenges. *IEEE Communications Magazine*, 55(5):80–87.

[8] Abidi, M. H., Alkhalefah, H., Moiduddin, K., Alazab, M., Mohammed, M. K., Ameen, W., & Gadekallu, T. R. (2021). Optimal 5G network slicing using machine learning and deep learning concepts. *Computer Standards & Interfaces*, 76:103518.

The correlation between uremic toxins with CRP level in patients with chronic kidney disease

Zainab ABDULKAREEM AHMED [1], ***Volkan EYUPOGLU*** [2*]

[1] *Graduate School of Natural and Applied Sciences, Chemistry, Çankırı Karatekin University, Çankırı, Turkey*

[2] *Graduate School of Natural and Applied Sciences, Chemistry, Çankırı Karatekin University, Çankırı, Turkey*

Abstract

The kidneys play an important role in fluid control as well as the removal of harmful waste products which known as (uremic toxins). Our study was focused on the measurement the concentrations of some uremic toxins which accumulates in the blood of the patients with chronic kidney disease. The concentration of blood urea, serum creatinine and protein bound uremic toxin (indoxyl sulfate) were measured and the results is compared with results of samples taken from healthy people (control group). Then, correlation between uremic toxins with CRP was studied. The results showed that the levels of uremic toxins were significantly higher ($P < 0.05$) in patients' group than in healthy group. The results were respectively (132.49± 32.59), (5.72± 1.57) and (1.432 ± 0.392). Also, the mean of CRP was measured and the findings showed, the CRP concentration was significantly higher ($P < 0.05$) in patients (15.32 ± 6.48) compared to the control group (1.02 ± 0.48). The correlation between uremic toxins and CRP also determined, there were positive correlation between each of blood urea, serum creatinine and indoxyl sulfate concentration with CRP.

Keywords: *uremic toxins, CRP, chronic kidney disease*

1. Introduction

The kidneys play an important role in fluid control as well as the removal of harmful waste products which known as (uremic toxins) [1]. Chronic kidney disease (CKD) is defined as defective kidney structure or function that lasts more than three months and has health consequences [2]. Chronic kidney disease (CKD) is one of the worldwide public health problems. Kidney disease, which develops when kidneys damaged for various reasons become untreatable, results in the loss of nephrons, renal dysfunction or structural damage to the kidneys [3]. In the developing world, the exact number of people with chronic renal failure who require renal replacement treatment (RRT) is unknown. In contrast to the developed world, the majority of underdeveloped countries lack kidney registries [4]. In the United States, approximately one in three adults aged 65 years or older has chronic kidney disease (CKD), which is defined as a glomerular filtration rate (eGFR) of less than 60 mL/min/1.73 m2. Most patients with CKD do not progress to advanced stages of the disease because death precedes progression to end-stage renal disease (ESRD) [5]. The retention of many solutes ordinarily discharged by healthy kidneys causes uremic syndrome. Although hemodialysis can relieve many of these anomalies, it should be noted that dialysis can exacerbate or even worsen some uremic consequences [6]. Uremic toxins are defined as organic or inorganic substances, that accumulate in the body fluids of patient with acute or chronic kidney disease and impaired kidney function. They collectively contribute to the diverse clinical manifestations of the uremic syndrome [7]. The uremic syndrome is characterized by the retention of many solutes that would normally be released by the kidneys, but in case of kidney failure these substances or solutes (uremic toxins) are accumulated and interfered with biological activity [8]**.** In case of advanced CKD and kidney failure, dialysis can remove tiny water-soluble uremic toxins but not intermediate molecules or protein-bound uremic toxins. Hemodialytic removal of protein-bound chemicals, such as indoxyl sulfate (IS) is difficult due to their high protein-binding properties [9]. Hemodialysis (HD) is the conventional procedure used worldwide to remove metabolic wastes. The creatinine and urea levels have been routinely monitored to estimate

* Corresponding author. *e-mail address: volkan@karatekin.edu.tr*

kidney function and effectiveness of the HD process [10]. Because of IS capacity to attach to proteins, forming large molecular weight its elimination by hemodialysis is less efficient than that of non-protein bound uremic toxins [11]. IS, based on its physiological concentration in serum, has been demonstrated to have antioxidant effects, balancing oxidative stress in CKD. In patients with CKD and end-stage renal disease (ESRD), increased IS buildup contributes significantly to CV risk. IS significantly enhances superoxide production in endothelial cells while attenuating vasorelaxation mediated by sodium nitroprusside via the AhR and NOX activation [12]. On the other hand, the CKD group had a significantly elevated median serum level of hsCRP in comparison to the control group without CKD. In 20-65% of ESRD patients (pre-dialysis, hemodialysis, and peritoneal dialysis), serum CRP levels are elevated. The increase in blood CRP and other acute-phase proteins is caused by underlying factors that cause acute phase responses and the activation of the inflammatory cascade [13]. The findings of some studies in this regard, indicated that the inflammatory process in chronic kidney disease (CKD) begins prior to dialysis and is not only caused by dialysis, as the CKD patients in the study had not yet undergone dialysis treatment. There was a strong positive association seen between CRP and serum creatinine, as well as a negative correlation with estimated GFR. This study identified that Estimated Glomerular Filtration Rate (GFR) was a significant predictor of C-reactive protein (CRP) levels in kidney failure [14]. This study demonstrated a positive correlation between decreased renal function and inflammation, as indicated by elevated CRP levels, in patients with chronic kidney disease.

2. Materials & methods

2.1 Sampling

Our study was performed on two groups of participants, the patients' group was composed of 100 patients with kidney failure. The ages of the patients ranged from 13-79 years and they were treated with dialysis in Kirkuk General Hospital. The study also included measurement of the aimed parameters of samples taken from control group which consist of 50 healthy individuals who haven't any disease, with the same demographic properties, in order to compare the results. Each participant in this study had five milliliters of blood drawn from a vein without the use of a tourniquet. The blood sample was placed into sterile test tubes. After coagulation, the samples were placed into the centrifuge and spun at 3000 rpm for 15 minutes until the serum could be extracted. The biochemical measurements of blood urea, serum creatinine, indoxyl sulfate and CRP were performed.

2.2. Estimation of Kidney Function Tests

The concentration of serum creatinine and blood urea were measured by using a commercially available assay kits from (AGAPPE, Switzerland).

2.3. Indoxyl Sulfate Assay

The sandwich enzyme-linked immune-sorbent assay technology was used in this kit. 96-well plates were pre-coated with capture antibody. As detecting antibodies, biotin conjugated antibodies were utilized. Following that, the standards, test samples, and biotin conjugated detection antibody were added to the wells and rinsed with wash buffer. HRP-Streptavidin was used. Wash buffer was used to remove added and unbound conjugates. HRP enzymatic activity was visualized using TMB substrates. reaction. TMB was catalyzed by HRP to create a blue product that became yellow after the addition of an acidic stop solution. The yellow density is related to the amount of sample collected in the plate. In a laboratory, measure the O.D. absorbance at 450 nm. The concentration of the target parameter can then be estimated using a microplate reader.

2.4. CRP

C-reactive Q is a quantitative turbidimetric test used for the measurement of C-reactive protein (CRP) concentration in human serum or plasma. Latex particle in the reagent coated with specific anti-human CRP agglutinates with samples containing CRP when mixed together. An absorbance change happens due to the agglutination, and this

absorbance is dependent upon the CRP concentration of the patient sample that can be measured by comparison from a calibrator of known CRP concentration.

2.5. Statistical Analysis

The data was statistically analyzed using Minitab, a statistical analysis software, and Excel, a computer for making spreadsheets. The data were presented as mean and standard deviation. The current study used statistical analysis tools, specifically the Dunkin' multiple test and the ANOVA test, to compare the arithmetic means of the experimental groups to look for potential significant changes.

3. Results & Discussion

The levels of uremic toxins were significantly higher in patients with CKD than in the control group, as shown in the Table 3.1

Table 1. Levels of uremic toxins

Uremic toxins	Patints group	Control group	P.value
Urea	132.49± 32.59	31.58± 12.86	P<0.05
Creatinine	5.72± 1.57	1.06 ± 0.29	P<0.05
Indoxyl sulfare	1.432 ± 0.392	0.842 ±0.075	0.0001

The urea levels in these patients (132.49± 32.59) were significantly higher (P<0.05) compared to the control group (31.58± 12.86), also the creatinine levels in the patients (5.72± 1.57) were significantly elevated (P<0.05) compared to the control group (1.06 ± 0.29). our findings also showed that, the indoxyl-sulfate concentration was found to be significantly higher (P <0.05) in patients (1.432 ± 0.392) compared to the control group (0.842 ±0.075). Increased levels of blood urea and serum creatinine are widely recognized as reliable markers of compromised kidney function in individuals with chronic kidney disease (CKD), and there is widespread agreement among medical professionals regarding their significance in evaluating renal health. The metrics mentioned are commonly employed to assess kidney function in persons with diabetes and hypertension who are at a higher risk of developing chronic kidney disease [15]. The renal excretion, tubular secretion, and breakdown of creatinine are reduced in patients with chronic kidney disease (CKD), leading to an increase in creatinine levels. Furthermore, consumption of meat and protein supplements results in elevated levels of serum creatinine. Another factor contributing to elevated levels of creatinine is the use of drugs that impede the release of creatinine in the renal tubules and reduce the breakdown of creatinine by the gastrointestinal tract [16], [17]. Indoxyl-sulfate is produced in healthy individuals by the degradation of tryptophan by the microbiota residing in the colon. It is then removed by the kidneys and discharged in the urine. Hemodialysis effectively eliminates a significant number of uremic toxins from the bloodstream. Nevertheless, IS, due to its strong protein affinity, cannot be eliminated through the utilization of this approach [18]. The toxicity of IS can arise from its interaction with proteins [19].

3.1. CRP

The CRP concentration was significantly higher (P <0.05) in patients (15.32 ± 6.48) compared to the control group (1.02 ± 0.48). The study was carried out on a group of 100 individuals with chronic kidney disease (CKD) to investigate the importance of C-reactive protein in this condition. There was a strong positive association seen between CRP and CKD. In addition, CRP has a negative correlation with the estimated GFR. This study identified that Estimated Glomerular Filtration Rate (GFR) was a significant predictor of C-reactive protein (CRP) levels in

CKD [14]. This study demonstrated a positive correlation between decreased renal function and inflammation, as indicated by elevated CRP levels, in patients with chronic kidney disease (CKD).

3.2. The correlation between uremic toxins and CRP

The results of our study also showed that, CRP level is significantly correlated with each one of the measured uremin toxin concentrations. There were positive correlation between CRP levels with urea, creatinine and indoxyle sulfate, the r value of each correlation were 0.6748, 0.756 and 0.718 respectively (Figure1, Figure2, and Figure 3).

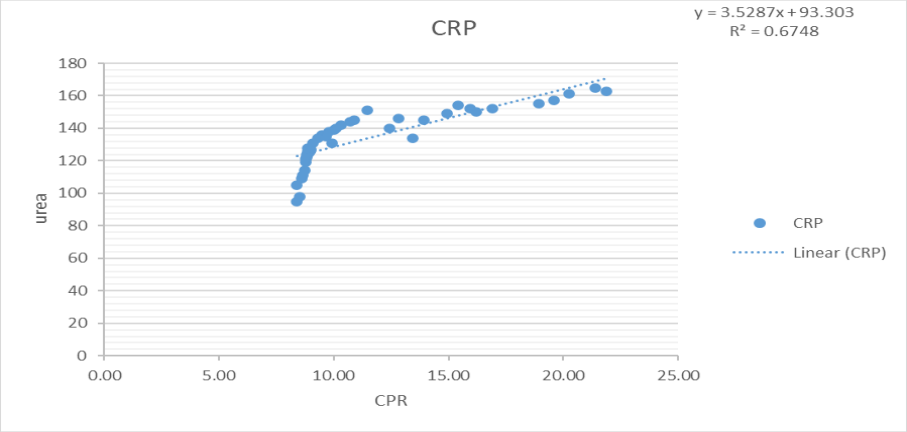

Figure 1. the correlation between CRP level and urea concentrations

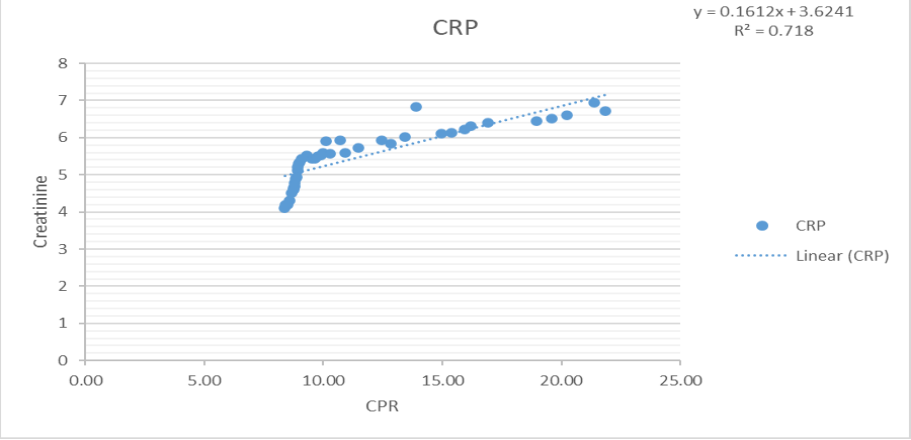

Figure 2. the correlation between CRP level and creatinine concentrations

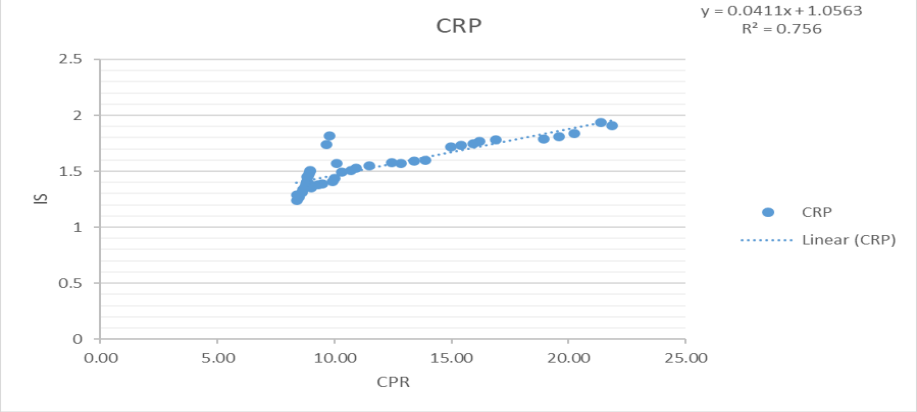

Figure 3. the correlation between CRP level and indoxyl sulfate concentrations

4. Conclusion

Chronic kidney failure is strongly associated with the levels of creatinine and urea, which are regarded as the initial laboratory tests for assessing renal function. Chronic renal failure leads to changes in the levels of indoxyl-sulfate, which can be regarded as an indicator of kidney failure based on the findings of the present investigation. The recent investigation revealed that chronic renal failure leads to elevated levels of inflammatory markers such as CRP. In addition, we can conclude from the results of this research, that high uremic toxins concentration leads to inflammatory reactions.

References

[1] Evans M. Prognosis and progression in chronic kidney disease. Institutionen för klinisk vetenskap/Department of Clinical Sciences; 2010 Sep 17.

[2] Gaitonde DY, Cook DL, Rivera IM, Eisenhower DD. Chronic Kidney Disease: Detection and Evaluation [Internet]. Vol. 96. 2017. Available from: www.aafp.org/afp.

[3] Yildirim N, O. 70 YAŞ VE ÜZERİNDEKİ KRONİK BÖBREK HASTALARINDA FİBROBLAST GROWTH FAKTÖR-23 VE β-2 MİKROGLOBÜLİN DÜZEYİNİN ÖLÇÜLMESİ VE YAŞAM KALİTELERİNİN DEĞERLENDİRİLMESİ. 2020.

[4] Kher V. End-stage renal disease in developing countries. Kidney Int. 2002;62(1):350–62.

[5] Dalrymple LS, Katz R, Kestenbaum B, Shlipak MG, Sarnak MJ, Stehman-Breen C, et al. Chronic kidney disease and the risk of end-stage renal disease versus death. J Gen Intern Med. 2011 Apr;26(4):379–85.

[6] Himmelfarb, J. (2005). Hemodialysis complications. American journal of kidney diseases, 45(6), 1122-1131.

[7] Richard J. Glassock, Shaul G. Massry, Chapter 6 - Uremic toxins: an integrated overview of classification and pathobiology, Editor(s): Joel D. Kopple, Shaul G. Massry, Kamyar Kalantar-Zadeh, Denis Fouque, Nutritional Management of Renal Disease (Fourth Edition), Academic Press, 2022.

[8] Duranton F, Cohen G, De Smet R, Rodriguez M, Jankowski J, Vanholder R, Argiles A, European Uremic Toxin Work Group. Normal and pathologic concentrations of uremic toxins. Journal of the American Society of Nephrology: JASN. 2012 Jul;23(7):1258.

[9] Lin YT, Wu PH, Tsai YC, Hsu YL, Wang HY, Kuo MC, et al. Indoxyl sulfate induces apoptosis through oxidative stress and mitogen-activated protein kinase signaling pathway inhibition in human astrocytes. J Clin Med. 2019;8(2).

[10] Ragi, N., Pallerla, P., Babi Reddy Gari, A. R., Lingampelly, S. S., Ketavarapu, V., Addipilli, R., ... & Sripadi, P. (2023). Assessment of uremic toxins in advanced chronic kidney disease patients on maintenance hemodialysis by LC-ESI-MS/MS. Metabolomics, 19(3), 14.

[11] Niwa T. Role of Indoxyl Sulfate in the Progression of Chronic Kidney Disease and Cardiovascular Disease: Experimental and Clinical Effects of Oral Sorbent AST-120. Therapeutic Apheresis and Dialysis. 2011 Apr;15(2):120–4.

[12] Lu, C. L., Zheng, C. M., Lu, K. C., Liao, M. T., Wu, K. L., & Ma, M. C. (2021). Indoxyl-sulfate-induced redox imbalance in chronic kidney disease. Antioxidants, 10(6). https://doi.org/10.3390/antiox10060936

[13] Razeghi, E., Parkhideh, S., Ahmadi, F., & Khashayar, P. (2008). Serum CRP levels in pre-dialysis patients. Renal Failure, 30(2), 193–198. https://doi.org/10.1080/08860220701810539

[14] Pravin B, Tushar D, Vijay P, Kishanchnad K. Review on Citrullus colocynthis. Int. J. Res. Pharm. Chem. 2013;3(1):46-53.

[15] Al-Obaidy F, Yazdani F, Mohammadi FA. Intelligent testing for Arduino UNO based on thermal image. Computers & Electrical Engineering. 2017 Feb 1;58:88-100.

[16] Pandya D, Nagrajappa AK, Ravi KS. Assessment and correlation of urea and creatinine levels in saliva and serum of patients with chronic kidney disease, diabetes and hypertension–a research study. Journal of clinical and diagnostic research: JCDR. 2016 Oct;10(10):ZC58.

[17] Webster AC, Nagler EV, Morton RL, Masson P. Chronic kidney disease. The lancet. 2017 Mar 25;389(10075):1238-52.

[18] Itoh, Y.; Ezawa, A.; Kikuchi, K.; Tsuruta, Y.; Niwa, T. Protein-bound uremic toxins in hemodialysis patients measured by liquid chromatography/tandem mass spectrometry and their effects on endothelial ROS production. Anal. Bioanal. Chem. 2012, 403, 1841–1850.
[19] Saldanha, J.F.; Yi, D.; Stockler-Pinto, M.B.; Soula, H.A.; Chambert, S.; Fouque, D.; Mafra, D.; Soulage, C.O. Determination of the binding properties of the uremic toxin phenylacetic acid to human serum albumin. Biochimie 2016, 125, 53–58.

Exploring Extracts as Lipase Inhibitors In Vitro: A Promising Approach for Obesity Management

Zeyad Adil Hameed HAMEED [1,*], ***Bedriye Seda KURŞUN AKTAR*** [2], ***Şevki ADIM*** [3], ***Zainab Falih ALKHAZAALI*** [4(A,B)]

[1] *Department of Chemistry Sciences, School of Natural and Applied Sciences, Çankiri Karatekin University, Iraq*

[2] *Department of Hair Care and Beauty Services, Yeşilyurt Vocational School, Malatya Turgut Özal University, Malatya, Turkey*

[3] *Department of Chemistry Sciences, School of Natural and Applied Sciences, Çankiri Karatekin University, Turkey*

[4 A] *Department of Chemistry Sciences, School of Natural and Applied Sciences, Çankiri Karatekin University, Iraq.*

[B] *Ibn Sina University for Medical and Pharmaceutical Sciences*

Abstract

In this study, three compounds, namely 5b, 5f, and 5g, were investigated for their potential to inhibit lipase enzyme activity. The motivation behind this research stems from the increasing prevalence of obesity due to sedentary lifestyles and the consumption of high-fat and high-sugar processed foods. Obesity is associated with various health risks, and inhibiting lipase activity is considered a potential approach for managing this condition. The results indicate that all three compounds, 5b, 5f, and 5g, demonstrated a reduction in lipase enzyme activity. The concentration-dependent inhibition is clearly illustrated in the graphical representations (Figures 1, 3, and 5). These findings suggest that these compounds have the potential to be utilized in the treatment of diseases linked to lipase enzyme activity, such as obesity. The 2D interaction maps (Figures 2, 4, and 6) provide insight into the specific amino acid interactions between each compound and the lipase enzyme. Notably, hydrogen bond interactions with amino acids like GLY 76, ARG 256, PHE 77, HIS 151, and SER 152 were identified, emphasizing their role in the inhibitory process. Additionally, the red separation contacts in the interaction maps suggest that the active site of the enzyme is no longer occupied by water molecules, leading to a change in enzyme shape and the cessation of catalytic reactions. The results of this study support the potential therapeutic use of compounds 5b, 5f, and 5g in treating conditions associated with elevated lipase activity, such as obesity. Further research, including in vivo studies and clinical trials, would be necessary to validate these findings and assess the safety and efficacy of these compounds as potential anti-obesity agents.

Keywords: *Lipase, Inhibition, Obesity*

1. Introduction

Our lifestyle has become more sedentary as a result of industrialization, urbanisation, and modernity. More and more of the food we eat every day is processed, fast food, which is heavy in fat and sugar for energy. Because of these shifts, the number of people classified as overweight or obese has almost quadrupled since 1975 [1]. An imbalance between caloric intake and expenditure is the primary cause of obesity, a complex and multifaceted condition. In addition to diabetes [2,3], cardiovascular illnesses [4,5], and certain malignancies [6], obesity increases the risk of additional significant diseases. Medications for obesity such as orlistat, phentermine/topiramate, naltrexone/bupropion, and liraglutide are now authorised by the FDA [7,8]. Among these medications, orlistat is unique in that it inhibits the action of human pancreatic lipase (HPL), an enzyme involved in the hydrolysis of triglycerides during fat digestion and absorption [9]. Flatulence, steatorrhea, nephrotoxicity, kidney stones, and pancreatitis are some of the unpleasant and unfavourable side effects of orlistat [7]. There have been zero new medicines approved using this technique since orlistat. There has been a lot of interest in finding drugs that block HPL as a means to restrict the digestion and absorption of dietary fats, which might lead to weight loss. The X-ray diffraction analysis of HPL (PDB ID: 1LPB) crystal structure was verified. The N and C regions of HPL, which are glycoproteins linked to colipases, include the amino acid residues 1–335 and 336–449, respectively [10,11]. Residues 247–258 in the N region form the active site, which includes the catalytic trial Ser152–Asp176–His263 (Figure 1). A disulfide bridge formed by residues Cys237 and Cys261 forms the surface loop that is the lid domain. The primary surface for colipase binding is located in the C region, which features a double-ring shape. Additionally, from amino acids 76 to 85, there are two hair-loop coils, and from amino acids

* Corresponding author. *e-mail address: .zeyad95adil@gmail.com*

204 to 224, there is a β9-loop [10]. There are two possible states for an HPL structure: closed and open. When the enzyme is in its open form, the catalytic site is opened when the lid domain interacts via van der Waals contact with the β5-loop and β9-loop coils [12,13]. As a lipase inhibitor, a C11 alkyl phosphonate (MUP) was co-crystallized at the HPL active site [12]. Orlistat, which was authorised by the FDA, forms a covalent connection with the lipase active site in the digestive tract lumen, making it an irreversible inhibitor of pancreatic and gastric lipase [14,15].

2. Materials and Methods

To determine if chemicals or substances inhibit lipase activity in vitro, the lipase enzyme inhibition test is a typical tool for the lab. Enzyme lipase catalyses the hydrolysis of triglyceride ester linkages, resulting in free fatty acids and glycerol. Treatments for diseases like obesity may benefit greatly by inhibiting lipase activity. A stock solution of the product or chemical to be evaluated for lipase inhibition is prepared by dissolving it in 1 mg/mL of dimethyl sulfoxide. A variety of concentrations for the test are obtained by diluting the stock solution. Recombinant enzymes, such as human pancreatic lipase, are a source of lipase. Lipase is isolated or purified using appropriate procedures to produce the enzyme source. It is common practice to freeze the enzyme and then defrost it before to the experiment. To ensure the lipase enzyme is active in the best possible environment, a buffer system is set up. The pH of the buffer is 8.0 and it comprises Tris-HCl and NaCl. It is common practice to evaluate lipase activity using a particular substrate, such 4-Nitrophenyl decanoate. Once the substrate is dissolved in the assay buffer to the correct concentration, it is ready to use. The test sample, D.W., substrate, buffer, and lipase enzyme are all combined to make the reaction mixture. Optimising the final enzyme and substrate concentration is important. Complete inhibition of lipase enzyme activity is shown by the positive control, whereas maximal enzyme activity without any inhibitory impact is represented by the negative control. To ensure the accuracy of the data, the assay incorporates these controls. To initiate the enzyme-substrate reaction, the reaction mixture is incubated at a controlled temperature, usually 37°C, for a predetermined duration. Optimal incubation times could vary from experiment to experiment. A proper detection technique is used to evaluate the lipase enzyme activity after the incubation time. A spectrophotometer is used to measure the product production by tracking the absorbance at a given wavelength, often around 405 nm. A compound's or substance's percentage of lipase inhibition at each concentration is determined using the absorbance values that were obtained. The inhibitory concentration (IC50), which is the concentration needed to block 50% of the lipase enzyme activity, may be calculated by generating a dose-response curve.

3. Results and Discussion

You may see the symbols utilized in this investigation and the results obtained for these samples in Table 1.

Table 1. Reveals the sample results and the signals used

Sample	Results μM
5b	210.045
5f	173.287
5g	135.911

Since 5b has been shown to reduce lipase enzyme activity, it might theoretically be used to treat pathological diseases like obesity that are linked to lipase enzyme activity. The connection between the percentage of enzyme activity and the concentration of 5b is shown graphically in Figure 1, which gives a comprehensive description of the activity. As the quantity of 5b increases, the enzyme lipase's activity decreases, as shown in the graph. The specific interactions between 5b and the enzyme's amino acids are shown by the 2D interaction map in Figure 2. Significant contributions to hydrogen bond interactions, which were shown to be critical to the binding process, were made by the following amino acids: GLY 76, ARG 256, PHE 77, HIS 151 and SER 152. Through these interactions, the inhibitory effects are increased and the binding is stabilised. In addition, the presence of red separation contacts indicates that the enzyme's active site is no longer occupied by water molecules. The outcome is that the enzyme changes shape and stops catalysing reactions. That is why 5b stops the lipase enzyme in its tracks.

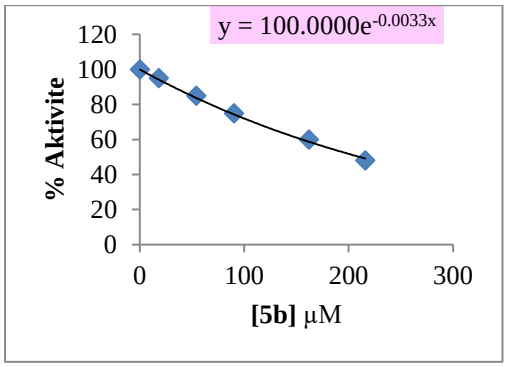

Figure 1. Reduce lipase enzyme activity from the 5b

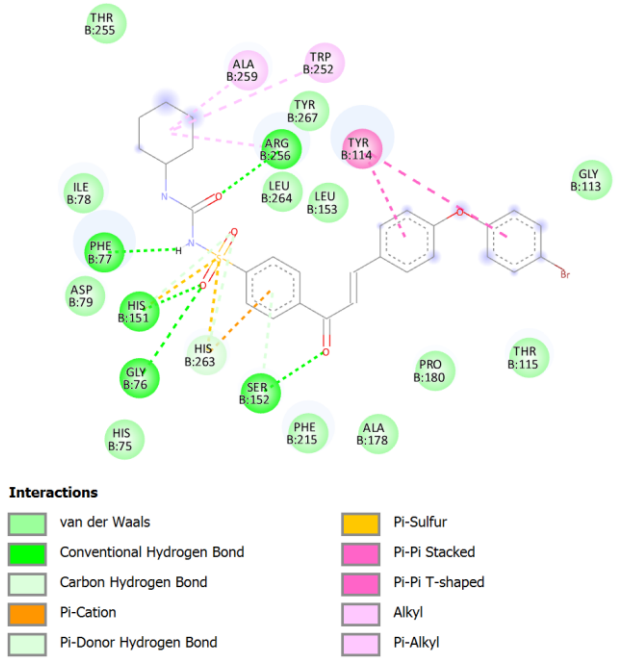

Figure 2. The 5b compound's two-dimensional structures with lipase enzyme

Since 5f has been shown to reduce lipase enzyme activity, it might theoretically be used to treat pathological diseases like obesity that are linked to lipase enzyme activity. The connection between the percentage of enzyme activity and the concentration of 5f is shown graphically in Figure 3, which gives a comprehensive description of the activity. As the quantity of 5f increases, the enzyme lipase's activity decreases, as shown in the graph. The specific interactions between 5f and the enzyme's amino acids are shown by the 2D interaction map in Figure 4. Significant contributions to hydrogen bond interactions, which were shown to be critical to the binding process, were made by the following amino acids: PHE 77 and HIS 263. Through these interactions, the inhibitory effects are increased and the binding is stabilised. In addition, the presence of red separation contacts indicates that the enzyme's active site is no longer occupied by water molecules. The outcome is that the enzyme changes shape and stops catalysing reactions. That is why 5f stops the lipase enzyme in its tracks.

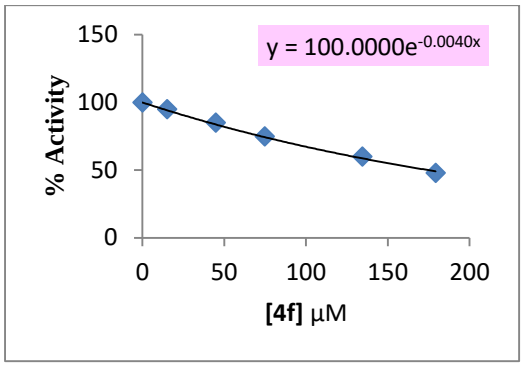

Figure 3. Reduce lipase enzyme activity from the 5f

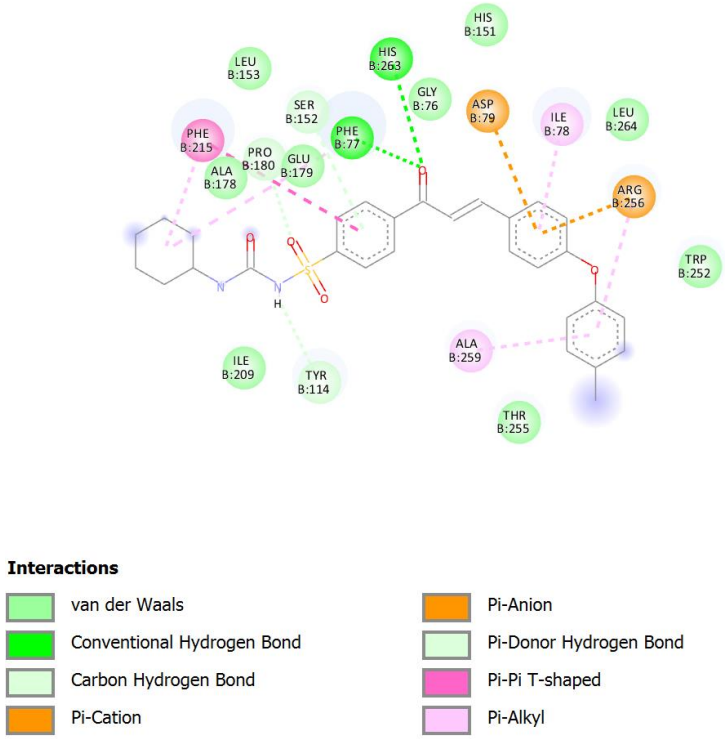

Figure 4. The 5f compound's two-dimensional structures with lipase enzyme

Since 5g has been shown to reduce lipase enzyme activity, it might theoretically be used to treat pathological diseases like obesity that are linked to lipase enzyme activity. The connection between the percentage of enzyme activity and the concentration of 5g is shown graphically in Figure 5, which gives a comprehensive description of the activity. As the quantity of 5g increases, the enzyme lipase's activity decreases, as shown in the graph. The specific interactions between 5g and the enzyme's amino acids are shown by the 2D interaction map in Figure 6. Significant contributions to hydrogen bond interactions, which were shown to be critical to the binding process, were made by the following amino acids: GLY 76, ARG 256, PHE 77, HIS 151 and SER 152. Through these interactions, the inhibitory effects are increased and the binding is stabilised. In addition, the presence of red separation contacts indicates that the enzyme's active site is no longer occupied by water molecules. The outcome is that the enzyme changes shape and stops catalysing reactions. That is why 5g stops the lipase enzyme in its tracks.

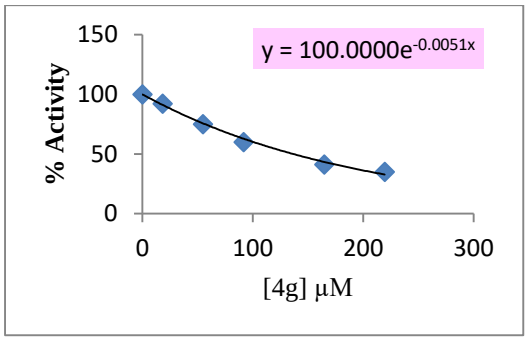

Figure 5. Reduce lipase enzyme activity from the 5g

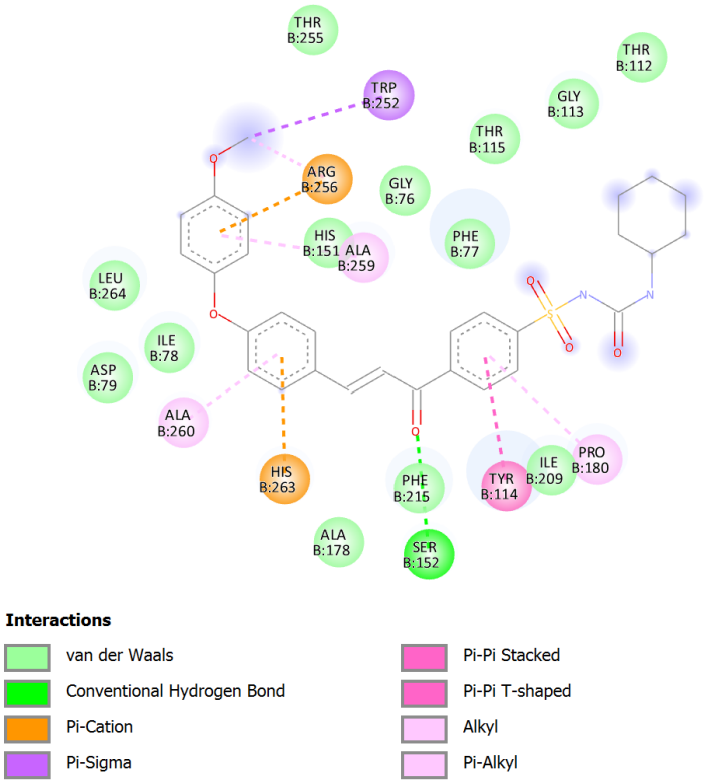

Figure 6. The 5g compound's two-dimensional structures with lipase enzyme

4. Conclusion

Three substances, 5b, 5f, and 5g, were studied for their ability to suppress lipase enzyme activity in this research. This opens up a new possibility for the management of obesity and other disorders associated with high lipase activity. The three drugs inhibited lipase activity in a concentration-dependent manner. The inhibitory mechanism was emphasised by the 2D interaction maps, which showed hydrogen bond interactions with certain amino acids. Enzyme catalytic activity was disrupted due to the displacement of water molecules from its active site, as shown by the red separation contacts. Compounds 5b, 5f, and 5g show promise as a treatment for obesity and other diseases linked to increased lipase activity, according to these results. To confirm these findings and evaluate the safety and effectiveness of these chemicals as anti-obesity drugs, more study is essential, such as clinical trials and in vivo investigations. People afflicted with lipase-related disorders may soon be able to enjoy better health and a higher quality of life thanks to this research, which is a giant leap forward in the quest for new treatment approaches.

References

[1] Keaver, L., Xu, B., Jaccard, A., & Webber, L. (2020). Morbid obesity in the UK: A modelling projection study to 2035. *Scandinavian journal of public health*, *48*(4), 422-427.

[2] Bell, J. A., Kivimaki, M., & Hamer, M. (2014). Metabolically healthy obesity and risk of incident type 2 diabetes: a meta-analysis of prospective cohort studies. *Obesity reviews*, *15*(6), 504-515.
[3] Abdullah, A., Peeters, A., de Courten, M., & Stoelwinder, J. (2010). The magnitude of association between overweight and obesity and the risk of diabetes: a meta-analysis of prospective cohort studies. *Diabetes research and clinical practice*, *89*(3), 309-319.
[4] Wilson, P. W., D'Agostino, R. B., Sullivan, L., Parise, H., & Kannel, W. B. (2002). Overweight and obesity as determinants of cardiovascular risk: the Framingham experience. *Archives of internal medicine*, *162*(16), 1867-1872.
[5] Lu, Y., Hajifathalian, K., Ezzati, M., Woodward, M., Rimm, E. B., Danaei, G., & D'Este, C. (2014). Metabolic mediators of the eff ects of body-mass index, overweight, and obesity on coronary heart disease and stroke: a pooled analysis of 97 prospective cohorts with 1.8 million participants.
[6] Calle, E. E., & Thun, M. J. (2004). Obesity and cancer. *Oncogene*, *23*(38), 6365-6378.
[7] Daneschvar, H. L., Aronson, M. D., & Smetana, G. W. (2016). FDA-approved anti-obesity drugs in the United States. *The American journal of medicine*, *129*(8), 879-e1.
[8] Woodard, K., Louque, L., & Hsia, D. S. (2020). Medications for the treatment of obesity in adolescents. *Therapeutic Advances in Endocrinology and Metabolism*, *11*, 2042018820918789.
[9] Pilitsi, E., Farr, O. M., Polyzos, S. A., Perakakis, N., Nolen-Doerr, E., Papathanasiou, A. E., & Mantzoros, C. S. (2019). Pharmacotherapy of obesity: available medications and drugs under investigation. *Metabolism*, *92*, 170-192.
[10] Winkler, F. K., d'Arcy, A., & Hunziker, W. (1990). Structure of human pancreatic lipase. *Nature*, *343*(6260), 771-774.
[11] Lowe, M. E. (1997). Structure and function of pancreatic lipase and colipase. *Annual review of nutrition*, *17*(1), 141-158.
[12] Egloff, M. P., Marguet, F., Buono, G., Verger, R., Cambillau, C., & van Tilbeurgh, H. (1995). The 2.46. ANG. resolution structure of the pancreatic lipase-colipase complex inhibited by a C11 alkyl phosphonate. *Biochemistry*, *34*(9), 2751-2762.
[13] van Tilbeurgh, H., Egloff, M. P., Martinez, C., Rugani, N., Verger, R., & Cambillau, C. (1993). Interfacial activation of the lipase–procolipase complex by mixed micelles revealed by X-ray crystallography. *Nature*, *362*(6423), 814-820.
[14] Heck, A. M., Yanovski, J. A., & Calis, K. A. (2000). Orlistat, a new lipase inhibitor for the management of obesity. *Pharmacotherapy: The Journal of Human Pharmacology and Drug Therapy*, *20*(3), 270-279.
[15] Hadvary, P., Sidler, W., Meister, W., Vetter, W., & Wolfer, H. (1991). The lipase inhibitor tetrahydrolipstatin binds covalently to the putative active site serine of pancreatic lipase. *Journal of Biological Chemistry*, *266*(4), 2021-2027.

Antioxidant Properties of Lycium barbarum Extracts

Serap ÇETİNKAYA [1*], ***Burak TÜZÜN*** [2]

[1]*Department of Molecular Biology and Genetics, Science Faculty, Sivas Cumhuriyet University, Sivas, Turkey*

[2]*Plant and Animal Production Department, Technical Sciences Vocational School of Sivas, Sivas Cumhuriyet University, Sivas, Turkey*

Abstract

Lycium barbarum (Goji berry) belongs to the Lycium genus. Lycium barbarum is a plant of Asian origin and its fruit has some pharmaceutical features exerting antioxidant and anticancer effects. To this end, the functional components constitute polysaccharides, polyphenols, flavonoids, carotenoids, and their derivatives. These compounds can neutralize free radicals by affecting the maintenance of cellular homeostasis and intracellular signalling pathways. Lycium barbarum is rich in antioxidants that fight free radicals in the body. Therefore, it may help slow the aging process, reduce cellular damage, and sustain overall health. The plant also produces vitamin C which helps strengthen the immune system. GC-MS analysis was performed to determine the content of Lycium barbarum extracts. Activities of the identified molecules against antioxidant proteins, PDB ID: 1HD2, and 4Z8D, were assessed.

Keywords: *Antioxidant, GC-MS, Lycium barbarum, Molecular docking.*

1. Introduction

Lycium barbarum L., is a medicinal plant, growing all over the world. It is famous with its fruit, called wolfberry or goji berry. Almost a hundred thousand tons of it is produced by China alone. This country knows this plant for almost 2,500 years. The fruit of this plant has been a traditional medicine as anti-aging, antioxidant, antidiabetic, anticancer, cytoprotective, neuroprotective, and immunomodulatory agent [1-3]. It contains carotenoids, phenylpropanoids, flavonoids, polyphenols, and polysaccharides. Its polysaccharides, vitamins, betaine and mixed extracts of goji berry elicit anti-aging effects and improve eyesight [4].

L. barbarum polysaccharides (LBPs) are a group of water-soluble glycoconjugates with a molecular weight between 10-2300 kDa and they form around 6% of dry fruit weight [5]. LBPs are the bioactive components of L. barbarum. The biological functions of LBPs appear to be complex and multifaceted.

2. Materials and Methods

2.1. Polysaccharides

Aqueous extractions at medium and high temperatures have revealed that L. barbarum L. possesses douzens of polysaccharides within a molecular range between 10 and 2300 kDa [3]. Additional means such as physical or enzymatic breakdown of the extracts have been added in some of the experimental procedures. Such treatments have seemed to increase the overall LBP yield. Some other extraction startegies have involved a combiantion of the several extraction methods [6]. Similar results have been reported from extractions with ultrasound-enhanced subcritical water [7].

In recent years sophisticated instrumental extraction approaches, involving gel permeation and ion exchange chromatography, high-performance liquid chromatography (HPLC), size exclusion chromatography (SEC), and hybrid membrane technology, have been introduced [8]. These novelties have also enabled the researchers to gather some information on the extracted LPS conformations [9,10].

2.2. Phenolic compounds

2.2.1. Flavonoids and Anthocyanidins

Flavonoids apigenin and luteolin possess 2-phenyl-1 benzopyran-4-one skeletons. L. barbarum L. flavones quercetin, myricetin, and routine, possess a 3-hydroxyflavone skeleton [11]. Routine and quercetin appear to dominate the fruit LPBs [12,13].

* Corresponding author. *e-mail address: serapcetinkaya2012@gmail.com*

Extraction yield and diversity of flavonoids have seemed to differ with the solvent, water, alcohols or their combinations, commonly used in earlier efforts. Recents studeis have preferred instrumental extractions, like gas chromatography-mass spectrometry (GC-MS), and capillary zone electrophoresis (CZE), HPLC-MS (Yang et al. 2021b), and solvents such as DESs (deep eutectic solvents), and "green solvents" including cheaper and biodegradable ingradients. Extraction in DESs has resulted in very high amounts of myricetin and routine, morin [14], and a very impportant flavanone naringenin [15].

Chromene pigments anthocyanidins is the coloring agent of L. ruthenicum. In some of the studies, a good number of anthocyanins have been extracted using UPLC-Triple-TOF/MS and UPLC-Q-Orbitrap methods [16]. These results have indicated that the type and yield of anthocyanin depended on the approach chosen [10].

2.2.2. Phenolic acids

Lycium species appear to be very good producers of phenolic acids: gallic acid, vanillic acid, 2,4-dihydroxybenzoic, veratronic acid, benzoic acid, salicylic acid, syringic acid, protocatechuic acid, chlorogenic acid, caffeic acid, p-coumaric acid, and ferulic acid [13]. Extraction methods have generally involved sophisticated instrumentation, mainly HPLC-MS, and GC-MS as weel as electrophoresis chemiluminescence (CE-CL) with solid phase extraction (SPE) [10,17].

2.2.3. Other phenolic compounds

As well as Lycium fruit, its roots have aslo been used as the phenolic compound source. And so far, fruit phenolics have included cannabicin D, cannabicin E, cannabicin F, threo-cannabicin H, erythro-cannabicin H, melongenamide D, grosamide, O-hydroxybenzene acetic acid, phloretic acid, dihydroferulic acid, and ethyl dihydroferulate. In other parts of the plant phenolic acid amides N-trans-feruloyl tyramine, N-trans-feruloyl 3-methoxytyramine, lysiumite A, N-trans-p-coumaroyl tyramine, N-cis-p-coumaroyl tyramine, N-feruloyl agmatine have been found [10,13].

2.3. Molecular docking

Molecular docking calculations are performed to compare the biological activities of molecules against biological materials. The program developed by Maestro Molecular modeling platform (version 12.8) by Schrödinger [18] was used for molecular docking calculations. Calculations are made up of several steps. Each step is done differently. In the first step, the protein preparation module [19] was used in the preparation of proteins. In this module, the active sites of the proteins were determined. In the next step, the studied molecules are prepared. First, the molecules are optimized in the gaussian software program, then the LigPrep module [20] is prepared for calculations using optimized structures. The Glide ligand docking module [21] was used to examine the interactions between the molecules and the cancer protein after preparation. Calculations were made using the OPLS4 method in all calculations. Finally, ADME/T analysis (absorption, distribution, metabolism, excretion and toxicity) will be performed to examine the drug potential of the studied molecules. The Qik-prop module [22] of the Schrödinger software was used to predict the effects and reactions of molecules in human metabolism.

3. Results and Discussion

3.1. Antioxidant activity of goji leaves

Goji leaves also appear to be a very rich source of both polyphenols and polysaccharides. Detection methods have mainly involved DPPH (free radical scavenging activity assay), TEAC (Trolox equivalent antioxidant capacity), HAPX (hemoglobin ascorbate peroxidase activity inhibition assay), and superoxide anion scavenging capacity assay. The compounds identified with the antioxidant activity mainly comprised polyphenols [23]. Here some other observations made have suggested that room temperature influenced the molecular diversity of the phenolic content [24]. Environmental samples have also been found to yield superior phenolic yields. Polysaccharides have been proven to be a significant DPPH, superoxide, and hydroxyl radicals scavengers in in vitro assays. Their in vivo antioxidant performance however remains a mystery for some of the researchers [25]. Evidence in this direction supports this concern [26]. One in vivo result however has pointed to the other direction that in diabetic rats ethyl acetate fraction of LCL could meaningfully lessen the amount of malondialdehyde at certain concentrations and increase the activities of radical scavenging enzymes, including catalase, superoxide dismutase, and glutathione peroxidase [27,28].

3.2. The potential of goji in the food industry

Industrial products of Goji fruit have found place in the shelves of food markets. In comparison, the leaves lag far behind and most of it is currently thrown away as waste, probably because Goji is a seasonal product and its leaves constitute a mass that is difficult to harvest and to preserve. On the other hand, the chemical composition and biological activities of Goji leave extracts, including above–mentioned compounds, flavonoids, alkaloids, polysaccharides, promise a brighter future as to its industrial use especially in bakery [29], because it can justly replace synthetic flour supplements. It can also lengthen the shelf life of meat products [30]. Calcium bind to LBLP through ionic interactions, and LBLP binds abundant calcium with uronic acid. Besides, crystallized cellulose contain high amounts of silicon and [31]. These findings might imply that Goji leaves are rich in mineral-based macromolecules [28].

Goji leaves, when used directly, can be toxic and decompose in gastrointestinal tract [32]. Encapsulation of leave extracts can avoid this problem [33]. Liposomes can also be used as efficient carriers of polyphenolic extracts [33-35].

3.3. Molecular docking result

The outcomes from the GC-MS analysis have unveiled a diverse array of chemical compounds within the Coriandrum sativum. Each of these compounds has been identified, and their names are meticulously presented in Table 1, offering comprehensive details for each.

Molecular docking is a computer simulation method that models the interaction of a target molecule (usually a protein) and a small molecule (ligand) [36,37]. This method is used in many areas such as drug design, understanding biological interactions and discovery of biochemical processes [38].

Essentially, molecular docking attempts to predict how a ligand binds to a target protein and how stable that binding is [39]. This is used to identify potential drug candidates or understand biological interaction mechanisms [40].

In this investigation, the effectiveness of the compounds enumerated in Table 1 was individually appraised against prostate cancer proteins via molecular docking computations [41,42]. These computations generated a multitude of parameters alongside their associated numerical values, playing a pivotal role in appraising the interactions and potential effectiveness of these compounds against prostate cancer proteins [43-45].

Table 1. Numerical values of the docking parameters of molecule against enzymes

1HD2	Docking Score	Glide ligand efficiency	Glide hbond	Glide evdw	Glide ecoul	Glide emodel	Glide energy	Glide einternal	Glide posenum
Butanal, 3-methyl	-4.14	-0.69	-0.32	-10.61	-2.73	-16.91	-13.34	0.52	229
3-Hydroxy-2-butanone	-4.67	-0.78	-0.15	-7.90	-8.11	-21.12	-16.01	0.15	383
2-Methyltetrahydrofuran-3-one	-4.72	-0.67	-0.12	-13.12	-1.78	-19.48	-14.90	0.00	221
1-Methoxy-2-propanone	-4.29	-0.71	-0.39	-10.18	-4.20	-18.55	-14.38	0.46	124
2,3-Butanediol	-3.65	-0.61	0.00	-1.77	-13.87	-18.56	-15.65	1.92	267
1-Butanol, 3-methyl-	-3.14	-0.52	-0.40	-9.83	-5.11	-16.84	-14.94	1.44	60
1-Pentanol	-1.55	-0.26	-0.37	-9.63	-4.17	-14.48	-13.80	1.21	210
Ethyl lactate	-3.30	-0.41	-0.28	-5.59	-10.98	-20.40	-16.57	0.50	376
2-Pentanone	-4.00	-0.67	-0.07	-11.22	-1.50	-15.57	-12.71	1.94	286
Pentanal	-2.61	-0.43	-0.07	-11.65	-1.71	-14.70	-13.35	2.20	287
4Z8D	Docking Score	Glide ligand efficiency	Glide hbond	Glide evdw	Glide ecoul	Glide emodel	Glide energy	Glide einternal	Glide posenum
Butanal, 3-methyl	-5.41	-0.90	-0.32	-12.80	-3.08	-21.12	-15.89	0.01	191
Acetic Acid	-3.84	-0.96	-0.40	-0.72	-7.10	-14.48	-7.82	0.00	4
3-Hydroxy-2-butanone	-5.28	-0.88	-0.30	-10.92	-6.44	-22.85	-17.36	0.20	259
2-Methyltetrahydrofuran-3-one	-5.91	-0.84	-0.42	-15.62	-1.48	-23.29	-17.10	0.00	123
1-Methoxy-2-propanone	-4.97	-0.83	-0.61	-12.43	-3.10	-20.38	-15.54	0.10	371
2,3-Butanediol	-4.57	-0.76	-0.84	-13.42	-7.75	-26.61	-21.17	0.62	219
1-Butanol, 3-methyl-	-4.54	-0.76	-0.86	-8.74	-6.97	-19.10	-15.71	1.60	291
1-Pentanol	-3.29	-0.55	-0.85	-9.78	-6.82	-19.42	-16.60	0.73	222
Ethyl lactate	-3.76	-0.47	0.00	-14.40	-6.55	-25.54	-20.95	1.03	165
2-Pentanone	-5.32	-0.89	-0.32	-11.51	-3.11	-19.75	-14.61	0.06	285
Pentanal	-4.69	-0.78	-0.61	-12.81	-2.72	-19.51	-15.53	1.00	27

The docking score, a vital metric derived from the calculations, holds a pivotal role in the comparative analysis of the activities of the molecules examined in your research [46,47]. It is noteworthy that the molecule exhibiting the most negative numerical value for the docking score is regarded as having the highest activity among the tested compounds [48,49]. This parameter serves as a key tool in evaluating the potential effectiveness of these molecules in their designated roles, such as inhibiting prostate cancer proteins [50,51].

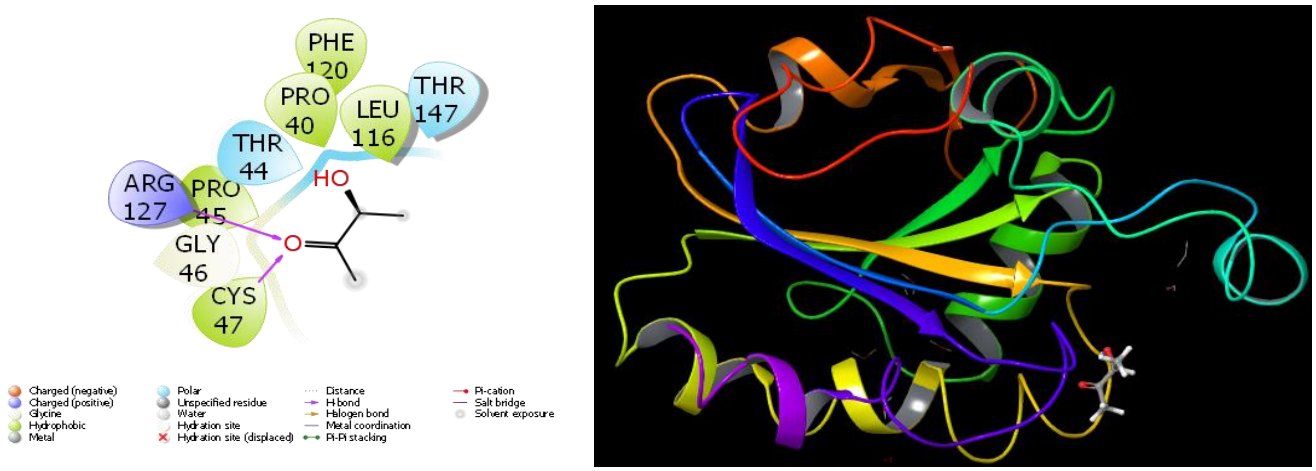

Figure 1. 2-Methyltetrahydrofuran-3-one's Interactions with Proteins Related to anti-oxidant protein (PDB ID: 1HD2)

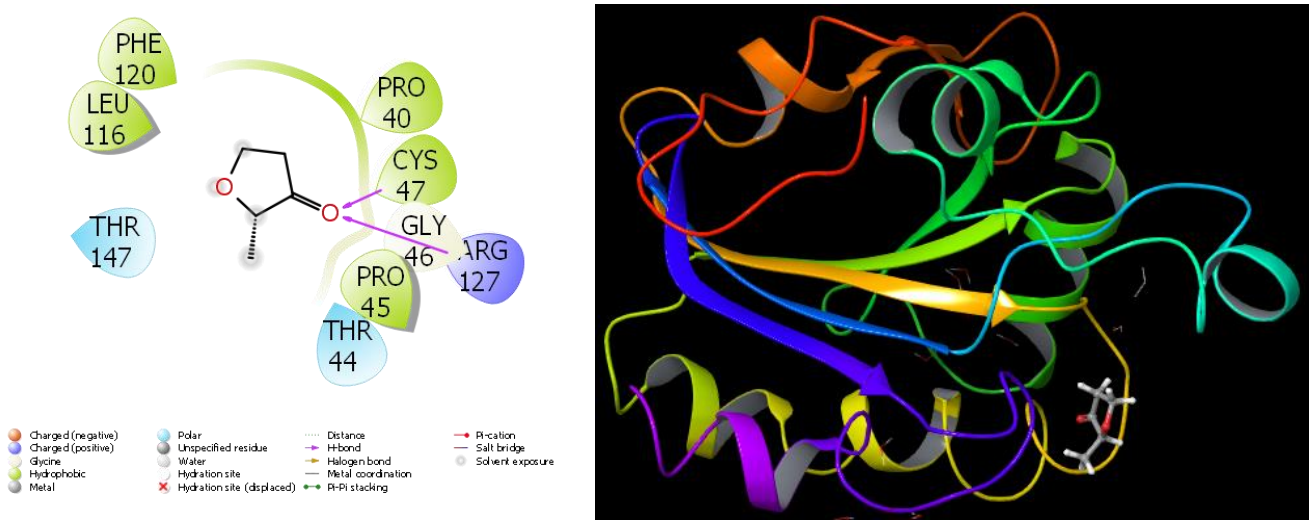

Figure 2. 3-Hydroxy-2-butanone 's Interactions with Proteins Related to anti-oxidant protein (PDB ID: 1HD2)

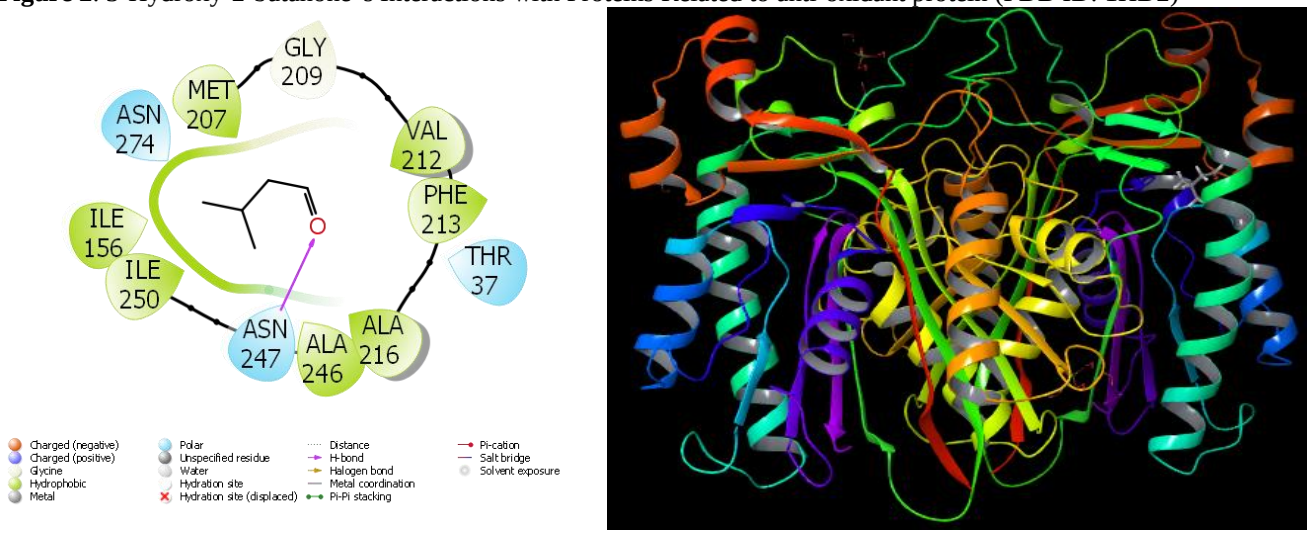

Figure 3. 2-Methyltetrahydrofuran-3-one's Interactions with Proteins Related to anti-oxidant protein (PDB ID: 4Z8D)

4. Conclusion

Goji fruit and leaves are rich in mineral-rich polysaccharides, phenolic compounds, alkaloids and minerals and exhibit various biological activities such as antioxidant, anti-inflammatory, anti-diabetic and anti-microbial activities. Moreover, the proteins obtained from Goji leaves deserve to be researched and studied. Goji leaves may be a good alternative to Goji berries for people who prefer to consume less sugar and more dietary fibre. However, before any use recommendations can be made for products based on Goji leaves, clinical evidence and strict procedures for their safety and quality are indispensable.

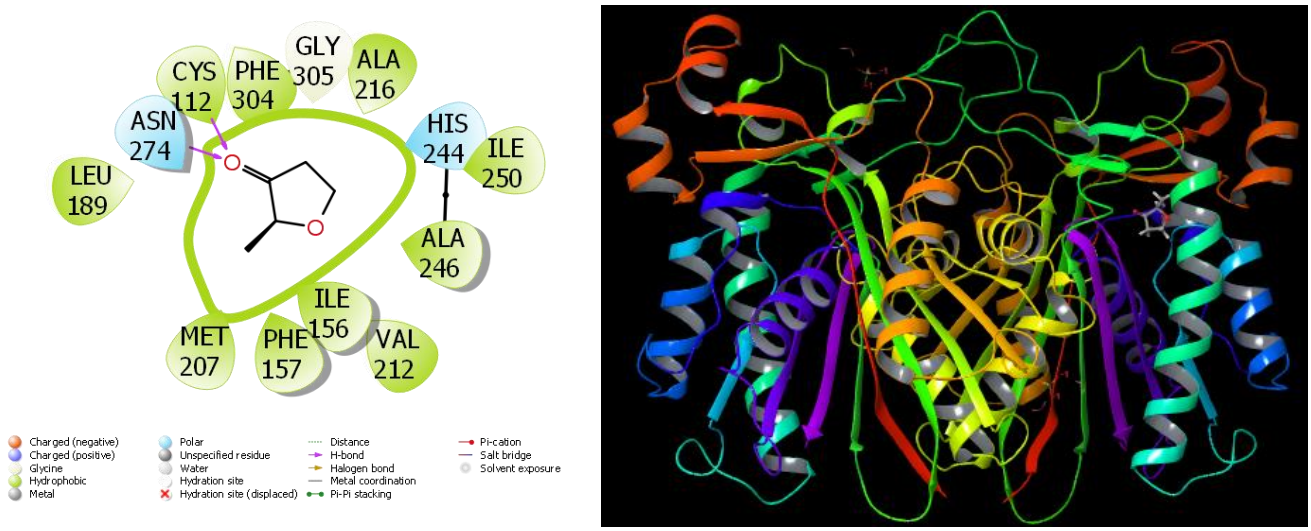

Figure 4. Ethyl linolenate's Interactions with Proteins Related to anti-oxidant protein (PDB ID: 4Z8D)

References

[1] Amagase, H., & Farnsworth, N. R. (2011). A review of botanical characteristics, phytochemistry, clinical relevance in efficacy and safety of Lycium barbarum fruit (Goji). Food research international, 44(7), 1702-1717.

[2] Wu, D. T., Guo, H., Lin, S., Lam, S. C., Zhao, L., Lin, D. R., & Qin, W. (2018). Review of the structural characterization, quality evaluation, and industrial application of Lycium barbarum polysaccharides. Trends in Food Science & Technology, 79, 171-183.

[3] Tian, X., Liang, T., Liu, Y., Ding, G., Zhang, F., & Ma, Z. (2019). Extraction, structural characterization, and biological functions of Lycium barbarum polysaccharides: A review. Biomolecules, 9(9), 389.

[4] Yao, R., Heinrich, M., & Weckerle, C. S. (2018). The genus Lycium as food and medicine: A botanical, ethnobotanical and historical review. Journal of ethnopharmacology, 212, 50-66.

[5] Wang, Q., Chen, S., & Zhang, Z. (1991). Determination of polysaccharide contents in Fructus Lycii. Chin Tradit Herb Drugs, 22, 67-8.

[6] Zhou, Z. Q., Fan, H. X., He, R. R., Xiao, J., Tsoi, B., Lan, K. H., ... & Gao, H. (2016). Lycibarbarspermidines A–O, new dicaffeoylspermidine derivatives from wolfberry, with activities against Alzheimer's disease and oxidation. Journal of agricultural and food chemistry, 64(11), 2223-2237.

[7] Wen, L., Zhang, Z., Sun, D. W., Sivagnanam, S. P., & Tiwari, B. K. (2020). Combination of emerging technologies for the extraction of bioactive compounds. Critical Reviews in Food Science and Nutrition, 60(11), 1826-1841.

[8] Liu, J., Pu, Q., Qiu, H., & Di, D. (2021). Polysaccharides isolated from Lycium barbarum L. by integrated tandem hybrid membrane technology exert antioxidant activities in mitochondria. Industrial Crops and Products, 168, 113547.

[9] Liu, W., Liu, Y., Zhu, R., Yu, J., Lu, W., Pan, C., ... & Gao, X. (2016). Structure characterization, chemical and enzymatic degradation, and chain conformation of an acidic polysaccharide from Lycium barbarum L. Carbohydrate Polymers, 147, 114-124.

[10] Ma, R. H., Zhang, X. X., Ni, Z. J., Thakur, K., Wang, W., Yan, Y. M., ... & Wei, Z. J. (2022). Lycium barbarum (Goji) as functional food: a review of its nutrition, phytochemical structure, biological features, and food industry prospects. Critical Reviews in Food Science and Nutrition, 1-15.

[11] Yang, L., Gao, Y., Bajpai, V. K., El-Kammar, H. A., Simal-Gandara, J., Cao, H., ... & Xiao, J. (2023). Advance toward isolation, extraction, metabolism and health benefits of kaempferol, a major dietary flavonoid with future perspectives. Critical Reviews in Food Science and Nutrition, 63(16), 2773-2789.

[12] Protti, M., Gualandi, I., Mandrioli, R., Zappoli, S., Tonelli, D., & Mercolini, L. (2017). Analytical profiling of selected antioxidants and total antioxidant capacity of goji (Lycium spp.) berries. Journal of pharmaceutical and biomedical analysis, 143, 252-260.

[13] Jiang, Y., Fang, Z., Leonard, W., & Zhang, P. (2021). Phenolic compounds in Lycium berry: Composition, health benefits and industrial applications. Journal of Functional Foods, 77, 104340.

[14] Ali, M. C., Chen, J., Zhang, H., Li, Z., Zhao, L., & Qiu, H. (2019). Effective extraction of flavonoids from Lycium barbarum L. fruits by deep eutectic solvents-based ultrasound-assisted extraction. Talanta, 203, 16-22.

[15] Bajkacz, S., & Adamek, J. (2018). Development of a method based on natural deep eutectic solvents for extraction of flavonoids from food samples. Food analytical methods, 11, 1330-1344.

[16] Dong, Y., Gu, J., Wang, P., & Wen, H. (2019). Developed functionalization of wool fabric with extracts of Lycium ruthenicum Murray and potential application in healthy care textiles. Dyes and Pigments, 163, 308-317.

[17] Yang, S., Han, Y., Wang, K., Wang, Y., Li, L., Li, N., & Xu, X. (2021). Simultaneous determination of four phenolic acids in traditional Chinese medicine by capillary electrophoresis-chemiluminescence. RSC advances, 11(54), 33996-34003.

[18] Mocan, A., Zengin, G., Simirgiotis, M., Schafberg, M., Mollica, A., Vodnar, D. C., ... & Rohn, S. (2017). Functional constituents of wild and cultivated Goji (L. barbarum L.) leaves: Phytochemical characterization, biological profile, and computational studies. Journal of enzyme inhibition and medicinal chemistry, 32(1), 153-168.

[19] Liu, S. C., Lin, J. T., Hu, C. C., Shen, B. Y., Chen, T. Y., Chang, Y. L., ... & Yang, D. J. (2017). Phenolic compositions and antioxidant attributes of leaves and stems from three inbred varieties of Lycium chinense Miller harvested at various times. Food Chemistry, 215, 284-291.

[20] Harnly, J. (2017). Antioxidant methods. Journal of Food Composition and Analysis, 64, 145-146.

[21] Ruskovska, T., Maksimova, V., & Milenkovic, D. (2020). Polyphenols in human nutrition: from the in vitro antioxidant capacity to the beneficial effects on cardiometabolic health and related inter-individual variability–an overview and perspective. British Journal of Nutrition, 123(3), 241-254.

[22] Olatunji, O. J., Chen, H., & Zhou, Y. (2017). Effect of the polyphenol rich ethyl acetate fraction from the leaves of Lycium chinenseMill. on oxidative stress, dyslipidemia, and diabetes mellitus in streptozotocin-nicotinamide induced diabetic rats. Chemistry & biodiversity, 14(10), e1700277.

[23] Lei, Z., Chen, X., Cao, F., Guo, Q., & Wang, J. (2022). Phytochemicals and bioactivities of Goji (Lycium barbarum L. and Lycium chinense Mill.) leaves and their potential applications in the food industry: A review. International Journal of Food Science & Technology, 57(3), 1451-1461.

[24] Al-Wraikat, M., Hou, C., Zhao, G., Lu, H., Zhang, H., Lei, Y., ... & Li, J. (2021). Degraded polysaccharide from Lycium barbarum L. leaves

improve wheat dough structure and rheology. Lwt, 145, 111372.
[25] Niu, Y., Chen, J., Fan, Y., & Kou, T. (2021). Effect of flavonoids from Lycium barbarum leaves on the oxidation of myofibrillar proteins in minced mutton during chilled storage. Journal of Food Science, 86(5), 1766-1777.
[26] Song, P., Zhou, F., Li, F., Han, Z., Wang, L., Xu, J., ... & Zhang, B. (2021). Superfine pulverisation pretreatment to enhance crystallinity of cellulose from Lycium barbarum L. leaves. Carbohydrate Polymers, 253, 117207.
[27] Păvăloiu, R. D., Sha'at, F., Neagu, G., Deaconu, M., Bubueanu, C., Albulescu, A., ... & Hlevca, C. (2021). Encapsulation of polyphenols from Lycium barbarum leaves into liposomes as a strategy to improve their delivery. Nanomaterials, 11(8), 1938.
[28] Yadav, M., Bhatia, V.J., Doshi, G. & Shastri, K. (2014). Novel techniques in herbal drug delivery systems. International Journal of Pharmaceutical Sciences Review and Research, 28, 83–89.
[29] Dumitriu, B. O., & Dima, S. (2016). Biopolymer-based techniques for encapsulation of phytochemicals bioacive in food and drug. Revista de materiale plastice, 53, 126-12.
[30] Al Ati, G., Chkirate, K., El-Guourrami, O., Chakchak, H., Tüzün, B., Mague, J. T., ... & Essassi, E. M. (2024). Schiff base compounds constructed from pyrazole–acetamide: Synthesis, spectroscopic characterization, crystal structure, DFT, molecular docking and antioxidant activity. Journal of Molecular Structure, 1295, 136637.
[31] Saraç, H., Demirbaş, A., & Tüzün, B. (2023). Could Zingiber officinale plant be effective against Omicron BA. 2.75 of SARS-CoV-2?. Turkish Computational and Theoretical Chemistry, 7(3), 42-56.
[32] Kanzouai, Y., Chalkha, M., Hadni, H., Laghmari, M., Bouzammit, R., Nakkabi, A., ... & Al Houari, G. (2023). Design, synthesis, in-vitro and in-silico studies of chromone-isoxazoline conjugates as anti-bacterial agents. Journal of Molecular Structure, 1293, 136205.
[33] Tapera, M., Kekeçmuhammed, H., Sarıpınar, E., Doğan, M., Tüzün, B., Koçyiğit, Ü. M., & Çetin, F. N. (2023). Molecular hybrids integrated with imidazole and hydrazone structural motifs: Design, synthesis, biological evaluation, and molecular docking studies. Journal of Molecular Liquids, 391, 123242.
[34] Majumdar, D., Philip, J. E., Tüzün, B., Sutradhar, D., & Roy, S. (2023). Two adamantan-1-amine-based scaffolds: Synthesis, crystallographic synthons, TD/DFT calculations, in-depth molecular docking/ADME/T simulations, and shedding light on antibacterial/fungal activities. Results in Chemistry, 101228.
[35] Chalkha, M., Chebbac, K., Nour, H., Nakkabi, A., El Moussaoui, A., Tüzün, B., ... & El Yazidi, M. (2023). In Vitro and In Silico Evaluation of the Antimicrobial and Antioxidant Activities of Spiropyrazoline Oxindole Congeners. Arabian Journal of Chemistry, 105465.
[36] Karataş, H., Kiliç, H. K., Tüzün, B., & Kökbudak, Z. (2023). Schiff Base Derivatives against Monkeypox Virus: Synthesis, In silico, MM-GBSA and SAR properties. Journal of Molecular Structure, 137073.
[37] Aksu, A., Çetinkaya, S., Yenidünya, A. F., Çetinus, Ş. A., Gezegen, H., & Tüzün, B. (2023). Immobilization of pectinase on chitosan-alginate-clay composite beads: Experimental, DFT and molecular docking studies. Journal of Molecular Liquids, 390, 122947.
[38] Mermer, A., Tüzün, B., Daştan, S. D., Koçyiğit, Ü. M., Çetin, F. N., & Çevik, Ö. (2023). Piperazin incorporated Schiff Base derivatives: Assessment of in vitro biological activities, metabolic enzyme inhibition properties, and molecular docking calculations. Journal of Biochemical and Molecular Toxicology, 37(11), e23465.
[39] Erdoğan, M., Yeşildağ, A., Yıldız, B., Tüzün, B., & Özden, Ö. (2023). Synthesis and characterization of some benzidine-based azomethine derivatives with molecular docking studies and anticancer activities. Chemical Papers, 77(11), 6829-6847.
[40] Yalazan, H., Koç, D., Aydın Kose, F., Fandaklı, S., Tüzün, B., Akgül, M. İ., ... & Kantekin, H. (2023). Design, syntheses, theoretical calculations, MM-GBSA, potential anti-cancer and enzyme activities of novel Schiff base compounds. Journal of Biomolecular Structure and Dynamics, 1-14.
[41] Arukalam, I. O., Uzochukwu, I. N., Tüzün, B., Dagdag, O., & Oguzie, E. E. (2023). Influence of ZnO Nanoparticle Size on Barrier Performance and Corrosion Protection of Poly (dimethylsiloxane)-Coated Q235 Steel in Chloride Environment: Bode and Computational Simulation Investigations. Chemistry Africa, 1-11.
[42] Tuzun, B., Taş, N. A., Taslimi, P., & Karadağ, A. (2023). Synthesis, enzyme inhibition, and in silico studies of Amino Acid Schiff Bases. Iranian Journal of Chemistry and Chemical Engineering.
[43] Tokalı, F. S., Taslimi, P., Tuzun, B., Karakuş, A., Sadeghian, N., & Gulçin, İ. (2023). Novel Quinazolinone Derivatives: Potential Synthetic Analogs for the Treatment of Glaucoma, Alzheimer's Disease and Diabetes Mellitus. Chemistry & Biodiversity, 20(10), e202301134.
[44] Tokalı, F. S., Taslimi, P., Tüzün, B., Karakuş, A., Sadeghian, N., & Gulçin, İ. (2023). Synthesis of new carboxylates and sulfonates containing thiazolidin-4-one ring and evaluation of inhibitory properties against some metabolic enzymes. Journal of the Iranian Chemical Society, 20(10), 2631-2642.
[45] Manap, S., Medetalibeyoğlu, H., Kılıç, A., Karataş, O. F., Tüzün, B., Alkan, M., ... & Yüksek, H. (2023). Synthesis, molecular modeling investigation, molecular dynamic and ADME prediction of some novel Mannich bases derived from 1, 2, 4-triazole, and assessment of their anticancer activity. Journal of Biomolecular Structure and Dynamics, 1-15.
[46] Arukalam, I. O., Uzochukwu, I. N., Izionworu, V. O., Tüzün, B., & Dagdag, O. (2023). Corrosion protection of Q235 steel in Pseudomonas aeruginosa-laden seawater environment using high barrier PDMS nanocomposite coating. Safety in Extreme Environments, 1-11.
[47] Durmaz, L., Gulçin, İ., Taslimi, P., & Tüzün, B. (2023). Isofraxidin: Antioxidant, Anti-carbonic Anhydrase, Anti-cholinesterase, Anti-diabetic, and in Silico Properties. ChemistrySelect, 8(34), e202300170.
[48] Aksu, A., Çelik, M. S., Polat, Z. A., Yenidünya, A. F., & Tuzun, B. (2023). Experimental and theoretical evidence on the amoebicidal activity of synthesized tRNA-palmitic acid esters. Iranian Journal of Chemistry and Chemical Engineering.
[49] Majumdar, D., Philip, J. E., Tüzün, B., & Roy, S. (2023). Synthesis, characterization, crystallographic aspects, Fukui function, and photodynamic antifungal chemotherapy investigation of Cd (II)-tricyanomethanide coordination polymer: Insights from DFT. Inorganic Chemistry Communications, 155, 111057.
[50] Yuriy, K., Kusdemir, G., Volodymyr, P., Tüzün, B., Taslimi, P., Karatas, O. F., ... & Sayın, K. (2023). A biochemistry-oriented drug design: synthesis, anticancer activity, enzymes inhibition, molecular docking studies of novel 1, 2, 4-triazole derivatives. Journal of Biomolecular Structure and Dynamics, 1-17.
[51] Amrulla, F. P., Akber, M. A., Huseyn, I. R., Taslimi, P., & Tuzun, B. et all.(2023). Cu (II), Ni (II) and Co (II) Complexes of Malonic Acid Dihydrazide with bis-Br-Salicylhydrazone. Adv Neur Neur Sci, 6(2), 228-242.
[52] Ozmen, U. O., Tuzun, B., Ayan, E. B., & Cevrimli, B. S. (2023). Eco-friendly and potential colin esterase enzyme inhibitor agent sulfonyl hydrazone series: Synthesis, Bioactivity Screening, DFT, ADME properties, and Molecular Docking study. Journal of Molecular Structure, 1286, 135514.
[53] Hermi, S., Mrad, M. H., Alotaibi, A. A., Tüzün, B., Böhme, U., Alotaibi, K. M., ... & Nasr, C. B. (2023). A new 1-D polymeric chains of (C5H6ClN2)[CdCl3H2O]. H2O perovskite: Synthesis, Structure, Physico-Chemical Characteristics, theoretical calculations, and biological effects. Inorganic Chemistry Communications, 111122.

Exploring the Lipid Profile Parameters in the Serum of Iraqi Leukemic Patients

Basma Jawad AMEEN [1,*], ***Volkan EYÜPOĞLU*** [2], ***Ahmed Fadhil Neama ALSHANON*** [3]

[1] *Department of Chemistry Sciences, School of Natural and Applied Sciences, Çankiri Karatekin University, Iraq*

[2] *Department of Chemistry Sciences, School of Natural and Applied Sciences, Çankiri Karatekin University, Turkey*

[3] *Plant Biotechnology department, Center of Biotechnology Research, Alnahrain University, Iraq*

Abstract

This study investigates the potential differences in lipid profile parameters between Iraqi leukemia patients and healthy controls to understand their association with the disease and its progression. The study included 200 Iraqis, including 150 leukemia patients. 50 healthy individuals aged 6–68 were the control group. Medical patient got six milliliters of blood collected from Al-Yarmuk Teaching Hospital. Lipid profile test showed that leukemia patients had higher cholesterol, triglycerides, and VLDL (239.7, 40.53, and 189.2) than controls (170.8, 20.68, and 104.9) but no significant differences in HDL or LDL. This study suggests potential alterations in lipid profile parameters in Iraqi leukemia patients, which may contribute to understanding the disease's mechanisms and developing personalized treatment approaches. Further research is needed to confirm these findings and elucidate the complex interplay between lipid metabolism and leukemia pathogenesis.

Keywords: *Leukemia, Lipid Profile, Cholesterol, Iraqi*

1. Introduction

Leukemia is a cancer of the hemopoietic tissues characterized by an increase of aberrant white blood cells (WBCs) in the bone marrow [1]. The bone marrow produces all blood cells. in order to maintain the required number of blood cells. Bone marrow is a spongy substance found within bones. In adults, a tiny number of stem cells, which can give rise to aberrant cells and induce bone marrow failure, They're in charge of creating 120,000 WBC and three million red blood cells per seconds [2]. When leukemia cells die, they continue to reproduce rapidly, creating new leukemic cells that might gather and choke healthy blood cells. The primary methodThe bone marrow assay or numerous full blood counts are used in determining the presence of leukemia. If concerns appear, both of these examinations are performed. However, on rare cases, blood examinations might not produce reliable results for leukemia or might not indicate if the patient is thought of having leukemia. That occurs either while leukemia is just starting to progress or after it has reached remission [3]. In certain circumstances, further procedures, such as a lymph node biopsy, may be utilized to identify and investigate particular forms of leukemia [4]. After the diagnosis is made more focused assays are carried out to establish the extent of liver and kidney destruction, such as blood chemistry testing., in addition to the patient's response to treatment with chemotherapy, such as reticulocyte numbers and blood sample analysis, iron investigations, including Fe. in Iraq, accounting for 8.97% of all new cancer diagnoses. The most prevalent of them was leukemia (10499), which accounts for 29.65% of all cases, on average, 524 kids are diagnosed with leukemia each year. Leukemia accounted for 2088 (30.94%) of all pediatric cancer cases from 2000 to 2004, this number slightly decreased to 2174 (30.50%) from 2005 to 2009, then increased to 3020 (32.82%) from 2010 to 2014, and finally decreased to (3217) 25.60% from 2015 to 2019. According to the World Health Organization, leukemia was the third most prevalent illness in 2020, with 1545 fatalities and 2027 new cases (WHO 2020). Oxidants are known to contribute to several phases of carcinogenesis [5]. OS is linked to a number of medical conditions, including infection, inflammation, exposure to UV and gamma radiation, and an increase in mutation frequency [6] and acute promyelocytic leukemia [7]. Mild OS is signified by elevated levels of anti-oxidant enzymes, which is an adaptive protective response, and enhanced free radical production, notably the production of superoxide anion in leukemia patients [8]. OS has been linked to the development of cancer in several studies [9]. Endogenous oxidants can play a role in several stages of malignant transformation and are thought to be major naturally occurring carcinogens [10]. ROS have the ability to cause chromosomal and genetic changes, which can lead to cancer formation in multistep carcinogenesis [11]. AdditionallyROS can activate intercellular secondary messengers, which can alter a range of cellular processes such as apoptosis, gene expression, and cell development [12]. OS begin the carcinogenesis process by activating kinases and

* Corresponding author. *e-mail address: .....@.....*

denaturing DNA via chromosomal protein poly ADP-ribosylation [13]. OFR frequently causes cell damage and may have.

2. Materials and Methods

The collection of blood was performed in Al- Yarmuk Teaching Hospital and Medical and Health in Baghdad 150 samples were collected from Patients were diagnosed with leukemia by a consultant medical staff at center. their ages rangedwere between 6 years to 68 years. All patients were attended to the laboratoryof hospital in order to diagnosis and treatment. To act as a control group, fifty healthy males and females were examined. Their ages ranged from 6 to 68 years. None of them had any clinical or lab indication of an illness that might have an impact on the measurement parameters. After cleaning the skin with 70% alcohol and drawing blood from each patient's vein, the blood was allowed to clot for about 30 minutes at room temperature before being centrifuged for 5 minutes at 3000 (rpm) to separate the serum and then transferred into additional tubes. In total, 150 patients and 50 controls had their blood samples drawn. To assess the quantities of chemical components in the blood, clinical chemistry employs chemicals. It is particularly helpful for tracking organ function and early illness diagnosis. Blood and urine are the most typical specimens utilized in clinical chemistry. The typical blood tests and things that can be measured using UV/Vis spectroscopy instruments.In this program note, the LAMBDATM 465 UV/Vis Spectrophotometer and UV LabTM software were used to detect the quantity of cholesterol in human serum using an enzymatic approach. concept of Cholesterase hydrolyzes the cholesterol esters in the sample. Cholesterol oxidase then converts the liberated free cholesterol into 4-cholesteren-3-one and H2O2. Hydrogen peroxide (H2O2) is converted into a quantifiable red quinoneimine compound with an absorbance of 500 nm. Triglycerides are measured by enzymes in either plasma or serum through a series of related processes in how triglycerides are digested to produce glycerol. Then, glycerol is exposed to oxidation using glycerol oxidase, and one of the byproducts, H2O2, is identified as being associated with cholesterol. The absorbance is calculated at 500 nm. Regional atherosclerotic and CHD-risk-raising illnesses can be recognized by high blood triglyceride levels. High triglycerides are related to an increased risk for coronary artery disease (CAD) among persons who have other risk factors, such as low levels of HDL cholesterol, specific patient groups with higher levels of apolipoprotein B, and those with LDL kinds that may be particularly atherogenic. Borderline overnight levels of triglycerides, which are those below 200 mg/dL, are regarded to be ideal., High is 400–1,000 mg/dL, Very High is >1000 mg/dL, and Low is 200–400 mg/dL. Extremely elevated levels of triglycerides ought to be investigated and dealt with right away since they can cause pancreatitis. Although the value is applied to determine the level of low density lipoprotein (LDL)-cholesterol concentrations, triglycerides are evaluated as well. Using the Direct HDL method. For a direct HDL test, serum is utilized. The basic concept of the approach is as follows. According to the assay's requirements, a taking up reagent is utilized to interact with the material's apoB-containing lipoproteins and make them non-reactive with the enzyme cholesterol reagent. As a result, when the test conditions are satisfied, the procedure effectively eliminates the lipoproteins that contain apoB, leaving just HDL-chol. Roche/Boehringer-Mannheim Diagnostics is where the reagents are bought. The method uses sulfate alpha-cyclodextrin in the presence of Mg+2, which forms complexes with apoB-containing lipoproteins, as well as polypropylene glycol-coupled cholesterol levels esterase and cholesterol oxidase as substrates for the detection of HDL cholesterol. According to the following connection, LDL cholesterol is estimated from measured values of total cholesterol, triglycerides, and HDL cholesterol. Very low-density lipoproteins (VLDL), LDL, and HDL are the three main lipoprotein fractions that contain the majority of the circulating cholesterol. Total cholesterol is the sum of VLDL, LDL, and HDL cholesterol. As a result, this mathematical equation could used to determine the value ofVLDL.

3. Results and Discussion

First, cholesterol levels were assessed. The patients had elevated cholesterol levels. based on the outcomes we came up with. The findings demonstrate that there were considerable gains. According to Figure 1, the cholesterol values in the healthy control and patient were (170.8 and 239.7), Pg/ml respectively (P=0.0009). The percentage in difference between the healthy group and the sufferers was 71%, as it explained below.

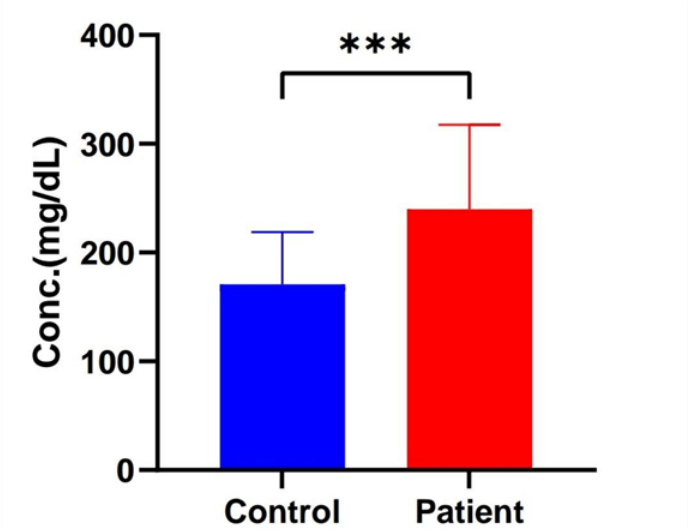

Figure 1. Cholestoral concentration in different studied groups

Also, an increase in VLDL levels was observed, according to the obtained resultsThere was significant differences (P=0.0043) between control leukemia patients and it was (58.7and55.78) Pg/ml respectively. as it showen in Figur 2.

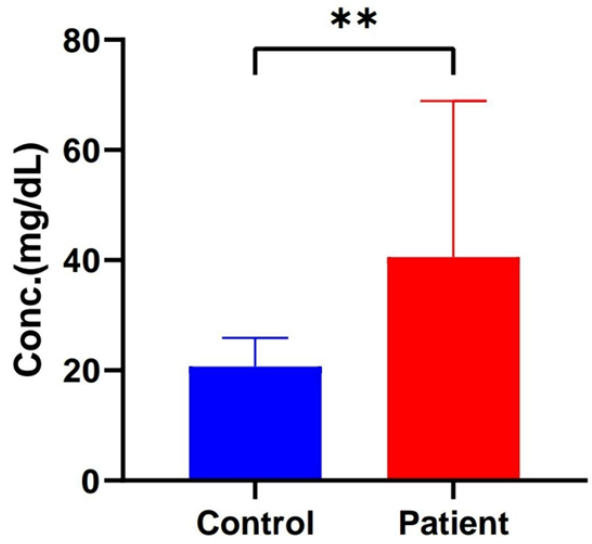

Figure 2. VLDL concentration in different studied groups

There were also similar results in the Estimate of triglycerides, where there was a clear increase in triglyceride levels. According to the results obtained (P=0.0028)and the difference between control and leukemia patient was (104.9and 189.2) Pg/ml Figure 3.

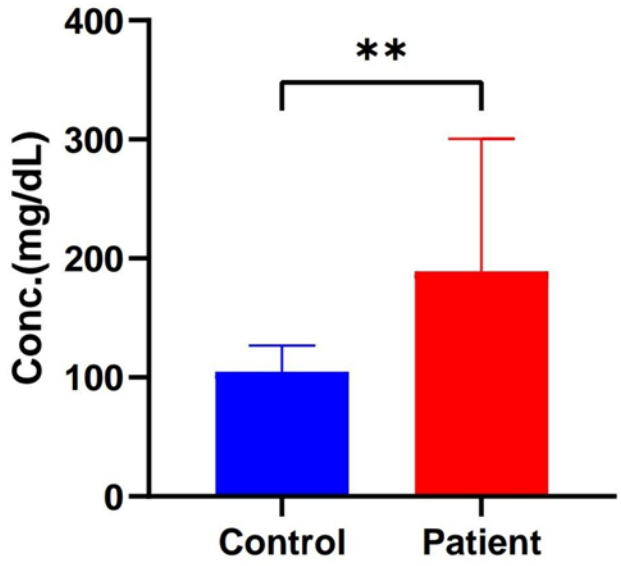

Figure 3. Triglyceride concentration in different studied groups

while While the result was different in HDL and LDL.from obtained data there is no significant differences in HDL(P= 0.8254)and the HDLlevel in patien group Not a clear difference For the healthy group (55.78 and 58.70) Pg/ml as it shown in Fiuger 4.

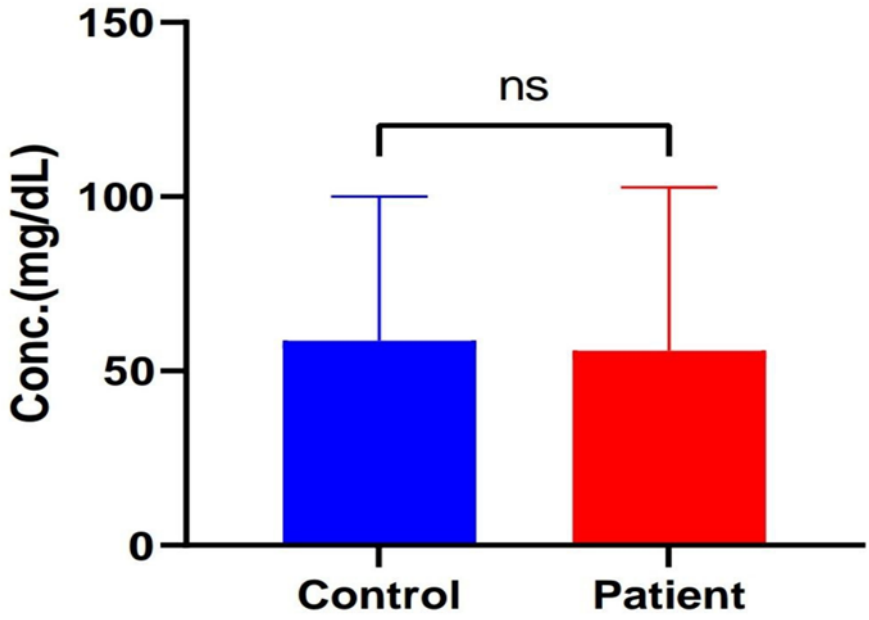

Figure 4. HDL concentration in different studied groups

The result in LDL was similar to HDL Also, there was no significant difference (P= 0.4082) and LDL value is comparing with the healthy control and it was(112.4and 99.90) Pg/ml as it shown in Figure 5.

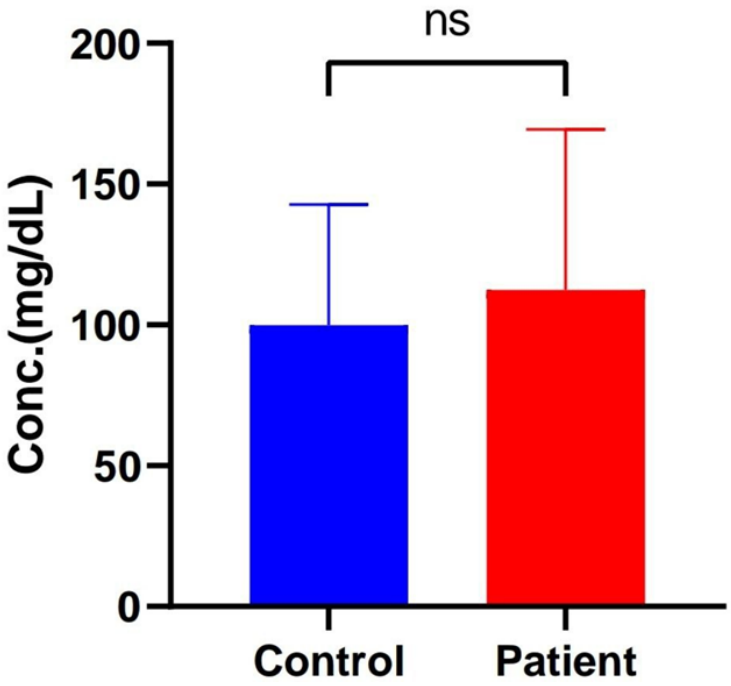

Figure 5. LDLconcentration in different studied groups

First of all, for cholesterol compared to those in good health. With a rise in tumor stage, the amount of cholesterol decreases even more [14]. On the other hand, 75% of patients attending a clinic of Chronic Lymphocytic had elevated cholesterol levels [15]. According to reports, CLL patients are more likely to survive if they use cholesterol-lowering medication and had hypercholesterolemia before their diagnosis [16]. Numerous molecules related to cholesterol metabolism were shown to be dysregulated in blood cancer cells at the cellular level. When compared to control, lympho-cytes from people with chronic lymphocytic leukemia express more LDLR, SREBP-2, and the nu\clear cholesterol channel protein PBR. As a result, cholesterol accumulation was also ``discovered in the cytoplasm and nucleus [17]. It was observed in most studies that the increase in VLDL and TG was associated with most patients with leukemia. Taking chemotherapeutic medicines such as asparginase may cause lipid problems. Asparginase has been shown by [18]. to result in hypertriglyceridemia, in their study, plasma LDL was considerably raised following treatment with asparginase. Additionally, it has been shown that AML patients have much smaller amounts of lipoproteins with a high density than acute lymphocytic leukemia (ALL) patients do.

4. Conclusion

The comprehensive investigation into the lipid profile and oxidative stress parameters in the serum of Iraqi leukemic patients sheds light on the intricate relationship between leukemia and systemic metabolic alterations. The findings underscore the potential impact of leukemia on lipid metabolism and oxidative stress, providing valuable insights into the underlying pathophysiological mechanisms. The observed changes in lipid levels and oxidative stress markers could serve as potential diagnostic and prognostic indicators, aiding in the development of targeted therapeutic strategies. Moreover, this study emphasizes the importance of exploring novel avenues for intervention and management that extend beyond traditional approaches, offering new perspectives for improving the overall health outcomes of Iraqi leukemic patients. Future research endeavors should continue to unravel the intricate interplay between leukemia, lipid metabolism, and oxidative stress, paving the way for innovative approaches to enhance patient care and treatment efficacy.

References

[1] Attar, M. N. 2022. The role of the guanine nucleotide exchange factors DOCK2 and DOCK5 in acute myeloid leukemia and their interactions with epigenetic regulation. Staats-und Universitätsbibliothek Hamburg Carl von Ossietzky.

[2] Bosi, A. and Bartolozzi, B. 2010. Safety of bone marrow stem cell donation: a review. Transplantation Proceedings, 42(6): 2192–2194.

[3] Suttorp, M., Schulze, P., Glauche, I., Göhring, G., von Neuhoff, N., Metzler, M., Sedlacek, P., de Bont, E. S. J. M., Balduzzi, A. and Lausen, B. 2018. Front-line imatinib treatment in children and adolescents with chronic myeloid leukemia: results from a phase III trial. Leukemia, 32(7): 1657–1669.

[4] Quinquenel, A., Aurran-Schleinitz, T., Clavert, A., Cymbalista, F., Dartigeas, C., Davi, F., de Guibert, S., Delmer, A., Dilhuydy, M. S. and Feugier, P. 2020. Diagnosis and treatment of chronic lymphocytic leukemia: recommendations of the French CLL Study Group (FILO). Hemasphere, 4(5): 87-91.

[5] Reuter, S., Gupta, S. C., Chaturvedi, M. M. and Aggarwal, B. B. 2010. Oxidative stress, inflammation, and cancer: how are they linked? Free Radical Biology and Medicine, 49(11): 1603–1616.

[6] Chung, Y. J., Robert, C., Gough, S. M., Rassool, F. V, and Aplan, P. D. 2014. Oxidative stress leads to increased mutation frequency in a murine model of myelodysplastic syndrome. Leukemia Research, 38(1): 95–102.

[7] Wrede, J. E., Sundram, U., Kohler, S., Cherry, A. M., Arber, D. A. and George, T. I. 2005. Fluorescence in situ hybridization investigation of cutaneous lesions in acute promyelocytic leukemia. Modern Pathology, 18(12): 1569–1576.

[8] Devi, G. S., Prasad, M. H., Saraswathi, I., Raghu, D., Rao, D. N. and Reddy, P. P. 2000. Free radicals antioxidant enzymes and lipid peroxidation in different types of leukemias. Clinica Chimica Acta, 293(1–2): 53–62.

[9] Zhang, B., Pan, C., Feng, C., Yan, C., Yu, Y., Chen, Z., Guo, C. and Wang, X. 2022. Role of mitochondrial reactive oxygen species in homeostasis regulation. Redox Report, 27(1): 45–52.

[10] Irigaray, P. and Belpomme, D. 2020. Circulating free methylglyoxal as a metabolic tumor biomarker in a rat colon adenocarcinoma model. Molecular and Clinical Oncology, 12(4): 311–316.

[11] Alhmoud, J. F., Woolley, J. F., Al Moustafa, A.-E. and Malki, M. I. 2020. DNA damage/repair management in cancers. Cancers, 12(4): 1050.

[12] Checa, J. and Aran, J. M. 2020. Reactive oxygen species: drivers of physiological and pathological processes. Journal of Inflammation Research, 1057–1073.

[13] Zhou, D. R., Eid, R., Miller, K. A., Boucher, E., Mandato, C. A. and Greenwood, M. T. 2019. Intracellular second messengers mediate stress inducible hormesis and Programmed Cell Death: A review. Biochimica et Biophysica Acta (BBA)-Molecular Cell Research, 1866(5): 773–792.

[14] Yavasoglu, I., Tombuloglu, M., Kadikoylu, G., Donmez, A., Cagırgan, S. and Bolaman, Z. 2008. Cholesterol levels in patients with multiple myeloma. Annals of Hematology, 87: 223–228.

[15] Chow, S., Buckstein, R. and Spaner, D. E. 2016. A link between hypercholesterolemia and chronic lymphocytic leukemia. Leukemia and Lymphoma, 57(4): 797–802.

[16] Mozessohn, L., Earle, C., Spaner, D., Cheng, S. Y., Kumar, M. and Buckstein, R. 2017. The association of dyslipidemia with chronic lymphocytic leukemia: a population-based study. JNCI: Journal of the National Cancer Institute, 109(3): 1856-1858.

[17] Sankanagoudar, S., Singh, G., Mahapatra, M., Kumar, L. and Chandra, N. C. 2017. Cholesterol homeostasis in isolated lymphocytes: A differential correlation between male control and chronic lymphocytic leukemia subjects. Asian Pacific Journal of Cancer Prevention: APJCP, 18(1): 230.

[18] Demirci-Çekiç, S., Özkan, G., Avan, A. N., Uzunboy, S., Çapanoğlu, E. and Apak, R. 2022. Biomarkers of oxidative stress and antioxidant defense. Journal of Pharmaceutical and Biomedical Analysis, 209: 114477.

Banana Peel as an Adsorbent for Brilliant Black Removal in Aqueous Solutions

Tiba SALEH GHANI AL-OKAIDAT [1], *Suhad JUMBAZ* [1], *M. Bora AKIN* [1*]

[1] *Department of Chemical Engineering, Çankırı Karatekin University, Çankırı, Turkiye*

Abstract

Banana peels have been used as a potential adsorbent for the removal of various pollutants from aqueous solutions. In the literature, the efficacy of banana peel-based adsorbents in removing cyanide, selected metals, dyes, Fe (II) ions, cadmium, lead (II), brilliant green, and congo red from wastewater has been demonstrated [1-5]. This study investigates the adsorption capacity of the adsorbent produced by simply drying the banana peel without any pre-treatment, in the removal of Brilliant Black dye from wastewaters. The effects of variables such as time, initial dye concentration, amount of adsorbent, and temperature on the adsorption of Brilliant Black onto banana peel from wastewater have been examined.

Keywords: *Wastewater, Adsorption, Congo Red, Banana peel, Adsorbent*

1. Introduction

The effectiveness of banana peels as an adsorbent for the removal of various pollutants from aqueous solutions has been investigated in numerous studies. A study by Arunakumara et al. (2013) demonstrated the efficacy of banana peels in removing metals from contaminated waters [1]. Additionally, Deshmukh et al. (2017) examined the removal of cadmium from aqueous solutions using dried banana peels as an adsorbent [2]. Moreover, Abdelaziz et al. (2022) explored the removal of Fe+3 and Pb+2 ions from aqueous solutions using banana peels [3]. Furthermore, a study conducted by Singh et al. (2022) has shown that banana peels are effective in decontaminating the cationic dye brilliant green [4]. Similarly, Mondal and Kar (2018) have demonstrated the potential of banana peels in removing Congo red from aqueous solutions [5]. Other studies have found them to be effective as adsorbents for the removal of copper from water [6] and the removal of atrazine and ametryne [7].

In this study, the adsorption capacity of banana peels for brilliant black was investigated, while examining the effect of parameters such as temperature, initial dye concentration, amount of adsorbent, and time.

2. Materials and Methods

Brilliant Black was obtained from Sigma Aldrich. The bananas obtained were separated from their peels, which were then dried at a temperature of 80 °C using a vacuum oven. Subsequently, they were ground and then used in adsorption experiments. In the Brilliant Black adsorption experiments, a magnetic stirrer (IKA) and a UV spectrophotometer (Shimadzu) were used.

In this study, calibration curves for Brilliant Black adsorption experiments were created in light of different concentrations by diluting from a 1000 mL stock solution. The wavelength on the spectrometer was set to 571 nm for measuring the absorbance values of Brilliant Black. In the experiments determining the adsorption capacity, the initial concentrations were prepared as 10, 25, 50, 100, 200, 300, 400, 500, 750, and 1000 mg/L, respectively. The experiments were carried out at a temperature of 25 °C with 0.5 mg/L of adsorbent used in 100 mL of solution. In time-dependent experiments, measurements were recorded at 0, 2, 5, 10, 20, 30, 45, 60, 90, 180, 240, 300, 360, 420, and 1440 minutes using a dye concentration of 200 mg/L. Subsequently, concentration values were calculated using the calibration curve. Experiments were conducted at temperatures of 5 °C, 25 °C, and 40 °C to examine the effect of temperature on the adsorption process. Adsorbent doses of 0.3, 0.5, 1, and 2.5 mg/L were used to study the effect of adsorbent dose. The adsorption capacity was calculated from the equation below:

* Corresponding author. *e-mail address: mbakin@karatekin.edu.tr*

$$q_e = \frac{(C_0 - C_e)}{m} \cdot V \quad (1)$$

Here, q_e represents the capacity of the adsorbent (mg/g), C_0 is the initial concentration of the adsorbate (mg/L), C_e is the equilibrium concentration of the adsorbate (mg/L), V (mL) is the volume of the solution, and m is the weight of the adsorbent used (g).

3. Results and Discussion

3.1. Effect of Initial Dye Concentration

g/L of adsorbent for different concentrations. The q_e values obtained against the concentrations studied are presented in Figure 1. The highest adsorption capacity within the initial concentrations was achieved with 0.0111 mol/kg at 750 mg/L. An increase in the q_e value is observed up to an initial concentration of 750 mg/L. A concentration of 200 mg/L was chosen as the working concentration, and this concentration was used in the examination of the other parameters.

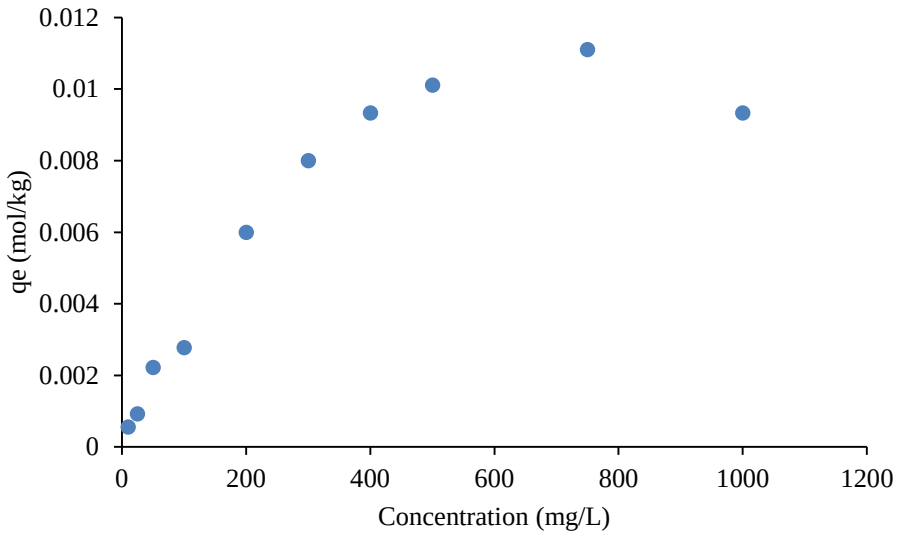

Figure 1. Effect of dyestuff initial concentrations on adsorption capacity.

3.2. Effect of Time

For the experiment in which the effect of time on q_e was examined, 200 mg/L was chosen as the initial concentration. To find the q_e value at the selected concentration, concentration values were found by measuring samples taken at certain times. When Figure 2a is examined, it is understood that the concentration decreases over time, meaning that the adsorbent does its job. At the end of 1440 minutes, the dye concentration decreases to 184.37 mg/L. The calculation made using concentrations shows the change of q_e value with time (Figure 2b). At the end of 1440 minutes, the q_e value is 0.0193 mol/kg at an initial dye concentration of 200 mg/L.

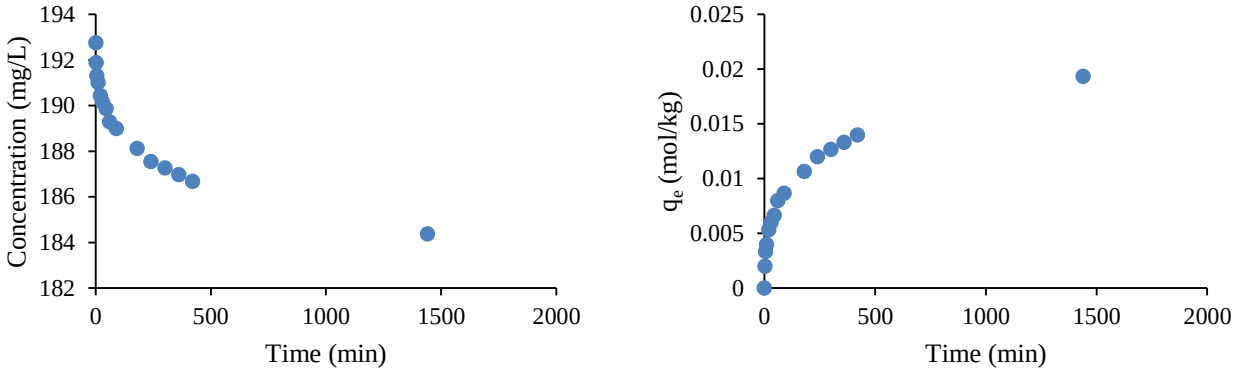

Figure 2. Effect of 0.5 mg/L adsorbent at 200 mg/L initial dye concentration: a) Concentration and b) adsorbent capacity

3.3. Effect of Adsorbent Amount

As the amount of adsorbent increases, the q_e value becomes 0.022 at 0.3 mg/L and 0.019 mol/kg at 0.5 mg/L. While the q_e value is 0.008 mol/kg in the amount of 1 mg/L adsorbent, this value decreases to 0.003 mol/kg in the amount of 2.5 mg/L adsorbent (Figure 3a). The decrease in q_e appears to be linear. The regression coefficient was obtained as 0.82. It is seen that the highest adsorption percentage is 4.35% with the use of 0.5 mg/L adsorbent, and the closest value to this value is 3.45% with the use of 1 mg/L adsorbent (Figure 3b).

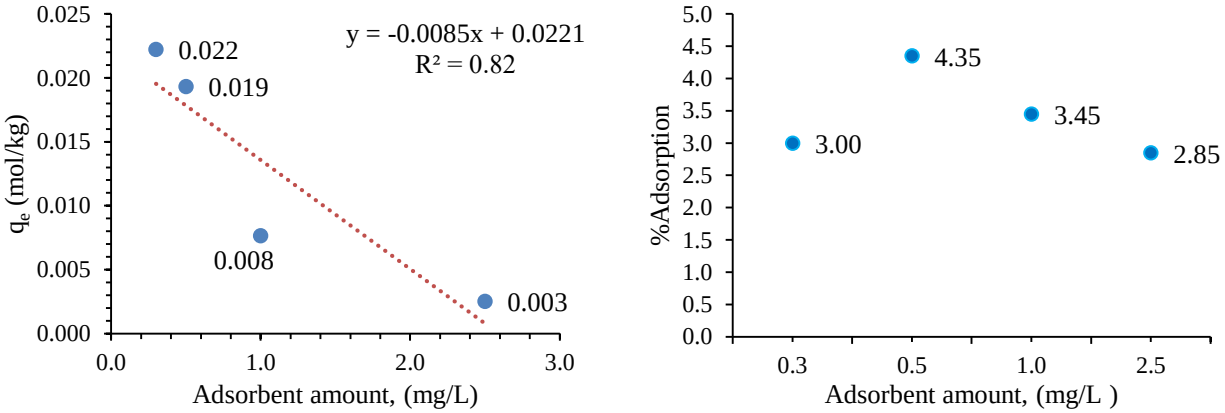

Figure 4. Effect of adsorbent amount a) adsorption capacity, b) Adsorption percentage

3.4. Effect of Temperature

In experiments conducted at 5 °C, 25 °C and 40 °C, where the effect of temperature on adsorption capacity was examined, q_e values were 0.013 mol/kg at 5 °C, 0.006 mol/kg at 25 °C and 0.002 mol/kg at 40 °C, respectively. According to the data obtained, the q_e value decreases as the temperature increases (Figure 4).

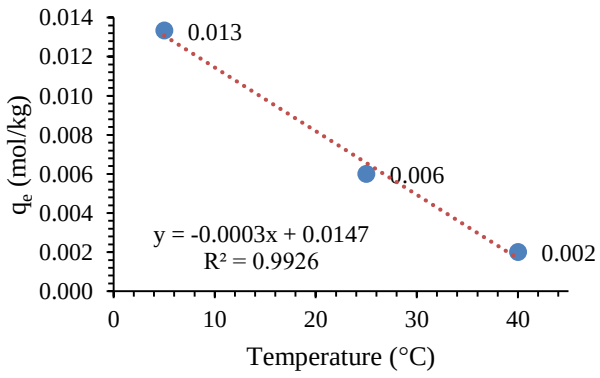

Figure 4. Effect of temperature on adsorption capacity

4. Conclusion

The data obtained in the study show that it is possible to use dried banana peels in the adsorption of Congo Red. It was observed that the q_e value increased with increasing initial dye concentration. The highest q_e value was found to be 0.0111 mol/kg at a dye concentration of 750 mg/L. By using 0.5 mg/L adsorbent at an initial concentration of 200 mg/L, the q_e value was obtained as 0.019 mol/kg. With this amount of adsorbent, the adsorption efficiency is 4.35%. The q_e value was obtained as 0.013 mol/kg at 40 °C. The q_e value was found to be 0.002 mol/kg at 5 °C. Adsorption capacity decreases with increasing temperature.

Acknowledgement

All experimental work was conducted in the Chemical Engineering Department Laboratory at Çankırı Karatekin University. The authors would like to thank the Chemical Engineering Department.

References

[1] I. Arunakumara, K.K., Walpola, B.C., Yoon, M-H. (2013). Banana Peel: A Green Solution for Metal Removal From Contaminated Waters. Korean J Environ Agric. https://doi.org/10.5338/kjea.2013.32.2.108.
[2] Deshmukh, P.D., Khadse, G.K., Shinde, V.M., Labhasetwar, P. (2017). Cadmium Removal From Aqueous Solutions Using Dried Banana Peels as an Adsorbent: Kinetics and Equilibrium Modeling. J Bioremediation \& Biodegrad. https://doi.org/10.4172/2155-6199.1000395.
[3] Abdelaziz, M.A., Taha, M., Gahly, M.S., Hefnawy, H.T. (2022). Removal of Fe+3 And Pb+2 Ions From Aqueous Solutions by Adsorption Using Banana Peels. Zagazig J Agric Res. https://doi.org/10.21608/zjar.2022.278248.
[4] Singh, S.K., Gupta, H., Dhiman, S., Sahu, N.K. (2022). Decontamination of Cationic Dye Brilliant Green From the Aqueous Media. Appl Water Sci. https://doi.org/10.1007/s13201-022-01596-5.
[5] Mondal, N.K., Kar, S. (2018). Potentiality of Banana Peel for Removal of Congo Red Dye From Aqueous Solution: Isotherm, Kinetics and Thermodynamics Studies. Appl Water Sci. https://doi.org/10.1007/s13201-018-0811-x.
[6] Hossain, MA. (2012). Removal of Copper From Water by Adsorption Onto Banana Peel as Bioadsorbent. Int J Geomate. https://doi.org/10.21660/2012.4.3c.
[7] Silva, C.R., Gomes, T.F., R. Andrade, G.C., Monteiro, S.H., Dias, A.C., Zagatto, E.A.G., et al. (2013). Banana Peel as an Adsorbent for Removing Atrazine and Ametryne From Waters. J Agric Food Chem 2013. https://doi.org/10.1021/jf304742h.

Effect of Pressure on Optoelectronic Properties of Ir3ZrC Compound

Yasemin Öztekin ÇİFTCİ [1*], ***İlknur Kars DURUKAN*** [1]

[1] *Science Faculty, Physics Department, Gazi University, Ankara, Turkey*

Abstract

Ever since their discovery by Russian mineralogist Perovski in 1839, perovskite materials have been the subject of extensive study. This diverse class includes various structures like perovskite, antiperovskite, inverse perovskite, double perovskite, and anti-double perovskite, each characterized by unique compositions and coordination geometries. Ternary nitrides or carbides with a cubic antiperovskite structure fall into a distinct class of materials described by the general formula AXM3 or M3AX, where A represents a main group III-V element, X stands for carbon or nitrogen, and M is a transition metal. Our focus in this study is on the compound Ir3ZrC, which adopts an antiperovskite structure, belongs to the Pm3m space group, and exhibits a cubic arrangement. Using the first-principles method with Density Functional Theory (DFT), we conducted a comprehensive theoretical analysis of the compound. This investigation delved into the effects of pressure on its structural, electronic, and optical properties. Understanding how compounds deform under compression and the consequent changes in their physical and chemical characteristics is crucial for comprehending the nature of solids, given the importance of pressure as a key parameter. We compared lattice constants, volumes, bulk modulus, and its first derivative under pressure with both experimental and theoretical data at zero pressure, providing a detailed analysis of their variations. The values of the studied compound at zero pressure were consistent with literature values, and Ir3ZrC demonstrated stability according to Born criteria across different pressure values. Furthermore, its electronically metallic nature was maintained even under the influence of pressure. In conclusion, we utilized the complex dielectric function to explore the optical properties of Ir3ZrC, presenting a thorough evaluation of optical parameters under pressure. The study not only examines the pressure effect but also investigates the optical properties of the perovskite cubic compound Ir3ZrC for the first time, contributing valuable data for experimental studies and enriching the existing literature.

Keywords: *: DFT, B2 structure, electronic properties, elastic, properties, vibrational properties*

1. Introduction

Antiperovskites have become a subject of widespread interest due to their distinct physical, chemical, and thermodynamic properties. Representing electronically inverted perovskites, they constitute a growing class of versatile materials, offering an active and promising research field for materials scientists. The inverse counterparts, antiperovskites X3BA, are derivatives of electronically inverted perovskites, with A as a cation located at (0, 0, 0), B (C, N) at (1/2, 1/2, 1/2), and the transition metal atom X at (0, 1/2, 1/2). The ideal antiperovskites exhibit a cubic structure with the Pm-3m space group [1].

The unique coordination environment of cation X, characterized by the X-X distance and linear two-fold coordination, plays a pivotal role in determining crystal field strength. Their inherent structural flexibility, accommodating diverse elements from the periodic table, has garnered substantial research interest on a global scale [2]. Recent progress in antiperovskite research has unveiled exceptional properties, including giant magnetoresistance (GMR), nearly zero temperature coefficients of resistivity, and magnetostriction. These properties position them as promising candidates for various industrial applications, particularly in magnetic field sensors used for data reading in hard disk drives, biosensors, and microelectromechanical systems (MEMS). Furthermore, owing to their favorable thermoelectric properties, antiperovskites hold potential for addressing the energy crisis through electricity generation and solid-state refrigeration [3].

A decade ago, the authors of [4] predicted a diverse range of new ternary carbides, denoted as M_3AC, utilizing empirical structural criteria for evaluating the stability of cubic antiperovskites. This assessment, based on the tolerance factor (t), determined whether the sizes of octahedral voids in closely packed M_3A crystals could accommodate B, C, or N atoms. In the specified tolerance factor interval ($0.899 < t < 1.123$), it was suggested

* Corresponding author. *e-mail address:yasemin@gazi.edu.tr.*

that four Ir-based Ir3MC carbides—Ir3TiC, Ir3ZrC, Ir3NbC, and Ir3TaC—could potentially exist. It is imperative to underscore that the empirical methodology employed in this context does not yield substantive insights into the intrinsic physical properties of the envisioned materials. Rather, it is contingent upon the judicious selection of constituent elements based on their fitting atomic radii. However, the projected distinctive electronic and magnetic attributes of Ir3MC compounds emanate from the intricate interplay within the antiperovskite structure, wherein two sub-lattices are configured, featuring open-shell 5d-(3d,4d)-atoms. The technological significance of Ir3MC compounds is premised on the inclusion of the platinum-group metal Ir, renowned for its exceptional hardness, coupled with carbon. The heightened attention directed towards carbides and nitrides of platinum group metals (M = Ru, Rh, Pd, Os, Ir, Pt) has gained momentum, notably subsequent to the successful synthesis of platinum monocarbide PtC under high pressure and temperature conditions utilizing the laser-heated diamond anvil cell technique, as documented by Ono et al. [5]. This focus is distinctly oriented towards materials exhibiting potential superior hardness and minimal compressibility. These considerations derive from the guiding principle that prospective ultra-hard materials should amalgamate concise and robust covalent bonds, involving 2p-atoms such as B, C, or N, with the heightened valence charge density characteristic of transition metal compounds [6-8]. Moreover, given the chemical stability and notably high melting point (circa 2454o C) of iridium, materials encompassing Ir-based alloys and compounds are of particular interest for applications necessitating extreme temperature resilience.

Here, we have studies pressure effects on structural, electronic and optical properties of Ir3ZrC compound using first-principles methods.

2. Materials and Methods

In this investigation, we conducted structural optimizations, electronic property calculations, and evaluations of optic properties using the Vienna ab initio simulation package (VASP) code [9-11], based on density functional theory. For describing exchange and correlation effects, the Perdew-Burke-Ernzerhof (PBE) [12] generalized gradient approximation (GGA) [13] was implemented. Electron-ion interactions were addressed using the all-electron projector augmented-wave (PAW) [14] method, treating the valence electrons of B, C, and N atoms ($2s^2 2p^1$, $2s^2 2p^2$, and $2s^2 2p^3$, respectively).To maintain total energy convergence at around 2 meV/atom, we utilized a plane-wave kinetic energy cutoff of 800 eV and 18 × 18 × 18 k-point grids under the Monkhorst-Pack scheme [15].

3. Results and Discussion

3.1. Structural and ElectronicProperties

The Ir3ZrC anti-perovskite compound exhibit an ideal cubic structure characterized by the space group (Pm-3m). In this structure, X ions are situated at the corner positions, carbon resides at the body center, and Rh occupies the face center of the cube. The specific Wyckoff positions for these elements are Zr: 1a (0,0,0); C: 1b (1/2,1/2,1/2); Ir: 3c (1/2,1/2,0), respectively as seen in Fig.1. To determine the equilibrium lattice constants, geometric optimizations calculation were performed using full relaxations by minimizations of energies. Table 1 includes some experimentally reported lattice constants for comparative purposes. Our computed lattice parameter is comparable with the values reported in Ref. [16], attributed to the utilization of the GGA functional. The total energy of the unit cell is calculated by varying the unit-cell volume(see Fig.2). Subsequently, the computed total energies plotted against volume are fitted using Murnaghan's equation of state (EOS) [17]. This fitting process is crucial for determining fundamental ground state properties, including the equilibrium lattice constant (a_0), bulk modulus (B_0), and ground state unit cell energy (E). These parameters are presented in Table 1, along with theoretical results.The determined bulk modulus for Ir3ZrC as 260.78 GPa is lower than compared to values in [16]. The pressure derivative of bulk modulus, indicative of resistance to volume change under mechanical effects, is 4.54.

Table 1. Structural parameters for Ir3ZrC

	a(A)	B(GPa)	B’	Etot (eV)/atom
This study	4.169	260.76	4.54	-44.61
Theory [16]	4.164	266.5	-	-

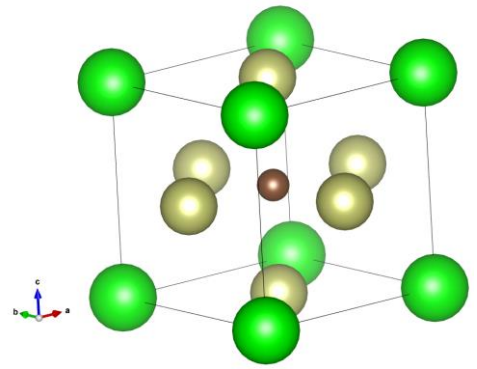

Figure. 1 Unitcell of Ir3ZrC

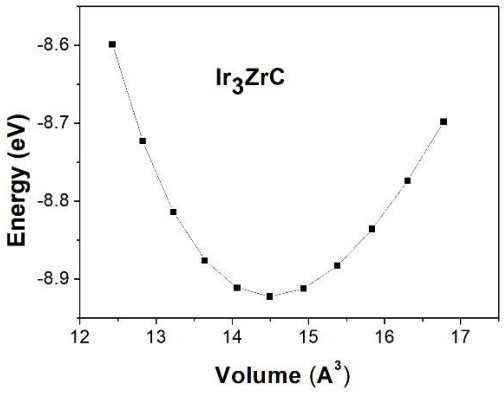

Figure.2 Energy- volume curves for Ir3ZrC

The technological relevance of solid-state materials hinges significantly on the intricate behavior exhibited by valence and conduction electrons within the material matrix. This behavior, in turn, is intricately tied to the energy dispersion characteristics (E(k)) within the Brillouin zone. Our investigative focus is dedicated to the computational analysis of the electronic band structure of Ir3ZrC, leveraging an optimized crystal structure for precision. Illustrated in Figure 3 are the electronic energy dispersion curves under varying pressures along high-symmetry directions within the Brillouin zone of Ir3ZrC. By aligning the Fermi level at 0 eV, the metallic nature of Ir3ZrC becomes evident, with overlapping valence and conduction bands suggesting electron conductivity proximate to the Fermi level, as showcased in Figure 3. The distinctive features discerned in the presented band structure unequivocally affirm the existence of multiple bands with diverse degrees of dispersion intersecting the Fermi level, thereby corroborating the metallic character of the Ir3ZrC ternary compound. Bands exhibiting heightened dispersion along the M and R directions underscore their pivotal role in influencing charge transport properties, whereas those intersecting the Fermi level in the vicinity of the Γ-X and Γ-L directions display reduced dispersion. The conspicuous dispersion observed in specific bands implies a diminished effective mass for charge carriers, indicative of heightened charge mobility. Noteworthy is the presence of lowly dispersive E(k) regions around the Γ points, emphasizing substantial anisotropy in charge transport along distinct crystallographic directions and within the momentum space of the scrutinized material.

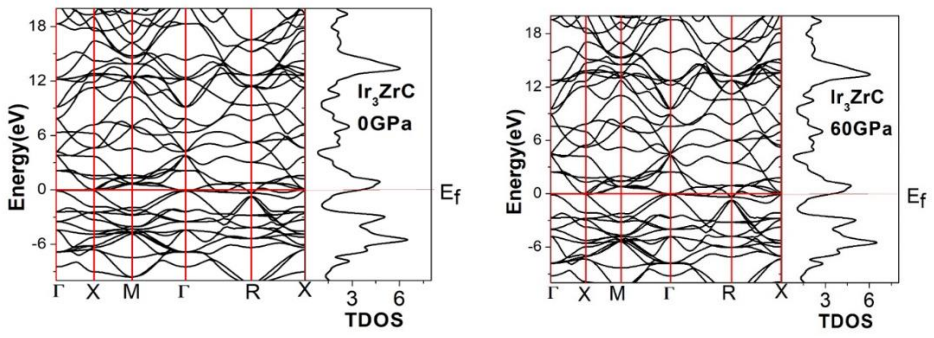

Figure 3. Electronic band structure for Ir3ZrC at 0GPa and 60 GPa

In Figure 4, we present the partial density of states (PDOS) for Ir3ZrC, illustrating distinct contributions from the Fermi level, valence band, and conductivity band. Examining the total density of states (TDOS) and PDOS plots for Ir3ZrC reveals that its metallic nature primarily stems from the occupancy of Ir-d, Zr-d, and C-p states at the Fermi level. Specifically, Ir-d and C-p states contribute significantly to the valence band, while Zr-d states play a major role in the conduction band. Upon scrutinizing Figure 4 at 0 and 60 GPa, we observe slight changes in the shapes of the peaks under pressure. This suggests that the structural integrity of the Ir3ZrC compound remains largely unaffected, with no discernible structural phase transformation observed under pressures up to 60 GPa. Notably, an increase in pressure leads to a noticeable shift of the peaks toward the Fermi level.

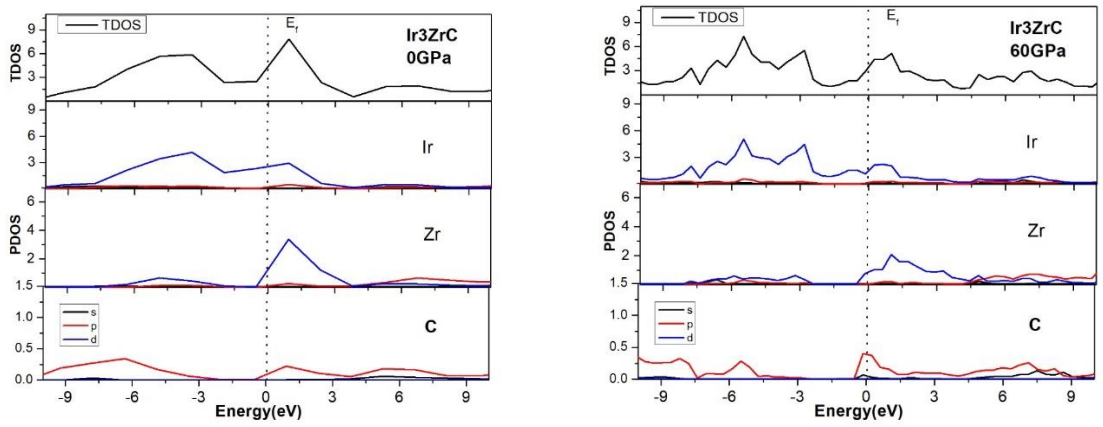

Figure 4. Total and partial DOS for Ir3ZrC at 0GPa and 60GPa

3.3 Optical Properties

The potential application of a material in optoelectronic devices is contingent on its optical characteristics under varying pressure conditions. In this study, we investigate the pressure-dependent optical properties, including absorption, photoconductivity, reflectivity, refractive index, and dielectric function, providing insights across various application fields. Our examination of optical spectra reveals shifts in electrical states, band constructions, bond types, and internal material structures. The Kramers–Kronig transformation enables the derivation of the frequency-dependent complex dielectric function, denoted as $\varepsilon(\omega) = \varepsilon 1(\omega) + i\varepsilon 2(\omega)$, and is linked to relative permittivity.

In Figures 5, the real and imaginary parts of the dielectric function for Ir3ZrC perovskites are presented under varying pressures, covering photon energies up to 20 eV. A Gaussian smearing of 0.5 eV is applied in all calculations, with the analysis focused on the [100] polarization vector. The real part exhibits an initial increase at low photon energy, followed by a rapid decline with higher photon energy. The pressure-induced perovskite displays an increased dielectric constant within the visible range. At 0, 30, and 60 GPa pressures, the static dielectric constants are measured at 170.3, 176.2, and 155.4, respectively, suggesting the potential of Ir3ZrC as a promising dielectric material. The imaginary part, indicative of optical absorption/transitions and the material's band gap, exhibits heightened values and shifted peaks towards lower incident photon energy under applied pressure. Conversely, in the higher photon energy region, the imaginary part diminishes to zero around 20 eV, indicating the material's transparency beyond this threshold. These findings provide valuable insights into the pressure-dependent optical properties of Ir3ZrC and their implications for optoelectronic devices.

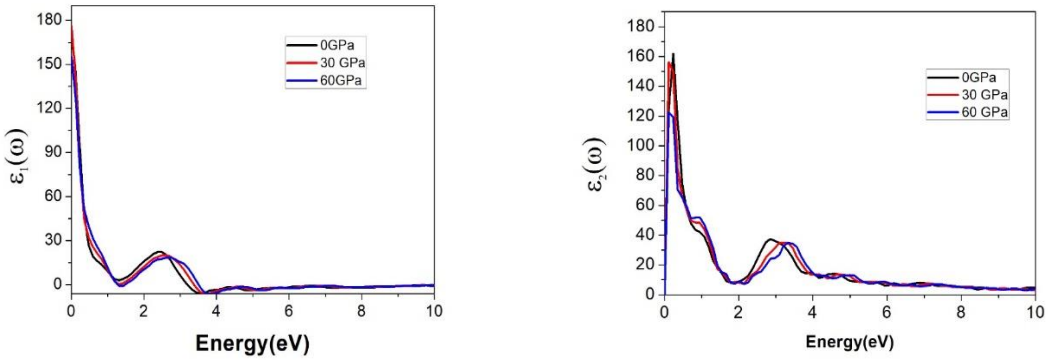

Figure 5. Real and imaginary dielectric function for different pressure of Ir3ZrC

In Figure 6, the real part of the refractive index is depicted, representing the phase velocity of electromagnetic wave propagation within Ir3ZrC. The maximum value of n is attributed to electron transitions from the valence to the conduction band. Peaks in the refractive index correspond to the generation of electron-hole pairs for conduction and interband optical transitions between valence and conduction bands. The fourth peak around 14.0 eV, known as the plasmon peak, arises from the collection of excitons of free carriers. These distinct responses

among materials contribute to variations in their band gaps. At 0, 30, and 60 GPa pressures, the maximum refractive index values are observed at zero photon energy, suggesting potential applications of Ir3ZrC in devices such as QLEDs, OLEDs, solar cells, and waveguides. Additionally, a noticeable pressure effect is evident, with the refractive index decreasing under pressure.

Reflectivity, a pivotal optical property determining material surface characteristics for applications in optoelectronics and solar cells, is presented in Fig. 6(b). reflectivity is determined by considering the ratio of incident to reflected power. At zero pressure, reflectivity was consistently low for Ir3ZrC compound. Upon the application of pressure, reflectivity and loss function values experienced significant increases, potentially attributed to changes in structural alterations. The appearance of peaks at 4.8 eV is attributed to the inter-band transition among valence and conduction bands. In contrast, energy ranging from 35 eV to 45 eV exhibits the minimum value of reflectivity as a consequence of collective plasma resonance. The presence of L(ω) peaks below 2 eV underscores the efficiency of the Ir3ZrC component as an optical absorption layer within the visible photon spectra and infrared (IR) range. Notably, the loss function of I3ZrC remains relevant for photon energies up to 50 eV. In essence, the loss function of Ir3ZrC plays a pivotal role in its performance, underscoring its importance in the design and optimization of this materials for specific applications.

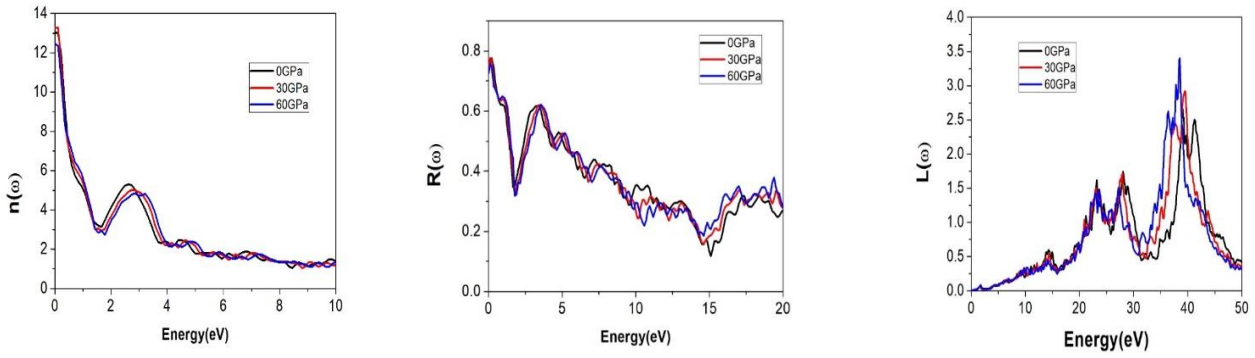

Figure 6. Refractive index, reflectivity and loss function for different pressure of Ir3ZrC

4. Conclusion

We conducted a thorough examination of the impact of hydrostatic pressure on the structural, electronic, and optical properties of Ir3ZrC using rigorous first-principles methods. The results obtained for the structural parameters are in excellent agreement with previously reported data. Analysis of the electronic band structure and density of states unveiled the metallic nature of Ir3ZrC. Notably, an observed reduction in lattice constant was identified with an increase in hydrostatic pressure. Furthermore, as the pressure was elevated up to 60 GPa, there was a discernible upward trend in static dielectric constant, plasma frequency, and static refractive indices. These findings offer valuable insights for the comprehension and advancement of optoelectronic devices utilizing Ir3ZrC, particularly those engineered to operate effectively under varying pressure conditions..

References

[1] D. Cherrad, L. Selmani, D. Maouche, M. Maamache, First principles calculations on elasticity, electronic structure and bonding properties of antiperovskites ANTi3 (A= Al, in and Tl), J. Alloys Compd. 509 (2011) 4357–4362.
[2] Y. Wang, H. Zhang, J. Zhu, X. Lü, S. Li, R. Zou, Y. Zhao, Antiperovskites with exceptional functionalities, Adv. Mater. 32 (2020), 1905007.
[3] M. Bilal, S. Jalali-Asadabadi, R. Ahmad, I. Ahmad, Electronic properties of antiperovskite materials from state-of-the-art density functional theory, J. Chem. (2015) 1–11, 2015.
[4] K. S. Alexandrov, and B. V. Besnosikov. *Perovskites: present and future*. Siberian Branch, Russ. Acad. Sci, Novosibirsk, 2004 *(in Russian).*
[5] S. Ono, T. Kikegawa, and Y. Ohishi, Solid State Commun. **133**, 55 (2005).
[6] R. B. Kaner, J. J. Gilman, and S. H. Tolbert, Science **308**, 1268 (2005).

[7] J. J. Gilman, R. W. Cumberland, and R. B. Kaner, Int. J. Refract. Met. Hard. Mater. **24**, 1 (2006).
[8] J. B. Levine, S. H. Tolbert, and R. B. Kaner, Adv. Funct. Mater. **19**, 3519 (2009)
[9] G. Kresse, J. Hafner, (1993) Ab initio molecular dynamics for liquid metals, Phys. Rev. B 47 558.
[10] G. Kresse, J. Hafner, (1994) Ab initio molecular-dynamics simulation of the liquid metal–amorphous-semiconductor transition in germanium, Phys. Rev. B 49 14251.
[11] G. Kresse, J. Furthmuller, (1996) Efficiency of ab-initio total energy calculations for metals and semiconductors using a plane-wave basis set, Comput. Mater. Sci. 6 15.
[12] J.P. Perdew, J.A. Chevary, S. Vosko, K.A. Jackson, M.R. Pederson, D.J. Singh, C. Fiolhais, (1992) Atoms, molecules, solids, and surfaces: applications of the generalized gradient approximation for exchange and correlation, Phys. Rev. B 46 6671.
[13] J. P. Perdew, in *Electronic Structures of Solids'91*, Ed. by P. Ziesche and H. Eschrig (Akademie, Berlin, 1991), p. 11.
[14] G. Kresse and D. Joubert, Phys. Rev. B **59**, 1758 (1999).
[15] H.J. Monkhorst, J.D. Pack, (1976) Special points for Brillouin-zone integrations, Phys. Rev. B 13 5188
[16] V.V. Bannikov, I.R. Shein, D.V. Suetin, Structural, elastic and electronic properties of Ir-based carbides-antiperovskites Ir3MC (M= Ti, Zr, Nb and Ta) as predicted from first-principles calculations, Computat. Condens. Matter. 11 (2017) 60–68.
[17] F.D. Murnaghan, Proc. Natl. Acad. Sci. USA 30, 244, (1944).

Column-Author Matching in Turkish Texts Using SVM and MLP Algorithms

İbrahim DOĞAN[1,*], ***Sedat KORKMAZ***[2]

[1] *Institute of Graduate Studies, Faculty of Engineering and Natural Sciences, Computer Engineering, Konya Technical University, Konya/Turkey*

[2] *Institute of Graduate Studies, Faculty of Engineering and Natural Sciences, Computer Engineering, Konya Technical University, Konya/Turkey*

Abstract

In this study, a column-author matching was performed using columns taken from the website of a newspaper. A data set containing more than 3 thousand data was created by combining the articles written by people who are newspaper writers in different fields, some other information about the articles and the names of the authors. Data pre-processing work was carried out on the created data set and data set optimisation was achieved. By running Zemberek library functions on the optimised data set, morphological analysis was performed, stop words were removed from the text and new attributes were extracted and included in the data set. The data was normalized using the Min-Max Normalization technique and digitised with TF-IDF, Word Bag and Word-Sentence Distribution Vectors. The 67% of the dataset was used to train the machine learning classification algorithms, while the remaining 33% was used to measure the author-artwork matching success of the algorithm. Support Vector Machines (SVM) and Multilayer Perceptrons (MLP) were used in the study and the highest success rate was obtained with the SVM algorithm with 83%.

Keywords: *Machine Learning, Natural Language Processing, Text Classification, Zemberek Library.*

1. Introduction

Language is an advanced communication tool that enables people to express their feelings and thoughts using words or signs. Languages are categorized under two main headings: natural languages and artificial languages.

Natural language is a decodable multi-level system with a certain rule structure that people use in their daily lives to share their ideas, wishes and thoughts with each other. English, German, Spanish, French and Chinese are examples of natural languages that are widely used in the world.

Artificial languages, on the contrary to natural languages, are languages whose source is known, created and developed by some people or communities for a purpose. It is possible to analyze artificial languages in two different categories. These are programming languages used in computer science (Java, C#, C++, Python, HTML, etc.) and languages used by some communities as spoken languages (Esperanto, Bâleybelen, Ido, Elvish, Klingon, etc.).

When the history of humanity is analyzed, the leaps provided by some developments draw attention. Language is one of these developments. Thanks to language, changes and progress have been made in many fields such as faith, culture, art and positive sciences. Today, many applications are being developed in the field of Natural Language Processing (NLP) due to the intensification of studies in the field of machine learning, linguistics and artificial intelligence, the rapid development of technology and the increase in human-computer interaction.

Many sciences and disciplines are utilized in the development of NLP applications. NLP is a bridge that works interactively with the fields of artificial intelligence, linguistics, cognitive psychology and data science and establishes the relationship between machine language and spoken language by taking text or audio data as input and providing the desired outputs within certain rules. NLP is a combination of Natural Language Understanding (NLU) and Natural Language Generation (NLG) processes [1]. Although we are not aware of it, NLP is frequently encountered in our daily lives. For example; voice response systems, text summarisation applications, spell checking and word suggestion systems are just some of the areas of use. Considering the studies carried out, it is better understood how intertwined NLP is with our lives and how it is a factor that facilitates our lives.

* Corresponding author. *e-mail address: ibrahimdgn023@gmail.com*

The working steps of NLP are generally analyzed under four main headings. These are respectively; Vocabulary Science, Syntactic Analysis, Semantic Analysis and Discourse Analysis. In the morphological analysis stage, the smallest structural units of words, roots and affixes, are examined separately to determine the type and form. In the syntactic analysis stage, the relationship between the words in the sentence is interpreted. Semantic analysis is the method used to determine which feelings and thoughts are intended to be expressed in the sentences in the texts. Discourse analysis is the method aiming to analyse the main idea of the text correctly.

The rapid development of technology and the widespread use of the internet has led to the provision of many services in this field, easy access to data and the number of data has increased exponentially day by day. This situation has brought with it the difficulty of accessing the correct and desired data. For this reason, especially the extraction of meaningful data from meaningless data and the classification of such data according to certain qualities have gained importance.

In this study, the articles written by newspaper writers in different fields were analyzed by using Numerical Style Analysis (Stylometry), NLP, a sub-branch of artificial intelligence, and machine learning methods, and it was aimed to accurately match the authors of the articles in question.

2. Materials and Methods

2.1. Software Packages

The coding of the project was done using Anaconda distribution version 1.9.0, Python version 3.9.12 and Jupyter Notebook version 6.4.11 development environment. The Java-based Zemberek library version 0.17.1 was downloaded as a Jar file, the Zipfile library was used to read the modules in the Jar file, and version 1.3 of the Jpype library was used to integrate it into Python. Version 1.4.1 of the Pandas library was used for data manipulation, version 1.20.3 of the Numpy library was used for high-level mathematical operations, and version 1.0.2 of the Scikit-learn library was used for machine learning models and some preprocessing modules.

2.2. Data Set

The data set was obtained from the digital platform of a newspaper using Web Scraping method. There are 208 columnists writing in different fields (agenda, sports, market, etc.) in the dataset. The dataset includes a total of 3417 columns, with each columnist having at least 1 and at most 40 columns. The data are kept in table format and consist of the columns of the date the column was written, the name of the author, the headline of the column, the link to the newspaper website from which the column was taken and finally the text of the column.

2.3. Data Preprocessing

Data preprocessing is defined as a set of methods that should be applied before starting to work with the data set in order to ensure that machine learning algorithms can benefit from the data set at the highest level and obtain the most accurate results [2, 3]. The data preprocessing techniques used in this study are listed below.

2.3.1. Cleaning Stop Words from the Data Set

Insignificant words that are used for grammatical rules or to ensure sentence integrity and do not carry any information about the text they are found in are labelled as stop words. These stop words are removed from the data set in the data preprocessing stage in order to increase the classification success and reduce the processing time and data size.

2.3.2. Min-Max Normalization

Normalization is used to reduce data size, to reduce data clutter by formatting within a scale without proportionally distorting the difference between very distant numerical values, to make the data set more meaningful and interpretable and to provide better results of machine learning applications [4].

In this study, the data set is scaled between 0 and 1 using the Min-Max Normalization technique. The minimum is the smallest value that the data can take and the maximum is the largest value that the data can take [5]. The Min-Max Normalization technique was performed using Equation 1. [6, 7].

$$x' = \frac{x_i - x_{min}}{x_{max} - x_{min}} \quad (1)$$

2.4. Zemberek

Zemberek was developed by Ahmet Afşın AKIN using Java programming language and it is a library that enables the application of NLP methods on Turkish texts [8]. With the help of the library, operations such as spell checking, sentence separation, correction of misspelled words, detection of written language, finding word roots and affixes can be easily performed.

2.4.1. Morphological Analysis

Morphological analysis is defined as the separation of roots and affixes of a word in order to determine its morphological structure. Since Turkish is a suffixal language, the suffixes to the word can cause changes in the structure of the word and change its meaning. For this reason, it becomes difficult to find the root and affixes of the word in suffixal languages such as Turkish [9].

In the Zemberek library, there is a special tree model designed to find the roots of Turkish words. The roots are placed and labeled on the tree according to their letter-based content. For example, the noun root "balo" is added to the tree and labelled with the letters B-A-L-O respectively. One of the most important advantages of the model is that it can be used by using or adding existing nodes without having to create separate nodes for each root. Thus, unnecessary nodes are not used and memory is saved [10].

2.4.2. Sentence Extraction/Splitting

Zemberek library can split the text into its sentences as well as its roots and suffixes. TurkishSentenceExtractor class is used for this. The class takes a text as input and returns separated sentences of the text as output [11]. At this stage, rule-based simple combinations and the Binary Averaged Perceptron model are used to determine the start and end points of the sentence.

2.5. Term Frequency-Inverse Document Frequency (TF-IDF)

Term Frequency-Inverse Document Frequency (TF-IDF) is a statistical method used to determine the importance of a term in a text within a dataset. TF refers to the frequency of the relevant term in the processed text and is calculated using Equation 2. When calculating the TF value, all words in the text are considered equally important [12].

$$f_{t,d} = \frac{Number\ of\ repetitions\ of\ the\ term}{Total\ word\ count\ in\ the\ document} \quad (2)$$

Document Frequency (DF) is the frequency of the related word in other texts and IDF (Inverse Document Frequency) is the logarithm of the DF value. IDF is a factor that decreases the weight of terms that occur frequently in the whole document and therefore have a higher frequency than other words in the text, and increases the weight of words that rarely occur in the document with low frequency and are more important for the document. As seen in Equation 3, the IDF value is calculated by taking the logarithm of the result obtained by dividing the total number of documents by the number of documents in which the relevant word occurs [13].

$$IDF = \log\left(\frac{Total\ number\ of\ documents}{Document\ with\ the\ term}\right) \quad (3)$$

TF-IDF is a frequency obtained by multiplying these two values and varies between 0 and 1. A higher TF-IDF value indicates that the word is more important for the text and represents the text more.

2.6. Classification Algorithms

This study employed two distinct classification algorithms, which are described below.

2.6.1. Support Vector Machine (SVM)

SVM is a supervised machine learning algorithm used to solve classification and regression problems. The method utilizes vectors to separate data clustered around certain attributes. These vectors separating the classes are characterised as hyperplanes. In order to increase the success of the classification, SVM prefers the vector that is the farthest distance from the data of all classes. This preferred vector is called the optimum hyperplane. The points or data closest to the optimum hyperplane are called support vectors. The gap between the supports is called Margin.

2.6.2. Multi-Layer Perceptron (MLP)

The MLP algorithm consists of 3 main parts. These are respectively: Input Layer, Hidden Layer and Output Layer.

The number of neurons in the input layer is equal to the length of the vector received as input. The number of neurons in the output layer is designed to be equal to the length of the vector to be obtained as a result of the model. The intermediate layers, consisting of at least one layer between the input and output layers, are called hidden layers. There should be at least one neuron in the hidden layer, but one neuron may not be enough to achieve the desired success rate. For this reason, various experiments are performed to determine the optimal number of neurons in the hidden layer of the model and the design that gives the most successful result is applied to the model. In other words, the number of hidden layers and the number of neurons in the hidden layer are determined by trial and error [14].

2.7. RandomizedSearchCV

In order to ensure that classification algorithms can work with maximum performance, parameter adjustment is needed. The number of parameters may vary according to the algorithms. However, depending on the technical characteristics of the data set used in the study, many parameters may need to be adjusted. In such cases, it is very unlikely that the optimal parameter set can be found manually due to the large number of possible combinations. Therefore, methods have been developed to find the optimal parameters for algorithms. In this study, the RandomizedSearchCV method is used, which is often preferred for hyperparameter analysis. The RandomizedSearchCV method tests a certain number of randomly selected parameter combinations on the data set. In the RandomisedSearchCV method, the number of iterations is determined by the user in order to find the most successful hyperparameter set.

3. Results and Discussion

This study consists of 3 basic process steps. These are; data collection and creation of the dataset, feature extraction from the pre-processed data and finally classification of the dataset using machine learning algorithms.

The dataset was obtained from a newspaper's website using the Requests and BeautifulSoup libraries. While news articles written in different fields were collected for data diversity, the last 40 articles of the authors (if the columnist has less than 40 published articles, all of their existing works were taken) were added to the dataset to ensure the timeliness of the news.

Since some of the data in the obtained data set showed an unbalanced distribution, 96 authors with less than 15 columns and 330 columns of these authors were considered as outlier data and removed from the data set. As a result of this process, a total of 112 authors and 3087 columns remained in the dataset.

Using Zemberek, an NLP library, the texts in the dataset were separated into words and sentences, stop words were cleaned and word roots were extracted. In addition, numerical attributes such as word richness, root richness, punctuation marks used and number of stop words were extracted and added to the dataset. In addition, the numerical attributes were scaled using the Min-Max Normalization method in order to maximize the classification success.

In text-based classification studies, the most information about the scope of the text is usually contained in word roots. For this reason, word roots have an important place as a distinguishing feature in text classification applications. However, since most of the classification algorithms cannot work on categorical data, such data must be transformed. For this reason, the word roots in the dataset were digitised using TF-IDF and Word Bag methods.

The data set, which was made suitable for classification, was divided into two parts as training (67%) and test (33%) and SVM and MLP algorithms were trained on the training data set. The trained classification algorithms were run on the test data with the default parameters and the success rates were calculated. As a result of this process, the MLP algorithm achieved a success rate of 79.2%, while the SVM algorithm achieved a success rate of 65.5%.

In order to further increase the success rates, hyperparameter analysis was performed with the RandomisedSearchCV method and reclassification was performed using the optimum parameters obtained. As a result of the classification, a success rate of 83% was obtained with the SVM algorithm, while a success rate of 82.4% was obtained with the MLP algorithm. The classification success rates of these algorithms before and after hyperparameter analysis are given in Table 1. In the hyperparameter analysis phase, the number of iterations for the RandomizedSearchCV method was set to 20.

Table 1. Success rates obtained before and after hyperparameter analysis.

	Default parameters	Success Rates	Parameter Pool	The Best Parameters	Success Rates After Parameter Analysis
SVM	Kernel=rbf C= 1.0	%65.5	Kernel=[rbf, linear, sigmoid, poly] C= Between(1-1000) Gamma= Between (0.0001-0.01)	Kernel=linear C=216 Gamma= None	%83
MLP	hidden_layer_sizes=100 activation='relu' solver='adam' alpha=0.0001	%79.2	hidden_layer_sizes=[(10,30,10),(20,)] activation=[tanh, relu] solver=['sgd', 'adam'] alpha=[0.0001,0.001,0.01]	hidden_layer_sizes=(20,) activation='relu' solver='adam' alpha=0.001	%82.4

4. Conclusion

In this study, author-artwork matching was performed using the columns published on the website of a newspaper. For this purpose, firstly, the dataset was organised with basic machine learning libraries and some data preprocessing techniques to make it suitable for classification. Then, the Zemberek NLP library and feature extraction methods (TF-IDF and Word Bag) were used in order to obtain maximum efficiency from the dataset. SVM and MLP algorithms were used in the classification phase. Hyperparameter analysis was used to improve the classification success rate. As a result of the parameter analysis, the highest success rate was obtained by using the SVM algorithm with 83%.

References

[1] Talan, T. ve Aktürk, C., 2021, Bilgisayar Bilimlerinde Teorik Ve Uygulamalı Araştırmalar, p.

[2] Oğuzlar, A., 2003, Veri ön işleme, Erciyes Üniversitesi İktisadi ve İdari Bilimler Fakültesi Dergisi (21).

[3] Famili, A., Shen, W.-M., Weber, R. ve Simoudis, E., 1997, Data preprocessing and intelligent data analysis, Intelligent data analysis, 1 (1), 3-23.

[4] Dondurmacı, G. A. ve Çınar, A., 2014, Finans sektöründe veri madenciliği uygulaması, Akademik Sosyal Araştırmalar Dergisi, 2 (1), 258-271.

[5] Yavuz, S. ve Deveci, M., 2012, İstatiksel Normalizasyon Tekniklerinin Yapay Sinir Ağin Performansina Etkisi, Erciyes Üniversitesi İktisadi ve İdari Bilimler Fakültesi Dergisi (40), 167-187.

[6] Gültepe, Y., 2019, Makine öğrenmesi algoritmaları ile hava kirliliği tahmini üzerine karşılaştırmalı bir değerlendirme, Avrupa Bilim ve Teknoloji Dergisi (16), 8-15.

[7] Erdal, H. ve Yapraklı, T. Ş., 2016, Firma başarısızlığı tahminlemesi: Makine öğrenmesine dayalı bir uygulama, Bilişim Teknolojileri Dergisi, 9 (1), 21.

[8] Akın, A. A. ve Akın, M. D., 2007, Zemberek, an open source NLP framework for Turkic languages, Structure, 10 (2007), 1-5.
[9] Gündoğdu, Ö. E. ve Duru, N., 2016, Türkçe Metin Özetlemede Kullanılan Yöntemler, 18. Akademik Bilişim Konferansı-AB'16.
[10] Ekin, M. F., 2020, Türkçe morfolojik analiz için yeni bir yöntem, Maltepe Üniversitesi, Lisansüstü Eğitim Enstitüsü.
[11] Uludogan, G., Özçelik, R., Parlar, S., Ercan, G. ve Yıldız, O. T., 2017, Türkçe Dogal DilIsleme için Arayüzler User Interfaces for Turkish Natural Language Processing, IEEE.
[12] Taşkıran, S. F., 2021, Doğal dil işleme ile akademik metinlerin kümelenmesi, Konya Teknik Üniversitesi.
[13] Christian, H., Agus, M. P. ve Suhartono, D., 2016, Single document automatic text summarization using term frequency-inverse document frequency (TF-IDF), ComTech: Computer, Mathematics and Engineering Applications, 7 (4), 285-294.
[14] Ataseven, B., 2013, Yapay sinir ağlari ile öngörü modellemesi, Öneri Dergisi, 10 (39), 101-115.

Internet Based Door Automation System

Çağatay ERSİN[1,], Mehmet GÜNEŞ[2]*

[1]*Vocational School, Department of Design Interior Design Program, Cankiri Karatekin University, Cankiri, Turkey*

[2]*Vocational School, Department of Electronic and Automation Mechatronics Program, Cankiri Karatekin University, Cankiri, Turkey*

Abstract

The internet of things (IoT) has become an application that is included in our daily lives thanks to rapidly developing technology. IoT has an important place in the development of internet-based smart home applications. In this study, it is aimed to control the exterior door of the apartment using a smartphone with the NodeMCU development card integrated into the door automaton systems at home. By connecting to the home network with the built-in Wi-Fi receiver on the development board, the automatic exterior door can be controlled via a single-channel relay with the software on the designed circuit board. The development card used in the smart home system was preferred because it was economical and open source. It is thought that the system can be designed by users using simple circuit elements and software code.

Keywords: *Internet of Things, IoT, Door, Automation, NodeMCU*

1. Introduction

With the increase and development of the speed and bandwidth of the Internet, the IOT (Internet of Things) market moves to a new point and continues to offer new ideas and opportunities [1]. IoT consists of web-enabled smart devices that can use sensors and communication hardware to collect, send and act on data. Thanks to a gateway, objects in the system enable the transfer and processing of this data via online storage service. The developing technology of the Internet allows all kinds of objects or devices to connect with it. IoT is the communication of addressable objects over the internet, built on standard communication protocols [2]. It was introduced in the AutoID laboratories of the Massachusetts Institute of Technology (MIT) in the early 1990s, and its first application, "Trojan Room Coffee Pot", was developed in 1999. In the same year, the world's first internet-controlled device, the toaster, was designed. However, today the concept of IoT has taken its place at the center of the concepts of object, human and internet [3].

As the Internet of Things finds application with rapidly developing technologies, new generation urbanization brings more and new opportunities in business, life and many areas of our lives (smart factories, building energy management systems, e-health systems, precision agriculture, smart homes, etc.). reveals [4]. Nowadays, smart home systems and internet of things automations are increasing the number of users and continue to be integrated into our lives with the popularity they have achieved [5]. The main idea of Smart Home Technology is to introduce network devices and equipment at home for a better quality of life. Smart home allows the entire house to be automated, thus providing benefits to disabled individuals as well as a comfortable life. In the future, more innovations and developments are expected in the field of internet of things and smart home systems. These technologies will make significant contributions to areas such as energy efficiency, security, comfort and quality of life. Additionally, as these technologies become widespread, it will be inevitable for our homes to become smarter and make our lives easier [6].

Current door locking systems are all legacy ways of accessing the system via a traditional key, passcode pads or some RFID (Radio Frequency Identification) chip [7]. In this study, an automatic door-opening system that is integrated with in-home doorphones and works online is designed. With this system, the user will be able to open the exterior door of the apartment via mobile device while being away from the intercom. When the studies in the literature were examined, it was observed that similar studies had been conducted. However, in the circuit designed in this study, the door opening signal is sent by connecting the line given as output directly to the

[1]* Corresponding author. *e-mail address: cagatayersin@karatekin.edu.tr*

doorphone data line, without the need for any door lock or motor. In this way, the cost of the system was reduced and it was integrated into the ready-made system.

2. Materials and Methods

NodeMCU microcontroller was used as the controller in the system design. The main reason for using this microcontroller is that it can communicate with objects without the need for an additional module, thanks to the integrated Wi-Fi. Since the microcontroller operates with 5v DC voltage, a 7805 regulator was used to reduce the voltage coming from the doorphone to this voltage. Additionally, a 5v relay was preferred to open the automatic door.

2.1. NodeMCU ESP32

It is an open source, low-cost IoT platform. It can connect objects over the internet and enable them to transfer data using the Wi-Fi protocol. Later, 32-bit ESP32 MCU support was added. The relay that regulates AC power is managed by a NodeMCU. Relays are electrical switches used to protect electrical equipment. Typically relay modules use 5V/12V. Electrical devices are switched mechanically using electromagnets. The main function of relays is to manage high voltage and operate low voltage equipment. Since there is no direct contact between NodeMCU and the device, it is considered safe to use [8].

NodeMCU is an open source programmable electronic circuit. It is produced to realize internet of things applications economically. The programming language called “lua” is used to program the NodemCU circuit. Lua is a programming language written in C, generally designed for embedded systems and clients [9]. In addition, it can also be programmed with the Arduino IDE program [10]. The most important reason why this circuit is preferred is that it can connect to wireless networks and spread its own internet network, allowing other devices to connect.

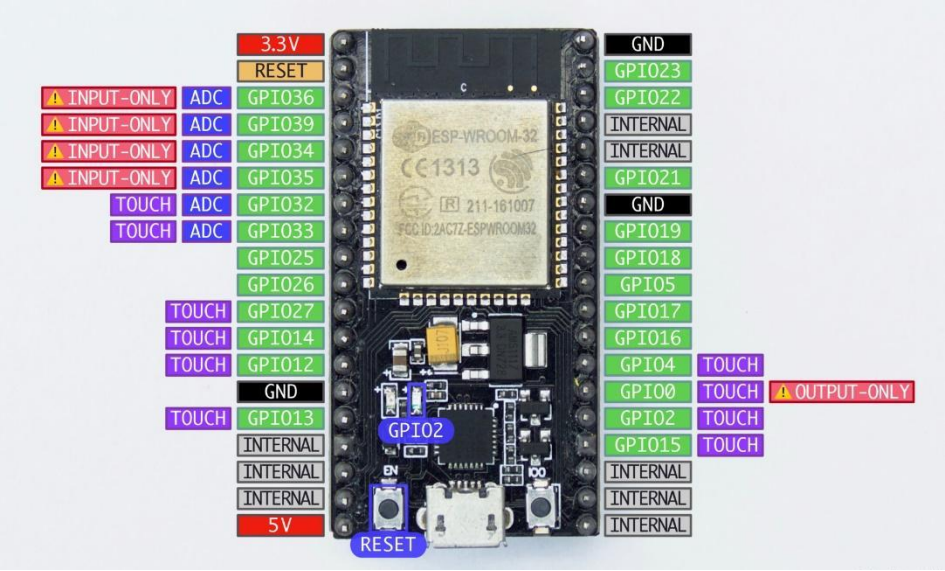

Figure 1. ESP32 Wifi Module.

The NodeMCU card, relay and 7805 voltage regulator circuit integrated on an example video call intercom system is shown in Figure 2. The +24v received via the doorphone was reduced to 5v, which the NodeMCU and relay could use, using a 7805 voltage regulator. The development board and relay were fed with this voltage obtained. GPIO pin 14 on the NodeMCU was used as an output and connected to the In1 input of the relay card. When the user logs in to the interface created on the web address and uses the open button, a signal is sent to the data entry on the intercom and the apartment entrance door is opened.

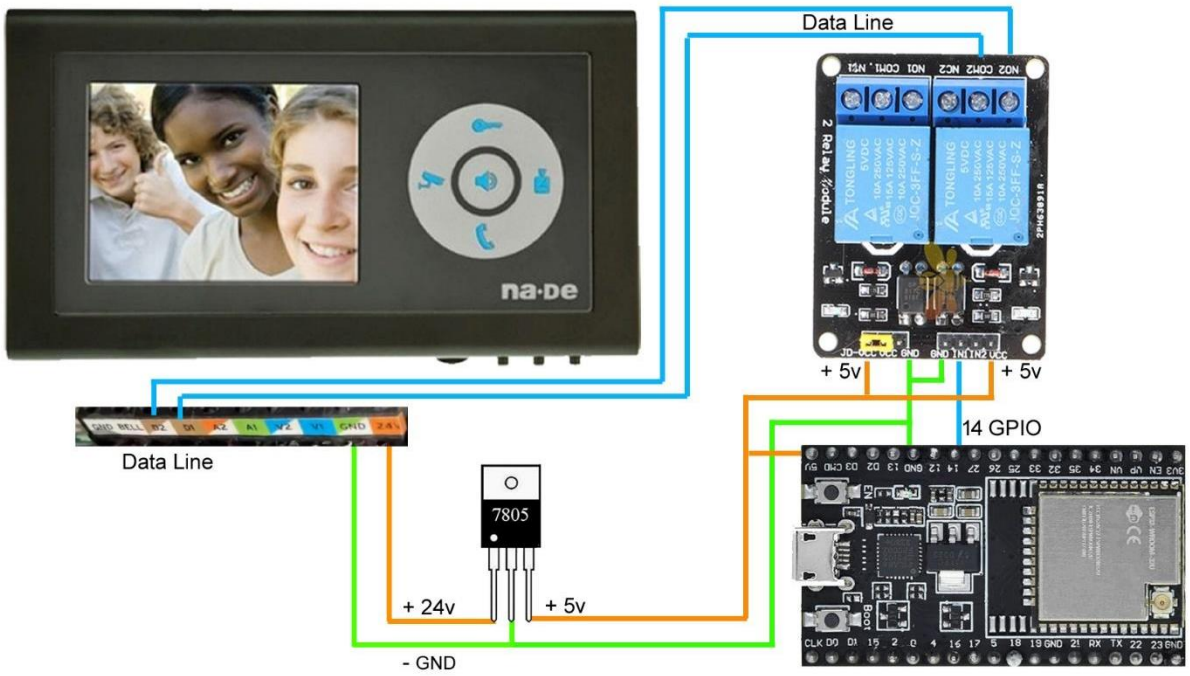

Figure 2. Circuit diagram.

2.2. Circuit Software

In this study, Arduino IDE program was used to upload software to the Esp32 microcontroller development board. The Esp32 plug-in was installed in the Arduino Ide program and the door automatic software shown in Figure 3 was written in C language.

```
#include <WiFi.h>
const char* ssid = "********";
const char* password = "*******";
WiFiServer server(80); // Port 80
#define LED2  2    // LED2 is a Built-in LED.
#define Role 14
String estado = "";
int wait30 = 5000; // time to reconnect when connection is lost.
void setup() {
  Serial.begin(115200);
  pinMode(LED2, OUTPUT);
  pinMode(Role,OUTPUT);
  Serial.println();
  Serial.print("Connecting with ");
  Serial.println(ssid);
  WiFi.begin(ssid, password);
  while (WiFi.status() != WL_CONNECTED) {
    delay(500);
    Serial.print(".");
  }
  Serial.println("Connected with WiFi.");
  server.begin();
  Serial.println("Web Server started.");
  Serial.print("This is IP to connect to the WebServer: ");
  Serial.print("http://");
  Serial.println(WiFi.localIP());
}
void loop() {
  if ((WiFi.status() != WL_CONNECTED) && (millis() > wait30)) {
    Serial.println("Trying to reconnect WiFi...");
    WiFi.disconnect();
    WiFi.begin(ssid, password);
    wait30 = millis() + 30000;
  }
  WiFiClient client = server.available();
  if (!client) {
    return;
  }
  Serial.print("New client: ");
  Serial.println(client.remoteIP());
  String req = client.readStringUntil('\r');
  Serial.println(req);
       if (req.indexOf("on2") != -1) {digitalWrite(LED2, HIGH);
       digitalWrite(Role, HIGH); estado = "ON";}
       if (req.indexOf("off2") != -1){digitalWrite(LED2, LOW);
       digitalWrite(Role, LOW);; estado = "OFF";}
     if (req.indexOf("consulta") != -1){
         if (digitalRead(LED2)){estado = "LED2 now is ON";}
         else {estado = "LED2 now is OFF";}
          }
  //  WEB PAGE. ////////////////////////////
  client.println("HTTP/1.1 200 OK");
  client.println("Content-Type: text/html");
  client.println(""); //  Important.
  client.println("<!DOCTYPE HTML>");
  client.println("<html>");
  client.println("<head><meta charset=utf-8></head>");
  client.println("<body><center><font face='Arial'>");
```

```
  client.println("<h1>Servidor web con ESP32.</h1>");
  client.println("<h2><font color='#009900'>KIO4.COM - Juan A. Villalpando</font></h2>");
  client.println("<h3>Página web.</h3>");
  client.println("<br><br>");
  client.println("<a href='on2'><button>Click to ON LED2</button></a>");
  client.println("<a href='off2'><button>Click to OFF LED2</button></a>");
  client.println("<a href='consulta'><button>Consult status LED2</button></a>");
  client.println("<br><br>");
  client.println(estado);
  client.println("</font></center></body></html>");

  Serial.print("Client disconnected: ");
  Serial.println(client.remoteIP());
  client.flush();
  client.stop();
}
```

Figure 3. Door automatic codes.

In order for the door vending system, which is implemented in C language, to work on the internet, HTML codes have been added to the software and an opening button has been added. When the user accesses the internet address in a location away from the intercom and presses the button on the interface created with HTML codes, the door automatic will be activated and the door will open. The image of the interface created with HTML codes implemented in the Arduino IDE software is shown in Figure 4.

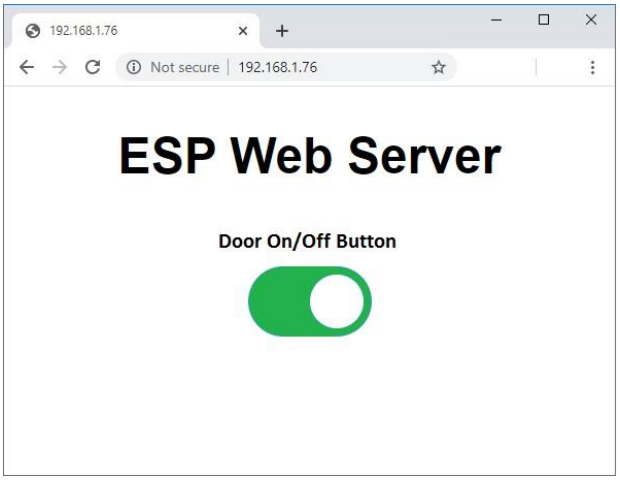

Figure 4. Interface created with HTML codes.

3. Result

The internet of things can be seen in examples where it is widely used in smart home systems, as in every aspect of our lives. With the system designed and implemented in this study, homeowners will be able to open the exterior doors of the building when they are not at home with the help of a smartphone and a simple interface. The user will also be able to operate the system remotely without going to the intercom when he is at home. The biggest advantage of the system is that it is designed with low-cost hardware. It can also be integrated into the intercom systems in the apartment. Video and audio features on the intercom can be added to similar studies by making the necessary software and coding on the system later.

References

[1] Gupta, A. K., & Johari, R. IOT based Electrical Device Surveillance and Control System, 4th International Conference on Internet of Things: Smart Innovation and Usages (IoT-SIU), Ghaziabad, India, 2019, pp. 1-5

[2] Bassi, A., & Horn, G. (2020). Internet of Things in 2020: A Roadmap for the Future. *European Commission: Information Society and Media*, *22*, 97-114.

[3] Erdal, E., & Ergüzen, A. Nesnelerin İnterneti (IoT). (2020). *International Journal of Engineering Research and Development*, *12*(3), 24-34.

[4] Karakoç, E., & Çeken, C. (2021). Black hole attack prevention scheme using a blockchain-block approach in SDN-enabled WSN. *International Journal of Ad Hoc and Ubiquitous Computing*, *37*(1), 37-49.

[5] İlkbahar, F., Ünal, Ş., Karakaya, A. T., & Eren, B. (2021). Akıllı Ev Sistemleri Üzerine Bir Model Önerisi. *AJIT-e: Academic Journal of Information Technology*. *12*(45), 90-105.
[6] Alaçakal, İ., & Doğan, H. (2023). Nesnelerin İnterneti Tabanlı Akıllı Kapı Uygulaması. *Türk Bilim ve Mühendislik Dergisi, 5(*1), 21-28.
[7] Gupte, N. N., & Shelar, M. R. (2013). Smart door locking system. *International Journal of Engineering Research & Technology, 2*(11), 2214-2217.
[8] Niranjana, R., Arvind, S., Vignesh, M., & Vishaal, S. Effectual Home Automation using ESP32 NodeMCU, 2022 International Conference on Automation, Computing and Renewable Systems (ICACRS), Pudukkottai, India, 2022, 1-5,
[9] Oral, O., & Çakır, M. (2017). Nesnelerin interneti kavramı ve örnek bir prototipin oluşturulması. *Mehmet Akif Ersoy Üniversitesi Fen Bilimleri Enstitüsü Dergisi, 8*(1), 172-177.
[10] Kayaalp, K., & Özkorucuklu, S. (2015). Arduino Teknolojisi Kullanılarak Tarla İçin Radyasyon Kapı Kontrolü Tasarımı. *Uluslararası Teknolojik Bilimler Dergisi*, *7*(2), 39-47.

Mechanical Properties of Hydrothermally Grown Carbon Reinforced Polypropylene Composites

Nurettin ELTUĞRAL[1]*

[1] *Engineering Faculty, Medical Engineering Department, Karabuk University, Karabük, Türkiye*

Abstract

This study reports mechanical properties of composites produced by adding certain amounts (10, 15 and 20 wt%) of hydrothermall grown carbon spheres (HTCs) into polypropylene (PP) were investigated. Composites were prepared by means of melt-mixing method. The effect of HTC amounts was also investigated. Scanning electron microscopy (SEM) was employed to study morphological and structural properties of the obtained composites. Thermal stabilities of the composites were studied by thermogravimetric analsysis under nitrogen atmosphere. Mechanical properties of the composited were evaluated by means of tensile tests. Although, PP/HTC composites yielded lower tensile strength compared to pristine PP, they showed improved performance as the HTC content increased, their performance increase as more HTC was added. Addition of HTC caused a remarkable reduction in elongation of PP. Thermal stabilities of the composites were found to be higher than that of pristine PP. MFI values of the composites were shown to increase as more HTC added. This study could be assessed as a means of useful data for future applications of HTC as potential filler in polymer science and technology.

Keywords: *Hydrothermal carbon, polypropyle, melt-mixing, composite, mechanical properties.*

1. Introduction

Polypropylene (PP) as being a thermoplastic polymer, has very useful properties such as low density, easy processability, low cost, resonable mechanical strength heat distortion temperature, transparency, flame resistance, dimentional stability and high impact strength [1–3]. These properties widen its application in many areas including automotive, medical, construction and packaging industries [4]. PP is also a very promising material which serves as a useful matrix for reinforcing to produce composites with improved mechanical properties to enlarge its applications [5–7]. Reinfrocements are used to tune and improve mainly physical and mechanical properties of plastics. In general, their inclusions led to increase the mechanical performance of polymer composites.

Carbon-based reinforcements (CBRs) including carbon nanotubes (CNTs), graphene, graphite, carbon fibers and carbon black have been considered in a number of prospective applications due to their excellent properties such as low mass density and improved mechanical properties [8–10]. Therefore, CBRs have been the subject of a large number of studies to illustrate their potential as reinforcers for polymer matrix. Their intrinsic properties and morphologies may play an important role in determining the ultimate properties of polymer composites. For instance, Juan Li prepared PP composites reinforced with multiwalled CNTs and their hydroxyl-modified ones [11]. An increase in tensile strength, bending strength, and impact strength was observered as CNT concentration increases. A further improvement in those properties resulted in with addition of hydroxyl-modified CNTs. However, elongation at break is reported to decrease upon addition of multiwalled CNTs and hydroxyl-modified multiwalled CNTs as well. Similarly, Yang et al. studied the mechanical properties of PP/CNTs composites (0.5-2 wt%) nanocomposites in the presence of maleic anhydride (0.6 wt%) [12]. Again, an enhancement in tensile strength, toughness and Young's modulus was observed. However, there appears to be some major issues that limit the mechanical properties of the resulting composite. For instance, strong tendency of the carbon nanotubes to form bundles even at low loadings such as 1 wt% which in turn may cause reduction in hardness and crystallinity while improved tensile strength is attained at higher filler loadings [3,11,13]. In a recent study, J. Wang et al. introduced graphene nanoplates into PP by melt compounding method and then self-reinforced polymer composites were produced by film stacking technique [14]. It was reported that graphene-reinforced PP composites exhibited an improvement in mechanical properties. Similar findings were reported also in other research studies [10,15]. In some cases, post chemical procedures are necessary to modify graphene into graphene

* Corresponding author. *e-mail address: nurettineltugral@karabuk.edu.tr*

oxide form to improve compatibility. Mechanical properties of PP-based composites fabricated by introducing carbon fibers or carbon black as the reinforcement were also reported in the literature [16,17].

Hydrothermal carbons (HTCs) can be considered as another set of CBRs whicah can be produced under mild conditions [18–21] whereas methods for the synthesis of other CBRs need challenging procedures. In most cases HTCs can be fabricated in the form of microspheres [22]. HTCs have several advantages over the afformentioned CBRs, i.e. (1) they can be prepared at mild conditions in water at low temperatures (180-220 °C) under autogenic pressures from different types of biomass; (2) HTCs production is very simple, and since the reaction medium is water, the process is pronounced to be environmentally friendly; (3) production cost is cheap in comparison with other processess for the preparation of other CBRs. HTCs have been extensively studied for their potential in energy and environment [23] due to these advantages. To the best of our knowledge, effect of HTCs as a reinforcement material on the mechanical properties of PP has not been studied in literature. This study aims to postulate the processability and mechanical performance of PP/HTC. In this regard, first of all, HTCs were produced from glucose precursor, and PP/HTC composites at different compositions (10, 15, and 20 wt%) were fabricated by melt blending method. Surface characteristics of the produced HTCs as well as the morphology of PP/HTC composites were investigated using scanning electron microscopy (SEM). Mechanical properties of the obtained composites were evaluated by tensile test, melt flow index (MFI) test, thermogravimetric analysis (TGA).

2. Materials and Methods

2.1. Materials

Polypropylene used in this research study was obtained from Borealis, Belgium under the trade name of BP 335 SA. This injection-grade homopolymer has a density of 0.905 g cm^{-3} according to supplier. HTC synthesis was carried out using D(+)-glucose (Merck) as a precursor. Ultra pure water was used throughout the experiments.

2.2. Preparation of HTCs

Synthesis of HTCs was produced from glucose as the feedstock. HTC experiments were carried out in a Teflon-lined stainless steel autoclave. Accordingly, in each set, 1.5 g of glucose was dissolved in 20 mL of ultrapure water and transferred in to the autoclave. Then, it was placed into a pre-heated oven at 200 °C and kept at that temperature for 24 h. HTC conversion occurs almost within 24 h which was reported by one of our previous study [21] . After the conversion was complete, the autoclave was taken out of the oven and cooled down to ambient temperature. The resulting product was filtered off and solid residue was washed with ultrapure water several times and the recovered solid product (HTCs) were dried at 105 °C for 3 h.

2.3. Preparation of PP/HTC composites

PP pellets and HTC powder were placed at 100˚C for 2 hours to eliminate the moisture prior processing. Composite samples were produced via melt-blending technique by the help of lab-scale counter rotating twin screw micro-compounder (MC 15 HT, Xplore Instruments, Netherlands). The process parameters used in compounding including screw rate, mixing temperature and mixing time summerized in Table 1. The compositions of HTC in PP matrix were 10, 15 and 20 weight percent. Fabricated composite samples were shaped via compression molding using lab-scale hydraulic hot-press device (AtsFaar, Italy) and mold with the thikness of 1.5 mm. The dog-bone shape casts were used to obtain test specimen with dimensions of 70×6.0×1.5 mm^3 according to ASTM 638-M 91a standard.

Table 1. Processing parameters applied during fabrication of PP and PP/HTC composites

Parameters	Specification	Unit
Mixing Temperature	200	˚C
Mixing Time	5	min
Screw Speed	100	rpm
Compression Temperature	200	˚C
Compression Pressure	10	bar
Holding Time	2	min

2.4. Characterization methods

Tensile test measurements of composites were done by universal tensile test device (Lloyd LR30K, England) using load cell with 5 kN and crosshead speed of 5 cm min^{-1} testing parameters. Tensile strength, percentage strain and tensile modulus values were recorded as an average of at least five samples or each composite. TGA tests were carried out using STA 7300 thermogravimetric analyzer (Hitachi, Japan). During TGA analysis, heating range of 25-600 ºC and heating rate of 10°C min-1 under argon atmosphere. MFI measurements were conducted by MFI measurement equipment (Coesfeld Meltfixer LT, Germany) using standard specified load of 2.16 kg at temperature of 200 °C. MFI values were recorded as an average value of at least ten samples for each composite. Fracture surface of composites and morphological properties of HTCs were examined using field emission-scanning electron microscope (FESEM) (Carl Zeiss Ultra Plus Gemini, Germany). All the samples were coated with a layer of gold deposited by sputtering under vacuum prior to the analysis. Wear test was applied in accordance with ASTM G133 standard in UTS Tribometer T10 test device with 5 N load, 10 mm stroke and total sliding distance 20 m back and forth. Wear volume and specific wear rate were calculated with the formulas given in equations 1 and 2, respectively.

$$W = A \times Stroke\ (mm^3) \tag{1}$$

$$W_R = \frac{W}{F_N \times l}\ (mm^3/Nm \tag{2}$$

Where, W is wear volume in mm^3, A is wear surface area in mm^2, W_R is specific wear rate, FN is applied load in Newtons, and I is total slide distance in meters.

3. Results and Discussion

3.1. Characterization of HTCs

Figure 1 show morphologies of HTCs. The formed HTCs by hydrothermal method were confirmed to be accumulated in the form of hard spheres with an average size of 0.67 ± 0.06 µm.

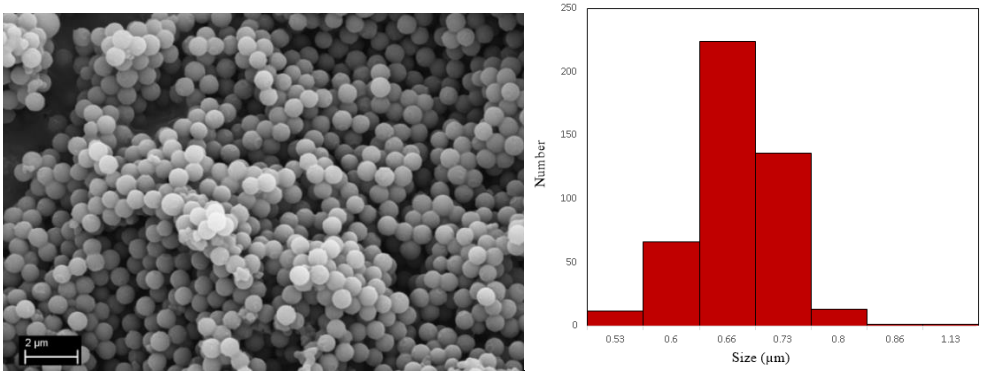

Figure 1. SEM image of prepared HTCs and their particle size distribution histogram.

3.2. Mechanical Properties of PP/HTC composites

Table 2 shows the Young's modules values of PP/HTC composites. Addition of HTC increased this property up to 109%. Improvements in the Young's modulus favours the rigidity of the polymer which could be attributed to brittle behaviour of the samples which in turn results in a large reduction of elongation as compared to pure PP. Elongation at break was observed to decrease gradually with the increase of HTC content. Movement of polymer chain is supposed to be restricted by the HTCs which leads to a decrease in the this property [16]. However, composites which contain 15 and 20% HTC revealed almost close values in elongation at break.

3.3 MFI measurements

MFI parameter provides an insight for viscosity and processibility of polymers. MFI values of PP and PP/HTC composites are given in Figure 2. HTC addition at lower loading ratios caused a decrease in MFI values of the PP/HTC composites. This effect is almost compensated by 15% HTC loading compared to pristine PP and after that, a slight increase in MFI was obtained for 20% HTC loading which is comparable to that of PP itself. These results suggest that HTC reinforcers seem to have no significant problems during the processing or manufacturing of the PP/HTC composites even at higher HTC concentrations [24,25].

Table 2. Tensile properties of the PP and its composites.

Samples	Tensile Strength (MPa)	Elongation at break (%)	Young's modulus (MPa)
PP	20.7 ± 0.4	24.4 ± 2.1	293.7 ± 8.3
PP/10 HTC	11.8 ± 1.1	8.2 ± 0.1	310.5 ± 6.6
PP/15 HTC	12.9 ± 0.3	6.3 ± 0.3	381.5 ± 4.6
PP/20 HTC	14.3 ±0.1	6.1 ± 0.1	427.6 ± 4.9

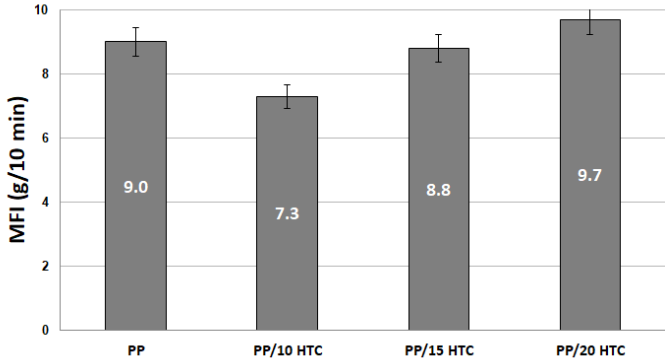

Figure 2. Melt flow index results of the PP and PP/HTC composites.

3.3. Morphological characterization of PP/HTC composites

SEM analysis of the fracture surface of the composites was employed to investigate the dispersion of HTCs in the PP matrix. Figure 3 shows the SEM micrographs of PP/HTC composites with varying weight percentages of the HTCs. SEM micrographs indicate that HTC spheres are well dispersed throughout the PP phase. For 20% HTC loading, the HTCs appear in the form of aggregates to some extent. Nevertheless, they are observed to be covered by the PP matrix. SEM surveys represent a good interfacial adhesion with the spherical HTCs. This can be attributed to compatibility of HTCs with the PP matrix due to increased surface area of the HTCs. These observations are in good agreement with the results from tensile strength measurements.

3.4. Thermal characteristics

Figure 4 shows the melting behavior of the PP and its composites with varying HTC concentrations. It was observed that the initial decomposition temperature increases as the HTC content increases. The weight loss for pristine PP starts at about 330 °C. Our findings agrees the litereture as well [2]. The onset degredation behaviour of composites including 10 – 20 wt% HTC has a very similar melting profile. They almost start to decompose around 370 °C. Our results depicts no significant changes in thermal decomposition of the composites however, thermal stability increases compared to pristine PP.

3.5. Wear properties of the PP/HTC composites

Table 4 shows the wear properties values of PP and PP/HTC composites. As the specific wear rate increases, wear resistance decreases [26]. Specific wear rates were shown to decrese as HTC content increased in the composite. Therefore, wear resistance increases as the composite is reinforced with increasing amount of HTC. Among the composites, the specific wear rate of the composite containing 20% HTC showed the best improvement (30%).

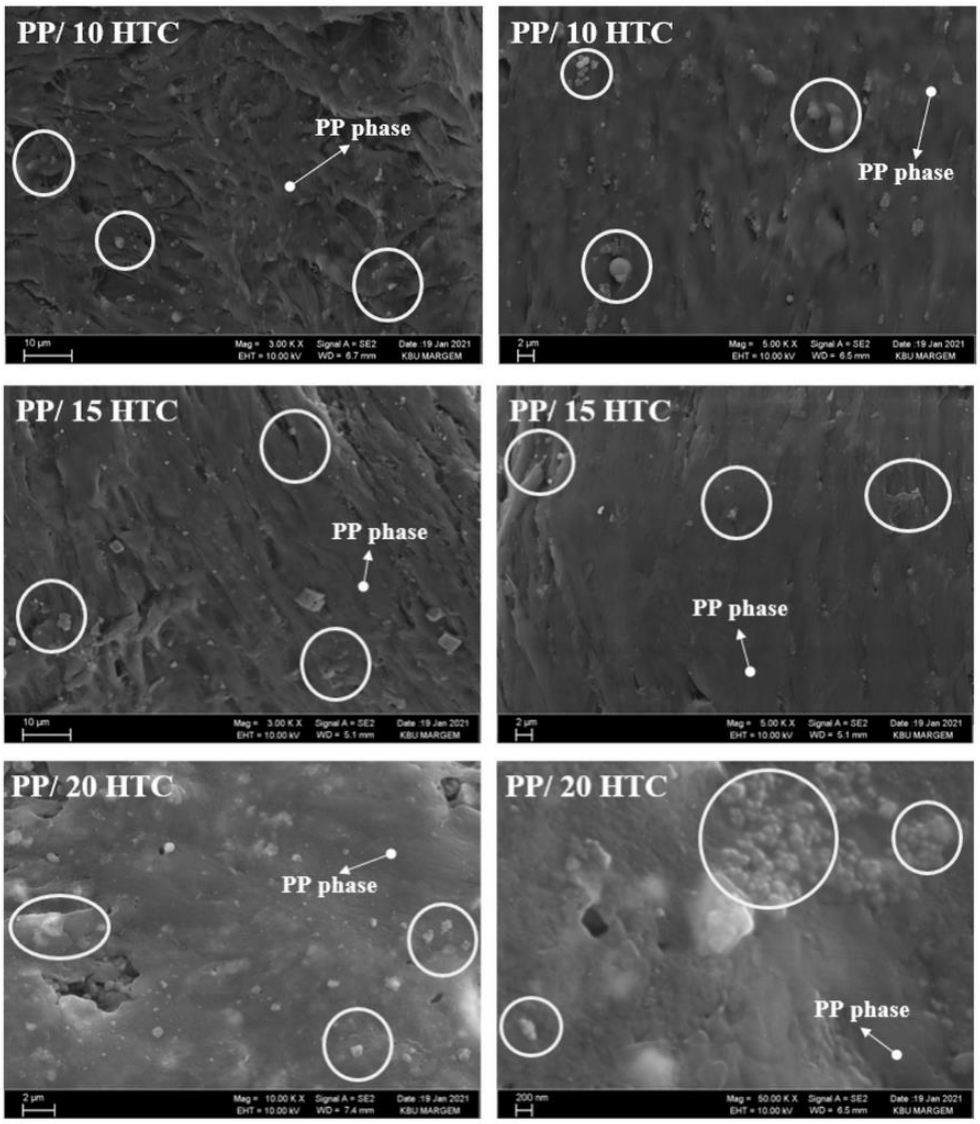

Figure 3. SEM micrographs of the composites with varying weight fractions of the HTC.

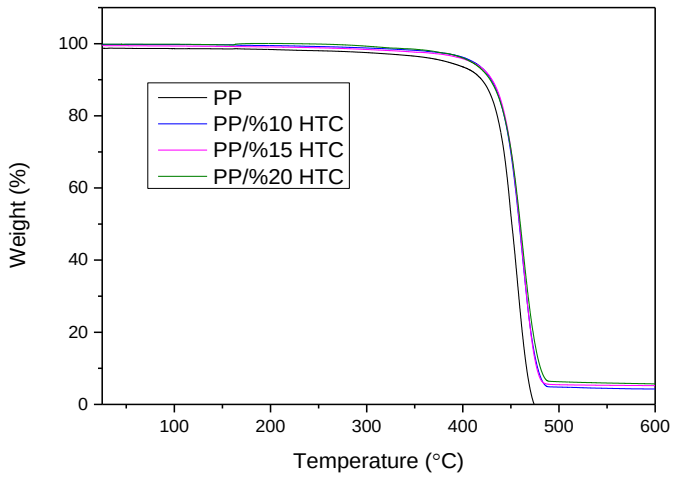

Figure 4. TGA analysis of pristine PP and of its composites at different loadings of HTC.

Table 3. Wear properties of PP and its composites

Samples	Stroke (mm)	Surface area of wear (A) (mm^2)	Volume of wear (W) (mm^3)	Specific wear rate (W_R) (mm^3/Nm)
PP	10	0.001	0.1	0.4
PP/%10HTC	10	0.006	0.06	0.24
PP/%15HTC	10	0.005	0.05	0.2
PP/%20HTC	10	0.003	0.03	0.12

4. Conclusion

In this work, hydrothermally grown carbons were considered as reinforcers to investigate mechanical properties of PP/HTC composites. The interfacial adhesion between reinforcers and a polymer matrix influence the mechanical properties of the overall composite. Alternatively, a novel approach based on incorporation of HTCs into PP matrix has been developed to improve mechanical, thermal and wear strength of the resulting composite. The results showed that HTC loading lowers the tensile strenght with respect to pristine PP however, as the HTC content increases tensile strength of the resulting composites increases as well. Addition of 20% HTC causes some agglomeration. Addition of more HTC increases the wear resistance. Thermal stability of the composites has improved with respect to PP itself, however there was no significant change among the composites having different amount of HTC loadings. This study presents insightful information about possible potential application of HTCs in the polymer composite technology.

Acknowledgements

The author acknowledges the funding (grant no. KBÜBAP-21-DS-049) from Karabük University.

References

[1] Shubhra QTH, Alam AKMM, Quaiyyum MA. Mechanical properties of polypropylene composites: A review. J Thermoplast Compos Mater 2013;26:362–91. https://doi.org/10.1177/0892705711428659.
[2] Mertens AJ, Senthilvelan S. Mechanical and tribological properties of carbon nanotube reinforced polypropylene composites. Proc Inst Mech Eng Part L J Mater Des Appl 2018;232:669–80. https://doi.org/10.1177/1464420716642620.
[3] Yunus R, Zahari NH, Salleh MAM, Ibrahim NA. Mechanical properties of carbon fiber-reinforced polypropylene composites. Key Eng Mater 2011;471–472:652–7. https://doi.org/10.4028/www.scientific.net/KEM.471-472.652.
[4] Kanbur Y, Tayfun Ü. Polipropilen/Huntit Kompozitlerinin Mekanik, Fiziksel ve Morfolojik Özellikleri. SAÜ Fen Bilim Enstitüsü Derg 2017;21:1–1. https://doi.org/10.16984/saufenbilder.281035.
[5] Menyhárd A, Varga J. The effect of compatibilizers on the crystallisation, melting and polymorphic composition of β-nucleated isotactic polypropylene and polyamide 6 blends. Eur Polym J 2006;42:3257–68. https://doi.org/10.1016/J.EURPOLYMJ.2006.09.003.
[6] Martínez-Colunga JG, Sánchez-Valdés S, Ramos-Devalle LF, Muñoz-Jiménez L, Ramírez-Vargas E, Ibarra-Alonso MC, et al. Simultaneous polypropylene functionalization and nanoclay dispersion in PP/Clay nanocomposites using ultrasound. J Appl Polym Sci 2014;131:1–8. https://doi.org/10.1002/app.40631.
[7] Barkoula NM, Alcock B, Cabrera NO, Peijs T. Flame-Retardancy Properties of Intumescent Ammonium Poly(Phosphate) and Mineral Filler Magnesium Hydroxide in Combination with Graphene. Polym Polym Compos 2008;16:101–13. https://doi.org/10.1002/pc.
[8] Papageorgiou DG, Li Z, Liu M, Kinloch IA, Young RJ. Mechanisms of mechanical reinforcement by graphene and carbon nanotubes in polymer nanocomposites. Nanoscale 2020;12:2228–67. https://doi.org/10.1039/c9nr06952f.
[9] Rao CNR, Sood AK, Subrahmanyam KS, Govindaraj A. Graphene: The New Two-Dimensional Nanomaterial n.d. https://doi.org/10.1002/anie.200901678.
[10] Galpaya D, Wang M, Liu M, Motta N, Waclawik E, Yan C. Recent Advances in Fabrication and Characterization of Graphene-Polymer Nanocomposites. Graphene 2012;01:30–49. https://doi.org/10.4236/graphene.2012.12005.
[11] Li J. Multiwalled Carbon Nanotubes Reinforced Polypropylene Composite Material. J Nanomater 2017;2017. https://doi.org/10.1155/2017/2171356.
[12] Yang BX, Shi JH, Pramoda KP, Goh SH. Enhancement of the mechanical properties of polypropylene using polypropylene-grafted multiwalled carbon nanotubes. Compos Sci Technol 2008;68:2490–7. https://doi.org/10.1016/J.COMPSCITECH.2008.05.001.
[13] Moniruzzaman M, Winey KI. Polymer Nanocomposites Containing Carbon Nanotubes. Macromolecules 2006;39:5194–205. https://doi.org/10.1021/ma060733p.
[14] Wang J, Song F, Ding Y, Shao M. The incorporation of graphene to enhance mechanical properties of polypropylene

self-reinforced polymer composites. Mater Des 2020;195:109073. https://doi.org/10.1016/j.matdes.2020.109073.
[15] Huang CL, Lou CW, Liu CF, Huang CH, Song XM, Lin JH. Polypropylene/graphene and polypropylene/carbon fiber conductive composites: Mechanical, crystallization and electromagnetic properties. Appl Sci 2015;5:1196–210. https://doi.org/10.3390/app5041196.
[16] Pérez-Rocha D, Morales-Cepeda AB, Navarro-Pardo F, Lozano-Ramírez T, Lafleur PG. Carbon Fiber Composites of Pure Polypropylene and Maleated Polypropylene Blends Obtained from Injection and Compression Moulding. Int J Polym Sci 2015;2015. https://doi.org/10.1155/2015/493206.
[17] Kanbur Y, Küçükyavuz Z. Electrical and mechanical properties of polypropylene/carbon black composites. J Reinf Plast Compos 2009;28:2251–60. https://doi.org/10.1177/0731684408092378.
[18] Bai CX, Shen F, Qi XH. Preparation of porous carbon directly from hydrothermal carbonization of fructose and phloroglucinol for adsorption of tetracycline. Chinese Chem Lett 2017;28:960–2. https://doi.org/10.1016/j.cclet.2016.12.026.
[19] Hu B, Wang K, Wu L, Yu SH, Antonietti M, Titirici MM. Engineering carbon materials from the hydrothermal carbonization process of biomass. Adv Mater 2010;22:813–28. https://doi.org/10.1002/adma.200902812.
[20] Wei L, Sevilla M, Fuertes AB, Mokaya R, Yushin G. Hydrothermal carbonization of abundant renewable natural organic chemicals for high-performance supercapacitor electrodes. Adv Energy Mater 2011;1:356–61. https://doi.org/10.1002/aenm.201100019.
[21] Simsir H, Eltugral N, Karagoz S. Hydrothermal carbonization for the preparation of hydrochars from glucose, cellulose, chitin, chitosan and wood chips via low-temperature and their characterization. Bioresour Technol 2017;246. https://doi.org/10.1016/j.biortech.2017.07.018.
[22] Mi Y, Hu W, Dan Y, Liu Y. Synthesis of carbon micro-spheres by a glucose hydrothermal method. Mater Lett 2008;62:1194–6. https://doi.org/10.1016/j.matlet.2007.08.011.
[23] Maniscalco MP, Volpe M, Messineo A. Hydrothermal carbonization as a valuable tool for energy and environmental applications: A review. Energies 2020;13. https://doi.org/10.3390/en13164098.
[24] Ahmed SA, Tirkes S, Tayfun U. Reinforcing effect of polyurethane sizing on properties of acrylonitrile–butadiene–styrene composites involving short carbon fiber. SN Appl Sci 2020;2:1–9. https://doi.org/10.1007/s42452-020-03809-5.
[25] Türk DA, Brenni F, Zogg M, Meboldt M. Mechanical characterization of 3D printed polymers for fiber reinforced polymers processing. Mater Des 2017;118:256–65. https://doi.org/10.1016/J.MATDES.2017.01.050.
[26] Karabeyoğlu SS, Ekşi O, Feratoğlu K. Eriyik yığma modelleme ile imal edilen PLA-Cu kompozitlerinin farklı sıcaklık şartları altında aşınma karakteristikleri. Balıkesir Üniversitesi Fen Bilim Enstitüsü Derg 2021;23:358–65. https://doi.org/10.25092/baunfbed.854829.

Treatment of excessive gingival display and diastema closure: a case report

Basak KARASU [1,*], ***Musa ACARTÜRK*** [2]

[1]*Faculty of Dentistry, Department of Periodontology, Çankırı Karatekin University, Çankırı, Turkiye*

[2]*Faculty of Dentistry, Department of Restorative Dentistry, Çankırı Karatekin University, Çankırı, Turkiye*

Abstract

Smile is an important facial expression and affects a person's self-confidence. Excessive gingival display while smiling and the gap between the proximal surfaces of the maxillary incisors are among the most notable aesthetic concerns. In this case report, the gingivectomy procedure and diastema closure were performed on a 23-year-old male patient who applied to our department with the chief complaint of excessive gingival display, short clinical crowns and spacing in the upper front tooth region.

Keywords: *Diastema, Gingivectomy, Gummy smile*

1. Introduction

The primary concern for many people these days is facial aesthetics. The smile has a significant impact on one's self-confidence and facial appearance. In terms of appearance, patients, particularly younger ones, find diastema between teeth disturbing. Differences in the space between teeth and arch sizes, as well as variations in tooth morphology (such as narrow or cone-shaped teeth), can result in diastema [1]. A peg-shaped lateral, proclination of the upper labial segment, an enlarged labial frenum, a missing tooth, midline supernumerary teeth, and habits like lip or finger sucking, tongue thrusting can all result in midline diastema. Conservative and prosthetic approaches are used for diastema closure [2].

A gummy smile (GS) has an impact on one's appearance as well as psychological well-being because it results in a decrease in self-confidence that makes one hide or control their smile. A gummy smile is defined as having more than 2 mm of exposed gingiva [3]. The appearance of less than 3 mm of gingiva in the front area is considered a normal smile. When the gingiva between the canine teeth appear more than 3 mm while smiling, it is considered GS. [4]. GS can caused by various reasons including altered passive eruption of teeth, short or hyperactive upper lip muscles, short clinical crowns, dentoalveolar extrusion and vertical maxillary excess or combinations of them. Therefore, in order to accurately diagnose and treat GS, dentists must identify its primary causes [5].

The harmony of teeth and periodontium, as well as their interaction with perioral structures, particularly extraoral soft tissues, are critical factors in enhancing the aesthetics of a smile [6]. A person's smile greatly influences their facial appearance. Front teeth, maxillary alveoler bone, and upper lip (levator) muscles work together to produce a smile that is pleasing to the eye. An unpleasant smile may result from dysfunction in any one of these areas [7]. When designing an aesthetically pleasing smile, it's crucial to have a proportionate, symmetrical tooth arrangement where the proper dominance of particular teeth is recognized. Teeth differ in size and proportion from person to person and even within a single individual over the course of their life due to pathological or physiological tooth wear. In every smile, the dominant teeth should be the maxillary central incisors [8]. The relationship between the incisal edge slope of the upper incisors and the upper edge slope of the lower lip during smiling is expressed as the smile line. [9]. The lower edge of a person's upper lip when smiling is defined as the lip line. This line affects the appearance of the teeth and gingiva [10]. The maxillary central incisor's visibility during smiling ranges from showing 2 mm of gingival tissue to showing 3/4 of the clinical crown [11].

Gingivectomy refers to excision of the gingiva [12]. In order to perform gingivectomy, a sufficient amount of bone level, gingival thickness of more than 3 mm (from bone tissue to gingival crest) and a sufficient amount of attached gingival tissue are required. [13, 14]. Nonetheless, gingivectomy is contraindicated if osseous levels are approximate the cementoenamel junction because this could violate the biologic width [15].

* Corresponding author. *e-mail address: basakkarasu.@karatekin.edu.tr*

Diastema and gummy smile are multifactorial conditions that adversely impact the sense of aesthetics. This case report demonstrates the multidisciplinary approach to treating a patient with a gummy smile, short crown lengths, and a diastema between the maxillary central incisors.

2. Materials and Methods

A 23-year-old male patient applied to Çankırı Karatekin University Faculty of Dentistry department of Periodontology with a chief complaint of excessive gingival display, short clinical crowns, and spacing in the upper front tooth area. As a result of the medical and dental history taken from the patient, no systemic or dental disorders were detected. Midline spacing between the maxillary central incisors and gummy smile was observed during the clinical examination.

The phenotype of the gingiva was thick, pink, and firm. Minimal amounts of calculus and plaque deposits were recorded during the periodontal evaluation. Relatively 2-3 mm were measured by the Williams probe during the first probing depth measurements without any bleeding or clinical attachment loss. The cementoenamel junction-alveoler bone crest distance were in a normal range. While smiling, the patient's teeth were visible from maxillary right first premolar to the maxillary left first premolar. Additionally, 5–6 mm of vertical exposure of gingiva was recorded from the inferior border of the upper lip and gingival margins of maxillary anterior teeth.

After the clinical evaluation was completed, the patient was informed about all surgical and restorative procedures. Written consent form was obtained from the patient before starting dental treatment. Supragingival and subgingival scaling were performed by curettes and scalers. Oral hygiene instructions were given following the treatment.

In the second visit, local anesthesia (ultracain-articain HCl 40 mg/ml, epinephrine HCI 6 mcg/ml) was first administered in the vestibular mucosa between the maxillary right canine and the maxillary left canine. In order to prepare an excision, bleeding points were secondarily marked. The surgical blade #15c was positioned at a 45° angle to the tooth's long axis, apically to the bleeding points, and gingivectomy incisions were made in the anterior area on the facial surface only. After that, the excised gingiva tissue was removed with forceps. The gingiva was recontoured. 600 mg ibuprofen three times a day for three days was prescribed for the postoperative pain. For the first twenty-four hours following the surgery, the patient was advised to abstain from hot beverages. The patient was instructed to rinse with 0.12% Chlorhexidine Gluconate twice daily for 2 weeks. Follow-up examinations showed exposure of the complete anatomical crowns of upper anterior teeth, thus enhancing the esthetics of the teeth and correcting the excessive gingival display. The patient was consulted to the department of Restorative Dentistry.

First, a restorative dental examination was performed on the patient, whose gingivoplasty procedure was completed and the anatomical crown lengths reached a sufficient length, in order to close the diastema between the upper central teeth. Although no tooth decay was found in the upper central teeth in the mouth, an uncomplicated tooth fracture was detected at the enamel-dentin level in the mesial part of the incisal edge in the right upper central tooth. No pathological findings were detected in the radiological examination. After the patient was informed about the treatment options, it was decided to restore the diastema and the tooth fracture in the incisal area with composite resin.

The mesial regions of 1/3 of the mesiodistal length of the teeth and the fractured area were bevelling process performed with a flame-tipped diamond bur (858 H, 014, Bosphorus, Turkey). After bevelling process, cotton rolls were placed between the upper central teeth and the upper lip. In order to increase the roughness of the enamel surface, the beveled incisal edges and 1/3 mesial parts of the teeth were etched with Panora 200 Etching Gel (IMICRYL, Turkey) for 30 seconds. After etching, the teeth were washed for 30 seconds and then dried. Wet cotton rolls were replaced. Before the restoration, the color selection process was made for the composite resin to be applied to the teeth and it was decided to use the composite resin in A1 color tone (Estelite Sigma Quick, Tokuyama Dental, Italy).

After a transparent tape (Dispodent, Turkey) was placed on the upper right central tooth, where color selection was made and saliva isolation was provided, bonding agent (Hybrid Bond One, Sun Medical Co., Ltd., Japan) was applied and then a suitable form was given to the tooth with composite resin. The same procedures were applied to the upper left central tooth. Following the composite application, the approximal surfaces of the teeth were polished with composite sandpaper (Ref. 8276, KG Sorensen, Brazil) and the vestibule surfaces were

polished with composite discs (No 1.075, Tor VM, Russia). Finally, the restoration was completed by polishing the vestibule surfaces of the teeth with the help of yellow rubber (Ref. 905.C.100, Kenda AG, Liechtenstein).

3. Results and Discussion

Minimally invasive procedures present several advantages compared to more destructive traditional therapies by minimizing unnecessary loss of dental tissue, violation of the dentin-pulp complex, and lowering the risk of iatrogenic harm to adjacent hard and soft tissues. In order to restore function and aesthetics with restorations in the long term, these approaches preserve the maximum amount of dental tissue while utilizing the best restorative materials[16].

Composite resins were used for diastema closure in this clinical case, and they have clear advantages as a more conservative, quicker, and economical option than ceramic veneers [17]. The use of direct composite resin to close midline diastema is a minimally invasive procedure. This method creates a significant bond strength at the tooth/adhesive system interface and extends the life of the restoration because the enamel connection provides greater retention even though it does not have dentin collagen fibers [18].

Anterior crown lengthening is indicated in patients with excessive gingival display or insufficient clinical crowns [19]. Gingivectomy is a surgical procedure used to remove excessive gingival tissue. The physiological contour can be restored with this method. Gingivectomy and gingivoplasty are efficient treatment options to provide gingival aesthetics [12]. The purpose of the gingival surgery is to establish an sufficient relationship between the gingival margin and the lip, to enhance the appearance of the crown, and to achieve aesthetic harmony between the height and width of the crowns of the front teeth. Composite resins can improve aesthetic results in diastema closure cases, as in this case [20].

When combined with the direct composite resin technique, periodontal surgery offered patients satisfactory functional and aesthetic outcomes while requiring less time and money for treatment than alternative approaches. This multidisciplinary approach to improving smile esthetics proved to be an excellent treatment option. In aesthetic dentistry, the participation of various specialties in diagnosis and treatment planning allows the dentist to give each patient the best possible care and meet their expectations for the outcome.

4. Conclusion

In this case report, the diastema was closed with the direct application of composite resin, and the excessive gingival appearance was eliminated with gingivectomy, providing highly satisfactory results without requiring extensive surgery or ceramic veneer.

References

[1] de Araujo Jr, E.M., et al., *Direct adhesive restoration of anterior teeth: Part 2. Clinical protocol.* Practical Procedures & Aesthetic Dentistry: PPAD, 2003. **15**(5): p. 351-7; quiz 359.

[2] Izgi, A.D. and E. Ayna, *Direct restorative treatment of peg-shaped maxillary lateral incisors with resin composite: A clinical report.* The Journal of prosthetic dentistry, 2005. **93**(6): p. 526-529.

[3] Allen, E.P., *Use of mucogingival surgical procedures to enhance esthetics.* Dental Clinics of North America, 1988. **32**(2): p. 307-330.

[4] Mangano, A. and A. Mangano, *Current strategies in the treatment of gummy smile using botulinum toxin type A.* Plastic and reconstructive surgery, 2012. **129**(6): p. 1015e.

[5] Silberberg, N., M. Goldstein, and A. Smidt, *Excessive gingival display--etiology, diagnosis, and treatment modalities.* Quintessence Int, 2009. **40**(10): p. 809-18.

[6] Parekh, S.M., *The perception of selected aspects of smile esthetics-smile arcs and buccal corridors*. 2005, The Ohio State University.

[7] Mate, P.P., et al., *Clinical and electromyographic evaluation of botulinum toxin type A in the treatment of gummy smile: A prospective clinical study.* Journal of dental research, dental clinics, dental prospects, 2021. **15**(2): p. 122.

[8] Sharma, P.K. and P. Sharma. *Dental smile esthetics: the assessment and creation of the ideal smile*. in *Seminars in orthodontics*. 2012. Elsevier.

[9] Sarver, D.M., *The importance of incisor positioning in the esthetic smile: the smile arc.* American journal of orthodontics and dentofacial orthopedics, 2001. **120**(2): p. 98-111.
[10] Sabri, R., *The eight components of a balanced smile.* J Clin Orthod, 2005. **39**(3): p. 155-67.
[11] Peck, S. and L. Peck. *Selected aspects of the art and science of facial esthetics*. in *Seminars in orthodontics*. 1995. Elsevier.
[12] Newman, M., H. Takei, and P. Klokkevold, *Periodontología clínica de Carranza. Vol 1 y 2*. 2014, Mexico: Mc Graw-Hill. Interamericana.
[13] Duruel, O., et al., *Treatment of various types of gummy smile with botulinum toxin-A.* Journal of Craniofacial Surgery, 2019. **30**(3): p. 876-878.
[14] Dolt, A.H. and J.W. Robbins, *Altered passive eruption: an etiology of short clinical crowns.* QUINTESSENCE INTERNATIONAL-ENGLISH EDITION-, 1997. **28**: p. 363-374.
[15] Mostafa, D., *A successful management of sever gummy smile using gingivectomy and botulinum toxin injection: A case report.* International journal of surgery case reports, 2018. **42**: p. 169-174.
[16] Mackenzie, L. and A. Banerjee, *Minimally invasive direct restorations: a practical guide.* British dental journal, 2017. **223**(3): p. 163-171.
[17] Durán, G., et al., *The use of direct composite resin to close maxillary midline diastema complementary to orthodontic treatment.* Revista clínica de periodoncia, implantología y rehabilitación oral, 2019. **12**(2): p. 106-108.
[18] Prabhu, R., et al., *Clinical evaluation of direct composite restoration done for midline diastema closure–long-term study.* Journal of pharmacy & bioallied sciences, 2015. **7**(Suppl 2): p. S559.
[19] Mantovani, M.B., et al., *Use of modified lip repositioning technique associated with esthetic crown lengthening for treatment of excessive gingival display: A case report of multiple etiologies.* Journal of Indian Society of Periodontology, 2016. **20**(1): p. 82.
[20] Storrer, C.L.M., et al., *Treatment of gummy smile: Gingival recontouring with the containment of the elevator muscle of the upper lip and wing of nose. A surgery innovation technique.* Journal of Indian Society of Periodontology, 2014. **18**(5): p. 656.

In Vitro Effects of Some Chemotherapy Drugs on Glutathione Reductase Enzyme Activity Purified from Sheep Spleen Tissue

Çiğdem ÇOBAN [1], *Mehmet ÇİFTCİ* [2*]

[1]*Bingol University, Solhan Health Services Vocational School, Bingol, Türkiye*

[2]*Bingol University, Faculty of Veterinary Science, Bingol, Türkiye*

Abstract

In this study, the in vitro effects of some drugs used in chemotherapy on glutathione reductase (GR; EC 1.8.1.7) enzyme activity purified from sheep spleen tissue were investigated. Purification was carried out using homogenate preparation, 20-70% ammonium sulfate precipitation and 2', 5' ADP-Sepharose 4B gel affinity chromatography steps. In the second stage of the study, the effects of some chemotherapy drugs such as ibandronic acid, oxaliplatin, carboplatin and cisplatin on the activity of the pure enzyme were investigated. As a result of the in vitro studies, the Activity%-[I] graph was drawn for the drug oxaliplatin, which has an inhibitory effect on the enzyme, and the IC_{50} value was calculated as 4.53 mM. In addition, it was detected that the drugs ibandronic acid, carboplatin and cisplatin did not have a significant effect on the enzyme.

Keywords: *Glutathione reductase, Ibandronic acid, Oxaliplatin, Carboplatin*

1. Introduction

Glutathione reductase (E.C. 1.8.1.7; GR) enzyme, which belongs to the oxidoreductase enzyme group, is the most important enzyme that carries out the metabolic reactions of glutathione (GSH) metabolism, which forms the basis of antioxidant metabolism [1]. GSH molecule, which contains most of the free –SH groups in the cell; It consists of γ-glutamine-cysteine-glycine. By transferring the H in the –SH group in this molecular structure to the radical precursors, the radicals are broken down and transformed into water and oxygen, and it itself turns into a reducing form. The glutathione molecule is found in the cell in more than 99% reduced form. The GSH/GSSG ratio is kept at a certain level in the cell. According to research, this ratio for erythrocyte cells is approximately 500/1, and a decrease in this ratio causes hemolysis [2]. The GR enzyme is vital in keeping this ratio constant. For this, the GR enzyme catalyzes the conversion of oxidized glutathione (GSSG) into reduced glutathione (GSH) in the presence of the nicotinamide adenine dinucleotide phosphate (NADPH) molecule produced in the pentose phosphate pathway and malic enzyme step [3]. Thus, the cell is cleared of radicals that attack vital structures such as DNA, especially to prevent aging [4, 5, 6]. The fact that the GR enzyme requires the NADPH coenzyme molecule in its operation reveals the relationship of this enzyme with the glucose 6-phosphate dehydrogenase (G6PD) enzyme. Two molecules of NADPH are formed from each glucose 6-phosphate molecule oxidized in the oxidative part of the pentose phosphate pathway. Therefore, a malfunction in the functioning of the G6PD enzyme will cause the GR to be negatively affected. In this case, it directly affects GSH formation [7, 8]. Many purification and inhibition studies have been carried out on vital enzymes such as GR, which serve at key points of cell metabolism These inhibitors are antibiotics and drugs generally used in human and animal treatment [4, 5, 9]. Our research aimed to investigate the effects of some chemotherapy drugs such as ibandronic acid, oxaliplatin, carboplatin and cisplatin on GR enzyme activity. The main purpose of chemotherapy is to suppress protein production by preventing the transcription of DNA and thus stopping the spread of cancer cells. Increasingly in recent years, chemotherapy drugs have different cytotoxic effects on cells.

Among these drugs, Cisplatin is from the antineoplastic drug group and is the chemotherapy drug with the most known nephrotoxic side effects. In patients taking cisplatin, the rate of nephrotoxicity decreases significantly when hydrated with physiological saline (150-200 mL/hour). Ibandronic acid is used in the prevention and treatment of skeletal fractures associated with cancer-related hypercalcemia and osteolytic bone metastases. Carboplatin belongs to the antineoplastic drug group and is much less nephrotoxic than cisplatin. It is used instead of cisplatin in patients with renal failure. Oxaliplatin, a third-generation platinum analogue, is a cancer drug used to treat colorectal cancer [10].

* Corresponding author. *e-mail address: mciftci@bingol.edu.tr*

2. Materials and Methods

2.1. Preparation of Hemogenate

The sheep spleen tissue used in this study was obtained from Bingöl Provincial Combined Meat and Milk Institution according to cold chain rules. For the GR enzyme, 15 grams of tissue was taken and cut into small pieces and suspended in the homogenator with 45 mL of 50 mM KH_2PO_4 (pH = 8.0) homogenate buffer. The resulting suspension was centrifuged at 10,000xg for 1 hour, then the pellet was discarded to form homogenate [2, 9, 11].

2.2. 2', 5'-ADP Sepharose 4B Affinity Chromatography

The enzyme sample, which was partially purified after ammonium sulfate precipitation, was purified by 2', 5' ADP Sepharose-4B affinity chromatography. For this method, first an affinity column was prepared. For a bed volume of 10 mL; 2', 5'-ADP sepharose 4B gel was weighed 2 g dry. Then, the gel was washed several times with 400 mL of distilled water to remove solids and the gel was swollen during this time. The air resulting from inflation was removed by vacuuming and the suspension was made by adding equilibration buffer (50 mM KH_2PO_4/1 mM EDTA, 1mM DTT, pH: 6.0) to the gel. The prepared gel was packed into a refrigerated column and the gel was waited to precipitate. It was understood that the column was balanced by approximately equalizing the absorbance and pH of the eluate and buffer at 280 nm. The enzyme sample was applied to the prepared column. Then, the column was washed with three separate washing solutions of 25 mL each. The column was first washed with 0.1 M K-acetate/0.1 M K-phosphate (pH=6) buffer. Then, 0.1 M K-phosphate/0.1 M KCl (pH=7.85) buffer was used for washing and finally it was washed with 50 mM KH_2PO_4/1 mM EDTA (pH=7) buffer. The washing process was monitored on a spectrophotometer and the absorbance values were determined to be approximately equal to the blank. After the washing process was completed, the enzyme was eluted with elution buffer (50 mM KH_2PO_4/1 mM EDTA, 1mM GSH and 0.5 mM NADPH, pH 7.3)[9, 11, 12, 13, 14]. The elutions were placed in 1.5 mL Eppendorf tubes and their activity values were checked.

2.3. Activity Determination

To determine the activity, 2 mM NADPH solution, 0.1 M KH_2PO_4 (pH 8.0) buffer, 20 mM GSSG solution were prepared and 200 µL KH_2PO_4 buffer, 100 µL GSSG solution, 100 µL NADPH solution, 20 µL homogenate were added to a 1000 µL cuvette. and 580 µL of pure water was added and measurements were made spectrophotometrically at 340 nm. This situation was determined by the decreasing amount of NADPH due to the oxidation of NADPH in the presence of GSSG [6, 15, 16].

2.4. Kinetic Studies

In kinetic studies, the effects of some chemotherapy drugs such as ibandronic acid, oxaliplatin, carboplatin and cisplatin on GR enzyme activity purified from sheep spleen tissue were investigated. These drugs were taken in different concentrations and added to the bathtub environment. As a result of activity measurements, trials were made up to the highest possible inhibitor concentration, and the % Inhibition – [I] graph was drawn and the IC_{50} value was calculated for the drug oxaliplatin, which showed an inhibitory effect.

3. Results

In kinetic studies, the effects of some chemotherapy drugs such as ibandronic acid, oxaliplatin, carboplatin and cisplatin on GR enzyme activity at different concentrations were investigated and % Activity-[I] graphs were drawn (Figures 1, 2, 3 and 4). Using the graphic equation, the IC_{50} value for oxaliplatin, which has an inhibitory effect, was calculated as 4.53 mM. In addition, it was determined that the drugs ibandronic acid, carboplatin and cisplatin did not have a significant effect on the enzyme (Table 1).

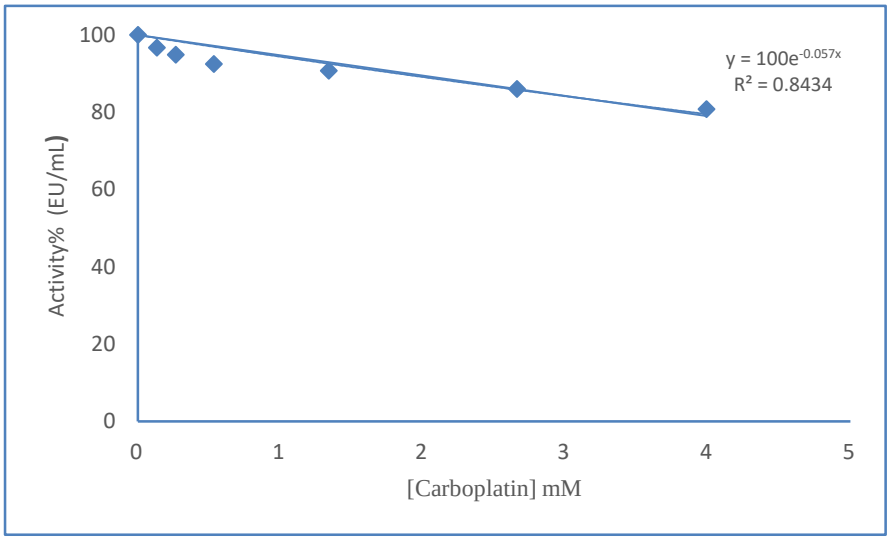

Figure 1. Activity%-[I] graph obtained for carboplatin

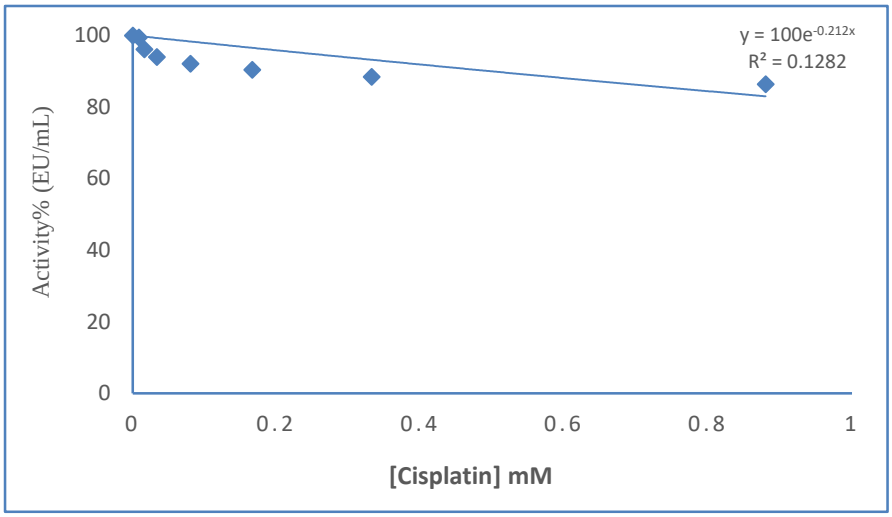

Figure 2. Activity%-[I] graph obtained for cisplatin

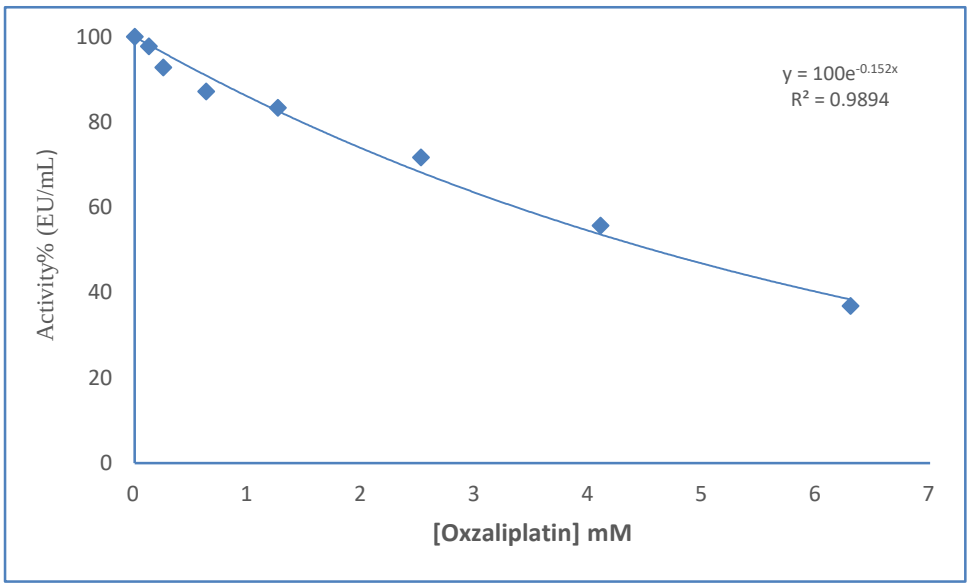

Figure 3. Activity%-[I] graph obtained for oxaloplatin

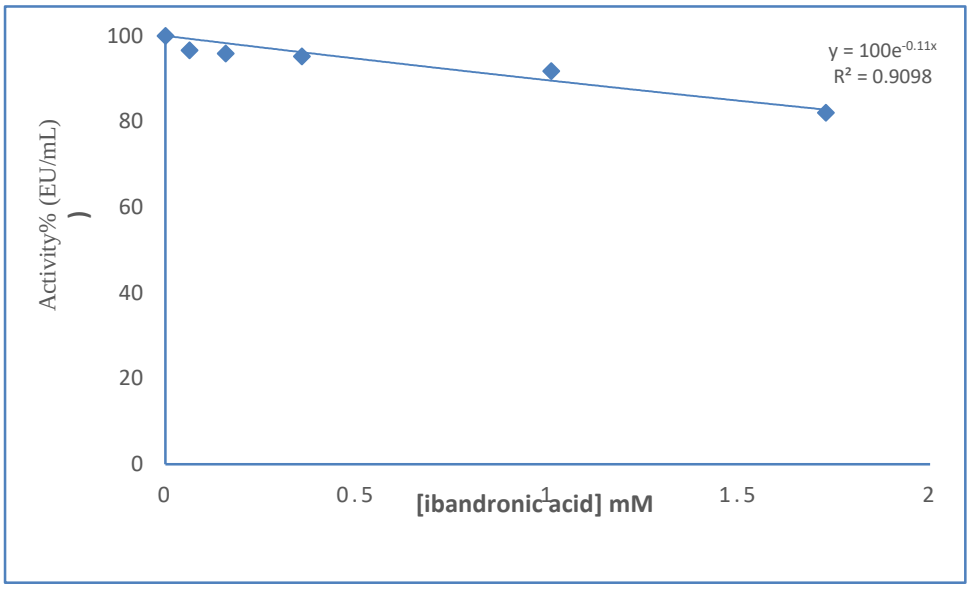

Figure 4. Activity%-[I] graph obtained for ibandronic acid

Table 1. Obtained IC_{50} values

Drug	IC_{50} (mM)
Oxzaliplatin	4,53

4. Conclusion

GR enzyme is a very important enzyme for glutathione metabolism, which plays a major role in the balanced and orderly conduct of biochemical events within the cell by converting oxidized glutathione (GSSG) into the reduced glutathione (GSH) molecule, which is more than 99% in reduced form in the cell [2]. In this metabolism, it is vital for the cell that the GSH/GSSG ratio remains at a certain level. Thus, the continuity of several vital functions of the cell, such as protein and DNA biosynthesis as well as detoxification of reactive oxygen species, is ensured [17]. This is especially important for erythrocytes. In a study, when erythrocytes were exposed to oxidative stress for various reasons, there was a decrease in the enzymes of antioxidant systems such as G6PD and GR. This situation was determined by the increase in malondialdehyde (MDA), which is an indicator of lipid peroxidation [18]. GR enzyme has been purified from many different tissues and its biochemical properties have been examined. In addition, inhibition studies have been conducted on enzyme activity with different drugs and chemicals [6, 13, 19]. In our study, the effects of some chemotherapy drugs such as ibandronic acid, oxaliplatin, carboplatin and cisplatin on GR enzyme activity purified from sheep spleen tissue were investigated. It was determined that the GR enzyme precipitated by 20-70% with the homogenate prepared first in the purification of the enzyme. The precipitation value we found between 20-70% is compatible with the literature review we conducted [6].Additionally, in literature reviews, the ammonium sulphate range of the GR enzyme purified from sheep liver is 0-60% [20], the ammonium sulphate precipitation range of the GR enzyme purified from human and bovine erythrocytes is 30-70% [7]. and the ammonium sulphate range of the GR enzyme purified from sheep brain is 30-70% [7]. The range was found to be 35-55% [21]. In the next stage of purification, 2', 5'-ADP Sepharose 4B affinity chromatography was applied, which provides very fast and high-yield purification [6].After the purification process, kinetic studies were carried out. Here, the IC_{50} value for the oxaliplatin drug based on GR enzyme activity purified from sheep spleen tissue was calculated as 4.53 mM. In addition, it was determined that the drugs ibandronic acid, carboplatin and cisplatin did not have a significant effect on the enzyme. In a literature review conducted on sheep spleen tissue, the effects of some antibiotics and anti-inflammatory drugs were investigated on GR enzyme activity. These; ampicillin, lincomycin, novamizole, gentamicin, streptomycin sulfate, cefazolin sodium, Cefoperazone sodium, prekort-lyo, amoxicillin, tylosin, cefuroxime sodium, ketogesik and clindamycin. Among these drugs, those that have an inhibitory effect on enzyme activity are prekort-lyo (1.27 mM), ampicillin (3.22 mM), streptomycin sulfate (7.95 mM), cefoperazone sodium (16.97 mM) and gentamicin (17.20 mM).) Of these; Ampicillin and gentamicin inhibited non-competitively, while streptomycin sulfate, cefoperazone sodium and precort-lyo inhibited competitively [6].

In conclusion; Inhibitors are of great importance for enzyme therapeutic approaches. Since the GR enzyme keeps the vital GSH/GSSG ratio under control, the use of inhibitors that can disrupt this balance by inhibiting the GR enzyme must be controlled.

References

[1] Taser P, &., Ciftci , M. (2012). Purification and characterization of glutathione reductase from turkey liver. *Turkish Journal of Veterinary ve Animal Science*, 36(5): 546-553.

[2] Keha, EE., Küfrevioğlu, Öİ. Biyokimya, Aktif Yayınevi, 6. Baskı, İstanbul, 2010.

[3] Demir, H., Erat, M., & Şakiroğlu, H. (2006). In vitro effects of some antibiotics on glutathione reductase obteined from chicken liver. *Turk. J. Vet. Anim. Sci*, (30):513-519.

[4] Ciftci, M., Kufrevioglu, OI., Gundogdu, M., & Ozmen, I. (2000). Effects of some antibiotics on enzyme activity of glucose-6-phosphate dehydrogenase from human erythrocytes. *Pharmacological Research.* 41(1):109-113.

[5] Sevki, A., & Ciftci, M. (2012). Purification of rat kidney glucose 6 phosphate dehydrogenase, 6-phosphogluconate dehydrogenase, and glutathione reductase enzymes using 2', 5'-ADP sepharose 4B affinity in a single chromatography step. *Protein Expression and Purification.* 81(1):1-4.

[6] Çoban Ç., *Glutatyon Redüktaz Enziminin Koyun Dalak Dokusundan Saflaştırılması, Karakterizasyonu ve Bazı Antibiyotiklerin Enzim Aktivitesi Üzerine Etkilerinin Araştırılması* Doktora Tezi, Bingöl Üniversitesi, Fen bilimleri Enstitüsü, Kimya Anabilim Dalı, 2022, s. 88, Bingöl.

[7] Erat M., *İnsan ve sığır eritrosit glutatyon redüktaz enziminin saflaştırılması, bazı ilaç ve kimyasal maddelerin inhibisyon veya aktivasyon etkilerinin araştırılması,* Doktora tezi, Atatürk Üniversitesi, Fen Bilimleri Enstitüsü, Kimya Anabilim Dalı, 2002, 112-11, Erzurum.

[8] Temel, Y., Bozkuş, T., Karagözoğlu, Y., & Çiftçi M. (2017). Glutatyon redüktaz (GR) enziminin japon bıldırcın (Coturnix coturnix japanica) eritrositlerinden saflaştırılması ve karakterizasyonu. *Journal of the Institute of Science and Technology,* 7.3: 143-150.

[9] Çoban, Ç., & Çiftci, M. (2022). Bazı İlaçların Koyun Dalak Dokusundan Saflaştırılan Glukoz-6-Fosfat Dehidrogenaz Enzimi Üzerine *İn Vitro* Etkileri. *Türk doğa ve fen dergisi,* 11: 1, 29 – 35

[10] Kayaalp, SO. (2002) *Rasyonel tedavi yönünden tıbbi farmakoloji.*10. Baskı. Kitabın muhtelif bölümleri

[11] Smith, LL. (1987) Cholesterol autoxidation. *Chem. Phys.* Lipids 44: 87-125

[12] Bradford, MM. (1976) A rapid and sensitive method for the quantitation of microgram quantities of protein utilizing the principle of protein dye binding. *Anal. Biochem.* 72(1 2): 248–254

[13] Temel, Y., & M.Ş. Taysi. 2019. The Effect of Mercury Chloride and Boric Acid on Rat Erythrocyte Enzymes. *Biological Trace Element Research* 191(1).

[14] Demir, H., Erat, M., & Şakiroğlu, H. (2006). In vitro effects of some antibiotics on glutathione reductase obteined from chicken liver. *Turk. J. Vet. Anim. Sci*, 30):513-519.

[15] Carlberg, I., & Mannervik, B. (1981). Purification and characterization of glutathione reductase from calf liver. An improved procedure for affinity chromatography on 2', 5'-ADP-Sepharose 4B. *Anal. Biochem*, 116:531–536

[16] Çoban, Ç., Teme,l Y., & Çiftci, M. (2022). Koyun Dalak Dokusundan Saflaştırılan Glukoz-6-Fosfat Dehidrogenaz ve Glutatyon Redüktaz Enzimi Üzerine Diklofenak Sodyumun *İn Vitro* Etkileri. *Journal of the Institute of Science and Technology.* 12:3, 1624 – 1634.

[17] Çakmak, R., Durdagi, S., Ekinci, D., Şentürk, M., & Topal, G. (2011). Design, synthesis and biological evaluation of novel nitroaromatic compounds as potent glutathione reductase inhibitors. *Bioorganic & medicinal chemistry letters*, 21(18): 5398- 5402.

[18] Stocks, J., Offerman, EL., Modell, CB., & Dormandy, TL. (1972) The Susceptibility to Autoxidation of Human Red Cell Lipids in Health and Disease. *Brit J Haematol* 23: 713-24.

[19] Ekinci, D., & Şentürk, M. (2013). Assesment of metal inhibition of antioxidant enzyme glutathione reductase from rainbow trout liver. *Journal of Enzyme Inhibition and Medicinal Chemistry* , 28(1): 11-15.

[20] Ulusu, NN., & Tandogan, B. (2007). Purification and kinetic properties of glutathione reductase from bovine liver. *Mol Cell Biochem*, 303: 45-51

[21] Acan L., & Tezcan, EF. (1989). Sheep brain glutathione reductase: purification and general properties. *FEBS Lett* 250(1): 72-74

Pomegranate Peel Waste: A Study on Methylene Blue Adsorption in Wastewater

Tiba SALEH GHANI AL-OKAIDAT [1], *Jussie Berna MOULENDA MOULENDA*[1]

M. Bora AKIN [1*]

[1] *Department of Chemical Engineering, Çankırı Karatekin University, Çankırı, Turkiye*

Abstract

While overall, biosorbents offer an environmentally friendly, sustainable and cost-effective solution, appropriate biosorbent selection and temperature of process conditions are important to ensure maximum efficiency in certain applications. The type of biosorbent, preparation type and concentration, temperature and pH have an impact on the removal rate.

The results of this effect on the removal of dyes from pomegranate peel in wastewater were investigated. The aim of the study is to evaluate the processes of removing methylene blue from water using pomegranate peel. In the study, what are the characteristics of adsorption distributions of variables such as dyestuff temperature, adsorbent amount and temperature. The findings show that pomegranate peel can be used in the adsorption of methylene blue in water without any pretreatment under the examined conditions.

Keywords: *Adsorption, Wastewater, Methylene Blue, Pomegranate peel, Adsorbent*

1. Introduction

The presence of dyes in wastewater is a critical problem due to their effects on ecosystems and human health. In recent years, research on cheap and environmental-friendly adsorbents for the removal of dyes from wastewater has attracted attention. Pomegranate peel is being studied as a potential adsorbent in the removal of dyes from aqueous solutions. Various studies have demonstrated the potential of pomegranate peel as a low-cost and renewable biosorbent in the removal of various pollutants from wastewater [1]. It is possible to use waste pomegranate peel as an adsorbent for dyes found in wastewater [2]. Extensive studies including isotherms, kinetics and thermodynamics on methylene blue adsorption with pomegranate peel also support this situation [3].

In this study, the use of pomegranate peel for the adsorption of dyes in wastewater treatment by changing various parameters is revealed and the adsorption capacity for methylene blue in water is examined. The parameters of the study were chosen as time, temperature, adsorbent dose and initial dye concentration.

2. Materials and Methods

Metileb was obtained from Blue Sigma Aldrich. Pomegranate peels were dried using a vacuum oven at 80 °C. After drying, the size was reduced by grinding in a mortar. A magnetic stirrer (IKA) and UV spectrophotometer (Shimadzu) were used in methylene blue adsorption experiments.

In this study, experiments on the adsorption of Methylene Blue were carried out comprehensively. First, 1000 mL of Methylene Blue stock solution was prepared at a concentration of 1 g/L. In order to obtain different concentrations from this stock solution, a calibration chart was created by dilution processes. The wavelength of the UV spectrophotometer used in the measurement of Methylene Blue was determined as 665 nm.

In the experiments conducted to determine the adsorption capacity, the initial concentrations of Methylene Blue were set as 10, 25, 50, 100, 200, 300, 400, 500, 750 and 1000 mg/L, respectively. Experiments were carried out at 25 °C using 0.5 mg/L adsorbent in 100 mL solutions prepared.

In time-dependent experiments, a concentration of 200 mg/L Methylene Blue was used and the samples taken during the removal process were examined at the following time periods: 0, 2, 5, 10, 20, 30, 45, 60, 90, 180, 240, 300, 360, 420 and 1440 minutes. The samples taken were measured with a UV spectrophotometer.

* Corresponding author. *e-mail address: mbakin@karatekin.edu.tr*

Additionally, experiments were conducted at temperatures of 5 °C, 25 °C and 40 °C to examine the temperature effect on the adsorbent. In order to investigate the effect of adsorbent dosage, the amounts of adsorbent used were determined as 0.3, 0.5, 1 and 2.5 mg/L.

The parameters used in the experiments and the values chosen for these parameters has been given Table 1.

Table 1. Parameters and levels of the study

Temperature (°C)	Adsorbent Dose (mg/L)	Init. Dye Conc. (mg/L)	Time(min)
5	0.3	10	0
25	0.5	25	2
40	1	50	5
	2.5	100	10
		200	20
		300	30
		400	45
		500	60
		750	90
		1000	180
			240
			300
			360
			420
			1440

3. Results and Discussion

3.1. Effect of Initial Dye Concentration

In the study, adsorption capacities (q_e) were examined using adsorbent with 0.5 mg/L for different concentrations. The q_e values obtained for the concentrations examined in the study are given in Figure 1. Among the initial concentrations, the highest adsorption capacity was obtained at 0.4321 mol/kg and 500 mg/L. A rapid increase is observed in the q_e value up to the initial concentration of 500 mg/L. 200 mg/L was chosen as the working concentration and this concentration was used to examine other parameters.

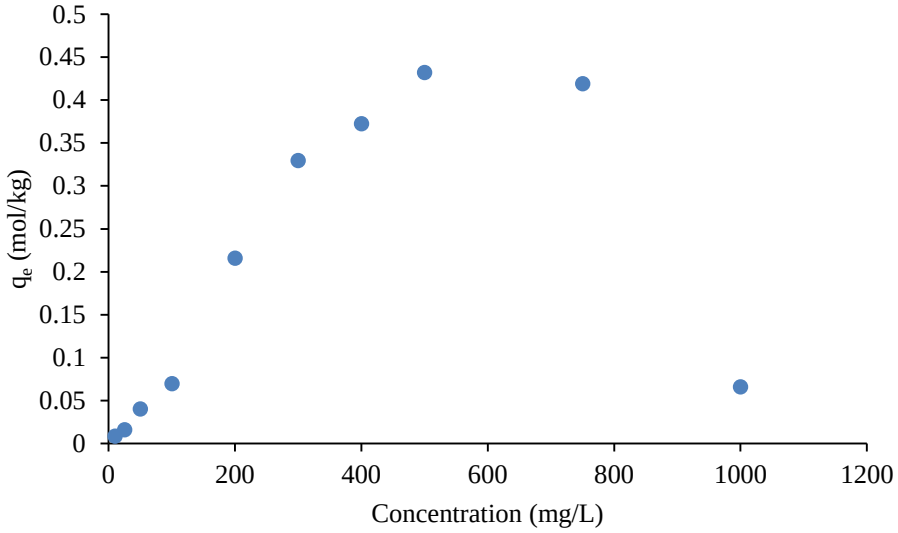

Figure 1. Effect of dyestuff initial concentrations on adsorption capacity.

3.2. Effect of Time

For the experiment in which the effect of time on q_e was examined, 200 mg/L was chosen as the initial concentration. To find the q_e value at the selected concentration, concentration values were found by measuring samples taken at certain times. When Figure 2a is examined, it is understood that the concentration decreases over time, meaning that the adsorbent does its job. At the end of 1440 minutes, the dye concentration decreases to 159.28 mg/L. The calculation made using concentrations shows the change of q_e value with time (Figure 2b). At the end of 1440 minutes, the q_e value is 0.2161 mol/kg at an initial dye concentration of 200 mg/L.

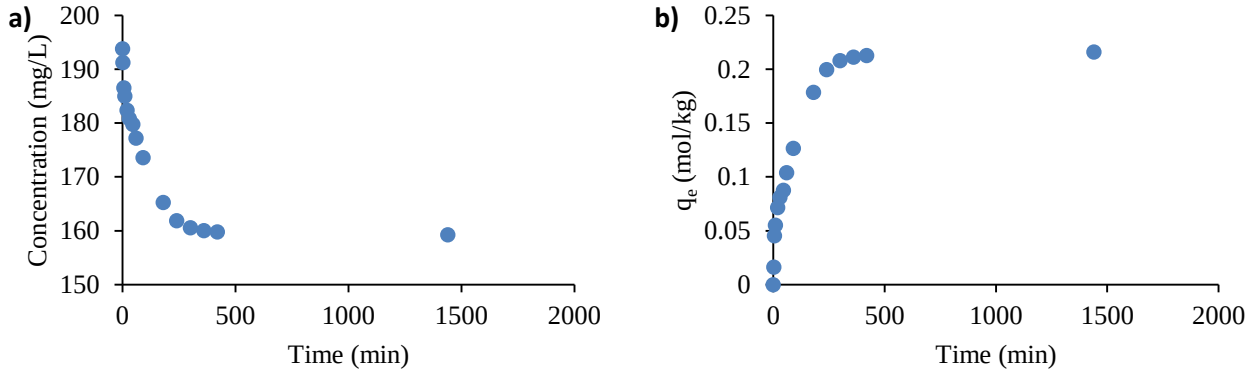

Figure 2. Effect of 0.5 mg/L adsorbent at 200 mg/L initial dye concentration: a) Concentration and b) adsorbent capacity

3.3. Effect of Adsorbent Amount

As the amount of adsorbent increases, the q_e value becomes 0.2383 at 0.3 mg/L and 0.2161 mol/kg at 0.5 mg/L. While the q_e value is 0.1324 at 1 mg/L adsorbent amount, this value decreases to 0.0608 at 2.5 mg/L adsorbent amount (Figure 3a). The decrease in q_e appears to be linear. The regression coefficient was obtained as 0.9149. It is seen that the highest adsorption percentage is 25.1% with the use of 2.5 mg/L adsorbent, and the closest value to this value is 21.8% with the use of 1 mg/L adsorbent (Figure 3b).

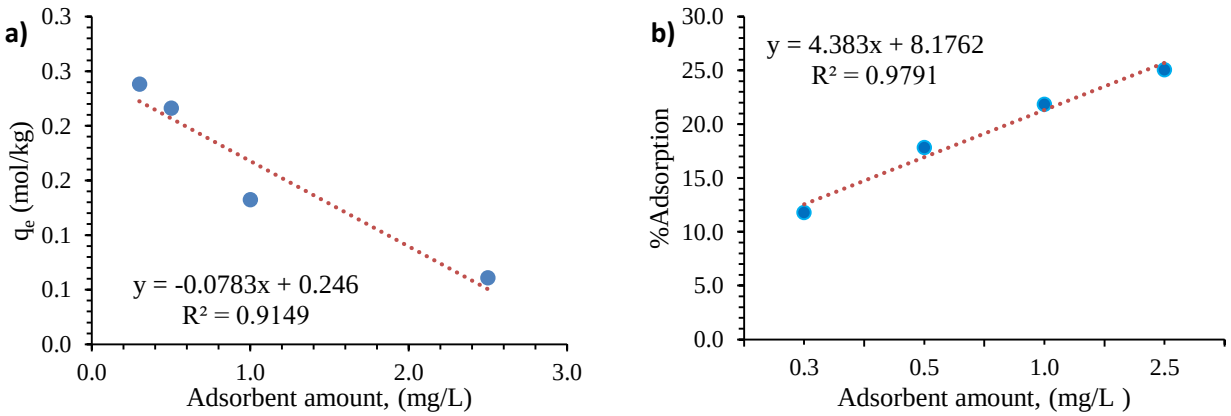

Figure 3. Effect of adsorbent amount a) adsorption capacity, b) Adsorption percentage

3.4. Effect of Temperature

In experiments conducted at 5 °C, 25 °C and 40 °C, where the effect of temperature on adsorption capacity was examined, q_e values were 0.3542 mol/kg at 5 °C, 0.2161 mol/kg at 25 °C and 0.1186 mol/kg at 40 °C, respectively. According to the data obtained, the q_e value decreases as the temperature increases (Figure 4).

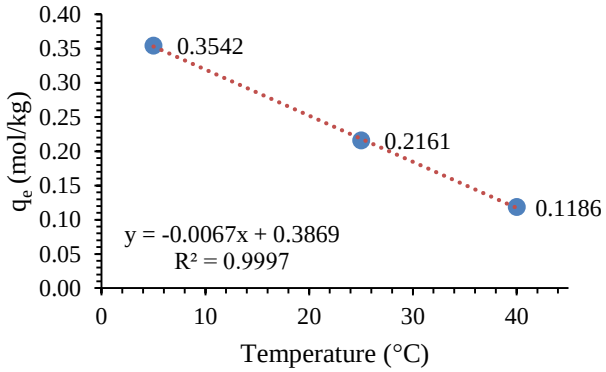

Figure 4. Effect of temperature on adsorption capacity

4. Conclusion

The data obtained in the study show that the adsorption of dyestuff from dried pomegranate peels and Methylene Blue solutions is possible. It was observed that the q_e value increased with increasing initial dye concentration. The decrease begins after 500 mg/L. By using 0.5 mg/L adsorbent at an initial concentration of 200 mg/L, the q_e value was obtained as 0.2161 mol/kg. As the amount of adsorbent used as adsorbent increases to 2.5 mg/L, the adsorption efficiency increases and reaches 25.1%. At this yield, the q_e value is 0.0608 mol/kg. While the adsorption capacity decreased with increasing temperature, the q_e value was obtained as 0.1186 mol/kg at 40 °C. The q_e value was found to be 0.3542 mol/kg at 5 °C.

Acknowledgement

All experimental work was conducted in the Chemical Engineering Department Laboratory at Çankırı Karatekin University. The authors would like to thank the Chemical Engineering Department.

References

[1] Bhatnagar A, Sillanpää M, Witek-Krowiak A. Agricultural Waste Peels as Versatile Biomass for Water Purification – A Review. Chem Eng J 2015. https://doi.org/10.1016/j.cej.2015.01.135.
[2] Msaadi R, Sassi W, Hihn J-Y, Ammar S, Chehimi MM. Valorization of Pomegranate Peel Balls as Bioadsorbents of Dyes in Aqueous Media 2020. https://doi.org/10.26434/chemrxiv.13117691.
[3] Jawad Al-Taie AH, Waheeb AS, Rashid RA, Nawawi WI, Yousif E. Equilibrium Isotherms, Kinetics, and Thermodynamics Studies of Methylene Blue Adsorption on Pomegranate (Punica Granatum) Peels as a Natural Low-Cost Biosorbent. DWT 2018. https://doi.org/10.5004/dwt.2018.22021.

Experimental and modeling investigation of mass transfer during hot air drying of Ahlat pear

***Osama T. A. ALSHAMHAZI*[1,*], *İlknur KÜÇÜK*[2], *İbrahim DOYMAZ*[3]**

[1,2,3] *Chemical Engineering Department, Yıldız Technical University, İstanbul, Turkey*

Abstract

Drying is an energy-intensive process involving both heat and mass transfer, widely employed as a technique for preserving food. Ahlat pear (*Pyrus elaegrifolia* L), naturally grown in Turkey and contains C and B vitamins, caroten, pectin, fruit acid, sugar and tannin. It can be consumed in dried or fresh form. The focus of this study is examining the efficacy of a cabinet dryer under diverse air temperatures (45, 55, and 65°C) with a consistent air velocity of 2 m/s in the drying process of Ahlat pears. The initial moisture content of Ahlat pears' samples was successfully reduced from 68.75% to 20% (wet basis), and a comprehensive analysis was made for their drying characteristics and kinetics. The impact of drying air temperature on drying time is clearly substantiated by the results. Drying curves illustrate a falling-rate period during the drying process without noticing any constant-rate period. The study further elucidates the effective moisture diffusivity, evaluated via Fick's second law, revealing a range from 3.25×10^{-9} to 7.04×10^{-9} m²/s across the investigated conditions. Activation energy was estimated by an Arrhenius type equation as 35.51 kJ/mol. Five different mathematical models (Alibas, Aghbashlo, Logarithmic, Logistic, Page ve Henderson and Pabis) were evaluated for moisture ratios using nonlinear regression analysis. The results of regression analysis indicated that the Alibas model is the best model to describe the drying behaviour with the lowest χ^2 and RMSE values and highest R^2 values.

Keywords: *Hot-air drying, Ahlat pear, effective diffusivity, mathematical modelling, Alibas model.*

1. Introduction

Ahlat pear is a species of wild pear that has a wide distribution area in the region, starting from Southeastern Europe to Anatolia, the Caucasus and Crimea, and can survive in dry and unfavorable conditions. This thorny tree, belonging to the Rosaceae family, helps to solve many health concerns [1-4]. Ahlat pear is traditionally used for treating diarrhea while its leaves are employed for anti-inflammatory purposes and its bark infusion is prescribed for intestinal ulcers and palpitations. Additionally, it exhibits diverse biological activities such as analgesic, anti-inflammatory, antioxidant, antispasmodic, antimicrobial, antibacterial, and wound-healing properties. After Ahlat pear is collected from the tree, it can be consumed both fresh and dried [3,5].

Drying is a traditional or industrial preservation method that is used in the food industry. The reduction of moisture content through drying is essential for increasing the shelf life of food products, thereby reducing transportation, packaging, and storage costs. Various drying techniques such as spray-drying, freeze-drying, and non-thermal methods have gained importance in the food industry [6-8]. Hot-air drying is a commonly used method in the food industry due to its cost-effectiveness [8].

Mathematical models play a crucial role in understanding and optimizing the drying process of food products. These models can be categorized into theoretical, semi-theoretical, and empirical models, each considering different aspects of the drying phenomenon [9]. Thin-layer drying models have been widely used to describe the drying process of agricultural products. These models are essential for determining effective moisture diffusivity and understanding the kinetics of the drying process [10]. There is very few information in the literature regarding mathematical modeling of Ahlat pear drying. In this present study, the main objectives were to investigate the effect of air temperature on the drying time, fit the experimental data to five drying models, and compute effective moisture diffusivity and activation energy.

2. Materials and Methods

2.1. Preparation of samples and drying procedures

* Corresponding author. *e-mail address: osama7alshamhazi@gmail.com.*

Good quality Ahlat pears were bought from a local market in Istanbul, Turkey. The initial moisture content of Ahlat pear was determined by using an oven at 105°C for 6 hours. Triplicate samples were used for the determination of moisture content and the average values were reported as 68.75%, w.b.

Drying experiments were carried out in a cabinet dryer (APV & PASILAC, UK) at Yıldız Technical University Department of Chemical Engineering. The experiments were conducted with about 50±0.9 g of ahlat pear samples and samples dried at 45, 55, and 65°C air temperatures. The moisture losses were recorded at 15 minute intervals during the drying process, using a digital balance (Mettler-Toledo AG, Switzerland) during drying. After achieving 20% moisture content, drying process was stopped and dried samples were waited to cool down then packed into polyethylene bags and stored at ambient temperature. The experiments data was collected and used to draw the drying curves.

2.2. Mathematical modelling and data analysis

Six models were evaluated to describe the drying kinetics of the Ahlat pear samples (Table 1). The moisture content (M) and moisture ratio (MR) of Ahlat pear slices were computed by the following equations:

$$M = \frac{W - W_d}{W_d} \quad (1)$$

$$MR = \frac{M_t - M_e}{M_0 - M_e} \quad (2)$$

where M represents the moisture content (kg water/kg dry matter), W is the sample weight (kg), W_d is the dry matter content of the sample (kg), and t is the drying time (min). M_e and M_t stand respectively for equilibrium moisture content and moisture content at time t (kg water/kg dry matter). Considering that M_e is significantly smaller than both M_0 and M_t values, M_e can be ignored, allowing the expression of MR as M_t/M_0 [11].

Table 1. Mathematical models designed for fitting to the drying of Ahlat pear

Reference	Model Name	Model
[12]	Alibas	$MR = a\exp((-kt^n) + bt) + g$
[13]	Aghbashlo et al.	$MR = \exp(-at/(1+bt))$
[14]	Henderson and Pabis	$MR = a\exp(-kt)$
[11]	Logarithmic	$MR = a\exp(-kt) + c$
[15]	Page	$MR = a\exp(-kt^n)$
[16]	Logistic	$MR = a/(1 + b\exp(kt))$

The experimental data underwent analysis utilizing the Statistica 10 software package (StatSoft Inc., USA). Model parameters were determined through a non-linear regression procedure employing the Levenberg-Marquardt algorithm. The assessment of the fitting accuracy of experimental data to all models was conducted using metrics such as the coefficient of determination (R^2), reduced chi-square (χ^2), and root mean square error (RMSE). The R^2, χ^2 and RMSE were calculated from the following formulas that are given in Table 2:

Table 2. The R^2, χ^2 and RMSE formulas

$R^2 = 1 - \frac{\sum_{i=1}^{N}\left(MR_{pre,i} - MR_{\exp,i}\right)^2}{\sum_{i=1}^{N}\left(\overline{MR}_{pre} - MR_{\exp,i}\right)^2}$	$\chi^2 = \frac{\sum_{i=1}^{N}\left(MR_{\exp,i} - MR_{pre,i}\right)^2}{N - z}$	$RMSE = \left[\frac{1}{N}\sum_{i=1}^{N}\left(MR_{pre,i} - MR_{\exp,i}\right)^2\right]^{1/2}$

where $MR_{exp,i}$ represents the experimental dimensionless moisture ratio, $MR_{pre,i}$ denotes the predicted dimensionless moisture ratio, N stands for the number of observations, and z signifies the number of constants. A superior fit is indicated by a higher R^2 value, accompanied by lower χ^2 and RMSE values [17].

2.3. Determination of effective moisture diffusivity and Computation of activation energy

The values of the effective moisture diffusivity (D_{eff}) for dried Ahlat pear are based on the application of Fick's second law of diffusion equation. The analytical solution for Fick's second law in the context of unsteady-state diffusion within Cartesian coordinates, assuming moisture migration occurs through diffusion, with negligible shrinkage, constant effective diffusivity, and temperature throughout the drying process is reformulated in logarithmic form as follows:

$$ln(MR) = ln\left(\frac{8}{\pi^2}\right) - \left(\frac{\pi^2 D_{eff}}{4\,L^2}\right)t \tag{3}$$

The effective moisture diffusivity is determined by graphing the experimental drying data as *ln* (*MR*) against time (min). According to Eq. (3), the plotted *ln* (*MR)* versus time yields a linear relationship with a slope represented by (K), where:

$$K = \left(\frac{\pi^2 D_{eff}}{4\,L^2}\right) \tag{4}$$

The relationship between effective diffusivity and temperature is commonly expressed by the Arrhenius equation:

$$D_{eff} = D_0\, exp\left(-\frac{E_a}{R(T + 273.15)}\right) \tag{5}$$

where D_0 represents the pre-exponential factor in the Arrhenius equation (m^2/s), E_a expresses the activation energy (kJ/mol), *R* stands for the universal gas constant (kJ/(mol×K)), and *T* represents the temperature (°C).

3. Results and Discussion

3.1. Analysis of drying curves and Evaluation of models

Figure 1(A) presents variations in the moisture content as a function of drying time at 45, 55 and 65°C. It can be noticed that drying time was reduced along with the increase in the air-drying temperatures as awaited. The drying times were found to be 855, 630 and 405 minutes at air temperatures of 45, 55 and 65°C, respectively. The moisture content decreases constantly with drying time. The drying time at 45°C temperature was 2.111 times bigger than the drying time of 65°C temperature. A similar result was observed in the study done by Doymaz and İsmail [18], when the air temperature was increased by 20°C, the drying time at the first temperature was 2.5 bigger than the drying time of the second temperature.

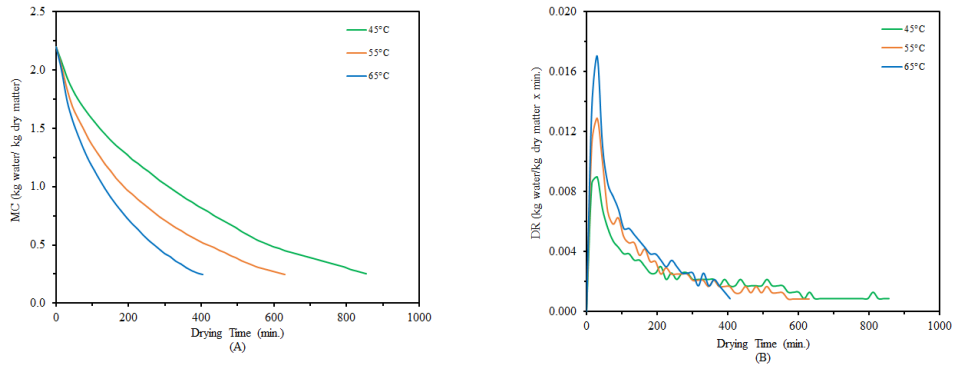

Figure 1. (A) Moisture content versus drying time, (B) Drying rate versus drying time of Ahlat pear samples at 45,55,65°C.

Figure 1(B) illustrates the drying rate curves of Ahlat pear. The drying rate exhibits a continual decrease throughout the drying period. Initially, higher drying rates are observed, followed by a decline corresponding to the reduction in sample moisture content. This decline is attributed to the shrinking of samples, leading to decreased porosity and an increased resistance to water movement, resulting in a further reduction in drying rates. The complete prevalence of the falling-rate period suggests that moisture movement in Ahlat pear slices is predominantly governed by diffusion as the primary physical mechanism [19].

The best model selected is based on the highest R^2 and the lowest χ^2 and RMSE values. Results of the statistical computing are shown in Table 3. The R^2 values for all models were above 0.99. Among the drying models tested, Alibas model obtained the R^2 values as 0.9994 and the lowest $\chi 2$ values as 0.000037 and RMSE values as 0.037659 describe best model for 45°C. For 55 and 65°C, Alibas model is also the best model and the R^2 values are 0.9997 and 0.9994, χ^2 values are 0.000017 and 0.000041 and RMSE values are 0.015918 and 0.022185 for 65°C and 75°C, respectively.

Table 3. Statistical parameters of models for different temperatures.

T (°C)	Model	R^2	χ^2	RMSE
45°C	Alibas	0.9994	0.000037	0.037659
	Aghbashlo et al.	0.9969	0.000177	0.088279
	Henderson and Pabis	0.9968	0.000183	0.066819
	Logarithmic	0.9968	0.000185	0.068799
	Page	0.9961	0.000222	0.067127
	Logistic	0.9936	0.000360	0.114856
55°C	Alibas	0.9997	0.000017	0.015918
	Aghbashlo et al.	0.9991	0.000053	0.038997
	Henderson and Pabis	0.9981	0.000112	0.057381
	Logarithmic	0.9956	0.000244	0.084117
	Page	0.9951	0.000279	0.088475
	Logistic	0.9909	0.000507	0.110386
65°C	Alibas	0.9994	0.000041	0.022185
	Aghbashlo et al.	0.9988	0.000075	0.036828
	Henderson and Pabis	0.9983	0.000116	0.046981
	Logarithmic	0.9970	0.000191	0.058423
	Page	0.9966	0.000223	0.062423
	Logistic	0.9950	0.000319	0.069941

3.2. Effective moisture diffusivity and activation energy

The effective moisture diffusivity of the was calculated by plotting ln(MR) against drying time and employing the slope method. The calculated values of effective moisture diffusivity (D_{eff}), determined using Eq. (3), are presented in Figure 2(A). Within the drying temperature range of 45-65°C, the D_{eff} values for Ahlat pear ranged from 3.25×10^{-9} to 7.04×10^{-9} m²/s. The highest D_{eff} value was observed at 65°C and the lowest at 45°C. Furthermore, the D_{eff} values obtained for Ahlat pear slices are like those proposed by Toğrul et al. [19].

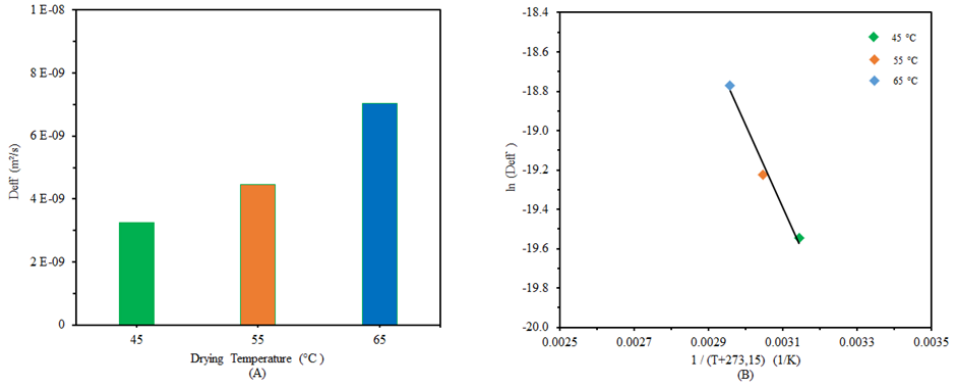

Figure 2. (A) Variation of effective moisture diffusivity with air temperatures, (B) Arrhenius-type relationship between effective diffusivity and reciprocal absolute temperature.

Graphing ln(D_{eff}) against 1 / (T+273.15) results in a linear relationship with a slope equivalent to ($-E_a/R$), facilitating the straightforward estimation of E_a (Figure 2.(B)). Equation 6 shows the impact of temperature on D_{eff} for the samples, with the associated coefficients:

$$D_{eff} = 1.4657 \times 10^{-3}\, exp\left(-\frac{4150.4}{(T+273.15)}\right) \quad (R^2 = 0.9859) \tag{6}$$

The determined activation energy value is 35.51 kJ/mol, which closely aligns with activation energy values reported in the literature for pear drying [18,19].

4. Conclusion

Drying characteristics of Ahlat pear were examined using a cabinet dryer at varieous temperatures of 45, 55, and 65°C, with a consistent air velocity of 2 m/s. Air temperature emerged as a crucial factor influencing the drying process of Ahlat pear, where higher drying temperatures led to shorter drying times. To elucidate the drying kinetics of Ahlat pear, six drying models were applied and fitted to the experimental data. Statistical analysis revealed that the Alibas model effectively predicted the experimental data across all air temperatures. The effective diffusivity values for Ahlat pear samples ranged from 3.25×10^{-9} to 7.04×10^{-9} m²/s. Additionally, the activation energy was determined to be 35.51 kJ/mol. These findings contribute valuable insights into the drying behavior of Ahlat pear under various conditions.

References

[1] Beigi, M. (2016). Energy efficiency and moisture diffusivity of apple slices during convective drying. *Food Science and Technology*, 36(1), 145-150.

[2] Ilhan, M., Akkol, E.K., Taştan, H., Dereli, F.T.G., & Tümen, I. (2019). Efficacy of Pyrus elaeagnifolia subsp. elaeagnifolia in acetic acid–induced colitis model. *Open Chemistry*, 17(1), 13-22.

[3] Yerliturk, F.U., Arslan, O., Sinan, S., Gencer, N., & Ozensoy, O. (2008). Characterization of polyphenoloxidase from wild pear (Pyrus elaegrifolia). *Journal of Food Biochemistry*. 32(3), 368-383.

[4] Anşin, R., & Özkan, Z. C. (1993). Seed Plants (SPERMATOPHYTA) Woody Taxa, *Karadeniz Technical University, Faculty of Forestry*, Publication No: 19, Trabzon, Turkey.

[5] Siddiq, M., & Cash, J.N. (2000). Physico-chemical properties of polyphenol oxidase from D'anjou and Bartlett pears (*Pyrus communis* L.). *Journal of Food Processing and Preservation*, 24(5), 353-364.

[6] Witrowa-Rajchert, D., Wiktor, A., Sledz, M., & Nowacka, M. (2014). Selected emerging technologies to enhance the drying process: a review. *Drying Technology*, 32(11), 1386-1396.

[7] Kandasamy, S., & Naveen, R. (2022). A review on the encapsulation of bioactive components using spray-drying and freeze-drying techniques. *Journal of Food Process Engineering*, 45(8), e14059.

[8] Martínez-Sánchez, C., Solis-Ramos, A., Rodríguez-Miranda, J., Juárez-Barrientos, J., Ramírez-Rivera, E., Ruiz-López, I., Gomez-Aldapa, C.A., & Herman-Lara, E. (2022). Evaluation of ascorbic acid impregnation by ultrasound-assisted osmotic dehydration in plantain. *Journal of Food Processing and Preservation*, 46(10), e16839.

[9] Wang, Z., Sun, J., Liao, X., Chen, F., Zhao, G., Wu, J., & Hu, X. (2007). Mathematical modeling on hot air drying of thin layer apple pomace. *Food Research International*, 40(1), 39-46.

[10] Kara, C., & Doymaz, İ. (2014). Effective moisture diffusivity determination and mathematical modelling of drying curves of apple pomace. *Heat and Mass Transfer*, 51(7), 983-989.

[11] Afolabi, T.J., Tunde-Akintunde, T.Y., & Adeyanju, J.A. (2015). Mathematical modeling of drying kinetics of untreated and pretreated cocoyam slices. *Journal of Food Science and Technology*, 52, 2731-2740.

[12] Alibas, I. (2012). Microwave drying of grapevine (*Vitis vinifera* L.) leaves and determination of some quality parameters. *Journal of Agricultural Sciences*, 18(1), 43–53.

[13] Aghbashlo, M., Kianmehr, M.H., Khani, S., & Ghasemi, M. (2009). Mathematical modeling of thin-layer drying of carrot. *International Agrophys*, 23, 313-317.

[14] Henderson, S.M., & Pabis, S. (1961). Grain drying theory I: Temperature effect on drying coefficient. *Journal of Agricultural Engineering Research*, 6, 169–174.

[15] Page, G. (1949). Factors influencing the maximum rates of air-drying shelled corn in thin layer. M.S. Thesis. *Department of Mechanical Engineering, Purdue University*, West Lafayette, IN, USA.

[16] Chandra, P.K., & Singh, R.P. (1995). Applied numerical methods for food and agricultural engineers. *CRC Press. Boca Raton*, FL. pp. 163-167.

[17] Marianni, V.C, Perussello, C.A., Cancelier, A., Lopes, T.J., & Silva, A. (2015). Hot-air drying characteristics of soybeans and influence of temperature and velocity on kinetic parameters. *Journal of Food Process Engineering*, 37, 619-627.

[18] Doymaz, İ., & İsmail, O. (2012). Experimental characterization and modelling of drying of pear slices. *Food Science and Biotechnology*, 21, 1377-1381.

[19] Toğrul, İ. T., Çelebi, R.S., & Toğrul, H. (2018). Modeling of drying and shrinkage behavior of Ahlat with applied various pretreatment. *Journal of the Faculty of Engineering and Architecture of Gazi University*,

33(4), 1231-1245.

Political Discourse in the Kazakh Language: A Review of the Literature and the Creation of a Text Corpus

***Ayaulym SAIRANBEKOVA*[1,*], *Laura ORYNBAY*[1], *Banu YERGESH*[2], *Gulmira BEKMANOVA*[2], *Altynbek SHARIPBAY*[1]**

[1]*Faculty of Information Technology, Department of Artificial Intelligence Technologies, L. N. Gumilyov Eurasian National University, Astana, Kazakhstan*

[2]*Digital Development and Distance Learning Department, L. N. Gumilyov Eurasian National University, Astana, Kazakhstan*

Abstract

The corpus of political discourse texts is a collection of text documents containing texts related to political topics, debates and discussions. Such texts can be political speeches, laws, political programs, articles, discussions on social networks, news materials, interviews with political figures and much more.

In this article, the results of a study on the review of literature at the world and local level are written, the work of various researchers is analyzed and examples of their work are given.

This article also provides an overview of the analysis of Internet resources devoted to political discourse in the Kazakh language, as well as describes the initial steps to create a corpus of texts for research in this area. The study's significance lies in supporting the concept of a "hearing state" and contributing to scientific and technological development in Kazakhstan.

Keywords: *political discourse, a text corpus, analysis, Kazakh language, Internet source*

1. Introduction

Political discourse, or the language of power and governance, is critical to understanding the complexities of politics, ideology, and public opinion. In the age of the digital revolution, the Internet has become a valuable repository of political discourse. It allows us to understand the beliefs, aspirations and debates that influence countries and communities.

This article is devoted to a comprehensive study of political discourse analysis in the Kazakh language and this research is funded by the Science Committee of the Ministry of Science and Higher Education of the Republic of Kazakhstan (Grant No. AP19679847).

The first part of the article reviews relevant studies and methodologies related to the creation of structured semantic databases for analyzing political discourse.

The second section is devoted to the study of online resources devoted to political discourse. The issues of categorization and statistical analysis of the huge array of Internet resources collected for the analysis of political discourse in Kazakhstan are considered.

The third part then examines the process of creating a corpus of political texts in Kazakh. The methodology of creating a corpus of political discourse texts is revealed, and the use of a synonymizer containing typical examples of synonymous words in socio-political discourse is demonstrated.

2. Literature Review

Political discourse analysis (PDA) is an interdisciplinary field that plays a key role in understanding political communication, ideology and public opinion [1]. Creating structured semantic databases for political discourse in a specific language, such as Kazakh, involves various linguistic, computational and socio-political challenges. This literature review provides an overview of relevant studies and methodologies related to the creation of structured semantic databases for political discourse analysis.

Political Discourse Analysis and Semantics. An overview of key theoretical and methodological approaches to analyzing political discourse was presented by Chilton [2]. This book provides detailed case studies of how

* Corresponding author. *e-mail address: sairanbekova98@gmail.com.*

political discourse shapes public opinion and policy outcomes. For example, he analyzes how the discourse of European integration has evolved over time, from the early days of the European Union to the present day, and how it has been shaped by different actors and ideologies.

Regarding key studies on semantics in the PDA, one study examined the argument that in political contexts metaphor can be used and is often used for ideological purposes because it activates unconscious emotional associations and thereby contributes to the creation of a myth: politicians use metaphor to tell the right story [3].

Semantic approaches have also been applied to analyze political speeches in the context of emotional expression [4]. The study used an affective computing approach to automatically detect emotional content in political speeches and identify rhetorical strategies through semantic analysis. The results showed the importance of emotional language in political communication and emphasized the value of using semantic approaches for PDA.

Language Resources and NLP. Fundamental knowledge about language processing methods and technologies needed to analyze, categorize and extract information from political texts, speeches and debates can be found in the book by Jurafsky and Martin [5]. The comprehensive coverage of speech and language processing concepts provides a solid foundation for the development of tools and systems that meet the specific requirements of analyzing political discourse in the Kazakh language.

Sentiment Analysis in Political Discourse. Sentiment analysis, especially in the context of political discourse, is a crucial area of research. Bekmanova et al. [6] discuss sentiment processing in socio-political discourse and public speeches, emphasizing the importance of understanding public and social media sentiment. They propose methods and tools for analyzing emotional states and opinions expressed through textual data.

Analyzing emotional states in social networks. The work of Yergesh and Kenjina [7] deals with analyzing the emotional states of users on social media. The study focuses on identifying and understanding the emotions expressed by users on social platforms. This study is in line with the broader task of analyzing sentiments in socio-political contexts, as it aims to identify sentiments in society.

Text Corpus and Corpus Linguistics. A foundational text that discusses the methodology, theory, and practical applications of corpus linguistics can be found in McEnery and Hardie [8], whereas Baker and Egbert [9] provide valuable insights into the methods and techniques used in corpus linguistic research. These works serve as foundational texts for researchers and linguists interested in studying language patterns, usage, and discourse within large datasets called corpora. Although these studies do not specifically focus on political discourse, they provide important insights into corpus linguistics, which is highly relevant in the context of creating a structured semantic database of political discourse in Kazakhs.

Information Sources for Political Discourse in Kazakhstan. Valuable resources for collecting data on political discourse in Kazakh are various online news agencies, political party websites and social media platforms. These sources are analyzed in more detail in the next section.

3. Examination of Online Resources regarding Political Discourse

A variety of sources can be used to create a text corpus of political discourse via the Internet. For example, official government websites can provide access to laws, regulations, official statements, and other policy documents; News websites and agencies provide news, analysis, and commentary on political events and topics; Websites of political parties and organizations contain political programs, speeches of leaders and other materials; Publications and comments on social networks where users discuss political topics; Political blogs and forums may contain opinions and discussions about current political issues; Digital libraries and databases that provide access to academic articles and research in political science and sociology; Videos of political speeches, interviews and discussions on platforms such as YouTube; Online archives containing historical political documents and materials; Recordings of public speeches by political figures available online; Many newspapers and magazines have online versions where articles on political topics can be found.

In Kazakhstan, political texts can be found in such Internet resources as information portals, newspapers and magazines, the official website of the political party, and TV channels (Table 1).

Table 1. Categories of Internet resources and the Number of Resources Collected.

Type of Internet resource	Amount of resources collected
Information portal	439
Newspapers and magazines	128
Official website of the political party	269
TV channels	36
Total	872

In this article, not only the results of the text corpus are published, but also the statistics of Internet resources for creating the corpus are described in detail. Of these, 50% are information portals, such as news sites, district blogs, and official and unofficial sites of cities and 31% are official sites of political parties, the remaining 15% are data from newspapers and 4% are TV channels (Figure 1).

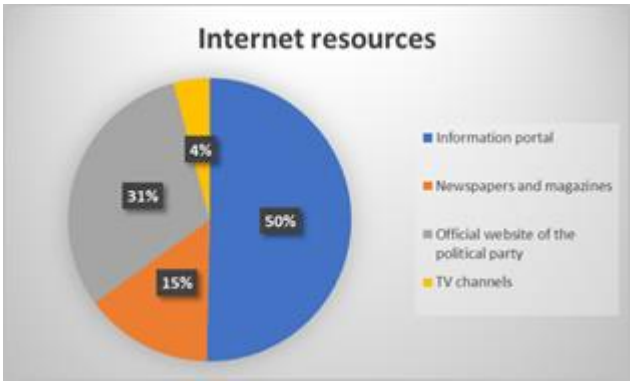

Figure 1. Categories of Internet resources and the Number of Resources Collected (in percentage).

Analyzing political discourse from online sources requires a discerning approach, considering factors like source evaluation, bias and objectivity, relevance, audience and intent, and cross-referencing. Reliable sources of political discourse in the Kazakh language include online publications like “Informburo.kz” [10], “Tengrinews” [11], “Kazpravda.kz” [12], “Sputnik” [13], “BAQ.KZ” [14], “Kazinform” [15], “Egemen Qazaqstan” [16] and more. Bias, objectivity, and the relevance of information must be assessed when evaluating these sources.

Political discourse occurs on the web pages of political parties in Kazakhstan, such as “AMANAT” [17], “Nation's Party of Kazakhstan” [18], “Ak Zhol” [19], “Auyl” [20], and “Baitaq” [21]. Additionally, political science journals and newspapers serve distinct audiences and purposes in shaping political discussions.

4. Establishing a Political Text Corpus in the Kazakh Language

To analyze political processes and opinions in Kazakhstan, a critical analysis of Internet resources related to political discourse was conducted, emphasizing the importance of evaluating sources, identifying bias, and using critical thinking [22]. Based on the analyzed sources, the work on creating a text corpus of political discourse in the Kazakh language was initiated. For this purpose, the previously created synonymizer of standard samples of synonymic words in socio-political discourse and public speech was used [6]. The synonymizer contains 1,000 dictionary entries on the topics “Pre-election advertising”, “Speech of political candidates”, and “Pre-election debates”.

The Synonymizer consists of several columns: “Word”, “Part of Speech”, “Status” (homonym, unambiguous, polysemic), “Meaning”, “Example”, “Synonym”, and “Periphrasis” (Figure 2). It serves as a valuable tool for analyzing and comparing synonyms in texts related to socio-political discourse and public speech.

Word	Part of speech	Status	Meaning	Example	Synonym 1	Synonym 2	Synonym 3	Synonym 4	Synonym 5	Synonym 6	Periphrase1	Periphrase2	Periphrase3	Periphrase4	Periphrase5
акт	noun	unambig	Белгілі бір оқиғаны	Әлепат шал әлі де	хаттама	хат	қағаз	хабарлам	ата-заң		қаулы				
заң	noun	unambig	тұтас алғанда барлық	Заңды, әдетте,	жарғы	низам	мизам	қаулы	құқықты		нормати	қаулы	жарғы		
Конституциялы	noun	unambig	ҚР Конституциясында	1995 жылы 30	Констит	Констит	Констит	Ата Заң			Ата Заң	Констит	Констит	Констит	
толықтыру	verb	unambig	Жетілдіру мақсатымен	Нақ осы кезеңде	толтыру	жетілдіру	аяғына	түгендеу	сұрыпта		жетілдіру	толтыру			
енгізу	verb	unambig	Қолданысқа кіргізу,	Кеншілер руда	қосу	іске қосу	құру	тарату	кірістіру	кіргізу	қолданы	тәжірбие			
жоба	noun	unambig	тиісті талаптарға сәйкес	Осы жобаның	проект	жоспар	схема	теория	чертеж		проект				
баяндалған	verb	unambig	Суреттеу арқылы оқиға	Ұлжан панфиловшыл	мазмұнд	айтылға	хабарлау	білдірген	суреттеу		айтылға	хабарлау	білдірген		
өткізу	verb	unambig	Өткіз етістігінің қимыл	Дүниені өткізу	жіберу	өңдеу	өтеусіз	қылғыту			өтеусіз	айырбас			
азамат	noun	unambig	Кәмелетке толып, ер	Асанжан, азаматсың	тұлға	кісі	адам	пенде	жігіт	ер	Кәмелет	бір елдің			
ерікті	adjective	unambig	Өз еркі өзінде,	Мен – қазақпын азат	ықтиярл	ырықты	құқылы	тәуелсіз	күштеусіз	зорлықс	өз еркі	құқылы	тәуелсіз	күштеусіз	
жасырын	adjective	unambig	Ашық түрде емес, құпия	Осы түн ел әбден	астыртты	құпия	бұғынықы	бүркеніш	ашық	ептеп-	ашық	құпия	көзден	Қалтары	
дауыс беру	verb	unambig	бұл ұсынылған	Бұл кездегі сайлау	сайлау	үміткер	еркін	өз	қолдау		сайлау				
негізделеді	verb	unambig	Негізге алыну, сүйеніну.	Әрбір қимыл өз	айқында	бағдарла	нақтыла	дәлелден			айқында	бағдарла	нақтыла	дәлелден	
дауыс	noun	unambig	Адамның көмейден	Ойын қалған, елең-	үн	дыбыс	саңқылд	дабырла	дабыр-	шуылдау	үн	дыбыс			
баға	noun	polysem	Қазақ тілінде	Алманың бағасы	нарық	бәс	құн	көрсеткі	қаражат		құн	парқы	көрсеткі	бәс	
баға	noun	polysem	білім алушының	Баға көтермелеу	нарық	бәс	құн	көрсеткі	қаражат						
баға	noun	polysem	Адамның қадір-қасиеті,	Нелер ұрпақ әлі де	нарық	бәс	құн	көрсеткі	қаражат						
кеңес	noun	homony	Нұсқаулық, нұсқау,	Жергілікті жердегі	нұсқау	ақыл	пікір	ұсыныс			одақ	қоғам	сот		

Figure 2. A segment from the synonymizer containing standard examples of synonymous words commonly used in socio-political discourse and public speaking.

5. Conclusion

As a result of this research, the sources for the corpus of texts were identified and its formation was successfully carried out. However, since the goal of the project is to develop methods for analyzing political discourse in Kazakh-language social networks to identify both official and unofficial sources of political discourse, as well as to determine the mood of discussions in these sources, the work on this topic will still continue. To achieve this goal, the following tasks will be solved in the future: creation of ontological models on election topics, such as “Pre-election advertising”, “Speeches of political candidates”, and “Pre-election debates”; development of knowledge bases with semantic attributes; formal representation of logical rules for drawing conclusions from these knowledge bases; development of a processor for processing official and unofficial sources of political discourse; creation of a tool (software application) for analyzing the mood of official and unofficial sources of political discourse; creation of a tool (software application) for analyzing the mood of official and unofficial sources of political discourse.

References

[1] Wodak, R. (2015). Critical discourse analysis, Discourse-historical approach. *The International Encyclopedia of Language and Social Interaction*, 1–14.

[2] Chilton, P. (2004). *Analysing political discourse: theory and practice*. London, United Kingdom: Routledge.

[3] Charteris-Black, J. (2011). *Politicians and Rhetoric: The Persuasive Power of Metaphor*. Palgrave Macmillan.

[4] Preoţiuc-Pietro, D., Liu, Y., Hopkins, D., & Ungar, L. (2017). Beyond Binary Labels: Political Ideology Prediction of Twitter Users. In *Proceedings of the 55th Annual Meeting of the Association for Computational Linguistics (Volume 1: Long Papers)*. Stroudsburg, PA, USA: Association for Computational Linguistics.

[5] Jurafsky, D., & Martin, J. H. Speech and Language Processing (Draft-Version from Dec 2020).

[6] Bekmanova, G., Yergesh, B., Ukenova, A., Omarbekova, A., Mukanova, A., & Ongarbayev, Y. (2023). Sentiment Processing of Socio-political Discourse and Public Speeches. In *Computational Science and Its Applications – ICCSA 2023 Workshops* (pp. 191–205). Cham: Springer Nature Switzerland.

[7] Yergesh, B., & Kenzhina, L. (2021). Analysis of the users’ emotional state in social networks. In *ICEMIS'21: The 7th International Conference on Engineering & MIS 2021*. New York, NY, USA: ACM.

[8] Hardie, A., & McEnery, T. (2011). *Corpus Linguistics: Method, Theory and Practice*. Cambridge University Press.

[9] Egbert, J., & Baker, P. (2016). *Triangulating Methodological Approaches in Corpus Linguistic Research*. Taylor & Francis Group.

[10] News Informburo.kz - the latest news in Kazakhstan and the world. (n.d.). Retrieved October 25, 2023, from https://informburo.kz/kaz.

[11] Tengrinews.kz - The main news portal of Kazakhstan. (n.d.). Retrieved from https://kaz.tengrinews.kz/.

[12] Kazakhstan News - current, latest news about everything. (n.d.). Retrieved from https://kazpravda.kz/.

[13] Sputnik Kazakhstan. (n.d.). Retrieved from https://sputnik.kz.

[14] BAQ.KZ - News. Latest news from Kazakhstan. (n.d.). Retrieved from https://baq.kz.

[15] News of Kazakhstan and the world - latest news of the day on inform.kz. (n.d.). Retrieved from https://inform.kz.

[16] Sovereign Kazakhstan – Egemen Qazaqstan. (n.d.). Retrieved from https://egemen.kz.

[17] AMANAT. (n.d.). Retrieved from https://amanatpartiasy.kz.

[18] Official website of the People's Party of Kazakhstan (PPK) (n.d.). Retrieved from https://halykpartiyasy.kz/kz.

[19] Democratic Party of Kazakhstan NGO “Ak Zhol”. (n.d.). Retrieved from https://akzhol.kz.
[20] Party “Auyl”. (n.d.). Retrieved from https://auyl.kz.
[21] «Baytaq» The Green party of Qazaqstan. (n.d.). Retrieved from https://baytaq.kz/kk/main-kz/.
[22] Sairanbekova, A., Orynbay, L., Ukenova, A., Sharipbay, A., & Razakhova, B. (2023). Database Creation of Political Discourse in The Kazakh Language, The XI International Conference on Computer Processing of Turkic Languages “TurkLang 2023”, Bukhara, Uzbekistan (to be published).

Production calculation in non-hazardous waste recycling facility

Zehra Gülten YALÇIN [1]*, ***Mustafa DAĞ*** [2], ***Ercan AYDOĞMUŞ*** [3]

[1,2] *Institute of Science, Faculty of Engineering, Department of Chemical Engineering, Karatekin University, Çankırı, Turkey*

[3] *Institute of Science, Faculty of Engineering, Department of Chemical Engineering, Fırat University, Elazığ, Turkey*

Abstract

In this study, packaging waste collection, separation and pressing work is carried out in a business located in Çankırı. Packaging wastes from various productions are first weighed from the scale and discharged into the collection area. Here, the same size is passed through the appropriate number of separation belts. Packaging wastes from the separation belt are collected in prepared boxes. After the collection separation, it goes to the pressing belt. After the pressing process, the packaging waste is sent to the temporary storage area and the recycling facility. It is offered for sale to companies that are in special demand. Packaging waste, which is defined as non-hazardous waste, is used in the facility. Wooden packaging, metallic packaging, composite packaging, glass packaging, textile packaging wastes are also evaluated in the facility. Since heat treatment is not used in the facility, there is no harmful transfer that will cause air emissions. Despite the fact that domestic wastewater is generated at the facility, it is exempted from "wastewater discharge". The annual production amount, press calculation and necessities of the facility were calculated.

Keywords: *Packaging waste, Production capacity, Waste collection, Waste separation*

1. Introduction

Recycling is a current issue. Waste and pollution are of great importance to humans, the environment and society. For this reason, it concerns the individual, the smallest part of society, and ultimately the whole society. With the increase in industrialization, the world quickly faced this problem[1].

The definitions of waste and garbage are often confused. Not recycling has a negative impact on all living things. The waste collected during recycling is separated in the sorting center and processed into plastic, glass, paper, etc. It is classified as. Additionally, waste management is important in a sustainable economy. Garbage is an unwanted product that is no longer possible to use and cannot be recycled. Waste is defined as a material that is produced during industrial production and also as a result of consumption, and that can be recycled and used again in production. Most importantly, it is necessary to understand that "not all waste is garbage" and improve our evaluation perspective accordingly. Efforts to eliminate garbage or waste depend on the development level of societies. For this reason, all stages from the formation of garbage or waste to its collection, transportation, storage and processing require a certain work [2].

In Turkey, waste was defined for the first time in the Environmental Law No. 2872 dated 1983 as "harmful substances thrown or released into the environment as a result of any activity"[3].

Solid garbage that is an environmental and social problem; Within the waste cycle, from the moment they are produced to the final disposal step, they interact directly or indirectly with the environment and society. On an important issue, the increase in global warming, the decrease in energy resources and the resulting environmental pollution in the process of obtaining waste materials such as glass and paper constitute an important problem [4].In a study, there are various approaches for classification of waste. Solid garbage is divided into seven subheadings when separated according to where they occur. These; They are stated as domestic solid waste, industrial waste, hazardous waste, agricultural and garden waste, medical waste, special waste, construction residue and rubble waste [5].

1.1 Zero waste

The waste management strategy called zero waste has come to the fore in solid waste management. Zero waste is a management system that guides waste management efforts to eliminate waste on-site and prevent problems in burning and storing waste, and to reduce and eliminate waste at its source.

* Corresponding author. *e-mail address: zaltin@karatekin.edu.tr*

Zero waste is an inevitable fact that existing waste consumes natural resources by using water and electricity and creates pollution in terms of environment, soil, air and water. For this reason, it can be described as achieving a waste-free production and consumption structure. In short, minimizing waste is the process of resetting and reviewing resource use [5-7].

In the Zero Waste Regulation published in the Official Gazette No. 30829 dated 12.07.2019 in Turkey, zero waste; "An approach that aims to protect the environment and human health and all resources by preventing/reducing waste generation in production and consumption, prioritizing reuse, collecting the waste generated separately at the source, and reducing the amount of waste to be sent for disposal by ensuring recycling and/or recovery"; The zero waste management system is; It is defined as "a management system created by taking into account the benefit and cost factors, starting from the prevention of waste generation, reducing waste, segregating it at the source, temporary storage, separate collection, transportation and processing" [6-10].

In the current company, plastic, paper, cardboard, etc. obtained from the environment. The products are separated on the sorting band and sent to the pressing machines. Scrap paper and cardboard are pressed as secondary products in pressing machines. Baling was done by adjusting the bale size in the horizontal press machine. Plastic scrap is a secondary product and is pressed in a vertical press. As a result of the chronometry study carried out on the horizontal press machine, it was determined that the loading of 1 bale was completed in 2 minutes. In the chronometry study performed on the Vertical Press machine, it was determined that 1 pallet of product was removed from the press and strapped in 20 minutes. Capacity calculation was made by evaluating the separation process according to its capacity.

2. Materials and Methods

2.1 Annual production amounts:

Capacity calculation is calculated as 300 days and 8 hours per year. The efficiency was taken as 0.80. There is one separation band in the facility with a length of 10 m and a band width of 1 m (Equation 1).

B: 10 m (belt lenght) E: 1 m (bandwidth) H: 5 m/d belt speed
Ya: 0,3 m waste height on belt

$V\ belt$: $B\ x\ E\ x\ Ya\ x\ K$: 10 x 1 x 0,3 x 0,8 = 2,4 m^3 (1)
$V\ waste$: $Vbelt\ x\ H/B$: (2,4 x 5 / 10) x 60 = 72 m^3/hour

Total amount of separated waste per day (Equation 2).

$Vdaily$: $72\ x\ 8$ = 576 m^3/day

Annual total amount of separated waste (2)
$Annual$: $572\ x\ 300$ = 172.800 m^3/day

2.2. Press account

Scrap paper and cardboard Secondary Products:
K : $(60/2)\ x\ 8\ x\ 300\ x\ 0{,}8$ = 57600 piece/year (3)

1 bale of paper and cardboard is 1.6 x 1.2 x 0.9 in size (1.728 m3). Although there are differences in the weight of the waste product, the average pressed weight of 1 m3 of scrap paper and cardboard is 140 kg..

K: $57.600\ x\ 1{,}728$ = 99.532 m^3/year x 140 kg / 1000 = 13.934 ton/year (4)
99.532 m^3/year /300 day = 331,77 m^3/day

2.3. Scrap plastic secondary product:

$K:\ (60/20)\ x\ 8\ x\ 300\ x\ 0{,}8$ = 5.760 piece/year (5)

1 plastic bale is 2x1x1 in size (2 m3). Although there are differences in the weight of the waste product, the average pressed weight of 1 m3 of scrap plastic material is 110 kg. Its average weight is 220 kg.

K: $5.760\ x\ 2$ = 11.520 m3/year x 110 kg = 1.267 ton/year (6)
11.520 m3/year /300 day = 38,4 m^3/day

Separation capacity and press capacities were examined separately and production values were taken according to the press capacities.

2.4. Need items:

Scrap Paper and Cardboard = 5% excess (due to foreign material)
13,934 X 1.05 = 14,630 ton/year
Scrap Plastic = with 5% excess calculation (due to foreign material)
1,267 x 1.05 = 1,330 ton/year
Plastic strap = 12 meters are used in 1 bale
(57,600 + 5,760) x 12 = 760,320 m/year

3. Results

The company produces 13934 tons/year of scrap paper secondary product (Equation 3-4) and 1267 tons/year of scrap plastic secondary product (Equation 5-6). Annual consumption is calculated as 14630 tons of paper and cardboard waste, 1330 tons of plastic waste, and 760320 meters of plastic straps.

References

[1] Kavaklı Vatansever, B. & Ateş, A. (2018). Classification, labeling, packaging, storage, transportation of chemical substances and disposal of chemical wastes in R&D establishments. *Sakarya University Journal of Science*, 22 (2) , 159-173. DOI: 10.16984/saufenbilder.292664

[2] Steiner M. & Wiegel M. (2009). Solid Waste Management Guidebook to the Fundamentals of Waste Management.

[3] Gül, M. & Yaman, K. (2021). Evaluation of Waste Management and Zero Waste Project in Turkey: Ankara Example. Atatürk University Journal of Economics and Administrative Sciences, 35 (4) , 1267-1296 . DOI: 10.16951/atauniiibd.870434.

[4] Tufaner, F. (2019). Investigation of the contribution of informative studies on the collection of recyclable waste to the collection efficiency. *Climate Change and Environment*, 4 (1) , 33-40.

[5] Bilgili, M. Y. (2020). Some concepts and their explanations used in solid waste management. Eurasia Term Journal, 8 (2) , 88-97.

[6] Mısır, A., & Arıkan, O. (2022). Circular economy and zero waste management in the European Union (EU) and Turkey. *Environment, Climate and Sustainability*, 23(1), 69-78.

[7] Sarıyar, E. A., Odabaşı, S. U., & Büyükgüngör, H. (2021). Recycling of waste electrical and electronic equipment within the scope of zero waste: The public's attitude on this issue. *Karadeniz Science Journal,* 11(1), 257-276.

[8] Güllü, G. (2022). Zero waste management in urban transformation. *Journal of Istanbul Sabahattin Zaim University Institute of Science and Technology*, 4(2), 112-120.

[9] Bilgili, M. Y. (2021). The origins of the zero waste approach and its meaning today. *Istanbul Commerce University Journal of Social Sciences*, 20(40), 683-703.

[10] Gündüz, M. Y. (2021). Control of recyclable waste and zero waste project applications: Necmettin Erbakan University Example (Doctoral dissertation, Necmettin Erbakan University Turkey.

The effect of marula oil on the release of madecassoside

Gamze UYSAL [1,*], ***Emel AKYOL*** [1]

[1]*Institute of Science and Engineering, Faculty of Chemical and Metallurgical Engineering, Chemical Engineering, Yıldız Technical University, Istanbul, Turkey*

Abstract

Specifically, the impact of natural oils on drug release in cream formulations was investigated through UV-Vis Spectrophotometry analysis. The aim of this study was to enhance the drug release from creams, a commonly employed transdermal drug delivery method, by formulating them with marula oil. Specifically, the impact of marula oil on drug release in cream formulations was investigated through UV-Vis Spectrophotometry analysis. The experimental findings clearly indicate that the inclusion of marula oil enhances the drug release in creams. To compare the release profiles, various kinetic models such as zero-order, first-order, Higuchi, and Korsmeyer Peppas were employed. The focus of this study centered on investigating the release of the active ingredient madecassoside, derived from the Centella asiatica plant. In conclusion, the inclusion of marula oil in cream formulations was found to increase drug release compared to the base formulation. Release performance in the formulations was observed for 120 minutes. In the cream formulation reinforced with marula oil, it provided 38% permeability by mass at the end of the 120th minute. This study highlights the potential of marula oil as an effective ingredient in transdermal drug delivery, particularly for enhancing the release of madecassoside in topical creams. Further research and optimization of formulations can lead to improved therapeutic outcomes and enhanced patient convenience.

Keywords: *Topical Drug Delivery, Madecassoside, Kinetic model, Marula oil*

1. Introduction

Transdermal drug administration devices allow the medication to be applied to the skin without the need for a needle and manage the drug's blood flow, in contrast to routinely used methods like a hypodermic needle. [1,2] The medicine is loaded directly into instruments like patches, gels, creams, and microneedles for transdermal applications. For the medicine to penetrate the skin, several techniques have been tested and developed since antiquity. [3] Transdermal systems are gaining attention in research and development today because they provide a simple, painless, regulated, and efficient means of release. [4] These techniques have been utilized to create numerous medications, vitamins, and hormones that are used to treat several ailments. Patches are suitable for use throughout a range of time periods since they are made for continuous or intermittent drug administration. Contrarily, micron-sized drug delivery systems called microneedles were created by combining the benefits of patches and hypodermic needles. [5] It also distinguishes out because of its formulation, which is the most extensively used topical medicine in the cosmetics industry, and because of how simple it is to apply. With its composition employing several excipients, it helps the active component to go deeply into the stratum corneum while preventing direct skin penetration and regulating its blood flow. The stratum corneum, the skin's top layer, must first be penetrated by the medicine before it can reach the epidermis and dermis. [6,7] The drug's routes of transmission are crucial for efficient penetration. Three stages can be used to explain how the transmission via these techniques occurs. The drug's entry into the stratum corneum comes first. It also refers to the stratum corneum's permeation into the dermis and epidermis. [8,9] This leads to its resorption into the circulatory system as an outcome. Fick's first law, which is a brief explanation of the transmission mechanism, states that therapeutic molecules must continue to work on the skin until the concentration gradient vanishes. [9] Drug penetration is evaluated using in vitro techniques. Franz diffusion cell, which offers several benefits, is an appropriate technique for lab experiments. [10,11]

The purpose of this study was to monitor and assess the controlled release of cream formulated with the active component madecassoside, marula oil, and other excipients by using Franz diffusion cell method. Madecassoside is widely recognized in the cosmetic industry for its beneficial properties, including soothing the skin, promoting healing, and combating signs of aging. [12]

* Corresponding author. *e-mail address: gmzuysal@outlook.com.tr*

2. Materials and Methods

2.1 Materials

Chemicals that are used for the experiments are;

Table 1. Chemicals used in the experiment

RAW MATERIAL NAME	FUNCTION
Aqua (Water)	solvent
Cellulose Gum	gelling agent
Cetearyl Alcohol	emulsifier
Glyceryl Stearate SE	emulsifier
Pentylene Glycol	preservative
Glyceryl Caprylate/Caprate	preservative
Dimethyl Isosorbide	penetration enhancer
Madecassoside	active ingredient
Lactic acid	pH regulator
Marula Oil	natural oil

2.2 Methods

2.2.1 Preparation and formulation of cream

In Table 2., ingredients and their mass percentage in cream are given**.**

Table 2. Formulation

INGREDIENT	% W/W
Aqua (Water)	67.29
Cellulose Gum	0.2
Cetearyl Alcohol	12
Glyceryl Stearate SE	4
Pentylene Glycol	2.5716
Glyceryl Caprylate/Caprate	0.4284
Dimethyl Isosorbide	3
Marula Oil	10
Madecassoside	0.5
Lactic Acid	0.01

The cream consists of a water phase and an oil phase. The oil phase consisted of cetearyl alcohol, glyceryl stearate SE, dimethyl isosorbide, and marula oil. These ingredients were weighed according to their mass percentages and then heated to a temperature of 75-80 °C. Similarly, the water phase was prepared by mixing water and cellulose gum and heating them to the same temperature as the oil phase. Once both phases were heated, they were combined with suitable mixing rpm. The mixing rpm was gradually decreased, resulting in the formation of a creamy consistency. After completing the mixing stage, the cream was cooled to approximately 30°C. At this temperature, the active ingredient madecassoside and preservative is pentylene glycol and glyceryl caprylate/caprate used as a were added to the formulation. Finally, the pH of the cream was adjusted to 6.0 matching the pH of human skin, by incorporating lactic acid.

2.2.2 Drug Release experimentals

A cellulose acetate membrane with a 0.45 µm pore size and 47 mm diameter was select to fit the donor compartment of the Franz diffusion cell. This cellulose acetate membrane was used to simulate human skin. In order to replicate human blood, pH 7.4 buffer solution was placed in the receptor compartment of the Franz diffusion cell. The receptor compartment was covered with a manufactured cellulose acetate membrane. 1 gram of cream was applied to the membrane and donor compartment was placed above them. Then, Franz diffusion cell to simulate human body was placed into agitating hot water bath with a temperature of 36.8°C and shaken at 120 rpm. 1 ml of samples were collected into sample tubes and 2 ml of buffer solution is added to tube and diluted. Buffer solution is added instead of the sample taken at certain time intervals in the Franz diffusion cell. Sample collection is carried out at 10-minute intervals during the first hour and 20-minute intervals during the second hour. These collected samples were subsequently analyzed in the UV Spectrophotometer.

Figure 1. Franz diffusion cell and cream formulation

3. Results and Discussion

In-vitro release studies use UV-vis spectroscopy to investigate the presence and amount of madecassoside active released from the cream.

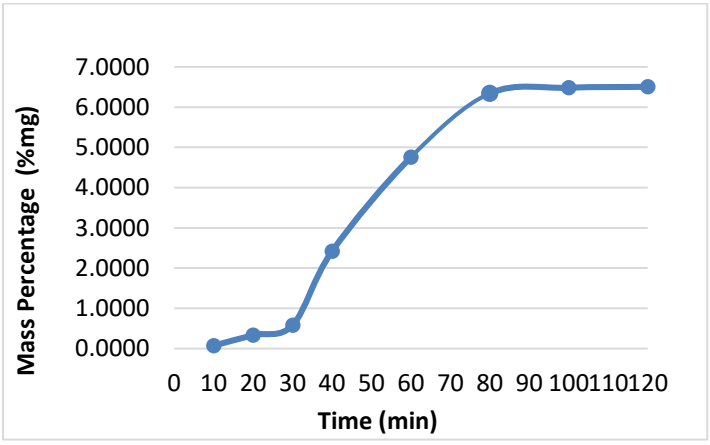

Figure 2. Mass percentage – time graph of base formulation

Figure 2 shows the mass percentage-time graph for the base formulation. From the graph, it is evident that the base formulation exhibits an increasing trend up to 80 minutes. However, after 80 minutes, the graph levels off, indicating an interruption of drug release. Notably, there are sharp increases observed at the 30-minute and 50-minute marks on the graph. These points indicate notable spikes in the drug release rate during those specific time intervals.

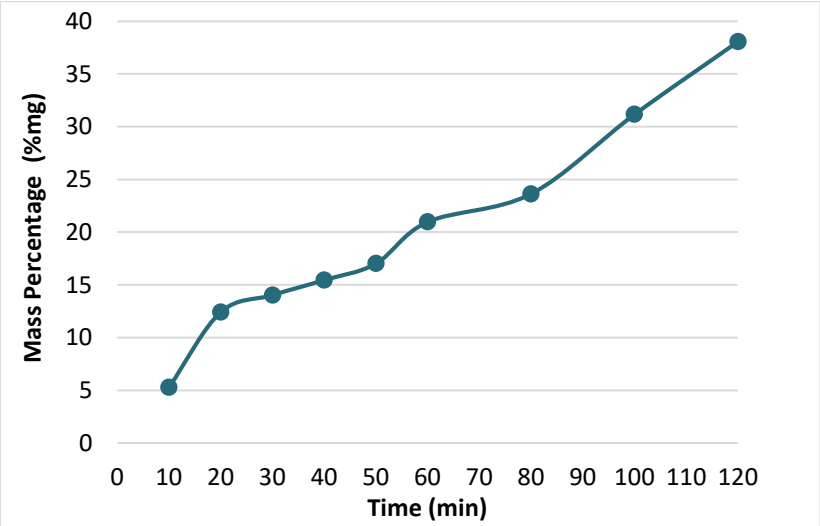

Figure 3. Mass percentage – time graph of cream with marula oil

Figure 3 presents the mass percentage-time graph for the marula oil formulation. Based on the graph, there is a sligtly increase in drug release up to 80 minutes. However, after 80 minutes, there is a rapid increase in drug release. The graph continues to show an increasing trend beyond 120 minutes. It can be concluded that the cream containing marula oil exhibits its maximum transdermal penetration at 120 minutes. The duration of the experiment was set at 2 hours since topical creams are typically applied to the skin for this duration. In the Cream with marula oil formulation, 38% permeability by mass was achieved at the end of the 120th minute.
In this study, the obtained data were fitted to the widely recognized Korsmeyer-Peppas equation and zero order equation, which is an exponential equation frequently used to describe drug release behavior. Additionally, the release kinetics of Madecassoside during the permeability study using pH 7.4 phosphate buffer were evaluated using the zero-order, first order, and Higuchi equations. The results indicate that the Korsmeyer-Peppas and zero order release kinetic models exhibit the highest R^2 values for base and marula oil formulations respectively.

Tablo 3. Regression coefficients according to release kinetic models

Formulations	R^2 Values			
	Zero Order	First Order	Higuchi	Korsmeyer Peppas
Base	0.8657	0.7058	0.9036	0.9235
Marula oil	0.9744	0.8527	0.9233	0.9602

This formulas have Korsmeyer-Peppas ve zero order kinetics models. R^2 values is better indicate that drug release is a diffusion-controlled process. When the emissivity (n) parameter value of the Korsmeyer-Peppas model was examined, it performed non-fickian diffusion. For non-Fickian diffusion, mass and rate of penetration are directly proportional to time. In this case, the diffusion rate of the penetrant is faster than the chain mobility. This chain mobility causes the polymer to swell. This non-Fickian state occurs during the mobility of the penetrant and the polymer chain. It occurs as a combination of diffusion and erosion controlled release. The cream with marula oil formula has zero-order drug kinetic model. Zero-order drug delivery systems have the potential to overcome the issues facing immediate-release by releasing drug at a constant rate, there by maintaining drug concentrations within the therapeutic window for an extended period of time.

4. Conclusion

In this study, topical drug delivery, which is one of transdermal drug delivery methods, was investigated. Various systems and formulations used in topical drug delivery are described. Creams, which are a highly frequent and simple approach for drug delivery systems, were preferred. The solvent, moisturizer, emulsifier, preservative,

and active component in the cream are all listed in detail. To examine its release, the madecassoside component was chosen because of its numerous advantageous and functional features. To examine the effect of the release, marula oil was employed as a moisturizer, penetration enhancer, and gives different advantages to the skin in the field of cosmetics and alternative medicine. investigated. The cream formulations were analyzed using the Franz diffusion cell method, and the release rate was monitored using a UV spectrophotometer. The results showed that marula oil improved the release rate of the active component, suggesting its potential in enhancing drug delivery in topical applications.

References

[1] Alkilani, A. Z., McCrudden, M. T., & Donnelly, R. F. (2015). Transdermal Drug Delivery: Innovative Pharmaceutical Developments Based on Disruption of the Barrier Properties of the Stratum Corneum. Pharmaceutics, 7(4), 438–470.

[2] Agrahari, S., Sharma, A., Kumar, S., Sharma, A., & Sagar, M. K. (2019). Formulation and Development of Transdermal Patches of Piroxicam. Asian Journal of Pharmaceutical Research and Development, 7(3), 119–128.

[3] Benson, H. a. E. (2005). Transdermal Drug Delivery: Penetration Enhancement Techniques. Current Drug Delivery, 2(1), 23–33.

[4] Adepu, S., & Ramakrishna, S. (2021, September 29). Controlled Drug Delivery Systems: Current Status and Future Directions. Molecules, 26(19), 5905.

[5] Donnelly, R. F., Singh, T. R. R., & Woolfson, A. D. (2010). Microneedle-based drug delivery systems: Microfabrication, drug delivery, and safety. Drug Delivery, 17(4), 187– 207.

[6] Bartošová, L., & Bajgar, J. (2012). Transdermal Drug Delivery In Vitro Using Diffusion Cells. Current Medicinal Chemistry, 19(27), 4671–4677.

[7] Osseiran, S., Cruz, J. D., Jeong, D. H., Wang, H., Fthenakis, C. G., & Evans, C. L. (2018). Characterizing stratum corneum structure, barrier function, and chemical content of human skin with coherent Raman scattering imaging. Biomedical Optics Express, 9(12), 6425.

[8] Bhowmik, D. (2013). TOPICAL DRUG DELIVERY SYSTEM. ResearchGate.

[9] Alkilani, A. Z., McCrudden, M. T., & Donnelly, R. F. (2015). Transdermal Drug Delivery: Innovative Pharmaceutical Developments Based on Disruption of the Barrier Properties of the Stratum Corneum. Pharmaceutics, 7(4), 438–470.

[10] Salamanca, C. H., Barrera-Ocampo, A., Lasso, J. F., Camacho, N., & Yarce, C. J. (2018). Franz Diffusion Cell Approach for Pre-Formulation Characterisation of Ketoprofen Semi- 49 Solid Dosage Forms. Pharmaceutics, 10(3), 148.

[11] Ng, S. F., Rouse, J., Sanderson, F. D., Meidan, V. M., & Eccleston, G. (2010). Validation of a Static Franz Diffusion Cell System for In Vitro Permeation Studies. Aaps Pharmscitech, 11(3), 1432–1441.

[12] Guangtao Jia, Xiuyang Lu. (2008). Enrichment and purification of madecassoside and asiaticoside from Centella asiatica extracts with macroporous resins *Journal of Chromatography A*, *1193*(1-2), 136-141.

Analysis of structural, electronic, mechanical and thermodynamic properties of Ir3TiC compound using DFT

***İlknur KARS DURUKAN*[1,*], *Yasemin ÖZTEKİN ÇİFTÇİ*[1]**

[1]*Science Faculty, Physics Department, Gazi University, Ankara, Turkey*

Abstract

Antiperovskite materials are a class of materials of great interest due to their unique physical, chemical and thermodynamic properties. These materials are electronically inverted perovskites and have emerged as a growing class of versatile materials, thus providing materials scientists with an effective and fruitful area of research. In our study, the compound Ir3TiC, an antiperovskite compound, was theoretically analysed. Our study is a purely theoretical study, no experimental parameters were used. The compound has Pm3m space group and has cubic structure. The structural, electronic, mechanical and thermodynamic properties of the compound were analysed by the DFT method using the first principles method. Firstly, the structural parameters were determined using geometrical optics. The lattice constant, Bulk modulus and the first derivative of the Bulk modulus were determined by fitting the Murnaghan equation. They were compared with the theoretical and experimental parameters available in the literature. Elastic constants were obtained by Stress-Strain method. The elastic constants were found to be structurally stable by determining their conformity with Born criteria. Young's modulus, Shear modulus, Bulk modulus, Paugh ratio, Caushy pressure and Poisson's ratio, anisotropy value, melting temperature, Debye temperature were obtained from elastic constants. Pugh ratio, Caushy pressure and Poisson's ratio indicated that the compound has a ductile structure. Electronic band structure calculations are important for understanding the physical properties of the crystal structure. By analysing the electronic properties, information such as the nature of the band gap and carrier density is obtained. Electronic band structure calculations showed that the compound is mechanical in nature. In addition, finally, parameters such as Bulk modulus, volume, Heat capacity were determined by detailed analysis of thermodynamic properties.

Keywords: *Antiperovskite, ductile, thermodynamics*

1. Introduction

Perovskites, denoted as ABX_3 materials, constitute a extensive group of crystalline substances renowned for their uncomplicated structure and captivating properties. This family of materials was named in honor of the Russian mineralogist L. A. Perovski in 1839[1].

Distinguished by their structural composition and coordination of constituent elements, perovskites manifest in various types, including simple perovskites like $KMnF_3$ and $SrTiO_3$, antiperovskites such as SbNCa3 and BiNCa3, inverse perovskites exemplified by $(Eu_3O)In$ and (Eu3O)Sn, double perovskites like $SrLaVMoO_6$, and double antiperovskites represented by $Na_6FCl(SO_4)_2$ [2]. The inverse counterparts, or antiperovskites (X_3BA), are essentially electronically inverted derivatives of perovskites. In these structures, A is a cation positioned at (0, 0, 0), B (C, N) at (1/2, 1/2, 1/2), and the transition metal atom X resides at (0, 1/2, 1/2). Ideal antiperovskites exhibit a cubic structure with a Pm-3m space group [3].

Antiperovskite materials, particularly those with metallic characteristics, exhibit the potential for semiconductor and magnetic properties. The distinctive properties of these materials are contingent on their crystal structure and the specific elements they incorporate. Notably, certain constituents of antiperovskites, exemplified by $LiGaO_2$, may showcase exceptional conductive attributes.

These materials can be intentionally tailored for application in diverse electronic, magnetic, or optical contexts. Exploring the properties of antiperovskite materials through research contributes to advancements in the realms of materials science and nanotechnology.

In our study, the structural, elastic, electronic and thermodynamic properties of the Ir_3TiC antiperovskite compound were studied theoretically using the DFT method. Detailed analysis of the material class, which has an important place in materials science, makes a great contribution to the literature.

* Corresponding author. *e-mail address: ilknurdurukan.@gazi.edu.tr*

2. Materials and Methods

All geometric optimization calculations were conducted utilizing the Density Functional Theory (DFT) method within the Vienna ab initio simulation package program (VASP) [4], [5]. The Perdew–Burke–Ernzerhof parameterization (PBE) was specifically employed for the exchange–correlation function, utilizing the generalized gradient approach (GGA). The calculations utilized a plane-wave basis set with an energy cut-off of 700 eV, and a 15 x 15 x 15 Monkhorst and Pack k-point grid in the Brillouin zone for the Ir3TiC compound.

The determination of mechanical properties employed the stress-strain method, facilitated by the implementation of IBRION = 6 commands in VASP 5.4. To explore the dependence of the thermodynamic properties of the Ir3TiC compound on pressure and temperature, a semi-harmonic Debye model approach was employed, utilizing the GIBBS code.

3. Results and Discussion

3.1. Structural Properties

Ir3TiC antiperovskite compound possess the ideal cubic structure with space group (Pm-3m), Ir ion occupying the corner positions, Ti at the body center and C at the face center of the cube. Their Wyckoff positions are Ir: 1a (0,0,0); Ti: 1b (1/2,1/2,1/2); C: 3c (1/2,1/2,0) respectively. Preceding any calculations, a geometric optimization was meticulously conducted to ascertain the most stable configuration of the CsCl crystal structure. The lattice constant of the compound was found to be 4.095 A and was determined to be compatible with the literature [1].

3.2. Elastic Properties Elastic properties play a crucial role in revealing the bonding characteristics among adjacent atoms, offering insights into a material's flexibility, hardness, and mechanical stability. In the case of the cubic Ir3TiC compound with a pm3m structure, the calculation of second-order elastic constants was carried out through the stress-strain method. Given its cubic structure, the Ir3TiC compound possesses three distinct elastic constants: C_{11}, C_{12}, and C_{44}. These constants adhere to the Born criteria, ensuring the material's stability ($C_{11} + C_{12} > 0$, $C_{44} > 0$, and C_{11}-$C_{12} > 0$)[6]. This analysis provides a comprehensive understanding of the compound's mechanical behavior and underscores its structural integrity.

Table 1. Calculated Elastic constants C_{11}(GPa), C_{12}(GPa) and C_{44}(GPa), Bulk modulus (B, GPa), Young modulus (E, GPa), Poisson's ratio (**ν**, GPa) of the Ir3TiC compound

Material	C_{11}	C_{12}	C_{44}	B	G	E	v
Ir3TiC	404.5	209	48.1	274.1	64.1	178.3	0.391
ref [1]	380.4	208	51.9	265.5	86.2	233.3	0.353

Table 1 showcases the mechanical properties derived from the elastic constants. The material exhibits elevated values for Bulk Modulus and Young's Modulus, suggesting a high resistance to volume and linear deformations, respectively. Simultaneously, the relatively low Shear Modulus implies a moderate resistance to shape distortion, classifying the compound as moderately hard. Notably, the Poisson's ratio exceeding 0.26 signifies ductility, indicating the material's ability to undergo significant deformation without compromising its structural integrity[7].

3.3. Electronic Properties

The nature of a material is revealed through its electronic properties, which in turn greatly influence the precision of its physical characteristics. To delve into the electronic structure and phase stability of Ir3TiC, Fig. 1 illustrates the energy band structure along the high symmetry direction (Γ-X-M-Γ-R), accompanied by the total electronic state density. The Fermi level is constantly set at 0 eV. The absence of any band gap at the Fermi level indicates that the compound has metallic character.

The changes in the partial DOS graphs of the Ir3TiC compound are seen in Figure 1. We can evaluate the given graph as Fermi level, valence band and conduction band. The biggest contribution to the Fermi level at zero

comes from the Ir-d and Ti-d bands. The largest contribution to the valence band comes from Ir-d states, while the largest contribution to the conduction band comes from Ti-d states.

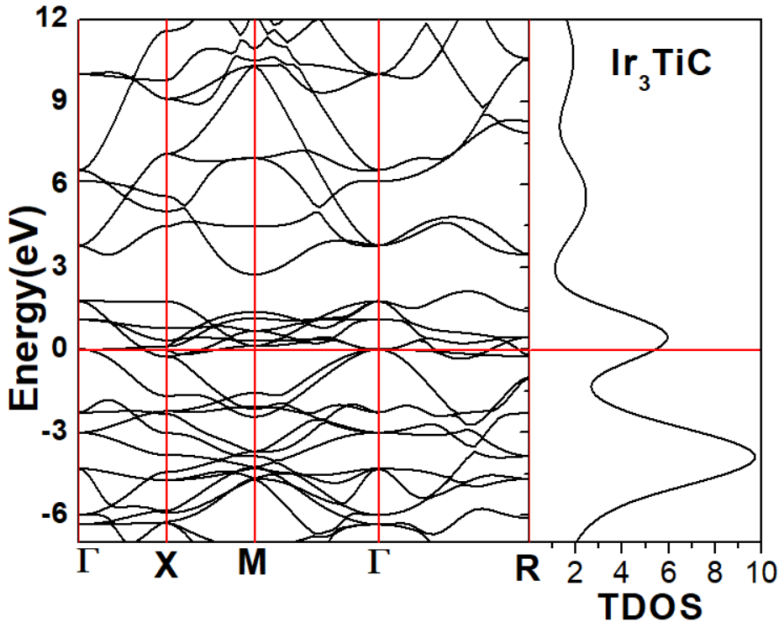

Figure 1. Electronic band structure and total density of Ir_3TiC

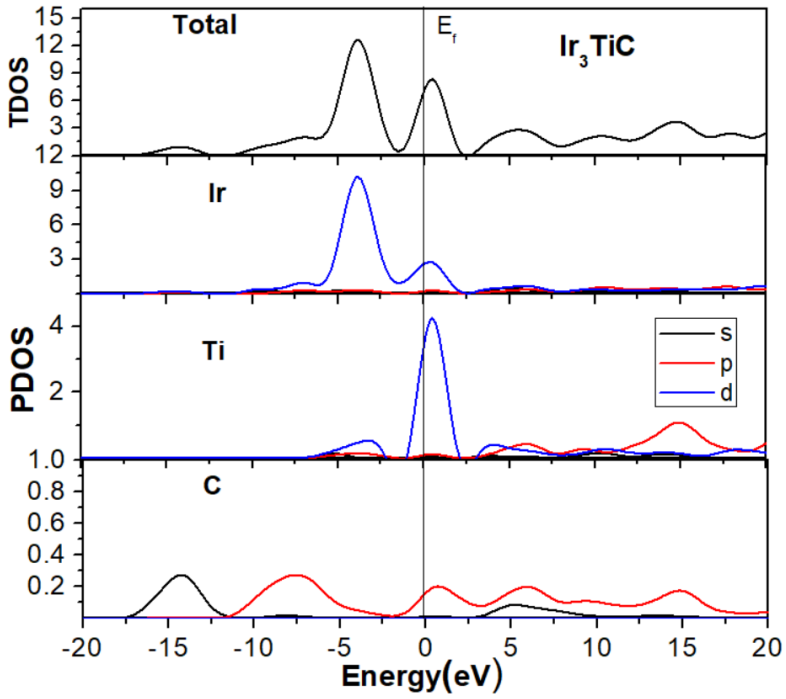

Figure 2. Partial density of states of Ir_3TiC

The effects of the Ir3TiC compound on thermodynamic properties when exposed to high temperature and high pressure were investigated. Thermal properties were calculated with the Gibbs code half-harmonic Debye model [8]. Thermodynamic properties were analyzed in the temperature range of 0–1000 K and the pressure range of 0–50 GPa.

The effect of pressure and temperature on volume change was investigated in Fig.3. When the pressure is kept constant, the volume decreases as the temperature increases. When the temperature is kept constant, the volume decreases as the pressure increases. The effect of pressure is greater in the compound.

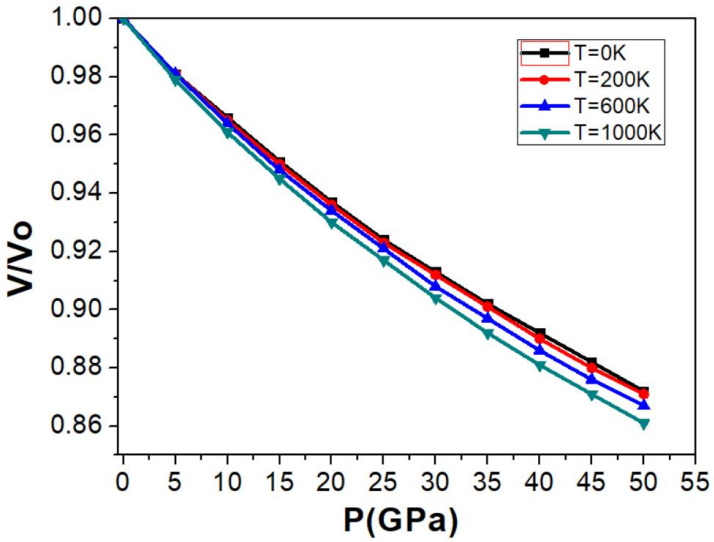

Figure 3. The variations of V/V0 with pressure at different temperature for Ir_3TiC

The change of bulk modulus against pressure and temperature is examined in Figure 4. When the pressure is kept constant, the bulk modulus decreases as the temperature increases. Bulk modulus increases as the pressure increases when the temperature is kept constant. The effect of pressure is greater in the compound. The results show that the studied compound is compressible.

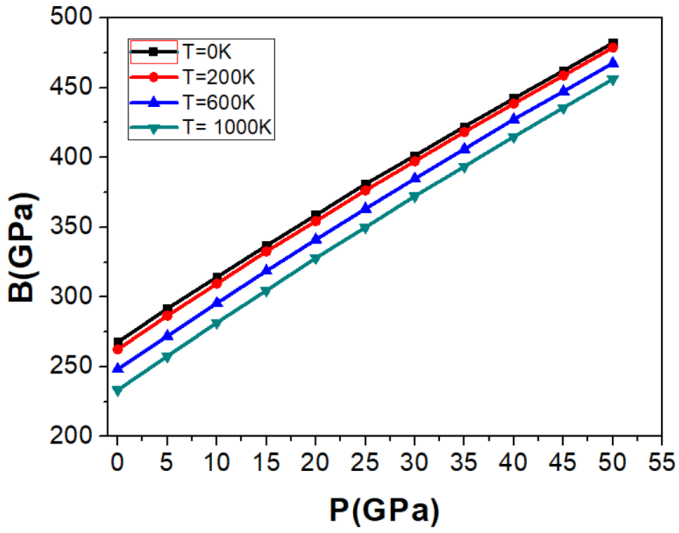

Figure 4. The variations of Bulk modulus with pressure at different temperature for Ir_3TiC

The Debye temperature, denoted as θ_D, serves as a key indicator of diverse physical properties in solids, encompassing elastic constants, specific heat, and melting temperature [9]. Figure 5 illustrates the Debye temperature values and their correlation with temperature. As temperature rises at a constant pressure, Debye temperatures decrease, whereas they ascend with increasing pressure at a constant temperature. Notably, the impact of pressure on the Debye temperature surpasses that of temperature, underscoring its predominant role in shaping the material's characteristics.

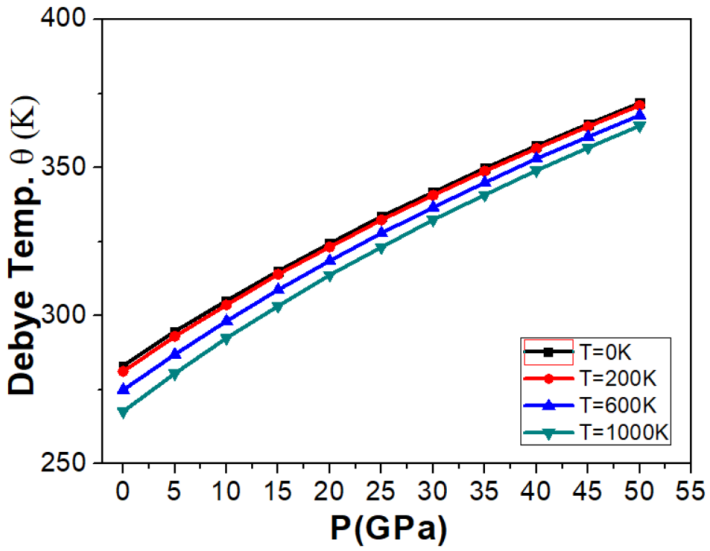

Figure 5. The variations of Debye temperature with pressure at different temperature for Ir_3TiC

Figure 6 illustrates the correlation between temperature and pressure concerning heat capacities (Cv). The Cv values exhibit a rapid increase with rising temperature, particularly up to 300 K, following a proportional relationship with T^3[10]. Beyond 300 K, the rate of increase gradually diminishes, reaching a stabilization point that aligns with the Petit and Dulong limit[11], a characteristic shared by many high-temperature solids[12]. For the compound, the calculated heat capacity values at 900 K and 0 GPa stand at 124.16 J/mol·K.

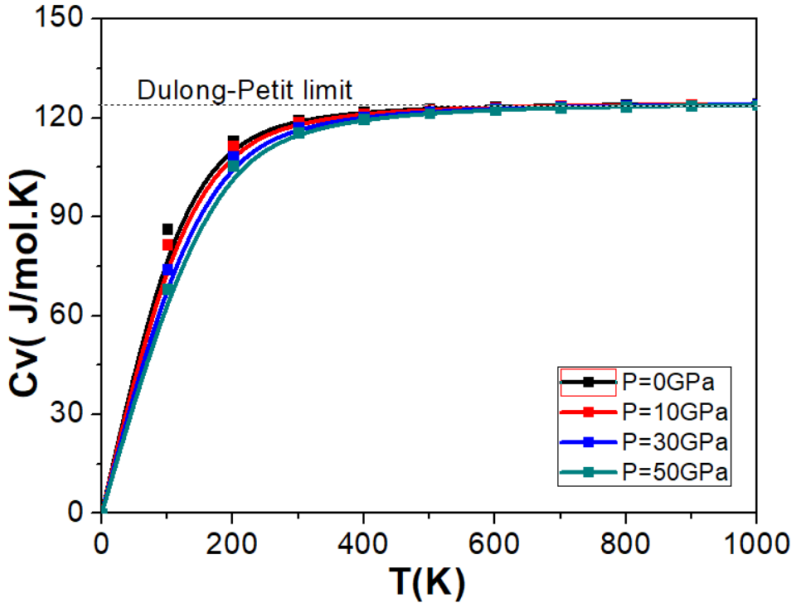

Figure 6. The variations of Cv with temperature at different pressure for Ir_3TiC

4. Conclusion

First principles calculations were performed using the GGA approach to study the structural, elastic, electronic and thermodynamic properties of Ir3TiC. It was determined that the compound was structurally stable. The compound has a ductile structure and showed metallic properties. Thermodynamic properties at high temperature and pressure values were evaluated in detail.

References

[1] Bannikov, V. V., Shein, I. R., & Suetin, D. V. (2017). Structural, elastic and electronic properties of Ir-based carbides-antiperovskites Ir3MC (M = Ti, Zr, Nb and Ta) as predicted from first-principles calculations, *Computational Condensed Matter*, *11*, 60–68.

[2] Rasul, M. N., Mehmood, M., Hussain, A., Rafiq, M. A., Iqbal, F., Khan, M. A., & Manzoor, A. (2022). Investigation of the Physical Properties of XCRh3 (X = Ti, V, Cr, Mn, Fe, Ni, Cu, Zn, Zr, Nb, Mo, Tc, Ru, Pd, Ag) Inverse Perovskites from First Principles, *Journal of Electronic Materials*, *51*, 5880–5896.

[3] Bannikov, V. V., Shein, I. R. Anionic state of platinum-group metal atoms in a series of ternary and quarternary compounds. *Computational Condensed Matter*, *22*, e00441.

[4] Mehmood, N., Ahmad, R., & Murtaza, G.(2017). Ab Initio Investigations of Structural, Elastic, Mechanical, Electronic, Magnetic, and Optical Properties of Half-Heusler Compounds RhCrZ (Z = Si, Ge), *Journal of Superconductivity and Novel Magnetism*, *30*, 2481–2488.

[5] Kresse, G., Hafner, J. (1993). Ab initio molecular dynamics for liquid metals, *Physical Review B*, *47*, 558–561.

[6] Mouhat, F., Coudert, F. X. (2014). Necessary and sufficient elastic stability conditions in various crystal systems," *Physical Review B - Condensed Matter and Materials Physics*, *90*, 4–7.

[7] Zeng, X., Peng, R., Yu, Y., Hu, Z., Wen Y., & Song, L.(2018). Pressure effect on elastic constants and related properties of Ti3Al intermetallic compound: A first-principles study, *Materials*, *11*, 10.

[8] Blanco, M. A., Francisco, E., & Luaña, V. (2004). GIBBS: Isothermal-isobaric thermodynamics of solids from energy curves using a quasi-harmonic Debye model, *Computer Physics Communications*, *158*, 57–72.

[9] Sahnoun, O., Bouhani-Benziane, H., Sahnoun, M., Driz, M., & Daul, C. (2018). Ab initio study of structural, electronic and thermodynamic properties of tungstate double perovskites Ba2MWO6 (M = Mg, Ni, Zn), *Computational Materials Science*, *77*, 316–321.

[10] Durukan, I. K., Ciftci, Y. O. (2021). Ab-initio study on physical properties of intermetallic LiPb compound, *Journal of Computational Science*, *54*, 101428.

[11] Sefir, Y. ,Terkhi, S., Zitouni, Z., Bekhti Siad, A., Seddik, T., Benani, M. A., Lantri, T., & Bentata, S. (2021). Structural, electronic, magnetic and thermodynamic properties of the new multifunctional half-Heusler alloy CoTcSn: Half-metallic and ferromagnetic behaviour, *Pramana - Journal of Physics*, *95*, 2.

[12] Touia, A., Benkhaled, M , Khobzaoui, C., & Fodil, M. (2021). Optical and Thermodynamic Properties of Half-Heusler Compound TaIrSn: Using Modified Becke-Johnson (mBJ), *Journal of Superconductivity and Novel Magnetism*, *34*, 2865–2877.

Molecular Docking and ADMET Studies of Podophyllotoxin Derivatives targeting Ribosomal Protein (RPL27A) in Triple Negative Breast Cancer Başlık farklı

Fatma SAAD MOHAMED BELHAJ [1,*], ***Şevki ADEM*** [2]

[1] *Natural and Applied Sciences, Science Faculty, Çankırı Karatekin University, Çankırı, Türkiye/Libya*

[2] *Natural and Applied Sciences, Science Faculty, Çankırı Karatekin University, Çankırı, Türkiye*

Abstract

Breast cancer is the most prevalent cancer in women worldwide, and Triple-negative breast cancer (TNBC) accounts for ~20% of all its cases. This study aimed to investigate the possible interaction potentials of podophyllotoxin derivatives with RPL27A target as an important therapeutic option that used in silico molecular techniques. Podophyllotoxin derivatives are found to have beneficial health effects in treating Cancer. An effort has been made to virtually screen podophyllotoxin derivative inhibitors by molecular docking in the current studies. The best binding score that has been resulted from the molecular docking analysis was by a Teniposide ligand with RPL27A target which is -9.1 kcal/mol , in addition to the lowest binding energies that were by Dihydrotaiwanin C, tetrahydrojusticidin B, Cleistantoxin, and Etop ligands with the same target , which are (-8.0, -7.1, -7.6, and -9.0 kcal/mol respectively) .This study reveals that these podophyllotoxin molecules can be developed as a novel multi-target RPs target inhibitors with greater potential and low toxicity.

Keywords: *Triple Negative Breast Cancer (TNBC), Ribosomal protein (RPL27A), Podophyllotoxine derivatives, molecular docking, ADMET studies*

1. Introduction

The management of triple- negative breast cancer represents a challenge due to its worse prognosis, heterogeneity and lack of targeted hormone therapy. [1,2] But Interestingly, TNBC is sensitive to drugs related to gene expression. Recent studies have linked mutations in ribosomal protein genes expression with poor prognosis, highlighting ribosome-targeted therapy as a promising approach for treating patients with cancer. [3-5] Fortunately, TNBC has strongly associated with specific ribosomal protein gene that is considered as a potential diagnostic and prognostic biomarker and potentially novel therapeutic target for TNBC. It is RPL27A which plays an important functional role in carcinogenesis in TNBC patients. [6] one of the drugs related to gene expression is podophyllotoxin and its derivatives which could not only inhibit the migration and invasion of triple-negative breast cancer but also affect the cell cycle and induce apoptosis. [7-9]

This study aimed to initiate a new direction for exploring the effect of podophyllotoxin and its derivatives as an anti-TNBC compound by in silico approach. Moreover, it provides theoretical support for further exploration of podophyllotoxin drugs as a vital part of the drug discovery method in cancer research field.

2. Materials and Methods

Five podophyllotoxin derivatives were selected and used as ligands to find the binding affinities with RPL27A target. The 3D structure of the RP (PDB ID: 8HTC) was selected as protein target that retrieved from the Protein Data Bank (PDB) (http://www.rcsb. org/) in PDB format. It is refined by preparing the protein for docking study by using Biovia

* *Corresponding author. e-mail address: fatmasuccess77@gmail.com*

Discovery Studio Visualizer (Biovia, 2021) and saved as PDB format. This processed protein structure is converted to the PDBQT file by selecting make macromolecule using the PyRx tool.
The 3D structure of the podophyllotoxin derivatives was obtained from the PubChem database (https://pubchem.ncbi.nlm.nih.gov), and then prepared by open babel in PyRx which minimized their energies and converted them into PDBQT formats for molecular docking analysis. The grid box parameter was set and adjusted for maximum binding affinity. The molecular docking study was carried out by using the Autodock PyRx docking tool. Best-predicted poses were screened to study the interaction of prepared ligands with target receptors.
The toxicity behavior of the selected podophyllotoxin derivatives was studied by ADMET parameters in the human body. The admetSAR prediction tool was used (http://lmmd.ecust.edu.cn:8000) to study ADMET parameters.

3. Results and Discussion

3.1. Molecular docking studies

RPL27A is targeted by the five podophyllotoxin derivatives predicted from previous studies' in silico screening data. AutoDock Vina in PyRx software, with an inbuilt docking algorithm, was employed for the purpose. The predicted free binding energy and hydrogen bonding were strongly focused on docking analysis. The values of docking binding energy and the interaction among the active site residues of the target receptor with podophyllotoxin derivatives are reported in Table 1.

Table 1. The Binding energy of different podophyllotoxin derivatives against the RPL27A target.

no	**Ligand name**	**PubchemID**	**RPL27A**
1	**ETOP**	5284558	-9.0
2	**Cleistantoxin**	71452884	-7.6
3	**TetrahydrojusticidinB**	54758663	-7.1
4	**Dihydrotaiwanin C**	163076341	-8.0
5	**Teniposide**	452548	**-9.1**

The binding affinity scores of all the formed ligand-protein complexes were compared with each other, one of them showed the lowest binding energy values that was by a Teniposide ligand with RPL27A target which is -9.1 kcal/mol, in addition to the lowest binding energy values of Dihydrotaiwanin C, tetrahydrojusticidin B, Cleistantoxin, and Etop ligands which are (-8.0, -7.1, -7.6, and -9.0 kcal/mol sequentially).

This comparative computational docking analyses gives insight into the efficacy of the podophyllotoxin derivatives over clinically approved reference drug molecules.

3.2 The docking analysis

The docking analysis was carried out using Discovery Studio (Biovia, 2021) for the best docked pose which was represented in Figure 1. Tenoposide docked well with the target binding pocket of RPL27A with the binding energy of -9.1 kcal/mol determines the ability of Teniposide to inhibit RPs.The podophyllotoxin derivative Teniposide stability in the binding site of RPL27A receptor is also recognized by common amino acids residue forming interactions like conventional hydrogen bond, hydrophobic interaction, Pi Sigma, Carbon-Hydrogen bond, and van der Walls interactions. The conventional hydrogen bonds with the amino acids at a distance of 4.90 Å, 4.61 Å, 3.94 Å ,3.96 Å, and 3.74 Å are interrelated with the high binding affinity of Tenoposide with RPL27A. The high binding affinity of Teniposide with the RP target may be due to the bond length distance between amino acid residues.

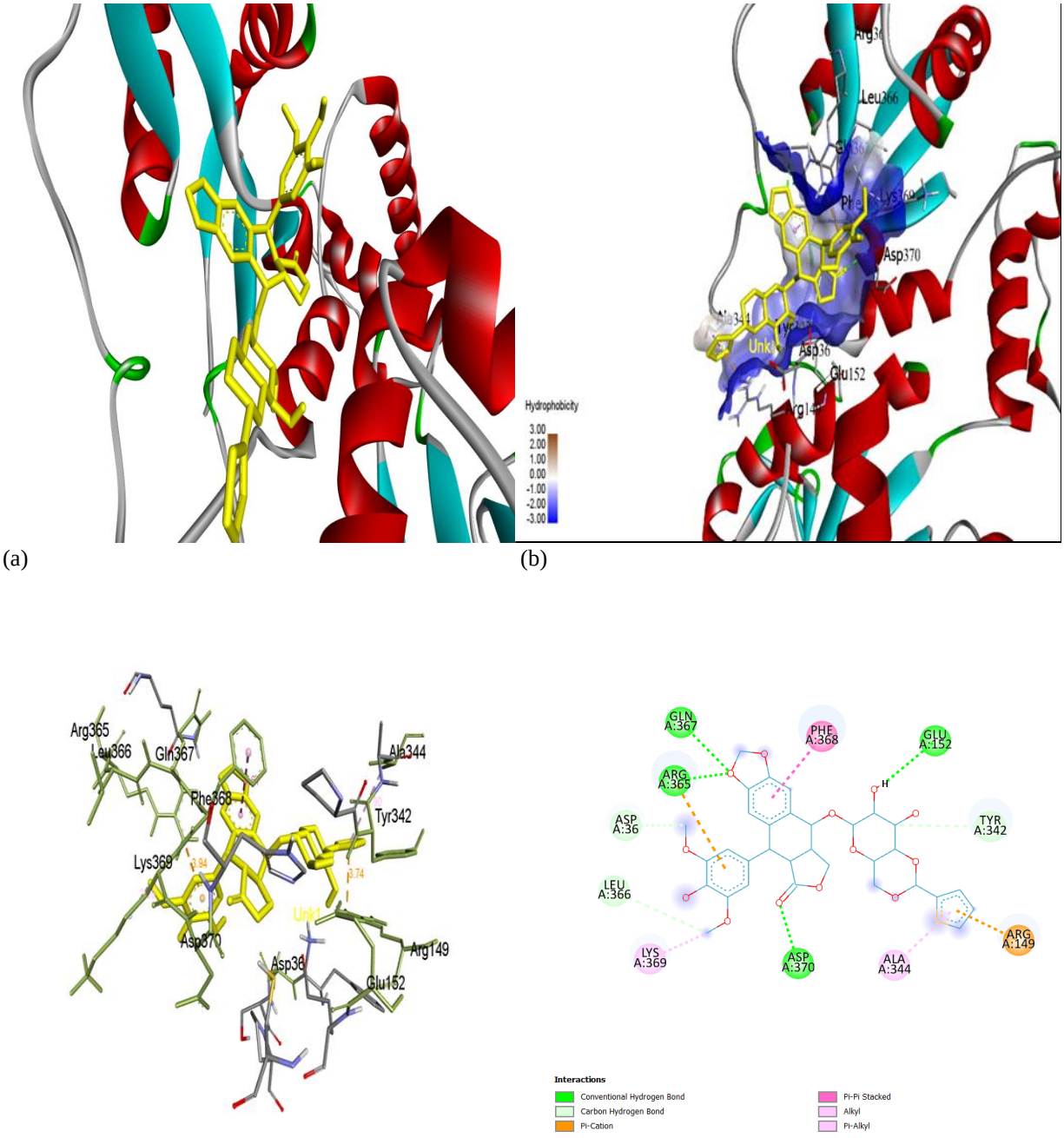

(a) (b)

(c) (d)

Figure 1. Docked poses of RPL27A (8BGH) with Teniposide (452548): (a) Teniposide docked to RPL27A (b) Hydrophobicity surface at the active binding site of RPL27A with Teniposde; (c) 3D stick diagram of surrounding RPL27A amino acids with Teniposide; (d) 2D view of surrounding RPL27A amino acids with Teniposide.

The reported docking results found that Teniposide exhibits the best binding interaction among the five podophyllotoxin derivatives as a common inhibitor for the RPL27A receptor. The lead compound was then assessed for ADME studies.

3.3 ADMET evaluation studies

Docking analyses showed Teniposide as the common inhibitor for RPL27A target. Teniposide was checked for the ADMET profile using admetSAR software. The admetSAR results were shown in Table 2. Teniposide may be capable of passing through BBB and able to absorb by intestine with probability score of 0.830. In addition, Teniposide is an inhibitor of P-glycoprotein with probability score of 0.53. Teniposide was an inhibitor of some CYP enzymes, two important biomarkers assessing the Teniposide's potential effects on the liver and renal functions accordingly, with probability score > 0.62. Drug toxicity is a great concern to the medical world. The toxicity prediction also indicated that Teniposde is a non-carcinogenic, and non- toxic to the body organs. Acute oral toxicity category-3 considered Teniposide is nontoxic for oral toxicity with a probability score of 0.74. Teniposide showed higher solubility with a log S value of -3.19, which affects Teniposide's movement from the site of administration into the blood.

Table 2. Predicted ADMET profile of Teniposide.

ADMET	**results**	**probability**
HIA	HIA+	0.8302
Caco 2	Caco 2-	0.8551
BBB	BBB -	0.8000
P-gp substrate	Substrate	0.8292
P-gp Inhibitor	inhibitor	0.5362
Plasma protein binding	1.071 100%	
CYP IP (inhibitory promiscuity)	low	0.9121
Renal clearance	10% of total body clearance	
hERG (Human ether-a-go-go-related gene) a prediction of arrhythmias	Weak Inhibitor	0.4338
Carcinogen	Non-Carcinogen	0.9700
Biodegradation	Not ready biodegradable	0.7750
Acute oral toxicity	III	0.7416
Aqueous solubility (logS)	-3.199	

4. Conclusion

Finally, based on the current computational study and obtained results, it can be predicted that the selected podophyllotoxin derivative drugs have shown potential inhibitory activity with TNBC specific target. Furthermore, this study could provide a new framework for discovering future solutions to the absence of targeted therapy problem for this aggressive type of breast cancer.

Acknowledgement

In this study, the scientific support was provided by my supervisor prof.Dr.Shevki Adem who was the sincere and kind mentor during my phD study, so a big thank for him, and thanks alot for Çankırı Karatekin University that gave me this great chance to participate in this conference. I would also like to thank all the supporters due to their precious contributions.

References

[1] Sylvia Annabel Dass , Kim Liu Tan , Rehasri Selva Rajan , Noor Fatmawati Mokhtar , Elis Rosliza Mohd Adzmi , Wan Faiziah Wan Abdul Rahman , Tengku Ahmad, Damitri Al-Astani Tengku Din, and Venugopal Balakrishnan. (2021). *Triple Negative Breast Cancer: A Review of Present and Future Diagnostic Modalities. Medicina journal*, 57- 62.

[2] Yun Li, Huajun Zhang, Yulia Merkher, Lin Chen, Na Liu, Sergey Leonov & Yongheng Chen. (2022). *Recent advances in therapeutic strategies for triple-negative breast cancer. Journal of Hematology & Oncology*, 33k Accesses, 87 Citations, 12 Altmetric, 15-121.

[3] Dolezal, J.M., Dash, A.P. and Prochownik, E.V. (2018) *Diagnostic and prognostic implications of ribosomal protein transcript expression patterns in human cancers*. *BMC Cancer* 18- 275.

[4] Lijuan Jiao, Yuzhe Liu, Xi-Yong Yu, Xiangbin Pan, Yu Zhang, Junchu Tu, Yao-Hua Song & Yangxin Li. (2023). *Ribosome biogenesis in disease: new players and therapeutic targets. Signal Transduction and Targeted Therapy*, 11k Accesses, 19 Citations, 11 Altmetric, 8-15.

[5] Elhamamsy1, Brandon J. Metge1, Heba A. Alsheikh1, Lalita A. Shevde1,2, and Rajeev S. Samant.(2022). *Ribosome Biogenesis: A Central Player in Cancer Metastasis and Therapeutic Resistance. Cancer Research journal* 82 (13): 2344-2353.

[6] Alkhatabi, H. A., McLornan, D. P., Kulasekararaj, A. G., Malik, F., Seidl, T., Darling, D., et al. (2016). *RPL27A is a target of miR-595 and may contribute to the myelodysplastic phenotype through ribosomal dysgenesis. Oncotarget* 7, 47875-47890.

[7] Zhang W., Liu C., Li J., Liu R., Zhuang J., Feng F., et al. (2020). *Target analysis and mechanism of podophyllotoxin in the treatment of triple-negative breast cancer. Front. Pharmacol*. 11:1211.

[8] Hua-yang Fan, † Zhuo-li Zhu, Hong-chun Xian, Hao-fan Wang, Bing-jun Chen, Ya-Jie Tang, Ya-ling Tang, and Xin-hua Liang. (2021). Insight into the Molecular Mechanism of Podophyllotoxin Derivatives as Anticancer Drugs. *Front. Pharmacol*.75-90.

[9] Li, Y., Chen, M., Yao, B., Lu, X., Zhang, X., He, P., et al. (2019). *Transferrin receptor-targeted redox/pH-sensitive podophyllotoxin prodrug micelles for multidrug-resistant breast cancer therapy. J. Mater. Chem*. B. 7 (38), 5814–5824.

Relationship between Age and the Risk of Diseases after Chemotherapy for Patients with Breast Cancer

***Jamal BASHIR MASAUD LAWAG*[1,*]**

Institute of Science, Faculity of Chemistry, Department of Biochemistry, Çankiri Karatekin University, Turkey

Abstract

Breast cancer is a common health problem that attacks women in the World, it is one of the most known malignancies with 23% of all types of cancers, with over one million new cases detected per year Roughly 4.4 million women are living with breast cancer and more than 400,000 died annually from the disease. This disease recorded 14% of all cancer deaths. It is the most common cause of female death in industrialized countries.

Small tumors are more treated successfully by early detection, Delayed detection of breast cancer is correlated with danger clinical stages and low survival percentage .Reports in developed countries indicated that the median time to the consultation was 21- 90 days. Delayed detection of breast cancer for more than few months before physician checking can lead to the occurrence of breast cancer mortality rates are higher than in developing countries.

Mortality rates are higher in Africa than in richer world regions and improved access to known effective therapy, efficiently delivered, would, therefore, save lives. They also reports that breast cancer also occurs in medium age Libyan women more than in other parts of the world

Keywords: *Breast cancer, Risk Factors, Libya, Treatment, Age*

1. Introduction

Breast cancer is rising within the lower socio-economic groups in Africa and may in the medium term become a problem for the African population. Although treatment is often considered to be connected to primary prevention, it has been estimated that between 2000 and 2020 approximately 10 million patients will die of cancer in Africa. Mortality rates are higher in Africa than in richer world regions and improved access to known effective therapy, efficiently delivered, would, therefore, save lives. They also report that breast cancer also occurs in medium age Libyan women more than in other parts of the world [1].

Breast cancer is a common health problem that attacks women in the World, it is one of the most known malignancies with 23% of all types of cancers, with over one million new cases detected per year [2]. Roughly 4.4 million women are living with breast cancer and more than 400,000 died annually from the disease. This disease recorded 14% of all cancer deaths. It is the most common cause of female death in industrialized countries [3].

The second most common cause in the world and the third most common in developing countries The protection from disease is by getting an early physical exam which makes therapy more beneficial. Despite development in the strategies for disease treatment, advanced breast cancer remains incurable and the goals of therapy range from symptom palliation to extending survival.

Breast cancer is the uncontrolled development of cells in the breast. It mostly, the disease affects females, but males also suffer from the disease. Different factors can indicate the occurrence of disease. The most important factor associated with breast cancer is a family history (Inheritance). Other risk factors that can lead to the occurrence of breast cancer are food, environment demographics, marital status, health condition, breast feeding, menarche, menopause, age and a number of children. The ratio of breast cancer in different areas differs based

* Corresponding author. *e-mail address: elawaj@yahoo.com*

on specific factors. Similarly, mortality rates are decreased and increased in different regions; in industrialized countries, the mortality rate is lower than in developing countries [4].

Small tumors are more treated successfully by early detection. Delayed detection of breast cancer is correlated with danger clinical stages and low survival percentage. Reports in developed countries indicated that the median time to the consultation was 21 - 90 days. Delayed detection of breast cancer for more than few months before physician checking can lead to the occurrence of breast cancer mortality rates are higher than in developing countries [5].

Risk factors by demographics

Gender has been found to be the most significant risk factor for breast cancer; while men can also develop breast cancer, women account for over 99% of cases.

The lifetime risk of breast cancer for a woman is typically estimated to be one in eight, but it does increase with age. In addition, the probability levels vary over the lifespan range, with one in 233 being between 30 and 39 years old and one in 27 being between 60 and 69 years old.

One of the few cancers that a ffects the wealthier social classes more frequently is breast cancer Breast cancer is rising within the lower socio-economic groups [6].

2. Material and Methods

The study viewpoint was conducted over a 12-month period from January -December 2023. For the purpose of the study a descriptive design had been employed. The participants included in this study were 540 women of Libyan nationality between the ages of 25-85 years.

- Sampling

A sample size of 540 Patient was estimated using a single there was samples collection from oncology centers in the study area. Sampling was used to select the study from the various ages and different to ensure representativeness the number of patients selected from oncology enter

- Patient Study

This study was conducted randomly on (540) women with breast cancer aged 25 - 85 years

- Statistical Analysis

Described the distribution of chemotherapy use by patient characteristics, including the median and inter quartile range (25th–85th percentile) for follow-up end time December 01, 2023).

We then used Cox proportional hazards regression to calculate hazard ratios (HRs) with 95% (CIs) for HF/CM associated with time-varying chemotherapy exposures. Each participant began accruing person-time on the date of chemotherapy initiation and stopped accruing person-time at the time, health plan disenrollment, death, or December 01, 2023. We used day 540 patient after diagnosis as a proxy for the index date for unexposed women. Using time-varying exposures allowed us to account for changes in chemotherapy use. For example, women were considered Adriamycin - 50 mg- based-only users until they started taxotere therapy 80 mg.

Data collection:

Data includes 540 patients diagnosed with one of the danger clinical stages of breast cancer. It collected between Januray 2023 and December 2023 from the same place (Oncology Centre) based on the psychology and physical aspects. Eight input variables will be predicted according to the clinical stages.

Age is a numerical variable between 25 and 85 years old with mean 44.1 and standard deviation 10.325. Menopausal status divided into two distinct, perimenopause 84 patients with a percentage of 64.61% and post-

menopausal 46 patients with a percentage of 35.38%. Tumor size is between 1.9 and 34, the mean is 13.88 and a standard deviation of 7.605 (Table 1).

Table1. Distribution of patients according on tumor size and clinical stages

Characteristics	Gender (Female)	Number of patients	Percentage %
Gender	Female	540	100%
Tumor Size	T1	155	28.5 %
	12	280	51.5%
	T3	56	10.5%
	T4	12	2.5%
	Tx	37	6.5 %
Stage	I	66	12%
	II	168	31.5%
	III	287	53.5%
	IV	19	3 %

Moreover, the clinical stage represents the response variable to predict all data by using data mining, it divided into four stages. Stage I with 66 patients and percentage 12%, stage II with 168 patients and percentage 31.5%, stage III with 287 patients and percentage 53.5% and stage IV with 19 patients with percentage 3 % (Figure 1).

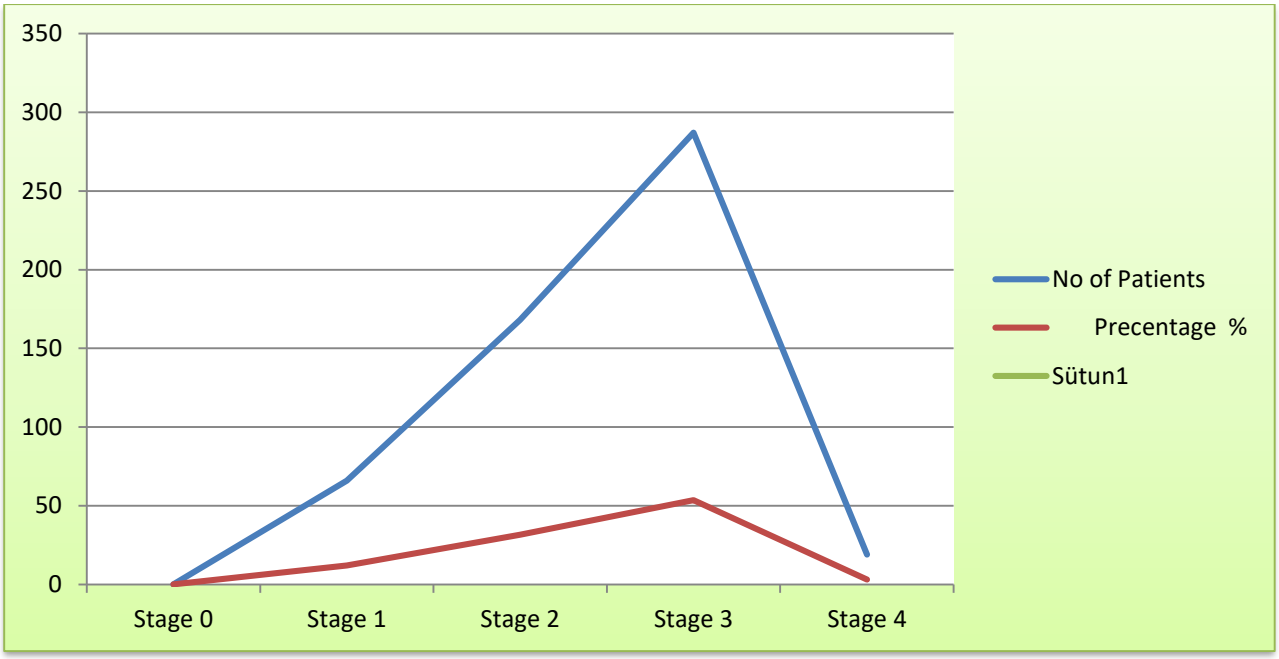

Figure 1. Patients' numbers categorized by tumor stage

3. Result and Discussion

Accounting for almost 26% in 2023 of all cancer cases, breast cancer is the most common cancer in Libya then second place colomn cancer and lung cancer is thirth place. Its incidence increases with age.

Less than 10% of newly diagnosed breast cancer in the arabic countries of Mediterranean Region, compared to 30% in Western societies, are diagnosed in women 40 - 60 years or older (The Global Burden of Disease, 2015). This group of older breast cancer patients remains underrepresented in clinical trials. their treatment plan is less clear and have poor outcomes.

Pathological features and clinical presentation among older patients with breast cancer are not the same as younger ones. With aging, the percentage of human epidermal growth factor receptor 2 (HER-2) positive disease decreases while estrogen receptors (ER) and progesterone receptors (PR)-positivity increases. Such features, though implicate a better prognosis, are not reflected in real clinical outcomes.

Many previously published studies have shown that older patients are more likely to receive non- standardized care and usually depends more on physician's preference.

Compliance to planned treatment is always an issue with increasing age.

The poor outcome observed among older patients can also be attributed to comorbidities and its associated medications. Such comorbidities have the potential to affect the mortality of older women regardless of their breast cancer or its treatment [7].

Women with early-stage breast cancer and comorbid conditions, are likely to die from causes other than breast cancer. In one study, using Surveillance, Epidemiology, and End Results (SEER). These comorbid conditions include cerebrovascular disease, paralysis, dementia, chronic obstructive pulmonary disease, chronic renal failure, myocardial infarction, congestive heart failure, peripheral vascular disease, diabetes, liver disease, previous cancer, rheumatoid arthritis, and ulcers. A total of 540 patients with breast cancer diagnosed at a median age of 55 years were included. The 540 individual comorbid conditions were associated with decreased overall survival and increased mortality [8].

To date, the consequences of treatment disparities, particularly the under treatment of the older patients, have been poorly assessed in population like ours. In this research, we describe clinical presentations, tumor characteristics, treatment modalities and outcomes among older Libyan patients with breast cancer. The mean age of patients with breast cancer at the time of diagnosis is 50 years old within the study period.

Comparing the results between different patients shows a great difference regarding the mean age at diagnosis time med zone ofLibya with mean of 40 ±10.47) which indicate that each Oncology Institute in Libya should evaluate and compare independently.

And this research it is the showed the higher age case at diagnosis in breast cancer patients (ranging from 50 to 69 years old) (Table 2).

Table 2. Distribution of patients according to the age

25 - 29	30	5.5%
30 - 39	45	8.5%
40 - 49	87	16%
50 - 59	123	22.5%
60 - 69	185	34.5%
70 - 79	50	9.5%
≥ 80	20	3.5%

4. Conclusion

Breast cancer came first with 26% (540 patients), also significantly higher than the 13.0% quoted for the rest of the world, that is, 33.3% more frequent breast cancers in med zone of Libya. Colorectal cancer was second in the study, with 19.3% (83 patients), significantly higher by 40% than the 11.5% reported worldwide. Respectively, and reported 11.2% and 9.6%, respectively, for colorectal cancers. 9 It is likely that both breast and colorectal

cancer rates may have been offset by the potential underestimation of lung cancer rates; for all we know, the country has no screening policies or cancer awareness programmes for breast, colorectal, or otherwise.

In med zone of Libya, cancer incidence stands at 71.7 per 100 000 populations with 540 cases during the 12-month survey period (January 2023–December 2023). This incidence rate is at least an underestimate, with differences in distribution by type populations. Furthermore, a single centre cancer registry is an unreliable alternative to a national or regional cancer registry that collects information from all healthcare facilities in the region. All the above should support strategic planning and decision-making in developing cancer care in the country.

The number of cancer case files registered in med zone of Libya from 2004 to 2023 is 14,689 cases.

The cumulative number of cancer cases reached 13,549 new cases.

The proportion of females is 55% of the total new cases recorded.

The service provided to residents of the central region represented only 20% of the total services, and the rest was for the western regions, 51%, the eastern regions, 16%, and the southern regions, 13%.

Finally, the largest age group affected by breast cancer in 2023 was between 50 and 69 years.

And breast cancer represents the most common type of cancer in Libya at a rate of 26%, followed by colorectal cancer and lung cancer.

Waste time from the patients without early detecting disease on breast cancer, The risk of death increases, especially if the patient neglected herself without getting treatment or taking ineffective medicine.

Less than 10% of newly diagnosed breast cancer in Libya, compared to 30% in Western societies,

The average diagnosis in Libyan women 50 - 69 years. This patients of older breast cancer patients remains underrepresented in clinical trials and their treatment plan is less clear and have poor outcomes.

References

[1] Kruger, W.M. and Apffelstaedt, J.P. (2007). Young breast cancer patients in the developing world: incidence, choice of surgical treatment and genetic factors. South African Family Practice, 49(9), 18.
[2] Benamer,H., (2012). Healthcare system in Libya. Annually factual report.
[3] Ermiah E., F. Abdalla, A. Buhmeida, E. Larbesh, S. Pyrhönen, Y. Collan, (2012). Diagnosis delay in Libyan female breast cancer. BMC Res. Notes.
[4] Salem, M., (2011). Data mining techniques and breast cancer prediction: A case study of Libya, Doctoral Dissertation. PhD Thesis, http://shura.shu.ac.uk/20611/1/10701258.pdf
[5] Ahmad G., T. Eshlaghy, A. Poorebrahimi, M. Ebrahimi and R. Razavi, (2013). Using three machine learning techniques for predicting breast cancer recurrence. J. Health Med. Inform.
[6] Yost, K. et al., (2001). Socioeconomic status and breast cancer incidence in California for different race/ethnic groups. Cancer Causes and Control, 12(8), 703-711.
[7] Danese M, O'Malley C, Lindquist K, et al, (2012). An observational study of the prevalence and incidence of comorbid conditions in older women with breast cancer. Ann Oncol ;23(7):1756–65.
[8] Patnaik JL, Byers T, Diguiseppi C, Denberg TD, Dabelea D, (2011). The influence of comorbidities on overall survival among older women diagnosed with breast cancer. J Natl Cancer Inst. ;103(14):1101.

Evaluation of Stroke Survivor Quality of Life and Perceived Stress

Mansoor OUDAH KADHIM AL ADILEE[1*] ***Songül KAMIŞLI***[2]

[1] *AlSadr Medical City, Staff training and Develop Mental Center, Al-Najaf Al-Ashraf, Iraq*

[2] *Çankırı Karatekin University Health Science Faculty, Gerontology Department, Çankırı, Turkey*

Abstract

Stroke survivors may experience changes in mood, personality, and cognitive abilities, affecting their overall mental health. This study aimed to evaluation stroke survivor's quality of life and perceived stress. A cross-sectional descriptive study was conducted between 1 April-30July 2022 in Iraq. The study sample consisted of 205 patients who agreed to participate in the study at the time of data collection. Personal Information Form and the Perceived Stress Scale, and Stroke Survivor Quality of Life were used to collect the data. It was observed that the average age of the participants was 55, 54.1% male and 57.6% married, 36.6% were high school graduates, 29.3% were university graduates and most of them had ischemic stroke. The perceived stress, and quality of life were affected by variables as gander, age, income, educational level, residence, type of stroke. There is a statistically significant and inverse relationship between the level of psychological stress and several aspects of quality of life such as energy, family role, language, movement, mood, personality, self-care, social role, upper limb function, and work/production ($p<0.01$) There was also an inverse and significant relationship between stroke-specific quality of life and the level of psychological stress ($p<0.01$). The evaluation of stroke survivors' quality of life and perceived stress is a complex process that requires a comprehensive understanding of the physical, mental, and social dimensions of their experiences. Psychosocial support programs and support systems should be tailored to address the unique challenges faced by stroke survivors, promoting not only physical recovery but also emotional well-being and social integration

Keywords: Stress, Quality of life, Stroke survivors

1. Introduction

Stroke still kills many people every year, it is the second most common cause of death worldwide [1]. According the report Iraq, there were 11,205 deaths (6.53%) due to stroke. and to the latest WHO data published in 2020 Stroke Deaths in Iraq reached 20,793 or 14.19% of total deaths [2, 3]. Stroke survivors may experience changes in mood, personality, and cognitive abilities, affecting their overall mental health. Also Stroke significantly reduces one's quality of life. Studies have also shown that people with negative cognitive ratings have worse mental health outcomes after a stroke. They also have higher symptoms of psychological stress after a stroke. Another study found a significant association between negative perceptions about oneself and the world and the severity of post-traumatic stress disorder symptoms after a stroke [3-4]. The study's goal was to address a gap in the literature about the quality of life of stroke survivors living in Iraq, which would be reflected in Arab societies.

2. Materials and Methods

The current study employed the descriptive research methodology. The study included 205 people who had undergone cerebrovascular accidents. The study included 205 stroke survivors who met the overall study requirements. The necessary official administrative approvals were obtained to conduct this study. Ethics committee approvals were also obtained to conduct the study from the public university (No:25; date:17/03/2022). Personal Information Form and the Perceived Stress Scale, and Stroke Survivor Quality of Life were used to collect the data. These measurement tools' Croncbach Alpha values were acceptable in this study (0.862-0965). All statistical analyses were conducted using SPSS Version 25 (IBM SPSS Statistics). The study samples included survivors of stroke in Al-Najaf Governorate. An independent sample t-test was performed to test whether our quantitative variables differed significantly from the scores obtained from Two independent samples. ANOVA (F) test was applied to test whether the mean of more than two unrelated samples differed significantly from each other. “Reliability Analysis” was conducted to test the reliability of the scales. Pearson correlation analysis was performed to test the relationship between the scales. Values with p values below 0.05 were considered significant in the study. The inclusion criteria were (1) Survivors of stroke, both haemorrhagic and ischemic, (2) ages 18 years and over. The exclusion critera were (1) People with dementia and mental illness, (2) People who have lost hearing and speech at the same time, (3) People with persistent memory loss.

* Corresponding author. *e-mail address: mansor222344@gmail.com*

3. Results and Discussion

Participants' characteristics are shown in Table 1. It was determined that 76.1% of the participants had ischemic stroke and 23.9% had hemorrhagic stroke. It was determined that 48.8% of the participants had a disease duration of 5-6 months, and 31.7% had 7 months or more.

Table 1. Participants' characteristics

Variables		Number	%
Age ($\overline{X}$:55.70; SS:14.37)	40 altı	24	11.7
	40-59	82	40.0
	60 ve üzeri	99	48.3
Gander	Male	111	54.1
	Female	94	45.9
marital status	Single	35	17.1
	Married	118	57.6
	Widow	52	25.4
Residence	Separate	83	40.5
	Urban	122	59.5
Job	Officer	45	22.0
	Employee	24	11.7
	Retired	44	21.5
	Unemployed	61	29.8
	Housewife	31	15.1
Education status	Illiterate	56	27.3
	Primary school	75	36.6
	High school	74	36.1
Diagnosis	hemorrhagic stroke	49	23.9
	ischemic stroke	156	76.1
Disease duration (months)	6 ay	140	68.3
	7+	65	31.7

Participants' score distributions of Perceived Stress and Stroke-spesific Quality of Life according to their gender are shown in Table 2.

Table 2. Participants' score distributions of Perceived Stress and Stroke-spesific Quality of Life according to their gender

	Men		Women		t	p
	$\overline{X}$	SS	$\overline{X}$	SS		
Energy	1.63	0.53	1.62	0.54	0.128	0.898
Family rol	1.77	0.57	1.93	0.56	-2.038	0.043*
Language	2.48	0.68	2.52	0.58	-0.386	0.700
Mobility	1.75	0.63	1.71	0.59	0.404	0.687
Mode	1.87	0.56	2.16	0.54	-3.718	0.000*
Personality	1.56	0.51	2.17	0.60	-7.702	0.000*
self-care	1.95	0.72	2.10	0.61	-1.608	0.109
social role	1.47	0.41	1.53	0.42	-1.034	0.302
Thinking	1.96	0.75	2.04	0.66	-0.845	0.399
Vision	2.64	0.67	2.74	0.57	-1.096	0.274
business/production	1.65	0.52	1.76	0.46	-1.548	0.123
Stroke-specific quality of life	1.90	0.32	2.01	0.29	-2.584	0.010*
perceived stress	13.23	3.55	8.43	4.64	8.223	0.000*

Independent Samples t Ttest was applied to determine whether the stroke-specific quality of life and perceived stress mean scores of the study participants differed according to gender. It was determined that the mean scores of the participants on the stroke-specific quality of life scale and its sub-dimensions, family role, mood, and

personality dimensions showed a statistically significant difference according to gender (p <0.05). Accordingly, it was observed that the average family role, mood, personality, and stroke-specific quality of life scores of women were higher than men. It was determined that the perceived stress scale average scores of the participants showed a statistically significant difference according to gender (p <0.05). A previous study conducted in Nigeria found that women prefer to stay at home due to religious, cultural and social customs, as these women tend to take care of the family and take care of internal family affairs [5]. But in another study conducted in the Republic of China, researchers found that women are more likely than men to develop psychological problems after surviving a stroke [6]. This study was also supported by researchers Breslow, which was conducted in the United States of America, and its results confirmed that women are more likely than men to suffer from psychological problems [7]. Other research has found sharp reductions in sad mood, anhedonia, fatigue, concentration difficulties, appetite changes, negative thoughts, and hopelessness, with higher levels as a function of increased stress. While men did not experience increases in sad moods associated with stress levels. Women experienced greater emotional reactivity, i.e., greater sadness, than men at both higher levels of stress [8].

Participants' mean score distributions of patients' stroke-specific quality of life and perceived stress scales according to marital status are shown in Table 3.

Our study also showed that marital history and marital status may have an important impact on survival after stroke. The researchers found that people who were single at the time of stroke may be more likely to die. These findings indicate the importance of considering social support and psychological factors associated with marital history or marital status in the influence of survival time after stroke [9]. The study showed that changes in marital status can have an impact on the risk of stroke. The results of this study showed that changing marital status may be associated with different stroke risks depending on current housing and employment status [10]. The results of our research differed from all previous research that addressed the issue of differences between married or single women after a stroke related to quality of life. The reason for this difference is the difference in social and environmental customs in Iraq from other European, Western, or Asian countries. Since single women live with their families throughout their lives, they cannot live in a house isolated from their families for customary and social reasons. Therefore, single women remain under the care and care of the family for life and are connected with their dependents by very strong social ties, unlike widowed or divorced women who live in homes separate from the rest of the family.

Table 3. Mean score distributions of participants' stroke-specific quality of life and perceived stress scales according to marital status

	Single (1)		Married (2)		Widow (3)		F	p	Multiple comparison
	$\bar{X}$	SS	$\bar{X}$	SS	$\bar{X}$	SS			
Energy	1.81	0.51	1.68	0.54	1.38	0.42	8.799	0.000*	3<1; 3<2
Family rol	1.82	0.65	1.91	0.57	1.72	0.49	1.929	0.148	-
Language	2.71	0.56	2.49	0.65	2.37	0.62	2.986	0.053	-
Mobility	2.03	0.58	1.75	0.62	1.49	0.52	9.001	0.000*	2<1; 3<1; 3<2
Mode	1.87	0.62	2.03	0.56	2.02	0.54	1.104	0.334	-
Personality	1.53	0.44	1.87	0.65	1.97	0.64	5.728	0.004*	1<3; 2<3
self-care	2.31	0.64	2.03	0.68	1.81	0.61	6.283	0.002*	3<1
social role	1.58	0.46	1.54	0.41	1.35	0.36	4.650	0.011*	3<1; 3<2
Thinking	2.26	0.74	2.07	0.70	1.65	0.58	10.195	0.000*	3<1; 3<2
Vision	2.88	0.43	2.79	0.53	2.32	0.78	13.602	0.000*	3<1; 3<2
business/production	1.90	0.48	1.73	0.47	1.50	0.51	7.491	0.001*	3<1; 3<2
Stroke-specific quality of life	2.01	0.29	1.99	0.31	1.82	0.29	6.463	0.002*	3<1; 3<2
perceived stress	12.57	4.17	10.92	4.92	10.23	4.47	2.676	0.071	-

Participants' mean score distributions of patients' stroke-specific quality of life and perceived stress scales according to educational level are shown in Table 4.
In our study we found that people who are better educated have a better quality of life after a stroke. Studies conducted in multiple countries, including the Republic of China, found that education for more than eight years has a good relationship with a reduced risk of developing mental illness after stroke [6]. In another research conducted in Switzerland, results showed that less education shows a higher incidence of psychological conditions after stroke [11]. There are many reasons why people with better education are given preference. Perhaps education is useful in understanding the health condition and dealing with it better, as education can increase people's understanding of the nature of stroke as well as its impact on their health. It can also help them deal with challenges and make appropriate decisions regarding treatment and health care better than their less educated peers.

Participants' relationship between stroke-specific quality of life and perceived stress' scores are shown Table 5. The results showed that there is a relationship between the level of perceived stress and depression in stroke patients. This study suggests that perceived stress may play a role in worsening depression after stroke [12]. Perhaps the possible reasons for the increase in perceived stress in people after a stroke is due to a completely or partial change in stroke survivors. They are exposed to several physical, psychological and emotional changes, in addition to the loss of control over the surrounding environment, which is represented by the loss of the family role, as well as the loss of the social role. In addition to high costs and financial deterioration. All of these reasons lead to the development of perceived stress, which greatly effects on the quality of life after a stroke.

Table 4. Mean score distributions of participants' stroke-specific quality of life and perceived stress scales according to educational level

	Primary school and under (1)		**secondary school (2)**		**Bachelor (3)**		**F**	**p**	**Multiple comparison**
	$\bar{X}$	**SS**	$\bar{X}$	**SS**	$\bar{X}$	**SS**			
Energy	1.45	0.53	1.62	0.49	1.77	0.54	6.220	0.002*	1<3
Family rol	1.65	0.56	1.89	0.48	1.95	0.63	5.043	0.007*	1<2; 1<3
Language	2.41	0.64	2.57	0.56	2.50	0.71	0.950	0.388	-
Mobility	1.60	0.55	1.73	0.64	1.84	0.62	2.368	0.096	-
Mode	1.98	0.59	2.01	0.55	2.01	0.58	0.056	0.945	-
Personality	1.90	0.68	1.81	0.64	1.82	0.58	0.424	0.655	-
self-care	1.91	0.68	1.99	0.67	2.13	0.66	1.913	0.150	-
social role	1.40	0.38	1.50	0.40	1.58	0.45	3.221	0.042*	1<3
Thinking	1.85	0.72	1.97	0.70	2.13	0.68	2.681	0.071	-
Vision	2.42	0.81	2.70	0.58	2.87	0.42	8.925	0.000*	1<2; 1<3
business/production	1.62	0.53	1.69	0.50	1.76	0.47	1.308	0.273	-
Stroke-specific quality of life	1.85	0.30	1.96	0.29	2.01	0.33	4.223	0.016*	1<3
perceived stress	11.13	4.84	11.13	4.41	10.85	5.00	0.081	0.922	-

Table 5. Relationship between stroke-specific quality of life and perceived stress' scores

	perceived stress	
	r	**p**
Stroke-specific quality of life	-0.574	0.000**
Energy	-0.219	0.002**
family role	-0.519	0.000**
Language	-0.254	0.000**
Mobility	-0.242	0.000**
Mode	-0.673	0.000**
Personality	-0.706	0.000**
self-care	-0.375	0.000**
social role	-0.455	0.000**
Thinking	-0.331	0.000**
Vision	-0.082	0.240
business/production	-0.407	0.000**

4. Conclusion

The perceived stress, and quality of life were affected by variables as gander, age, income, educational level, residence, type of stroke. It appears that people suffering from stroke could need extra attention to self-care. It is a good idea to provide additional support and services to improve personal care management for these patients. There is a statistically significant and inverse relationship between the level of psychological stress and several aspects of quality of life such as energy, family role, language, movement, mood, personality, self-care, social role, upper limb function, and work/production ($p<0.01$) There was also an inverse and significant relationship between stroke-specific quality of life and the level of psychological stress ($p<0.01$). The evaluation of stroke survivors' quality of life and perceived stress is a complex process that requires a comprehensive understanding of the physical, mental, and social dimensions of their experiences. Psychosocial support programs and support systems should be tailored to address the unique challenges faced by stroke survivors, promoting not only physical recovery but also emotional well-being and social integration.

References

[1] Panzeri, A., Rossi Ferrario, S., & Vidotto, G. (2019). Interventions for psychological health of stroke caregivers: a systematic review. *Frontiers in psychology*, 10, 2045

[2] World Health Rankings. (2021). Live Longer Live Better. Iraq Health Profile. https://www.worldlifeexpectancy.com/iraqcoronary-heart-disease

[3] Garton, A. L., Sisti, J. A., Gupta, V. P., Christophe, B. R., & Connolly Jr, E. S. (2017). Poststroke post-traumatic stress disorder: a review. Stroke, 48(2), 507-512. https://doi.org/10.1161/STROKEAHA.116.015234

[4] Goldfinger JZ, Edmondson D, Kronish IM, Fei K, Balakrishnan R, Tuhrim S, et al. 2014.Correlates of post-traumatic stress disorder in stroke survivors. J Stroke Cerebrovasc Dis.;23:1099–1105. doi: 10.1016/j. jstrokecerebrovasdis.2013.09.019.

[5] Abubakar, S. A., & Isezuo, S. A. (2012). Health related quality of life of stroke survivors: experience of a stroke unit. International journal of biomedical science: IJBS, 8(3), 183.

[6] Shi, Y., Yang, D., Zeng, Y., & Wu, W. (2017). Risk factors for post-stroke depression: a meta-analysis. Frontiers in aging neuroscience, 9, 218.

[7] Breslau N. (2001) The epidemiology of posttraumatic stress disorder: what is the extent of the problem J Clin Psychiatry.;62(suppl 17):16–22

[8] Mazure, C. M., Weinberger, A. H., Pittman, B., Sibon, I., & Swendsen, J. (2014). Gender and stress in predicting depressive symptoms following stroke. Cerebrovascular diseases, 38(4), 240-246.

[9] Dupre, M. E., & Lopes, R. D. (2016). Marital history and survival after stroke. Journal of the American Heart Association, 5(12), e004647.

[10] Honjo, K., Iso, H., Ikeda, A., Inoue, M., Sawada, N., Tsugane, S., & JPHC Study Group. (2016). Marital

transition and risk of stroke: how living arrangement and employment status modify associations. Stroke, 47(4), 991-998.

[11] Bruggimann L, Annoni JM, Staub F, von Steinbüchel N, Van der Linden M, Bogousslavsky J. (2006) Chronic posttraumatic stress symptoms after nonsevere stroke. Neurology.;66:513–516. doi: 10.1212/01.wnl.0000194210.98757.49.

[12] Laures-Gore, J. S., & DeFife, L. C. (2013). Perceived stress and depression in left and right hemisphere post-stroke patients. Neuropsychological rehabilitation, 23(6), 783-797

Gastric dilatation and volvulus with congestive splenomegaly in a Alabai dog

Fatih HATİPOĞLU [1,2*], **İsmail ŞEN** [3]

[1]*Faculty of Veterinary Medicine, Department of Pathology, Selcuk University, Konya, Türkiye*

[2]*Faculty of Veterinary Medicine, Department of Pathology, Kyrgyz-Turkish Manas University, Bishkek, Kyrgyzstan*

[3]*Faculty of Veterinary Medicine, Department of Internal Medicine, Kyrgyz-Turkish Manas University, Bishkek, Kyrgyzstan*

Abstract

Gastric dilatation and volvulus (GDV) is an acute, life-threatening condition that primarily affects large and giant breed dogs. In this case report, acute gastric dilatation due to ingested food and displacement of the stomach with congestive splenomegaly were described in a 2-year-old female Alabai dog. At necropsy; when the abdominal cavity was opened, it was observed that the stomach was on the right side of the abdominal cavity and extremely filled with gas, the stomach wall was tense, and large dark red congestive areas were observed through the serosa. When the stomach was opened, excessive gas accumulation in the lumen and occasional haemorrhages and congestion in the mucosa were detected. It was observed that the spleen was 3-4 times larger than normal, V-shaped and curved unlike its normal structure, the capsule was very tense and the sharp edges were blunt. In other parts of the intestine, the mucosa was hyperemic and a watery content was observed in the lumen. A foamy fluid was observed in the lumen of the trachea and bronchus (asphyxia). Costal imprints were also observed on the lung lobes. When the anamnesis and necropsy findings were evaluated, it was concluded that death was caused by acute gastric dilatation due to ingested food and consequent displacement of the stomach and acute passive hyperaemia in the spleen. It was also concluded that respiratory and circulatory disorders caused by the pressure of excessive dilatation of the stomach on the thoracic cavity played an important role in the development of death.

Keywords: *Gastric Dilatation-Volvulus, Congestive Splenomegaly, Alabai, Dog*

1. Introduction

Gastric dilatation and volvulus (GDV) is more commonly referred to as “bloat”. It occurs when a dog’s stomach becomes dilated and distended due to an accumulation of gas or fluid (dilation) and then rotates around its small axis (volvulus), trapping the gas or fluid inside. Dilatation without volvulus (simple bloat) can also occur separately [1, 2]. GDV is an enlargement of the stomach associated with rotation on the mesenteric access. GDV is an acute, life-threatening condition that primarily affects large- and giant-breed dogs, with a mortality rate of 20%–45% in treated animals. Immediate medical and surgical intervention is required to optimize survival in patients with GDV [1-3]. Although often referred to as bloat, there is a difference between the two conditions. Bloat is the accumulation of gas, food, and/or fluid in the stomach that cannot evacuate via esophagus or duodenum. A GDV includes torsion of the stomach that complicates the evacuation of gastric contents and obstructs blood flow. Gastric distension usually occurs first, and then the torsion follows. Pressure on the diaphragm can impair ventilation and cause a hypoxia. Venous blood return to the heart decreases, creating a hypovolemic shock that will lead to multiple organ dysfunction and death [2-4].

It causes pathology of multiple organ systems and is rapidly fatal. It is common in large- and giant-breed dogs. The disease appears to have a familial predisposition. Thoracic depth/width ratio also appears to predispose dogs to GDV [1]. The condition occurs most commonly in large, deep-chested dog breeds, such as German Shepherds, Great Danes and Doberman Pinschers. However, even small and medium breed dogs with a deep chest conformation can develop GDV [4, 5].

Gastric dilatation precedes development of volvulus and is the result of the accumulation of gas and fluid in the stomach as a result either of mechanical or functional disturbances in pyloric outflow. As the stomach distends and rotates about the distal esophagus, displacement and occlusion of the pylorus and duodenum occur. Necrosis and perforation of the stomach wall and peritonitis are common causes of death [2, 5-7].

* Corresponding author. *e-mail address: fhatip@selcuk.edu.tr, fatih.hatipoglu@manas.edu.kg*

2. Materials and Methods

The material of this case was a 2 years old female Alabai y dog which was found dead and brought to Kyrgyz-Turkish Manas University Veterinary Faculty for necropsy. Necropsy was performed after the anamnesis taken from the owner. External examination was performed before necropsy and observed changes were recorded. The dog was placed in the supine position and the skin incision was made along the median line from under the mandible to the anus. After incisions on the inner side of the forelimbs and hind limbs, the skin was skinned to the dorsal region. After the abdominal and thoracic cavities were opened according to known methods, changes in the organs were recorded. Tissue samples were taken from the affected organs in 10% buffered formaldehyde for histopathological examinations. After this process, 5-µm thick sections were taken from the paraffin blocks prepared by routine laboratory methods in the microtome, and were stained with Hematoxylin&Eosin (H&E).

3. Results and Discussion

According to the anamnesis, it was stated that carbohydrate-rich food was added to the dog's diet and that the dog's appetite had decreased for 3 days and enemas were given for treatment. Despite this treatment, the dog was found dead in the morning the next day and a necropsy was requested by the owner to find out the cause of death. Necropsy was performed on the same day.

In the external examination before necropsy, it was observed that the abdominal region of the dog was extremely distended and the skin was tense. At necropsy; when the abdominal cavity was opened, it was observed that the stomach was dilated due to extremely filled with gas (Figure 1) and there was a bloody fluid of the abdominal cavity.

It was noted that the stomach wall was tense, there were large and dark red congestive areas that could be seen through the serosa and in the abdominal cavity (Figure 1). When the stomach was opened, excessive gas accumulation in the lumen and congestion with occasional haemorrhages in the mucosa were observed.

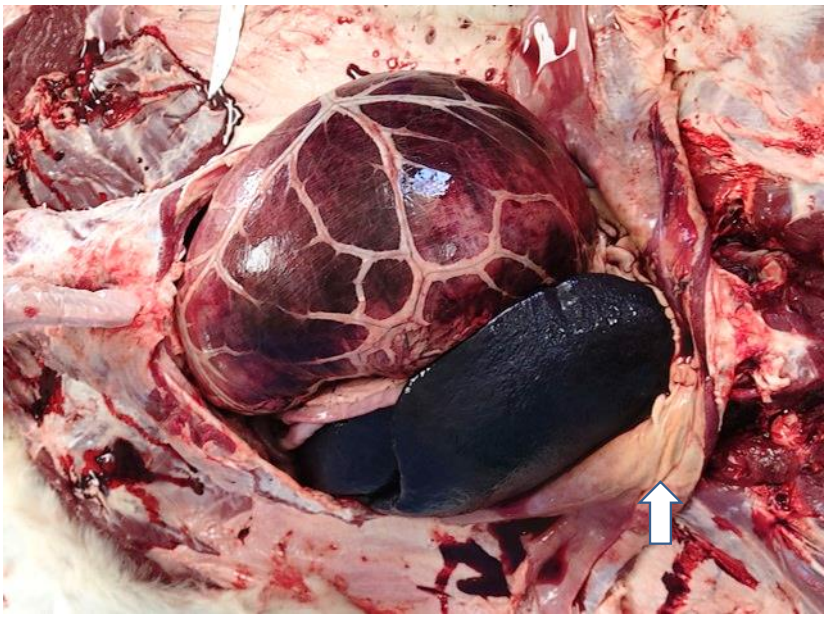

Figure 1. Gastric dilation-volvulus and congestive splenomegaly. Dilated stomach due to extremely filled with gas. Tense stomach wall and dark red congestive areas on serosa, and splenic congestion (arrow)

It was observed that the spleen was 3-4 times larger than normal, it was V-shaped and curved unlike its normal structure, its capsule was very tense and its sharp edges were blunt (Figure 2). A large amount of blood of dark red-black colour was oozing from the cut surface (Figure 3). In addition, a twisted and curved appearance was observed in the hilus region of the spleen.

A dark red coloured bloody content was observed in the lumen of duodenum. In other parts of the intestine, the mucosa was hyperemic and occasionally filled with a watery content. The liver was slightly pale and the liver tissue around the gallbladder was dark green in colour (biliary imbibition). At the thoracic cavity was opened, the right cranial and caudal lobes of the lung on the side where the animal was lying were well red and voluminous, with dark red blood leaking from the cut surface (hypostatic congestion) (Figure 4). A foamy fluid

was observed in the lumen of the trachea and bronchus (asphyxia). Costal imprints were also observed on the lung lobes.

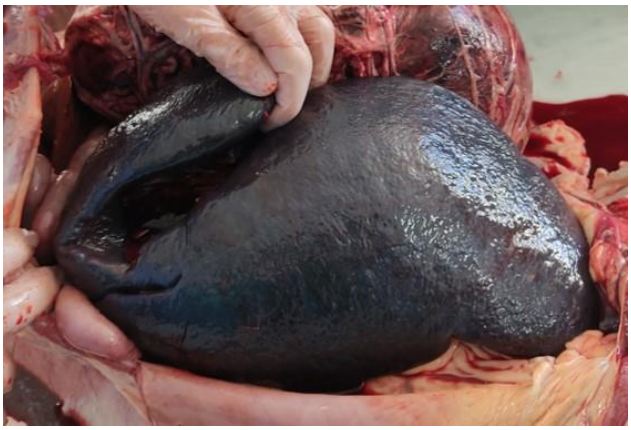

Figure 2. Congestive splenomegaly. Large, curled into a V shape, stretched capsule, blunt sharp edges.

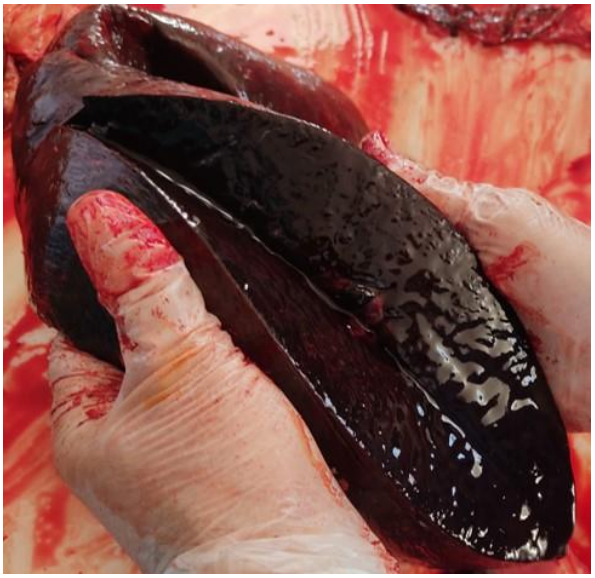

Figure 3. Congestive splenomegaly. An excessive amount of dark red-black colored blood on cut surface.

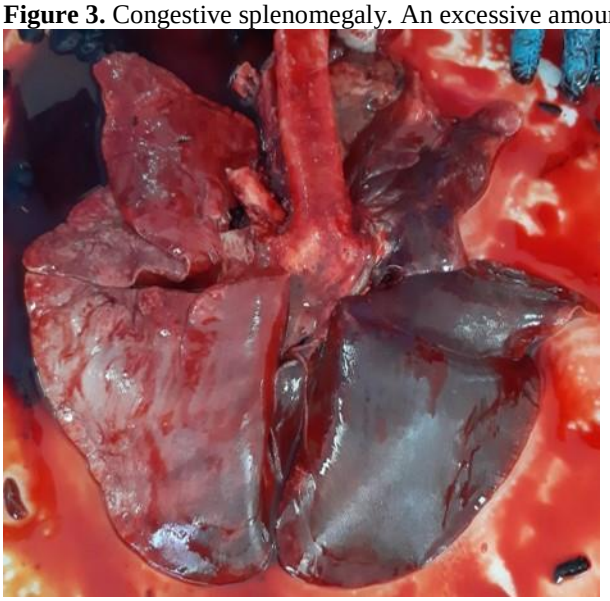

Figure 4. Lung, right cranial and caudal lobes, red-colored and voluminous appearance (hypostatic congestion).

Microscopic examinations showed a subcapsular hemorrhage in the spleen, as well as a dense accumulation of erythrocytes in the red pulp and macrophages loaded with hemosiderin (Figure 5). A depletion in lymphoid tissue

was observed in the white pulp (Figure 6). In the lung, hyperemia was observed in the interalveolar capillaries and pink edematous fluid in the alveolar lumens (Figure 7). Hyperemia was noted in the vena centralis lumen in the liver. In the stomach, degeneration of the lamina epithelialis and intense erythrocyte accumulation in the lumens of the veins and oedema in the submucosa were observed (Figure 8).

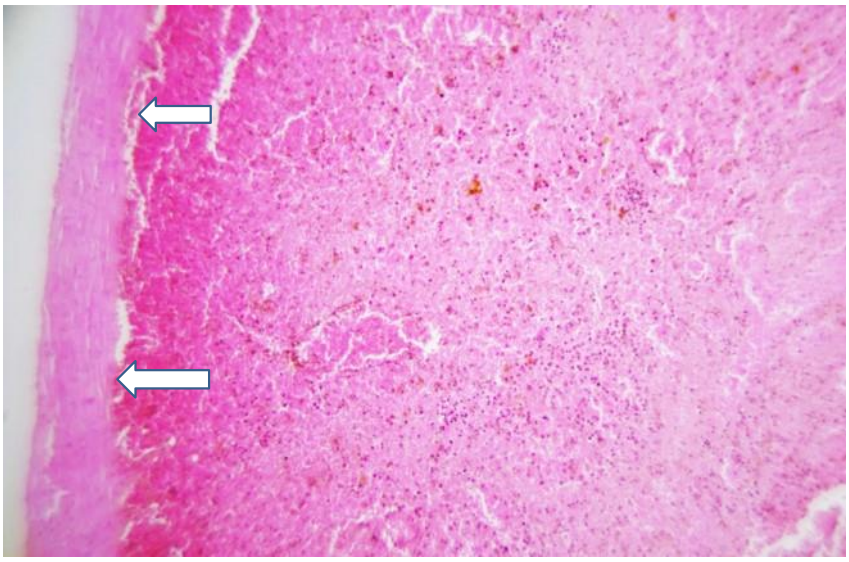

Figure 5. Spleen. Subcapsular hemorrhage (arrows) and dense erythrocytes accumulation in the red pulp and hemosiderin loaded macrophages.H&E, x100

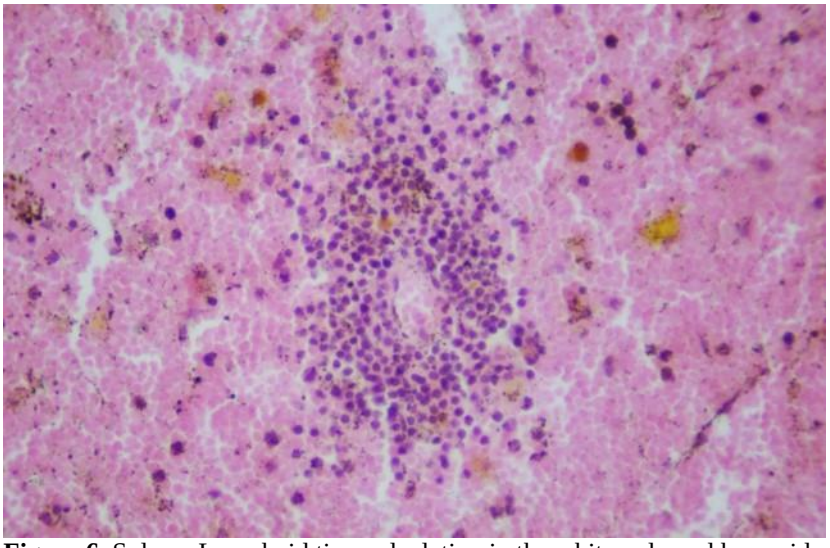

Figure 6. Spleen. Lymphoid tissue depletion in the white pulp and hemosiderin loaded macrophages, H&E, x400

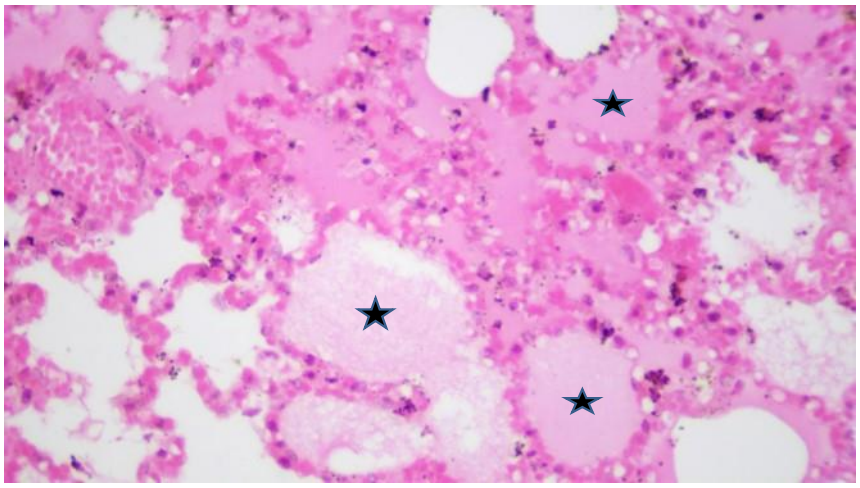

Figure 7. Lung. Hyperemic interalveolar capillaries and pink edematous fluid (asteriks) in the alveolar lumens, H&E, x400

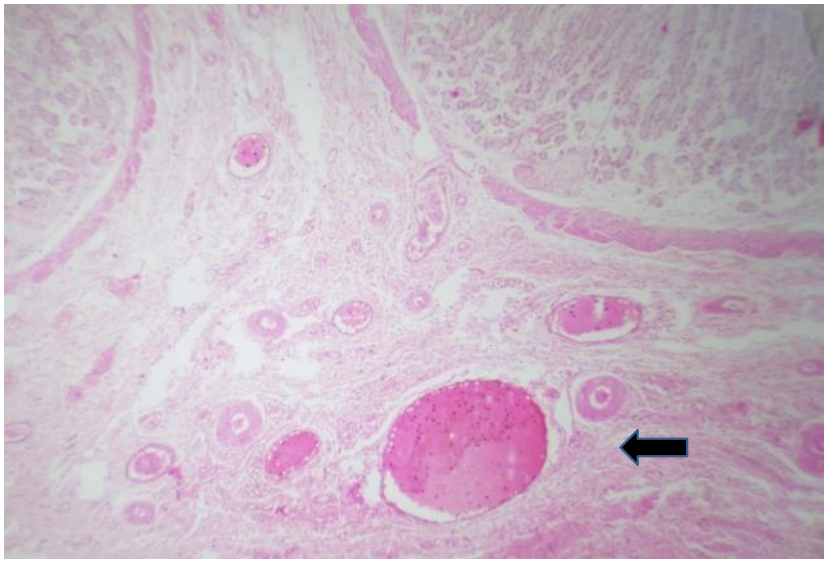

Figure 8. Stomach. Intense erythrocyte accumulation in the veins (arrow) and oedema in the submucosa, H&E, x40

Despite ongoing research, the specific cause of GDV remains unknown. The following risk factors are thought to contribute to bloat: overeating, eating very quickly, drinking a large quantity of water in a short period of time, raised food bowls, stress, exercising after eating, genetic factors and increased age. The conformation of the thorax appears to be a risk factor for GDV. Results from studies have shown that the risk of GDV is related to thoracic depth-to-width ratios, both for individuals [1, 4, 6]. In the presented case, the fact that the dog in which GDV occurs was from a large breed and there were problems with feeding supports the views stated above about the reasons.

Distension and displacement of the stomach cause obstruction of the caudal vena cava and portal vein resulting in venous stasis and sequestration of blood in splanchnic, renal, and posterior muscular capillary beds. This decrease in circulating blood volume (venous return) and subsequent decrease in cardiac output, arterial blood pressure, and tissue perfusion culminate in hypovolemic shock. Endotoxemia, a consequence of portal vein occlusion, contributes to the shock syndrome [2, 7]. The congestion observed in the spleen in this case supports the researchers' views and explains the cause of death of the dog in the presented case.

GDV develops without warning and can progress very quickly. Recognizing the early signs is essential to increasing the chances your dog will survive. Signs in the early stages of bloat can include: restlessness, pacing, swollen or distended abdomen painful abdomen, overall look of distress, retching or attempts to vomit with no success, excessive drooling, panting or rapid breathing, collapse/inability to stand [1, 3, 6].

Breed, history, and clinical presentation will aid in diagnosis. Radiographs will show gastric dilatation and possibly torsion. If passing a stomach tube is attempted, volvulus is suspected if the tube will not pass [1, 2, 6]. No matter what the order of treatment, the objectives remain the same. The goal is to correct circulatory shock, decompress the stomach, correct volvulus if necessary, and stabilize the patient. Decompression involves passing of a stomach tube (sedation may be required), temporary gastrotomy or trochar catheter, or surgical decompression. The stomach can be emptied through a stomach tube or surgically. Correction of volvulus requires a surgical fix. Additionally, if compromised a splenectomy can be performed during the surgical procedure [6-8].

Performing a gastropexy, to prevent future volvulus, completes the surgery. Correction of circulatory shock and supportive therapy includes oxygen therapy, IV fluids, and drug therapy. Antibiotics for endotoxemia, antiarrhythmic drugs, and antacids are used with GDV patients. The patients are hospitalized for monitoring and recovery and are monitored for continued gastric distension [6, 8]. Ultrasound-guided, temporary, percutaneous T-fastener gastropexy and gastrostomy catheter placement was safe and effective at providing sustained gastric decompression in dogs with GDV, suggesting that this technique would be ideal for dogs in which surgical delays are anticipated or unavoidable [9]**.**

4. Conclusion

As a result of the evaluation of the anamnesis and necropsy findings, it was concluded that death was caused by acute gastric dilatation due to ingested food and consequent displacement of the stomach and acute passive hyperaemia (splenic congestion) of the spleen. In addition, it was thought that respiratory and circulatory disorders due to the pressure on the thoracic cavity as a result of excessive dilatation of the stomach due to gas were also effective in the death of the dog. In cases where GDV is suspected as a result of clinical and laboratory examinations in dogs with digestive system problems, starting treatment as soon as possible will make a significant contribution to preventing fatal cases.

References

[1] Broome, C.J., & Walsh, V.P. (2003). Gastric dilatation-volvulus in dogs. *New Zealand Veterinary Journal, 51(6),* 275-283.

[2] Hornbuckle, W.E., Simpson, K.W., & Tennant, B.C. (2008). Gastrointestinal Function. In J.J. Kaneko, J.W. Harvey, & M. L. Bruss (Eds), *Clinical Biochemistry of Domestic Animals (*p.413-457)., 6th Ed. New York , USA, Academic Press.

[3] Gibson, T.W.G. (2022) Gastric Dilation and Volvulus in Small Animals (Bloat). *MSD Manual, Veterinary Manual* (MSD Veterinary Manual (msdvetmanual.com).

[4] Bell, J.S. (2 014).Inherited and predisposing factors in the development of gastric dilatation volvulus in dogs. *Top Companion Anim Med, 29,* 60-63

[5] Raghavan, M., Glickman, N. W., & Glickman, L. T. (2006). The effect of ingredients in dry dog foods on the risk of gastric dilatation-volvulus in dogs. *Journal of the American Animal Hospital Association, 42(1),* 28–36.

[6] Johnson A (2014). Small Animal Pathology for Veterinary Technicians. Blackwell Publishing, pp.60-62.

[7] Sharp, C.R. & Rozanski, E.A. (2014). Cardiovascular and systemic effects of gastric dilatation and volvulus in dogs. *Top Companion Anim Med, 29,* 67-70.

[8] Arıcan, M., Uzunlu, E.O., &İncekara, O. (2021). Köpeklerde gastrik dilatasyon-volvulus olgularında cerrahi girişimler ve postoperatif hasta yönetimi. In A.P. Gökçe (Ed), *Kedi ve Köpeklerde Gastrointestinal Hastalıklar (*p.48-56). 1. Baskı. Ankara, Türkiye, Türkiye Klinikleri.

[9] Fox-Alvarez, W. A., Case, J. B., Lewis, D. D., Joyce, A. C., Cooke, K. L., & Toskich, B. (2019). Evaluation of a novel technique involving ultrasound-guided, temporary, percutaneous gastropexy and gastrostomy catheter placement for providing sustained gastric decompression in dogs with gastric dilatation-volvulus. *Journal of the American Veterinary Medical Association, 255(9),* 1027-1034.

Estimation of survival times of covid-19 patients using some lifetime distributions

Caner TANIŞ[1,*]

[1] *Science Faculty, Statistics, Çankırı Karatekin University, Çankırı, Turkey*

Abstract

In this study, the survival time (in days) of Covid-19 patients from hospitalization and death were modeled with some known lifetime distributions such as Weibull, transmuted Weibull, exponentiated Weibull, and generalized Lindley distributions. The maximum likelihood method is considered for point estimation. We present four data sets on Covid-19 patients. The goodness of the fitted distribution is evaluated via some selection criteria such as Akaike information criterion, the Bayesian information criterion, the Kolmogorov-Smirnov test statistic, the Anderson Darling statistic, the Cramér von Mises statistic, and the p-value criteria Also, the estimated probabilities of the survival times of Covid-19 patients were calculated via the invariance property of maximum likelihood estimation. In dying Covid-19 patients, the average survival time is estimated approximately 15 days.

Keywords: *Covid-19, Lifetime distribution, Maximum likelihood, Point estimation*

1. Introduction

The new coronavirus, also known as the Covid-19 virus, appeared in Wuhan, China in December 2019 and rapidly exceeded its borders and affected the whole world. The WHO officially reported that Covid-19 is a global pandemic on March 11, 2020 [1]. As of March 27, 2023, it is globally announced that there have been 761,402,282 confirmed Covid-19 cases with 6,887,000 deaths by the World Health Organization (WHO) [2]. Tian et al. [3] analyzed the findings of many studies on mortality in hospitalized Covid-19 patients. They reported that patients with damaged organs such as the heart, liver, kidney, had a high risk of death due to Covid-19. Covino et al. [4] investigated the clinical properties and prognostic indicators in Covid-19 patients aged more than 80 years. The findings of Covino et al. [4] show that the risk of death could be not age dependent in Covid-19 patients aged more than 80 years while severe dementia emerged as a risk factor in this group. Cheng et al. [5] investigated the death periods in hospitalized Covid-19 patients. In the literature, many statistical distributions are used to model data obtained in many fields such as biology, chemistry, engineering, and medical sciences. Some of the popularly used lifetime distributions can be shown as Weibull, Lindley, and various modified versions of these distributions. In this study, different from other studies in the literature, the estimates will be provided about the survival times of Covid-19 patients using some known lifetime distributions including Weibull, transmuted Weibull, and generalized Lindley distribution. The rest of this paper is organized as follows: In Section 2, we describe the emphasized lifetime distributions. In Section 3, the point estimation of the examined distributions is given. In Section 4, Model evaluation is given. In Section 5, the results and discussion are presented. Finally, the conclusions are given in Section 6.

2. Materials and Methods

2.1. Weibull Distribution

Weibull distribution is one of the most popular distributions used to model lifetime data. The cumulative distribution function (CDF) and probability density function (PDF) and first moment of the Weibull distribution are given by

$$F_{Weibull}(x) = 1 - \exp\left\{-\left(\frac{x}{\beta}\right)^{\alpha}\right\}, \tag{1}$$

$$f_{Weibull}(x) = \frac{\alpha}{\beta}\left(\frac{x}{\beta}\right)^{\alpha-1} \exp\left\{-\left(\frac{x}{\beta}\right)^{\alpha}\right\}, \tag{2}$$

* Corresponding author. *e-mail address: canertanis@karatekin.edu.tr*

and

$$E_{Weibull}(X) = \beta\Gamma\left(1+\frac{1}{\alpha}\right), \tag{3}$$

respectively, where, $\alpha > 0$ is a shape parameter, $\beta > 0$ is a scale parameter, and $x > 0$.

2.2. Exponentiated Weibull Distribution

The EW distribution suggested by Pal et al. [6] is a generalization of Weibull distribution. The CDF and PDF and first moment of the EW distribution are given by

$$F_{EW}(x) = \left\{1-\exp\left(-\alpha x^{\beta}\right)\right\}^{\theta}, \tag{4}$$

$$f_{EW}(x) = \alpha\beta\theta x^{\beta-1}\left\{1-\exp\left(-\alpha x^{\beta}\right)\right\}^{\theta-1}, \tag{5}$$

and

$$E_{\mathrm{W}}(X) = \begin{cases} \theta\alpha^{-1}\Gamma\left(\frac{1}{\beta}+1\right)\sum_{i=0}^{\theta-1}\binom{\theta-1}{i}(-1)^{i}(i+1)^{-\frac{1}{\beta}-1}, & \text{if } \theta \in \square \\ \theta\alpha^{-1}\Gamma\left(\frac{1}{\beta}+1\right)\sum_{i=0}^{\infty}\frac{(\theta-2)(\theta-3)\cdots(\theta-i+2)}{i!}(-1)^{i}(i+1)^{-\frac{1}{\beta}-1}, & \text{if } \theta \notin \square \end{cases}, \tag{6}$$

where, $\square$ denote natural number. $\beta > 0$ and $\theta > 0$ are shape parameters, $\alpha > 0$ is a scale parameter, and $x > 0$ [7]. The EW distribution is reduced Weibull distribution for $\theta = 1$.

2.3. Transmuted Weibull Distribution

Transmuted Weibull (TW) distribution proposed by Aryal and Tsokos [8] is another generalization of Weibull distribution. The CDF, PDF and first moment of TW distribution are

$$F_{TW}(x) = \left[1-\exp\left\{-\left(\frac{x}{\beta}\right)^{\alpha}\right\}\right]\left[1+\theta\exp\left\{-\left(\frac{x}{\beta}\right)^{\alpha}\right\}\right], \tag{7}$$

$$f_{TW}(x) = \frac{\alpha}{\beta}\left(\frac{x}{\beta}\right)^{\alpha-1}\exp\left\{-\left(\frac{x}{\beta}\right)^{\alpha}\right\}\left[1-\theta+2\theta\exp\left\{-\left(\frac{x}{\beta}\right)^{\alpha}\right\}\right], \tag{8}$$

and

$$E_{\mathrm{TW}}(X) = \beta\Gamma\left(\frac{1}{\alpha}+1\right)\left(1-\theta+\theta 2^{-\frac{1}{\alpha}}\right), \tag{9}$$

respectively, where, $\theta \in [-1,1], \alpha, \beta > 0$ and $x > 0$. The TW distribution is reduced Weibull distribution for $\theta = 0$.

2.4. Generalized Lindley Distribution

Lindley distribution introduced by [9] can be used in various fields such as biology, engineering, and medical sciences is another popular lifetime distribution. Ghitany et al. [10] mentioned that Lindley distribution is particularly useful for modeling mortality data.

The GL distribution proposed by [11] is a generalization of Lindley distribution. The CDF, PDF and first moment of the GL distribution are

$$F_{GL}(x) = \left[1-\frac{(\alpha+\alpha x+1)\exp\{-\alpha x\}}{\alpha+1}\right]^{\beta}, \tag{10}$$

$$f_{GL}(x) = \frac{\alpha^{2}\beta(x+1)\exp\{-\alpha x\}}{1+\alpha}\left[1-\frac{(\alpha+\alpha x+1)\exp\{-\alpha x\}}{\alpha+1}\right]^{\beta-1}, \tag{11}$$

and

$$E_{GL}(X)=\frac{\beta\alpha^{2}}{1+\alpha}\mathrm{K}(\beta,\alpha,1,\alpha), \tag{12}$$

where, $\mathrm{K}(\beta,\alpha,1,\alpha)=\sum_{i=0}^{\infty}\binom{\beta-1}{i}\frac{(-1)^{i}}{(1+\alpha)^{i}}\sum_{j=0}^{i}\binom{i}{j}\alpha^{j}\sum_{k=0}^{j+1}\binom{j+1}{k}\int_{0}^{\infty}x^{1+k}\exp(-\alpha ix-\alpha x)\,dx$, $\alpha,\beta>0$, and $x>0$ [11].

3. Point Estimation

$X_1, X_2,\cdots, X_n$ denote a random sample from the Weibull (α,β) distribution and $x=x_1, x_2\cdots, x_n$ indicate the observed value of X_i for $i=1,2,\cdots,n$. For the Weibull (α,β) distribution, the log-likelihood function is

$$\ell(\alpha,\beta\mid x)=\mathrm{In}(\alpha)-\mathrm{In}(\beta)+(\alpha-1)\sum_{i=1}^{n}\mathrm{In}\left(\frac{x_i}{\beta}\right)-\sum_{i=1}^{n}\left(\frac{x_i}{\beta}\right)^{\alpha}. \tag{13}$$

For the Weibull (α,β) distribution, the maximum likelihood estimators of the α and β parameters maximize the $\ell(\alpha,\beta\mid x)$ function in Eq. (13).

$X_1, X_2,\cdots, X_n$ denote a random sample from EW (α,β,θ) distribution and $x=x_1, x_2\cdots, x_n$ indicate the observed value X_i for $i=1,2,\cdots,n$. The log-likelihood function is

$$\ell(\alpha,\beta,\theta\mid x)=\mathrm{In}(\alpha)+\mathrm{In}(\beta)+\mathrm{In}(\theta)+(\beta-1)\sum_{i=1}^{n}\mathrm{In}x_i+(\theta-1)\sum_{i=1}^{n}\mathrm{In}\left(1-\exp\left(-\alpha x_i^{\beta}\right)\right). \tag{14}$$

For EW (α,β,θ) distribution, the maximum likelihood estimators of the α,β, and θ parameters maximize the $\ell(\alpha,\beta,\theta\mid x)$ function in Eq. (14).

$X_1, X_2,\cdots, X_n$ denote a random sample from TW (α,β,θ) distribution and $x=x_1, x_2\cdots, x_n$ indicate the observed value X_i for $i=1,2,\cdots,n$. The log-likelihood function is

$$\ell(\alpha,\beta,\theta\mid x)=\mathrm{In}(\alpha)+\mathrm{In}(\beta)+(\alpha-1)\sum_{i=1}^{n}\mathrm{In}\left(\frac{x_i}{\beta}\right)-\sum_{i=1}^{n}\left(\frac{x_i}{\beta}\right)^{\alpha}+\sum_{i=1}^{n}\mathrm{In}\left(1-\theta+2\theta\exp\left(-\left(\frac{x_i}{\beta}\right)^{\alpha}\right)\right). \tag{15}$$

For the TW (α,β,θ) distribution, the maximum likelihood estimators of the α,β, and θ parameters maximize the $\ell(\alpha,\beta,\theta\mid x)$ function in Eq. (15).

$X_1, X_2,\cdots, X_n$ denote a random sample from GL (α,β) distribution and $x=x_1, x_2\cdots, x_n$ indicate the observed value X_i for $i=1,2,\cdots,n$. The log-likelihood function is

$$\ell(\alpha,\beta\mid x)=\ln\left(\frac{\beta\alpha^{2}}{1+\alpha}\right)+\sum_{i=1}^{n}\ln(x_i+1)-\alpha\sum_{i=1}^{n}x_i+(\alpha-1)\sum_{i=1}^{n}\ln(\mathrm{V}(x_i)), \tag{16}$$

where $\mathrm{V}(x_i)=1-\frac{1+\alpha+\alpha x_i}{1+\alpha}\exp(-\alpha x_i)$.

For GL (α,β) distribution, the maximum likelihood estimators of the α and β parameters maximize the $\ell(\alpha,\beta \mid x)$ function in Eq. (16). The optim function in the R program is used to maximize the log-likelihood functions in Eqs. (13, 14, 15, 16).

4. Model Evaluation

We consider some selection criteria including Akaike information criterion (AIC), Bayesian information criterion (BIC), Anderson-Darling statistics (A*), Cramér-von Mises statistics (W*), Kolmogorov-Smirnov statistics (K-S), and p-values (A*, W*, KS) for Covid-19 patients data analysis.

4.1. Data Description

We consider two Covid-19 patients data sets (the survival time of 75-84 aged Covid-19 patients (100 observations), the survival time of 85+ Covid-19 patients (100 observations)). The survival time (in days) refers to the time between deaths and hospitalizations of Covid-19 patients. The survival time of 75-84 aged Covid-19 patients data consist of 100 individuals of 1047 patients with certain characteristics (Age: 74-85, Source of Covid-19: Contact with confirmed) were selected by simple random sampling method. The survival time of 85+ Covid-19 patients data consist of 100 individuals of 1323 patients with certain characteristics (Age: 85+, Source of Covid-19: Contact with confirmed) were selected by simple random sampling method. The survival time of 75-84 aged Covid-19 patients and the survival time of 85+ Covid-19 patients data sets were collected between June 15, 2020 and January 20, 2021 and released to the public by the Israel Ministry of Health on 20 January 2021 (anonymous and open-access data, [12]). The descriptive statistics of the data sets are given Table 1.

Table 1. Descriptive statistics of Covid-19 data sets

Data set	Minimum	Maximum	Mean	Median
Data set 1	1	58	15.20	13
Data set 2	1	41	14.48	13

5. Results and Discussion

In this subsection, we present the results of data analysis for described data sets in Section 4. Table 6 shows the maximum likelihood estimates (MLEs) of fitted models for four data sets. In Table 7, the selection criteria statistics to assess the fits of models to data sets are given. From Table 7, the EW distribution is the best-fitted model according to the KS statistic and its p-value. From Table 7, it is seen that the GL distribution is the best-fitted model according to all criteria except A *, W * statistics, and their p values. The best model was determined as TW according to A *, W *, and their p values for the first data set. In the second data analysis, the GL distribution is the best-fitted model according to AIC, BIC, A *, and its p-value while the EW distribution is the best-fitted model according to KS and its p-value. The W * statistics of the TW and EW distributions are very close to each other. According to this criterion, TW and EW distributions are the two best-fit models due to the higher number of the selection.

Table 2. MLEs and standard errors (SE) of parameters of all models for data sets

Data set	Model	$\hat{\alpha}$	$\hat{\beta}$	$\hat{\theta}$	$SE(\hat{\alpha})$	$SE(\hat{\beta})$	$SE(\hat{\theta})$
Data set 1	Weibull	1.461815	16.84369	-	0.109226	1.216951	-
	TW	1.074265	10.79041	-0.94037	0.14124	1.649272	0.211835
	EW	0.088046	1.038861	2.003125	0.083591	0.240331	0.935173
	GL	0.136562	1.206187	-	0.013607	0.183067	-
Data set 2	Weibull	1.730377	16.28494	-	0.131714	0.993283	-
	TW	1.861176	19.98046	0.596923	0.142753	2.965782	0.370521
	EW	0.036983	1.322898	1.677508	0.040665	0.295992	0.726261
	GL	0.162691	1.599501	-	0.015149	0.253754	-

The invariance property of the maximum likelihood estimator is used to estimate the mean survival time of Covid-19 patients and the probabilities of dying for data sets. We compute the estimated probabilities of survival times in Covid-19 patients for data sets using the following procedure.

Table 3. Selection criteria of fitted models for data sets

Data	Model	AIC	BIC	KS	A*	W*	p-value (KS)	p-value (A*)	p-value (W*)
Data set 3	Weibull	727.3092	732.5196	0.0758	0.6560	0.0923	0.6131	0.5963	0.6247
	TW	726.7592	734.5747	0.0593	**0.3627**	**0.0431**	0.8737	**0.8845**	**0.9175**
	EW	726.8427	734.6582	0.0596	0.3820	0.0426	0.8701	0.8661	0.9201
	GL	**724.8983**	**730.1087**	**0.0562**	0.3711	0.0450	**0.9102**	0.8766	0.9071
Data set 4	Weibull	699.3657	704.5761	0.0800	0.4140	0.0678	0.5437	0.8343	0.7663
	TW	700.1762	707.9917	0.0689	0.2932	**0.0469**	0.7288	0.9430	**0.8957**
	EW	700.2063	708.0218	**0.0640**	0.2896	**0.0469**	**0.8080**	0.9456	**0.8957**
	GL	**698.4261**	**703.6365**	0.0666	**0.2878**	0.0472	0.7673	**0.9469**	0.8938

Let define X be a random variable from one of the examined distributions (Weibull, TW, EW, GL) with estimated parameters given in Table 6, and t denotes the survival times of Covid-19 patients. In this regard, we can calculate the probability via the following equation.

$$\Pr(X < t) = \int_0^t f(x)\,dx, \tag{17}$$

where $f(x)$ denotes the PDF of the relevant distribution (Weibull, TW, EW, GL). Thus, we provide the estimated probabilities given in Tables 4-5 for data sets. Further, we estimate the average survival times of dead Covid-19 patients for the first and second data sets (Table 6).

Table 4. Estimated probabilites of survival times in Covid-19 patients for data set 1

Survival time	*Weibull*	*TW*	*EW*	*GL*
<7 days	0.241981	0.232418	0.235266	0.226725
<8 days	0.285923	0.280867	0.284638	0.274363
<9 days	0.329706	0.329238	0.333658	0.322227
<10 days	0.3729	0.376798	0.381606	0.369567
<11 days	0.415158	0.422988	0.427953	0.415795
<12 days	0.456198	0.4674	0.472325	0.460462
<13 days	0.495802	0.509744	0.514471	0.503238
<14 days	0.533799	0.549833	0.55424	0.543894
<15 days	0.570064	0.587558	0.591556	0.582283
<16 days	0.604511	0.622875	0.626405	0.618327
<17 days	0.637088	0.655789	0.658818	0.652
<18 days	0.667769	0.686344	0.688856	0.683321
<19 days	0.696554	0.71461	0.71661	0.71234
<20 days	0.723462	0.74068	0.742182	0.739133
<21 days	0.748531	0.764659	0.765688	0.763793
<4 weeks	0.8778	0.883842	0.882602	0.886159
<5 weeks	0.945679	0.944485	0.942626	0.947507
<6 weeks	0.977684	0.973993	0.972355	0.976499
<7 weeks	0.991465	0.987981	0.986797	0.989696
<8 weeks	0.996943	0.994502	0.993732	0.995553

According to Tables 4-5, it was observed that the patients died with a probability of almost 90% within 4 weeks. We estimated that patients over 85 years of age died within 14.5 days and patients in the 74-85 age group died within approximately 15.2 days. (Table 6). The purpose of this paper is to estimate the survival times (in days) of Covid-19 patients by modeling some lifetime distributions. In a previous research, Cheng et al. [5] emphasized that the median of days from illness onset to admission was 10 days, and the median of stay in hospital was 5 days for dead Covid-19 patients. This means that a patient dies approximately 15 days after being infected [5]. Our results support previous studies, the survival time of an infected patient has been estimated at about 15 days. It can be said that this result is similar to Cheng's [5] findings. Another subject of discussion is that there are other factors affecting survival times in Covid-19 patients such as the presence of chronic disease and treatment method. We have provided a new study on the survival times of Covid-19 patients only in terms of age and gender.

Table 5. Estimated probabilites of survival times in Covid-19 patients for data set 2

Survival time	*Weibull*	*TW*	*EW*	*GL*
<7 days	0.207055	0.20091	0.201186	0.200513
<8 days	0.253461	0.249238	0.251857	0.252803
<9 days	0.301197	0.299307	0.303951	0.306571
<10 days	0.349531	0.350188	0.356379	0.360542
<11 days	0.397804	0.40104	0.408227	0.413675
<12 days	0.44544	0.451126	0.458754	0.465156
<13 days	0.491945	0.499816	0.507381	0.514376
<14 days	0.536902	0.546596	0.553674	0.560908
<15 days	0.57997	0.591061	0.597329	0.604479
<16 days	0.620886	0.632915	0.638151	0.644943
<17 days	0.65945	0.671958	0.676041	0.682253
<18 days	0.695529	0.708081	0.710972	0.716441
<19 days	0.729046	0.74125	0.742981	0.747596
<20 days	0.759973	0.771495	0.772149	0.775851
<21 days	0.788327	0.798899	0.798596	0.801365
<4 weeks	0.922258	0.924054	0.92083	0.918609
<5 weeks	0.976673	0.974378	0.971797	0.968443
<6 weeks	0.994213	0.992304	0.990696	0.988173
<7 weeks	0.998802	0.997993	0.997122	0.995668
<8 weeks	0.999792	0.999554	0.999159	0.998439

Table 6. The estimated average survival times of Covid-19 patients for data sets

Data Set	*Weibull*	*TW*	*EW*	*GL*
Data set 1: The estimated average of the survival times (in days)	15.2556	15.1888	15.1972	15.1887
Data set 2: The estimated average of the survival times (in days)	14.5134	14.4496	14.4774	14.4896

6. Conclusion

In conclusion, we also have shown that some statistical distributions (Weibull, TW, EW, GL) have the potential to be used in modelling the Covid-19 data. We recommend using GL distribution and EW distributions to model and estimate the survival time of Covid-19 patients in the data sets due to the high number of select according to selection criteria in Section 4. The study has the limitations. Firstly, the Covid-19 data sets are anonymous and open access URL-1, (2021). The datasets on Israeli Covid-19 patients are consisted by filtering variables (age and gender). Secondly, the sample size is limited and an accurate assessment of the survival time of Covid-19 patients is not accurate. The survival time may vary depending on age, ethnicity, country, and other global factors. The study is designed to show the survival time can be estimated by lifetime distributions. Extensive research should be conducted on the survival time of Covid-19 patients.

References

[1] World Health Organization, (2020) WHO Director-General's Opening Remarks at the Media Briefing on Covid 19 - 11 March 2020. World Health Organization, Geneva.

[2] World Health Organization, (2023) Available at: https://Covid19.who.int/, Retrieved March 27, 2023.

[3] Tian, W., Jiang, W., Yao, J., Nicholson, C. J., Li, R. H., Sigurslid, H. H., ... , & Malhotra, R. (2020) Predictors of mortality in hospitalized COVID-19 patients: A systematic review and meta-analysis. *Journal of medical virology*, 92(10), 1875-1883.

[4] Covino, M., De Matteis, G., Santoro, M., Sabia, L., Simeoni, B., Candelli, M., ... , & Franceschi, F. (2020) Clinical characteristics and prognostic factors in COVID-19 patients aged≥ 80 years. *Geriatrics & gerontology international*, 20(7), 704-708.

[5] Cheng, Y., Luo, R., Wang, K., Zhang, M., Wang, Z., Dong, L., ... , & Xu, G. (2020) Kidney impairment is associated with in-hospital death of COVID-19 patients. *MedRxiv*. https://doi.org/10.1101/2020.02.18.20023242.

[6] Pal, M., Ali, M. M., & Woo, J.. (2006) Exponentiated weibull distribution. *Statistica*, 66(2) (2006) 139-147.

[7] Gradshteyn, I. S., & Ryzhik I. M. (2014) Table of integrals, series, and products. London: Academic press.

[8] Aryal, G. R., & Tsokos, C. P. (2011) Transmuted Weibull distribution: A generalization of the Weibull probability distribution. *European Journal of pure and applied mathematics*, 4(2), 89-102.

[9] Lindley, D.V. (1958) Fiducial distributions and Bayes theorem. *Journal of the Royal Statistical Society B*, 20, 102.

[10] Ghitany M. E., Alqallaf F., Al-Mutairi D. K., & Husain H. A. (2011) A two-parameter weighted Lindley distribution and its applications to survival data, *Mathematics and Computers in Simulation*, (81) 6, 1190-1201.

[11] Nadarajah, S., Bakouch, H. S., & Tahmasbi, R. (2011) A generalized Lindley distribution. *Sankhya B*, 73(2), 331-359.

[12] Israel Ministry of Health. (2021) Available at: https://data.gov.il/dataset/COVİD-19, Retrieved January 25, 2021.

Evaluation of Traditional Wooden Toys and Laser Cut Wooden Toys In Terms of Production

Mehmet GÜNEŞ[1,*], *Çağatay ERSİN*[2]

[1]*Vocational School, Department of Design Interior Design Program, Cankiri Karatekin University, Cankiri, Turkey*

[2]*Vocational School, Department of Electronic and Automation Mechatronics Program, Cankiri Karatekin University, Cankiri, Turkey*

Abstract

Wooden toys have survived from the earliest periods of history to the present day. Toys are involved in many stages of human life, starting from infancy to childhood and adulthood. With the development of materials and production technology, the design and production of toys changed. Wooden toys are preferred today because they are natural materials and are easy to process. Although production tools are changing, traditional production techniques are still used in wooden toys. In addition to traditional workshop-type production, laser-cutting machines can produce more products in less time during the toy design and production stages. This research mentions the advantages and disadvantages of solid wooden toys produced by traditional methods and wood-based toys produced by laser cutting machines.

Keywords: *Wooden, Toys, Laser Cut, Traditional, Production*

1. Introduction

The concepts of games and toys for children are as old as human history. Toys are objects that have existed since the first moments of human history [1]. So much so that it is possible to take the history of toys back to the ancient stone age. However, due to the problems arising from the shelter and security needs of the people of this period, the concept of toys could not be fulfilled [2]. Therefore, when we look at the history of toys, it is thought that the first toys known in history belonged to the Egyptians [3]. Games and toys play a very important role in the development of children by contributing to their mental, emotional and physical development [4]. Toys are materials that children use for play purposes, such as wood, rubber, soil, plastic, cloth, metal, etc. They are play tools made of materials [5].

Toys have changed over time not only in terms of their usage areas and appearance, but also in terms of the materials used in their construction. Various advances in human life have also been reflected in production methods, changes in production methods have affected all areas, and have rearranged the function and form relations of objects that we frequently encounter in daily life [6]. For this reason, it is possible to say that the materials used in toy making are affected by these changes.

As toymaking came to the fore in Germany in the 18th century, toys made of wood began to appear [7]. With the spread of moving toys in the same century, mechanical materials began to be used in toys, but the use of paper and cardboard in toy making continued [8]. While glass and handmade marbles were seen in Germany in the 19th century [9], the use of plastic in toys began to become widespread along with polystyrene in the 20th century [6]. It is noticeable that in the 21st century, chips began to be used in toys, as well as many other materials in toy making. Nowadays, the material mostly used in toy making is plastic. However, considering the damage caused by plastic to the environment, it seems that toys have largely turned to wood [9].

This study aims to comparatively evaluate traditional wooden toys and wooden toys produced by laser cutting in terms of their design features and use by children. Taking into account various parameters, the technical features of both toy groups such as production processes, costs, variety of details, durability, as well as their level of preference by children and their contribution to play experiences will be examined.

2. Use of Wooden Materials in Toy Making

The toy must have features suitable for the child in every respect. However, with the increasing interest in cheaper and easier to process raw materials, the use of plastic materials in toy production has surpassed other materials

* Corresponding author. *e-mail address: mehmetgunes@karatekin.edu.tr*

used in toy production. Being cheaper, providing ease of production due to its suitability for mold-supported manufacturing, allowing the use of advanced machinery suitable for mass production, being recyclable in some types, and being able to easily change its properties in the desired direction have made plastic the most commonly used material in toy making [10].

With the social, environmental and economic changes in recent years, people have become more aware of the harms of plastic toys, and families have turned to toys made of wooden materials in their toy preferences [4].

The fact that wood is a natural and renewable material makes it preferred in its production and purchasing. It is difficult to produce bacteria and therefore does not need to be disinfected. When used naturally, it does not contain any material harmful to health. Touching and playing with wood leads to a positive effect [11]. In addition to these, the reasons why wooden toys are preferred are listed below.

-It is environmentally friendly, made of natural wood material. It is a material that is harmless to the environment in its production, use and at the end of its useful life.

-There is no need for special facilities to destroy wooden products. It is possible to recycle wooden toys into nature. Wood is a material that can be used for many purposes.

-Wooden products have always seemed to people as a warm, cute and natural material with their different colors, textures and smells. It provides richness of imagination with its variety of patterns and harmony in its designs.

-It is possible to capture different formations in Figures and objects with color differences, as it is noticeable in gift ornaments, carving and market production.

-Wooden products, with their different odors, play a role in the development of the sense of smell, especially in developing children.

-It helps children develop their learning skills by improving their sense of touch with a variety of different weights and surfaces.

-It is possible to repair broken wooden toys. In addition to the white glue used in its repair, other glues are also used (D2-D3). Repairing a broken toy not only helps the communication between the child and his parents, but also helps his development.

-Wooden toys are products that are passed down from generation to generation and have continuity. Wooden play tools also enable integration between generations and cultures.

-It is completely recyclable. It is also possible to make wooden toys from carpenter's scraps, lumber and wood scraps.

-Wooden toys can be exhibited in showcases and living areas because they look beautiful and resemble a work of art.

-It is durable, does not deteriorate, can be glued when broken and you can change its color.

-Wooden toys can be used not only as toys and educational tools but also for therapy purposes.

-It is not necessary to use advanced production tools and systems to produce wooden toys. Handmade, chipped and carved items are especially valuable.

-Wooden toys without surface treatment can be purchased for children. Since the “acrylic paint” you will purchase is water-based, a product that the child can paint and contribute to can be obtained.

-It is always possible to change the shape of all kinds of wooden products using any tool and to obtain new products (hobby and model toys). It plays a role in the development of imagination [5].

3. Traditional Wooden Toys

Traditional wooden toys are generally handcrafted toys made of natural wood materials. They can generally be produced in small workshop environments. For their production, small hand tools as well as production tools such as circular saw machine, band saw machine, planer thickness machine, sanding machine are required. These types of toys are generally designed to develop children's creativity and imagination. Wooden toys are usually painted with colored paint or natural oils and attract attention with their simple designs. If wooden toys are categorized in detail, they can be defined as follows [12]:

Wooden Blocks Category: Shape-Size Different Blocks, Shape-Size Same Blocks, Lego (Interlocking Blocks), Tegu (Magnet Blocks). Bulyap Category: Geometric Shaped Bulyap, Traced/Notched Bulyap, Noah's Ark. Instrument Category: Rattle, Maracas, Singing, Castanets, Guiro, Xylophone, Drum, Tambourine, Whistle. Nail Drilling Category: Tapping Sticks, Dropping Spheres into the Channel, Stamping with a Seal. Çöğüncek Category: Balance Board, Scale-Weighing Scale Examples, Seesaw (Lever). Stringing and Threading Category: Stringing Beads on a String, Threading Objects through Wire, Twisted and Spiral Threading, Stringing with Notched Pieces, Threading a String on a Perforated Wooden Table. Organized Category: Pull and Drop Vehicles, Wind-Up Vehicles, Pedal Tricycle, Sound Puzzles, Sound Puzzles. House Category: Two-Storey (Roof and Open Sides) House, Floorless-Roofless (Top View) House, Three-Storey (Roof and Open Sides) House. Pinwheel Category: String Pinwheel, Handle Pinwheel, Spinning Top, Yoyo. Figures Category: Baby Figures, Soldier Figures, Animal Figures, Human Figures, Professional Figures. Letter Teaching Category: Letter Cubes, Slotted Letter Tray. Nesting Category: Matryoshka, Colored Boxes, Wooden Cups. Slide Category: Multi-layer Curved Channel Marble Roller, Layered Ramp Car Slide, Rotational Ball Rolling Tower, Layered Conical Sound Tree. Puppets Category: Pinocchio, Animal Figure Puppet, Human Figure Puppet, Robotic Puppet [13].

Wooden blocks are one of the most used educational toys in preschool and infancy. Figure 1 shows blocks made of one piece of solid wood. Figure 2 and Figure 3 show traditional type wheeled wooden toys. These toys are generally produced by adding wheels to a single piece. Figure 4 shows the wooden miniature children's house, which has more parts than other toys. Since its assembly and durability are lower than other toys, it may not be preferred by parents.

Figure 1. Solid wooden cubes.

Figure 2. Solid toy car.

Figure 3. Wooden toy rabbit

Figure 4. Wooden house with solid pieces

It is known that wooden toys produced from a single body have a longer lifespan than toys with multiple and more complex components.

4. Laser Cut Wooden Toys

In recent years, laser technology has been at the forefront of material processing. It is conceivable that it will probably replace traditional techniques such as sawing in the near future [14]. With computer numerically controlled (CNC) machine technology, manpower in production has started to decrease and be replaced by information processing. With the spread of laser technology, non-contact, precise and chip-free production methods have become widespread.

Laser technology is currently used in many fields such as automotive, shipping, aviation, military equipment, energy industry and medicine [15]. In addition, it has also found a place in applications such as semiconductor production, electronics and communications [16]. Hobby woodworking has also been involved in areas such as advertising and entertainment shows. With its use in measuring devices in industry, it has become a technology that has no alternative in most cases. Its use has gained importance especially in applications requiring high precision. As can be seen, laser technology has found its place in daily life for many different purposes, from small to large. In recent years, with the development of technology, there has been a trend towards the use of laser in industry [17].

Figure 5. Laser cut wooden block

Figure 6. Laser cut toy car

Figure 7. Laser cut layered wooden rabbit

Figure 8. Plywood laser cut house

Toys produced by laser cutting are produced in a shorter time than traditional toys. As seen in Figure 5, Figure 6, Figure 7 and Figure 8, the high number of parts and low part thickness create a disadvantage in terms of strength.

Result and Discussion

Some of the main reasons why solid wooden toys have been used for centuries are that they are natural, renewable, can be easily applied on the surface, are healthy and can be easily repaired. With technological developments, the processing of wood has become easier and the production technique of most wooden toys has changed. It is understood that toy design and production with laser cutting and 3D programs, in addition to the traditional production technique, has many advantages but also disadvantages. The production and design of laser cut wooden toys is faster and simpler, saving time. However, a computer and a separate cutting device are required for design and production. In addition, its disadvantages are that it has a higher number of parts and is less durable than solid wood. Poisonous gases released during toy production by laser cutting must be removed from the workshop environment. Since toys produced with traditional hand tools and laser cutting have different advantages and disadvantages compared to each other, the selection should be made taking into account production costs and health procedures.

References

[1] Vatandaş, S. (2020). Oyun ve oyuncak: teknolojik ve toplumsal dönüşüm sürecinde oyun ve oyuncağin anlamsal ve işlevsel değişimi. *Süleyman Demirel Üniversitesi Vizyoner Dergisi, 11(28)*, 913-930.

[2] Bekir, O. (1992). Tarih boyunca oyunlar ve oyuncaklar. *Ankara University Journal of Faculty of Educational Sciences (JFES), 25(2)*, 365-386.

[3] Kırman, A., *Çocuk kitaplarında oyun ve oyuncak kavramının incelenmesi*, PhD Thesis, Hacettepe Üniversitesi, Sağlık Bilimleri Enstitüsü, 2019, 190, Ankara.

[4] Dalğar, T., & Kaya, A. İ. (2017). Oyuncak tercihinde ahşap malzeme özelliklerinin incelenmesi. *İleri Teknoloji Bilimleri Dergisi, 6(3)*, 9-16.

[5] Tuncer, Y. *Ahşap oyuncaklar*, Lisans tezi, Dumlupınar Üniversitesi, Simav Teknik Eğitim Fakültesi Mobilya ve Dekorasyon Eğitimi Bölümü, 2012, Kütahya.

[6] Ak, D. *Oyun ve oyuncak kavramlarının tarihsel ve kültürel değişimine endüstriyel tasarım açısından bir bakış*, Yüksek Lisans Tezi, Anadolu Üniversitesi, Endüstriyel Sanatlar Anabilim Dalı, 2006, 84.

[7] Erdoğdu, N. Ö., & Renda, F. Ş. (2021). Rönesans'tan modern döneme batı resim sanatında oyuncağın görünürlüğü. *Ulakbilge Sosyal Bilimler Dergisi, 58(9)*, 406-423.

[8] Gorman, A. B. (1985). Toys are us. *Time Machines: Artifacts and Culture, Volume VI, 2-18.*

[9] Aydın, H. S. *Oyuncak tasariminda sürdürülebilirlik esaslarinin uygulanmasi: ahşap oyuncak örneği,* Yüksek Lisans Tezi, Anadolu Üniversitesi, Endüstriyel Sanatlar Anabilim Dalı, 2012, 104.
[10] Elibol, G. C., Kılıç, Y., & Burdurlu, E. (2006). Okul öncesi çocuk oyuncaklarında malzeme kullanımı ve 4-6 yaş çocuklarının renk tercihleri. *Sosyal Politika Çalışmaları Dergisi, 9(9),* 35-44.
[11] İlker, U., (2018). Genç yetişkinlerin bakışıyla okul öncesi çocuklar için ahşap oyuncaklar. *Mesleki Bilimler Dergisi (MBD),* 7(2), 99-122.
[12] İlker, U. (2020). Çocukluk deneyimi yaşamiş genç yetişkinlerin okul öncesi dönem bağlaminda yeğledikleri ahşap oyuncak çeşitleri. *Mesleki Bilimler Dergisi (MBD), 9(1):* 1-28.
[13] İlker, U. (2022). Ahşap oyuncak kategorizasyonu. *Avrasya Sosyal ve Ekonomi Araştırmaları Dergisi, 9(4),* 97-126.
[14] Gaff, M., Rezaei, F., Sikora, A., Hýsek, Š., Sedlecký, M., Ditommaso, G., Corleto, R., Kamboj, G., Sethy, A., & Vališ, M. (2020). Interactions of monitored factors upon tensile glue shear strength on laser cut wood. *Composite Structures, 234,* 1-9.
[15] Aniszewska, M., Maciak, A., Zychowicz, W., Zowczak, W., Mühlke, T., Christoph, B., Lamrini, S., & Sujecki, S. (2020). Infrared laser application to wood cutting. *Materials, 13(22),* 5222.
[16] Knowles, M., Rutterford, G., Karnakis, D., & Ferguson, A. (2007). Micro-machining of metals, ceramics and polymers using nanosecond lasers. *The International Journal of Advanced Manufacturing Technology, 33,* 95-102.
[17] Yurdakul, M., Tükel, T., İç, Y. T., İbrahim, Ü., Balcı, A., & Güneş, S. (2022). Bir imalat firmasında en iyi ürün kalitesi için lazer ile kesim parametrelerinin en iyilenmesi. *Journal of Turkish Operations Management, 6(1),* 977-996.

Design and implementation of fuzzy logic-controlled smart solar tracking system

Zaid AL-IBRAHIME[1,*], Fatih KORKMAZ[2]

[1] *Electrical and Electronics Engineering, University of Çankiri, Çankiri, Turkiye*

[2] *Electrical and Electronics Engineering, University of Çankiri, Çankiri, Turkiye*

Abstract

This paper proposes to build a multi-axis, closed-loop smart solar tracking system capable of moving 360° horizontally and 180° vertically with a starting angle of 90° so that the system can know the start angle without the need to know the azimuth angle. In addition to the system being able to protect the photovoltaic cells from damage, it continuously changes the direction of the solar panel by 180° if the solar temperature exceeds 45°C and then returns to track after the temperature drops below that. The fuzzy logic controller will be responsible for controlling and directing all elements of the system and determining the time to move the panels so that they face direct sunlight. and collecting data using a recording unit (SD card) and storing it on a memory card, which may be accessed at any time, to verify the system's efficiency and identify weak points.
The importance of the research is using 8 sensors (LDR) programmed according to a special mathematical algorithm instead of 4. This approach allows the system to effectively handle partial shading and maintain accurate tracking even if one of the sensors malfunctions. As a result, this system exhibits a high level of tracking accuracy. The system employs two motors: a DC motor with a gearbox for horizontal rotation and a servo motor for vertical rotation. The results of this study indicate that employing a fuzzy logic controller yielded superior precision in comparison to alternative software. Additionally, the utilization of 8 LDR sensors, two motors, and a temperature sensor resulted in enhanced practical accuracy for the system, enabling it to achieve maximum photovoltaic energy output over the longest possible period of time.

Keywords: *Solar tracking system, LDR sensors, DC Motor, SERVO Motor, Fuzzy logic*

1. Introduction

In recent decades, the focus has been on low-cost renewable solar energy technologies to reduce fossil fuel use and environmental damage. With diminishing resources, there's a need for environmentally friendly, cost-effective, and infinite energy sources. Solar energy is the best-developed renewable technology due to its accessibility, non-polluting, clean, and safe nature [1]. Researchers have developed closed-loop solar tracking systems to overcome the limitations of solar panels in wet or cloudy weather, utilizing various tracking technologies for improved efficiency [2]. A solar tracking system (STS) adjusts a solar panel's position or tilt to face the sun perpendicularly, enhancing its efficiency compared to a fixed system [3]. Previous studies have explored methods for optimizing photovoltaic energy generation. This study aims to identify and address the limitations of these previous studies in order to achieve higher accuracy. By doing so, we can increase the amount of energy obtained while also prolonging the lifespan of the solar cells. The most important differences that this study will focus on are:

Previous studies neglected the investigation of strategies to address the issue of partial shadowing or the failure of one of the Light Dependent Resistor (LDR) sensors. This study incorporated 8 Dependent Resistor (LDR) sensors that were operated by a specialized mathematical system utilizing fuzzy logic. The intelligent system in this study successfully navigated through all barriers and achieved direct perpendicularity with great accuracy. For example, the research conducted by Imron et al. utilized the solar panel's location, which is controlled by four Light Dependent Resistor (LDR) sensors, which adjust the strength of solar radiation. The control technique employed is fuzzy logic, which yields a settling time of 10 seconds and a steady-state error of 0.080%. This system enhances power output by more than 30% [4].

Previous studies have emphasized the pressing requirement to determine the azimuth angle, even when employing multi-axis tracking. To solve this issue in this study, the solar panel's initial angle was adjusted to 90 degrees relative to the horizon. Subsequently, the sensors detect the maximum light radiation without requiring knowledge of the azimuth angle. For example, the research conducted by Aprillia et al. discusses the optimization of the azimuth direction and tilt angle of photovoltaic panels at Telkom University in Bandung, West Java. The goal is to enhance the absorption of solar radiation by determining the maximum tilt angle using calculations [5].

* *Corresponding author. e-mail address: fihkorkmaz@yahoo.com*

Previous studies neglected the impact of elevated temperatures; this study addressed this issue by implementing a strategy of reorienting the panel by 180 degrees when the temperature exceeded 45 degrees Celsius. This approach was adopted due to the fact that high temperatures cause a 3% decrease in the efficiency of photovoltaic cells for every 10 degrees Celsius above their optimal operating conditions. For example, the research conducted by Huang et al. proposed a two-axis sun-tracking solar energy system using fuzzy logic as an intelligent quality policy. The system uses dual-axis solar panels for mechanical movement, with fuzzy logic controlling timing and database theory. This system is more accurate and simpler than traditional sensor systems and can reduce energy loss even in poor weather conditions, but without focusing on the impact of the high temperatures [6].

Significantly, the key distinction between this study and most comparable studies lies in the fact that, in the former, the control devices, sensors, and motors were simulated through computer programs, and tests were conducted under ideal conditions. Conversely, in this study, the testing was carried out in a practical and realistic manner, accounting for variations in the internal resistance values of the sensors. Consequently, this discrepancy in sensor readings resulted in an elevated error rate. Furthermore, elevated temperatures have an impact on the internal resistance value of the sensor. A mathematical approach has been implemented to compare the sensors and resolve this issue. For example, the research conducted by Asyadi and Muliadi used Matlab/Simulink R2018b software for simulation testing, focusing on selecting solar modules, modeling boost converters, designing FLC methods, and comparing FLC results with P&O for maximum power point [7]. Nevertheless, the project for this study has employed a sophisticated approach to guarantee that the system is fully prepared to maximize energy output, irrespective of the associated expenses, operational range, and reliability of the sensors.

2. Materials and Methods

The reagents, 1H-imidazole This research designed an external structure that supports the concept of the solar tracking system and is characterized by freedom of movement in all needed axes and directions. Moving the solar panel in both directions requires the use of two motors, provided that these two motors are controlled by smart devices (Arduino) that are coded in a smart language by employing fuzzy logic to boost the accuracy of the instructions controlling the system. In order to determine the necessary angle and direction, 8 (LDR) sensors were evenly positioned around the solar panel. These 8 LDRs were distributed as follows:

- 4 LDRs sensors around the corners of the solar panel
- 4 LDRs sensors in the middle of the outer ribs of the panel and between the first four sensors.

Furthermore, the utilization of specific plastic pieces to manipulate the angle of light that enters the (LDR) serves to enhance the sensitivity of the device in the intended direction, as shown in Figure 1. To enhance the precision of identifying the necessary movement direction of the solar panel, it is vital to employ specific mathematical equations, as shown below:

Horizontal LDR ERROR ((A1-A0) + (A3-A2)) / 2

Vertical LDR ERROR ((A2-A0) + (A3-A1)) / 2

Center-Horizontal LDR Error (A7)

Center: Vertical LDR ERROR (A5) (A4)

The term "error" is used to denote the value of the difference between the sensor and the other sensor in a certain direction.

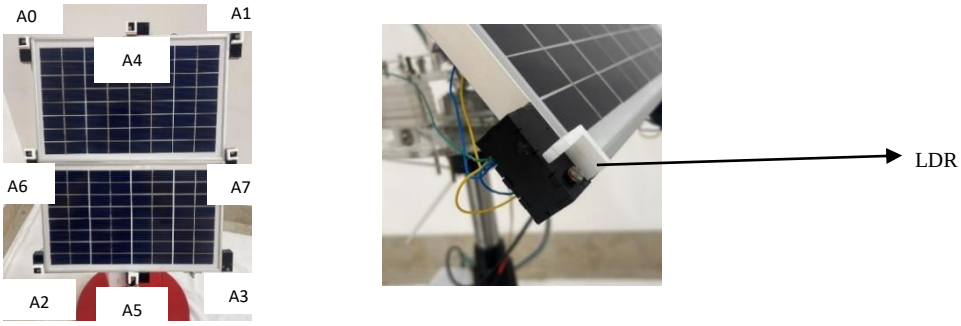

Figure 1. Distribution of the LDR with the specific plastic pieces of the solar tracking system used in the study (Researcher)

The distribution of 8 LDR and utilization of the mathematical algorithm above can be attributed to several fundamental reasons, with the most significant ones being:

- First: the variation in values arises from differences in the manufacturing and production processes of LDR sensors by the company. This discrepancy is primarily caused by variations in the internal resistance, resulting in different sensing and reading values for sensors under the same conditions. Consequently, this discrepancy leads to inaccuracies in the instructions sent to the horizontal and vertical motors through an Arduino device, as it becomes challenging to select the optimal angle perpendicular to the source of solar radiation as shown in Figure 2.

Figure 2. The difference in the value of the internal resistance for each LDR sensor, and for the same LDR sensor values used in this study (Researcher)

- Second: in the event of partial shading, the system can effectively address this issue by increasing the number of LDR sensors using the technique outlined before.
- Third: in the event of damage or malfunction in one of the LDR sensors, the system will remain unaffected due to the presence of other LDR sensors and an algorithm that can establish the necessary angle using the functioning sensors.
- Fourth: oscillation and delayed reaction in practice can be mitigated by implementing the aforementioned mathematical technique, which effectively minimizes the fluctuations caused by many and varying readings.

In addition, a temperature sensor has been installed in the solar system to prevent the photovoltaic cells from overheating and potentially causing harm. Furthermore, a rechargeable battery has been included to power the entire system. The sun-tracking device utilized in this study was devised and executed via a 3D printer. The solar tracking system utilized in this investigation comprises a solar panel, light-dependent resistor (LDR), liquid crystal display (LDC), temperature sensor, current sensor, servo motor, DC motor with gearbox, Arduino microcontroller interfaced with a micro-SD card, Arduino Mega 2560 Rev3, L298N DC Motor Driver Module interfaced with Arduino, DC-DC converter, battery, and printed circuit board (PCB). Figure 3 show the elements of the system from the front and back perspectives. Furthermore, Figure 4 illustrates the constituent parts of the system's controller box.

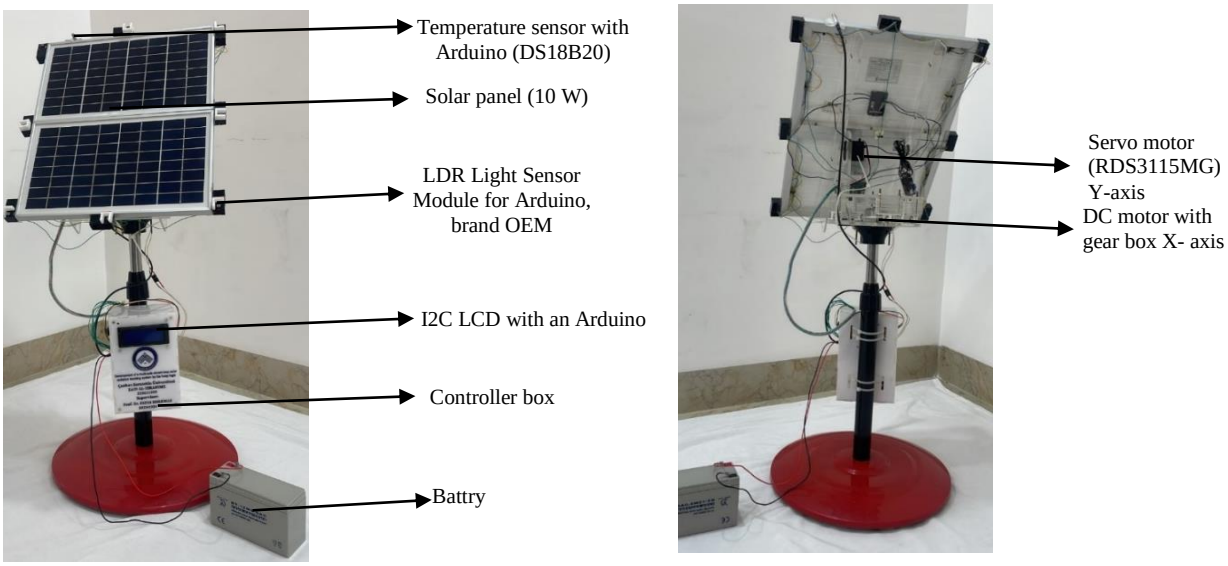

Figure 3. The front and back elevation of the solar tracking system used in the study (Researcher)

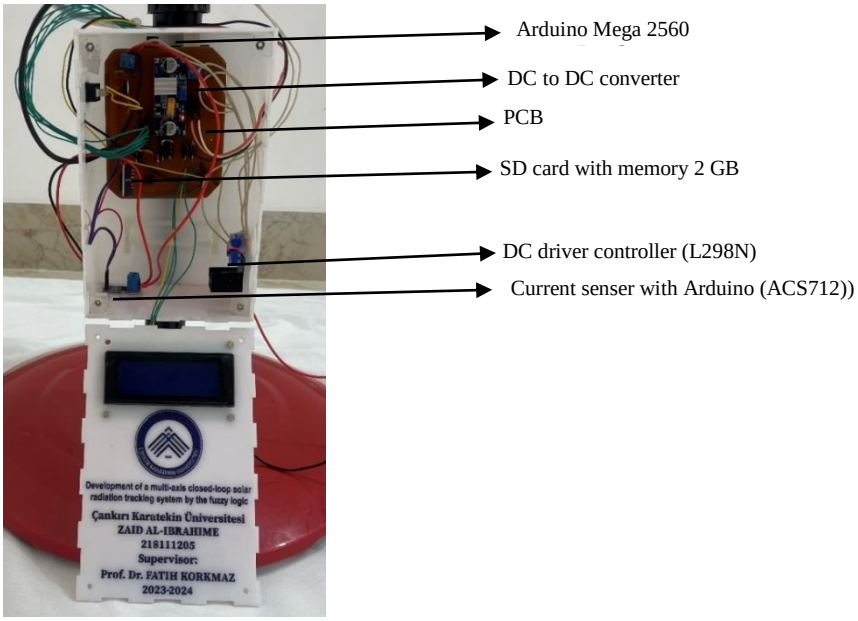

Figure 4. The controller box components of the solar tracking system used in the study (Researcher)

3. Results and Discussion

The results of the study that was conducted in Iraq, Mosul (36.405255, 43.150255), on November 5, 2023, from 8:30 a.m. to 18:00 p.m. through reading the system's LDR sensors.

Table 1. Solar tracking system data utilized in this study

Time	Temperature	A0	A1	A2	A3	A4	A5	A6	A7	V-E	H-E	C-V-E	C-H-E	mAin	V- in
8:30	23.19	959	966	955	948	972	958	954	919	-11	0	-14	-35	97	13.38
9:00	27.56	960	968	958	951	975	961	958	934	-9	0	-14	-24	97	13.29
9:30	28.19	962	969	959	953	976	962	959	945	-9	0	-14	-14	97	13.25
10:00	26.88	963	970	960	955	978	963	960	953	-9	1	-15	-7	97	13.2
10:30	27.94	963	970	960	955	978	963	959	957	-9	1	-15	-2	97	13.11
11:00	28.75	961	965	959	954	978	958	951	958	-6	0	-20	7	97	13.07
11:30	31.56	942	946	958	955	975	952	920	958	12	0	-23	38	97	13.07
12:00	31.06	943	948	958	954	976	953	922	958	10	0	-23	36	97	12.97
12:30	30.69	923	934	956	954	973	947	911	957	26	4	-26	46	97	12.93
13:00	30.94	925	934	956	954	973	948	908	957	25	3	-25	49	97	12.7
13:30	30.94	926	934	957	954	974	949	906	957	25	2	-25	51	97	12.88
14:00	32	931	936	957	954	974	949	907	952	22	1	-25	45	97	12.84
14:30	31.19	938	939	956	952	973	949	915	944	15	-1	-24	29	97	12.84
15:00	29.94	944	945	954	950	972	950	925	929	7	-1	-22	4	97	12.79
15:30	29	925	926	949	944	966	941	895	908	21	-2	-25	13	97	12.84
16:00	26.75	892	892	926	928	948	920	869	865	35	1	-28	-4	97	12.57
16:30	23.5	769	781	781	777	783	785	727	723	4	4	2	-4	97	12.79
17:00	22.13	489	544	557	525	496	551	434	425	24	11	55	-9	97	11.93
17:30	21.5	35	57	61	47	35	48	35	33	8	4	13	-2	97	11.61
18:00	20.31	27	36	36	29	26	30	27	26	1	1	4	-1	97	11.2

Table 1 shows the system data obtained from the SD card. It includes the recorded values of the eight LDR sensors and the temperatures experienced by the system during the practical test period. Additionally, it presents the vertical error (V-E), horizontal error (H-E), center vertical error (C-V-E), and center horizontal error (C-H-E), which indicate the panel's movement directions relative to solar radiation. These directions were determined using specialized mathematical equations based on fuzzy logic to enhance tracking precision.

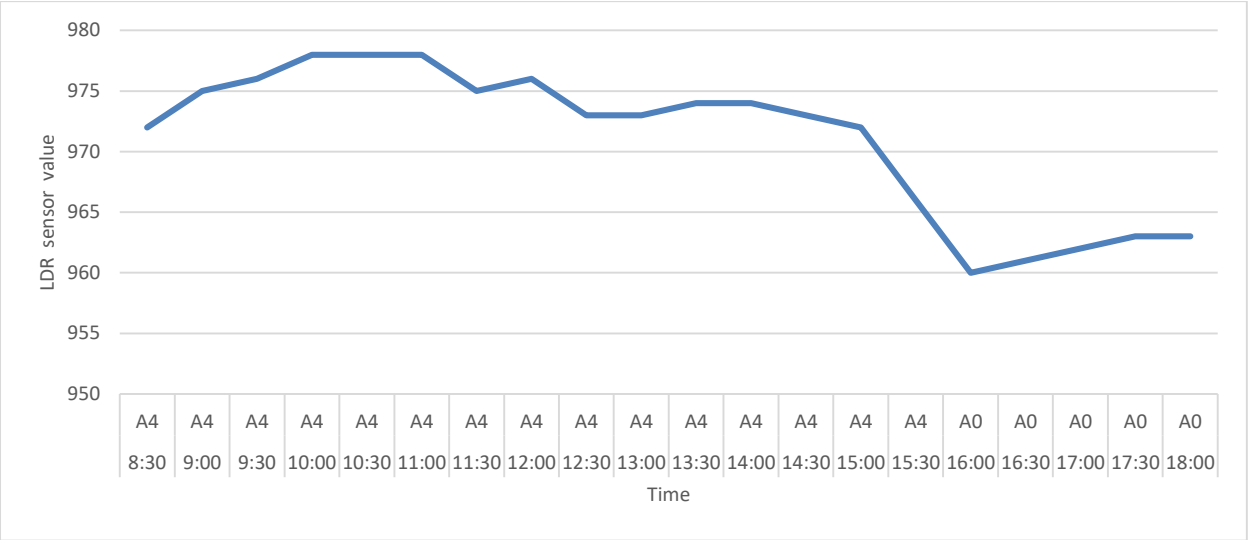

Figure 5. The highest reading for LDR sensor value in relation to time (Researcher)

Figure 5 shows the readings from the eight LDR sensors in the smart system during the practical test, taken at various time intervals. The LDR sensors were programmed via fuzzy logic, with the value of 0 representing total darkness and the value of 1024 representing the highest level of light exposure. The system successfully monitored a collective. The highest recorded value was observed at sensor A4, reaching a peak of 978 during the time interval of 10:00 to 11:00. The lowest sensitivity value, on the other hand, was found between sensors A4 and A7, occurring at 18:00. The following conclusions can be elucidated by conducting tests on the smart system:

1- The greatest reading LDR sensor value was obtained during the system's operating period, reaching (978 unit) out of (1024 unit), which is the ideal value for the intensity of light radiation.
2- The system was able to track the source of solar radiation without the need to know the azimuth angle.
3- Generating the greatest electrical energy for the longest possible period of time from the beginning of the system's operation at 8:30 a.m. until 17:00 p.m., then the production capacity decreased to its lowest at 18:00 p.m. as shown in Figure 6.

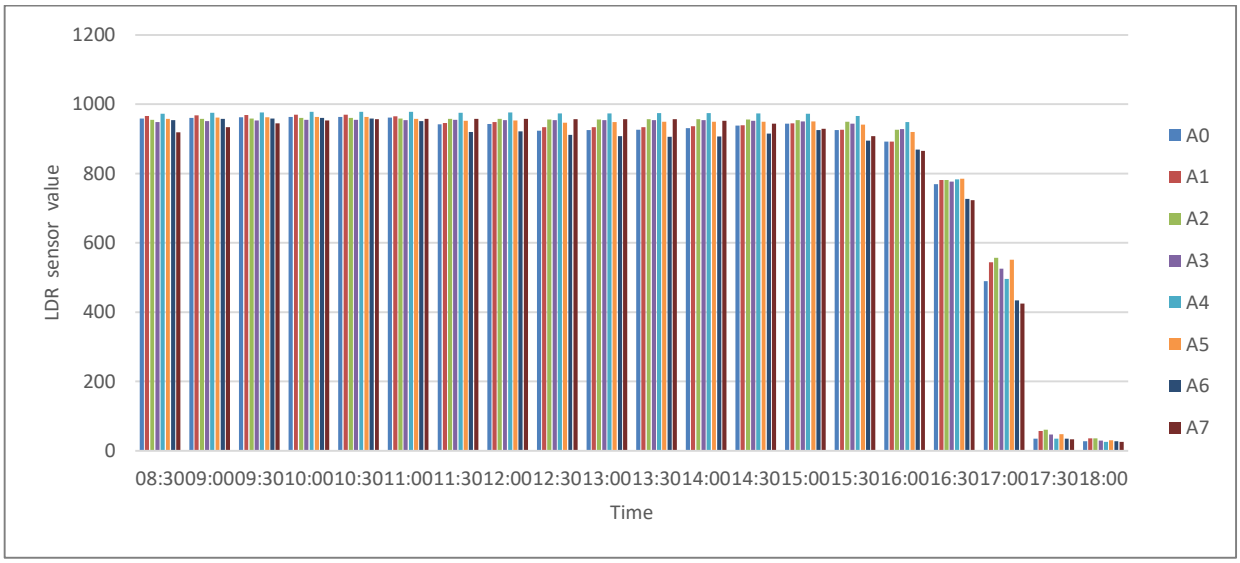

Figure 6. Reading of 8 LDR sensor values in relation to time (Researcher)

4- If the V-E value is positive, it means that the solar panel will move toward the north, and if it is negative, it will move toward the south.

5- If the H-E value is positive, it means that the solar panel will move toward the east, and if it is negative, it will move toward the west.
6- If the C-V-E value is positive, it means that the solar radiation value directed toward the bottom of the panel is higher than the solar radiation value directed towards the top.
7- If the C-H-E value is positive, it means that the solar radiation value directed toward the west of the panel is higher than the solar radiation value directed toward its east.

4. Conclusion

After employing the intelligent solar tracking system on the ground, we can assert that it surpasses conventional tracking systems in terms of its superior ability to locate the sun's position and its heightened precision. This result was detected by analyzing the data collected during the practical experiment. The alignment of the system with the radiation source was achieved through a sophisticated mathematical algorithm controlled by fuzzy logic. This algorithm considered various factors, such as partial shadowing or sensor damage, to ensure accurate alignment. Furthermore, the study suggests including 8 LDR sensors, using a fuzzy logic system, constructing an exterior structure capable of rotating 360° horizontally and 180° vertically, and utilizing two motors (specifically, a DC motor with a gearbox and a servo motor). Based on the results of this study, the proposed system offers numerous benefits in an intelligent framework that allows tracking to commence without requiring knowledge of the azimuth angle. Furthermore, it provides accurate results for the maximum point of electrical power generation over an extended period of time. In addition, the system can be used to effectively manage a substantial quantity of solar panels in order to maximize the generation of photovoltaic energy.

References

[1] Elzein, I. A. (2014). A study of Maximum Power Point Tracking Algorithm for Photovoltaic Systems Using a Fuzzy Logic Controller.*WIT Transaction on Engineering Sciences*, Vol.96, WIT Press.P.409-419.
[2] Zakariah, A., Jamian, J. J., & Yunus, M. A. M. (2015, December). Dual-axis solar tracking system based on fuzzy logic control and Light Dependent Resistors as feedback path elements. In 2015 *IEEE* Student Conference on Research and Development (SCOReD) (pp. 139-144). IEEE.
[3] Kumar, D. N., & John, M. S. (2020, August). A Review on Solar Tracking Methods. In *IOP Conference Series: Materials Science and Engineering* (Vol. 912, No. 4, p. 042045). IOP Publishing.
[4] Imron, C., Abadi, I., Brillianti, N., Asy'ari, M. K., Nor, Y. A., & Uyun, A. S. (2020). Fuzzy Logic Controller Application for an Active Two-Axis Solar Tracking System. *In E3S Web of Conferences* (Vol. 190, p. 00004). EDP Sciences.
[5] Aprilia, B. S., Romdlony, M. Z., Raharjo, J., & Sidik, Y. G. (2021). Fuzzy based sensorless tracking controller on the dual-axis PV panel for optimizing the power production. *JURNAL INFOTEL*, 13(4), 230-238.
[6] Huang, C. H., Pan, H. Y., & Lin, K. C. (2016). Development of intelligent fuzzy controller for a two-axis solar tracking system. *Applied Sciences*, 6(5), 130.
[7] Asyadi, T. M., & Muliadi, M. (2023, June). The maximum power point tracking (MPPT) on changes in radiation and temperature of solar modules based on fuzzy logic controller (FLC). *In AIP Conference Proceedings* (Vol. 2691, No. 1). AIP Publishing.

Some physical properties of B2 type AgY intermetallic compound from Ab-initio Calculations

***Yasemin Öztekin ÇİFTCİ**[*], İlknur Kars DURUKAN*[1]

[1] *Science Faculty, Physics Department, Gazi University, Ankara, Turkey*

[2]*Science Faculty, Physics Department, Gazi University, Ankara, Turkey*

Abstract

Intermetallics have superior physical important properties than ordinary metals. Due to interesting properties such as high tensile strength, high melting point and stifness, good oxidation resistance , low mass density, these intermetallic compounds are suitable for many applications in engineering. and industry. Among the B2-type intermetallic compounds, there is a theoretical study on the defect properties of AgY . Here, we have studied structural, mechanics, electronic, vibrational and thermodynamic properties of AgY compound using first-principles methods based on density-functional theory. It can be concluded that AgY in B2 structure are metallic compounds from electronic band structure. AgY is also stable mechanically and dynamically.

Keywords: *: DFT, B2 structure, electronic properties, elastic, properties, vibrational properties*

1. Introduction

The discovery of high ductility and fracture toughness at room temperature in certain B2 type- compounds, as described by Gschneidner et al. in 2003, is indeed noteworthy. The compounds mentioned exhibit promising mechanical properties without the need for additional elements or complex processing techniques[1-3]. The challenge of brittleness in intermetallic compounds has historically limited their practical applications. The improvement in ductility for these specific compounds is a significant advancement. The fact that these properties can be achieved by simply arc-melting equal amounts of pure elements in normal-humidity air without the addition of third elements adds to the practicality of these materials. Typically, methods to enhance ductility in intermetallic compounds involve techniques such as testing at high temperatures, zero-humidity atmospheres, adding dopants, introducing non-stoichiometry, or inducing metastable disorder. However, the mentioned compounds seem to exhibit desirable properties at room temperature without the need for such complex procedures. Understanding the ductility mechanism of these alloys is crucial for furthering their applications and optimizing their properties. While the elastic properties of YAg have been investigated by Russel and Gschneidner[4], it is highlighted that the ductility mechanism of these alloys has been reported very little. Further research and investigation into the underlying mechanisms responsible for the observed ductility in these intermetallic compounds can provide valuable insights for the development of new materials with improved mechanical characteristics. In summary, the discovery of intermetallic compounds with high ductility and fracture toughness at 300K opens up new possibilities for their use in various applications. The simplicity of the synthesis process and the absence of additional elements make these compounds particularly interesting for further exploration and development in the field of materials science[5-7].

The intermetallic compounds YM (where M represents Cu, Zn, and Ag) adopt a cubic CsCl-type structure characterized by a space group symmetry of Pm3m (No. 221). Extensive experimental and theoretical analyses have been conducted to explore their electronic, elastic, and mechanical properties, as documented in several studies [8–13]. There is no study onvibrational properties and thermodynamic properties of DyAg in B2 structure. We have aimed to investigate structural, mechanical, electronic, vibrational and thermodynamic properties of AgY intermatallic compound in B2 structure using ab-initio methods.

2. Materials and Methods

We have used the density functional theory (DFT) method to investigate of the B2-structured YAg compound's physical. The calculations were performed with the VASP software [14-17], employing the Generalized Gradient Approximation (GGA) for the exchange-correlation function [18]. Y and Ag exhibit valence-electron

* Corresponding author. *e-mail address:yasemin@gazi.edu.tr.*

configurations of $4s^2 4p^6 4d^2 5s^1$ and $4d^{10} 5s^1$ respectively. To optimize lattice parameters and atomic positions, a 17 × 17 x17 Monkhorst and Pack k-points grid [19] was applied for integration into the irreducible Brillouin region. The kinetic energy cutoff for the plane-wave basis set was set at 850 eV. Elastic constants were investigated using the stress-strain method [20,21]. For the analysis of vibrational properties, a supercells approach was employed, and phonon dispersion curves were calculated using the PHONOPY code [22]. This methodology provides a comprehensive exploration of both the physical and vibrational characteristics of AgY.

3. Results and Discussion

3.1. Structural and Mechanical Properties

AgY adopts the B2 phase CsCl structure within the (2 2 1) space group. The atomic positions are designated as Ag(0, 0, 0) and Y(0.5, 0.5, 0.5) as illustrated in Fig. 1(a). To optimize the lattice constants of AgY, comprehensive structural relaxations were conducted. The resulting total energies-volume graphs, presented in Fig. 1(b), were fitted to the Murnaghan state equation [23] for determining the bulk modulus and its first derivative. The obtained data, detailed in Table 1, were compared with findings from literature. Our computed lattice parameter is comparable with the values reported in Ref. [24], attributed to the utilization of the GGA functional. Throughout subsequent calculations, this determined lattice parameter was consistently applied. The determined lower bulk modulus for YAg, at 66.08 GPa, signifies a slightly higher compressibility compared to values in [24]. The bulk modulus, indicative of resistance to volume change under mechanical effects, is accompanied by a first derivative of 4.32, which is lower than the corresponding result in Ref. [24].

Table 1. Structural parameters for AgY in B2 structure

	a(A)	B(GPa)	B’	Etot (eV)/atom
This study	3.653	66.08	4.32	-4.985
Theory (YAg)[24]	3.641	68.5	5.0	

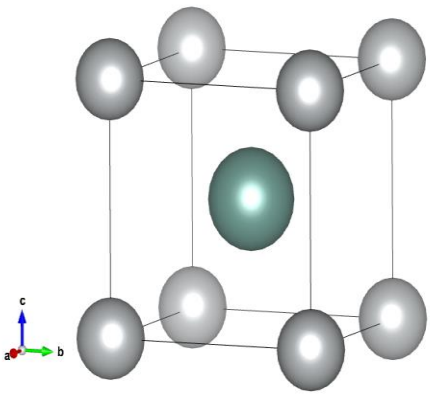

Figure 1. Unitcell of AgY

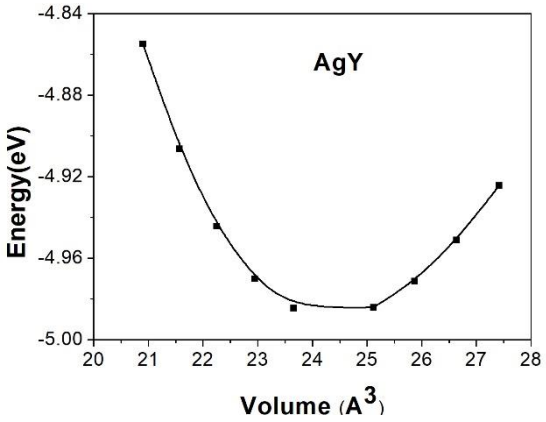

Figure 2. Energy- volume curves for AgY

Understanding elastic properties is crucial for comprehending a material's physical response, particularly in device applications. Elastic properties not only influence the material's effectiveness but also offer insights into its thermodynamic behavior. In the cubic system, three elastic constants play a pivotal role in characterizing the material's response to stress. C_{11} indicates the material's rigidity, C_{12} determines transverse expansion, and C_{44} is associated with shear deformation. These constants collectively contribute to the material's stability. The stability conditions of the cubic system encapsulated in the Born-Huang criteria [25], hinge on satisfying four essential criteria. These criteria provide a comprehensive framework for assessing the stability of the material and are integral to understanding its overall performance and reliability. Table 2 presents the our obtained findings of

calculated elastic constants and mechanical properties, with C_{11}, C_{12}, and C_{44} satisfying the stability criteria for AgY.

Table 2. Obtained elastic constants (C_{11}, C_{12}, C_{44} in GPa unit), Young's modulus (E in GPa), Anisotropy factor (A), Poisson ratio (v) and Hardness (Hv in GPa) for AgY

	C_{11}	C_{12}	C_{44}	E	B/G	A	v	Hv
This study	96.5	50.8	35.2	77.0	2.237	1.540	0.3054	3.2
Theory [24] YAg	99.30	54.3	38.5	81.0	2.209	1.71	0.305	-

Young's modulus (E, GPa) gauges the stress- strain ratio, primarily reflecting the chemical bonds between atoms in the material and providing information about the material's hardness. Notably, the AgY compound exhibits a lower Young's modulus, signifying its not hardness. Determination of ductile / brittle property involves factors like the B/G ratio showing the Paugh ratio, AgY is categorized as ductile based on the Paugh ratio. The Poisson ratio (v), which characterizes bonding forces in solids, serves as a key indicator. When v ranges from 0.25 to 0.50, it signifies the center of interatomic force, while a v of 0.5 indicates nearly incompressible material. Since limit values of Poisson's ratio are 0.10 for covalent bonds, 0.25 for ionic bonds and 0.33 for metallic bonds [26], AgY has ionic bonding.The Hv parameter defines stiffness against deformation, and in the B2, hardness increases with C_{44}. AgY, with a parameter value of 3.2 GPa, exhibits a soft structure. Values above 10 indicate hardness, and those exceeding 40 imply super-hardness. Zener anisotropy A, derived from elastic constants, indicates isotropy at a value of 1 and anisotropy at smaller or larger values. AgY displays an anisotropic nature.

3.2 Electronic Properties

Electronic energy band structure along the high symmetry direction, accompanied by the total density of states, provides insights into the electronic properties of AgY. Setting the Fermi level at 0 eV reveals the metallic nature of AgY, where the valence and conduction bands overlap, signifying conductivity contributed by electrons near the Fermi level as seen in Figure 3. In Fig. 4, the partial density of states (PDOS) for AgY is presented, showcasing distinct contributions from the Fermi level, valence band, and conductivity band. Predominantly, the Y-d states significantly influence the Fermi level, while the valence band is dominated by Ag-d states. The metallic character of AgY, attributed to conductivity, is primarily associated with Y-d and Y-p states in the conductivity band. The density of states (DOS) at the Fermi level registers at 1.58, a lower value of which typically indicates a more stable structure.

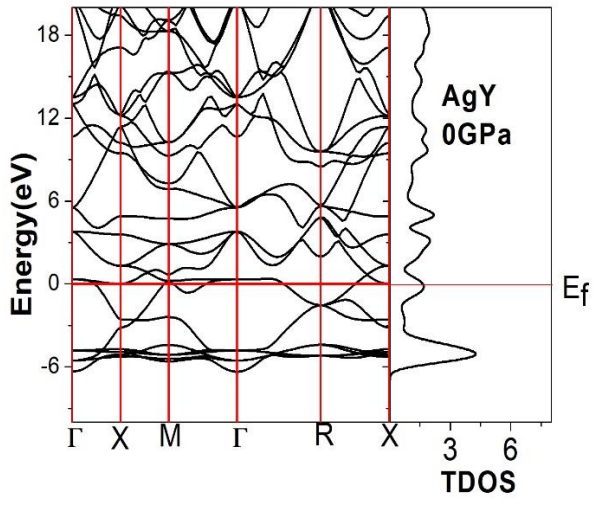

Figure 3. Electronic band structure for AgY

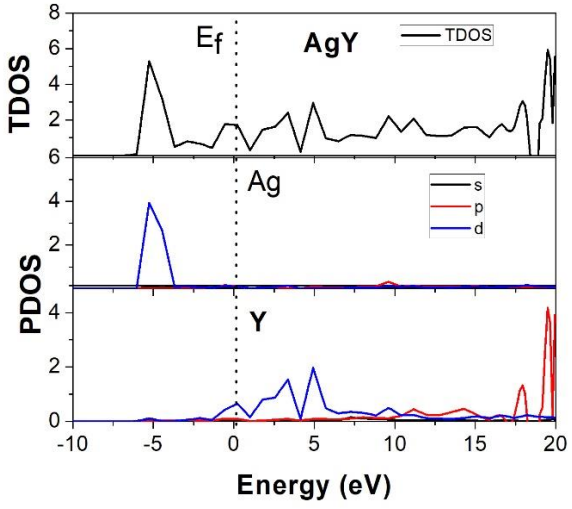

Figure 4. Total and partial DOS for AgY

The charge density map for (100) planes of AgY, as sgiven in Figure 5, is crucial for analyzing the bond structure between atoms. Understanding the bond type involves considering electronegativity and inter-atomic charge transfer. When the electronegativity values differ significantly, as in this case, an ionic bond is formed; otherwise, a covalent bond is established. Figure 5 illustrates an ionic bond structure with varying electron densities.

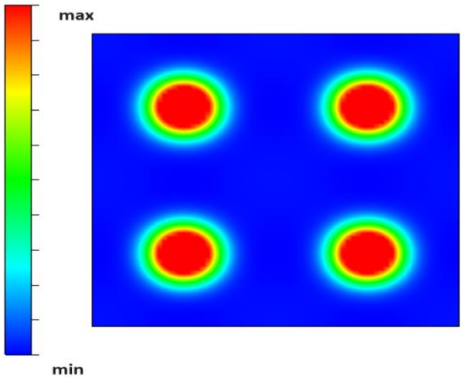

Figure 5. Charge density map along [100] direction for AgY

3.3 Vibrational Properties

The PHONOPY open-source code [22] was employed to determine the phonon distribution spectrum of AgY compound. Analyzing this spectrum provides insights into various physical properties, including phase transitions, dynamic stability, and specific heat within the compound. Figure 6 illustrates phonon distribution curves along high symmetry directions, generated using 2 × 2 × 2 supercells. YbAu, characterized by two atoms in its unit cell, exhibits three acoustic vibration modes and three optic modes among the available six vibration modes. Here, all obtained frequencies for first Brillouin region are positive, indicating the absence of imaginary frequencies. Thus, AgY is dynamically stable at 0 GPa. From the PDOS of AgY, Y atoms in the region between 2.5-4.5 THz contributed more to the acoustic modes. Lower frequencies region of acoustic modes are mostly detected by vibrations of Ag atoms.

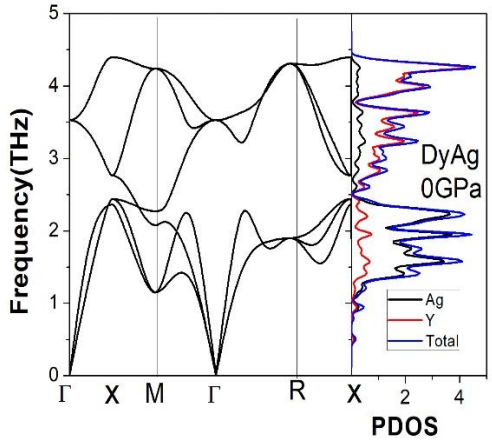

Figure 6. Phonon dispersion curves for AgY

The properties dependent on temperature are explored through the quasi-harmonic approach, considering thermal electronic excitations. Thermodynamic parameters like heat capacity (Cv) and entropy (S) are calculated using phonon frequencies within the framework of the quasi-harmonic approximation. Figure 7 visually represents how lattice vibrations contribute to the entropy and heat capacity of AgY. To minimize the potential influence of

anharmonicity, the temperature is limited to the range of 1000 K. The contribution of lattice vibrations to heat capacity follows the Debye model and gradually approaches the Dulong–Petit limit at higher temperatures. This analysis offers a thorough understanding of the system's temperature-dependent characteristics, especially concerning its thermodynamic parameters

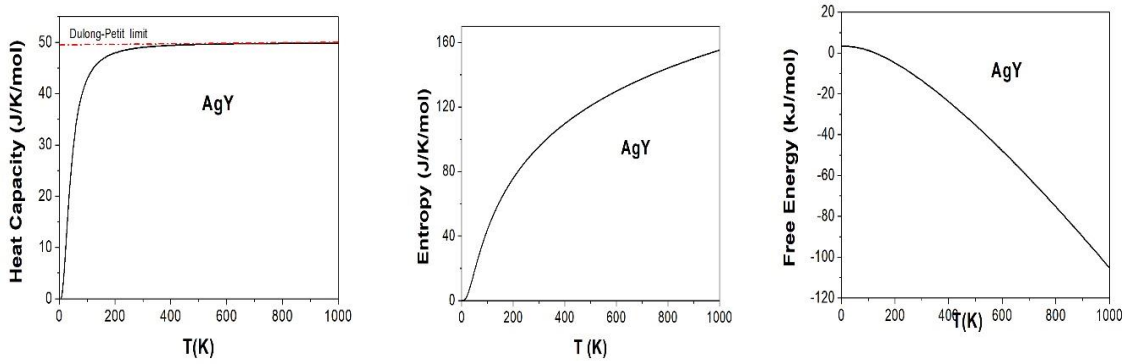

Figure 7. Thermodynamic properties for AgY

4. Conclusion

We conducted a thorough exploration of AgY's structural, elastic, vibrational, electronic, and thermodynamic properties using first-principles methods. Our investigation into zero-pressure second-order elastic constants and related parameters confirmed the compound's malleable characteristics. In contrast, Poisson's ratio (ν) values pointed towards the presence of ionic bonds, while elastic anisotropy (A) values indicated the compound's elasticity is anisotropic. The calculated structural and elastic constants results exhibited consistent agreement with previously reported data. Electronic band structure and density of state calculations brought to light the metallic nature of AgY. Despite observing a decline in free energy, both enthalpy and entropy demonstrated an increase at temperatures exceeding 1000 K.

References

[1] C. T. Liu, E. P. George, P. J. Maziasz and J. H. Schneibel (1998), Mater. Sci. Eng. A **258** 84–98.
[2] N. S. Stoloff, C. T. Liu and S. C. Deevis(2000), Intermetallics **8** 1313–1320.
[3] D. B. Miracle, (1993) Acta Metall. Mater. **41** 649–684.
[4] K. Gschneidner, A. Russell, A. Pecharsky, J. Morris, Z. Zhang, T. Lograsso, D. Hsu, C. H. Chester, Y. Y. Ye, A. Slager and D. Kesse (2003)Nature Mater. **2** 587–590.
[5] Z. Zhang, A. M. Russell, S. B. Biner, K. Gschneidner and C. C. H. Lo (2005)Intermetallics **13** 559–564.
[6] A. M. Russell, Z. Zhang, T. A. Lograsso, C. C. H. Lo, A. O. Pecharsky, J. R. Morris, Y. Ye, K. A. Gschneidner and A. J. Slager (2004)Acta Mater. **52** 4033–4040.
[7] A. M. Russell, Z. Zhang, K. A. Gschneidner, T. A. Lograsso, A. O. Pecharsky, A. J. Slager and D. C. Kesse (2005)Intermetallics **13** 565–571.
[8] J.R. Morris, Y.Y. Ye, Y.B. Lee, B.N. Harmon, K.A. Gschneidner, A.M. Russell, (2004)Acta Mater. 53 4849.
[9] Z. Zhang, A.M. Russell, S.B. Biner, K.A. Gschneidner, H.C.C. Lo, (2005) Intermetallics 13 559.
[10] S. Ugur, G. Ugur, F. Soyalp, R. Ellialtioglu, (2009) J. Rare Earths 27 664.
[11] G. Ugur, M. Civi, S. Ugur, F. Soyalp, R. Ellialtioglu, (2009) J. Rare Earths 27 661.
[12] C. Ritter, M.R. Ibarra, R.M. Ibberson, (1992) J. Phys. Condens. Matter 4 L39.
[13] Y.J. Shi, Y.L. Du, G. Chen, G.L. Chen, (2007) Phys. Lett. A 368 495.
[14] G. Kresse, J. Hafner, (1993) Ab initio molecular dynamics for liquid metals, Phys. Rev. B 47 558.
[15] G. Kresse, J. Hafner, (1994) Ab initio molecular-dynamics simulation of the liquid metal–amorphous-semiconductor transition in germanium, Phys. Rev. B 49 14251.
[16] G. Kresse, J. Furthmuller, (1996) Efficiency of ab-initio total energy calculations for metals and semiconductors using a plane-wave basis set, Comput. Mater. Sci. 6 15.
[17] G. Kresse, J. Furthmuller, (1996) Efficient iterative schemes for ab initio total-energy calculations using a plane-wave basis set, Phys. Rev. B 54 11169.

[18] J.P. Perdew, J.A. Chevary, S. Vosko, K.A. Jackson, M.R. Pederson, D.J. Singh, C. Fiolhais, (1992) Atoms, molecules, solids, and surfaces: applications of the generalized gradient approximation for exchange and correlation, Phys. Rev. B 46 6671.
[19] H.J. Monkhorst, J.D. Pack, (1976) Special points for Brillouin-zone integrations, Phys. Rev. B 13 5188.
[20] L. Page, P. Saxe, (2002)Symmetry-general least-squares extraction of elastic data for strained materials from ab initio calculations of stress, Phys. Rev. B 65 104104.
[21] M.J. Mehl, J.E. Osburn, D.A. Papaconstantopoulos, B.M. Klein, (1990) Structural properties of ordered high-melting-temperature intermetallic alloys from first-principles total-energy calculations, Phys. Rev. B 41 10311.
[22] A. Toga, F. Oba, I. Tanaka, (2008) First-principles calculations of the ferroelastic transition between rutile-type and CaCl2-type SiO2 at high pressures, Phys. Rev. B 78 (134106) 1–9.
[23] F.D. Murnaghan, (1944) The compressibility of media under extreme pressures, Proc. Natl. Acad. Sci. U.S.A. 30 244–247.
[24] S.Singh Chouhan, P. Soni, G. Pagare, S.P. Sanyal, M. Rajagopalan, (2011) Ab-initio study of electronic and elastic properties of B2-type ductileYM (M=Cu, Zn and Ag)intermetallics, Physica B 406 339–344
[25] Mouhat, F., Coudert, F.X. (2014). Necessary and sufficient elastic stability conditions in various crystal systems. Physical Review B - Condensed Matter and Materials Physics, 90(22), 1-4.
[26] P. Ravindran, L. Fast, P.A. Korzhavyi, B. Johansson, J. Wills, O. Eriksson, (1998)Density functional theory for the calculation of elastic properties of orthorhombic crystals: application to TiSi 2, J. Appl. Phys. 84 (9) 4891–4904.

Exploring the Adsorption Efficiency of Dried Banana Peel Against Methylene Blue in Water

Tiba SALEH GHANI AL-OKAIDAT [1], *Gisela Mylene EYANG MINSO* [1]
M. Bora AKIN [1*]

[1] *Department of Chemical Engineering, Çankırı Karatekin University, Çankırı, Turkiye*

Abstract

Removal of methylene blue from wastewater using various adsorbents has been a subject of extensive research. As biosorbents, polyaniline/walnut shell waste composites [1], Urfa stone [2], chemically activated carbon from pomegranate peel [3], peach seed shell [4] and Chaff [5] was used in the removal of methylene blue.

In this study, the adsorption capacity of banana peel is examined by drying it without any pretreatment. Time, temperature, initial concentration of methylene blue and the amount of banana peel were used as parameters in the study. Adsorbent capacities were calculated through experiments performed by changing the parameters and the trends caused by the changes were found.

Keywords: *Adsorption, Wastewater, Methylene Blue, Banana peel, Biosorbent*

1. Introduction

Pollution of water resources with dyes poses a significant environmental problem. Cost-effective and efficient methods are required to eliminate paint-related pollution. In recent years, the use of food waste materials in the removal of dyes from aqueous solutions has attracted attention. Banana is among the most traded fruits in the world. According to Faostat, total banana consumption in the world reached 100,332 kt in 2021. This is 3.88% more than the previous year and 13.4% more than 10 years ago [6].

The use of dried banana peel in removing various pollutants from water is included in various studies. Massocatto et al. (2013) demonstrated the effectiveness of using banana peels to remove lead from aqueous solutions. They also made kinetic and thermodynamic calculations [7]. Additionally, Mondal and Kar (2018) used banana peel to remove Congo red from banana peel [8]. Additionally, Deshmukh et al. (2017) removed cadmium from aqueous solutions using dried banana peels [9]. Similarly, Hossain (2012) used banana peel as a bioadsorbent in removing copper from water [10]. All of these studies provide information that banana peel is effective in removing various pollutants from water when used by drying.

In the light of the information in the literature, in this study, the effects of various parameters on the adsorption capacity were examined using dried banana peel.

2. Materials and Methods

Methylene blue was obtained from Sigma Aldrich. Banana peels were dried using a vacuum oven at 80 °C. After drying, the size was reduced by grinding in a mortar. A magnetic stirrer (IKA) and UV spectrophotometer (Shimadzu) were used in methylene blue adsorption experiments.

In this study, experiments on the adsorption of methylene blue were carried out comprehensively. First, 1000 mL of Methylene Blue stock solution was prepared at a concentration of 1 g/L. In order to obtain different concentrations from this stock solution, a calibration chart was created by dilution processes. The wavelength of the UV spectrophotometer used in the measurement of Methylene Blue was determined as 665 nm.

* Corresponding author. *e-mail address: mbakin@karatekin.edu.tr*

In the experiments conducted to determine the adsorption capacity, the initial concentrations of Methylene Blue were set as 2.5, 5, 10, 25, 40, 60, 90, 100, 150 and 250 mg/L, respectively. Experiments were carried out at 25 °C using 0.5 mg/L adsorbent in 100 mL solutions prepared.

In time-dependent experiments, a concentration of 40 mg/L Methylene Blue was used and the samples taken during the removal process were examined at the following time periods: 0, 2, 5, 10, 20, 30, 45, 60, 90, 180, 240, 300, 360, 420 and 1440 minutes. The samples taken were measured with a UV spectrophotometer.

Additionally, experiments were conducted at temperatures of 5 °C, 25 °C and 40 °C to examine the temperature effect on the adsorbent. In order to investigate the effect of adsorbent dosage, the amounts of adsorbent used were determined as 0.3, 0.5, 1 and 2.5 mg/L.

3. Results and Discussion

3.1. Effect of Initial Dye Concentration

In the study, adsorption capacities (q_e) were examined using adsorbent with 0.5 mg/L for different concentrations. The q_e values obtained for the concentrations examined in the study are given in Figure 1. Among the initial concentrations, the highest adsorption capacity was obtained at 0.0897 mol/kg and 250 mg/L. A rapid increase is observed in the q_e value up to the initial concentration of 250 mg/L. 40 mg/L was chosen as the working concentration and this concentration was used to examine other parameters.

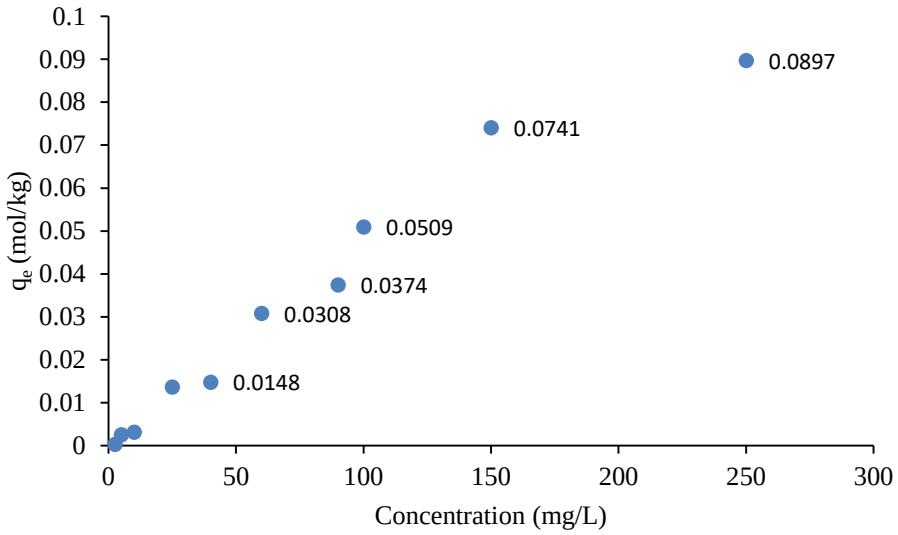

Figure 1. Effect of dyestuff initial concentrations on adsorption capacity.

3.2. Effect of Time

For the experiment in which the effect of time on q_e was examined, 40 mg/L was chosen as the initial concentration. To find the q_e value at the selected concentration, concentration values were found by measuring samples taken at certain times. When Figure 2a is examined, it is understood that the concentration decreases over time, meaning that the adsorbent does its job. At the end of 1440 minutes, the dye concentration decreases to 34.23 mg/L. The calculation made using concentrations shows the change of q_e value with time (Figure 2b). At the end of 1440 minutes, the q_e value is 0.0534 mol/kg at an initial dye concentration of 40 mg/L.

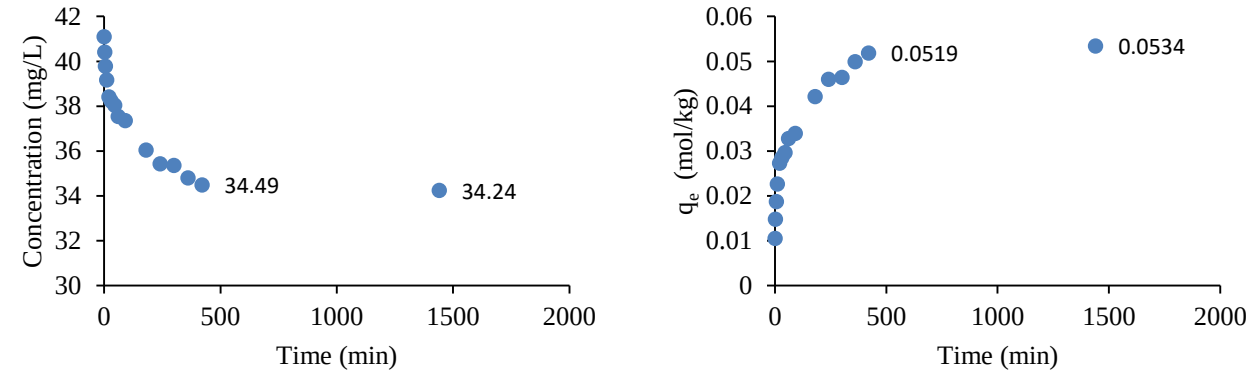

Figure 2. Effect of 0.5 mg/L adsorbent at 200 mg/L initial dye concentration: a) Concentration and b) adsorbent capacity

3.3. Effect of Adsorbent Amount

As the amount of adsorbent increases, the q_e value becomes 0.0175 at 0.3 mg/L and 0.0148 mol/kg at 0.5 mg/L. While the q_e value is 0.0111 at 1 mg/L adsorbent amount, this value decreases to 0.0041 at 2.5 mg/L adsorbent amount (Figure 3a). The decrease in q_e appears to be linear. The regression coefficient was obtained as 0.9681. It is seen that the highest adsorption percentage is 8.3% with the use of 1 mg/L adsorbent, and the closest value to this value is 7.7% with the use of 2.5 mg/L adsorbent (Figure 3b).

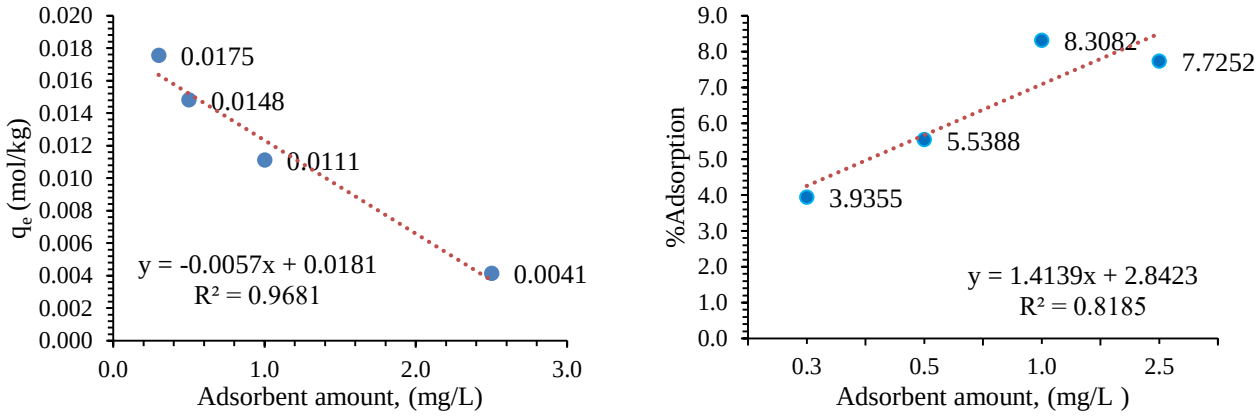

Figure 3. Effect of adsorbent amount a) adsorption capacity, b) Adsorption percentage

3.4. Effect of Temperature

In experiments conducted at 5 °C, 25 °C and 40 °C, where the effect of temperature on adsorption capacity was examined, q_e values were 0.0265 mol/kg at 5 °C, 0.0148 mol/kg at 25 °C and 0.0101 mol/kg at 40 °C, respectively. According to the data obtained, the q_e value decreases as the temperature increases (Figure 4).

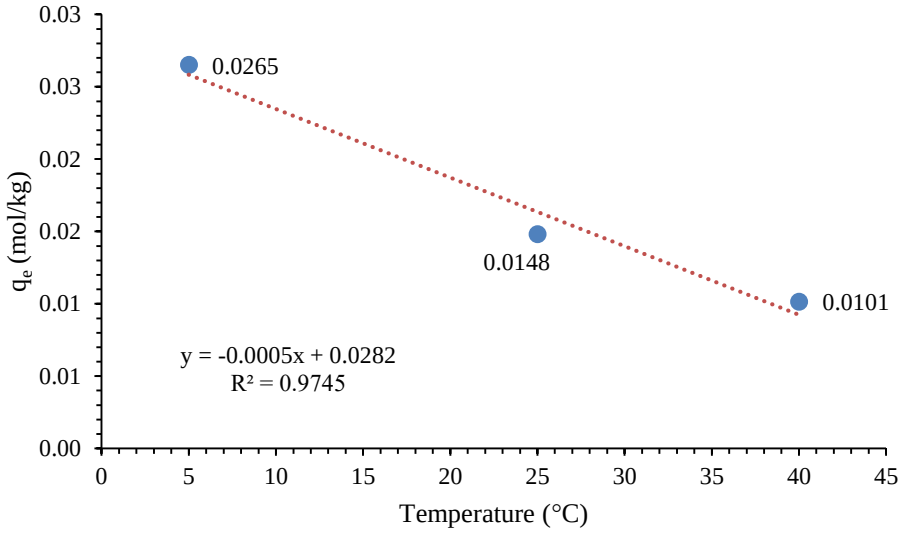

Figure 4. Effect of temperature on adsorption capacity

4. Conclusion

The data obtained in the study successfully examines dye adsorption from Methylene Blue solutions using dried banana peels. The q_e value increases with increasing initial dye concentration. Using 0.5 mg/L adsorbent at an initial concentration of 250 mg/L, the q_e value was obtained as 0.0897 mol/kg. This value was the highest value when the initial concentrations were considered. As the amount of banana peel used as adsorbent increases to 1 mg/L, the adsorption efficiency increases and reaches 8.3%. At this yield, the q_e value is 0.0111 mol/kg. While the adsorption capacity decreased with increasing temperature, the q_e value was obtained as 0.0101 mol/kg at 40 °C. The q_e value at 5 °C was found to be 0.0265 mol/kg.

Acknowledgement

All experimental work was conducted in the Chemical Engineering Department Laboratory at Çankırı Karatekin University. The authors would like to thank the Chemical Engineering Department.

References

[1] Cerit A. Atık Sulardan Metilen Mavisi Gideriminde Polianilin/Ceviz Kabuğu Atığı Kompozitlerinin Kullanımı. Gazi Üniversitesi Mühendislik-Mimarlık Fakültesi Derg 2021. https://doi.org/10.17341/gazimmfd.845443.

[2] Dilekoğlu MF. Harran Ovasi Tarim Arazileri Etrafinda Bulunan Urfa Taşi'nin Metilen Mavisi Boyar Maddesini Adsorpsiyonu. Türkiye Tarımsal Araştırmalar Derg 2018. https://doi.org/10.19159/tutad.333988.

[3] Yılmaz N, Alagöz O. Nar Kabuklarından Kimyasal Aktivasyon Ile Hazırlanan Aktif Karbon Üzerinde Metilen Mavisinin Adsorpsiyonu. El-Cezeri Fen Ve Mühendislik Derg 2019. https://doi.org/10.31202/ecjse.583102.

[4] Polat İ, Orhan R. Şeftali Çekirdeği Kabuğu Kullanarak Metilen Mavisi Boyasının Giderilmesi İçin Sabit Yataklı Kolonun Adsorpsiyon Performansı. Afyon Kocatepe Univ J Sci Eng 2019. https://doi.org/10.35414/akufemubid.605325.

[5] Han R, Wang Y, Han P, Shi J, Yang JW, Lu Y. Removal of Methylene Blue From Aqueous Solution by Chaff in Batch Mode. J Hazard Mater 2006. https://doi.org/10.1016/j.jhazmat.2006.02.029.

[6] Https://www.helgilibrary.com/. Which Country Eats the Most Bananas? Https://WwwHelgilibraryCom/ 2023:https://www.helgilibrary.com/charts/which-country-. https://www.helgilibrary.com/charts/which-country-eats-the-most-bananas.

[7] Massocatto CL, Paschoal EC, Buzinaro N, Oliveria TF, Teixeira Tarley CR, Caetano J, et al. Preparation and Evaluation of Kinetics and Thermodynamics Studies of Lead Adsorption Onto Chemically Modified Banana Peels. Desalin Water Treat 2013. https://doi.org/10.1080/19443994.2013.770614.
[8] Mondal NK, Kar S. Potentiality of Banana Peel for Removal of Congo Red Dye From Aqueous Solution: Isotherm, Kinetics and Thermodynamics Studies. Appl Water Sci 2018. https://doi.org/10.1007/s13201-018-0811-x.
[9] Deshmukh PD, Khadse GK, Shinde VM, Labhasetwar P. Cadmium Removal From Aqueous Solutions Using Dried Banana Peels as an Adsorbent: Kinetics and Equilibrium Modeling. J Bioremediation \& Biodegrad 2017. https://doi.org/10.4172/2155-6199.1000395.
[10] Hossain MA. Removal of Copper From Water by Adsorption Onto Banana Peel as Bioadsorbent. Int J Geomate 2012. https://doi.org/10.21660/2012.4.3c.

Optimization of electropolymerization conditions for enhanced anticorrosive resistance of 2,6-Benzphenone on AISI316L: A Response surface methodology approach

Ibrahim FILAZI [1,2,*], ***Ali Tuncay OZYILMAZ*** [2], ***Gul OZYILMAZ*** [2], ***Cumali CELIK*** [3]

[1] *Cankiri Karatekin University, Central Research Laboratory (ÇANKAM), Cankiri, TÜRKİYE*

[2] *Hatay Mustafa Kemal University, Science & Art Faculty, Chemistry Department, Antakya, TÜRKİYE*

[3] *Yalova University, Yalova Vocational School, Property Protection and Security Department, Yalova, TÜRKİYE*

Abstract

This study researched the effect of electropolymerization conditions (monomer concentration, scan rate and electropolymerization time) of 5-hydroxy-2,2-diphenyl-4h-benzo[d][1,3]dioxin-4-one on the anti-corrosive performance via using response surface methodology (RSM). The coatings were carried out on the surfaces of AISI 316L working electrodes in the acetonitrile medium presence of 0.15 M $LiClO_4$ electrolyte by cycling voltammetry (CV) technique according to the designed parameters. Electrodes monitored in 3,5% NaCl solution for 240h immersion time via AC impedance. Corrosion resistance data calculated from equivalent circuits representing the data obtained were analyzed with a quadratic model in the Box-Behnken technique. It was determined that the model obtained as a result of the study could explain the corrosion resistance, which is affected by 97.0% of the independent parameters studied, with 91.6% accuracy and high sensitivity. According to the obtained models, it was seen that the monomer concentration had the biggest effect on corrosion resistance and the electropolymerization time had the least effect. In addition, it was determined that the individual effects of monomer concentration and scan rate on the response were close to each other, but their combined changes were high. However, it was observed that this effect was less than the effect of the joint change of electropolymerization time and scan rate. The results were converted into response surface graphs and formulations that allowed parameters to be optimized to achieve the desired corrosion resistance.

Keywords: *corrosion, response surface methodology, electropolymerization, stainless steel, 5-hydroxy-2,2-diphenyl-4h-benzo[d][1,3]dioxin-4-one*

1. Introduction

Corrosion, represents an electrochemical phenomenon that transpires when metals interact with their surroundings, causes various significant damages on metals. This intricate electrochemical reaction poses a significant threat to structures, equipment, and infrastructure, as metals exhibit a proclivity to revert to more stable oxide or sulfide forms, resulting in the formation of corrosion byproducts, such as rust. Beyond its visual impact, corrosion inflicts substantial damage on the structural integrity of materials and components, thereby eliciting repercussions that extend beyond mere aesthetics, encompassing economic and safety concerns. This omnipresent challenge in metal usage has prompted the development of innovative strategies for safeguarding metal structures and components, aligning with advancements in technology and science. Among these approaches, conductive polymer coatings through electropolymerization have emerged as a noteworthy solution recently. This method not only establishes a protective barrier against corrosive forces prevalent in diverse environments but also introduces some distinctive electrical properties that augment corrosion resistance. [1], [2]

Electropolymerization serves as a sophisticated technique for the controlled deposition of polymer layers onto metal surfaces, a crucial aspect in achieving optimal corrosion protection while preserving the integrity and functionality of the underlying metal substrate. The effectiveness of this technique in corrosion mitigation is intricately tied to several key parameters, including polymerization time, applied potential, and electrolyte composition. Fine-tuning these parameters enables the customization of coatings with regard to film thickness, adhesion, and chemical composition, thereby influencing the overall corrosion resistance of the metal. A nuanced understanding and manipulation of electropolymerization parameters hold significant promise in optimizing the protective performance of these coatings. [3]

* Corresponding author. *e-mail address: mail@ifilazi.com*

This study examined the effect of electropolymerization & bath conditions of 5-hydroxy-2,2-diphenyl-4h-benzo[d][1,3]dioxin-4-one on the anti-corrosive performance of the resulting coating via using response surface methodology. Response surface methodology (RSM) offering distinct advantages over classic methods by efficiently resolving interactions among variables on complex data sets and identifying optimal conditions for enhanced outcomes. In contrast, with classic methods researchers often struggle to resolve intricate parameter relationships, leading to suboptimal results and requiring extensive experimental resources. The versatility and precision of RSM thus present a significant advancement in experimental design, providing a more systematic and resource-efficient approach compared to traditional methods [4].

2. Materials and Methods

In the study, medium obtained by dissolving 0.15 M $LiClO_4$ in acetonitrile was used as the electrolyte solution. All chemicals were purchased from Merck in analytical purity. Freshly synthezied 5-hydroxy-2,2-diphenyl-4h-benzo[d][1,3]dioxin-4-one [5] was used as monomer (Figure 1). Cylindrical AISI 316L grade stainless steel (SS) electrodes with a surface area of 0.30 cm^2 were used as working electrodes in 3-electrode cell setup, which were insulated with a thick polyester layer so that the working and connection surfaces were exposed. Before the study, the working surfaces of the electrodes were finely sanded and polished and then washed with bi-distilled water. A square platinum plate (99,9%) with a surface area of 0.50 cm^2 was used as the counter electrode and Ag/AgCl (3M KCl, SI Analytics B3520+) electrode was used as a reference. Electropolymerization was performed by cyclic voltammetry (CV) technique with CHI608C electrochemical workstation. The experimental set of the electropolymerization conditions and bath parameters (monomer concentration, scan rate and electropolymerization time) were designed in the Design-Expert software using the ranges in Table 1 and Box-Behnken technique. The designed experiment set is given in Table 2. 2 parallel electrodes obtained for each experiment in the set were immersed in 3.5% NaCl solution and kept for 240 hours in. Corrosion performance at the end of that time was monitored by A.C. impedance (EIS) technique at an open circuit potential of 7 mV amplitude in the range of 100 kHz - 1 mHz with CHI608C electrochemical workstation. The data obtained were converted into equivalent circuits in ZView2 software and the resistance values obtained from these circuits were entered as responses to the designed experimental set. The experimental set was analyzed with a quadratic model and response surface plots and ANOVA data were obtained.

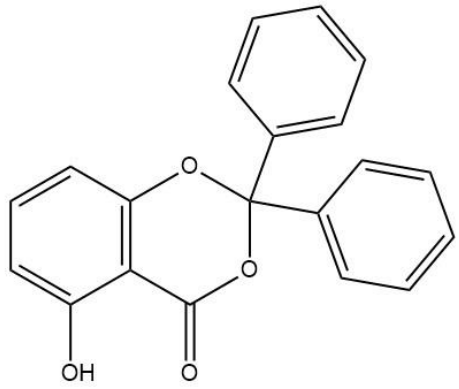

Figure 1. 5-hydroxy-2,2-diphenyl-4h-benzo[d][1,3]dioxin-4-one

Table 1. Design Parameters

Code	Factor	Unit	-1	0	+1
A	Monomer Concentration	mM	3,125	7,8125	12,50
B	Scan Rate	mV/s	50	100	150
C	Electropolymerization Time (Deposition Time)	seconds	500	1000	1500

Table 2. Designed Experiment Set

Experiment Number (R)	Factor A	Factor B	Factor C
1	7,8125	100	1000
2	12,5	100	500
3	12,5	150	1000
4	3,125	50	1000
5	7,8125	100	1000
6	7,8125	100	1000
7	3,125	100	500
8	7,8125	50	500
9	7,8125	150	1500
10	7,8125	50	1500
11	12,5	100	1500
12	7,8125	100	1000
13	12,5	50	1000
14	7,8125	150	500
15	3,125	100	1500
16	3,125	150	1000
17	7,8125	100	1000

3. Results and Discussion

Electropolymerization was carried out at a potential in the range of -0.5 to 2 V in the bath prepared for the relevant experiment according to the designed experimental parameters at the relevant scan rate and time. Figure 2 shows the first 4 segments of the cyclic voltammetry voltammograms obtained for the working electrodes with a potential applied at a scan rate of 50 mV/s in the range from -0.2 to 2 V in an electrolyte medium containing 12.5 mM monomer and no-monomer. When the voltammograms were analyzed, a significant current increase peak around 1.06 V was observed in the first segment of monomer-containing medium. Based on the fact that this peak does not appear in the monomer-free medium, it can be said that this peak corresponds to monomer oxidation. Since a single monomer oxidation peak is observed, it is thought that the monomer used can be considered to be of high purity. It is also thought that the change in current behavior of surface following this peak is due to the formation of a layer on the surface. The current change starting around -0.08 V before the appearance of the peak is considered to be due to the change of electrolyte conductivity because of the monomer. In the return peak in the second segment, the peak seen in both electrolyte environments at a potential of 1.6V is thought to be the re-formation peak of the oxide layers disrupted on the surface. The high current value of this peak in the monomer-containing medium is thought to be due to the behavior of the layer formed on the surface. The current decreases seen in the following segments show that this layer on the surface grows. [6]

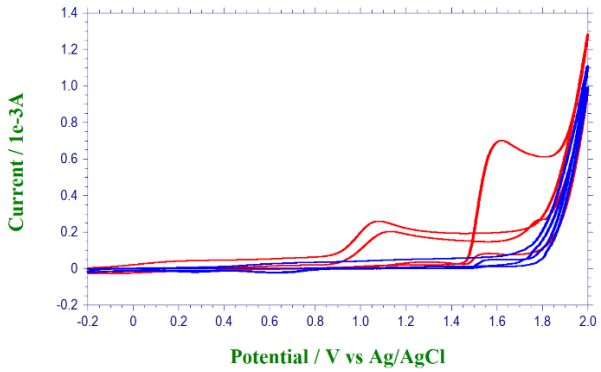

Figure 2. Cyclic voltammetry voltammograms of SS in monomer-containing (—) and monomer-free (—) medium

Following the immersion of the electrodes, which worked as per the parameters in Table 2, in a corrosive environment for 240 hours, the corrosion resistance calculated from equivalent circuits representing the AC impedance data was entered as responses to the experimental set. The obtained ANOVA results, following analysis using a quadratic model and the Box-Behnken technique, are presented in Table 3. When the data were analyzed, it was seen that the corrosion resistance was affected by 96.99% of the independent variables studied, and the quadratic model used for the analysis could explain this effect with 91.58% accuracy. The p-value of the model is lower than 0.05 and the Lack-of-Fit p-value is higher than 0.05, indicating that the model is significant and usable for analysis. Adeq Precision value much higher than 4 indicates that the signal to noise ratio of the model is low, while the CV% value indicates that the results may deviate by 37.08% from the average. The formula designed according to this model, which allows the calculation of corrosion resistance according to the studied parameters, is given in Equation 1. The graph showing the comparison of the predicted values calculated using this formula with the actual values studied is given in Figure 3. As can be seen from this graph, the graph points obtained in accordance with the ANOVA results intersect with the line. This shows that the model can explain the study with high accuracy and precision. [4], [7]

When the ANOVA data in Table 3 are analyzed in terms of decreasing p-value and increasing F-value of the factors, it is seen that the monomer concentration and scan rate affect the corrosion resistance most individually, and the variation of these factors together has a high effect, but less effect than the variation of scan rate and electropolymerization time together. In the light of these data, when the response surface graphs are examined, it can be clearly seen that the variation of scan rate and electropolymerization time together affects the corrosion resistance in parallel with the ANOVA results as can be seen in Figure 4. For all monomer concentrations, corrosion resistance is high at the limit values of scan rate and electropolymerization time together, while corrosion resistance is low at their intermediate values. The highest corrosion resistance was obtained at medium values of monomer concentration, high scan rate and high electropolymerization time. When the effect of the changes in monomer concentration and electropolymerization time on corrosion resistance is examined in Figure 5, it is observed that there is high corrosion resistance at the middle values of the limit values, the maximum and minimum values at the limit values give low corrosion resistance; At the middle values, a similar behavior is observed, but corrosion resistance cannot be obtained as high as the limit values. When values are given to the scan rate in the graphs, it is seen that as the scan rate increases, the corrosion resistance increases on the high electropolymerization time side of the graph and decreases on the low time side of the graph. When the effect of monomer concentration and scan rate changes on corrosion resistance in Figure 6 is examined, it is seen that there is a similar changes with Figure 5. While the scan rate was low and the monomer concentration was at low-medium values, low electropolymerization time gave the highest corrosion resistance, while medium monomer concentrations at high scan rate with increasing electropolymerization time increased the corrosion resistance.

When all the results were evaluated, it was seen that, depending on the electropolymerization time, high scan rate at high electropolymerization times and low scan rate at low electropolymerization times gave better results, and monomer concentration gave the best corrosion resistance at medium values, independent of other factors. When the ion formation rate of the scan rate is evaluated, it is thought that these results are compatible; at high monomer concentrations, the monomer creates an inhibition effect and creates insulation on the surface, and at low monomer concentrations, ionized monomer in the environment is insufficient for the valid electropolymerization conditions and forms a thin and porous film.

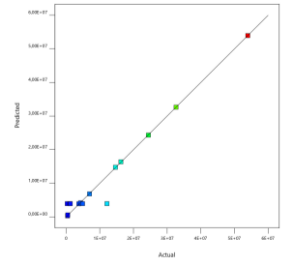

Figure 3. Predicted – Actual values

$$\boldsymbol{R_{corr}} = 3{,}94061e{+}06 + -5{,}03388e{+}06 * A + -6{,}82845e{+}06 * B + 1{,}06918e{+}06 * C + 5{,}17706e{+}06 * AB + 259.675 * AC + 9{,}58082e{+}06 * BC + -1{,}81164e{+}07 * A\text{^}2 + 2{,}14637e{+}07 * B\text{^}2 + 2{,}47212e{+}07 * C\text{^}2 \quad (1)$$

Table 3. ANOVA Results

Source	Sum of Squares	df	Mean Square	F-value	p-value	
Model	3,109E+15	9	3,454E+14	17,92	0,0027	*significant*
A-Monomer Conc.	2,027E+14	1	2,027E+14	10,52	0,0229	
B-Scan Rate	1,865E+14	1	1,865E+14	9,68	0,0265	
C-Electropolymerization Time	4,573E+12	1	4,573E+12	0,2372	0,6468	
AB	1,072E+14	1	1,072E+14	5,56	0,0649	
AC	2,697E+11	1	2,697E+11	0,0140	0,9104	
BC	1,224E+14	1	1,224E+14	6,35	0,0532	
A^2	9,054E+14	1	9,054E+14	46,97	0,0010	
B^2	1,271E+15	1	1,271E+15	65,93	0,0005	
C^2	1,686E+15	1	1,686E+15	87,46	0,0002	
Residual	9,638E+13	5	1,928E+13			
Lack of Fit	1,091E+11	1	1,091E+11	0,0045	0,9496	*not significant*
Pure Error	9,628E+13	4	2,407E+13			
Cor Total	3,205E+15	14				
Std. Dev.	4,391E+06			**R^2**	0,9699	
Mean	1,184E+07			**Adjusted R^2**	0,9158	
C.V. %	37,08			**Adeq Precision**	14,9603	

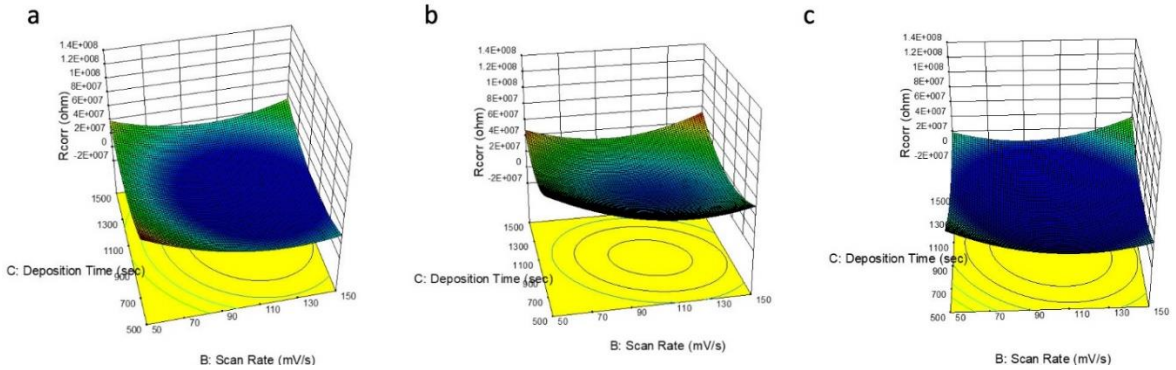

Figure 4. Response surface graph of variation of scan rate and electropolymerization (deposition) time together while monomer concentration (B) 3,125 mM (a), 7,8125 mM (b) and 12,5 mM (c)

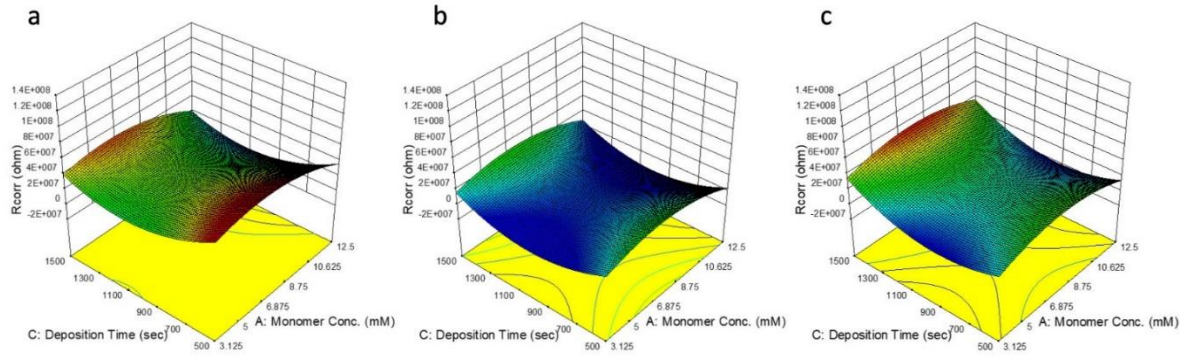

Figure 5. Response surface graph of variation of monomer concentration and electropolymerization (deposition) time together while scan rate (B) 50 mV/s (a), 100 mV/s (b) and 150 mv/S (c)

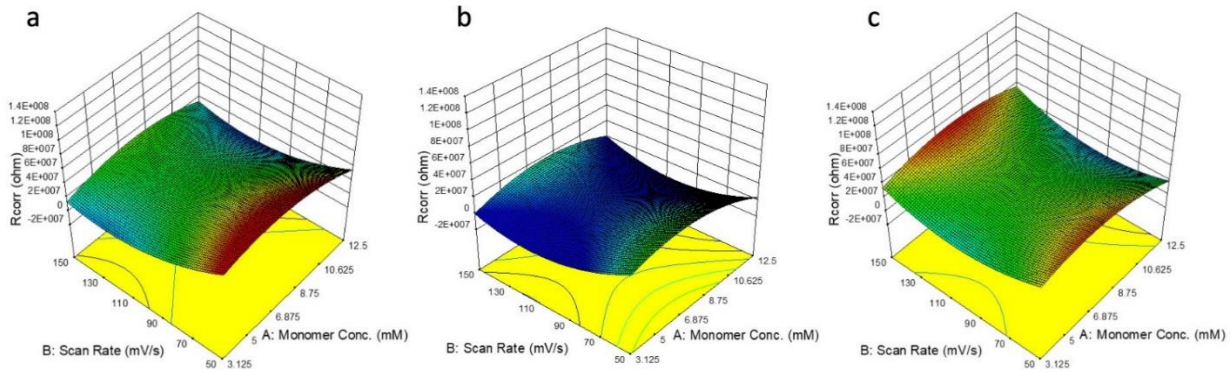

Figure 6. Response surface graph of variation of scan rate and monomer concentration together while electropolymerization time (C) 500 sec. (a), 1000 sec. (b) and 1500 sec. (c)

4. Conclusion

As a result of this study, a response surface model was able to explain the corrosion resistance, which was influenced by 97.0% of the independent parameters studied, with 91.6% accuracy and high sensitivity was determined for the electropolymerization of 5-hydroxy-2,2-diphenyl-4h-benzo[d][1,3]dioxin-4-one on the surface of AISI 316L to give the best corrosion resistance. According to the obtained model, it was seen that the monomer concentration had the biggest effect on corrosion resistance and the electropolymerization time had the least effect for 5-hydroxy-2,2-diphenyl-4h-benzo[d][1,3]dioxin-4-one electropolymerization. In addition, it was determined that the individual effects of monomer concentration and scan rate on the response were close to each other, but their combined changes were high. However, it was observed that this effect was less than the effect of the joint change of electropolymerization time and scan rate. The results were converted into response surface graphs and formulation that allowed parameters to be optimized to achieve the desired corrosion resistance.

References

[1] M. G. FONTANA, "Corrosion Engineering And Corrosion Science," *Corrosion*, vol. 19, no. 6, pp. 199t-204t, Jun. 1963, doi: 10.5006/0010-9312-19.6.199.

[2] M. Ates, "A review on conducting polymer coatings for corrosion protection," *J. Adhes. Sci. Technol.*, vol. 30, no. 14, pp. 1510–1536, Jul. 2016, doi: 10.1080/01694243.2016.1150662.

[3] A. T. Ozyilmaz, İ. Filazi, C. Surmelioglu, and G. Ozyilmaz, "Optimization of Anticorrosive PANi and PPy Synthesis Conditions on ZnNiMo Coated Copper Electrode Surface with Box Behnken Design," *Prot. Met. Phys. Chem. Surfaces*, vol. 58, no. 4, pp. 883–897, Aug. 2022, doi: 10.1134/S2070205122040177.

[4] R. H. Myers, D. C. Montgomery, and C. M. Anderson-Cook, *Response surface methodology: Process and product optimization using designed experiments*, 3rd ed. New Jersey, USA: John Wiley & Sons, Inc., 2009.

[5] V. Kumbaraci, N. Talinli, and Y. Yagci, "Photoinduced Synthesis of Oligoesters," *Macromolecules*, vol. 39, no. 18, pp. 6031–6035, Sep. 2006, doi: 10.1021/ma0607721.

[6] A. T. Özyılmaz, B. Özgen, and C. Çelik, "Poly(o-aminobenzyl alcohol) Films with and without Organic Compound on AISI 316 Surface; Synthesis and the Corrosion Performances," *J. Turkish Chem. Soc. Sect. A Chem.*, vol. 7, no. 2, pp. 375–382, Jun. 2020, doi: 10.18596/jotcsa.641851.

[7] A. Aygün, "Tekstil endüstrisi reaktif ve dispers boya banyo atıksularının elektrokoagülasyon prosesi ile arıtımı: Yanıt yüzey yöntemi ile optimizasyon," Doktora Tezi, Selçuk Üniversitesi Fen Bilimleri Enstitüsü, Konya, Türkiye, 2012.

The effect of adding cinnamon extract on the texture profile analysis of oil cake

Fatemeh GHANNADIASL [1,*], ***Banafshe BORDBAR LOMER*** [2]

[1] *Faculty of Agriculture and Natural Resources, Department of Food Sciences and Technology, University of Mohaghegh Ardabili, Ardabil, Iran*

[2] *Faculty of Agriculture, Department of Food Science and Technology, Urmia University, Urmia, Iran*

Abstract

Bakery products, especially oil cakes, are among the most widely consumed food products. The production of functional bakery products with physiological effectiveness and consumer acceptance requires careful consideration of their appearance, taste, and texture. The quality of these products mainly depends on the ingredients used in the recipe, the dough mixing conditions, and the baking conditions. Determining the optimal formulation to have healthy properties, maintain tissue properties, and improve the flavor of these products is very important. Cinnamon is a spice that has been shown to have antioxidant, anti-inflammatory, and antidiabetic effects, as well as enhance the sensory attributes of bakery products. This study aimed to evaluate the impact of different concentrations of cinnamon extract (0%, 0.1% and 0.2%) on the hardness, adhesiveness, cohesiveness, and resilience of oil cake. We hypothesized that adding cinnamon extract would improve the texture characteristics of oil cake. Texture profile analysis (TPA) was performed using the TEXTURE ANALYZER model Brook field-CT310K. The results showed that adding cinnamon extract reduced the hardness of the cake samples, while the adhesiveness increased compared to the control sample. The cohesiveness and resilience of the cake samples also decreased with increasing extract levels. Results suggest that using cinnamon extract can enhance the texture and stability of oil cakes.

Keywords: *Oil cake, Cinnamon extract, Texture profile analysis.*

1. Introduction

Bakery products, especially oil cakes, are among the most widely consumed food products globally due to their favorable texture and taste (Rios, Garzón, Lannes, & Rosell, 2018). Researchers are always looking to optimize the technology for preparing these products, to improve the variety, quality, and taste (Dhillon & Amarjeet, 2013). The production of functional bakery products with physiological effectiveness and consumer acceptance is essential (Siró, Kápolna, Kápolna, & Lugasi, 2008). The quality of these products mainly depends on the ingredients used in the recipe, the dough mixing conditions, and the baking conditions (Doweidar, Amer, & Tawfek, 2016). Therefore, determining the effective formulation to have healthy properties, maintain tissue properties, and improve the flavor of these products is very important (Škrbić & Cvejanov, 2011).

Cinnamon (C. Verum or C. Zeylanicum) belongs to the Lauraceous family. This brown substance has a pleasant aroma and sweet taste (Sharma, Mandal, Kant, Jachak, & Jagzape, 2020). Cinnamon is considered as an widespread spices in the world. It is used in traditional and modern medicine (Dhillon & Amarjeet, 2013). In medicine, cinnamon is mentioned as a traditional herbal medicine with different biological properties (Sadeghi et al., 2019) that has been shown to have antioxidant, anti-inflammatory, and antidiabetic effects (Muhammad & Dewettinck, 2017), as well as enhancing the sensory attributes of bakery products (Ghannadiasl & Bordbar Lomer, 2023). For a long time, researchers have been doing much research on cinnamon as a suitable flavoring for various foods and medicinal agents (Stevens & Allred, 2022). Due to the significant increase in the use of extract (Haddi, Faroni, & Oliveira, 2017), the present study aimed to prepare a cake formulation using cinnamon extract and to evaluate its texture characteristics.

2. Materials and Methods

2.1. Preparation of cinnamon extract

In order to extract, samples of Cinnamon bark (Golestan brand, Kian Badas Company of Tehran) were purchased and pulverized in suitable conditions and away from the sun with an electric grinder (France Moulinex Company,

* *Corresponding author. e-mail address: ghannadiasl@uma.ac.ir*

A320R1). The resulting powder was soaked in distilled water for 48 hours to prepare an aqueous extract (for every 100 g of powder, 300 ml of distilled water as solvent). Then, the soaked powder was transferred to the Buchner funnel machine and filtered using Whatman 42 filter paper. The aqueous cinnamon suspension was centrifuged for 15 minutes at 5000 rpm to separate the solids from the aqueous cinnamon solution. The resulting extract was concentrated using a rotary evaporator (EV400-Labtech-Italy) at a temperature of 75℃ and a speed of 200 rpm in a vacuum to 15 Brix. Brix measurements were performed with a refractometer (Onderoglu, Sozer, Erbil, Ortac, & Lermioglu, 1999).

2.2. Preparation of cake formulations

Cake dough was prepared by the sugar-dough method according to the instructions in Table 1 (Peyghambardoust, 2010). The studied samples included the control sample (without extract) and cake samples in 2 different concentrations of cinnamon extract (0.1% and 0.2%), which were added during the preparation of cake dough. After preparing the cake batter, the batter was poured into a greased pan and baked in a preheated oven at 180 °C for 20-25 minutes. Then, the cakes place in a clean space to cool. After reaching ambient temperature, it was completely covered with cellophane and prepared for tissue analysis.

Table 1. Formulation of oil cake by the sugar-dough method

Material	Percentage based on flour weight	Weight (g)	Method
Oil	57	263	Step 1) Warm up until a light color is produced (about 10 minutes).
Sugar	72	330	
Egg	72	330	Step 2) will be added in 4-5 parts.
Flour	100	425.6	Step 3) All the powdered ingredients will be sifted and then added to make the dough semi-smooth.
Baking powder	1.34	7.5	
Milk powder	2	9.2	
Vanilla	0.5	2.3	
Whey powder	4	18.4	
Water	25 (Variable)	114	Step 4) is added and mixed to form the desired dough.

2.3. TPA of oil cake samples

Texture analysis for cake samples was performed by TEXTURE ANALYZER model Brook field-CT310K. TPA is a time-force curve used to quantify texture properties related to sensory evaluation results (Vácha, Stejskal, Vejsada, Kouřil, & Hlaváč, 2014).

TPA of oil cake samples (2×2×2 cm) were pressed twice from the middle of the cakes, using a 38.1 mm diameter cylindrical probe (Probe: TA4/1000). Test Target 50%, Trigger Load 7g, Return Speed 2 mm/s, Test Speed 2.00 mm/s, Pretest Speed 1 mm/s, Fixture: TA-RT-KI. Finally, the TPA was determined from the curves using Texture Expert 1.05 (Stable Microsystems) software. Tissue measurement parameters, includeding hardness, adhesiveness, cohesiveness, and resilience were performed with an average of 3 replications per sample.

2.4. Statistical Analysis

For statistical analysis of data from a completely randomized design, the data were subjected to one-way analysis of variance (ANOVA) at the significant level of 5%. If there was a significantly different, it will be continued by Fisher's Least Significant Differences (LSD) test at the 0.05 probability. Quantitative data were reported as mean ± standard deviation.

3. Results and Discussion

The dimensions of the analyzed cakes (length, width, and depth) are shown in Table 2. According to the results, the addition of aqueous cinnamon extract in most cases does not affect on the Length, Width and Depth of oil cakes.

Table 2. Dimensions of cake samples

Dimensions (mm)	Samples		
	Control sample	0.1% extract	0.20% extract
Length	22.49±3.52[a]	23.70±6.51[a]	22.80±5.94[a]
Width	20.83±5.21[a]	21.10±3.49[ab]	25.28±0.25[ab]
Depth	18.45±4.84[a]	21.90±3.03[a]	21.69±5.99[a]

Dissimilar letters in each line indicate a significant mean difference (P<0.05).

Modifying the formulation of cake samples can change the texture properties related to physicochemical or structural phenomena (Soukoulis, Gaiani, & Hoffmann, 2018). Changes in the textural properties of the oil cake by adding aqueous cinnamon extract are shown in Table 3. TPA of the measured cake samples showed that by increasing the level of cinnamon extract in the oil cake, its hardness decreased, and the cake became softer. So, the cake hardness in the control sample decreased from 3816.33 to 2964.00 g in 0.20% sample. This result shows the improvement of the texture and hardness of the cake by adding the cinnamon extract to the oil cake. Our results were consistent with other findings (Majzoobi, Hedayati, Habibi, Ghiasi, & Farahnaky, 2014). In this study, the hardness of cakes decreased with increasing the percentage of resistant corn starch. Nakov et al. (2016), showed that the hardness of the measured cake samples becomes softer by increasing the level of button mushroom powder (Fakhreddin Salehi, Kashaninejad, Asadi, & Najafi, 2016). Different results have been reported in other studies. Adding different amounts of guar gum to carrot sponge cake is directly related to increasing the hardness of the cake (F Salehi & Kashaninejad, 2021). Also, increasing the amount of grape pomace powder increased the hardness of the cake (Nakov et al., 2020). Lu et al. (2010) found that the texture of sponge cake becomes harder by increasing the level of green tea powder (Lu, Lee, Mau, & Lin, 2010). The difference in the results was related to the type of added material. Adhesiveness is a surface property that depends on the combined effect of adhesive forces and other factors, including viscosity and viscoelasticity (Huang, Kennedy, Li, Xu, & Xie, 2007). The adhesiveness of the oil cake did not show a significant difference with increasing the percentage of cinnamon extract. However, all measured values for all concentrations were higher than the control sample. In the Slima et al. (2021) study, Lepidium sativum polysaccharide in cake formulation leads to increased cake adhesion (Slima et al., 2021). Cohesiveness indicates the internal strength of the food structure (F Salehi & Kashaninejad, 2021). One of the reasons for cake cohesion may be due to moisture or its circular cells (Slima et al., 2021). Thus, it can be inferred that cake samples with large amounts of small air cells show less dense structure than more cohesive cake samples (Moza & Gujral, 2017). In our study, the results of TPA showed a decrease in cake cohesion by increasing the level of cinnamon extract. In addition, the resilience of cakes decreased with increasing the percentage of extract. The results of our study were consistent with the study of Lu et al. (2010) in reducing the cohesiveness and resilience values in sponge cake samples by increasing the level of green tea powder (Lu et al., 2010).

Table 3. Textural properties of oil cakes with different levels of cinnamon extract

Parameters of texture	Samples		
	Control sample	0.1% extract	0.2% extract
Hardness (g)	3816.33±8.89[a]	3042.00±0.95[ab]	2964.00±3.12[ab]
Adhesiveness (mj)	0.20±0.26[b]	0.86±0.49[a]	0.47±0.31[ab]
Cohesiveness	0.73±0.13[a]	0.62±0.06[a]	0.58±0.02[a]
Resilience	0.24±0.02[a]	0.21±0.15[ab]	0.19±0.02[b]

Dissimilar letters in each line indicate a significant mean difference (P<0.05).

4. Conclusion

Considering the importance of bakery products worldwide, in this study, we investigated the texture characteristics of oil cakes enriched with cinnamon extract. According to the results obtained in this research, with the increase in the level of cinnamon extract, the hardness, cohesiveness, and resilience decreased compared to the control sample. However, the amount of adhesiveness increased compared to the control sample. These results suggest that using cinnamon extract can enhance the texture and stability of oil cakes.

Acknowledgement

The authors express their gratitude to Iran High-Tech Laboratory Network, central laboratory of Mohaghegh Ardabili University and Gilan University for supporting and providing laboratory facilities and equipment.

References

[1] Dhillon, G. K., & Amarjeet, K. (2013). Quality Evaluation Of Bread Incorporated With Different Levels Cinnamon Powder. *Int. J. Food Sci. Nutr. Diet*, 2, 70–74.
[2] Doweidar, M. M., Amer, A. M., & Tawfek, A. (2016). Preparation and evaluation of healthy cinnamon cake. *Egyptian Journal of Nutrition*, 31(4), 157–195.
[3] Ghannadiasl, F., & Bordbar Lomer, B. (2023). Physicochemical and sensory properties of oil cake enriched with cinnamon extract. *Journal of Food Research*, 33(2), 43–55.
[4] Haddi, K., Faroni, L. R. A., & Oliveira, E. E. (2017). Cinnamon oil. In *Green pesticides handbook* (pp. 117–150). CRC Press.
[5] Huang, M., Kennedy, J. F., Li, B., Xu, X., & Xie, B. J. (2007). Characters of rice starch gel modified by gellan, carrageenan, and glucomannan: A texture profile analysis study. *Carbohydrate Polymers*, 69(3), 411–418.
[6] Lu, T.-M., Lee, C.-C., Mau, J.-L., & Lin, S.-D. (2010). Quality and antioxidant property of green tea sponge cake. *Food Chemistry*, 119(3), 1090–1095.
[7] Majzoobi, M., Hedayati, S., Habibi, M., Ghiasi, F., & Farahnaky, A. (2014). Effects of corn resistant starch on the physicochemical properties of cake. *Journal of Agricultural Science and Technology*, 16(3), 569–576.
[8] Moza, J., & Gujral, H. S. (2017). Influence of barley non-starchy polysaccharides on selected quality attributes of sponge cakes. *LWT-Food Science and Technology*, 85, 252–261.
[9] Muhammad, D. R. A., & Dewettinck, K. (2017). Cinnamon and its derivatives as potential ingredient in functional food—A review. *International Journal of Food Properties*, 20(sup2), 2237–2263.
[10] Nakov, G., Brandolini, A., Hidalgo, A., Ivanova, N., Stamatovska, V., & Dimov, I. (2020). Effect of grape pomace powder addition on chemical, nutritional and technological properties of cakes. *Lwt*, 134, 109950.
[11] Onderoglu, S., Sozer, S., Erbil, K. M., Ortac, R., & Lermioglu, F. (1999). The Evaluation of Long-term Effects of Cinnamon Bark and Olive Leaf on Toxicity Induced by Streptozotocin Administration to Rats. *Journal of Pharmacy and Pharmacology*, 51(11), 1305–1312.
[12] Peyghambardoust, S. H. (2010). Cereal Products Yechnology. Volume 2. *Tabriz University of Medical Science*. 250p.
[13] Rios, R. V, Garzón, R., Lannes, S. C. S., & Rosell, C. M. (2018). Use of succinyl chitosan as fat replacer on cake formulations. *LWT*, 96, 260–265.
[14] Sadeghi, S., Davoodvandi, A., Pourhanifeh, M. H., Sharifi, N., ArefNezhad, R., Sahebnasagh, R., … Mirzaei, H. (2019). Anti-cancer effects of cinnamon: Insights into its apoptosis effects. *European Journal of Medicinal Chemistry*, 178, 131–140.
[15] Salehi, F, & Kashaninejad, M. (2021). Influence of Guar Gum on Texture Profile Analysis and Stress Relaxation Characteristics of Carrot Sponge Cake. *Journal of Food Biosciences and Technology*, 11(1), 1–10.
[16] Salehi, Fakhreddin, Kashaninejad, M., Asadi, F., & Najafi, A. (2016). Improvement of quality attributes of sponge cake using infrared dried button mushroom. *Journal of Food Science and Technology*, 53(3), 1418–1423.
[17] Sharma, S., Mandal, A., Kant, R., Jachak, S., & Jagzape, M. (2020). Is Cinnamon Efficacious for Glycaemic

Control in Type-2 Diabetes Mellitus? *JPMA. The Journal of the Pakistan Medical Association*, 70(11), 2065–2069.

[18] Siró, I., Kápolna, E., Kápolna, B., & Lugasi, A. (2008). Functional food. Product development, marketing and consumer acceptance—A review. *Appetite*, 51(3), 456–467.

[19] Škrbić, B., & Cvejanov, J. (2011). The enrichment of wheat cookies with high-oleic sunflower seed and hull-less barley flour: Impact on nutritional composition, content of heavy elements and physical properties. *Food Chemistry*, 124(4), 1416–1422.

[20] Slima, S. Ben, Ktari, N., Trabelsi, I., Chouikhi, A., Hzami, A., Taktak, M. A., & Msaddak, L. (2021). Antioxidant Activities, Functional Properties, and Application of a Novel Lepidium Sativum Polysaccharide Cake Formulation.

[21] Soukoulis, C., Gaiani, C., & Hoffmann, L. (2018). Plant seed mucilage as emerging biopolymer in food industry applications. *Current Opinion in Food Science*, 22, 28–42.

[22] Stevens, N., & Allred, K. (2022). Antidiabetic Potential of Volatile Cinnamon Oil: A Review and Exploration of Mechanisms Using In Silico Molecular Docking Simulations. *Molecules*, 27(3), 853.

[23] Vácha, F., Stejskal, V., Vejsada, P., Kouřil, J., & Hlaváč, D. (2014). Texture profile analyses in tench (Tinca tinca L., 1758) from extensive and intensive culture. *Acta Veterinaria Brno*, 82(4), 421–425.

Effect of PSSS concentration on $CaCO_3$-ZnO Partical Size Distribution

Maher JAWAD KADHIM KADHIM [1], ***Muhammed Bora AKIN*** [2*]

[1] *The Ministry of Oil, Nassiryh, Iraq*

[2] *Faculty of Engineering, Department of Chemical Engineering, Çankırı Karatekin University, Çankırı, Turkiye*

Abstract

Calcium carbonate is a material abundant in nature. Its main areas of use are the rubber industry, paint industry, paper industry and plastic industry. Zinc oxide is also used in similar areas. Improvements in material properties can be achieved by producing two materials together as a composite. Similar composites were produced in different studies and their properties and application areas were examined [1,2].

In this study, the effect of PSSS initial concentrations on the size distribution of crystals that spontaneously form $CaCO_3$-ZnO composite at low temperatures was examined. The sizes of the obtained crystals in SEM analyzes were measured and used to create size distributions. (This study was prepared from the student's master's thesis.)

Keywords: *Composite, CaCO3, Calcium Carbonate, ZnO, Zinc oxide*

1. Introduction

$CaCO_3$-ZnO composites are used in various application areas. In a study by Yulianti et al. (2014), $CaCO_3$-ZnO nanospheres were synthesized as catalysts and then used in the transesterification of refined palm oil and compared with $CaCO_3$ and ZnO catalysts used alone [3]. Additionally, in a study examining the hemostatic properties and wound healing performance of the porous chitosan-$CaCO_3$ (CS-$CaCO_3$) composite material developed by He et al. (2021), it was found that the synthesized composite material reduced wound healing from 12 days to 9 days. This result shows that this type of composites also have a future in medical applications [4]. However, it may be possible to use $CaCO_3$-ZnO composites in possible industrial applications. In a study by Alomayri (2021), the performances of basalt fiber reinforced geopolymer composites containing nano $CaCO_3$ were evaluated. Basalt fiber reinforced geopolymer paste using 3% nano $CaCO_3$ has high compressive strength and hardness values. The use of 2% Nano $CaCO_3$ improves bending strength, impact strength and fracture toughness values. These results reveal that geopolymer composite pastes can be an alternative to Portland cement in the construction industry [5]. In the light of this information, it is understood that $CaCO_3$-ZnO composites can be used as catalysts, as biocompatible composites, in medical applications and in different industrial applications. By changing the properties and components of composite materials during production, they can be optimized according to the needs of the application areas.

In this study, PSSS was used as an additive, calcium chloride dihydrate (ACS reagent >99%), sodium carbonate (ACS reagent >99.5%), zinc nitrate hexahydrate (ACS reagent >99%) and sodium hydroxide (ACS reagent >98%). $CaCO_3$-ZnO was synthesized as a result of a spontaneous low-temperature reaction with) reactants [6], and the effect of different amounts of PSSS additive on the size distribution of the synthesized crystals was demonstrated. SEM analyzes of the obtained crystals were used to measure crystal sizes. Size distributions were derived from the measured values. It was found that there were changes in crystal size distribution by changing the amount of PSSS.

2. Materials and Methods

In the experiments, a magnetic stirrer heater (Heidolph MR Hei Tech) and a circulator cooled water bath (Polyscience) were used. Calcium chloride dihydrate (ACS reagent >99%), sodium carbonate (ACS reagent >99.5%), zinc nitrate hexahydrate (ACS reagent >99%) and sodium hydroxide (ACS reagent >98%) were used in the experiments. Supplied from Sigma. The reactions were carried out by chemical precipitation method in a jacketed glass reactor with a capacity of 1 liter. During the experiments, the temperature was kept constant at 25

* Corresponding author. *e-mail address: mbakin@karatekin.edu.tr*

°C using chilled water bath circulation. The stirring speed was set at 300 rpm and the initial pH was set at 10. After the reaction, the precipitate was filtered and dried in a vacuum oven at 100 °C for about 12 hours.

SEM analyzes of the produced materials were performed using a Carl Zeiss Sigma 300 VP field emission scanning electron microscope [6]. In the previous study, XRD analyzes showed that the materials produced in all experiments were $CaCO_3$-ZnO composites [6].

3. Results and Discussion

The distributions of the diameters of the composite crystals were made with at least 144 measurements from SEM photographs. The obtained measurements were graphed by making statistical calculations. In the experiment performed without using additives for control purposes, the average diameter of the synthesized composite was found to be 8.89 ± 3.82 µm. Under the same conditions, the minimum diameter was 2.71 µm and the maximum diameter was 21.83 µm (Figure 1).

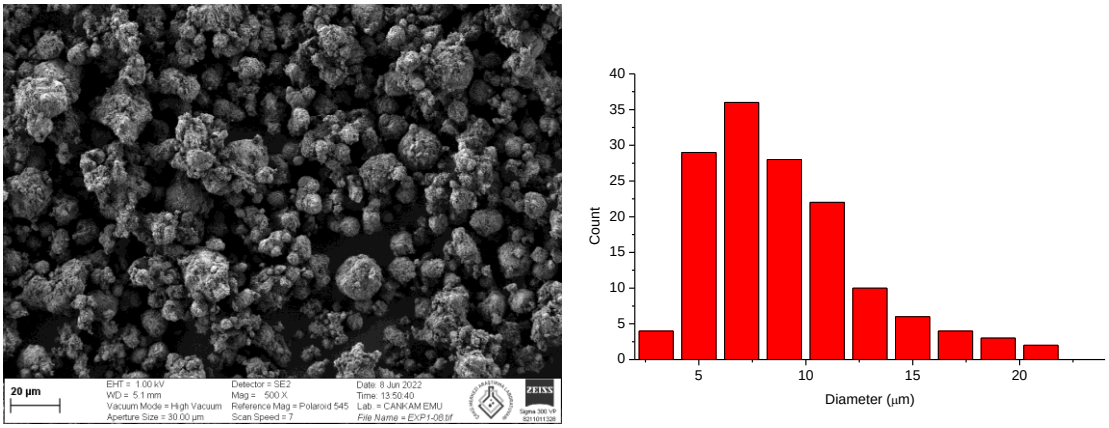

Figure 1. Morphology and size distribution of composite without additive

Figure 2 shows the SEM image of the composite produced in the experiments carried out in the presence of 5 ppm PSSS and the size distributions obtained. According to these results, the average diameter value was found to be 12.77 ±3.83 µm.

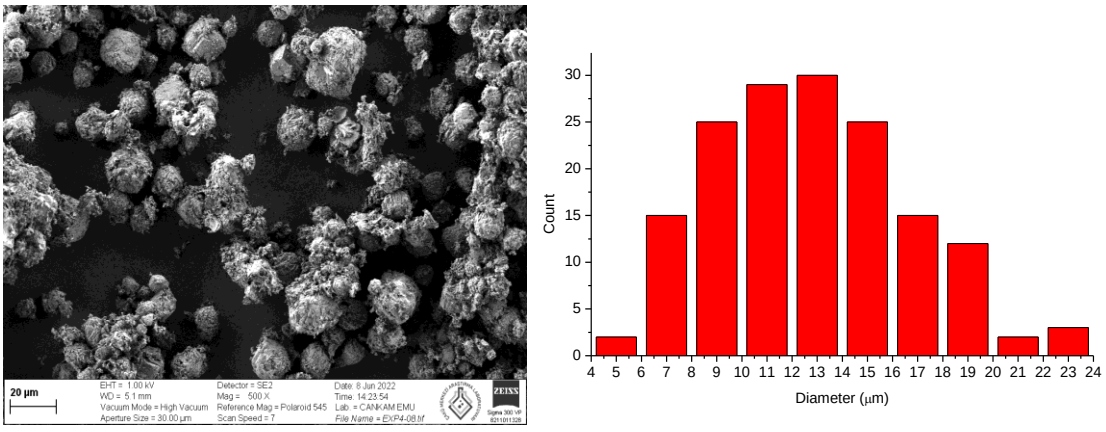

Figure 2. Morphology and size distiribution of synthesized composite in the presence of 5 ppm PSSS

Figure 3 shows the SEM image of the material produced in the presence of 50 ppm PSSS and the size distributions of the composite obtained by size analysis. The data show that the average diameter of the material is 11.12 ±3.17 µm. The minimum diameter was observed as 3.19 µm and the maximum diameter was 27.51 µm.

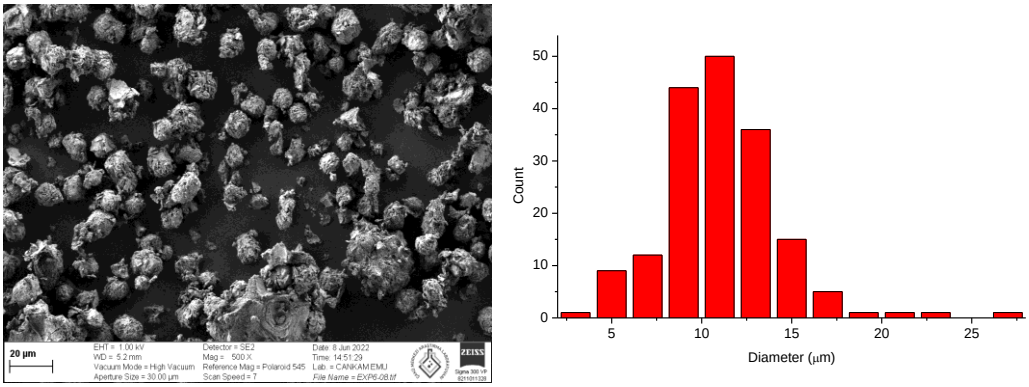

Figure 3. Morphology and size distiribution of synthesized composite in the presence of 50 ppm PSSS

The size distributions of the material produced in the presence of 150 ppm PSSS are shown in Figure 4. According to the statistical data obtained from the examination of the synthesized material, the average diameter was found to be 16.10 ±6.80 µm. The minimum diameter was measured as 4.79 µm and the maximum diameter was 37.47 µm.

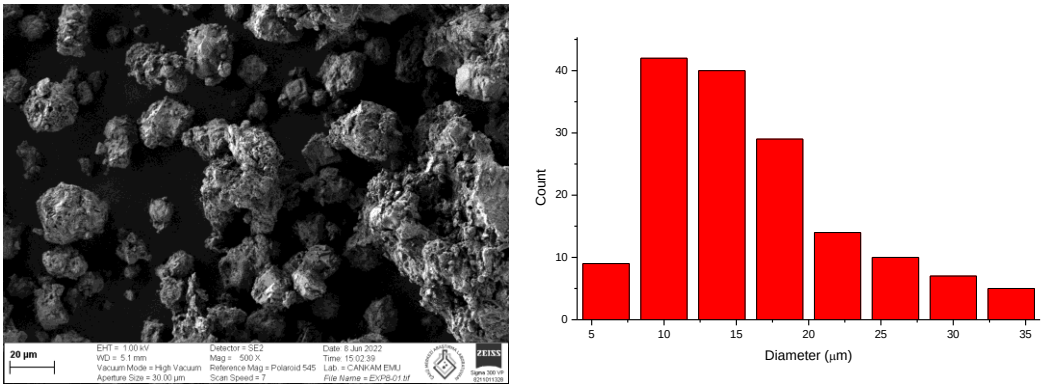

Figure 4. Morphology and size distiribution of synthesized composite in the presence of 150 mg/L PSSS

Data regarding the standard deviation, median, minimum and maximum values found when calculating the average diameter values as a result of the measurements are given in Table 1.

Table 1. Effect of PSSS concentration on dimensions

Initial PSSS Conc. (ppm)	N total	Mean (µm)	Sum	Minimum (µm)	Median (µm)	Maximum (µm)
Control	144	8.89 ± 3.82	2314.54	2.71	8.22	21.83
5	158	12.77 ± 3.83	3302.92	5.33	12.59	23.55
50	176	11.12 ± 3.17	3234.58	3.19	11.02	27.51
150	156	16.10 ± 6.80	3319.31	4.79	14.16	34.47

4. Conclusion

In this study, micron-sized calcium carbonate-zinc oxide composites were produced by spontaneous reaction using calcium chloride dehydrate, sodium carbonate, zinc nitrate hexahydrate and sodium hydroxide chemicals. Then, the measurements made from the SEM photographs were subjected to statistical analysis and size distributions were found. By examining these values, it was found that the average diameter values increased with the increase in the presence of PSSS in the experiments. It was observed that ZnO crystals were present in

nano size on the measured composite. It is planned to carry out studies to examine these crystals' sizes in the future.

Acknowledgement

All experimental work was conducted in the Chemical Engineering Department Laboratory at Çankırı Karatekin University. The authors would like to thank the Chemical Engineering Department.

References

[1] Shifu Chen Yunguang Yang, M.J., Liu, W. (2011). Preparation, characterisation and activity evaluation of CaCO3/ZnO photocatalyst. J Exp Nanosci 6: 324–36. https://doi.org/10.1080/17458080.2010.509873.

[2] Kumar, L.S., Shantha, V., Naik, C., Drakshayani, D.D.N., Kataraki, P.S., Janvekar, A.A., et al. (2020). Synthesis of calcite-zincite nano composite materials using sol-gel auto combustion method. IOP Conf Ser Mater Sci Eng 1003.

[3] Yulianti, C.H., Ediati, R., Hartanto, D., Purbaningtias, T.E., Chisaki, Y., Abdul Jalil, A., et al. (2014). Synthesis of CaOZnO Nanoparticles Catalyst and Its Application in Transesterification of Refined Palm Oil. Bull Chem React Eng Catal 9: 100–10. https://doi.org/10.9767/bcrec.9.2.5998.100-110.

[4] He, W., Huang, X., Zhang, J., Zhu, Y., Liu, Y., Liu, B., et al. (2021) CaCO3–Chitosan Composites Granules for Instant Hemostasis and Wound Healing. Materials (Basel) 14:3350. https://doi.org/10.3390/ma14123350.

[5] Alomayri, T. (2021). Performance evaluation of basalt fiber-reinforced geopolymer composites with various contents of nano CaCO3. Ceram Int 47: 29949–59. https://doi.org/10.1016/j.ceramint.2021.07.169.

[6] Jawad Kadhim Kadhim, M., Akın, M. B. (2022). Production and Characterization of Nano-Sized Calcium Carbonate-Zinc Oxide Composites. 1st Int. Karatekin Sci. Technol. Conf., Çankırı, p. 160–4.

Investigation of in Vitro Effects of Some Antibiotics on Chicken Heart Glutathione S-Transferase Enzyme Activity

Suat ZOR[1], ***Mehmet ÇİFTCİ***[2,*]

[1]*Batman University, Social Sciences Vocational School, Batman, Türkiye*

[2]*Bingol University, Faculty of Veterinary Science, Bingol, Türkiye*

Abstract

Glutathione S-transferase enzyme (GST; EC 2.5.1.18) is a very important antioxidant enzyme that plays important functions in living metabolism. Glutathione S-transferases have been identified as a Phase-II detoxification enzyme family. Xenobiotics, which originate from exogenous or endogenous sources, transform into metabolites with lower toxicity that are easily excreted from the living organism as a result of Phase II reactions. During this event, GST takes part in reactions that enable the conjugation of glutathione with many metabolites that may cause toxicity.

This study was carried out in two stages. First of all, the GST enzyme was purified and then the in vitro effects of some antibiotics on the purified GST enzyme activity were examined. GST enzyme was purified from chicken heart tissue by preparation of homogenate, ammonium sulfate precipitation and glutathione-agarose affinity chromatography. In the kinetic studies conducted with the purified GST enzyme, it was determined that the antibiotics amoxicillin, cefuroxime sodium and cefazolin sodium had an inhibitory effect on the enzyme. Activity%-[I] graphs were drawn with the data obtained as a result of the kinetic studies, and the IC50 values for the antibiotics in question were calculated as 0.66, 2.07 and 2.09 mM, respectively.

Keywords: *Glutathione S-transferase, Antibiotic, Inhibition*

1. Introduction

Living organisms encounter endogenous or exogenous substances containing toxicity throughout their life processes. They carry out their defense mechanisms against such harmful substances through their detoxification systems. Thus, xenobiotics that form in the body of the living thing or enter the body from outside are detoxified. To get rid of harmful substances, there are reactions called Phase I, Phase II and Phase III. The GST enzyme is involved in Phase II reactions. GST can bind with many organic anions to carry out detoxification reactions with compounds arising from endogenous and exogenous sources [1]. As a result of phase II reactions, the living organism is protected from the attacks of electrophilic substances with very high toxicity [2]. GST binds glutathione (GSH) and its substrate by bringing them closer together in its active site [3]. In this case, the sulfhydryl group on GSH becomes active and the aggressive electrotrophic substrate reacts with GSH [4].

GSH is endogenously synthesized in the liver through anabolic pathways using glutamic acid, cysteine and glycine [5]. Reduced glutathione (GSH) is a thiol-containing tripeptide of low molecular weight that is found in almost all living cells [6]. Glutathione (GSH) is considered an antioxidant because it eliminates free radicals such as H2O2, which cause serious damage to tissues, and eliminates the effects of reactive oxygen species (ROS) that cause damage to tissues [7]. The GSH/GSSG ratio is approximately 500 in erythrocytes. If a decrease in GSH level is observed, the onset and progression of many degenerative diseases are observed [8]. For example, aging causes symptoms of many diseases, including diabetes, renal failure, pneumonia, malignancy, amyotrophic lateral sclerosis, Parkinson's, Alzheimer's, and cataracts [9].

The aim of this study is to examine the effects of antibiotics such as amoxicillin, cefazolin sodium and cefuroxime sodium on GST enzyme activity.

2. Materials and Methods

2.1. Procuring Chicken Heart and Preparing the Homogenate

The chicken hearts used in the experiments were obtained from Bingöl Meat and Milk Institution in accordance with the cold chain rules and kept in the deep freezer at -20°C. To prepare the homogenate solution, the frozen

* *Corresponding author. e-mail address: mciftci@bingol.edu.tr*

heart was cut into small pieces, 5 g of chicken heart was taken and 3 times the amount of homogenate buffer was added. The homogenate, which was made homogeneous using a homogenizer, was placed in Ependorf tubes and centrifuged at 13,000 x g for one hour. The precipitate was separated and homogenate was obtained. These processes were carried out at +4 °C.

2.2. Purification of the Enzyme and Determination of Activity

The enzyme sample was applied to the glutathione agarose affinity column equilibrated with 10 mM KH2PO4 and 0.1M KCl, pH: 8.0 buffer. Gradient elution was performed to obtain the enzyme pure. The solution for the prepared elution was created from a solution containing 50 mM Tris-HCl and (1.25-10 mM, pH: 9.5) GSH. The activities of the obtained eluates were measured on a spectrophotometer set to 340 nm wavelength. Enzyme activity was performed according to the method used by Habig et al. [10].

2.3. Kinetic Studies

To prepare the IC_{50} chart, the activity value of the purified enzyme was measured as a control in the inhibitor-free environment. This measured value was accepted as 100%. Afterwards, IC50 values were calculated by measuring the values of antibiotics at different concentrations. These concentration values; for cefuroxime sodium; 0.896, 1.792, 4.48 and 8.96 mM, 0.419, 0.838, 1.676, 4.19 and 8.38 mM for cefazolin sodium, 0.228, 0.456, 0.912, 1.14, 1.368 and 1,596 mM for amoxicillin. The graphic equation was obtained by creating % Activity-[I] concentration graphs with these concentration values obtained. IC_{50} values were calculated using this equation.

3. Results and Discussion

In the study, GST enzyme was purified from chicken heart tissue according to the processes mentioned above. In the kinetic study, % Activity - inhibitor concentration graphs were drawn for the antibiotics amoxicillin, cefuroxime sodium and cefazolin sodium, which inhibit enzyme activity, and Figure 1, Figure 2 and Figure 3 were created. With the help of these graphs, IC_{50} values for the antibiotics amoxicillin, cefuroxime sodium and cefazolin sodium were calculated as 0.66, 2.07 and 2.09 mM, respectively. These values are shown in Table 1.

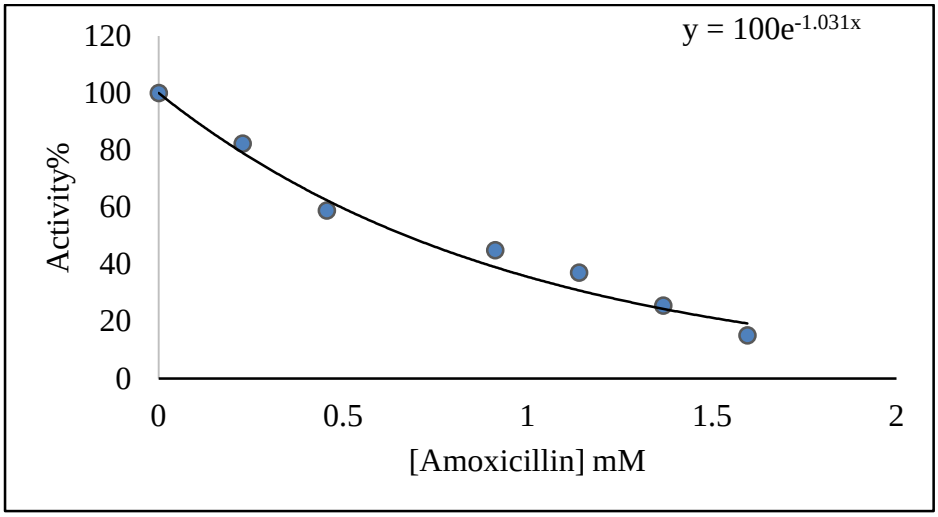

Figure 1. Effect graph of amoxicillin antibiotic on GST enzyme activity

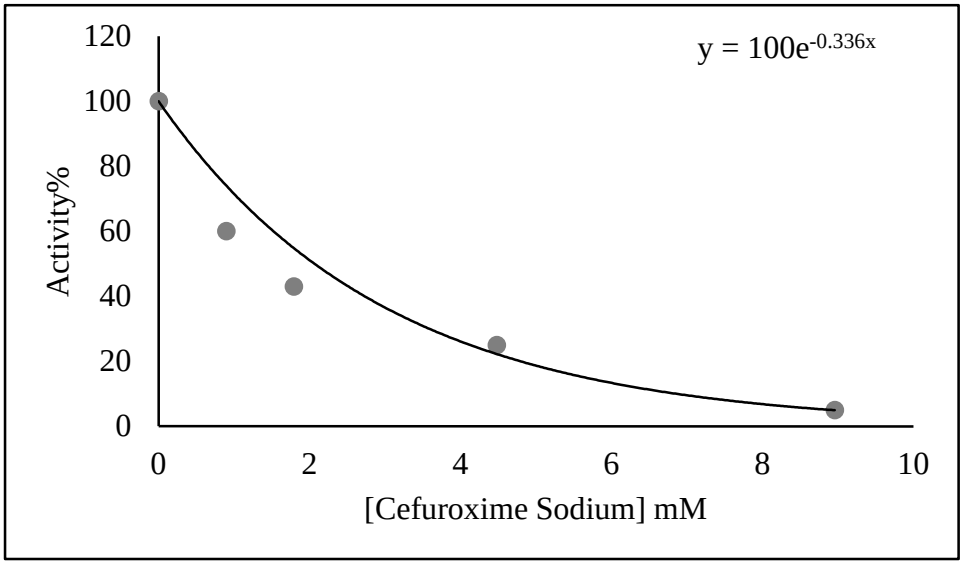

Figure 2. Effect graph of cefuroxime sodium antibiotic on GST enzyme activity.

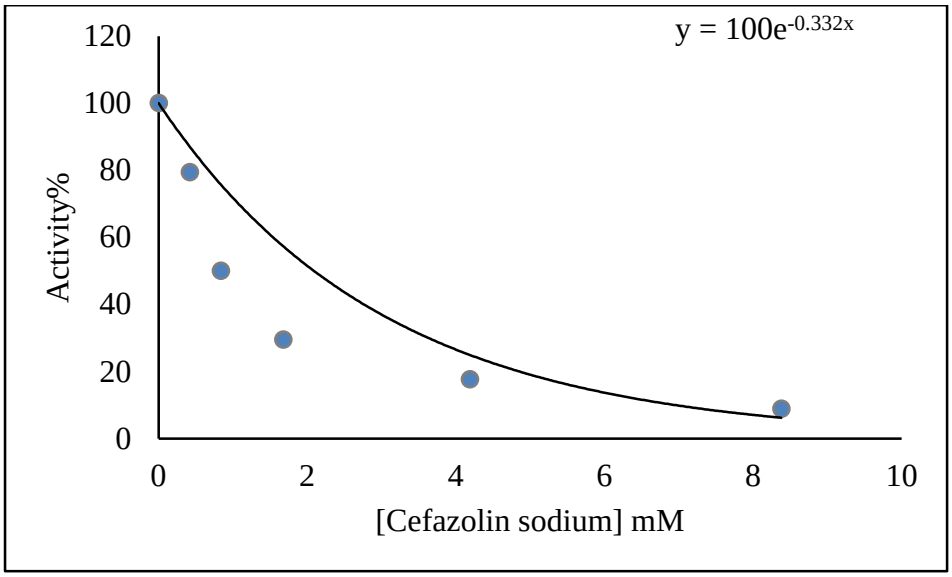

Figure 3. Effect graph of cefazolin sodium antibiotic on GST enzyme activity

Table 1. Effects of antibiotics on GST enzyme activities

Antibiotic	**IC_{50} (mM)**
Amoxicillin	0.66
Cefuroxime sodium	2.07
Cefazolin sodium	2.09

Today, many different substances have been identified that activate and inhibit the GST enzyme. Scientific studies have been conducted showing that while some of these are cations, most of them are drugs. In a study conducted by Casalino et al., the effects of Cd^{+2} and Mn^{+2} heavy metal cations on the activity of the GST enzyme isolated from rat liver tissue were examined. The rat was given 2.5 mg/kg $CdCl_2$ or 2.0 mg/kg $MnCl_2$ salts as a single dose. As a result, it was measured that the enzyme activity increased by approximately 36% one day after the experiment [11]. Türkanoğlu examined the GST enzyme activity purified from human blood serum with some

metal cations. As a result of the research, it was reported that Cd^{+2}, Hg^{+2} and Ni^{+2} cations reduced the activity of the GST enzyme [12]. Again, Chun-hua Zhang and his colleagues examined the effect of Cd^{+2} cation on the activity of GST purified from rice. As a result of the study, it was revealed that Cd^{+2} cation inhibits the enzyme [13]. In their study, Türkan and his colleagues isolated GST enzymes from the liver, heart muscle and kidney tissues of the albino rat species and examined the in vivo effects of the antibiotics cefuroxime sodium and cefoperazone sodium on this enzyme. They found that enzyme activity decreased seven hours after drug use [14]. In their study, Bayindir et al. examined the effects of gentamicin and clindamycin on GST enzyme activity isolated from rat erythrocyte tissue in vitro and calculated IC_{50} values. As a result of the experiment, it was reported that both antibiotics inhibited the enzyme. As a result of the experiment, IC_{50} values were found to be 1.69 and 6.9 mM, respectively [15].

4. Conclusion

In this study, the in vitro effects of antibiotics such as cefuroxime sodium, cefazolin sodium and amoxicillin on the GST enzyme isolated from chicken heart tissue were examined and IC_{50} values were calculated. Experimental results showed that these antibiotics inhibited enzyme activity. IC_{50} values of amoxicillin, cefuroxime sodium and cefazolin sodium were calculated as 0.66, 2.07 and 2.09 mM, respectively. Today, the therapeutic properties of antibiotics against bacterial infections have been demonstrated by many studies. However, the dose factor is very important in drug use. It is recommended that IC_{50} values be taken into consideration when using antibiotics whose kinetic effects on GST are examined.

References

[1] Rebbeck, T. R. (1997). Molecıılar Epidemiology of the Human Glutathione S-Transferase Genotypes GSTM1 and GSTT1 in Cancer Susceptibility, Cancer Epidemiology, Biomarkers and Prevention, 6(9), 733-743.

[2] Awasthi, Y. C., Dao, D. D., and Saneto, R. P. (1980). Interrelationship between anionic and cationicforms of glutathione S-transferases of human liver. Biochem J., 191(1): 1-10.

[3] Eaton, D. L., and Bammler, T. K. (1999). Concise review of the glutathione S-transferases and their significance to toxicology. Toxicol Sci. Jun; 49(2), 156-64.

[4] Armstrong, R. N. (1997). Structure, Catalytic Mechanism, and Evolution of the Glutathione Transferases. Chem. Res. Toxiol., 10(1), 2-18.

[5] Lu, S. C., 2009. Regulation of glutathione synthesis. Molecular aspects of medicine, 30(1-2), 42-59.

[6] Meister, A., Anderson, M. E., (1983). Glutathione, Annual Review of Biochemistry, 52, 711-760.

[7] Giblin, F. J. (2000). Glutathione lens transparency: cataracts. J Ocul Pharmacol Ther.16:121–135.

[8] Flagg, E. W., Coates, R. J., and Jones, D. P. (1994). Dietary glutathione intake and the risk of oral and pharyngeal cancer. Am J Epidemiol. 139:453–465.

[9] Ballatori, N., Krance, S. M., Notenboom. S., Shi, S., Tieu, K., and Hammond. C. L. (2009). Glutathione dysregulation and the etiology and progression of human diseases. Biol. Chem. 390, 191–214.

[10] Habig WH, Pabst MJ, Jakoby WB. Glutathione STransferases. Journal of Biological Chemistry. 1974 Nov;249(22):7130–9.

[11] Casalino, E., Sblano, C., Landriscina, V., Calzarettı, and G., Landriscina. C. (2004). Rat Liver Glutathione S-transferase Activity Stimulation Following Acute Cadmıum or Mangenese İntoxication. Toxicology, 200, 29-38.

[12] Türkanoğlu, A. (2007). Human Serum Arylesterase And Glutathıone S-transferase actıvıtıes in patıents wıth ıschemıc stroke compared to healthy controls. Approval of the Thesis Master of Science in Biochemistry Department, Middle East Technical University. Ankara.

[13] Chun-hua, Z., W. Ze-ying, J., and Ting, G. (2013). Purification and Identification of Glutathione S-transferase in Rice Root under Cadmium Stress. Ying, Rice Science, 20(3), 173-178.

[14] Türkan, F., Huyut, Z., Taslimi, P., Huyut, M. T., & Gülçin, İ. (2020). Investigation of the effects of cephalosporin antibiotics on glutathione S-transferase activity in different tissues of rats in vivo conditions in order to drug development research. Drug and Chemical Toxicology, 43(4), 423–428.

[15] Bayindir, S., Temel, Y., Ayna, A., & Ciftci, M. (2018). The synthesis of N-benzoylindoles as inhibitors of rat erythrocyte glucose-6-phosphate dehydrogenase and 6- phosphogluconate dehydrogenase. Journal of Biochemical and Molecular Toxicology, 32(9), 1–9. https://doi.org/10.1002/jbt.22193.

Synthesis of Graphene Oxide by Hummers Tour Method and Reduced Graphene Oxide by Chemical Reduction Method

Haluk KORUCU [1] *Esra YILMAZ MERTSOY* [1] *Mohammad Ruhul Amin BHUİYAN* [2]

[1] *Department of Chemical Engineering, Faculty of Engineering, Çankırı Karatekin University, Uluyazı, Çankırı 18100, Turkey*
[2] *Department of Electrical and Electronic Engineering, Islamic University, Kushtia 7003, Bangladesh*

Abstract

The purpose of this work was to compare the effectiveness of synthetic graphene oxide synthesis using the Hummers Tour technique from graphite and reduced graphene oxide synthesis using sodium boron hydride and ascorbic acid in the Chemical reduction method from synthesized graphene oxide. FTIR structure characterization, BET surface area measurement, Zeta Potential, and particle size distribution investigations were carried out for the synthesis of reduced graphene oxide and graphene oxide. The graphene oxide and reduced graphene oxide synthesis is successful, as can be seen from the FTIR graphs. The graphene oxide sample shows a BET surface area improvement rate of 76.64%. Because graphene oxide is hydrophilic, it can be readily dissolved in water, which has improved its Zeta Potential property by 114%. This provided a sample of reduced graphene oxide with a 41% increase in rag size due to the synthesis of sodium boron hydride. Sodium boronhydride performed better than ascorbic acid in manufacturing reduced graphene oxide. However, ascorbic acid is even better when its reduction performance is evaluated in terms of expenses and eco-friendly manner.

Keywords: *Graphene Oxide,Reduced Graphene Oxide, Hummers TOUR Method, Chemical reduction method*

1. Introduction

Graphene oxide (GO) is commonly synthesized through methods such as the Hummers' method. In this approach, natural graphite is oxidized with a mixture of strong acids, typically sulfuric acid and potassium permanganate. The resulting graphene oxide contains oxygen-containing functional groups such as hydroxyl, epoxy, and carboxyl, imparting hydrophilicity to the material [1]. GO serves as a precursor for various applications due to its dispersibility in water and the ease with which it can be functionalized. However, for certain applications where enhanced electrical conductivity and reduced oxygen content are crucial, GO is further subjected to a reduction process to produce reduced graphene oxide (rGO) [2].

The reduction of graphene oxide is often achieved through chemical or green reduction methods. Chemical reduction commonly employs agents like hydrazine or hydroiodic acid to remove oxygen groups and restore graphene-like properties [3]. On the other hand, green reduction methods utilize environmentally friendly agents such as ascorbic acid or green tea extract, offering a safer and more sustainable approach. These reduction processes lead to the formation of reduced graphene oxide with improved electrical conductivity while retaining some of the inherent properties of graphene, making it suitable for applications in sensors, energy storage devices, and other advanced technologies [4].

In the literature, studies using hydrazine and hydrazine hydrate for the reduction of graphene oxide have been conducted. However, these chemicals are known to be highly toxic and explosive, requiring extensive precautions when used in large quantities. Therefore, there is a search for a more environmentally friendly and non-toxic reducing agent to convert graphene oxide to reduced graphene oxide. L-ascorbic acid (L-AA), with its mild reduction capability and non-toxic nature, is used as the primary reducing agent for converting graphene oxide to reduced graphene oxide. Importantly, compared to traditional reducers used in GO reduction, such as hydrazine and hydrazine hydrate, L-AA itself and its oxidized products are environmentally friendly [5] In the reduction process, ascorbic acid serves as a mild and environmentally friendly reducing agent for GO. Its non-toxic nature and ability to efficiently reduce graphene oxide while minimizing environmental impact make it an attractive choice. Additionally, ascorbic acid introduces oxygen-containing functional groups, enhancing the hydrophilicity and reactivity of the resulting reduced graphene oxide (rGO). Sodium borohydride, another green reducing agent, is employed in the reduction of GO to rGO. It offers advantages in terms of being a mild and selective reducing agent. The reduction process with sodium borohydride generates fewer by-products and is less environmentally harmful compared to traditional methods using hazardous chemicals [6].

In this study, graphene oxide synthesis using the Hummers method and subsequent chemical reduction using ascorbic acid and sodium borohydrate were performed. The reduced graphene oxide samples were analyzed by different characterization techniques such as zeta potential measurement and particle size distribution analysis, FTIR analysis, surface area measurement.

2. Materials and Methods

This work will use the produced graphene oxide sample to carry out reduced graphene oxide production and graphene oxide synthesis from graphite using the Hummers method. Ascorbic acid and sodium boron hydride will be used in the chemical reduction process to create reduced graphene oxide. All synthesized materials will undergo surface area analysis using the BET technique and structure characterization by FTIR spectrum scanning. The graphite Hummers Tour method involved circulating water in a double-walled glass reactor to maintain a temperature of 5°C. Ten grams of graphite samples were combined with 30 grams of $KMnO_4$ 100 milliliters of H_2SO_4 and 10 milliliters of H_3PO_4. The mixture was then left to work for sixteen hours. After raising the reaction temperature to 95°C and mixing for six hours, 100 milliliters of distilled water was added to the combinations. The mixture was allowed to cool at the end of the reaction period, and 10 milliliters of H_2O_2 and 10 milliliters of HCl acid were added to them to stop the process. Until the Ph was 3, each experimental solution was cleaned using the decantation method. The samples underwent the final steps of centrifugation, washing, and oven drying at 60°C. After adding five grams of sodium boronhydride and ascorbic acid to two grams of manufactured graphene oxide sample, tests were carried out for twenty-four hours at ninety degrees Celsius in order to synthesize reduced graphene oxide. After the experiment was over, the samples were cleaned one last time with ethyl alcohol and acetone until their pH reached 7. After that, they were dried in a vacuum oven set at 70 °C. The quality standards that were established for the characterization of samples of reduced and graphene oxide are listed in Table 2.1.

Table 2.1 Quality criteria of the graphene oxide and reduced graphene oxide

Quality Criteria	Symbol	Explanation	Information	The goal for GO	The goal for RGO
1	FTIR	Characatarizaton of the structure	Functional groups		
2	PB	Particle Size	Feature improvement	Larger is better	Larger is better
3	ZP	Zeta Potential	Stable distribution	Smaller is better	Larger is better
4	BET	Surface Area	Degree of porosity	Larger is better	Larger is better

3. Results and Discussion

Figure 3.1 The FT-IR analysis pattern in the synthesized graphene oxide samples shows that the vibration peak C=O at 1721 cm^{-1}, the vibration and deformation peaks of the O-H groups 3391 cm^{-1} and 1410 cm^{-1}, the stress peak C-O at 1221 cm^{-1}, the stress peak C-O at 1046 cm^{-1}, and the stress peak C=C at 1680 - 1620 do not belong to the graphite structure [9]. In contrast, when observed in cm^{-1}, it was found that in the synthesis of reduced graphene oxide, for sodium boron hydride and ascorbic acid, the peaks formed by the synthesis of graphene oxide have largely disappeared and take on an appearance similar to that of graphite. The FTIR analysis results indicate that the synthesis of reduced graphene oxide utilizing sodium boron hydride and ascorbic acid by the chemical reduction method, as well as the synthesis of graphene oxide from graphite by the Hummers-TUOR method, have both been successful [6].

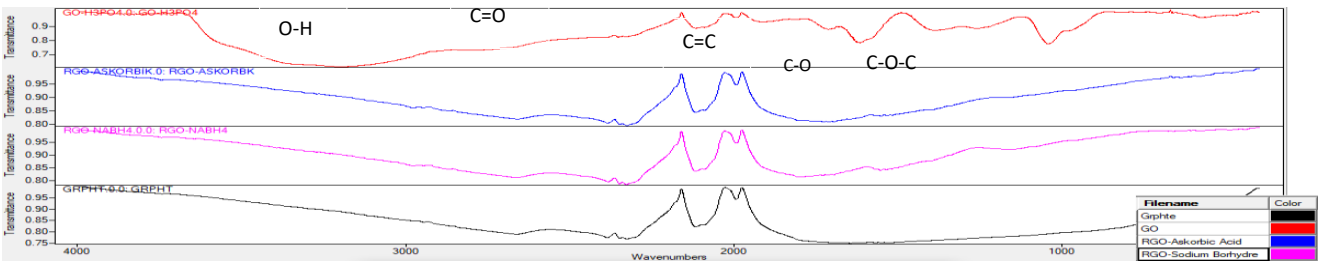

Fig 3.1. FTIR images of graphite samples of different purity

BET surface area measurements of graphite, graphene oxide, and reduced graphene oxide samples are shown in Figure 3.2.The synthesis mechanism of reduced graphene oxide and graphene oxide is predicted to improve surface areas from graphite. The maximum surface area is desired in the manufacture of reduced graphene oxide and graphene oxide.Surface areas increased during the synthesis of graphene oxide from graphite, but decreased during the production of reduced graphene oxide in comparison to graphene oxide. The creation of a porous structure is responsible for the huge surface area; however, contaminants may have closed the pores in the decreased graphene oxide samples, preventing an increase in surface area from being seen.

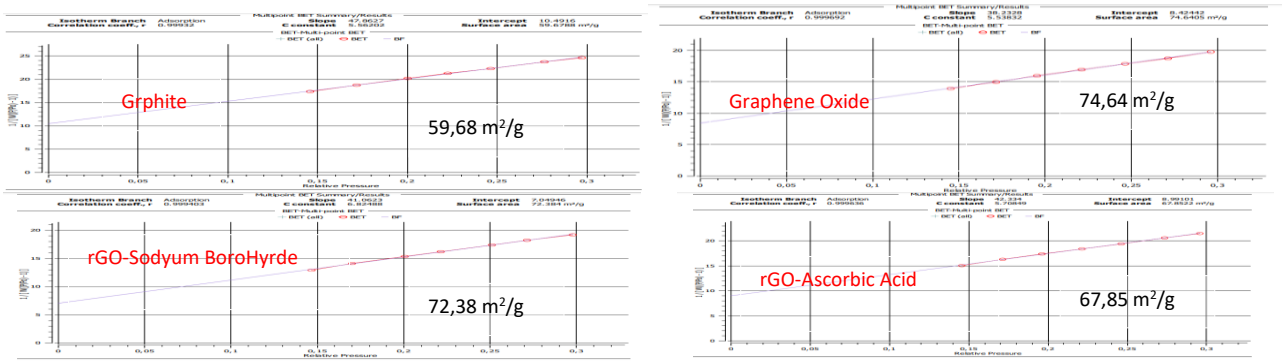

Fig 3.2. BET images of experimental samples

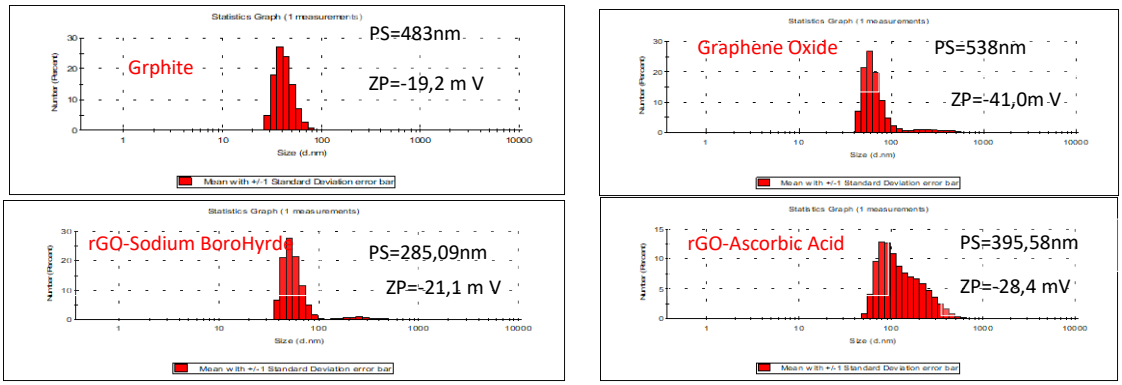

Fig 3.3. Zeta sizer and Particle size results of experimental samples

Figure 3.3 displays the findings from the investigation of particle size and Zeta Potential. The zeta potential values have decreased negatively as a result of graphene oxide's hydrophilic and water dispersible characteristics. However, the reduced graphene oxide structure, which is inimical to water, results in a negative increase in Zeta Potential values. Graphene oxide and reduced graphene oxide exhibit opposite-directional properties in their Zeta Potential target values. Because of this, the zeta potential value of graphene oxide was used to calculate recovery rates rather than graphite as the reference criterion for the synthesis of reduced graphene oxide. Better results in terms of particle size values were obtained in the sample of sodium boron hydride and in the production of reduced graphene oxide. Reduced graphene oxide production is anticipated to perform better than graphene oxide and graphite due to the particle size and surface area. The recovery rates are provided in Table 3.1 with reference to the synthesized graphite sample of graphene oxide samples.

Table 3.1 Recovery rates between graphene oxide and reduced graphene oxide samples

Answers	Ref[a] Grphite	GO	rGO-Askorbic Acid	rGO-Sodium Bprhydre	Recovery Rate GO-(%)	Recovery Rate rGO-Askorbic Acid (%)	Recovery Rate rGO-Sodium Bprhydre (%)
BET (SA-m²/g)	59,68	74,64	67,85	72,38	25[b]	13,7	**21,3**
ZP (ZP-mV)	-19,2	**-41**	**-28,4**	**-21,1**	113,5	30,7	**48.5**
ZP (PS-nm)	483	538	396	285	-11.4	18	**41**

Calculation of the % recovery rate of the experiment performed reference graphite

[b] *((74,64-59,68) / 59,68)*100 =25.06 (plus value means improvement)*

Because of this, the zeta potential value of graphene oxide was used to calculate recovery rates rather than graphite as the reference criterion for the synthesis of reduced graphene oxide. Better results in terms of particle size values were obtained in the sample of sodium boron hydride and the production of reduced graphene oxide. Reduced graphene oxide production is anticipated to perform better than graphene oxide and graphite due to the particle size and surface area. The recovery rates are provided in Table 3.1 regarding the synthesized graphite sample of graphene oxide samples. While a little rise in the synthesis of graphene oxide has been observed, a drop in particle size values is anticipated in the synthesis of reduced graphene oxide and graphene oxide from graphite. The analysis's findings demonstrated the effectiveness of both the chemical reduction approach and the Hummers method for synthesizing graphene oxide. Ascorbic acid is more advantageous for use due to its cost-effective and environmentally friendly nature, even if sodium boron hydride yields more successful outcomes with reduced graphene oxide.

Acknowledgment

This research was carried out with the support of the Scientific Research Project (MF081123B33) funded by Çankırı Karatekin University. Authors thank to Çankırı Karatekin University, Scientific Research Project Management Unit (ÇAKÜ-BAP).

References

[1] Hummers WS Jr, Ofeman RE (1958) Preparation of graphitic oxide. J Am Chem Soc 80:1339–1339

[2] De Silva K.K.H., Huang H.H., Yoshimura M. 2018. Progress of reduction of graphene oxide by ascorbic acid., Applied Surface Sicence 447,338-346

[3] Kanishka Desilva K.H., Huang H.H. and Yoshimura M., 2018. Progress of reduction of graphene oxide by ascorbic acid, Applied Surface Sceince 447,338-346

[4] F. Farjadian *et al.*, "Recent Developments in Graphene and Graphene Oxide: Properties, Synthesis, and Modifications: A Review," *ChemistrySelect*, vol. 5, no. 33, pp. 10200–10219, 2020, doi: 10.1002/slct.202002501.

[5] Surekha, G., Krishnaiah, K. V., Ravi, N., & Suvarna, R. P. (2020, March). FTIR, Raman and XRD analysis of graphene oxide films prepared by modified Hummers method. In Journal of Physics: Conference Series (Vol. 1495, No. 1, p. 012012). IOP Publishing.

[6] Das, B., Kundu, R., & Chakravarty, S. (2022). Preparation and characterization of graphene oxide from coal. Materials Chemistry and Physics, 290, 126597.

Optically Transparent FSS-Based Absorber for Electromagnetic Shielding in 5G Applications

Ömer Faruk GÜNAYDIN[1,*], ***Sultan CAN***[2]

[1] *Institute of Science, Engineering, Electrical and Electronics, Ankara University, Ankara, Turkey*

[2] *Institute of Science, Engineering, Electrical and Electronics, Ankara University, Ankara, Turkey*

Abstract

In this study, a frequency selective surface (FSS)-based absorber that can be used in 5G applications is proposed. The FSS-based absorber is designed to shield 3.5 GHz, the most used frequency in 5G applications. The purpose of the application is to create an electromagnetic shield for the 3.5GHz frequency and to protect devices that can be used at this frequency from electromagnetic interference. Parametric analysis is conducted employing three-dimensional full-wave electromagnetic simulation software (CST Studio Suite®). This analysis aims to verify the suitability of the chosen ground thickness and FSS pattern in meeting the specified frequency requirements. Simulation results indicate that both the ground line thickness and the diameter of the circular ring play pivotal roles in shaping the frequency characteristics of the frequency selective surface. In the design of the FSS-based absorber, transparent PVC with a dielectric constant of 2.77 was used as the dielectric material and copper as the conductor. The measurements taken from the fabricated sample were aligned with the simulation outcomes, showcasing a consistent agreement between the two sets of data.

Keywords: *Frequency selective surface, Absorber, Electromagnetic shielding, Electromagnetic interference, 5G applications*

1. Introduction

Metamaterials are a new class of functional materials designed around macro- and nanoscale patterns or structures that cause them to interact with light and other forms of energy in ways not found in nature[1]. They are artificial materials that can achieve electromagnetic properties that do not occur naturally, such as a negative refractive index or electromagnetic cloaking. These artificially engineered composite materials derive their properties from internal micro- and nanostructures rather than the chemical composition found in natural materials[2]. Their shape, geometry, size, orientation and arrangement give them properties that can manipulate electromagnetic waves. They can be used more efficiently than traditional materials by blocking, absorbing, enhancing or bending electromagnetic waves. The two-dimensional or surface counterpart of metamaterial are called metasurface[3]. It is also called metafilm in the literature [4]. Metasurface is defined as periodic structures in which the thickness and periodicity of unit cells are smaller than the wavelength[3-5]. Frequency selective surface(FSS) is a periodic surface with identical two-dimensional arrays of elements arranged on a dielectric substrate[6]. They are frequently used in communication systems for spectral filtering. FSS are designed to reflect, transmit and absorb electromagnetic fields depending on the frequency of the field[7].

Manipulation of electromagnetic waves(EM) is one of the important topics in modern optics and photonics[8]. Conventional materials generally use properties of light such as propagation and refraction to manipulate EM waves, meaning their ability to manipulate the waves is limited[9]. Metasurfaces which have unique abilities to block, absorb, concentrate, scatter, or direct the waves have emerged as an alternative application for controlling EM waves[10-11]. The amplitude, phase or polarization of EM waves can be easily controlled by changing the structural parameters of the metasurface or the constituent materials of the meta-atoms that make up the metasurface[12]. Electromagnetic emissions have the potential to impact the operation of electronic devices, electrical systems, and radio frequency (RF) systems. Due to the inherent nature of circuit electricity, virtually all electronic devices emit a certain degree of electromagnetic radiation.

Absorbers are materials that are used to attenuate/absorb signals up to a specific frequency when passed through an absorbing material and they are designed and shaped to absorb incoming electromagnetic radiation. Metamaterial absorbers have found a lot of use in the stealth technology due to their features such as ease of production, easy design and good, broadband absorption. Also there are many studies in the literature where metamaterials are used as radio frequency absorbers[13-14]. Parameters such as frequency range, surface

* Corresponding author. *e-mail address: ofgunaydin.@ankara.edu.tr*

resistance, operating temperature, form factor and thickness play an active role in determining the design of a metamaterial-based radio freaquency(RF) absorber. RF absorbers are critical in a variety of applications across multiple industries. For example, in aerospace and defense, RF absorbers are used in the design and testing of radar systems and stealth technologies. In the telecommunications sector, RF absorbers help prevent interference in signal transmission, improving the quality and reliability of communication networks[8-15]. Metamaterial absorbers are used to improve the isolation of antennas. Radiated power from nearby antennas, coupled through radiation and passing through the common ground plane, can be absorbed by absorber structures. And so the unwanted power between the antennas is isolated, which improves the quality of the communication[15].

In this study, FSS-based absorber is presented to provide electromagnetic shielding in 5G applications. Electromagnetic (EM) shielding offers a reliable method for safeguarding delicate electronic devices against electromagnetic interference (EMI), serving as a spatial filter to block specific frequency ranges. While many FSS-based EM shielding structures are devised to reflect incoming waves, this reflective approach can potentially create EMI issues for nearby devices and equipment, especially in densely populated electronic environments. On the contrary, absorptive FSS shielding presents a viable solution in such settings, offering an effective alternative that mitigates these concer. The study focused on 3.5GHz (n77), which is the most used 5G band. Transmission of other frequency bands is allowed. The aim of the study is to minimize the effect of electromagnetic interference on devices operating with the 5G frequency band 3.5GHz, which is widely used today.

2. Materials and Methods

In the unit cell structure proposed in this study, transparent PVC, a dielectric material, is used as the substrate material and copper is used as the conductor material. The transparent PVC was cut according to the dimensions of the WR229 waveguide used in the measurements. Copper tape was used in the production of the conductive material. The 2D drawing of the proposed design was drawn in Autocad with actual dimensions. This 2D drawing and the copper tape were sent to the printer at the same time and the drawing was made on the copper tape. Thus, the required conductive parts were cut according to the reference drawing on the copper tape. The cut conductive copper patches were glued to the actual position on the transparent PVC. After production was completed, the dimensions of the design were tested with the WR229 waveguide. Minor problems caused by production were resolved using waveguide. Simulation studies and parameter analyzes for the designed model were carried out using the CST Microwave Studio program.

3. Results and Discussion

3.1. Unit Cell Design

The geometry of the top and bottom surface of the proposed unit cell design is given in Figure 2. The optically transparent PVC used as substrate has width W, length L and thickness h_s. In the conductor part, the diameter of the circle seen on the top surface is d, the width of the ground line on the buttom surface is W and the length is k. The thickness of the transparent PVC is 1.48 mm and the dielectric constant is 2.77. In the conductor part, copper is used as the material and its thickness is 35 microns.

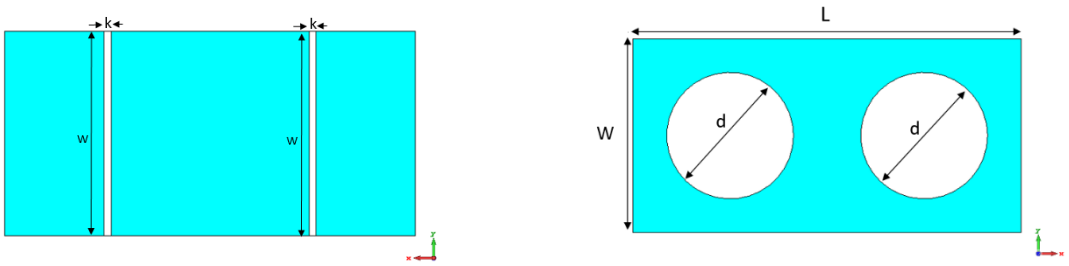

a) b)

Figure 1. a) Unit cell geometry bottom view of proposed design, b) Unit cell geometry top view of proposed design

The design parameters of the proposed design was given in Table1. As can be seen in the figure, the diameters of the circles used on the top surface are equal to each other and are d. In addition, the thickness of all the

conductive shapes used is the same, 35microns. Single-layer absorbers using FSS incorporate sheets that offer both resistive and reactive elements. The resistive aspect connects to the material's lossy properties, while the reactive component corresponds to the lengths and gaps between the elements.

Table1. Design parameters of the proposed unit cell

Design Parameters					
W	**L**	**k**	**d**	**hs**	**hc**
29.083 mm	58.166 mm	1 mm	19 mm	1.48 mm	0.035mm

3.2. Boundary Conditions

The surface current distributions of the structure are presented in Figure 2a and Figure 2b for the FSS and conducting plate. As can be seen in the figure, the current density on the bottom side of the design, called the conducting plate, is much higher than the circles on the front surface. To simplify, the illustration shows the current path of each element at its specific resonant frequency, offering an explanation for the resonance mechanism behind the proposed design of the FSS unit cell. The E and H field directions for TE polarization are presented in Figure 4.

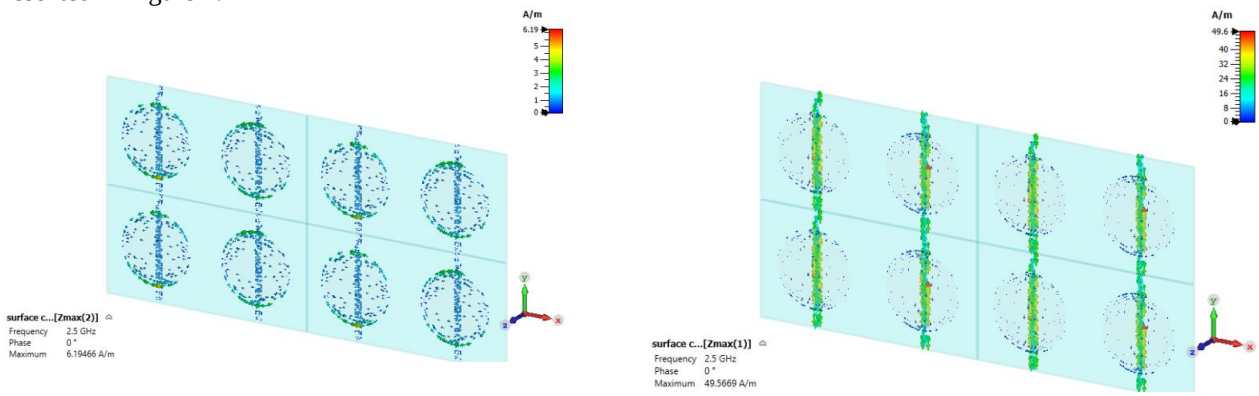

a) b)

Figure 2. Surface current distrubition a) FSS, b) Conducting plate

3.3. Absorption S11 and S21

Electromagnetic waves directed at the absorber undergo reflection, transmission, or absorption. The absorption coefficient (A) signifies the proportion of incident power absorbed by the frequency selective surface. It's represented by equation (1). As a copper layer exists at the absorber's base, minimal power is transmitted through, resulting in S21=0.

$$A = 1 - |S_{11}|^2 - |S_{21}|^2 \quad (1)$$

This equation indicates that a decrease in return loss corresponds to increased absorption. In the proposed design, a return loss below -10 dB is consistently observed within the 3.4 -3.7 GHz. range. The design parameters in the design were varied and their effects on the frequency characteristics were observed by simulation.

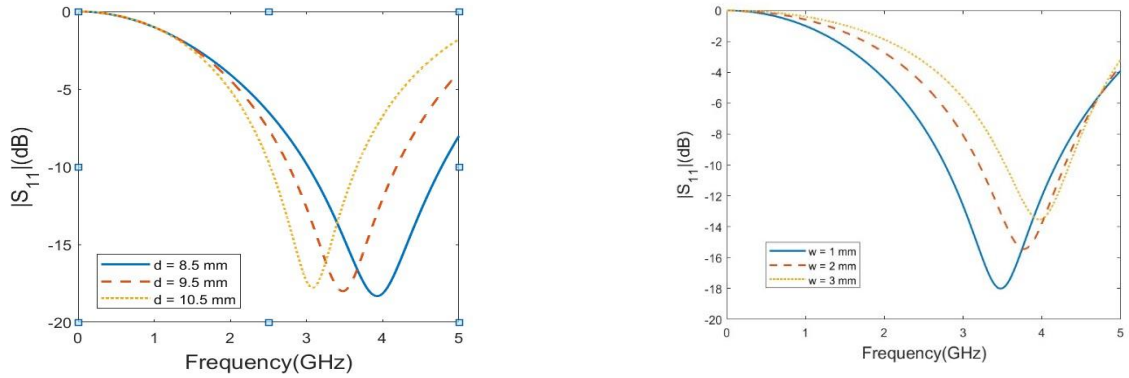

a) b)

Figure 3. a) The effect of diameter to frequency, b) The effect of copper patch width of ground plate

Figure 3a explored the impact on resonance frequency by altering the diameter of the circle on the front surface. As the diameter decreases, the resonance frequency rises, and conversely, as it increases, the resonance frequency declines. A change of about 1mm in diameter led to an approximate shift of 0.5GHz in the resonance frequency. In Figure 3b, the influence of copper patch thickness on the ground plane's rear surface on resonance frequency was investigated. It was noted that as the copper patch thickness increases, the resonance frequency also increases.

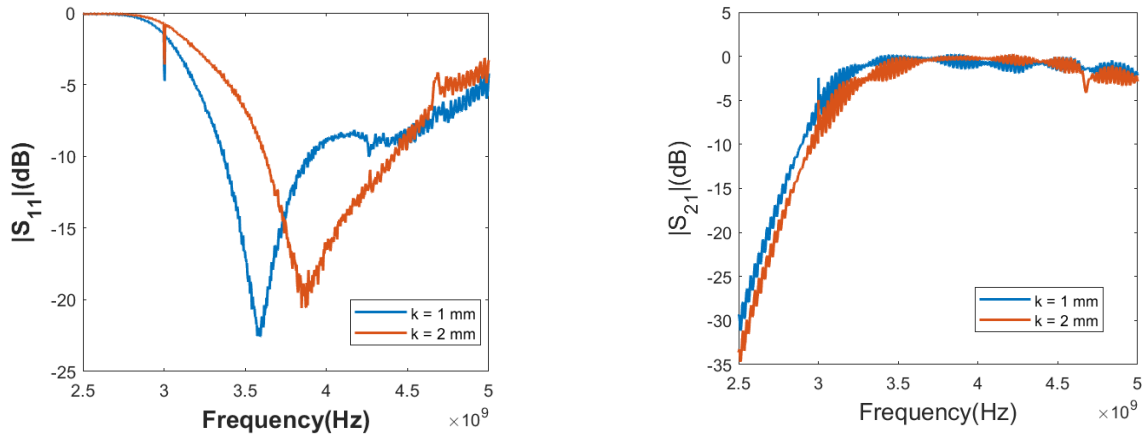

a) b)

Figure 4. a) S11 comparasion of the different copper patches, b) S21 comparison of the copper patches

Figure 4a presents a comparison of resonance frequencies between two unit cells differing in copper patch thickness. Consistent with simulation outcomes, experimental findings confirm that resonance frequency escalates with an increase in copper patch thickness. Measurements conducted with copper patch thicknesses of 1 mm and 2 mm revealed a resonance frequency difference of 0.25GHz. Figure 4b juxtaposes the transmission characteristics of these two distinct designs using the S21 parameter. The figure illustrates that both designs showcase S21 parameters hovering around 0 at the resonance frequency. This signifies the effective absorption capability of the proposed design within the specified frequency band. Referring to Formula 1, the proximity of the S21 parameter to 0 further substantiates the heightened absorptive nature of the design.

3.4. Prototype and the experimental results

The proposed design was fabricated in the laboratory using transparent PVC and copper tapes. After fabrication, measurements were performed. Rohde Schwarz network analyzer, which can measure up to 14GHz, was used to measure dispersion characteristics such as reflection and transmission. WR229 waveguide was used to measure the frequency characteristics. The image of the fabricated prototype in the waveguide is shown in figure a.

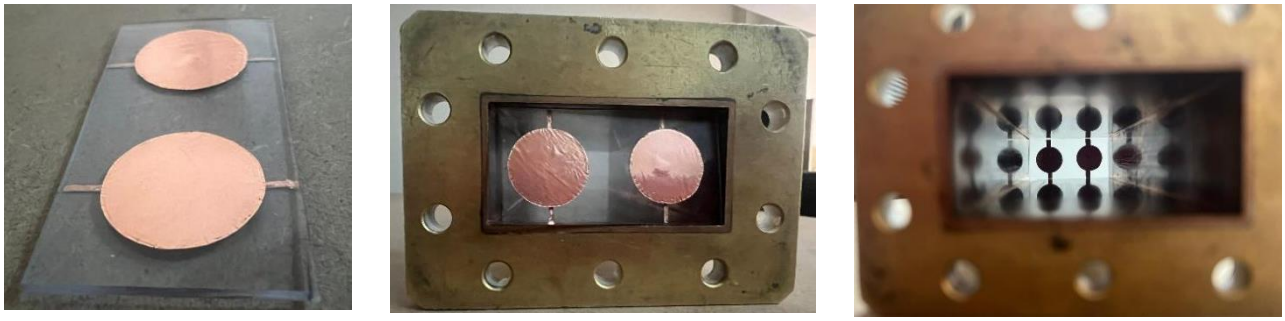

a) b) c)

Figure 5. a) Unit cell prototype b) Prototype in waveguide, c) Prototype in waveguide.

In the unit cell design given above, the thickness of the conductor on the bottom surface, k, is 1mm. In the simulations, this thickness was varied and its effect on the frequency characteristics was examined. At the same

time, two more unit cells were produced for k values of 2 and 3 mm and measurements were performed. Simulation results and measurement results are compared.

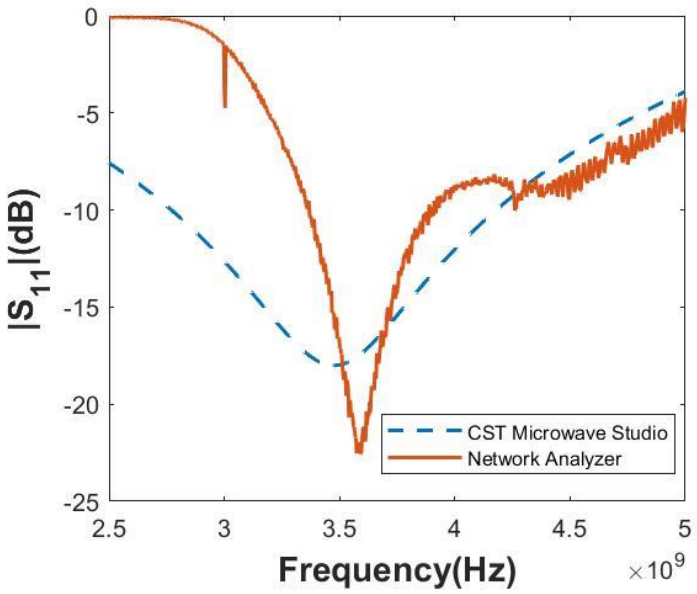

Figure 6. S_{11} comparison of the simulation and experimental result

Simulation studies and experimental measurements for different copper patch thicknesses were compared, and it was determined that the copper patch thickness of the most suitable design for the 3.5GHz band, which is one of the 5G applications to be used in practice, was 1 mm. As seen in Figure 6, the simulation results and measurement results are very close to each other. The difference in resonance frequency between the two results is approximately 0.1GHz, and it is thought that this difference is due to possible errors in production. As a result, looking at the measurement results and S parameters, an FSS-based absorber with a bandwidth of 0.2GHz for the 3.5GHz frequency band was produced.

4. Conclusion

In this study, an FSS-based absorber was specifically crafted to serve as electromagnetic shielding for the 3.5GHz frequency band, widely utilized in 5G applications. Through experimental studies, a noteworthy correlation between the experimental and simulation data was observed. A unique aspect of this research lies in the utilization of transparent PVC as a dielectric material, diverging from the conventional use of FR-4. This work revealed an easily fabricated structure that is not only low-cost but also capable of distinguishing transparency in the visible spectrum. Due to the flexibility of this structure used in the design, it is very suitable for use in many different shapes or different coating technologies. It is also possible to design a double band absorber by choosing different diameters of the circles used in the FSS part of the proposed design.

References

[1] Chaturvedi, P., Hsu, K., Zhang, S., & Fang, N. (2008), New frontiers of metamaterials: design and fabrication, *MRS BULLETIN,Volume 33*, pp. 915-920.

[2] Gangwar, K., Paras Dr., & Gangwar, Dr. R.P.S. (2014), Metamaterials: characteristics, process and application, *SSN 2231-1297, Volume 4*, pp. 97-10.

[3] Bukhari, S. S., Vardaxoglou, J., & Whittow, W. (2019), A metasurfaces Review : Definitions and Applications, *Appl. Sciences*.

[4] Kuester, E., Mohamed, M., Piket-May, M., & Holloway, C. (2003), Averaged transition conditions for electromagnetic fields at a metafilm, *IEEE Trans. Antennas Propag., Volume 51*, pp. 2641–2651.

[5] Yu, N., & Capasso, F. (2014), Flat optics with designer metasurfaces, *Nat. Mater.*, *Volume 13*, pp. 139–150.
[6] Hussein, M., Hung, Y., & Zhou, J., Frequency selective surface with miniaturize different elements: a different approach.
[7] Kohlgraf, D.C. (2005), Design and testing of a frequency selective surface (FSS) based wide-band multiple antenna system, pp. 6-8.
[8] Zheludev, N.I. (2015), Obtaining optical properties on demand, *Science 348*, pp. 973-974.
[9] Yu, S., Cheng, J., Li, Z., Liu, W., Cheng, H., Tian, J., & Chen, S.(2022), Electromagnetic wave manipulation based on few-layer metasurfaces and polyatomic metasurfaces, *ChemPhysMater*, *Volume 1*, pp. 6-16.
[10] Luo, K.(2015), Principles of electromagnetic waves in metasurfaces, *Sci. China Phys. Mech. Astron.*, *Volume 58.*
[11] Chen, S., Li, Z., Liu, W., Cheng, H., & Tian, J.(2019), From single-dimensional to multidimensional manipulation of optical waves with metasurfaces, *Adv. Mater.*, *Volume 31*, 1802458.
[12] Ozden, K., Yucedag, M.O., & Kocer, H.(2016), Metamaterials based broadband RF absorber at X-band, *AEU-International Journal of Electronics and Communications, Volume 70,* pg. 1062-1070.
[13] Jorwal, S., Dubey, A., Gupta, R., & Agarwal, S.(2023), A review:Advancement in metamaterial based RF and microwave absorbers, *Sensor and Actuators, Volume 354*.
[14] Costa, F., Genovesi, S., Monorchio, A., & Manara, G.(2019), A circuit-based model for the interpretation of perfect metamaterial absorbers, *IEEE Trans. Antennas Propag.*, *Volume 61*, pp. 1201–1209.
[15] Agarwal, M., & Meshram, K.M. (2016), Isolation improvement of 5GHz WLAN Antenna Array using Metamaterial Absorber", *URSI Asia-Pasific Radio Science Conference*.

A density functional theory analysis of the pressure-induced mechanical stability of $KNiF_3$ perovskite compound

Belgin KOÇAK [1,*] ***and Yasemin Öztekin ÇİFTCİ*** [2]

[1]*Vocational School of Higher Education, Department of Electronics and Automation, Ostim Technical University, Ankara, Turkey*

[2]*Faculty of Science, Department of Physics, Gazi University, Ankara, Turkey*

Abstract

In this study, we employed density functional theory to evaluate the structural, electronic, and mechanical properties of the $KNiF_3$ cubic perovskite compound, which belongs to the *Pm3m* space group, under high-pressure conditions ranging from 0 to 100 GPa. The results were calculated employing the GGA-PBE approximation in the Vienna Ab initio Simulation Package (VASP) code. Our findings were compared with existing research, and consistent results were obtained. The mechanical properties that our calculations determine are the following: Cauchy pressure, bulk modulus, Young's modulus, shear modulus, Pugh's ratio, Poisson's ratio, hardness, machinability index, Zener anisotropy factor, sound velocities, and Debye temperature. $KNiF_3$ compound was found to meet the criteria for mechanical stability and exhibited consistent mechanical stability across the entire 0 to 100 GPa pressure range. The computed mechanical properties suggest that $KNiF_3$ is a ductile material, and its ductility increases with pressure. The elastic anisotropic mechanical properties were visually represented. The estimation of electronic properties has been performed through spin-polarized calculations.

Keywords: *$KNiF_3$, density functional theory, structural properties, mechanical stability*

1. Introduction

$KNiF_3$ compound has a member of fluoride perovskite family, which has drawn a lot of interest in technological applications [1-11]. Despite the interest in fluoride perovskite alloys, the physical properties of the $KNiF_3$ compound have been researched poorly under pressure, to the best of our knowledge. A few experimentally measured reports on this compound's band structure [2-5]. Experimentally, Onuki et al. [2] have studied absorption sprectra of KMF_3 (M=Mn, Fe, Co, Ni, Cu, and Zn) compounds. Shulman et al. [3] measured x-ray-absorption spectra of KMF_3 (M=Mn, Fe, Co, Ni, and Zn) compounds via synchrotron radiation. Using X-ray diffraction data, the topological analysis of the electron density of $KNiF_3$ were reported by Tsirelson et al. [4]. They noticed that the K-F interaction is ionic and the Ni-F bond shows polar covalent type in $KNiF_3$. Rousseau et al. [5] were reported on the elastic constants of perovskite AMF_3 (A =K, Rb; M=Mg, Ni, Co, Zn, Mn) compounds by long waves method. Kitamura et al. [6] studied electronic properties of KMF_3 (M = Mn, Fe, Co, Ni, Cu, and Zn) compounds.

The electronic properties, magnetic properties and elastic properties of $KNiF_3$ has been obtained by Ref [7] using the ab initio method within Hartree-Fock approach as implemented in the CRYSTAL code. They found that $KNiF_3$ is a large gap insulator in ferromagnetic and antiferromagnetic phase [7]. Pari et al. [8] is theoretically investigated antiferromagnetic electronic structure of title compound. Moreira et al. [9] studied the magnetic coupling of $KNiF_3$ via an ab initio method within cluster model approach. Erum and Iqbal [10] calculated the elastic, optic and magneto-electronic features of $KNiF_3$ via an ab initio method. They point out that $KNiF_3$ compound shows ductile and anisotropic characteristic. The first principle calculation of electronic and magnetic properties for title compound is also reported in Ref [11] using WIEN2K package. They reported $KNiF_3$ compound is elastically stable in Pm3m space group.

2. Materials and Methods

In this study, the properties being investigated include structural, electronic, elastic, and related properties of the $KNiF_3$ compound were obtained using first-principles calculations within Vienna Ab-initio Simulation Package

* Corresponding author. *e-mail address: belgin.kocak@ostimteknik.edu.tr*

(VASP) [12]. The study covers a pressure range from 0 to 100 GPa.The interaction between valence electrons and ionic cores is modeled using the projector-augmented-wave (PAW) [13, 14] approach. The generalized gradient approximation (GGA) is employed for the exchange-correlation energy. Specifically, the Perdew-Burke-Ernzerhof (PBE) functional is used [15]. The number of k-points was set to Monkhorst-Pack [16] scheme 16 x 16 x 16 after the convergence test, and the cut off energy was 700 eV. These numbers were sufficient to satisfy convergence criterion for $KNiF_3$ compound.

3. Results and Discussion

3.1. Geometric optimization

By employing fully geometrical relaxation, the predicted $KNiF_3$ lattice parameters are obtained. Table 1 present the computed values of lattice constant (a_0) with experimental and theoretical value. The experimental lattice constants coincide quite well our prediction. The pressure effect of lattice constant for this compound is depicted in Figure 1. It is shown clearly that lattice constant of $KNiF_3$ is decreased by increasing the pressure. This can be expressed that there exist stronger atomic interactions. Unfortunately, unavailability of theoretical or experimental results, the ambient pressure values of calculated lattice constants cannot be compared.

Table 1. Calculated structural equilibrium lattice constant a_0 (in Å) of $KNiF_3$.

$KNiF_3$	a_0 (Å)
Present-PBE	4.039
Experimental [5]	4.010
Experimental [17]	4.034
Theory [7]	4.10
Theory [8]	4.12
Theory [10]	4.013^{LDA} 4.018^{GGA}
Theory [11]	4.012

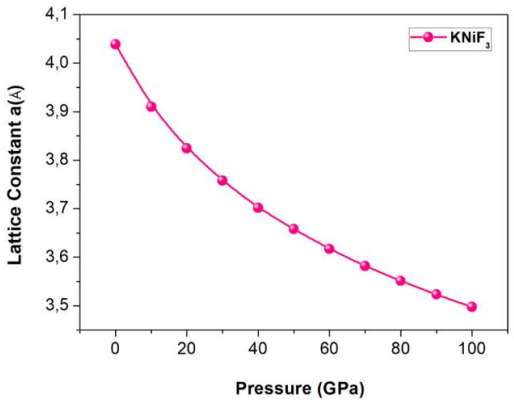

Figure 1. Pressure dependence of lattice constant of $KNiF_3$.

3.2. Mechanical stability

Through application of the "stress-strain" method [18], the mechanical properties of cubic perovskite $KNiF_3$ under high pressure are characterized by three independent elastic constants: C_{11}, C_{12}, and C_{44}. Table 2 shows the computed C_{ij} of $KNiF_3$ at P = 0 GPa. According Table 2, our predicted elastic constant values at 0 GPa correspond well with the published experimental values [5]. Thus, our calculation approach is plausible and accurate. The results obtained at 0 GPa also agree with prior theoretical studies in general [7, 10, 11]. The elastic constants of the title compound rise with increasing pressure, as shown in Figure 2. It's also worth noting that under 100 GPa, the obtained C_{11}, C_{12}, and C_{44} are all positive and fullfill the requirements [19] for the cubic structure. It's also found that C_{11} is more susceptible to pressure than C_{44} which has the least effect.

Table 2. Elastic properties of $KNiF_3$ at 0 GPa.

$KNiF_3$	Present- PBE	Exp. [5]	Theory [7]	Theory [10]	Theory [11]
C_{11} (GPa)	140.96	158.2	168	121.231	115.73
C_{12} (GPa)	54.771	48.5	60	58.989	53.85
C_{44} (GPa)	36.278	40.3	46	46.639	41.63
Cauchy Pressure (GPa)	18.49			12.06	
B (GPa)	83.50		79	80.217	89.26
G (GPa)	38.87			39.971	36.96
Y (GPa)	100.94			102.824	95.14
B/G	2.15			2.006	2.01
ν	0.299			0.29	0.2
μ_M	2.30				
A	0.84			1.55	1.35
H_v (GPa)	5.15				
v_l (m/s):	5890.22			5440	
v_t (m/s):	3156.71			2980	
v_m (m/s):	3525.32			4210	
θ (K)	444.3			320	

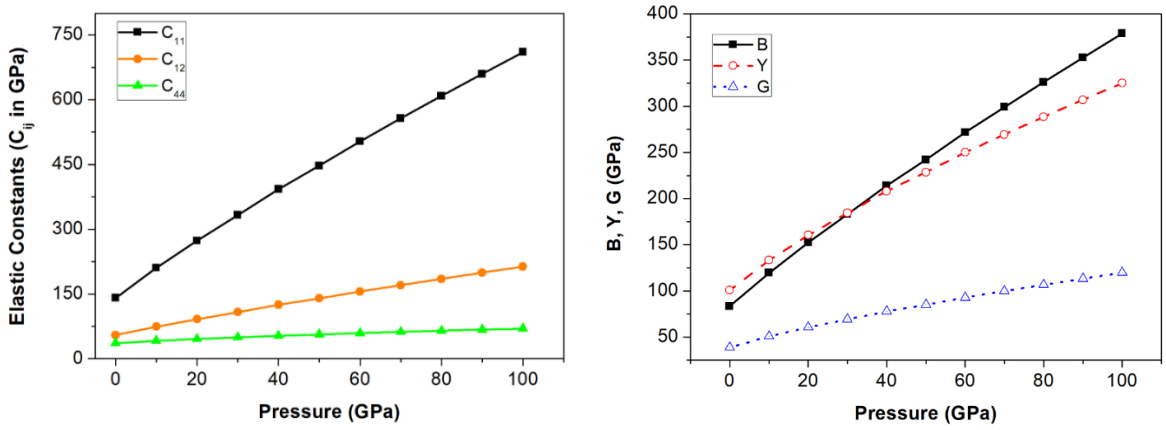

Figure 2. Pressure dependence of elastic properties of $KNiF_3$ compound.

Furthermore, various additional mechanical properties, such as Cauchy pressure, bulk modulus (B), shear modulus (G), Young's modulus (Y), machinability index (μ_M), Zener anisotropy factor (A), Poisson's ratio (ν), Pugh's ratio (B/G), hardness (H_v), longitudinal wave velocity (v_l), transverse wave velocity (v_t), average wave velocity (v_m), and Debye temperature (θ) were systematically calculated [20-27]. The corresponding values of these mechanical properties at 0 GPa are provided in Table 2, and their pressure dependence is illustrated in Figure 2. The bulk modulus (B), shear modulus (G), and Young's modulus (Y) exhibit an upward trend with increasing pressure within the specified pressure range.

Table 2 shows that the B/G ratios of $KNiF_3$ are more than 1.75, indicating that it is ductile [24, 25]. At 0 GPa, the B/G value of the title compound changes from 2.15 to 3.16 at 100 GPa. This suggests that as the pressure is increased, the $KNiF_3$ becomes more ductile. Cauchy pressure is found 18.49 GPa at zero pressure and 143.3 GPa at 100 GPa pressure. These values exhibit ductile nature and ductility of this compound increase also with pressure. The ductility of this compound is also confirmed since the obtained value of v is bigger than 0.26 [10, 25]. The elastic ansitropy properties [28] is also depicted in Figure 3 and 4.

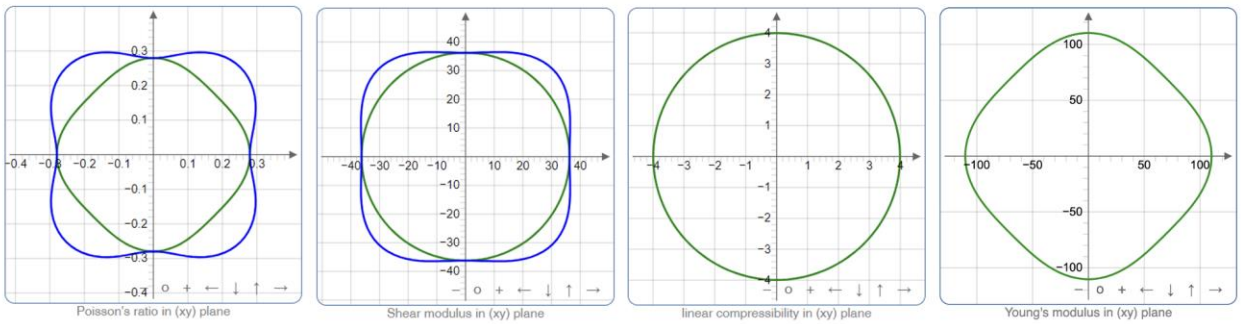

Figure 3. 2D elastic anisotropy properties of $KNiF_3$ compound at 0 GPa.

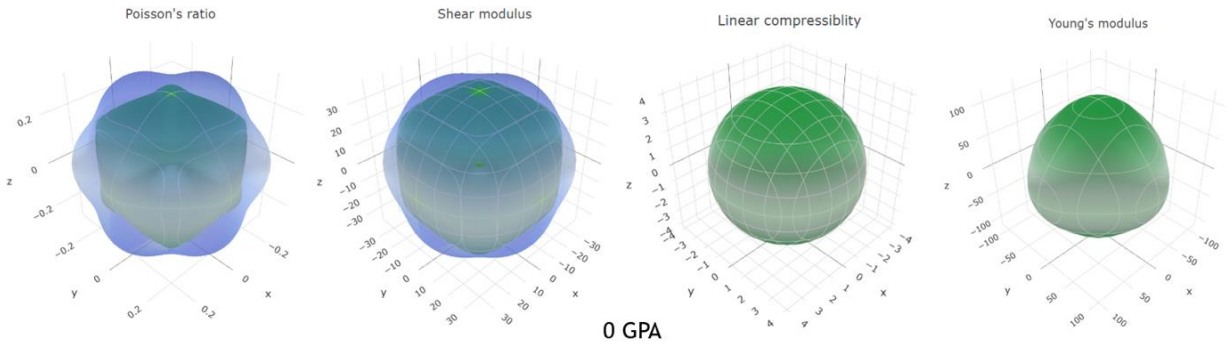

Figure 4. 3D elastic anisotropy properties of $KNiF_3$ compound at 0 GPa.

3.3. Electronic properties

The electronic properties were determined using spin-polarized calculations. The spin-up and spin-down electronic band structure presentation for $KNiF_3$ compound is given in Figure 5 and and total density of states (TDOS) is displayed in Figure 6. The computed electronic band structure aligns with the existing theoretical findings [10, 11] at 0 GPa.

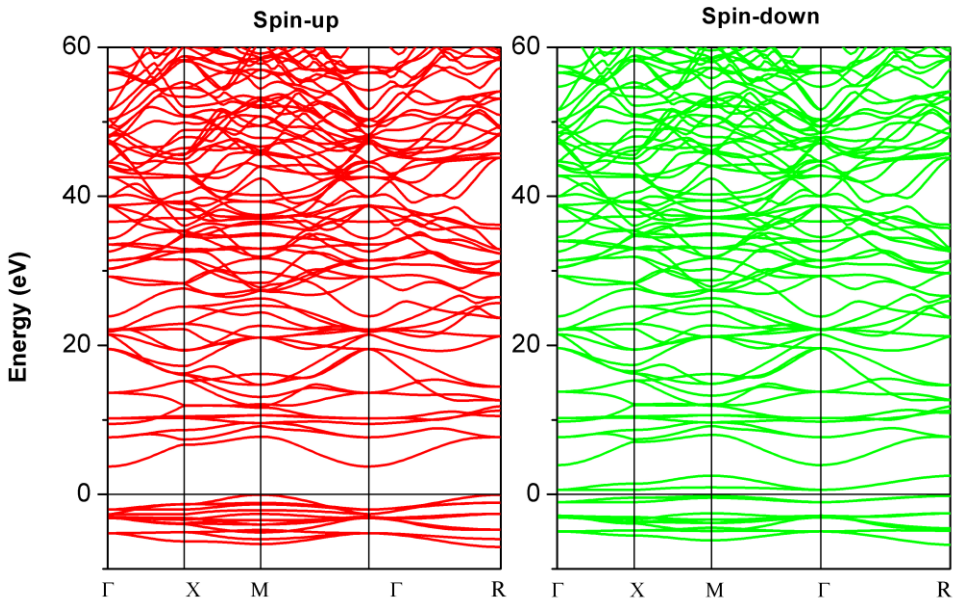

Figure 5. Electronic band structure of $KNiF_3$ compound at 0 GPa.

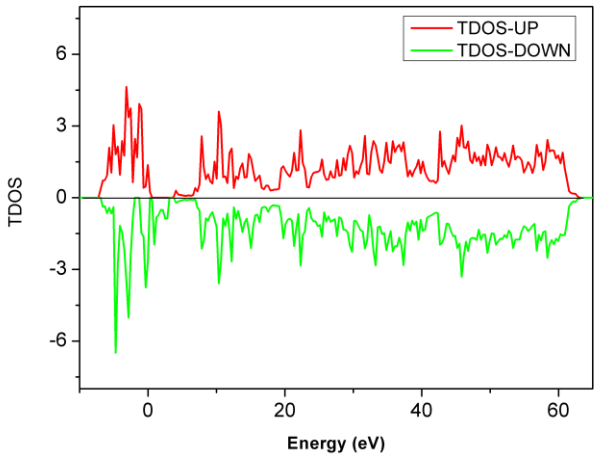

Figure 6. Total density of states of $KNiF_3$ compound at 0 GPa.

4. Conclusion

This study employed first principles calculations to investigate the impact of pressure (in the range of 0–100 GPa) on the physical properties of fluoroperovskite $KNiF_3$ compounds. The lattice constant, spin polarized electronic band structure, and elastic constants presented in this research consistent with both experimental structures and theoretical studies. The findings reveal a reduction in lattice constants under pressure, accompanied by an increase in elastic constants as the pressure rises. Importantly, at the assessed pressure levels, all elastic constants adhere to the conditions for mechanical stability.

Acknowledgement

The numerical calculations reported in this paper were performed at TUBITAK ULAKBIM, High Performance and Grid Computing Center (TRUBA resources).

References

[1] Rehman, J. U., Usman, M., Tahir, M. B., Hussain, A., Rehman, M. A., Sagir, M., Alrobei, H., Ullah, S., Assiri, M. A. (2022). First-principles calculations to investigate ultra-wide bandgap semiconductor behavior of $NaMgF_3$ fluoro-perovskite with external static isotropic pressure and its impact on optical properties. *Optik*, *252*, 168532.

[2] Onuki, H., Sugawara, F., Nishihara, Y., Hirano, M., Yamaguchi, Y., Ejiri, A., Takahashi, H., Abe, H. (1976). Absorption spectra of KMF_3 (M= Mn, Fe, Co, Ni, Cu, Zn) in the extreme ultraviolet region. *Solid State Communications*, *20*(1), 35-37.

[3] Shulman, G. R., Yafet, Y., Eisenberger, P., & Blumberg, W. E. (1976). Observations and interpretation of x-ray absorption edges in iron compounds and proteins. *Proceedings of the National Academy of Sciences*, *73*(5), 1384-1388.

[4] Tsirelson, V., Ivanov, Y., Zhurova, E., Zhurov, V., & Tanaka, K. (2000). Electron density of $KNiF_3$: analysis of the atomic interactions. Acta Crystallographica Section B: Structural Science, *56*(2), 197-203.

[5] Rousseau, M., Nouet, J., & Zarembowitch, A. (1974). Interatomic force constants studies of AMF_3 perovskite-type crystals (A= K, Rb; M= Mg, Ni, Co, Zn, Mn). *Journal of Physics and Chemistry of Solids*, *35*(8), 921-926.

[6] Kitamura, M., & Muramatsu, S. (1990). Electronic structure of perovskite-type compounds. *Physical Review B*, *41*(2), 1158.Ricart, J. M., Dovesi, R., Roetti, C., & Saunders, V. R. (1995). Electronic and magnetic structure of KNiF 3 perovskite. *Physical Review B*, *52*(4), 2381.

[7] Ricart, J. M., Dovesi, R., Roetti, C., & Saunders, V. R. (1995). Electronic and magnetic structure of $KNiF_3$ perovskite. *Physical Review B*, *52*(4), 2381.

[8] Pari, G., Jaya, S. M., & Asokamani, R. (1994). Electronic structure and magnetism of KMF_3 (M= Mn, Fe, Co, Ni). *Physical Review B*, *50*(12), 8166.

[9] Moreira, I. D. P. R., Illas i Riera, F. (1997). Ab initio theoretical comparative study of magnetic coupling in $KNiF_3$ and K_2NiF_4. *Physical Review B, 55 (7), 4129-4137.*
[10] Erum, N., Iqbal, M. A. (2017). Mechanical and magneto-opto-electronic investigation of transition metal based fluoro-perovskites: An ab-initio DFT study. *Solid State Communications*, *264*, 39-48.
[11] Murtaza, G., Khenata, R., Muhammad, S., Reshak, A. H., Wong, K. M., Omran, S. B., & Alahmed, Z. A. (2014). Structural, chemical bonding, electronic and magnetic properties of KMF_3 (M= Mn, Fe, Co, Ni) compounds. *Computational materials science*, *85*, 402-408.
[12] Hafner, J. (2008). Ab-initio simulations of materials using VASP: Density-functional theory and beyond. *Journal of computational chemistry*, *29*(13), 2044-2078.
[13] Kresse, G., Furthmüller, J. (1996). Efficient iterative schemes for ab initio total-energy calculations using a plane-wave basis set. *Physical review B*, *54*(16), 11169.
[14] Blöchl, P.E., "Projector augmented-wave method", *Physical Review B*, 50: 17953, (1994).
[15] Perdew, J. P., Burke, K., & Ernzerhof, M. (1996). Generalized gradient approximation made simple. *Physical review letters*, *77*(18), 3865.
[16] Monkhorst, H. J., & Pack, J. D. (1976). Special points for Brillouin-zone integrations. *Physical Review B*, *13*(12), 5188.
[17] Lee, J., Shin, H., Lee, J., Chung, H., Zhang, Q., & Saito, F. (2003). Mechanochemical Syntheses of Perovskite $KMIIF_3$ with Cubic Structure (MII= Mg, Ca, Mn, Fe, Co, Ni, and Zn). *Materials transactions*, *44*(7), 1457-1460.
[18] Le Page, Y., & Saxe, P. (2002). Symmetry-general least-squares extraction of elastic data for strained materials from ab initio calculations of stress. *Physical Review B*, *65*(10), 104104.
[19] Mouhat, F., & Coudert, F. X. (2014). Necessary and sufficient elastic stability conditions in various crystal systems. *Physical review B*, *90*(22), 224104.
[20] Reuss, A. (1929). Berechnung der fließgrenze von mischkristallen auf grund der plastizitätsbedingung für einkristalle. *ZAMM-Journal of Applied Mathematics and Mechanics/Zeitschrift für Angewandte Mathematik und Mechanik*, *9*(1), 49-58.
[21] Voigt, W., "Lehrbuch der Kristallphysik (mit Ausschluss der Kristalloptik)", Teubner, Leipzig, (1928).
[22] Hill, R. (1952). The elastic behaviour of a crystalline aggregate. *Proceedings of the Physical Society. Section A*, *65*(5), 349.
[23] Pettifor, D. G. (1992). Theoretical predictions of structure and related properties of intermetallics. *Materials science and technology*, *8*(4), 345-349.
[24] Pugh, S. F. (1954). XCII. Relations between the elastic moduli and the plastic properties of polycrystalline pure metals. *The London, Edinburgh, and Dublin Philosophical Magazine and Journal of Science*, *45*(367), 823-843.
[25] Bannikov, V. V., Shein, I. R., & Ivanovskii, A. L. (2010). Elastic properties of antiperovskite-type Ni-rich nitrides $MNNi_3$ (M= Zn, Cd, Mg, Al, Ga, In, Sn, Sb, Pd, Cu, Ag and Pt) as predicted from first-principles calculations. *Physica B: Condensed Matter*, *405*(22), 4615-4619.
[26] Ahmed, R., Mahamudujjaman, M., Afzal, M. A., Islam, M. S., Islam, R. S., & Naqib, S. H. (2023). DFT based comparative analysis of the physical properties of some binary transition metal carbides XC (X= Nb, Ta, Ti). *Journal of Materials Research and Technology*, *24*, 4808-4832.
[27] Tian, Y., Xu, B., & Zhao, Z. (2012). Microscopic theory of hardness and design of novel superhard crystals. *International Journal of Refractory Metals and Hard Materials*, *33*, 93-106.
[28] Gaillac, R., Pullumbi, P., & Coudert, F. X. (2016). ELATE: an open-source online application for analysis and visualization of elastic tensors. *Journal of Physics: Condensed Matter*, *28*(27), 275201.

Innovative Processing Techniques Unveil the Potential of Chickpea Aquafaba

Elif Gokcen Ates [1,2*], ***Gokcem Tonyali Karsli*** [1], ***Emin Burcin Ozvural*** [2], ***Mecit H. Oztop*** [1]

[1]*Department of Food Engineering, Middle East Technical University, 06800 Ankara, Turkey*
[2]*Department of Food Engineering, Cankiri Karatekin University, Uluyazi Campus, 18100, Cankiri, Turkey*

Abstract

Chickpea aquafaba, the residual liquid from cooked chickpeas, stands out as a noteworthy player in the dynamic landscape of plant-based ingredients, captivating the food science community with its distinct attributes. This study delves deeply into the physicochemical properties of chickpea aquafaba and its powder counterpart, highlighting the protein-rich profile. Chickpea aquafaba inherits these nutritional components, boasting 1-1.5% protein and 3.5% carbohydrates by weight, and distinguishing itself with exceptional foaming ability derived from a unique composition rich in soluble proteins, oligosaccharides, saponins, and starches. Aquafaba's foaming ability distinguishes it as a sought-after ingredient for vegan and egg-free recipes, excelling in achieving desirable textures. The investigation extends into cutting-edge technologies, with a focus on the transformative impact of microwave vacuum technology and custom-designed microwave equipment on aquafaba. These methods not only fine-tune critical parameters for optimized protein content and foaming ability, but they also improve protein extraction precision. The study delves deeper into spray-dried chickpea aquafaba, presenting a concentrated and shelf-stable powder that expands the benefits of this plant-based elixir. Chickpeas, aquafaba, advanced processing technologies, and custom-designed equipment have all come together to usher in a new era of plant-based innovation. The study emphasizes microwave vacuum technology which is a method that combines the advantages of microwave and vacuum drying and its superior performance, consistently yielding higher protein content and desirable properties in both liquid and powder forms of aquafaba. In the ever-changing landscape of food science, this comprehensive examination of composition, foaming ability, and advanced processing illuminates the path toward realizing the full potential of chickpea aquafaba.

Keywords: *Chickpea, Aquafaba, Microwave-Vacuum, Spray Drying, Powder*

1. Introduction

In the ever-evolving landscape of plant-based ingredients, chickpea aquafaba, the liquid residue derived from cooked chickpeas, has emerged as a valuable plant-based ingredient, captivating the food science world with its unique attributes. To comprehend the full scope of its potential, it is imperative to delve into the proximate composition of both chickpeas and their liquid counterpart. Chickpeas, scientifically known as *Cicer arietinum*, boast a nutrient-rich profile, serving as an excellent source of protein, dietary fiber, vitamins, and minerals. The proximate composition of chickpeas includes approximately 19-25% protein, making them a substantial plant-based protein option [1]. Furthermore, chickpeas contain essential amino acids, particularly lysine, which is often limited in grains. Albumin and globulins are the most abundant proteins, accounting for 8%-12% and 53%-60% of total protein content, respectively[2]. The transformation of chickpeas into aquafaba involves the infusion of water with these nutritional components. Aquafaba inherits the protein content of chickpeas, typically containing around 1-1.5% protein and approximately 3.5% carbohydrates by weight, rendering it a valuable alternative for individuals seeking plant-based protein sources [3,4]. What sets aquafaba apart is this remarkable foaming ability. This might seem modest, but its real magic lies in its unique composition, rich in soluble proteins, oligosaccharides, saponins and starches, which confer remarkable foaming and emulsifying properties [5,6]. The foaming ability of aquafaba makes it a sought-after ingredient for vegan and egg-free recipes, where aeration and stabilization are crucial for achieving desirable textures. From vegan meringues and macarons to plant-based mousses and mayonnaise, aquafaba stands out as a versatile ingredient capable of creating light and airy textures traditionally associated with egg-based formulations. In the quest to enhance the production and quality of chickpea aquafaba, innovative technologies have taken center stage. Microwave vacuum technology, a marriage of precision and efficiency, has become a transformative force in the extraction and preservation of the liquid's unique properties. This advanced method allows for fine-tuning of critical parameters like temperature, power and exposure time, ensuring an optimized protein content and foaming ability in the final aquafaba product. Microwave vacuum drying is a drying method that combines the advantages of microwave and vacuum drying.

* Corresponding author. *e-mail address: elifates@metu.edu.tr*

The microwave energy aids in the evaporation of the aquafaba's water content, while the vacuum atmosphere accelerates the drying process by lowering the boiling point of water [7]. This combination might result in a more effective and rapid aquafaba production than conventional techniques [8]. Microwave vacuum drying has been shown in studies to retain the nutritional value of heat-sensitive components and active substances in food items [9,10]. Moreover, aside from microwave vacuum technology, custom-designed microwave equipment is also taking a next step for production of aquafaba. Crafted specifically for pasteurization of food products, these specialized units offer unparalleled precision in the application of microwave energy for production of aquafaba from chickpea. The bespoke design allows for meticulous control over the cooking process, further enhancing the extraction of proteins and other essential components. Beyond the liquid form, the exploration extends to the realm of spray-dried chickpea aquafaba, a concentrated and shelf-stable iteration of this plant-based elixir. The spray-drying process encapsulates the magic of aquafaba in a versatile powder. Whether rehydrated or employed as a convenient ingredient in food, the spray-dried form brings the goodness of chickpea aquafaba to new horizons. As embarked on these excellent properties, the convergence of chickpeas, aquafaba, microwave vacuum technology, and custom-designed microwave equipment unveils a new era in plant-based innovation. Through a detailed examination of proximate composition, foaming ability, and advanced processing methods, it is illuminated the path toward unleashing the full potential of chickpea aquafaba in the food science landscape.

This paper explores the diverse attributes of chickpea aquafaba in the context of plant-based ingredients. It investigates the nutritional composition, with a focus on protein and highlights aquafaba's unique foaming ability. The study delves into innovative technologies, particularly microwave vacuum and custom-designed microwave equipment, as transformative tools in aquafaba extraction. Additionally, the paper explores spray-dried chickpea aquafaba, emphasizing advanced processing methods to enhance production and quality. The overarching goal is to contribute valuable insights to plant-based innovation, showcasing aquafaba's potential applications in food science.

2. Materials and Methods

2.1. Production of Aquafaba

With minor modifications, aquafaba was prepared as follows [11]. The chickpeas were washed first, and any excess water was discarded. The washed chickpeas were then soaked in distilled water for 16 hours at 4°C with a chickpea to water ratio of 1:3 (w/w) [12]. Following that, two different methods were used to increase the solid content of aquafaba namely microwave vacuum (MW-V) and custom designed microwave (MW-P).

Microwave-Vacuum

Chickpeas were cooked in a microwave-vacuum (MW-V) oven at a chickpea to water ratio of (1:2) (IF-TECH, Ankara, Turkey) for 50 minutes at 20 kPa vacuum pressure. Chickpea to water ratio, power and time were determined with preliminary experiments.

Custom Designed Microwave

Chickpeas were cooked in a microwave (MW-P) oven at a chickpea to water ratio of (1:2) (IF-TECH, Ankara, Turkey) for 50 minutes at 90% power. The unique fature of this equipment is where the magnetron stands. Chickpea to water ratio, power and time were determined with preliminary experiments

After employing two microwave processing techniques, the resulting aquafaba underwent two distinct treatments before the drying process. In the initial one, the aquafaba was promptly drained and separated from the chickpeas denoted as Standard Production (“SP”). In the second method, the chickpeas and water were left undisturbed overnight at 4°C, followed by filtration after a 24-hour period denoted as Overnight Production (“OP”).

2.2. Characterization of Aquafaba

2.2.1.Solid Content Analysis

The liquid samples' dry matter content was determined by placing them in an oven set at 105 °C for a duration of 3 hours. The process of measuring dry matter persisted until the variance between consecutive measurements fell below 0.5% [13].

2.2.2.Determination of Water and Oil Holding Capacities (WHC/OHC)

The assessment of water holding capacity (WHC) and oil holding capacity (OHC) was conducted on powder samples. For WHC, 0.1 gram of aquafaba powder was combined with 10 mL of distilled water. On the other hand, for oil holding capacity (OHC), 0.1 gram of the sample was mixed with 10 mL of sunflower oil [14].

Subsequently, these mixtures underwent centrifugation at 1960 x g for a duration of 30 minutes. Following the centrifugation process, the resulting supernatants were decanted, and the centrifuge tubes housing the sediment were weighed.

$$WHC/OHC = \frac{W_2 - W_1}{W_0} * 100$$

W_0 represents the weight of the dry sample, W_1 is the combined weight of the centrifuge tube and dry sample, and W_2 signifies the weight of the centrifuge tube and the sediment.

2.2.3.Soluble Protein Content

The soluble protein content was assessed employing the Lowry method [15,16]. 0.5 ml of the sample was combined with 2.5 ml of Lowry-ACR reagent in a tube, followed by a 10-minute incubation. Subsequently, 0.25 ml of Folin reagent (1/2 diluted) was introduced, and the mixture was thoroughly blended using a vortex. This concoction was then shielded from light and underwent a 30-minute incubation period. After completion, the absorbance at 750 nm was gauged using a spectrophotometer (Optizen Pop Nano Bio, Mecasys Co., Ltd., Daejeon, Korea). For calibration purposes, a curve was established utilizing a BSA (Bovine Serum Albumin) solution prepared at varying concentrations (0.03-10 g/L).

2.2.4.Foaming Ability and Stability

Foaming ability was determined for both liquid and powder aquafaba [17].In this context, a powder sample weighing 1.5 grams was blended with 30 ml of distilled water at a speed of 9,000 rpm for a duration of 5 minutes in a 100 ml graduated cylinder. For the liquid aquafaba, 100 ml of liquid aquafaba was blended for 10 minutes at a speed of 14000 rpm using a 250 ml graduated cylinder.The volumes were recorded at the initial stage, after 10 minutes and after 30 minutes. The foam capacity (FC) and stability (FS) were quantified as follows:

$$FC = \frac{v_f - v_i}{v_i} * 100$$

$$FS = \frac{v_{10}}{v_i} * 100$$

The volume values at the 30 minutes (Vf), first minute (Vi), and 10 minutes later (V10) were recorded as indicators of the foaming characteristics.

3. Results and Discussion

3.1. Solid Content Analysis

The dry matter content findings show notable differences amongst the samples. The production methods have resulted in varying levels of dry matter content in aquafaba (Table 1). The distinct processing techniques employed have led to differing dry matter contents, attributed to the unique mechanisms inherent in each method. MW-P yielded lower dry matter content than MW-V. This means that special design of microwave did not work as expected.

The effect of overnight soaking was also examined. It was observed that overnight soaking significantly increased the dry matter of aquafaba for all methods ($p<0.05$). The change in the dry matter content was greater for MW-V produced aquafaba (2.74% → 6.18%). This was attributed to the fact that higher amount of solid leached out due to the opening of the pores under the vacuum effect. Microwaves penetrate into food and cause the internal temperature to rise. High temperature generates water vapor inside the food and results in internal pressure gradient [18,19]. The internal pressure gradient is assumed to be higher in vacuum processes. Although the pores expanded during the process, time could have been insufficient for the dry matter to diffuse to the liquid phase. Hence, soaking overnight enhanced the dry matter transfer to a greater extent.

3.2. Determination of Water and Oil Holding Capacities (WHC/OHC)

WHC and OHC results of two different techniques were given in Table 2. Overnight storage was found to decrease WHC of MW-V. The decrease observed in microwave vacuum produced aquafaba is explained by the fact that the vacuum process expanded the pores more. With the opening of the pores, while dry matter transfer increased, the transfer of higher molecular weight constituents such as starch and insoluble fiber which can decrease WHC could also have taken place more. It is known that chickpea contains higher insoluble fiber content than soluble fiber [2]. Because insoluble fibers and starch are weak water binders, they might have decreased WHC [20,21]. The most known chickpea proteins are albumin and globulin which are water soluble and salt soluble fractions, respectively. With the opening of the pores, globulin transfer which is the larger and insoluble

protein fraction may have enhanced [22]. It has been also reported that as temperature increased, less amount of starch leaches out to the solution where boiling occurs. This is explained by the rupturing of granules due to the local temperature rise around each granule. Increase in temperature results in increase in local viscosity which restricts the mobility and prevents more leaching [23]. In addition to expanding of the pores, considering that the vacuum microwave operates at lower temperatures (~70°C), more starch transfer is likely to occur. Overnight soaking had a significant increase in MW-V sample ($p<0.05$). It was observed that overnight soaking had the opposite effect on WHC and OHC. It is possible to state that WHC and OHC work in opposite directions for aquafaba powders. This is expected since a decrease in WHC might mean a decrease in polar groups, while an increase in OHC might mean a decrease in these polar groups [24,25].

3.3. Soluble Protein Content

This study assessed the protein content of liquid (Table 1) and powder (Table 2) aquafaba derived from various production methods. For both, MW-V sample showed higher protein content than MW-P sample for both standard and overnight production. The application of vacuum treatment in conjunction with microwave heating contributes to enhancing the protein extraction process. Vacuum conditions could play a role in the enlargement of pores within the cellular structure of plant materials. This phenomenon is often referred to as "vacuum impregnation" or "vacuum infusion," and it can contribute to enhanced mass transfer of solutes, including proteins, from the interior of the cells to the surrounding liquid [26]. When vacuum is applied, the pressure is reduced, causing air and gases within the cellular structure to expand and escape. This can lead to the enlargement of cell pores and intercellular spaces. As a result, when the plant material is immersed in a liquid medium, such as water or an aqueous solution, the enlarged pores can facilitate the movement of solutes, including proteins, from the plant cells into the liquid. Vacuum conditions could promote the solubility of proteins in the aquafaba. It is known that vacuum conditions can alter the physical properties of substances by reducing the pressure and altering the intermolecular forces which eventually leading to increased solubility of proteins. This might be caused by the dissociation of the quaternary structure and depolymerization of the protein aggregates at a moderate power and vacuum level [27]. Also, while equilibrium between protein release and reabsorption occurs in all production methods, the microwave vacuum technique, characterized by its application of microwave heating and reduced pressure, offers distinct advantages. The vacuum environment in MW-V leads to lower boiling points and enhanced moisture evaporation, contributing to controlled and relatively lower temperatures within the sample. This environment, coupled with reduced oxygen exposure, potentially minimizes protein denaturation and degradation, resulting in stable protein content between immediate and overnight separations. In the MW-V-S samples, where immediate separation takes place, the protein content remains relatively stable. This stability can be attributed to the combined effects of microwave heating under reduced pressure. The vacuum conditions in MW-V-S likely contribute to the preservation of protein integrity by lowering the boiling point of liquids, leading to controlled moisture evaporation at lower temperatures. This mitigates the risk of excessive denaturation or degradation of proteins during the heating process. Intriguingly, even with overnight processing (MW-V-O), the protein content maintains its stability. The vacuum environment continues to play a crucial role in maintaining protein structure, preventing oxidation, and overall enhancing protein content stability. This consistency between immediate and extended separation underlines the potential of MW-V as a method capable of efficiently preserving and extracting proteins from chickpea aquafaba, making it a valuable option for applications demanding stable protein content.

3.4. Foaming Ability and Stability

The performance of four different samples (Mw-V-S, Mw-V-O, MW-P-S, and MW-P-O) reveals interesting differences in their foaming ability and foaming stability. Out of all the powder samples, Mw-V-S has the highest foaming ability, suggesting a tendency to create foam easily. Despite having a reduced foaming stability, the combination points to a dynamic interaction between adequate stability and rapid foam formation. Mw-V-O, on the other hand, has a lesser foaming ability but a greater foaming stability, indicating a more durable foam structure once created. The samples with moderate foaming abilities, MW-P-S and MW-P-O, suggest that there may have been a compromise in the initial creation of foam. However, their foaming stability values are on par with or even greater than the samples with higher foaming abilities. As mentioned above, the microwave-vacuum (MW-V) method resulted in relatively good foaming stability, implying that the vacuum treatment might contribute to maintaining the structural integrity of the foam. Pulse proteins could be a major factor contributing to the discrepancy between high foaming ability and low foaming stability. Proteins play a crucial role in both foam formation and stability due to their ability to interact with the air-water interface and stabilize the bubble structure. If the proteins at the interface do not form a strong network or film that effectively holds the bubbles

together, the foam can easily collapse over time. Also, proteins can interact with each other at the interface, either forming networks that stabilize the foam or aggregating in ways that weaken the foam structure.

4. Conclusion

The solid content analysis in this extensive investigation showed notable variations between aquafaba samples made using various techniques. The dry matter content of the microwave-vacuum (MW-V) methodology was found to be higher than that of the microwave-only (MW-P) method, indicating that the intended outcome of the microwave's particular design may not have been achieved. All techniques of aquafaba showed a considerable increase in dry matter after overnight soaking; however, MW-V showed the largest increase, which was attributed to pore opening under vacuum. Production techniques and overnight soaking have an impact on the water and oil holding capacities (WHC/OHC). Because of its larger pores and the transfer of components with higher molecular weights, MW-V showed a lower WHC. The results of the soluble protein content study demonstrated that MW-V consistently had a greater protein content than MW-P, highlighting the contribution of vacuum conditions. Additionally, even after processing for an entire night, the protein content of the microwave vacuum approach remained consistent, suggesting that it has the ability to effectively preserve protein. Evaluations of the samples' foaming ability and stability revealed subtle variations, with MW-V-S exhibiting a strong foaming ability and respectable stability. The integrity of the foam structure in MW-V was probably preserved in part by the vacuum treatment. Overall, our results highlight the complex interactions between manufacturing processes and aquafaba composition and qualities, providing important information for maximizing its use in a variety of sectors, including the food industry. The complex molecular and structural dynamics underlying these reported effects could be the subject of future investigation.

Table 1. Characterization of liquid aquafaba

Sample ID	Dry Matter (%)	Protein Content (mgBSA/L)	Foaming Ability	Foaming Stability
Mw-V-S	2.71 ± 0.11^{c}	5.25 ± 0.21^{a}	222.00 ± 1.51^{b}	97.03 ± 1.20^{b}
Mw-V-O	6.18 ± 0.04^{a}	5.18 ± 0.16^{a}	262.00 ± 6.71^{a}	106.73 ± 0.83^{b}
MW-P-S	1.21 ± 0.07^{d}	2.85 ± 0.22^{c}	120.83 ± 5.83^{d}	104.54 ± 6.13^{b}
MW-P-O	4.23 ± 0.07^{b}	4.30 ± 0.45^{b}	180.00 ± 3.41^{c}	$129.36\pm0.1.18^{a}$

Table 2. Characterization of powder aquafaba

Sample ID	WHC	OHC	Protein Content (mgBSA/g-powder)
Mw-V-S	2.14 ± 0.11^{a}	3.12 ± 0.12^{d}	1.69 ± 0.07^{b}
Mw-V-O	1.63 ± 0.15^{b}	4.84 ± 0.31^{a}	1.75 ± 0.07^{a}
MW-P-S	0.63 ± 0.06^{d}	3.31 ± 0.34^{c}	0.57 ± 0.06^{b}
MW-P-O	1.02 ± 0.08^{c}	3.73 ± 0.34^{b}	0.85 ± 0.11^{a}

Table 3. Foaming ability and stability of powder aquafaba

Sample ID	Foaming Ability	Foaming Stability
Mw-V-S	223.33 ± 5.77^{a}	99.58 ± 3.69^{b}
Mw-V-O	122.50 ± 4.19^{b}	106.51 ± 4.03^{a}
MW-P-S	111.67 ± 1.75^{c}	107.22 ± 1.24^{a}
MW-P-O	115.00 ± 4.08^{c}	104.56 ± 05.78^{a}

Acknowledgement

In this study, the financial support was provided by The Scientific and Technological Research Council of Turkey (TUBITAK), Project No. 121O024. The author would like to thanks to all supporters due to their precious contributions.

References

[1] Paredes-Lopez, O. et al. (1991). Chickpea Protein Isolates: Nutritional Characterization Functional and. *Journal of Food Science*.

[2] Grasso, N. et al. (2022). Chickpea protein ingredients: A review of composition, functionality, and applications. *Comprehensive Reviews in Food Science and Food Safety*. DOI: 10.1111/1541-4337.12878.

[3] Damian, J.J. et al. (2018). Phytochemical content and emulsifying ability of pulses cooking water. *European Food*

Research and Technology. DOI: 10.1007/s00217-018-3077-5.

[4] Mustafa, R. and Reaney, M.J.T. (2020). Aquafaba, from Food Waste to a Value-Added Product, in *Food wastes and by-products* (eds.Campos-Vega, R. et al.), John Wiley & Sons Ltd., pp. 93–126.

[5] Shim, Y.Y. et al. (2018). Composition and properties of aquafaba: Water recovered from commercially canned chickpeas. *Journal of Visualized Experiments*. DOI: 10.3791/56305.

[6] Mustafa, R. et al. (2018). Aquafaba , wastewater from chickpea canning , functions as an egg replacer in sponge cake. *International Journal of Food Science and Technology*. DOI: 10.1111/ijfs.13813.

[7] Sun, T. et al. (2023). Heat and mass transfer law during microwave vacuum drying of rice. *Quality Assurance and Safety of Crops and Foods*. DOI: 10.15586/qas.v15i1.1153.

[8] He, Y. et al. (2021). Standardization of Aquafaba Production and Application in Vegan Mayonnaise Analogs. *Foods*.

[9] Sui, W. et al. (2019). Effects of different drying methods on nutritional composition, physicochemical and functional properties of sweet potato leaves. *Journal of Food Processing and Preservation*. DOI: 10.1111/jfpp.13884.

[10] Zielinska, M. et al. (2018). The Effect of Microwave-Vacuum Pretreatment on the Drying Kinetics, Color and the Content of Bioactive Compounds in Osmo-Microwave-Vacuum Dried Cranberries (Vaccinium macrocarpon). *Food and Bioprocess Technology*. DOI: 10.1007/s11947-017-2034-9.

[11] He, Y. et al. (2019). Chickpea Cultivar Selection to Produce Aquafaba with Superior Emulsion Properties. *Foods*.

[12] Meurer, M.C. et al. (2020). Effects of ultrasound on technological properties of chickpea cooking water (aquafaba). *Journal of Food Engineering*. DOI: 10.1016/j.jfoodeng.2019.109688.

[13] Kestens, V. et al. (2008). Vaporisation coulometric Karl Fischer titration: A perfect tool for water content determination of difficult matrix reference materials. *Food Chemistry*. DOI: 10.1016/j.foodchem.2007.01.079.

[14] Bencini, M.C. (1986). Functional Properties of Drum-Dried Chickpea (Cicer arietinum L.) Flours. *Journal of Food Science*. DOI: 10.1111/j.1365-2621.1986.tb13849.x.

[15] Kusunoki, H. et al. (2012). Estimation of lactose interference in vaccines and a proposal of methodological adjustment of total protein determination by the lowry method. *Japanese Journal of Infectious Diseases*. DOI: 10.7883/yoken.65.489.

[16] Tas, O. et al. (2021). Glycation of soy protein isolate with two ketoses: d-Allulose and fructose. *International Journal of Food Science and Technology*. DOI: 10.1111/ijfs.15218.

[17] Koç, M. et al. (2011). Functional and physicochemical properties of whole egg powder: Effect of spray drying conditions. *Journal of Food Science and Technology*. DOI: 10.1007/s13197-010-0159-1.

[18] Teleken, J.T. et al. (2021). Mechanistic understanding of microwave-vacuum drying of non-deformable porous media. *Drying Technology*. DOI: 10.1080/07373937.2020.1728303.

[19] Monteiro, R.L. et al. (2020). Microwave vacuum drying of foods with temperature control by power modulation. *Innovative Food Science and Emerging Technologies*. DOI: 10.1016/j.ifset.2020.102473.

[20] Mudgil, D. (2017). *The Interaction Between Insoluble and Soluble Fiber*, Elsevier Inc.

[21] Chau, C.F. et al. (2007). Different micronization methods significantly improve the functionality of carrot insoluble fibre. *Food Chemistry*. DOI: 10.1016/j.foodchem.2005.11.034.

[22] Chang, Y.W. et al. (2011). Characterization of protein fractions from chickpea (Cicer arietinum L.) and oat (Avena sativa L.) seeds using proteomic techniques. *Food Research International*. DOI: 10.1016/j.foodres.2011.08.001.

[23] Palav, T. and Seetharaman, K. (2006). Mechanism of starch gelatinization and polymer leaching during microwave heating. *Carbohydrate Polymers*. DOI: 10.1016/j.carbpol.2006.01.024.

[24] D'Alessio, G. et al. (2023). High pressure homogenization to boost the technological functionality of native pea proteins. *Current Research in Food Science*. DOI: 10.1016/j.crfs.2023.100499.

[25] Stone, A.K. et al. (2015). Functional attributes of pea protein isolates prepared using different extraction methods and cultivars. *Food Research International*. DOI: 10.1016/j.foodres.2014.11.017.

[26] Panayampadan, A.S. et al. (2022). Vacuum Impregnation Process and Its Potential in Modifying Sensory, Physicochemical and Nutritive Characteristics of Food Products. *Food Engineering Reviews*. DOI: 10.1007/s12393-022-09312-4.

[27] Zheng, Y. et al. (2020). Effects of microwave-vacuum pre-treatment with different power levels on the structural and emulsifying properties of lotus seed protein isolates. *Food Chemistry*. DOI: 10.1016/j.foodchem.2019.125932.

Salt and Meat

Fatma BAYRAKÇEKEN NİŞANCI[1,*], ***Hüdayi ERCOSKUN***[2]

[1] *Ataturk University, Faculty of Sciences, Department of Chemistry, Erzurum, Turkey*

[2] *Karatekin University, Faculty of Engineering, Department of Food Engineering, Çankırı, Turkey*

Abstract

Meat and meat products with their high nutritional value are important food group in order to have a sufficient and balanced diet. Salt, on the other hand, is an ingredient used in foods as it has protective properties as well as flavoring foods. Sodium in the salt structure plays an important role in maintaining the body's electrolyte balance and regulating blood pressure. Excessive consumption of salt or sodium causes hypertension and cardiovascular diseases. Salt consumption is considerably above the maximum daily amount that individuals can consume in the world and Turkey. A significant portion of the salt taken in the diet is taken into the body as a result of the consumption of processed foods. Since meat products contain relatively high amounts of salt, various strategies have been developed for salt reduction in meat products. While reducing the salt content of meat and meat products, it is aimed to produce the desired products without the loss of quality characteristics of meat and flavor defects. This article reviews the human health effects of salt and the methods that can be applied to reduce salt in processed meat products.

Keywords: *Reduced Salt in Meat Products, Salt Reduction, Health*

1. Introduction

Meat products, which are among the foods of animal origin, are among the irreplaceable foods with the different tastes they offer to consumers in addition to providing a balanced diet [1]. Meat and meat products; rich in protein, essential fatty acids, mineral substances and vitamins with high biological value [2]. Salt is one of the indispensable food ingredients of traditional cuisines. Salt has preservative, flavor enhancing and bad taste masking properties in foods. In addition, salt is preferred to be used in foods because it is easily accessible and low cost. The most common raw material and/or additive used in meat products is salt. The first use of salt in meat products was for the preservation of the products. Another use of salt in meat products is to provide the desired taste and flavor to the product. Additionally, salt has a crispening function in meat products. Salt used in meat and meat products increases the water retention capacity of proteins by causing them to bind more water. On the other hand, salt increases the osmotic pressure of food and limits bacterial growth with the toxic effect created by chloride ions. It also prevents the development of undesirable microorganisms in foods by reducing the water activity value in meat and meat products. However, it has been reported that excessive salt consumption causes cardiovascular diseases, hypertension, stroke, stomach cancer, kidney diseases and indirectly obesity in individuals. The amount of salt taken into the body from food in the world and in our country is over 5g/day. On the other hand, the dietary guide prepared in the USA and the Canadian Health Authority have determined the tolerable upper sodium intake limit as 2300 mg/day. Recent data show that reducing daily salt intake to 1200 mg/day reduces cardiovascular risk and blood pressure. Consumers' desire to consume healthy products has led manufacturers to produce meat products with reduced sodium. Salt reduction in meat products occurs by directly reducing some or all of NaCl, using different chloride salts (KCl, $CaCl_2$, $MgCl_2$) and flavor enhancers instead of NaCl, or using new processing techniques. This article provides information about the effects of sodium reduction on sensory perception and product properties by applying various methods to meat and meat products[3].

* Corresponding author. *e-mail address: fbayrakceken@atauni.edu.tr*

1.1. Salt Reduction Strategies in Meat Products

The salt content of meat and meat products can be gradually reduced so that the consumer does not notice it. In a study on gradual salt reduction, it was determined that the taste of the mouth adapted to the salt reduction and consumers perceived the salt of the products as normal salinity [4]. It has been observed that the UK, which implemented this strategy, reduced the salt content of processed food products sold in markets by 20-30% over a 3-year period [5. This strategy for sodium reduction brings with it some limitations. Considering that 25% of individuals are sensitive to taste, it becomes difficult to reduce the amount of salt in the product without the consumers noticing. In addition, in order for this time-consuming strategy to be successful, it must be applicable on an industrial scale and to all products. On the other hand, even if consumers find the reduced sodium product acceptable, it is very difficult to reduce the amount of salt without damaging the taste of the product. As a result of reducing salt in foods, undesirable bitter tastes occur. Additionally, reducing salt in foods causes the shelf life to shorten [6,7]. By reducing the salinity in meat and meat products, both the perceived saltiness and the intensity of the product taste decrease. There are different approaches to reducing sodium content in meat and meat products, especially processed meats. These approaches;

1. Reducing the amount of sodium chloride used in meat products,
2.Reducing the amount of sodium chloride and replacing it with different chloride salts (KCl, $CaCl_2$, $MgCl_2$).
3. Flavor enhancing and masking agents used to eliminate saltiness that occurs when saltiness is reduced in foods.
4. Optimizing the physical structure of salt
5. It is realized as the use of new processing techniques.

1.2. Salt Substitutes Used Instead of Salt

One of the salt substitutes commonly used to reduce or lower the sodium content of foods is potassium chloride (KCl). However, it has been stated that the use of 50:50 sodium chloride/potassium chloride in foods causes bitterness and a decrease in salty taste. It has been concluded that patients with heart failure, chronic renal failure and type I diabetes increase their existing health problems with high potassium intake [8]. By partially replacing salt with KCl, the amount of sodium in meat products can be reduced. Mixing and using chloride salts in meat products is one of the methods used to reduce the amount of sodium. The most well-known and commercially produced mixture Pansalt® _ truck. Pansalt ® is a patented product prepared by removing almost half of the sodium chloride and replacing it with magnesium sulfate, potassium chloride and L-lysine hydrochloride from essential amino acids. The reason for using lysine hydrochloride in this mixture is to ensure easy excretion of sodium from the body, to increase the salinity of the product and to mask the taste perception of magnesium and potassium. Other commercially produced potassium chloride and sodium chloride mixtures are Morton Lite Salt ®, Losalt and Saxa So – Low salt. In a study, a mixture of 40% potassium chloride, 60% sodium chloride and Morton Lite Salt ® It was determined that turkey ham, veal ham, and bacon produced with meat were scored the same as the control groups [3]. A study was conducted on the effects of producing beef patties using low sodium salts. In the study, low-sodium and commercially used meatballs containing 12% magnesium sulfate, 28% KCl and 57% NaCl, Pansalt ®, NaCl , salt and without any added salt were used. Pansalt ® in the study It was observed that meatballs containing meatballs had a higher water retention capacity compared to other groups. This situation is thought to be caused by magnesium sulfate and potassium chloride in the formulation of Pansalt ® commercial salt [9]. Research has shown that the change in taste is not noticed when sodium chloride is replaced with other salts at a rate of 25-40%]. As the amount of potassium chloride in meat products increases to an acceptable level, there is an increase in acidic, spicy and salty taste [10]. Studies have shown that the addition of 50% potassium chloride, used instead of the salt component in cooked hams, helps to achieve high binding and quality sensory properties in the product. In a different study, no difference in

sensory taste, crispness, flavor, and acceptability was found between hams prepared using 100% sodium chloride and hams prepared from 70% sodium chloride + 30% magnesium chloride and 70% sodium chloride + 30% potassium chloride [11]. In a study conducted to reduce the salt content of bacon, it was concluded that adding KCL instead of 15% salt was acceptable in terms of textural properties, but it was not possible to use it in terms of texture because the use of KCl instead of 30% salt in the salt content of bacon gave negative results in terms of chewiness and hardness in the product [12]. Phosphates are used to reduce the amount of sodium chloride in meat and meat products. In a study, the use of phosphates in cooked meat products was investigated. Phosphates are generally used in foods for purposes such as increasing cooking efficiency and improving water retention capacity. Phosphates release negatively charged parts of meat proteins in fresh and cured meat products, thus increasing the ionic strength and causing an increase in water retention capacity. With the addition of salt, the functionality of phosphates increases [13]. Salt and phosphates create a synergistic effect in meat products. The phosphate rate used to reduce the amount of sodium in meat products is much lower than sodium chloride. While sodium chloride is used at a rate of 2-4% in meat products, sodium polyphosphate is used at a rate of 0.5%. The NaCl content of cooked salami and sausages made by adding phosphates can be reduced to 1.4% without losing taste. It is possible to reduce the salt content in cooked hams to 1.7% NaCl [14].

1.3. Flavor Enhancers and Enhancers

Taste masking and flavor enhancing agents are among the methods used to reduce the amount of sodium consumed in foods. Some of these products; monosodium glutamate, lactate, edible seaweed, yeast extracts and nucleotides. Taste enhancers used in foods activate receptors by showing various activities in the throat and mouth, and the loss of flavor caused by reducing the amount of salt in foods is prevented [15]. In a study, monosodium glutamate (MSG) or Ajiplus was used instead of some of the table salt to reduce sodium levels in the Singaporean dish mee soto and chicken rice. When the salt level of these dishes was reduced by 40%, it was observed that the spice aroma, umami and sweet taste, chicken flavor and saltiness decreased. On the other hand, it was determined that chicken aroma, umami taste and saltiness increased with the addition of flavor enhancers. There was no difference in salinity between the products in which the NaCl level was reduced by 40% and the same amount of monosodium glutamate was added. It was concluded that the addition of monosodium glutamate to the products had positive effects on the product in terms of umami taste, flavor intensity and mouth taste [16]. In a study on chicken nuggets, a salt mixture was created using potassium chloride, tartaric acid, citric acid and sucrose instead of 40% sodium chloride. Quality characteristics were examined on 3 samples by adding 12%, 10% and 8% apple pulp to the product. It has been determined that adding apple pulp to the products and reducing the salt significantly reduces the emulsion stability and cooking ability of the products. It has been concluded that the moisture content of nuggets containing 12g/100g of apple pulp with reduced salt content is high. Adding apple pulp to the products increased the dietary fiber content. Addition of apple pulp and reducing the amount of salt reduced the textural quality. It was concluded that products with inadequate properties in terms of sensory quality were obtained [17]. In a study conducted under naturally controlled conditions and using 3 different salts (70% NaCl-30% KCl, 85% NaCl-15% KCl, 100% NaCl) pastrami was produced with 2 different production techniques and the effects of these practices on quality characteristics were investigated. In the research, it was noted that the amount of sodium determined in the raw material increased during the production process depending on the sodium ratio in the salt mixture, and decreased with the fenugreek process. After sensory evaluation, pastrami produced under natural conditions with 100% NaCl was appreciated in terms of taste, while pastrami produced under controlled conditions with 85% NaCl-15% KCl was appreciated in terms of color [18]. In a study conducted on fermented sausages considering taste and textural properties, the amount of potassium chloride used as a substitute for sodium chloride was determined as 40%, the amount of potassium lactate was 30% and the amount of glycine was 20%. As a result of the evaluations, it was concluded that the 40% substitution for these three substances inhibited

pathogenic microorganisms in terms of food safety [19]. Lysine and succinic acid are among the substances used instead of salt to reduce sodium in meat and meat products. Lysine and succinic acid are substances that have antimicrobial and antioxidative properties. These substances can be used instead of 75% NaCl in dry curing of meat and meat products, ensuring that products with the same taste and flavor are obtained. Water binders such as phosphates, gums and starch must be used to preserve the water binding function lost by reducing the salt content in meat and meat products. Phosphates, gums and starch used for this purpose are used to improve the water retention capacity of meat products. The use of sodium and potassium lactate in meat products reduces the amount of sodium in the products [10,20]. In the study conducted to investigate the quality characteristics of low-sodium meatballs prepared using red meat, products with different contents were prepared using phosphate, sodium and fat. Analyzes were made on products with 10%, 15%, 20% fat and 0.8%, 0.42%, 0.04% salt content. Meatballs with 50% and 60% meat content were prepared. Meat and oils used in meatballs have different effects on the product. If the amount of meat used in the products increases, the perceived salty taste decreases, while if the amount of fat increases, the perceived saltiness increases. Although the use of phosphate does not have any effect on the perception of salinity, it has been found that it reduces cooking losses [3].

In a study conducted to reduce the amount of sodium chloride, potassium lactate was added to "Ham" with bones during the production stage. The purpose of using meat with bones here is to distribute the salts in the meat and apply an accelerated curing process. It was produced using 39.7 g/kg potassium lactate and 15 g/kg sodium chloride while preparing meats with bones. It has been determined that the addition of potassium lactate to meat with bones provides a positive improvement in sensory and physicochemical properties and positively affects microbial stability. [21]. A research was conducted on the sensory properties of fermented small sausages prepared by substituting sodium chloride with potassium chloride and potassium lactate at rates ranging from 0% to 50%. By increasing the amount of potassium lactate, an increase in sweetness, pH, doughy structure and the amount of disintegration of the product was observed, while a decrease in hardness, acidic taste, salty taste, ripe taste and sharpness in taste was observed. In addition, it was determined that products prepared by adding high amounts of potassium chloride were similar to the control group in terms of sensory properties [22].

1.4. Optimizing the Physical Structure of Salt

Among the methods used to reduce the amount of salt in meat and meat products, salt reduction in foods can be achieved by making changes in the physical structure of salt. One of the important parameters affecting the perception of salt is the size and shape of salt particles. Salt molecules with large surface areas and small ones dissolve quickly on the surface of the food, thus increasing the perception of saltiness [92]. In addition, applying salt to different layers of the food in varying concentrations can reduce the salt level without negatively affecting the perception of saltiness felt in the product. The salt used in meat and meat products must have a granular structure and the characteristics of refined salt. However, coarse salt is used in processed foods produced using traditional methods, such as pastrami. It has been determined that changes in the shape and crystal structure of the salt increase water binding in emulsion products more quickly, increase pH, increase protein solubility and positively affect cooking efficiency [23].

1.5. Using New Alternative Technologies

High pressure (HPP) and ultrasound applications, which are non-thermal food processing technologies, are used to reduce the salt level of meat products. High pressure (HPP) is applied to products with a value of 400-600 MPa at not very high temperatures (<45˚C) [24]. High pressure process is used in meat and meat products to prevent the development of pathogenic microorganisms in the products. In addition, this technology is used to preserve various features of meat products as a result of reducing salt levels. The interaction between sodium ions and proteins changes with the application of pressure, allowing sodium to enter the taste receptors on the tongue [25]. Proper distribution of salt on the meat

is ensured by the ultra sound technique used in the salting process. In this way, although the NaCl level of the product is reduced, the salinity perceived by the consumer increases [26]. The sodium in meat does not only come from sodium chloride. Sodium nitrate (preservative, colorant), sodium citrate (sweetener), sodium phosphate, sodium bicarbonate (leaving agent) and monosodium glutamate (flavoring) additives can also be used in the formulation of meat. In the study, the effects of high pressure application and changing the NaCl and phosphate content in different process steps on some quality criteria were examined. It was concluded that the application of high pressure treatment to raw meat negatively affected the structure and water retention capacity of reduced-salt ham. It was concluded that a 45% salt reduction in ham would be possible when KCl was used together with high pressure application [27].

References

[1] McNeill, S., Van Elswyk, M. E. (2012). Red meat in global nutrition, *Meat Science, 92*, 166– 173.

[2] Altunboy, A. and Sarıçoban, C., 2014, Muscle stretching techniques used in meat tenderization, *Electronic Journal of Food Technologies, 9* (2), 63-75.

[3] Ruusunen, M. and Puolanne, E. (2005). Reducing sodium intake from meat products. *Meat Science, 70,* 531–541.

[4] Israr, T., Rakha, A., Sohail, M., Rashid, S., Shedzad, A. (2016). Salt reduction in baked products: strategies and constraints. *Trends in Food Science & Technology, 5*1, 98-105.

[5] Ekmekçi, M. (2012). Effects of the Use of Potassium Chloride and Calcium Chloride on Some Quality Characteristics in the Production of Reduced Salt Pastrami. Ankara University, Institute of Science and Technology, Master's Thesis, Ankara, 77.

[6] Inguglia, E.S., Zhang, Z., Tiwari, BK, Kerry, J.P., Burgess, CM (2017). Salt reduction strategies in processed meat products-A review. *Trends in Food Science & Technology, 59*, 70-78.

[7] Doyle, M. E. (2008). Sodium reduction and its effects on food safety, food quality, and human health. FRI BRIEFINGS, 1-12.

[8] Anonymous. 2005. Salt and health: review of the scientific evidence and recommendations for public policy in Ireland. Food Safety Authority of Ireland.

[9] Ketenoğlu, O. and Candoğan, K. 2011. Effect of low-sodium salt utilization on some characteristics of ground beef patties. Food, 36 (2), 63-69.

[10] Price, J.F. 1997. Low-fat/only cured meat products. In AM Pearson & TR Dutson (Eds.), Advances in meat research. Production and processing of healthy meat, (Vol. 11, pp. 242–256). London: Blackie Academic & Professional.

[11] Collins, J. E. 1997. Reducing salt (sodium) levels in processing meat poultry and fish products. In AM Pearson & TR Dutson (Eds.), Advances in meat research. Production and processing of healthy meat, poultry and fish products (Vol. 11, pp. 283–297). London: Blackie Academic & Professional.

[12] Costa-Corredor, A., Serra, X., Arnau, J., Gou, P. 2009. Reduction of NaCl content in restructured dry-cured hams: Post-resting temperature and drying level effects on physicochemical and sensory parameters. *Meat Science 83*, 390–397.

[13] Ruusunen, M., Niemisto, M. and Puolanne, E. 2002. Sodium reduction in cooked meat products. *Agricultural and Food Science in Finland, 11*,199–207.

[14] Ruusunen, M., Vainionpa, J., Lyly, M., Lahteenmaki, L., Niemisto, M., Ahvenainen, R., Puolanne, E. 2005. Reducing the sodium content in meat products: The effect of The formulation in low-sodium ground meat patties. *Meat Science, 69,* 53–60.

[15] Ruusunen, M., Simolin, M. and Puolanne, E., (2001). The effect of fat content and flavor enhancers on the perceived saltiness of cooked bologna-type sausages, *Journal of Muscle Foods, 12,* 107–120.

[16] Leong, J., Kasamatsu, C., Ong, E., Hoi, J. T., Loong, M. N. (2015). A study on sensory properties of sodium reduction and replacement in Asian food using difference-from-control test. *Food Science & Nutrition, 4*(3), 469–478.

[17] Arun, K.V., Sharma, B. D. and Banarjee, R. (2010). Effect of sodium chloride replacement and apple pulp inclusion on the physico-chemical, textural and sensory properties of low fat chicken nuggets. *LWT - Food Science and Technology, 43*, 715–719

[18] Hastaoğlu, E. 2011. Effects of Potassium Chloride Use on Some Quality Characteristics of Pastrami.

Master's Thesis. Hacettepe University Institute of Science, Department of Food Engineering. 76p.
[19] Gelabert, J., Gou, P., Guerrero, L., Arnau, J., (2003). Effect of sodium chloride replacement on some characteristics of fermented sausages. *Meat Science, 65*, 833–839.
[20] Gou, P., Guerrero, L., Gelabert, J. and Arnau, J. (1996). Potassium chloride, potassium lactate and glycine as sodium chloride substitutes in fermented sauages and in dry-cured pork loin. *Meat Science, 42*(1), 37–48.
[21] Fulladosa, E., Serra, X., Gou, P. and Arnau, J. (2009). Effects of potassium lactate and high pressure on transglutaminase restructured dry-cured hams with reduced salt content. *Meat Science, 82*(2), 213–218.
[22] Guardia, MD, Guerrero, L., Gelabert, J., Gou, P. and Arnau, J. 2008. Sensory characterization and consumer acceptability of small caliber fermented sausages with 50% substitution of NaCl by mixtures of KCl and potassium lactate. *Meat Science, 80*, 1125−1230.
[23] Noort, M., Bult, J., Stieger, M. (2012). Saltiness enhancement by taste contrast in bread prepared with encapsulated salt. *Journal of Cereal Science, 55*, 218-225.
[24] Cruz, AG, Faria, JAF, Saad, SMI, Bolini, HMA, Sant'Ana, AS, Cristianini, M. (2010). High pressure processing and pulsed electric fields: potential use in probiotic dairy foods processing. *Trends in Food Science and Technology, 21*(10), 483-493.
[25] Clariana, M., Guerrero, L., Sárraga, C., Díaz, I., Valero, A., García-Regueiro, J. A. (2011). Influence of high pressure application on the nutritional, sensory and microbiological characteristics of sliced skin vacuum packed dry-cured ham. Effects along the storage period. *Innovative Food Science & Emerging Technologies, 12*(4), 456–465.
[26] Alarcon-Rojo, A.D., Janacua, H., Rodriguez, J.C., Paniwnyk, L., Mason, T.J. (2015). Power ultrasound in meat processing. *Meat Science 107*, 86-93.
[27] Tamm, A., Bolumar, T., Bajovic, B., Toepfl, S. (2016). Salt (NaCl) reduction in cooked crude by a combined approach of high pressure treatment and the salt replacer KCl. *Innovative Food Science and Emerging Technologies, 36*, 294–302

Different Methods Used for Increasing Gingival Tissue

Semra ESER [1,*], ***Başak KARASU*** [1]

[1] *Faculty of Dentistry, Department of Periodontology, Çankırı Karatekin University, Çankırı, Turkey*

Abstract

In the treatment of gingival recession, the goal is to cover the exposed root surface for aesthetic or sensitivity issues in some cases, while in other cases, the aim is to increase the amount of keratinized gingival tissue around the tooth or implant to enhance the survival rate of the respective tooth or implant. The purpose of our study is to present different soft tissue grafting methods used in various cases.

Keywords: *Free gingival graft, Keratinized gingival tissue, Subepithelial connective tissue graft, Soft tissue graft*

1. Introduction

Gingival recessions can lead to dentin hypersensitivity, root caries, and aesthetic issues [1,2]. When gingival recession occurs, maintaining hygiene in the affected area becomes challenging due to factors like sensitivity to mechanical and thermal stimuli or difficulty in reaching the area during brushing, leading to inflammation. Therefore, it is necessary to cover exposed root surfaces with gingival grafts.

The insufficiency of the attached keratinized gingiva around the tooth or implant causes the non-keratinized marginal gingiva around the tooth to move in the apical direction with lip and cheek muscle movements. This movement triggers plaque accumulation, complicating plaque elimination with difficulty in brushing the alveolar mucosa. The result is increased inflammation and gingival recession. According to the American Academy of Periodontology Regeneration Workshop Report, if plaque control cannot be achieved ideally, a minimum of 2mm keratinized gingiva is required to prevent attachment loss [3].

Free gingival grafts are commonly used to create keratinized gingiva, and pedicle grafts can be applied when adjacent gingival tissues are sufficient. Connective tissue grafts are applied to cover open root surfaces and thicken the gingival tissue [4]. Various methods, such as tunnel technique and advancement flaps, can be used to apply connective tissue grafts [5].

2. Materials and Methods

A 29-year-old female presented to our clinic with complaints of hot/cold sensitivity and pain while brushing her lower front teeth. Clinical examination revealed Miller Class 1 gingival recession on tooth 31 with 1mm of keratinized tissue. Due to inadequate keratinized gingiva around the tooth, the patient struggled to brush the area, leading to plaque accumulation and inflammation. Following Phase I periodontal treatment and oral hygiene education, inflammation was resolved at the follow-up session. Free gingival graft was planned. The free gingival graft obtained from the patient's palate was sutured to the recipient site and postoperative recommendations were made. The presence of keratinized gingiva was observed in the follow-up session 3 months later (Figure 1). The patient's pain complaint disappeared.

* Corresponding author. *e-mail address: semraeser@karatekin.edu.tr*

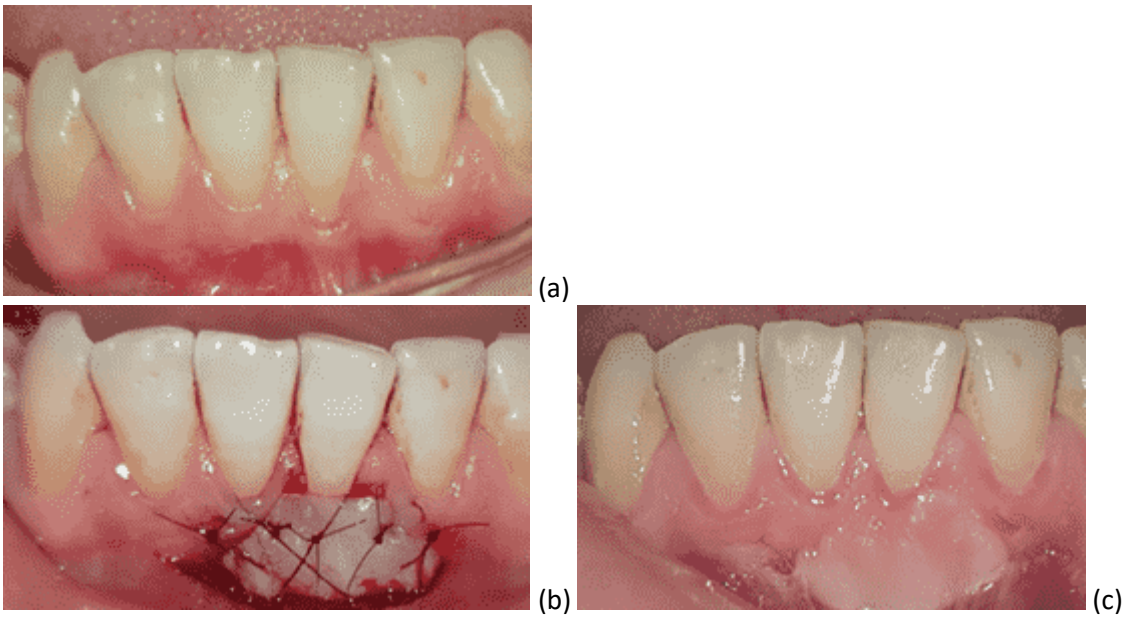

Figure 1. Gingival recession before surgery (a), post operation (b), 3 months post operation (c)

A 51-year-old female, who had dental implants and prosthetics placed one year ago, complained of pain while brushing and discomfort from lip movements during eating. Intraoral examination revealed no keratinized gingiva mesial to the implant, and lip movement caused mobility of the mucosa around the implant. Radiographic examination confirmed bone loss around the implant. Stemmed gingival graft around the implant was decided. After removing the prosthetics and attaching a healing abutment, a 4mm thick gingival tissue stemmed from the palate was buccally adapted and sutured. At three-week follow-up, healthy keratinized tissue had formed around the implant and lip movement did not mobilize the tissue (Figure 2).

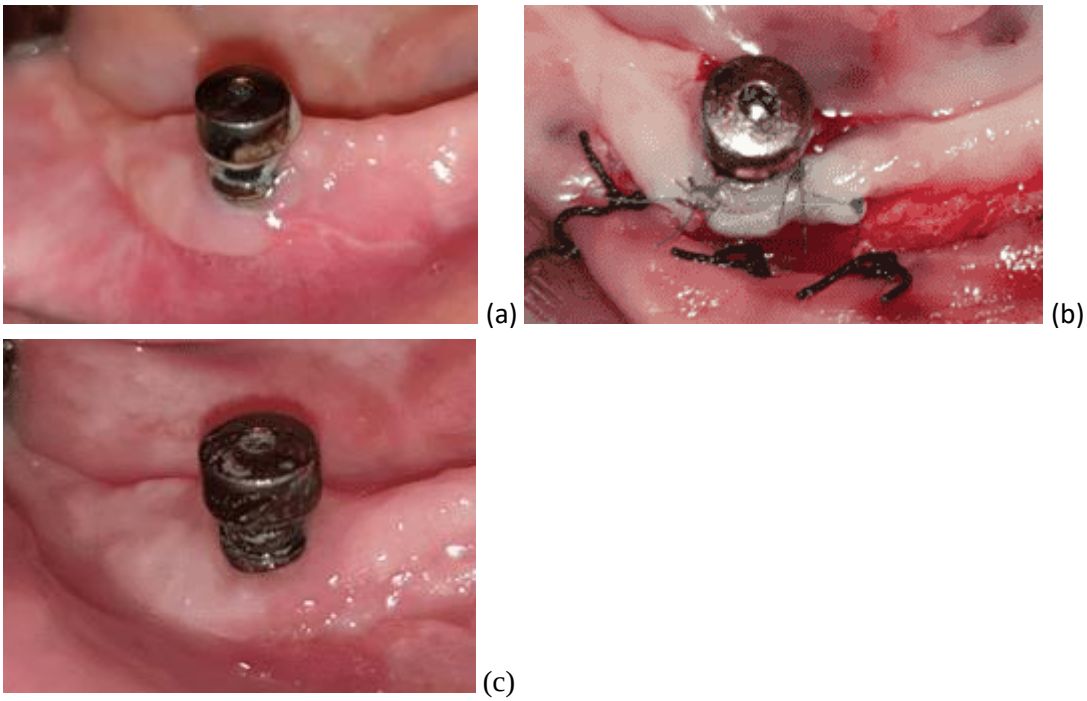

Figure 2. Around the implant before surgery (a), post operation (b), 3 weeks post operation (c)

In the intraoral examination of a 64-year-old male patient who applied to our clinic with the complaint of tooth sensitivity, it was observed that he had Miller Class 1 gingival recession in teeth number 13 and 14. It was planned

to perform a coronally advanced connective tissue graft on the patient in order to cover the exposed root surface. For this purpose, a subepithelial connective tissue graft was taken from the patient's palate and sutured to the recipient area. The half-thickness flap was closed by sliding it coronally. In the follow-up session 6 weeks later, it was observed that the open root surface was successfully closed (Figure 3).

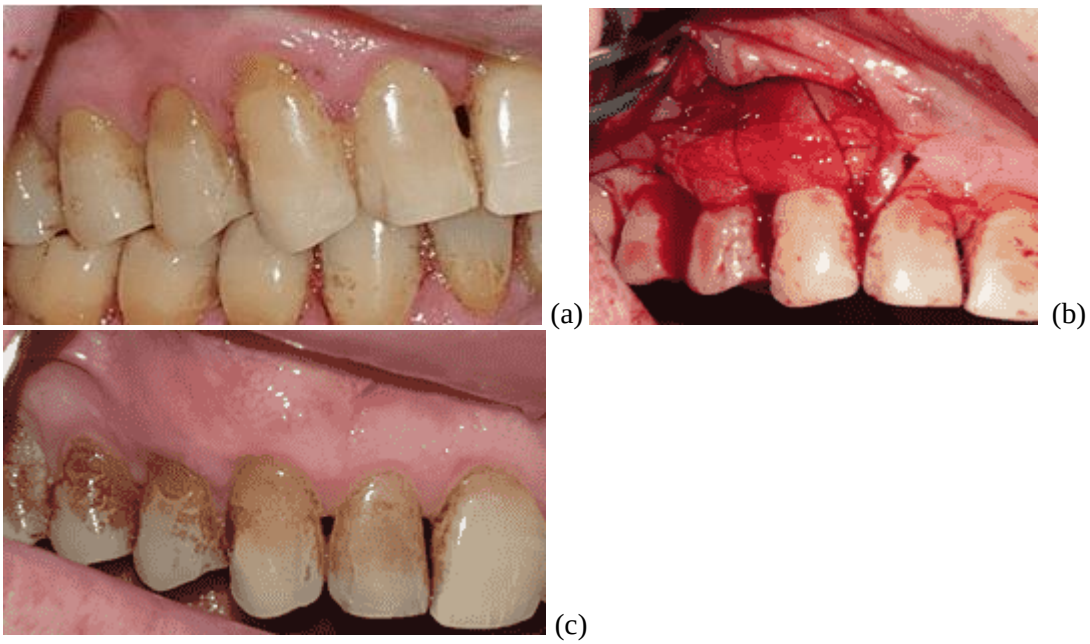

Figure 3. Gingival recession before surgery (a), post operation (b), 6 weeks post operation (c)

A 32-year-old female with complaints of tooth sensitivity and esthetic concerns presented with Miller Class 1 gingival recession around teeth 43, 44, 45, and 46. The recipient site was prepared with the tunnel technique and the subepithelial connective tissue graft obtained from the patient's palate was sutured to the relevant site. In the follow-up session 4 weeks later, it was observed that the open root surface was successfully closed (Figure 4).

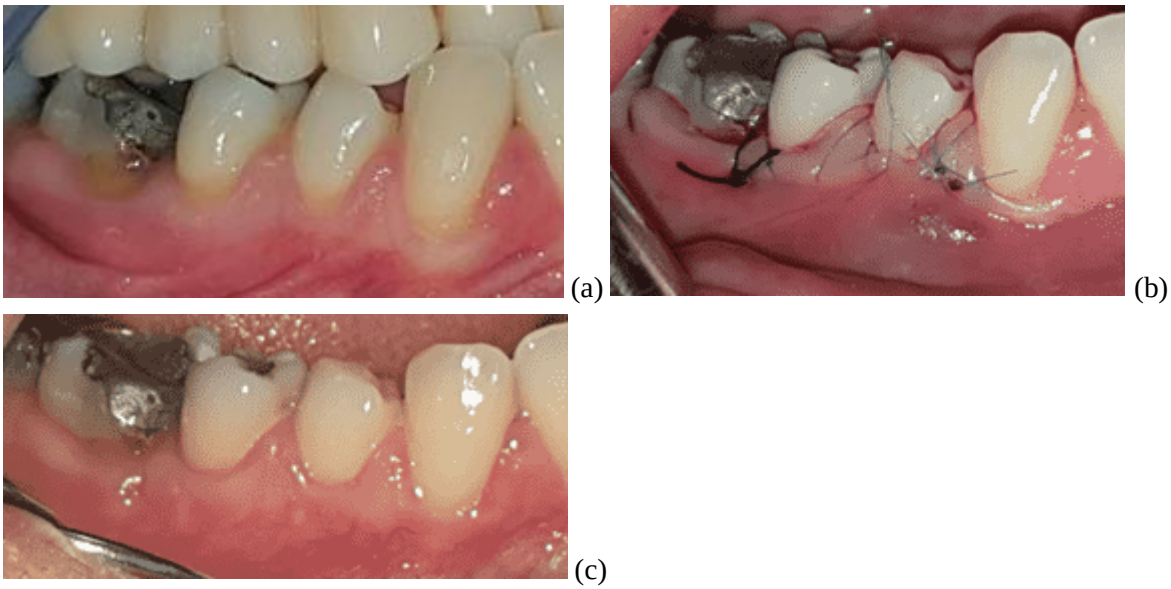

Figure 4. Gingival recession before surgery (a), post operation (b), 4 weeks post operation (c)

3. Conclusion

There are various soft tissue grafting methods available. The success of the treatment depends on the selection of the most appropriate method. Factors such as the amount and quality of keratinized gingival tissue, depth and width of gingival recession, and patient complaints should be evaluated together, guiding the selection of the method [6].

References

[1] Cortellini P, Bissada NF. (2018). Mucogingival conditions in the natural dentition: Narrative review, case definitions, and diagnostic considerations. J Clin Periodontol. Jun;45 Suppl 20:S190-S198.

[2] Jepsen, S, Caton, JG, et al. (2018). Periodontal manifestations of systemic diseases and developmental and acquired conditions: Consensus report of workgroup 3 of the 2017 World Workshop on the Classification of Periodontal and Peri-Implant Diseases and Conditions. *J Periodontol*. 89(Suppl 1): S237–S248.

[3] Scheyer ET, Sanz M, Dibart S, et al.(2015) Periodontal soft tissue non–root coverage procedures: a consensus report from the aap regeneration workshop.J Periodontol 86 : 73-76.

[4] Zucchelli G, Tavelli L, McGuire MK, Rasperini G, Feinberg SE, Wang HL, Giannobile WV. (2020). Autogenous soft tissue grafting for periodontal and peri-implant plastic surgical reconstruction. J Periodontol. Jan;91(1):9-16.

[5] Zadeh HH. (2011). Minimally invasive treatment of maxillary anterior gingival recession defects by vestibular incision subperiosteal tunnel access and platelet-derived growth factor BB. Int J Periodontics Restorative Dent. 31:653-660.

[6] Blanc A, Pare-Dargent C, Giovannoli JL.(1991). Traitement des recessions gingivales par lambeau positionne coronairement. J Parodontol. Sep;10(3):329-34.

Deep learning model for Tongue Cancer Classification

Sajad ABDLKADHIM*, ***Sait DEMİR***, ***Ashwan A. Abdulmunem***

[1] *Karabük University, Engineering Faculty, Sofware Engineering, Karabük, Türkiye.*

[2] *Karabük University, Engineering Faculty, Sofware Engineering, Karabük, Türkiye.*

[3] *University of Kerbala, College of Computer science and information technology, Kerbala, Iraq.*

Abstract

The advancement in computer vision and technology motivated its deployment in various life applications, medical uses of computer vision was one of the main focal of the technology. Image processing with artificial intelligence were the main tool used for medical diagnosis. In this paper, tongue images are used to classify the health. Two classifiers are used namely artificial neural network (FFNN) and Convolutional neural network (CNN). Features extraction also performed using two techniques namely wavelet and image coding. The results show that image coding-based features extraction has optimum results with both FFNN and CNN.

Keywords: *Tongue images, Wavelet, Coding, CNN.*

1. Introduction

Image processing technologies have been developed for many years and have been become vital to human daily routine. The population expansion in recent years triggered several challenges about living hood regulation [1]. The advancement of image processing and computer vision has motivated the integration of those techniques in medical diagnosis. It is being ages when medical diagnosed like virus detection in blood samples was performed in time consuming techniques that demand booth funds and man power [2]. So, it is becoming vital to search for alternative which reduce the man power and diagnosing cost. That is obvious in using computer vision based diagnosis system [3].

Microbiology is a field of tracking the unusual creatures inside the biological cells such as tracking virus inside a blood [4].

At [1] Traditional Chinese medicine (TCM) is well known for its use of tongue diagnosis, despite the results of this method's differential diagnosis being occasionally ambiguous and its effects being variable. The modernization of tongue diagnosis led to the development of technology that has standardized and established advantages in clinical settings using CNN.

At [2] The metabolic disorder diabetes mellitus is primarily caused by an increase in blood sugar levels (DM). The most significant health issue of the twenty-first century is swiftly emerging as diabetes mellitus (DM) and the consequences it causes, such as diabetic retinopathy (DR) using UNet-Conditional Random Field-Recurrent Neural Network (UNet-CRF-RNN).

At [4] Some tongue photos can be used for teaching and research in PM diagnosis, which is one of the first steps in standardizing PM diagnostic indices. Nonetheless, more research is necessary to improve the precision of diagnostic models.

Problem statement of this study can be listed in the hereinafter points:

First: detection of such creatures using image processing is troublesome task since the color of virus appears identical with background color which complicate the detection task.

Secondly: from the other hand, detection using deep learning technique e.g. transfer learning is demanding high-end computers with big processing power.

Thirdly, the deployment of virus detection system is required for long term to be integrated with microscopes which is small in size and need a small chip computer.so to say, powerful computers cannot be integrated with

* Corresponding author. *e-mail address: sajjad95.ab@gmail.com*

such machinery and then using the technology of deep learning in such applications is not possible practically in real life circumstances.

Lastly: The cost of deployment the application in powerful computer is high as compared to standard computer deployment.

2. Methodology

One of the efficient methods to diagnosis the human health is intensive image processing technology. Such technology is applied on the so-called electroluminescence images where the damages amount can be estimated. Three techniques are proposed in the literature to obtain that estimation, firstly analytical approach which tracks the cracks texture and secondly intelligent approach that works on deep learning that intake the image and provide the results without extra added features extraction tasks, lastly hybrid model to estimate cracks and damages is by features extraction integrated with deep/machine learning approach. In hybrid model, aims were to increase the accuracy of damages prediction/classification and reducing the computational costs reported in the first technique (analytical approach).

In this work, two types of features extraction approaches are proposed, using feed forward neural network (FFNN) and secondly using convolutional neural network (CNN). In each technology of above, two types of features extraction are used namely wavelet and features coding. Big data of images are used from open access resource to train the classifiers above. K-fold cross validation is used to obtain the best performance interpretation on the classifiers. Furthermore, in order to get accurate perception about every model performance, K-fold cross validation is to be used. With the mentioned number of database samples, K (folds) can be 10. Thus, accuracy, MAE, Precession can be measured for each fold.

Images are realized in different levels of damage and however, in order to use those images with supervised learning technology, each image need to be labeled with the level of damage. The same is being assigned as no damage (0 no sickness) and (1 with sickness).

2.1 Dataset

It includes pictures of the lips and tongue that are divided into malignant and non-cancerous categories. Photographs were taken in several ENT facilities in Ahmedabad, India, and were then classified with the aid of ENT specialists. The total cancerous images are 87 while the none cancerous images are 44, full dataset is available on [16].

2.2 Preprocessing

Following data processing, each image's records are examined in an effort to determine when the sickness will manifest itself. In this regard, the complete procedure can be summed up as follows:

1) The outcome is a class of "one" and a class of "zero," where "zero" denotes disease or the absence of a fault. Due to the organization of the photo data, each photo has an own class name (which indicate percent sickness occurrence) [5].

2) To reduce training times and lighten the load on the classifiers, image size is being reduced. Scaling an image is necessary for accuracy and to get rid of a lot of superfluous details. This procedure, which consists several coding phases, is utilized several times by the wavelet. We must resize the image for pre-processing in order to eliminate extraneous elements like background noise while keeping the image's proportions [6].

3) The images are normalized which means co images conversion into binary images (black and white) in order to reduce the data load on the training model. To normalize each image, the highest pixel value for a colored image, which is 225, was divided by each pixel [7]. Intelligent classifiers based on convolutional neural networks have been utilized to provide precise disease prediction [8]. The following sections, for instance, offer illustrations of various model settings.

This proposed model, which may be viewed as a more advanced version of an artificial neural network, slightly modified the same recurrent neural network design [9, 10]. It is capable of managing many data values at once. The numerous feedback loops between its layers set it apart from the traditional feed-forward neural network

paradigm. A typical (classical) feed-forward neural network's input and output gates are more likely to resemble the input and output layers. On the other hand, the forget layer is the chosen hidden layer in conventional feed-forward neural networks.

2.3 Features Extraction

Because image processing applications can automatically and without human intervention extract information from photos, their value has increased [11]. It also has the capacity to reveal information that is hidden from the naked eye. Thus, sophisticated computer programmes and algorithms must be used to process photographs in order to do the necessary duty. This could take several days of training time and a lot of computing power if the image data is huge [12]. To reduce the processing load, techniques like increasing the processor's memory or compressing the photographs by deleting unnecessary data are used. Yet, techniques like wavelet, which are also employed in this paper, can be applied in this situation. Nevertheless, picture coding can be utilized to improve training efficiency while reducing processing burden to the absolute minimum. This method can be used for supervised training if picture target information is given [13].

If $(n\ pixel \times n\ pixel)$ electroluminescent image $EIM_{n\times n}^{im=1}$ is present with prior target knowledge, such as 30% damage. The goal is to create a comparable, condensed version of this image that has all the necessary information for its identification $T^{im=1}$, makes it stand out from other photographs, and is comparable to the original. In light of this, $ID^{im=1}$ it is possible to state the following:

$$EIM_{n\times n}^{im=1} == \begin{matrix} t^{im=1} & t^{im=1} & T^{im=1} \\ id^{im=1} & CO & CO \\ ID^{im=1} & CO & CO \end{matrix} \quad (1)$$

As demonstrated in (1), $EIM_{n\times n}^{im=1}$ is representing the electroluminescent image with id=1 and size of $(n\ pixel \times n\ pixel)$. Which is converted into another matrix of other size (may be varying as per the need). The first row of the new matrix is representing the target information which is in our case reflecting the level of damage (e.g. 30%). The first column is reflecting the image identity e.g. image number 1. In order to mitigate the load on the classifier, the target and identity values are made in binary format. The size of new image was set to $(10\ pixel \times 10\ pixel)$. The same is represented in Figure 1.

Actual Image with 30% Defects

1 0 0 1 0 1 1 0 1 1
1 1 1 1 1 1 1 1 1 1
0 1 1 1 1 1 1 1 1 1
1 1 1 1 1 1 1 1 1 1
0 1 1 1 1 1 1 1 1 1
1 1 1 1 1 1 1 1 1 1
1 1 1 1 1 1 1 1 1 1
0 1 1 1 1 1 1 1 1 1
0 1 1 1 1 1 1 1 1 1
1 1 1 1 1 1 1 1 1 1

Coded Binary Image

Figure 1. Features codeing demonstration.

2.4 Model Classification

To achieve the health diagnosis by tongue image categorization, a model is created using a deep learning approach and is inspired by feed forward neural network and conventional neural network. As a result, a model is developed that forecasts case outcomes using picture analysis in order to establish diagnoses. The model is initially trained

with a large image library that comprises a significant number of colored images in order to give the neural network complete knowledge about the object and enable it to handle a range of photos.

Each layer of the model must be trained by allowing it to become popular with images in order for the network to use the knowledge acquired from all of the layers to recognize an image. As a result, the model may correctly predict the diagnosis during the test phase.

2.4.1 Model Training

The model will receive additional instruction until it is performing at its peak. In order to keep the error in the results from increasing, the optimization strategy may recalculate the weight until it achieves the lowest error in the output. The integrated training algorithm may evaluate the precision of the outcomes to gauge the efficacy of the neural network model [14].

The evaluation of the model's performance using the fitness function enables the determination of the final weight coefficients [15]. The initial stages of training involve producing random weight coefficients and assigning those figures to the weight values of the neural network. The training process is therefore continued throughout the training phases in order to achieve weight values that minimize the fitness function. In this case, the fitness function is represented by the mean square error. To begin testing, test data are provided to the neural network model's input, which seeks to ascertain the state of health. The neural network will assess the input data before making a prediction about the image class. This model was created to produce the diagnosis report and incorporate the dataset's photos. Figure 2 depicts the whole process proposed in this work.

3. Results

According to the obtained results from the above methods which is summarized in Table 1, the following points can be made.

(a) That maximum accuracy is 100 percent which is achieved in both proposed classifiers e.g. FFNN and CNN when Coding technique is used in Features extraction model.

(b) The minimum accuracy is seen in FFNN model when wavelet transform is used in features extraction.

(c) In case of wavelet features extraction, CNN is outperformed over the FFNN model in terms of time (248.232 percent) is achieved. However, the maximum accuracy is achieved in CNN in account of time where time required in CNN is 248.232 seconds for achieving of two-fold of FFNN accuracy.

(d) Coding techniques in features extraction is optimized both classifiers accuracy to 100 percent. Time required to perform the classification in the mentioned accuracy in FFNN is far less than it in case of CNN. Consequently, single hidden layer FFNN is outperformed when coding technique is used by obtaining of 100 percent accuracy of classification at 0.95993 seconds. FFNN is leading the other classifier in both accuracy of classification and time.

Table 1. performance assessment.

Tools	AC measure	MSE measure	Time measure	MSE measure	
FFNN	WL	33.333	1.8410	62.3201	1.00387
	Coding	100	0	0.95993	0
CNN	WL	63.953	0.3604	248.232	0.36046
	Coding	100	0	208.236	0

The same is graphically represented at Figure 3 .

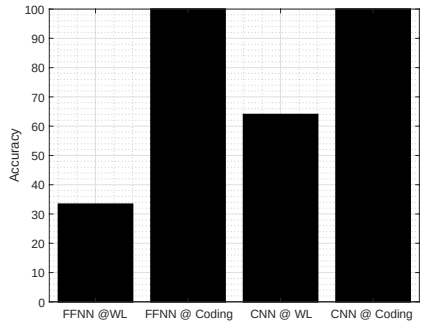

Figure 3. Accuracy measure of the tongue image classifier.

4. Conclusion

There have been various attempts to employ texture tracking features to diagnose diseases including eczema, scarlet fever, and the fairly common Kawasaki disease, which causes changes in tongue colour. All alleged detection techniques have been demonstrated to have a number of flaws, such as (time delay and high computational cost). The technology examines the body using photos of the tongue to discover disorders including Kawasaki disease, eczema, and scarlet fever that are invisible to the human eye. According to this study, automated anomaly detection would be a considerably more cost-effective alternative to human monitoring for carrying out the task of detection and ensuring excellent performance. Performance of the suggested state-of-the-art is compared to that of the Convolutional Neural Network (CNN) and Feed Forward Neural Network, for example, the Feed Forward Neural Network (FFNN). The proposed state of the art, such as coding-based features extraction, performs better in terms of abnormality/defect identification. The single hidden layer FFNN was able to attain the maximum level of recognition accuracy of 100% in the lowest amount of time, 0.95993 seconds, whereas both classifiers were capable of doing so. When the performance of the recommended model was assessed using tenfold validation, the aforementioned accuracy is the highest one that was attained in the fifth fold. The proposed state-of-the-art technique yields findings with the lowest mean absolute error (MAE), which is assessed for both techniques (zero).

References

[1] T.J.W. Klein Nulent et al. Intraoral ultrasonography to measure tumor thickness of oral cancer: a systematic review and meta-analysis, Oral Oncol (2018)
[2] Y. Shinozaki et al. Relationship between appearance of tongue carcinoma on intraoral ultrasonography and histopathologic findings, Oral Surg Oral Med Oral Pathol Oral Radiol (2014)
[3] A. Yesuratnam et al., Preoperative evaluation of oral tongue squamous cell carcinoma with intraoral ultrasound and magnetic resonance imaging—comparison with histopathological tumour thickness and accuracy in guiding patient management, Int J Oral Maxillofac Surg (2014)
[4] A. Kaneoya et al., Quantitative analysis of invasive front in tongue cancer using ultrasonography, J Oral Maxillofac Surg. (2009)
[5] S. Shintani et al., Intraoral ultrasonography is useful to evaluate tumor thickness in tongue carcinoma. Am J Surg. (1997)
[6] T.M. Pimenta Amaral et al., Predictive factors of occult metastasis and prognosis of clinical stages I and II squamous cell carcinoma of the tongue and floor of the mouth. Oral Oncol. (2004)
[7] L. Lam et al., Retrospective study of survival and treatment pattern in a cohort of patients with oral and oropharyngeal tongue cancers from 1987 to 2004. Oral Oncol (2007)
[8] T. T. Deng, “Basic theory of traditional Chinese medicine,” in Diagnostics of Chinese Medicine, pp. 5–11, Chih-Yin Publishing, Taipei, Taiwan, 1995.

[9] C. H. Li and P. C. Yuen, "Tongue image matching using color content," Pattern Recognition, vol. 35, no. 2, pp. 407–419, 2002.
[10] Y. Wang, Y. Zhou, and J. Yang, "A tongue analysis system for tongue diagnosis in traditional Chinese medicine," in Proceedings of the International Symposium Computational and Information Science (CIS '04), vol. 3314 of Lecture Notes in Computer Science, pp. 1181–1186, Springer, 2004.
[11] Y.-G. Wang, J. Yang, Y. Zhou, and Y.-Z. Wang, "Region partition and feature matching based color recognition of tongue image," Pattern Recognition Letters, vol. 28, no. 1, pp. 11–19, 2007.
[12] Q. Li and Z. Liu, "Tongue color analysis and discrimination based on hyperspectral images," Computerized Medical Imaging and Graphics, vol. 33, no. 3, pp. 217–221, 2009.
[13] M. F. Zhu and J. Q. Du, "A novel approach for color tongue image extraction based on random walk algorithm," Applied Mechanics and Materials, vol. 462-463, pp. 338–342, 2014.
[14] B. Pang, D. Zhang, and K. Wang, "Tongue image analysis for appendicitis diagnosis," Information Sciences, vol. 175, no. 3, pp. 160–176, 2005.
[15] C.-C. Chiu, "A novel approach based on computerized image analysis for traditional Chinese medical diagnosis of the tongue," Computer Methods and Programs in Biomedicine, vol. 61, no. 2, pp. 77–89, 2000.
[16] Dataset: https://www.kaggle.com/datasets/shivam17299/oral-cancer-lips-and-tongue-images

Analysis of one-dimensional photonic crystal biosensor for detection of SARS-CoV-2

Nurettin Bilgili [1*], **Ali Çetin** [2]

[1] *Graduate School of Natural and Applied Sciences, Eskişehir Osmangazi University, Eskişehir, Turkey*

[2] *Faculty of Science, Department of Physics, Eskişehir Osmangazi University, Eskişehir, Turkey*

Abstract

We theoretically investigate one-dimensional photonic crystal (1D PC) with a defect layer as a biosensor for the detection of COVID-19 (SARS-CoV-2) virus in the lungs. The composed of 1D photonic crystal is chosen as Silicon dioxide and Titanium dioxide, with a central defective layer. The defect layer is taken as healthy lung tissue and infected lung tissue. The different refractive indices of samples cause a shift in the transmission peak which can be used for the detection of COVID-19 (SARS-CoV-2). We optimized our structure and designed it in OptiFDTD software which uses the Finite-difference time-domain method (FDTD) to calculate the transmission spectrum of the biosensor. We show that the sensitivity of the biosensor is 101.46 nm/RIU, the quality factor is 3.22 × 105 and the detection limit is 1.97 × 10-4 RIU.

Keywords: *Photonic crystal, Transmittance, Defect modes, Biosensors, SARS-CoV-2*

1. Introduction

Corona virus (SARS-CoV-2) has spread rapidly and has become a pandemic since first confirmed in December 2019 [1]. According to a 2020 report by the World Health Organization (WHO), the SARS-CoV-2 virus, which causes COVID-19, is estimated to have killed more than 3.3 million people worldwide [2]. A lot of research is being done all over the world to control the spread [2]. Biosensors are key technologies for quick detection of virus [3]. Recently, photonic crystals (PCs) have been used as a biochemical sensor [4].

Photonic crystals (PCs) are multilayer structures which refractive indexes changes periodically [5]. There are three types of PCs depending on refractive index change directions; one-dimensional (1D), two-dimensional (2D) and three-dimensional (3D) [6]. PCs can control the propagation of electromagnetic waves of different frequencies. Because of the multiple Bragg scattering of light at the interface of different media photonic band gaps (PBGs) [7] occur which forbid the propagation of light at some frequencies. Today PC based devices used in technological applications such as high-efficiency semiconductor lasers, high-reflection mirrors, solar cells, light-emitting diodes, waveguides, optical filters, high-Q resonators, nano antennas, frequency-selective surfaces, amplifiers and antireflection coatings, biosensors, etc. [8 – 10].

Biosensors are devices with mechanisms that can measure changes in biological systems. PC-based Biosensor technology is recognized as a simple and cost-effective method for the detection of various diseases compared to conventional methods [11].

When we break the periodicity of the PCs by adding a different layer between the PCs structures, which called defect layer, a single transmission peak occurred which called the resonant mode inside PBG [12]. Any change in the refractive index of defect layer cause a shift in the position of the transmission peak in the PBG which is the basic principle of the PC biosensors [13]. Because of the low-cost and easily fabricated, 1D PC biosensors attract interest of the scientist worldwide [14].

In this study, we design 1D PC biosensor for detection of transmission peak shift in the PBG upon the change in the refractive index of lung tissues containing healthy and infected by SARS-CoV-2 virus under different concentrations based on FDTD Method approach. We optimized the relevant parameters to improve the sensitivity of this photonic biosensor.

* *Corresponding author. e-mail address: nurettinbilgili@gmail.com*

2. Materials and Methods

Finite-difference time-domain method (FDTD) divides the space and time in a regular grid for solving the Maxwell equations depending on time. Maxwell equations in isotropic and linear media are

$$\nabla \times \boldsymbol{H} = \varepsilon \frac{\partial \boldsymbol{E}}{\partial t} + \sigma \boldsymbol{E}$$
$$\nabla \times \boldsymbol{E} = -\mu \frac{\partial \boldsymbol{H}}{\partial t} + \sigma_m \boldsymbol{H} \quad \textbf{(1)}$$

where ε, σ, μ and σ_m are, the dielectric permittivity, the medium electrical conductivity, permeability of medium and magnetic loss of the medium, respectively. If we assume TEM wave propagates along z-direction we can write

$$\frac{\partial}{\partial x} = \frac{\partial}{\partial y} = 0$$

and Eq. 1 can be written as

$$-\frac{\partial \boldsymbol{H_y}}{\partial z} = \varepsilon + \frac{\partial \boldsymbol{E_x}}{\partial t} + \sigma \boldsymbol{E_x}$$
$$\frac{\partial \boldsymbol{E}}{\partial z} = \mu + \frac{\partial \boldsymbol{H_y}}{\partial t} + \sigma_m \boldsymbol{H_y}$$

A time step is determined for iterations and TE and TM fields can be calculated by using these iterations according to FDTD method

$$E_x^{n+1}(k) = \frac{1 - \frac{\sigma(m)\Delta t}{2\varepsilon(m)}}{1 + \frac{\sigma(m)\Delta t}{2\varepsilon(m)}} \times E_x^n(k) - \frac{\frac{\Delta t}{\varepsilon(m)}}{1 + \frac{\sigma(m)\Delta t}{2\varepsilon(m)}} \times \frac{H_y^{n+1/2}\left(k + \frac{1}{2}\right) - H_y^{n+1/2}\left(k - \frac{1}{2}\right)}{\Delta z}$$
$$H_y^{n+1/2}(k + 1/2) = \frac{1 - \frac{\sigma(m)\Delta t}{2\mu(m)}}{1 + \frac{\sigma(m)\Delta t}{2\mu(m)}} \times H_y^{n-1/2}\left(k + \frac{1}{2}\right) - \frac{\frac{\Delta t}{\mu(m)}}{1 + \frac{\sigma(m)\Delta t}{2\mu(m)}} \times \frac{E_x^n(k+1) - E_x^n(k)}{\Delta z}$$

where k and n are space step integer and time step integer respectively. Also transmission expressions of electric and magnetic fields can be written as [21]

$$R = \left|\frac{E_t(t)}{E_i(t)}\right|^2 \qquad R = \left|\frac{H_t(t)}{H_i(t)}\right|^2$$

3. Results and Discussion

We proposed a 1D defective PC which layout is shown in Fig.1 where vertical red line is input wave and green point is observation point to detect transmission waves. Since 700-780 nm wavelength laser diodes are widely used for biomedical measurement [15] we use $715\ nm$ as an input Gaussian modulated continuous wave. Our optimized PC designed as $(\mathrm{AB})^m/\mathrm{C}/(\mathrm{AB})^m$ where layer A is taken as SiO_2, layer B is taken as TiO_2 and layer C is defect layer which taken as healthy lung tissue and effected lung tissue with SARS-CoV-2 virus. m is the number of periods which taken as 6. The thickness and refractive indexes of SiO_2 and TiO_2 layers are $d_1 = 120\ nm,\ d_2 = 90\ nm$ and $n_1 = 1.4742, n_2 = 2.3609$ [16] respectively. The defect layer thickens taken

as 120 nm according to the maximum diameter of SARS-CoV-2 virus [17]. The healthy lung tissue refractive index taken as 1.39 [18] and infected lung tissue refractive indexes according to their concentrations (Nano Mole-nM) taken as shown in Table 1 [19, 20].

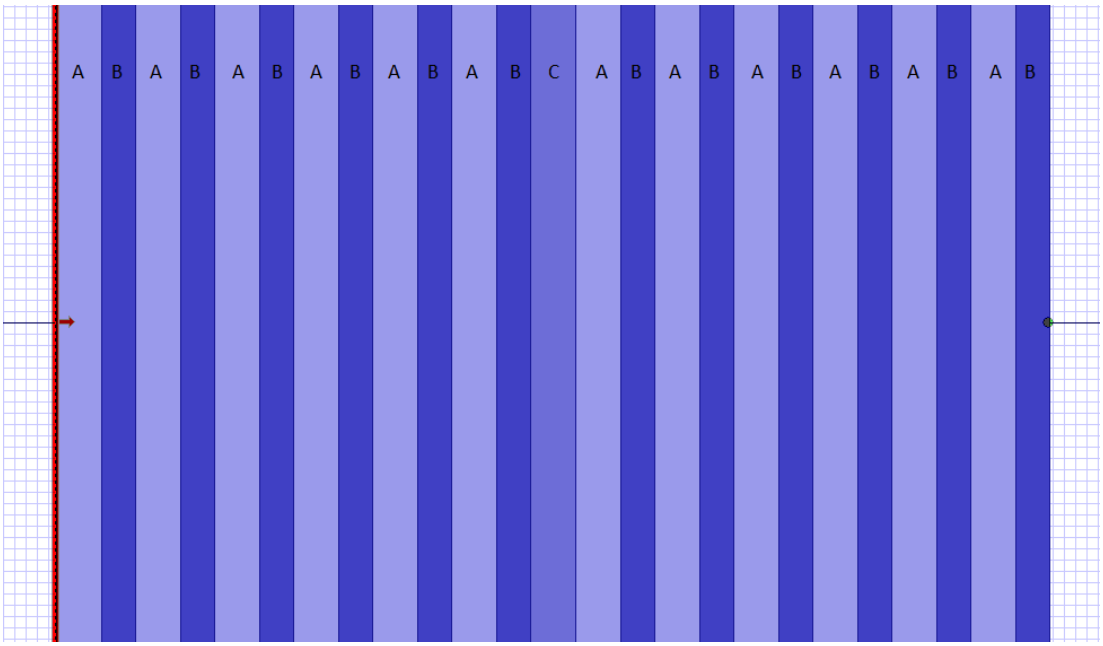

Figure 1. Schematic design of the proposed 1D PC biosensor with a defect layer

Table 1. Refractive index of blood cells in different SARS-CoV-2 concentrations

SARS-CoV-2 concentration (nM)	Refractive index
0	1.39
0.01	1.40
0.05	1.44
0.1	1.49
0.2	1.59
0.3	1.69

We theoretically investigated transmittance spectra of 1D PC with a defect layer for detecting SARS-CoV-2 in human lung tissues. We studied the refractive index for the normal and lung tissue samples at 715 nm.

We obtain defect mode in PBG at 762.53 nm which shown in Fig. 2 when we take defect layer as lung tissue sample.

Table 1 shows the refractive index of lung tissues at different SARS-CoV-2 concentrations. From Table 1, we can see that as SARS-CoV-2 concentrations in the lung tissue increase, the refractive index of the samples increases accordingly.

Fig. 3 shows that the transmittance spectrum of defective 1D PCs with different value of SARS-CoV-2 concentration in lung tissue samples which shown in Table 1. By increasing the blood SARS-CoV-2 concentration, the defect mode shifted towards longer wavelengths. The defect state is sharp as the quality factor is large [22].

Sensitivity (S) is an important parameter for a sensor. The sensitivity is defined as the change in defect state wavelength per unit refractive index [23]. We obtain the sensitivity of proposed biosensor from graph shown in Fig. 4. It is clear that wavelength peaks shift towards longer wavelengths by increasing the refractive index. We obtain sensitivity of proposed biosensor as 101,46 nm/RIU.

Quality factor (Q) shows the performance of the biosensors and calculated from $Q = \frac{\lambda_d}{\lambda_{FWHM}}$ formula where λ_d and λ_{FWHM} are the resonant wavelength and the full width at half maximum of defect mode. Table 2 shows the performance of our proposed biosensor as $1{,}864 \times 10^5$.

Finally, we calculated detection limit from $LOD = \lambda(20 \times S \times Q)$ formula [24] and obtain $1.97 \times 10^{-4}\ RIU$. According to value of LOD is very low, the proposed sensor is efficient as it can resolve very small changes in the refractive index.

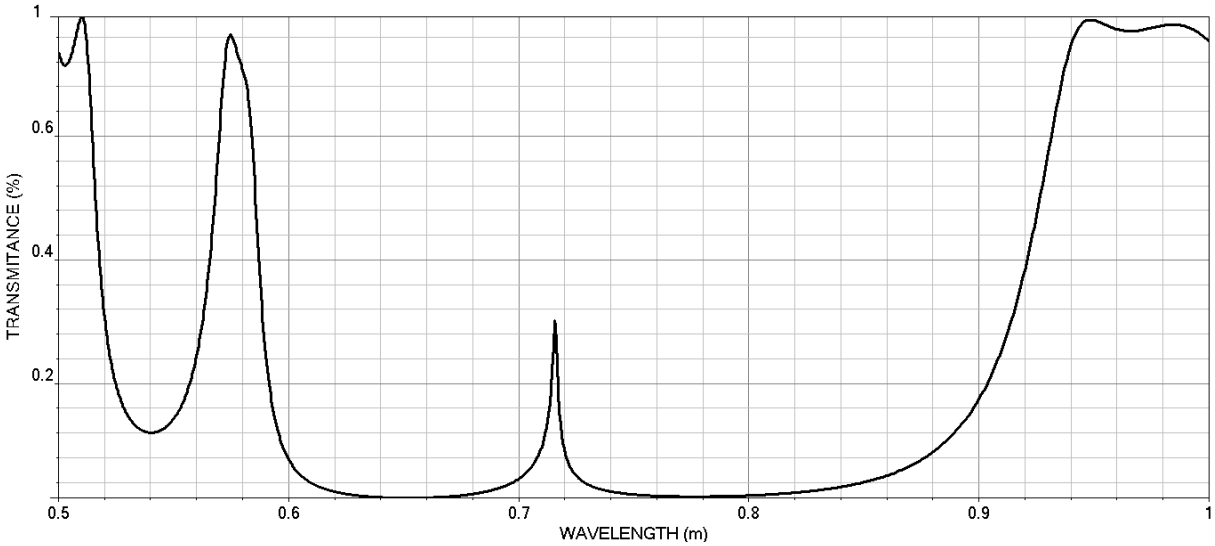

Figure 2. The transmittance spectrum (Y) of a defective photonic crystal as a function of wavelength (X) at healthy blood sample

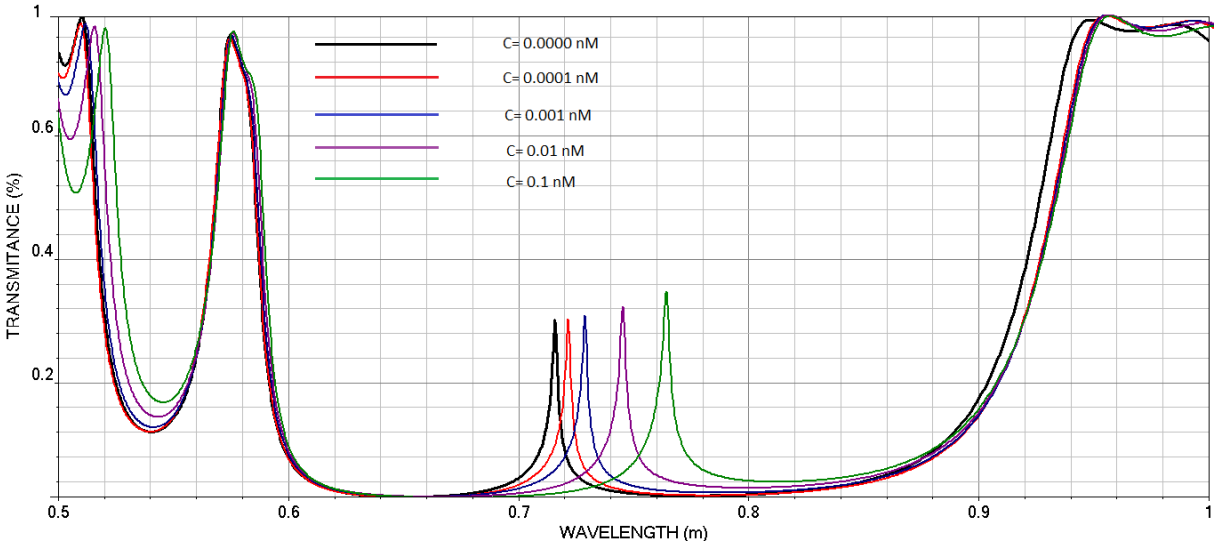

Figure 3. The transmittance spectrum of defective 1D PCs as a function of wavelength with different value of SARS-CoV-2 concentration (nM) in blood.

Table 2. The values of Quality factor at different SARS-CoV-2 virus concentrations

SARS-CoV-2 concentration	Refractive index	Wavelength (nm)	Quality factor
0	1.39	762.53	1.864
0.01	1.40	764.58	1.859
0.05	1.44	769.07	1.848
0.1	1.49	779.98	1.682
0.2	1.59	793.78	1.791
0.3	1.69	800.55	1.857

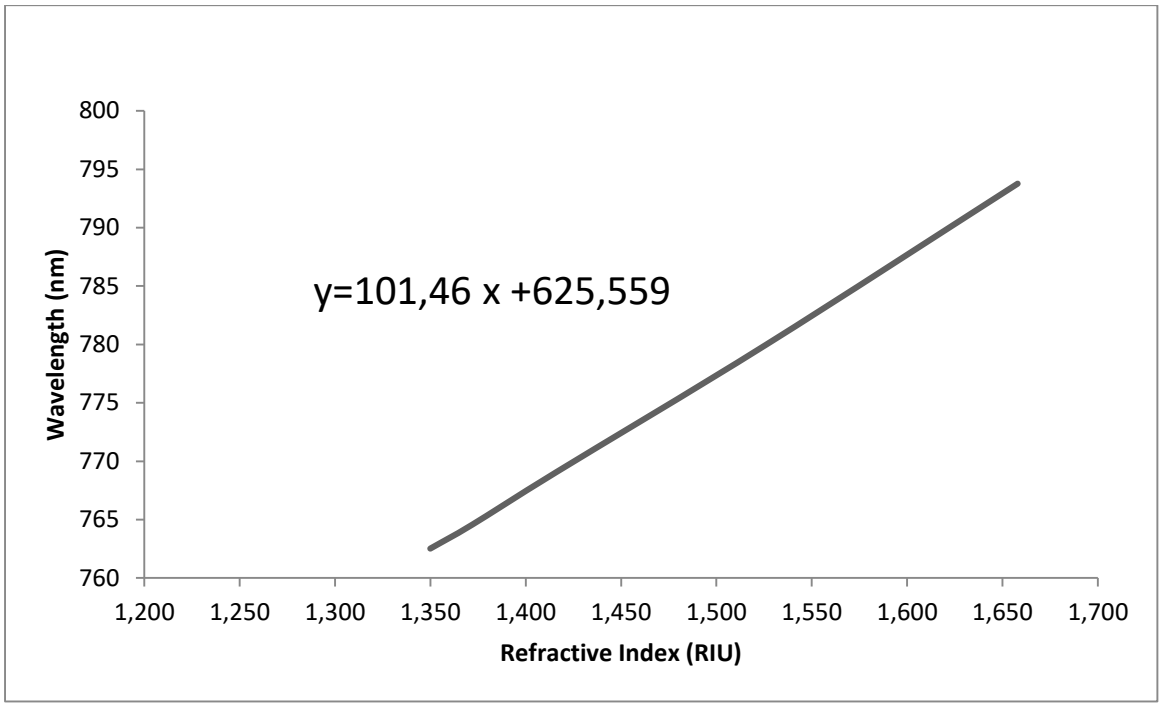

Figure 4. Sensitivity of the proposed biosensor due to transmission peak wavelength with refractive index of defect

4. Conclusion

In the present paper, the 1D defective PC studied as a biosensor for SARS-CoV-2. We theoretically investigated the performance of the PC using FDTD Method. We optimized the characteristics of the biosensor by keeping the layer type, layer thicknesses, incidence angles of input wave and number of periods constant expects the SARS-CoV-2 concentration in human lung tissues. The simulations showed that the position of defect mode increases linearly with the increase of SARS-CoV-2 concentration. Also, the sensitivity, quality factor and detection limit of the biosensor obtained as $101{,}46\, nm/RIU$, $1{,}864 \times 10^{5}$ and $1{,}97 \times 10^{-4}\, RIU$. The proposed device shows good results for the with SARS-CoV-2 ultra-fast response. This structure is conducive to the industrial design by using low-cost materials and high sensitivity. Therefore, this sensor may be desirable for bio/chemical sensing applications.

References

[1] WU, Fan, et al. A new coronavirus associated with human respiratory disease in China. *Nature*, 2020, 579.7798: 265-269.

[2] MACHHI, Jatin, et al. The natural history, pathobiology, and clinical manifestations of SARS-CoV-2 infections. *Journal of Neuroimmune Pharmacology*, 2020, 15.3: 359-386.

[3] VALERA, Enrique, et al. COVID-19 point-of-care diagnostics: present and future. *ACS nano*, 2021, 15.5: 7899-7906.

[4] TONG, Allison, et al. Research priorities for COVID-19 sensor technology. *Nature Biotechnology*, 2021, 39.2: 144-147.

[5] SHIN, Jinsub; BRAUN, Paul V.; LEE, Wonmok. Fast response photonic crystal pH sensor based on templated photo-polymerized hydrogel inverse opal. *Sensors and Actuators B: Chemical*, 2010, 150.1: 183-190.

[6] ZHANG, Yuping, et al. Optical properties of one-dimensional Fibonacci quasi-periodic graphene photonic crystal. *Optics Communications*, 2015, 338: 168-173.

[7] YABLONOVITCH, Eli. Inhibited spontaneous emission in solid-state physics and electronics. *Physical review letters*, 1987, 58.20: 2059.

[8] HUNG, Hui-Chuan; WU, Chien-Jang; CHANG, Shoou-Jinn. Terahertz temperature-dependent defect mode in a semiconductor-dielectric photonic crystal. *Journal of Applied Physics*, 2011, 110.9: 093110.

[9] BUSCH, Kurt, et al. (ed.). *Photonic crystals: advances in design, fabrication, and characterization*. John Wiley & Sons, 2006.
[10] BERGER, V. Photonic crystals and photonic structures. *Current Opinion in Solid State and Materials Science*, 1999, 4.2: 209-216.
[11] KATS, Mikhail A., et al. Nanometre optical coatings based on strong interference effects in highly absorbing media. *Nature materials*, 2013, 12.1: 20-24.
[12] ALY, Arafa H., et al. Biophotonic sensor for the detection of creatinine concentration in blood serum based on 1D photonic crystal. *RSC advances*, 2020, 10.53: 31765-31772.
[13] ALY, Arafa H.; ELSAYED, Hussien A. Defect mode properties in a one-dimensional photonic crystal. *Physica B: Condensed Matter*, 2012, 407.1: 120-125.
[14] MUKUNDAN, Harshini, et al. Waveguide-based biosensors for pathogen detection. *Sensors*, 2009, 9.7: 5783-5809.
[15] SINGH, R., et al. High-power, reliable operation of 730 nm AlGaAs laser diodes. *Applied physics letters*, 1999, 75.14: 2002-2004.
[16] PALIK, Edward D. (ed.). *Handbook of optical constants of solids*. Academic press, 1998.
[17] PANDEY, Amritanshu, et al. Analysis of ternary layer photonic band gap tunable filters for wavelength division multiplexing applications. *Journal of Nanoelectronics and Optoelectronics*, 2017, 12.4: 331-336.
[18] MALIK, Yasmin A. Properties of coronavirus and SARS-CoV-2. *The Malaysian journal of pathology*, 2020, 42.1: 3-11.
[19] LONDON, R. X-Ray Microimaging for the Life Sclences.
[20] TAGHIPOUR, Ata; HEIDARZADEH, Hamid. Design and Analysis of Highly Sensitive LSPR-Based Metal–Insulator–Metal Nano-Discs as a Biosensor for Fast Detection of SARS-CoV-2. In: *Photonics*.
[21] ÇETIN, Ali; BILGILI, Nurettin. TRANSMISSION PROPERTIES OF 1D DEFECT METALLIC-DIELECTRIC PHOTONIC CRYSTALS. *Anadolu University Journal of Science and Technology A-Applied Sciences and Engineering*, 2016, 17.4: 633-640.
[22] ARUNKUMAR, Rajendran; SUAGANYA, Thinakaran; ROBINSON, Savarimuthu. Design and analysis of 2D photonic crystal based biosensor to detect different blood components. *Photonic Sensors*, 2019, 9.1: 69-77.
[23] SUTHAR, Bhuvneshwer, et al. Biosensor application of one-dimensional photonic crystal for malaria diagnosis. *Plasmonics*, 2021, 16.1: 59-63.
[24] WHITE, Ian M.; FAN, Xudong. On the performance quantification of resonant refractive index sensors. *Optics express*, 2008, 16.2: 1020-1028.

Eco-Friendly Approach: Dried Lemon Peel as an Adsorbent for Methylene Blue in Aqueous Solutions

Tiba SALEH GHANI AL-OKAIDAT [1], *Abdulrhman ABDULKREEM MOHAMMED AL-MASWARI*[1]
M. Bora AKIN [1*]

[1] *Department of Chemical Engineering, Çankırı Karatekin University, Çankırı, Turkiye*

Abstract

The effect of dyestuffs in increasing environmental pollution is quite high. Moreover, they pollute the planet's scarce potable water resources. Therefore, cleaning wastewater has strategic importance. There are also adsorbents among various methods to clean dyestuffs in wastewater. Adsorbents can be produced from various materials. Cost and environmental impacts need to be taken into consideration during the production of these adsorbents. In this study, the adsorption of methylene blue from lemon peels, which are considered as waste, without being subjected to any other process other than drying, was examined. The results of this study show that dried lemon peels are insufficient for methylene blue adsorption. To obtain higher adsorption efficiency, pre-treatment of lemon peels is necessary. Additionally, the effects of initial concentration and amount of adsorbent on the adsorption capacity were determined and the effect of temperature on the adsorption capacity was examined. These findings show that adsorption of methylene blue from aqueous solutions with dried lemon peels is possible, but the removal efficiency is low. In this context, it is necessary to investigate and apply pre-treatment methods and different conditions to increase the adsorption capacity of lemon peels.

Keywords: *Adsorption, Wastewater, Methylene Blue, Lemon peel, Adsorbent*

1. Introduction

The removal of synthetic dyes from aqueous solutions is a significant environmental problem due to their potential adverse effects on ecosystems and human health. In recent years, there has been increasing interest in researching environmentally friendly and cost-effective adsorbents for the removal of dyes from wastewater. One such potential adsorbent is dried lemon peel, which is noted for its adsorption abilities. Lemon peel, a by-product of the citrus processing industry, offers advantages such as abundance, low cost and environmental friendliness.

There are studies in which various agricultural and food waste-based adsorbents, including activated carbons produced from pomegranate peel and agricultural waste, are suitable for dye removal. In a study, an adsorbent was produced from lemon peels as a biosorbent material to remove reactive blue 49 dye from aqueous solutions [1]. In another study, the seeds and peels of nance, an exotic fruit, were used in the removal of methylene blue [2]. Additionally, the adsorption capacity was examined in another study in the removal of lemon peel, methyl orange and congo red [3]. It was emphasized that pummelo peel pretreated with NaOH was effective in removing methylene blue from aqueous solutions and citrus peels were also effective adsorbents [4].

The use of methylene blue by drying lemon peel as an environmentally friendly adsorbent for use in wastewater treatment is a start for future research. This study investigates the adsorption capacity of dried lemon peel for methylene blue in aqueous solutions. Thus, dried lemon peels were used to adsorb methylene blue in water at 25 °C. During the study, temperature, adsorbent dose and initial dye concentration were examined. Additionally, the adsorption behavior of lemon peels used at 0.5 mg/L at a concentration of 200 mg/L was examined against time.

2. Materials and Methods

Metileb was obtained from Blue Sigma Aldrich. Lemon peels were dried using a vacuum oven at 80 °C. After drying, the size was reduced by grinding in a mortar. A magnetic stirrer (IKA) and UV spectrophotometer (Shimadzu) were used in methylene blue adsorption experiments.

In this study, experiments on the adsorption of Methylene Blue were carried out comprehensively. First, 1000 mL of Methylene Blue stock solution was prepared at a concentration of 1 g/L. In order to obtain different

* Corresponding author. *e-mail address: mbakin@karatekin.edu.tr*

concentrations from this stock solution, a calibration chart was created by dilution processes. The wavelength of the UV spectrophotometer used in the measurement of Methylene Blue was determined as 665 nm.

In the experiments conducted to determine the adsorption capacity, the initial concentrations of Methylene Blue were set as 10, 25, 50, 100, 200, 300, 400, 500, 750 and 1000 mg/L, respectively. Experiments were carried out at 25 °C using 0.5 mg/L leaf adsorbent in 100 mL solutions prepared.

In time-dependent experiments, a concentration of 200 mg/L Methylene Blue was used and the samples taken during the removal process were examined at the following time periods: 0, 2, 5, 10, 20, 30, 45, 60, 90, 180, 240, 300, 360, 420 and 1440 minutes. The samples taken were measured with a UV spectrophotometer.

Additionally, experiments were conducted at temperatures of 5 °C, 25 °C and 40 °C to examine the temperature effect on the adsorbent. In order to investigate the effect of adsorbent dosage, the amounts of adsorbent used were determined as 0.3, 0.5, 1 and 2.5 mg/L.

Table 1 summarizes the parameters used in these experiments and the values chosen for these parameters.

Table 1. Parameters and levels.

Parameter	Level
Temperature (°C)	5, 25, 40
Adsorbent dose (mg/L)	0.3, 0.5, 1, 2.5
Methylene Blue Conc. (mg/L)	10, 25, 50, 100, 200, 300, 400, 500, 750, 1000
Time (min)	0, 2, 5, 10, 20, 30, 45, 60, 90, 180, 240, 300, 360, 420, 1440

3. Results and Discussion

3.1. Effect of Initial Dye Concentration

In the study, adsorption capacities (qe) were examined using adsorbent with 0.5 mg/L for different concentrations. The qe values obtained for the concentrations examined in the study are given in Figure 1. Among the initial concentrations, the highest adsorption capacity was obtained at 750 mg/L with 0.2371 mol/kg. A rapid increase is observed in the qe value up to the initial concentration of 750 mg/L. 200 mg/L was chosen as the working concentration and this concentration was used to examine other parameters.

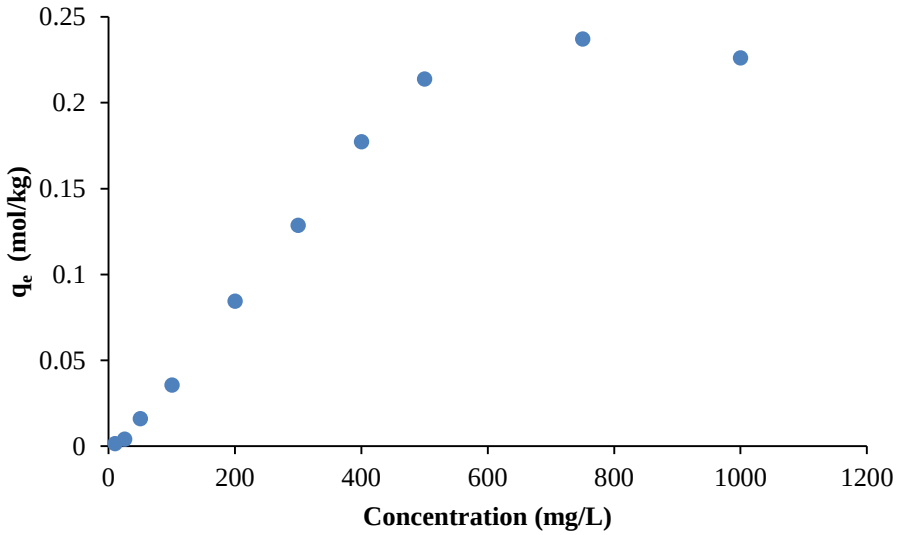

Figure 1. Effect of dyestuff initial concentrations on adsorption capacity.

3.2. Effect of Time

For the experiment in which the effect of time on qe was examined, 200 mg/L was chosen as the initial concentration. To find the qe value at the selected concentration, concentration values were found by measuring samples taken at certain times. When Figure 2a is examined, it is understood that the concentration decreases over time, meaning that the adsorbent does its job. At the end of 1440 minutes, the dye concentration decreases to 180.32 mg/L. The calculation made using concentrations shows the change of qe value with time (Figure 2b). At the end of 1440 minutes, the qe value is 0.0844 mol/kg at an initial dye concentration of 200 mg/L.

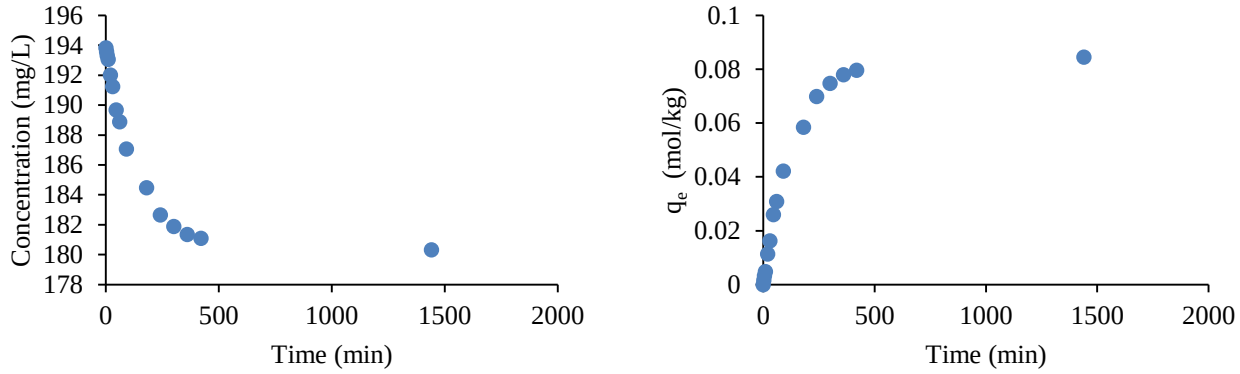

Figure 2. Effect of 0.5 mg/L adsorbent at 200 mg/L initial dye concentration: a) Concentration and b) adsorbent capacity

3.3. Effect of Adsorbent Amount

As the amount of adsorbent increases, the qe value becomes 0.0866 at 0.3 mg/L and 0.0845 mol/kg at 0.5 mg/L. While the qe value is 0.0536 at 1 mg/L adsorbent amount, this value decreases to 0.0221 at 2.5 mg/L adsorbent amount (Figure 3a). The decrease in qe appears to be linear. The regression coefficient was obtained as 0.9459. It is seen that the highest adsorption percentage is 9.1% with the use of 2.5 mg/L adsorbent, and the closest value to this value is 8.8% with the use of 1 mg/L adsorbent (Figure 3b).

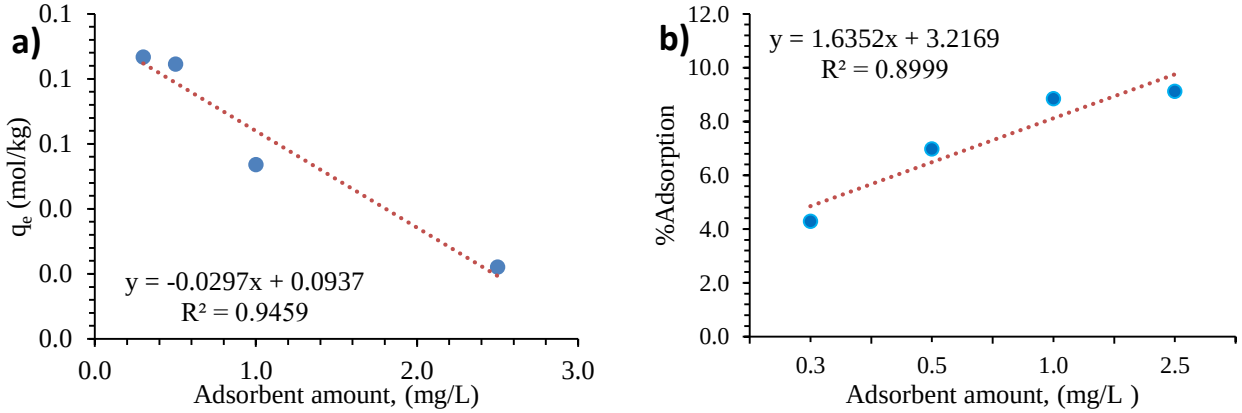

Figure 3. Effect of adsorbent amount a) adsorption capacity, b) Adsorption percentage

3.4. Effect of Temperature

In experiments examining the effect of temperature on the qe value, experiments were carried out at temperatures of 5 °C, 25 °C and 40 °C. qe values were 0.1088 mol/kg at 5 °C, 0.0845 mol/kg at 25 °C and 0.0422 mol/kg at 40 °C, respectively. According to the data obtained, the qe value decreases as the temperature increases (Figure 4).

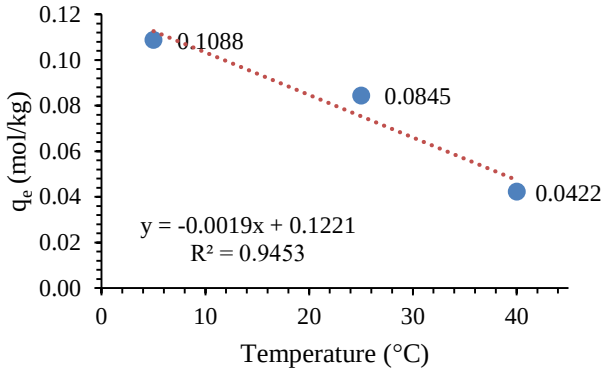

Figure 4. Effect of temperature on adsorption capacity

4. Conclusion

As a result of the study, it was revealed that the adsorption of dyestuff from dried lemon peels and Methylene Blue solutions was possible, but extremely insufficient. The fact that the removal efficiency does not exceed 10% indicates the need for pre-treatment of lemon peels. It was observed that the qe value increased with increasing initial dye concentration. After 750 mg/L, the rate of increase decreases. By using 0.5 mg/L leaf at an initial concentration of 200 mg/L, the qe value was obtained as 0.0845 mol/kg. As the amount of adsorbent used as adsorbent increases to 2.5 mg/L, the adsorption efficiency increases and reaches 9.1%. At this yield, the qe value is 0.0221 mol/kg. The qe value was obtained as 0.0422 mol/kg at 40 °C. The qe value was found to be 0.1088 mol/kg at 5 °C. The data indicate that the adsorption capacity decreases with increasing temperature.

Acknowledgement

All experimental work was conducted in the Chemical Engineering Department Laboratory at Çankırı Karatekin University. The authors would like to thank the Chemical Engineering Department.

References

[1] Taifi, A., A. Alkadir, O.K., Aljeboree, A.M., Al Bayaa, A.L., Alkaim, A.F., Abed, S.A.. (2022). Environmental Removal of Reactive Blue 49 Dye From Aqueous Solution by (Lemon Peels as Activated Carbon): A Model of Low Cost Agricultural Waste. Iop Conf Ser Earth Environ Sci. https://doi.org/10.1088/1755-1315/1029/1/012010.

[2] Robles-Melchor, L., Cornejo-Mazón, M., Hernández-Martínez, D.M., Gutiérrez-López, G.F., García-Pinilla, S., López-Villegas, E.O., et al. (2021) Removal of Methylene Blue From Aqueous Solutions by Using Nance (Byrsonima Crassifolia) Seeds and Peels as Natural Biosorbents. J Chem. https://doi.org/10.1155/2021/5556940.

[3] Latif, S., Rehman, R., Imran, M., Iqbal, S.. (2018). Biosorptive Decontamination of Acid Red-87 Dye From Wastewater byCitrus Limonum Peels:Ecofriendly Approach. Pakistan J Anal \& Environ Chem. https://doi.org/10.21743/pjaec/2018.06.04.

[4] Hu, C., Li, J., Zhou, Y., Mei, L., Feng, X., Li, H. (2009). Enhanced Removal of Methylene Blue From Aqueous Solution by Pummelo Peel Pretreated With Sodium Hydroxide. J Heal Sci. https://doi.org/10.1248/jhs.55.619.

Modelling and Simulation of Lorentz-Drude Dispersive Material as Nano waveguides by using FDTD Method

Nurettin Bilgili [1*], ***Ali Çetin*** [2]

[1] *Graduate School of Natural and Applied Sciences, Eskişehir Osmangazi University, Eskişehir, Turkey*
[2]*Faculty of Science, Department of Physics, Eskişehir Osmangazi University, Eskişehir, Turkey*

Abstract
In this work, we theoretically investigate the electric (TE) and magnetic (TM) field behaviours in linear nanowaveguides with different Lorentz-Drude dispersive materials using the finite difference time domain method (FDTD). We simulate the propagation of light in different materials to obtain the maximum efficient media. We investigate the amplitude, extinction and dissipation characteristics of the fields in the nanowaveguides and make comparisons to select the appropriate material for our needs. For electric field we obtain Titanium media for maximum amplitude, Silver media for minimum amplitude, Gold media for maximum extinction, and Titanium media for minimum extinction and Gold media for maximum dissipation, Silver media for minimum dissipation. For magnetic field we obtain Gold media for maximum amplitude, Silver media for minimum amplitude, Gold media for maximum extinction, and Chromium media for minimum extinction and Silver media for maximum dissipation, Chromium media for minimum dissipation.

Keywords: *Lorentz-Drude Materials, Nano waveguide, FDTD Method*

1. Introduction

In dispersive medium permittivity or permeability of medium depends on the wave frequency [1]. At optical frequencies, metals defined as dispersive [2]. At optical and near-infrared frequencies, the permittivity of metals can be describe by Lorentz-Drude (LD) model [3]. The refractive indexes of Lorentz-Drude dispersive materials continuously change under plasma frequency [4]. LD model studies free electrons (intra-band effects) and bounded electrons (inter-band effects). To investigate the metallic part of the plasmonic structure, LD model insert in the Maxwell equations.

To investigate the electromagnetic waves propagation in dispersive media, many various approaches developed [5] such as Finite Element Method (FEM) [6], Perturbation Method (PM) [7] , Beam Propagation Method (BPM) [8] and Finite-Difference Time-Domain Method [9, 10]. Losses of propagation fields in the other approximation methods are bigger than estimated value in FDTD method and can be apply many materials. Therefore, we prefer FDTD method to others [11]. FDTD method can be analyses metallic media at optical and infrared frequencies by solving Maxwell equations for complex geometries [12].

Because of wave propagation maintain in plasmonics at the interface of metal and dielectric boundaries, miniaturization of photonic devices can be made bellow the diffraction limits. From this characteristic properties of plasmonics, there have been many theoretical studies and fabricated works done on dispersive media in literature such as nanoantennas [13, 14], lenses [15, 16], resonators [17, 18], sensors [19] and waveguides [20-22].

In this paper, we design linear nanowaveguides which made of Lorentz-Drude dispersive materials such as Chromium, Titanium, Gold and Silver. We used OptiFDTD software [23] which based on FDTD method for simulation of TE and TM components in nanowaveguides. From obtained graphs, we compared amplitude, strength and dispersion properties of TE and TM through nanowaveguides according to time. We determined more suitable LD materials for nano-photonic devices.

* Corresponding author. *e-mail address: nurettinbilgili@gmail.com*

2. Materials and Methods

The frequency dependence of the dielectric permittivity can be described as sum of multiple resonances Lorentzian functions in Lorentz dispersion materials,

$$\varepsilon_r(\omega) = \varepsilon_\infty + \sum_{m=1}^{N} \frac{\chi_0 G_m \omega_{0m}^2}{\omega_{0m}^2 + j\Gamma_m \omega} \quad (1)$$

here ω_{0m} are the resonant frequencies, G_m are the oscillator strength coefficients, Γ_m are the damping coefficients, ε_∞ is the permittivity at infinite frequency and χ_0 is the permittivity at $\omega = 0$.

In the lossless case, Eq. (1) is directly related to Sellmeier equation. In lossy case, the Sellmeier equation can be written in a generalized form shown in Eq. (2).

$$n^2(\omega) = \varepsilon_\infty + \frac{\chi_0 G_1 \lambda^2}{\lambda^2 + j\Gamma_1 \lambda - \lambda_1^2} + \frac{\chi_0 G_2 \lambda^2}{\lambda^2 + j\Gamma_2 \lambda - \lambda_2^2} + \frac{\chi_0 G_3 \lambda^2}{\lambda^2 + j\Gamma_3 \lambda - \lambda_3^2} \quad (2)$$

Drude dispersive materials are characterized by dielectric function in Eq. (3),

$$\varepsilon_r(\omega) = \varepsilon_{r\infty} + \frac{\omega_p^2}{j\Gamma_\omega - \omega^2} \quad (3)$$

where, $\varepsilon_{r\infty}$ is permittivity for infinite frequency, ω_p is the plasma frequency and Γ collision frequency or damping factor.

Some metals complex can be expressed by dielectric function [24]

$$\varepsilon_r = \varepsilon_r^f(\omega) + \varepsilon_r^b(\omega)$$

Intraband effects and interband effects are separated from each other by above dielectric function. The intraband part of the dielectric function ($\varepsilon_r^f(\omega)$) is described by Drude model [25]

$$\varepsilon_r^f(\omega) = 1 + \frac{\Omega_p^2}{j\Gamma_0 \omega - \omega^2}$$

However, the interband part of the dielectric function is described by semi-quantum model which similar to Lorentz results for dielectrics [4]

$$\varepsilon_r^b(\omega) = \sum_{m=1}^{M} \frac{\Omega_p^2}{\omega_m^2 - -\omega^2 + j\Gamma_m \omega}$$

where Ω_p is the plasma frequency, M is the number of oscillators, ω_m is the m-th oscillator frequency and Γ_m is the m-th oscillator damping coefficient.

The plasma frequency associated with intraband transistions can be written as,

$$\Omega_p = \sqrt{G_0 \omega_P}$$

where G_0 is the oscillator strength.

Eq. (4) is more general expression for metals which named as Lorentz-Drude model [26]

$$\varepsilon_r(\omega) = \varepsilon_{r\infty} + \sum_{m=0}^{M-1} \frac{G_m \Omega_m^2}{\omega_m^2 - \omega^2 + j\Gamma_m \omega} \quad (4)$$

where Ω_m is the plasma frequency and G_m is the m-th oscillator strength coefficient. If only the term $m = 0$ exists and $\omega_0 = 0$ then the general equation describes the Drude model. If $m = 1 \ldots M$ terms exist and $\Omega_1 = \Omega_2 = \cdots = \Omega_M$, then the general model becomes the Lorentz model.

Above we described Lorentz-Drude model in frequency domain. For fullwave analysis of Lorentz-Drude materials we need to transpose from the frequency domain Lorentz-Drude model to time domain. This transformation can be made by using the polarization field within Maxwell's equations. Lorentz-Drude model in time domain can be expressed as,

$$-\nabla \times \mathbf{H} = \varepsilon_0 \varepsilon_{r\infty}(\omega) \frac{\partial \mathbf{E}}{\partial t} + \sum_{m=0}^{M-1} \frac{\partial \mathbf{P}}{\partial t} \tag{5}$$

$$\nabla \times \mathbf{E} = \mu_0 \frac{\partial \mathbf{H}}{\partial t} \tag{6}$$

We can write relations between polarization-electric field and polarization-magnetic field such as,

$$\mathbf{P}_m = \varepsilon_0 G_m \omega_m^2 \mathbf{E}$$

$$\mathbf{H} = \varepsilon_0 \mathbf{E} + \mathbf{P}_m$$

If we use relation between polarization and electric-magnetic fields then by taking the Fourier transform of the Maxwell's equations we obtained Eq. (7)

$$\frac{\partial^2 \mathbf{P}_m}{\partial t^2} + \Gamma_m \frac{\partial \mathbf{P}_m}{\partial t} + \omega_m^2 \mathbf{P} = \varepsilon_0 G_m \omega_m^2 \mathbf{E} \tag{7}$$

which FDTD algorithm can be derived from it.

3. Results and Discussion

In this work we have performed simulations in OptiFDTD tool. We take wafer dimension $10\ \mu m \times 10 \mu m$ and wafer material has taken air. The input plane has taken to be Gaussian modulated continuous wave.

We design linear nanowaveguides which materials are chosen dispersive Chromium, Titanium, Gold, Copper and Silver. The dimension of linear nanowaveguide has taken $1\mu m \times 1\mu m \times 8\mu m$. Fig. 1 shows the layout of the linear nanowaveguides.

We simulate the electric and magnetic field propagation throughout nanowaveguides. For all nanowaveguides the mesh delta along the x-axis and z-axis has taken $0.0135\ \mu m$. The number of mesh cells along x-axis and z-axis has taken 740 and the simulation selected to be run for 1582 steps.

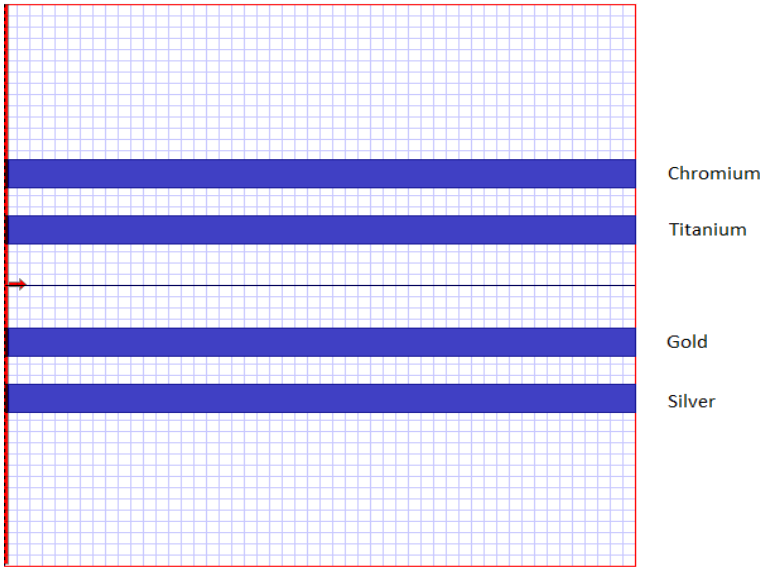

Figure 1. Layout of Nanowaveguides

Fig. 2 shows the propagation of electric field components E_y in Lorentz-Drude dispersive materials nanowaveguides.

From Fig. 2 we can see that maximum amplitude of E_y occurred in Titanium nanowaveguide and minimum amplitude of E_y occurred in Silver nanowaveguide. E_y amplitude quickly damped in Gold nanowaveguide as slowly damped in Titanium nanowaveguide.

Fig.3 shows the propagation of magnetic field components H_x in Lorentz-Drude dispersive materials nanowaveguides.

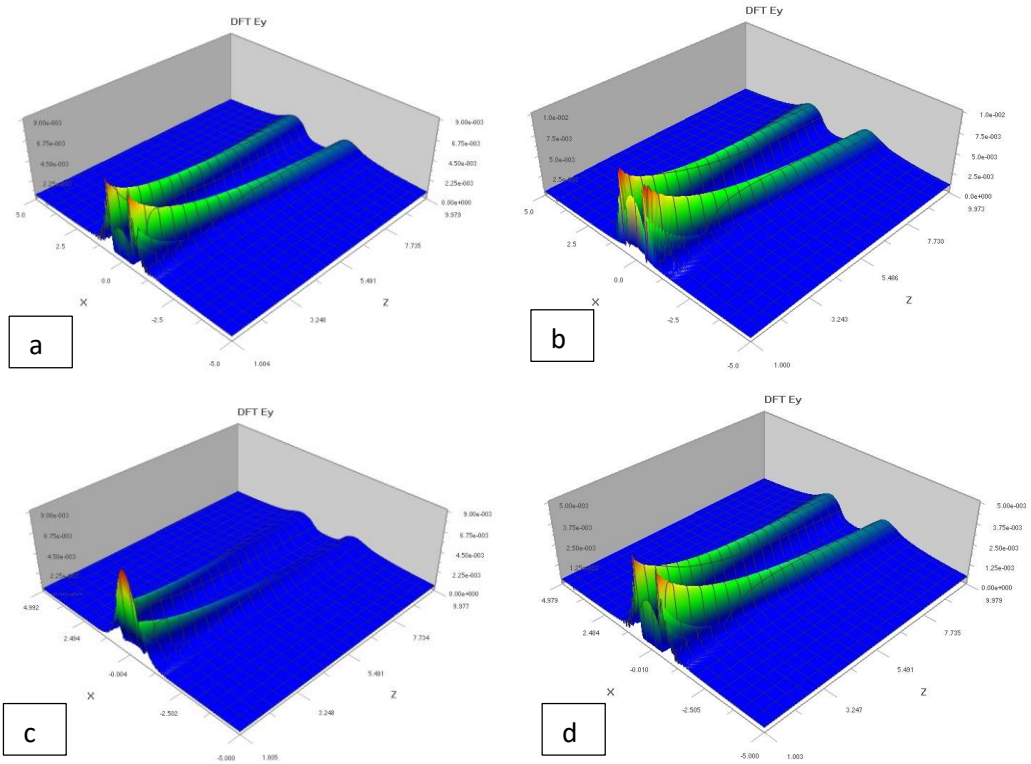

Figure 2. The propagation of E_y in (a) Chromium, (b) Titanium, (c) Gold and (d) Silver nanowaveguides.

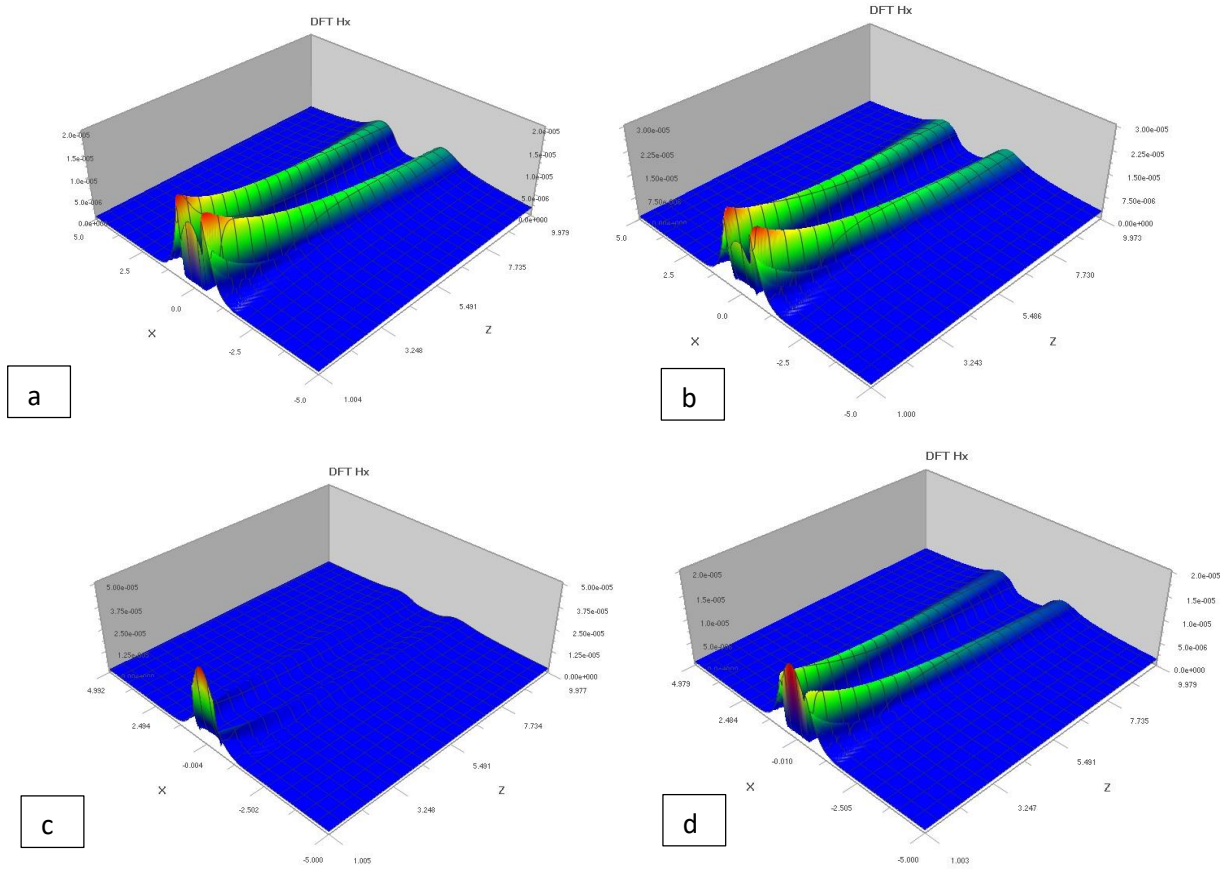

Figure 3. The propagation of H_x in (a) Chromium, (b) Titanium, (c) Gold and (d) Silver nanowaveguides.

From Fig. 3 we can see that maximum amplitude of H_x occurred in Gold nanowaveguide and minimum amplitude of H_x occurred in Silver nanowaveguide. H_x amplitude quickly damped in Gold nanowaveguide as slowly damped in Chromium nanowaveguide.

Electric fields dispersions can be seen clearly in Fig. 4 for Chromium, Titanium, Gold and Silver nanowaveguides.

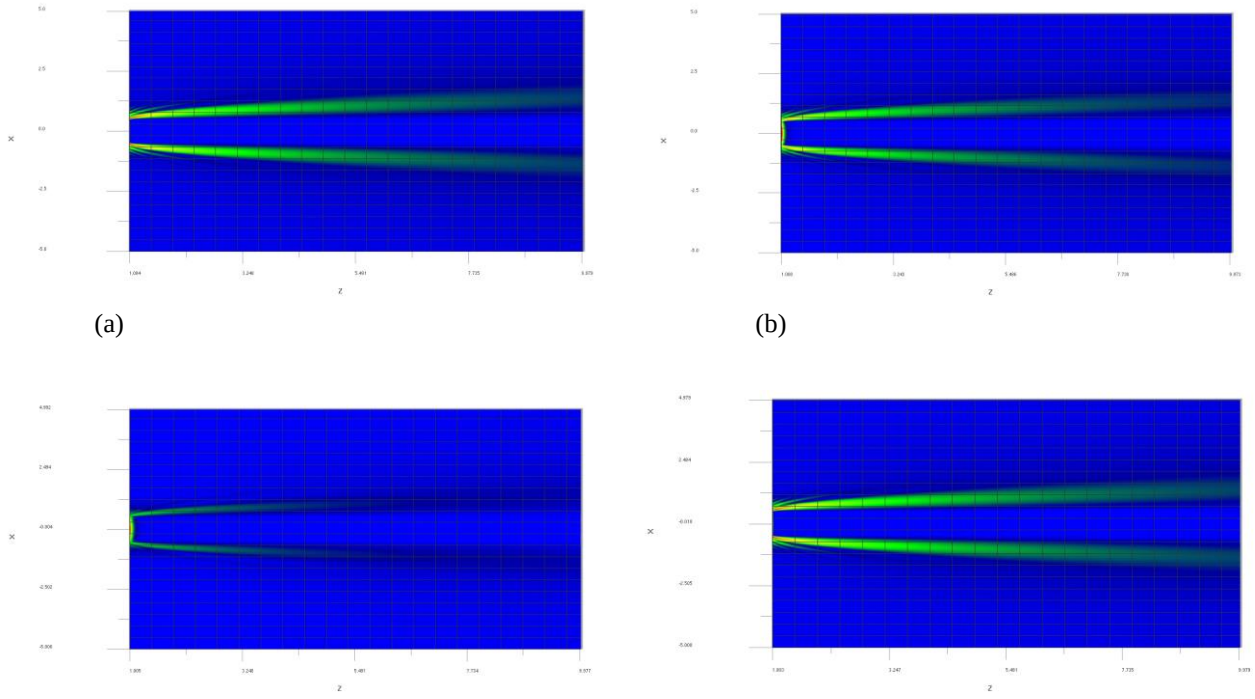

(a) (b)

(c) (d)

Figure 4. The dispersion of E_y in (a) Chromium, (b) Titanium, (c) Gold and (d) Silver nanowaveguides.

Maximum dispersion of E_y has seen in Silver nanowaveguide and minimum dispersion of E_y has seen in Gold nanowaveguide.

Also, magnetic fields dispersions can be seen clearly in Fig. 5 for Chromium, Titanium, Gold and Silver nanowaveguides.

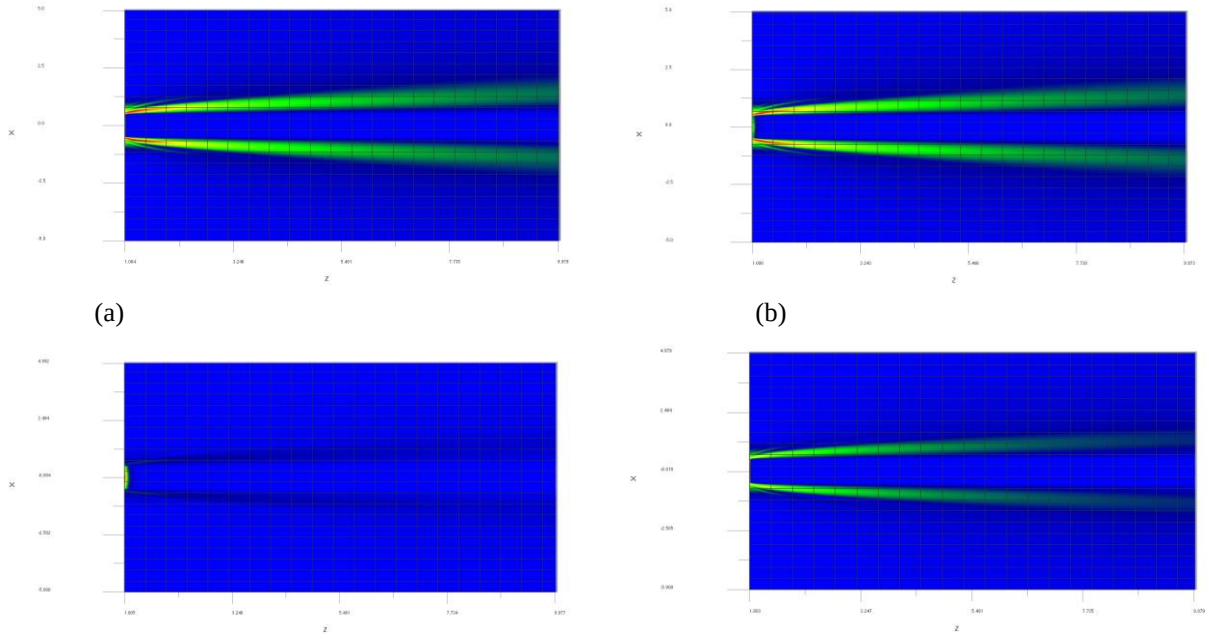

(a) (b)

(c) (d)

Figure 5. The dispersion of H_x in (a) Chromium, (b) Titanium, (c) Gold and (d) Silver nanowaveguides.

Maximum dispersion of H_x has seen in Silver nanowaveguide and minimum dispersion of H_x has seen in Chromium nanowaveguide.

4. Conclusion

We have theoretically studied maximum amplitude, damp and dispersion of E_y and H_x in Chromium, Titanium, Gold and Silver nanowaveguides. From our simulation results we compared these properties of Lorentz-Drude dispersive materials. We have determined maximum electric and magnetic field amplitudes at different materials. Also, we obtained damping and dispersions in different materials. Our results demonstrate that the maximum amplitude of E_y is observed in Titanium nanowaveguide and minimum amplitude of E_y is observed in Silver nanowaveguide. E_y amplitude quickly damped in Gold nanowaveguide as slowly damped in Titanium nanowaveguide. The maximum amplitude of H_x is observed in Gold nanowaveguide and minimum amplitude of H_x is observed in Silver nanowaveguide. H_x amplitude quickly damped in Gold nanowaveguide as slowly damped in Chromium nanowaveguide. The maximum dispersion of E_y has seen in Silver nanowaveguide and minimum dispersion of E_y has seen in Gold nanowaveguide. The maximum dispersion of H_x has seen in Silver nanowaveguide and minimum dispersion of H_x has seen in Chromium nanowaveguide. As a consequence, these results paved the way for us to choose more suitable materials for our purpose in nano optical devices.

References

[1] Rivzi S.: Handbook of Photomask Manufacturing Technology. CRC Press, Boca Raton (2005)

[2] Kolwas K., Derkachova A., Shopa M.: Size characteristics of surface plasmons and their manifestation in scattering properties of metal particles. J. Quant. Spectrosc. Radiat. Transfer. 110, 1490–1501 (2009)

[3] Taflove A.:Computational Electrodynamics. Artech House, Vol. 160, London (2000)

[4] Lee, K. H., Ahmed, I., Goh, R. S. M., Khoo, E. H., Li, E. P., and Hung, T. G. G.: Implementation of the FDTD method based on Lorentz-Drude dispersive model on GPU for plasmonics applications. Progress in Electromagnetic Research. 116, 441-456 (2011)

[5] Carcione, José M.: Wave fields in real media: Wave propagation in anisotropic, anelastic, porous and electromagnetic media. Elsevier, Vol. 38, (2007)

[6] Melenk, Jens M., and Ivo Babuška.: The partition of unity finite element method: basic theory and applications. Computer methods in applied mechanics and engineering. 139.1: 289-314 (1996)

[7] He, Ji-Huan.: A coupling method of a homotopy technique and a perturbation technique for non-linear problems. International journal of non-linear mechanics. 35.1: 37-43 (2000)

[8] Saitoh, Kunimasa, and Masanori Koshiba.: Full-vectorial imaginary-distance beam propagation method based on a finite element scheme: application to photonic crystal fibers. IEEE Journal of Quantum Electronics. 38.7: 927-933 (2002)

[9] Garcia, S. Gonzalez, Tae-Woo Lee, and Susan C. Hagness.: On the accuracy of the ADI-FDTD method. IEEE Antennas and Wireless Propagation Letters. 1.1: 31-34 (2002)

[10] Cetin, Ali, Ercan Ucgun, and M. Selami Kilickaya.: Determining the effective refractive Index of AlGaAs-GaAs slab waveguide based on analytical and finite difference method. Journal of Physical Science and Application. 2.9: 381 (2012)

[11] Oskooi, A. F., Roundy, D., Ibanescu, M., Bermel, P., Joannopoulos, J. D., and Johnson, S. G.: MEEP: A flexible free-software package for electromagnetic simulations by the FDTD method. Computer Physics Communications. 181(3), 687-702 (2010)

[12] Namiki, Takefumi.: 3-D ADI-FDTD method-unconditionally stable time-domain algorithm for solving full vector Maxwell's equations. IEEE Transactions on Microwave Theory and Techniques. 48.10: 1743-1748 (2000)

[13] Kinkhabwala, A., Yu, Z., Fan, S., Avlasevich, Y., Müllen, K., & Moerner, W. E.: Large single-molecule fluorescence enhancements produced by a bowtie nanoantenna. Nature Photonics. 3(11), 654-657 (2009)

[14] Li, Jingjing, Alessandro Salandrino, and Nader Engheta.: Shaping light beams in the nanometer scale: A Yagi-Uda nanoantenna in the optical domain. Physical Review B. 76.24: 245403 (2007)

[15] Smit, Meint K.: New focusing and dispersive planar component based on an optical phased array. Electronics letters. 24.7: 385-386 (1988)

[16] Neto, Andrea.: UWB, non dispersive radiation from the plenary fed leaky lens antenna—Part 1: Theory and design. IEEE Transactions on Antennas and Propagation. 58.7: 2238-2247 (2010)

[17] Drever, R. W. P., Hall, J. L., Kowalski, F. V., Hough, J., Ford, G. M., Munley, A. J., and Ward, H.: Laser phase and frequency stabilization using an optical resonator. Applied Physics B. 31(2), 97-105 (1983)

[18] Hakki, B. W., and P. D. Coleman.: A dielectric resonator method of measuring inductive capacities in the millimeter range. IRE Transactions on Microwave Theory and Techniques. 8.4: 402-410 (1960)

[19] Lu, X., Qi, H., Zhang, X., Xue, Z., Jin, J., Zhou, X., and Liu, X.: Highly dispersive Ag nanoparticles on functionalized graphene for an excellent electrochemical sensor of nitroaromatic compounds. Chemical Communications. 47(46), 12494-12496 (2011)

[20] Testa, Italo, Gianpaolo Evangelista, and Sergio Cavaliere.: Physically inspired models for the synthesis of stiff strings with dispersive waveguides. EURASIP Journal on Advances in Signal Processing. 2004.7: 1-14 (2004)

[21] Bernekorn, Peter, Anders Karlsson, and Gerhard Kristensson.: Propagation of transient electromagnetic waves in inhomogeneous and dispersive waveguides. Journal of electromagnetic waves and applications. 10.9: 1263-1286 (1996)

[22] Bartoli, I., Marzani, A., di Scalea, F. L., and Viola, E.: Modeling wave propagation in damped waveguides of arbitrary cross-section. Journal of Sound and Vibration. 295(3), 685-707 (2006)

[23] htpp://www.optiwave.com (2016)

[24] Kelly, K. L., Coronado, E., Zhao, L. L., & Schatz, G. C.: The optical properties of metal nanoparticles: the influence of size, shape, and dielectric environment. Journal of Physical Chemistry B-Condensed Phase. 107(3), 668-677 (2003)

[25] Bade, W. L.: Drude-Model Calculation of Dispersion Forces. I. General Theory. The Journal of Chemical Physics. 27.6: 1280-1284 (1957)

[26] Van Beijeren, Henk.: Transport properties of stochastic Lorentz models. Reviews of Modern Physics. 54.1: 195 (1982)

Assessment of Physical and Chemical Features of Unsaturated Polyester Resin Enhanced with Eggshell Components

Ercan AYDOĞMUŞ [1,*], ***Mustafa DAĞ*** [2], ***Zehra Gülten YALÇIN*** [2]

[1]*Fırat University, Faculty of Engineering, Department of Chemical Engineering, Elazığ, Türkiye*

[2]*Karatekin University, Faculty of Engineering, Department of Chemical Engineering, Çankırı, Türkiye*

Abstract

This study aims to investigate the physical and chemical properties of unsaturated polyester resin with the addition of eggshells. Eggshells were first crushed, dried, and then ground to particle sizes ranging from 50 to 100 mesh. The experiment was conducted by adding eggshell additives at proportions of 0 wt.%, 1 wt.%, 2 wt.%, 3 wt.%, and 4 wt.% to the unsaturated polyester resin. The properties examined include density, Shore D hardness, thermal conductivity coefficient, and activation energy values. According to the results obtained in this research, eggshell reinforcement increases the density of the polyester composite. As the filler ratio increases, Shore D hardness of the composite rises. The thermal conductivity coefficient of the polyester composite is also directly proportional to the filler ratio. Additionally, when thermal decomposition experiments of the samples are examined, eggshell reinforcement raises the activation energy of the composite. Accordingly, it can be said that the thermal stability of the composite is improved with the organic filler. The results indicate how the addition of eggshells affects the physical and chemical properties of unsaturated polyester resin. The study highlights the potential advantages of using materials in a more sustainable and environmentally friendly manner. This research offers a fresh perspective in the fields of materials science and chemistry, presenting innovative solutions for industrial applications.

Keywords: *Unsaturated Polyester Resin, Eggshell Additives, Chemical Properties, Natural Additives*

1. Introduction

Unsaturated polyester resins have gained significant attention in various industries due to their versatile applications and favorable mechanical properties. These resins are widely used in composite materials, coatings, and adhesives, among other fields. However, enhancing their properties and sustainability is a constant pursuit in material science and engineering [1-4].

One promising avenue in this quest is the incorporation of natural additives into the resin matrix. In this study, we focus on eggshells as a potential natural additive for unsaturated polyester resins. Eggshells are readily available and often discarded as waste, making them an environmentally attractive choice [5-8].

The objective of this research is to examine the impact of eggshell additives on the physical and chemical properties of unsaturated polyester resins. Specifically, we investigate the effects on hardness, thermal conductivity, and activation energy. Understanding how eggshell additions influence these characteristics is crucial for both enhancing the performance of the resin and contributing to sustainable material development [9-11].

This study contributes to the broader understanding of using natural additives in composite materials, offering a novel perspective on how waste materials can be repurposed for industrial use. The findings have the potential to open new avenues for sustainable material development and contribute to reducing environmental waste [12-14].

The polyester composite material has been obtained by reinforcing a synthesized eggshell with unsaturated polyester. Some thermophysical properties of the obtained product have been characterized according to the intended use. In this study, waste organic reinforcement filler is reinforced into the polyester composite.

* Corresponding author. *e-mail address: ercanaydogmus@firat.edu.tr*

2. Materials and Methods

Unsaturated polyester (UP), methyl ethyl ketone peroxide (MEKP), and cobalt octoate (Co Oc) used in experimental studies have been supplied from Turkuaz Polyester company. In this study, waste eggshells are prepared for composite production after being dried and ground. The filler, whose particle size range is between 297 μm and 149 μm, is added to the unsaturated polyester. After the mixture is homogenized, MEKP and Co Oc are added in certain proportions. After mixing for a short time, the sample is poured into standard molds. After waiting 24 hours for curing, physical and chemical tests are performed [15-17]. Figure 1 shows waste chicken egg shells and their ground form.

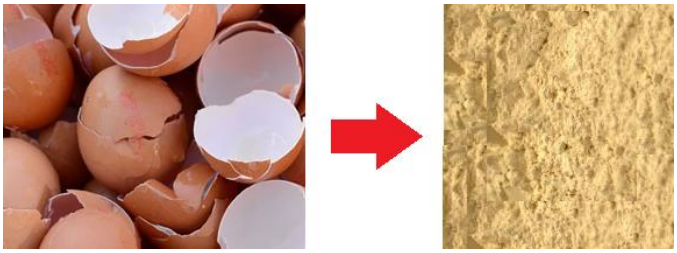

Figure 1. Eggshell and its ground powder.

Table 1 shows the experimental work plan and the proportions of each component in polyester composite production. Here, the ratios of MEKP and Co Oc in the mixture are constant, but the ratio of UP and filler varies. Additionally, the stages in polyester composite production are briefly schematized in Figure 2. The order of each component in composite production is easily understood.

Table 1. Experimental study plan

UP (wt%)	Filler (wt%)	MEKP (wt%)	Co Oc (wt%)
98	0	1.5	0.5
97	1	1.5	0.5
96	2	1.5	0.5
95	3	1.5	0.5
94	4	1.5	0.5

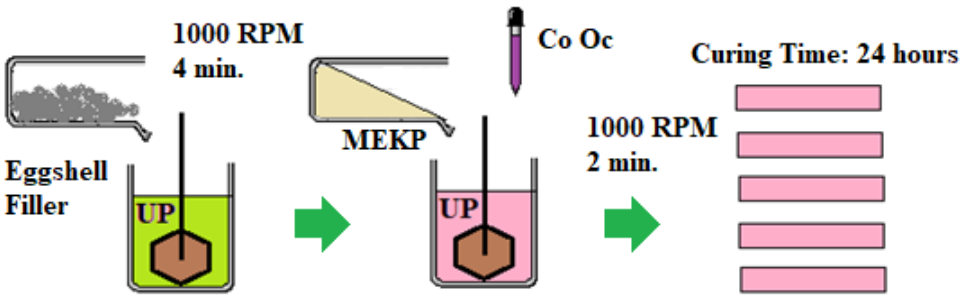

Figure 2. Polyester composite production scheme.

3. Results and Discussion

3.1. Density of polyester composite

After the resulting polyester composite is cured, physical and chemical tests are performed. Figure 3 expresses the relationship between the density of the composite and the proportion of eggshells. As the filler ratio increases, the density of the polyester composite also rises.

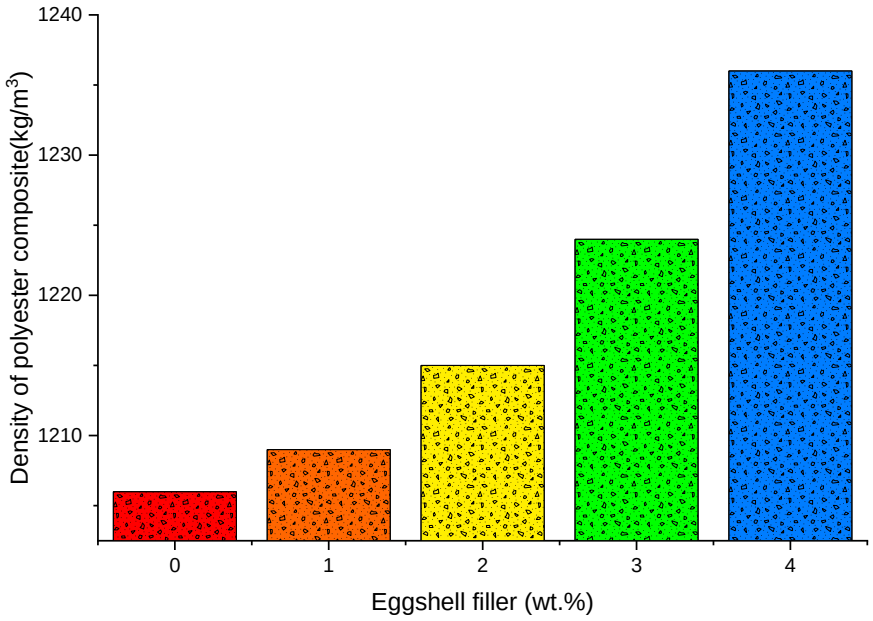

Figure 3. Change in the density of the eggshell reinforced the polyester composite.

3.2. Hardness of polyester composite

Shore D hardness tests are repeated five times for each sample and their average values are taken. The smooth surfaces of the composites removed from the molds are prepared according to standards. It has been determined that as the filling ratio in the polyester composite increases, Shore D hardness also goes up (Figure 4).

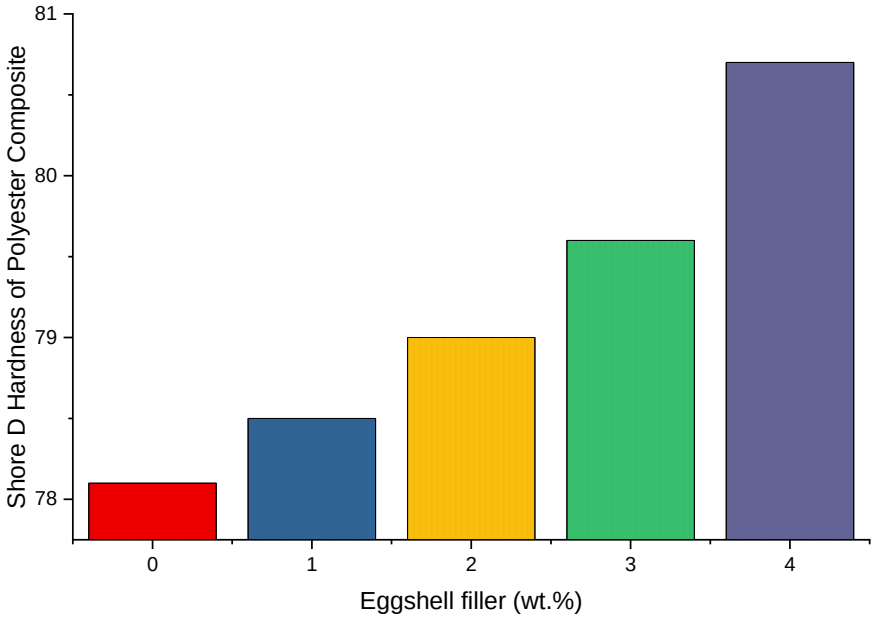

Figure 4. Variation of Shore D hardness of eggshell reinforced the polyester composite.

3.3. Thermal conductivity of polyester composite

When the thermal conductivity tests of the composites are examined, polyester without added filler has a thermal conductivity coefficient value of 0.056 W/m·K. As seen in Figure 5, as the filler ratio rises, the thermal conductivity coefficient also increases.

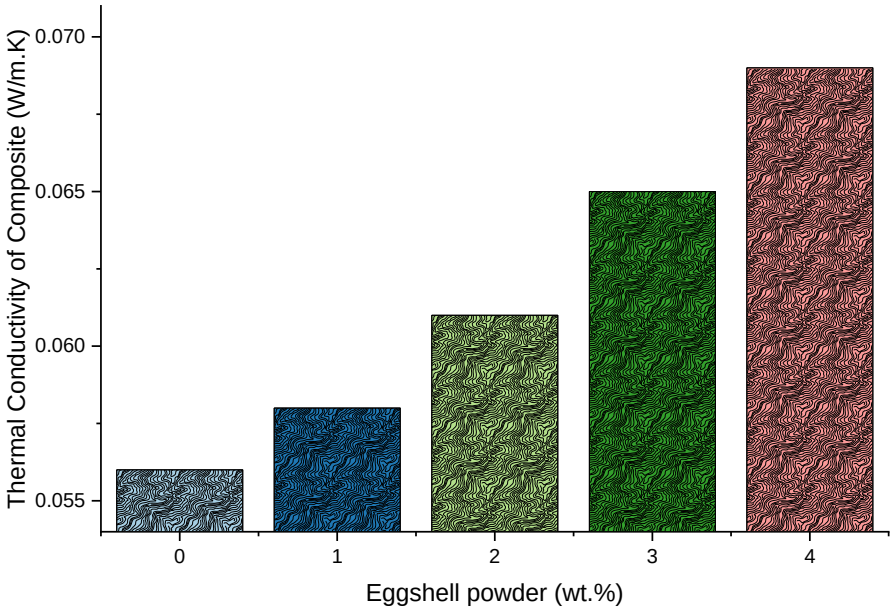

Figure 5. Change in the thermal conductivity of filler (eggshell) reinforced the composite.

3.4. Thermal decomposition of polyester composite

Activation energies of eggshell-reinforced polyester composites have been found in the range of 0.15 to 0.85 conversion ratio. Thermal decomposition experiments have been carried out at a heating rate of 10 K/min in the temperature range of 295 K to 875 K. The activation energies calculated in the thermal decomposition curves of polyester composites are given in Table 2. The activation energy values of the composites are found according to Coats-Redfern.

Table 2. Activation energy of the polyester composite

Eggshell (wt%)	Activation Energy (kJ/mol)
0	121.640
1	122.367
2	123.045
3	123.928
4	124.706

4. Conclusion

In this study, waste eggshells are used in polyester composite production. Environmentally friendly composite materials with low carbon footprint are produced. The thermal stability of the resulting composite is improved. Economical and high-density polyester composite production is achieved. In addition, composites with increased thermal conductivity coefficients can be preferred today. This research is important in terms of both thermal stability and waste evaluation. Eggshells used as fillers are not added to this study because they negatively affect the surface morphology of the composite when used in high amounts.

References

[1] Aydoğmuş, E., Arslanoğlu, H., & Dağ, M. (2021). Production of waste polyethylene terephthalate reinforced biocomposite with RSM design and evaluation of thermophysical properties by ANN. *Journal of Building Engineering*, 44, 103337.

[2] Orhan, R., Aydoğmuş, E., Topuz, S., & Arslanoğlu, H. (2021). Investigation of thermo-mechanical characteristics of borax reinforced polyester composites. *Journal of Building Engineering*, 42, 103051.

[3] Orhan, R., and Aydoğmuş, E. (2022). Investigation of some thermophysical properties of *Asphodelus aestivus* reinforced polyester composite, *Firat University Journal of Experimental and Computational Engineerin*g 1(3), 103-109.
[4] Orhan, R., and Aydoğmuş, E. (2022). Production and Characterization of Waste Corncob Reinforced Polyester Composite, *European Journal of Science and Technology*, 42, 176-179.
[5] Yanen, C., Dağ, M., and Aydoğmuş, E. (2022). Investigation of Thermophysical Properties of Colemanite, Ulexite, and Tincal Reinforced Polyester Composites, *European Journal of Science and Technology*, 36, 155–159, 2022.
[6] Aydoğmuş, E., and Arslanoğlu, H. (2021). Kinetics of thermal decomposition of the polyester nanocomposites, *Petroleum Science and Technology*, 39(13–14), 484–500.
[7] Şahal, H., and Aydoğmuş, E. (2022). Investigation of Thermophysical Properties of Polyester Composites Produced with Synthesized MSG and Nano-Alumina, *European Journal of Science and Technology*, 34, 95-99.
[8] Şahal, H., Aydoğmuş, E., and Arslanoğlu, H. (2022). Investigation of thermophysical properties of synthesized SA and nano-alumina reinforced polyester composites, *Petroleum Science and Tec*hnology, 1–17.
[9] Yanen, C., and Aydoğmuş, E. (2021). Characterization of Thermo-Physical Properties of Nanoparticle Reinforced the Polyester Nanocomposite, *Dicle University Journal of the Institute of Natural and Applied Science*, 10(2), 121–132.
[10] Aydoğmuş, E., Arslanoğlu, H., and Dağ, M. (2021). Production of waste polyethylene terephthalate reinforced biocomposite with RSM design and evaluation of thermophysical properties by ANN, *Journal of Building Engineering*, 44, 103337.
[11] Aydoğmuş, E. (2022). Biohybrid nanocomposite production and characterization by RSM investigation of thermal decomposition kinetics with ANN, *Biomass Conversion and Biorefinery*, 12, 4799-4816.
[12] Aydoğmuş, E., Dağ, M., Yalçın, Z.G., and Arslanoğlu, H. (2022). Synthesis and characterization of waste polyethylene reinforced modified castor oil-based polyester biocomposite, *Journal of Applied Polymer Science*, 139, e525256.
[13] Demirel, M.H., and Aydoğmuş, E. (2022). Production and Characterization of Waste Mask Reinforced Polyester Composite, *Journal of Inonu University Health Services Vocational School*. 10(1), 41-49.
[14] Demirel, M.H., and Aydoğmuş, E. (2022). Waste Polyurethane Reinforced Polyester Composite, Production and Characterization, *Journal of the Turkish Chemical Society Section A: Chemistry*, 9(1), 443–452.
[15] Buran, A., Durğun, M.E., and Aydoğmuş, E. (2022). *Cornus alba* Reinforced Polyester-Epoxy Hybrid Composite Production and Characterization, *European Journal of Science and Technology*, 43, 99-103.
[16] Buran, A., Durğun, M.E., Aydoğmuş, E., and Arslanoğlu, H. (2023). Determination of thermophysical properties of *Ficus elastica* leaves reinforced epoxy composite. *Firat University Journal of Experimental and Computational Engineering*, 2(1), 12-22.

Hybridization of Graphene Oxide and Silver Nanoparticles for Cementitious Composites

Taha Seham Ismail AL-BAYATI [1], ***Barış ŞİMŞEK*** [1,*], ***Ömer Faruk DİLMAÇ*** [1], ***Tayfun UYGUNOĞLU*** [2], ***Haluk KORUCU*** [1], ***Mücahit UĞUR*** [1], ***Özge BİLDİ CERAN*** [1]

[1] *Faculty of Engineering, Chemical Engineering Department, Çankırı Karatekin University, Çankırı, Türkiye*

[2] *Faculty of Engineering, Civil Engineering Department, Afyon Kocatepe University, Afyon, Türkiye*

Abstract

Graphene oxide (GO) and silver nanoparticles (AgNPs) are attractive nanomaterials due to their unique structure and physico-chemical properties. While the GO has a high surface area, AgNPs have antibacterial, thermal, and electrical properties. Hybridization of these materials' synergistic characteristics has proven beneficial in several applications such as electronics, catalysis, textiles, electrochemical biosensing, drug delivery, and antimicrobial agents. The GO-AgNPs dispersion with low particle size and high stability was important for such dispersion application. This study proposes Hummer's method-production of graphene oxide and silver nanoparticles dispersion. Four factors such as GO amount, AgNPs amount, and ultrasonic prop. time (UPT), and amount of distilled water (DIW) was determined to be effective on graphene oxide/silver nanoparticles dispersion features. Four quality criteria such as electrical conductivity, thermal conductivity, particle size, and zeta potential were selected. Taguchi method was applied for the first time to achieve the analyzed and optimized features of graphene oxide/silver nanoparticles. It was concluded that the optimum particle size and zeta potential of the GO/AgNPs dispersion are found as 164 ± 17 nm and -44 mV ± 0.4 mV, respectively. The hybridized GO/AgNPs dispersion zeta-potential varied between -30 mV and -60 mV. Furthermore, hybridized GO/AgNPs dispersion mixed cementitious composites were designed. The optimum GO and AgNPs hybrid usage was determined as 5 mg for each nanofiller and the highest compressive strength was determined as 22MPa by usage of 5 mg of GO and 5 mg of AgNPs. It was also concluded that compressive strength and ultrasonic pulse velocity of the GO-AgNPs dispersion mixed cementitious composites decreased with the GO and AgNPs usage of more than 5 mg due to the decrement in dispersion stabilities.

Keywords: *Cementitious composites, Graphene oxide silver nanocomposites, Hybrid nanoparticles, Synergistic effect*

1. Introduction

Graphene is one of the attractive 2D nanomaterials in both industrial and scientific fields is that it has unique mechanical, thermal, electrical, and optical properties [1, 2]. Monolayer graphene with a high thermal conductivity of 6000 $W*m^{-1}*K^{-1}$ [3], electrical conductivity of 5000 $S*cm^{-1}$ [4], and Young's modulus of ~1 TPa [5] makes that one of the most unique materials [6, 7]. Physical such as chemical vapor deposition or chemical methods such as oxidation and reduction processes can be mostly preferred in graphene synthesis. Since the production cost is taken into consideration, chemical methods are the most preferred method, especially Hummer's method. This method consists of the fact that graphite is chemically oxidized to graphene oxide (GO) and reduced with agents to reduced graphene oxide. GO is a kind of material that is very useful with functioning groups to obtain uniform and stable dispersion. Silver nanoparticles (AgNPs), on the other hand, are preferred because of their spherical structure, antibacterial activity, and relatively low-cost production [8]. AgNPS are preferred among all of the metal-based nanoparticles due to their low toxicity, and high electrical conductivity [9]. Moreover, AgNPs could be obtained with biosynthesis and green chemical reduction processes.

While cementitious composites are receiving increasing attention, nanofillers and the design of these composites play an important role. Nanofillers with their high surface area, ability to fill cracks, and superior mechanical properties give important properties to cementitious composites [10]. GO provides valuable properties to cementitious composites due to its relatively low production cost and ease of production [11]. AgNPs due to their antibacterial properties and low-size structure are preferred by the researchers [12]. Dispersion features such as particle size distribution and stability are very important in nanomaterial applications because unstable dispersion has a poor effect in many applications including building materials. Although GO and AgNPs are used to improve

* Corresponding author. *e-mail address: barissimsek@karatekin.edu.tr*

cementitious composites, statistical analysis of hybrid GO and AgNPS dispersion and combined application of GO and AgNPs in cementitious composites has not been encountered in the literature.

In the present study, it was aimed to analyze, characterize and optimize the hybridization of GO and AgNPs dispersion and, dipersed hybrid GO and AgNPs mixed cementitious composites (GACEC). For this purpose, the production of graphene oxide by the Hummers method by reacting graphite with potassium permanganate. Moreover, Glucose-reduced dispersed AgNPs were synthesized by a wet-chemical process. Zeta potential, particle size, electrical conductivity, and pH of the solution were preferred as responses. The amount of GO, amount of AgNPs, ultrasonic prop time (UPT), and distilled water amount (DI) as factors were analyzed by the Taguchi method based on main effect plots. Moreover, the dispersion properties of hybrid GO and AgNPs on cementitious composites were evaluated.

2. Materials and Methods

The chemicals used in the production of GO are high-purity graphite as a carbon source (< 50 μm, pure of 99%, Merck), sodium nitrate ($NaNO_3$), potassium permanganate ($KMnO_4$) and sulphuric acid (H_2SO_4) as oxidizers, hydrogen peroxide (H_2O_2: 30 wt. percent) as reaction terminator, and hydrochloric acid as a metal ions removal (HCl). Silver nitrate ($AgNO_3$, > 99.8%) as a precursor, soluble starch as a capable agent, sodium hydroxide pellets as pH adjuster (NaOH,>99%), D (+) glucose anhydrous as a reducer agent was used to obtain AgNPs. A water bath with a circulator (Polyscience 15-R) was used to control the reaction temperature in the experimental systems, and Merck Millipore brand pure water equipment was used to create the pure water. Hummer's method was used in the synthesis of GO [13, 14]. Hummer's method consists of strong oxidation of graphite with $KMnO_4$, termination of the reaction with H_2O_2, and removal of metal ions with HCl. AgNP synthesis consists of dissolving the starch solution and then adding $AgNO_3$ and glucose and pH adjustment (Figure 1).

Table 1. Taguchi orthogonal array for preparation of GO and AgNPs hybrid dispersion [15].

Exp. No*	GO (mg)	AgNPs (mg)	UPT (min.)	DI (mL)
GA1	5	5	5	300
GA2	5	10	15	400
GA3	5	15	30	500
GA4	10	5	15	500
GA5	10	10	30	300
GA6	10	15	5	400
GA7	15	5	30	400
GA8	15	10	5	500
GA9	15	15	15	300

* L_9 (3^4) Taguchi design

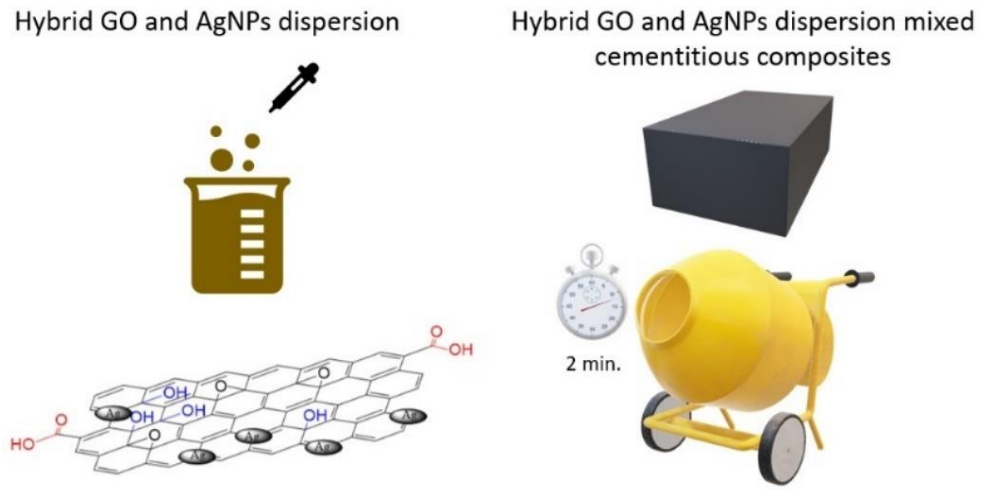

Figure 1. The following Methodology for GACEC production.

Hybrid dispersions were prepared according to the conditions designed according to the L_9 Taguchi design [15]. The amount of GO, amount of AgNPs, UPT, and distilled water amount DI with each having four levels was

selected as factors. Particle size and zeta potential were determined for each experimental run. After the characterization of dispersed hybrid GO and AgNPs, dispersed nanofillers were mixed with cement pastes (Figure 1). (Cement: water: superplasticizer 1: 0.45: 0.01). Pozzolanic type CEMIV/B (P) 32.5 cement and BASF 608 Masterglenium 608 superplasticizer were used to produce hybrid dispersed-GO and AgNPs mixed cementitious composites.

3. Results and Discussion

3.1. Characterization of hybrid GO and AgNPs dispersion

The UV-vis spectra obtained for each hybrid dispersed-GO and AgNPs considering the Taguchi design could be seen in Figure 2 [15]. The spectra showed a maximum absorption peak in the 215-275 nm regions and a weak peak in the 280-350 nm regions. The obtained absorption peaks indicate the presence of graphene oxide. The expected AgNPs peaks in the 390-420 nm regions were not found in the samples. However, the apparent shift in the peak around 320 nm show the hybrid GO and AgNPs presence [16].

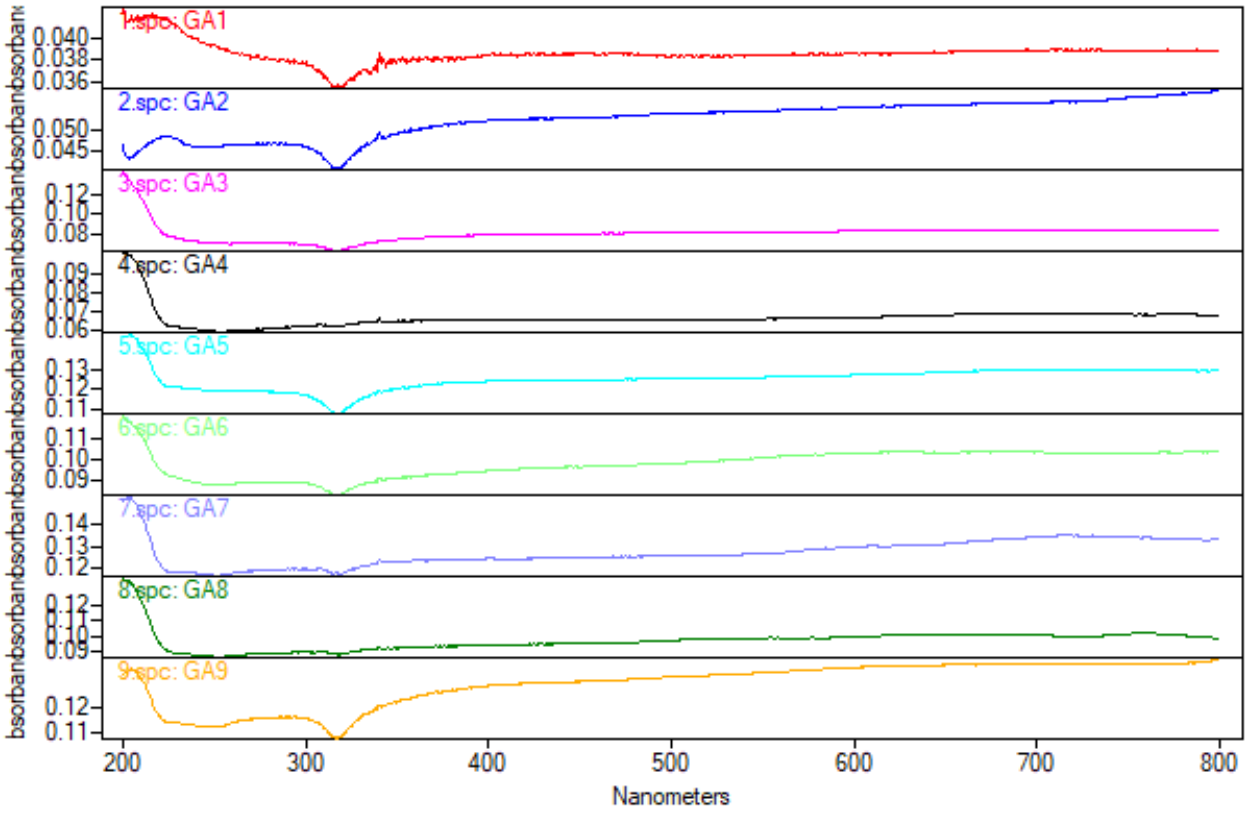

Figure 2. UV-Visible spectra for hybrid GO and AgNPs dispersion [15].

The main effect plots for the mean of particles size, zeta-potential and thermal conductivity drown by Minitab software could be seen in Figure 3 [15]. Particle size of hybrid dispersed-GO and AgNPs was decreased with the increasing of UPT and, increased with decreasing DIW amount (Figure 3a) [15]. Zeta-potential of hybrid dispersed-GO was decreased with the increasing of GO amount (Figure 3b) [15]. It has been observed that UPV treatment provides an advantage in dispersing nanofiller and ensuring homogeneous distribution. Thermal conductivity was decreased with the increasing of GO and AgNPs amount (Figure 3c) [15]. This result can be attributed to the oxygenated functional groups of GO.

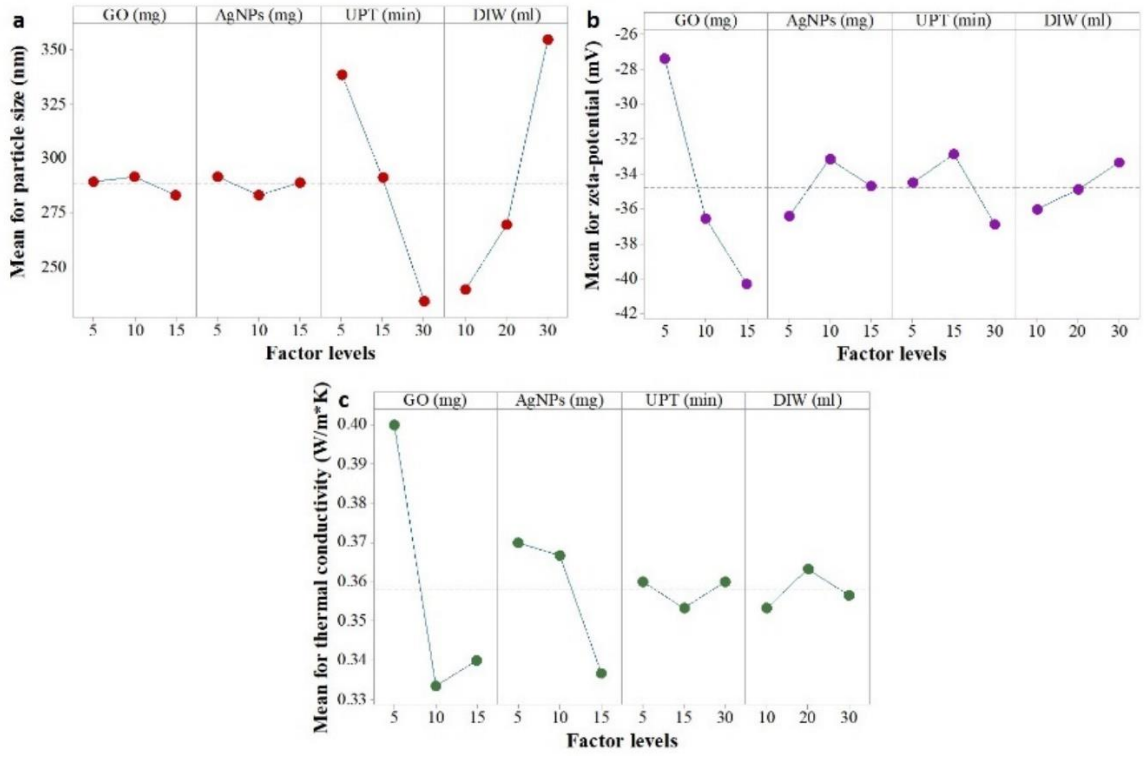

Figure 3. Main effect plots for hybrid GO and AgNPs: a) particle size, b) zeta-potential and c) thermal conductivity [15]

3.2. Features of hybrid GO and AgNPs dispersion mixed cementitious composites

All specimens were designed with a size of 5 cm^3 and cured at temperature 23ºC in tap water. The first quality criterion was selected as compressive strength at a day of 28 of GACEC, which should be maximized, was determined considering to the ASTM C109. Compressive tests were performed on 5 cm cubes. Second criterion was selected as ultrasonic pulse velocity and this test provide information about integrity of structures. Ultrasonic pulse velocity test, which should be maximized, was performed on 5 cm^3 cube specimens according to the ASTM C597-09.

The first point that draws attention is that the highest compressive strength average at 28 days was obtained when GO and AgNPs were used as 5 mg each. An average compressive strength value higher than 22 MPa was obtained in cementitious composites with a 5 mg of GO and 5 mg of AgNPs, which corresponds to C20 class concrete (Figure 4a). It should not be forgotten that obtaining this value without using fine aggregate, which increases the compressive strength of concrete, is remarkable. However, severe loss of strength is observed when using more than 5 mg of GO and AgNPs, which may be a result of the decrease in dispersion stability, in other words, the decrease in zeta potential of hybrid dispersion. Similarly, it is seen that the optimum usage rate for the ultrasonic pulse velocity at 28 days is 5 g for GO and AgNPs, respectively (Figure 4b). When using more than 5 mg for each nanofiller, there is probably a uniformity problem in cemet matrix due to the decrease in zeta potential, the structural integrity is disrupted and the ultrasonic pulse velocity decreases.

When the interaction graphs were analyzed, a very interesting result was encountered (Figure 4c). While the highest values in both compressive strength and ultrasonic pulse velocity were obtained with the use of 5 grams of GO and 5 g of AgNPs, a severe decrease in compressive strength and ultrasonic pulse velocity was observed, especially with the increase of AgNPs to 10 mg (Figure 4c and 4d). In other words, if AgNPs was used more than 10 mg, synergistic effect of hybridization of GO and AgNPs turned into an antagonistic effect on cementitious composite properties (Figure 4d). Especially when two nanomaterials are used at 10 mg, a sudden decrease in compressive strength and ultrasonic pulse velocity begins.

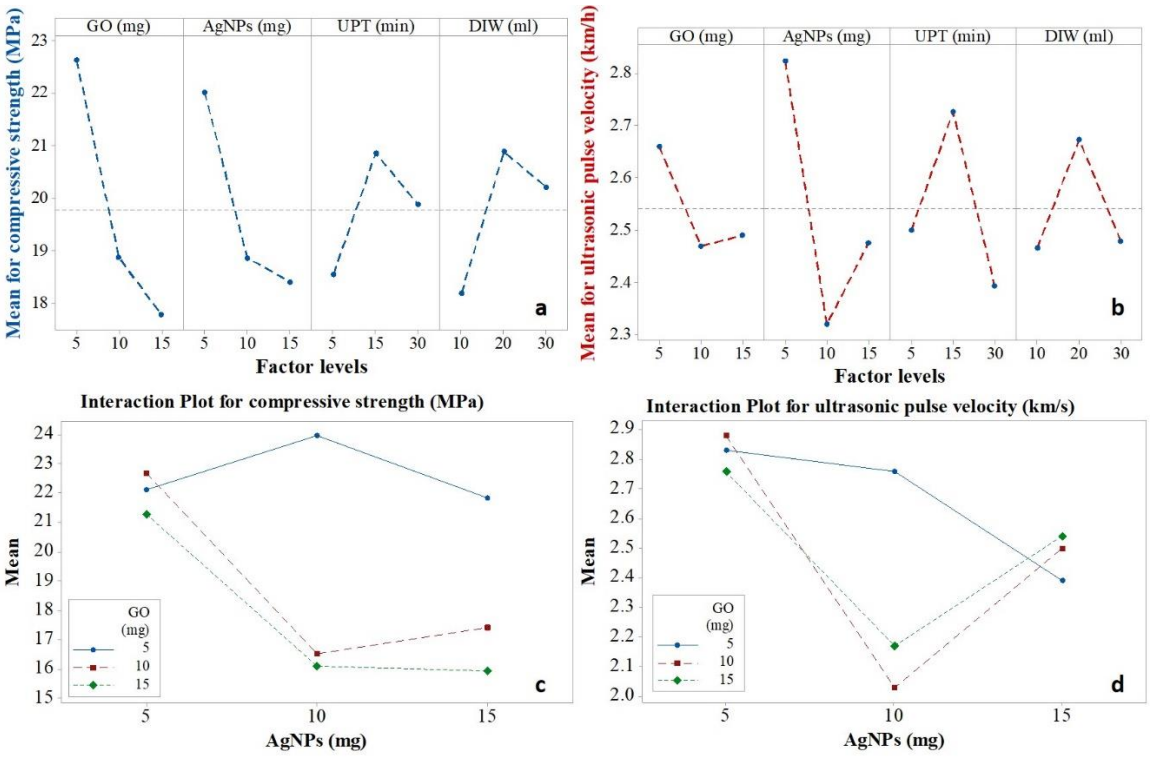

Figure 4. Factor effect analysis on GACEC using orthogonal arrays: a) mean plot for compressive strength, b) mean plot for ultrasonic pulse velocity, c) interaction plot for compressive strength, b) interaction plot for ultrasonic pulse velocity.

4. Conclusion

In this study, the hybrids dispersed GO and AgNPs was prepared according to the Taguchi design and the dispersion performance was analyzed statistically by the main effect plots systematically. Furthermore, hybrids dispersed GO and AgNPs mixed cementitious composites were designed and compressive strength and ultrasonic pulse velocity were assessed using main and interaction plots. It was concluded that the optimum particle size and zeta potential of the GO/AgNPs dispersion are found as 164.40 ± 17.38 nm and -44 mV ± 0.42 mV, respectively at a dosage of 5 mg of GO and 5 mg of AgNPs. Optimum dosages for preparing cementitious composites are determined as 5 mg each for GO and AgNPs. However, severe loss of strength was observed when using more than 5 mg of GO and AgNPs, which may be a result of the decrease in dispersion stability, in other words, the decrease in zeta potential of hybrid dispersion. Another result is that the synergistic effect that increases compressive strength and ultrasonic pulse velocity disappears more than this dosage levels.

Acknowledgement

In this study, the financial support was provided by Çankırı Karatekin University Scientific Research Projects Coordination Unit., Project No. MF210621L02. All experimental works were conducted in Çankırı Karatekin University Research Laboratory. The author would like to thank all supporters due to their precious contributions.

References

[1] Geim, A.K., & Novoselov, K.S. (2007). The rise of graphene. *Nature Materials (6)*, 183-191.
[2] Novoselov, K.S., . Geim, A.K, Morozov, S.V., Jiang, D., Zhang, Y., Dubonos, S.V., Grigorieva, I.V., & Firsov, A.A. (2004). Electric field effect in atomically thin carbon films. *Science 306*, 666-669.
[3] Ghosh, S., . Calizo, I., Teweldebrhan, D., Pokatilov, E.P., Nika, D.L., Balandin, A.A., Bao,W., Miao, F., & Lau, C.N. (2008). Extremely high thermal conductivity of graphene: Prospects for thermal management applications in nanoelectronic circuits, *Applied Physics Letters (92)*, 151911.

[4] Du, X., Skachko, I., Barker, A., & Andrei, E.Y. (2008). Approaching ballistic transport in suspended graphene, *Nature nanotechnology (3)*, 491-495.
[5] Zhu, Y., Murali, S., Cai, W., Li, X., Suk, J.W., Potts, J.R., & Ruoff, R.S. (2010). Graphene and graphene oxide: synthesis, properties, and applications. *Advanced materials (22)*, 3906-3924.
[6] Yıldız, B. *Application of graphene on journal bearings*, MSc Thesis, Pamukkale University, Institute of Science, 2006, pp. 97, Pamukkale, Türkiye.
[7] Liu, Z., & Zhou, X. (2014). *Graphene: energy storage and conversion applications*, USA: CRC Press.
[8] Padmavathi, J., Anantharaj, A., Velmurugan, S., Mariappan, G., & Gokulakumar, B. (2023). Synthesis of silver nanoparticles employing Bryophyllum pinnatum leaf extract and it's efficiency towards photocatalytic and antibacterial properties. *Chemical Data Collections (48)*, 101085.
[9] Karhan, Ö., Ceran, Ö.B., Şara, O.N., & Şimşek, B. (2017). Response Surface Methodology Based Desirability Function Approach To Investigate Optimal Mixture Ratio of Silver Nanoparticles Synthesis Process, *Industrial & Engineering Chemistry Research (56)*, 8180-8189.
[10] Joshaghani, A., Balapour, M., Mashhadian, M., & Ozbakkaloglu, T. (2020). Effects of nano-TiO_2, nano-Al_2O_3, and nano-Fe_2O_3 on rheology, mechanical and durability properties of self-consolidating concrete (SCC): An experimental study. *Construction and Building Materials (245)*, 118444.
[11] Korucu, H. Şimşek, B. Uygunoğlu, T. Güvenç, A.B., & Yartaşı, A. (2019). Statistical approach to carbon based materials reinforced cementitious composites: Mechanical, thermal, electrical and sulfuric acid resistance properties, *Composites Part B: Engineering (171)*, 347-360.
[12] Ceran, Ö.B., Şimşek, B., Doruk, S., Uygunoğlu, T., & Şara, O.N. (2019). Effects of dispersed and powdered silver nanoparticles on the mechanical, thermal, electrical and durability properties of cementitious composites, *Construction and Building Materials (222)*, 152-167.
[13] Hummers Jr, W.S., & Offeman, R.E. (1958). Preparation of graphitic oxide, *Journal of the American Chemical Society* (80), 1339-1339.
[14] Guerrero-Contreras, J., & Caballero-Briones, F. (2015). Graphene oxide powders with different oxidation degree, prepared by synthesis variations of the Hummers method. *Materials Chemistry and Physics (153)*, 209-220.
[15] Al-Bayati, T.S.I. *Synthesis and optimization of graphene oxide/silver nanoparticles nanocomposites*. MSc Thesis, Çankırı Karatekin University, Instute of Science, 2022, pp. 58, Çankırı, Türkiye.
[16] Chook, S.W., Chia, C.H., Zakaria, S., Ayob, M.K., Chee, K.L., Huang,N.M., Neoh, H.M., Lim, H.N., Jamal, R., & Rahman, R. (2012). Antibacterial performance of Ag nanoparticles and AgGO nanocomposites prepared via rapid microwave-assisted synthesis method. *Nanoscale Research Letters (7)*, 541.

In Vitro Effects of Some Cations on Glutathione S-Transferase Enzyme Purified from Chicken Heart

Suat ZOR [1] , ***Mehmet ÇİFTCİ*** [2, *]

[1]*Batman University, Social Sciences Vocational School, Batman,, Türkiye*

[2]*Bingol University, Faculty of Veterinary Science, Bingol, Türkiye*

Abstract

Glutathione S-transferase enzyme (GST; EC 2.5.1.18) is an important antioxidant enzyme in metabolism and takes part in reactions that enable the conjugation of glutathione with many metabolites that may cause toxicity. In this study, firstly, the GST enzyme was purified from chicken heart by homogenate preparation, ammonium sulfate precipitation and glutathione-agarose affinity chromatography. Then, the inhibition effects of Ag^+, Pb^{2+} and Na^+ ions on enzyme activity were examined in vitro. Enzyme activity was determined spectrophotometrically at 340 nm by the method of Habig et al. (1974). This method was applied in all kinetic studies. In the kinetic studies, it was found that Ag^+ (in the range of 0.1-0.7 mM), Pb^{2+} (in the range of 0.1-0.7 mM) and Na^+ (in the range of 1-5 mM) cations caused inhibition on the enzyme activity. IC_{50} values were found by drawing % Activity-[I] graphs for these cations showing inhibition effects. IC_{50} values for Ag^+, Pb^{2+} and Na^+ were found to be 0.239, 0.283 and 1.725 mM, respectively.

Keywords: *Glutathione S-transferase, Ag^+, Pb^{2+}, Na^+, Inhibiton*

1. Introduction

Since many products in today's world, from food and beverages to the items we wear, are produced synthetically, highly harmful chemicals are used in this production process. Many scientific studies have shown that these chemicals cause serious harm to humans and the environment. It has been reported that organic substances such as carbohydrates and proteins, especially those processed at high temperatures, have a carcinogenic effect [1]. In parallel with the development of technology, the amount of many toxic substances that threaten humans and the environment has inevitably increased in this process. Examples include substances such as heavy metals, plastic materials, pharmaceutical residues, pesticides and herbal medicines [2]. One of the sources that cause this toxicity is free radicals. Xenobiotics from exogenous sources are also involved in the formation of free radicals from endogenous and exogenous sources [3]. One of the main functions of the GST enzyme, which is the main subject of this thesis, is to render harmless these toxic substances entering the body through detoxification reactions [4]. As a result of the phase II reaction, the protection of the living organism from reactive electrophilic attacks occurs thanks to the GST enzyme [5]. The reason for the high GST rate in organs such as lung, liver, kidney and small intestine is the xenobiotics entering the body [6]. The GST enzyme has been accepted as a natural protective antioxidant because it eliminates these harmful substances as a result of a number of chemical reactions.

2. Materials and Methods

2.1. Quantitative Protein Determination

Quantitative protein determination was determined spectrophotometrically by the Bradford method at 595 nm [6].

2.2. Activity Determination

The activity of glutathione S-transferase (GST) enzyme was determined spectrophotometrically at a wavelength of 340 nm according to the method used by Habig et al. [7].

2.3. Procuring Chicken Heart and Preparing the Homogenate

* *Corresponding author. e-mail address: mciftci@bingol.edu.tr*

The heart used in the experiments was obtained from Bingöl Meat and Milk Institution in accordance with the cold chain rules and was kept in the deep freezer at -20°C. The frozen heart was cut into small pieces to prepare the homogenate solution. Then, 5 g of chicken heart was taken. Three times the amount of homogenate buffer was added to the amount of heart taken and it was made homogeneous using a homogenizer in an ice tray. Afterwards, the resulting homogenate was centrifuged at 13,000 x g for one hour. After this process, the precipitate was separated and homogenate was obtained.

2.4. Ammonium Sulfate Precipitation and Dialysis Procedures

The resulting homogenate was precipitated with ammonium sulphate between 20-80% to ensure that most of the chicken GST enzyme precipitated. At each step, the homogenate was centrifuged at 13500xg for 15 minutes. During these processes, the activities of the precipitate and supernatant were measured at each stage. Thus, tubes with activity were identified and merged. The mixture resulting from the precipitation process was dialyzed against dialysis buffer (10 mM K-phosphate, 1 mM EDTA pH = 7.5) for approximately two hours in the dialysis bag.

2.5. Purification of Enzyme by Affinity Chromatography

The enzyme sample obtained after dialysis was applied to the glutathione agarose affinity column, whose flow rate was 20 mL/hour with a peristaltic pump and balanced with 10 mM KH_2PO_4 and 0.1M KCl, pH: 8.0 buffer. The column was then subjected to washing. This process was carried out with a buffer solution of 10 mM KH_2PO_4 and 0.1M KCl, pH: 8.0. The washing process was completed after the absorbance values measured in the fractions during the spectrophotometric measurement were approximately equal to the blank. Gradient elution was performed to obtain the enzyme pure. Then, the enzyme was eluted from the column using the elution solution containing 50 mM Tris-HCl and (1.25-10 mM, pH: 9.5) GSH [8].

2.6. Kinetic Studies

Ag^+, Pb^{2+} and Na^+ cations were used in inhibition studies. First of all, appropriate solutions were prepared for each cation and activity measurements were made. Using the activity values obtained as a result of activity measurements and the applied concentrations, % Activity-[I] graphs were drawn and with the help of these graphs, IC_{50} values were found for each cation.

3. Results

Activity%-[I] graphs drawn for drugs showing inhibitory effects on chicken heart GST enzyme are shown in Figures 1, 2, and 3. The IC_{50} values obtained for the Ag^+, Pb^{2+} and Na^+ which have an inhibitory effect on the enzyme, were 0.239, 0.283 and 1.725 mM, respectively, and are shown in Table 1.

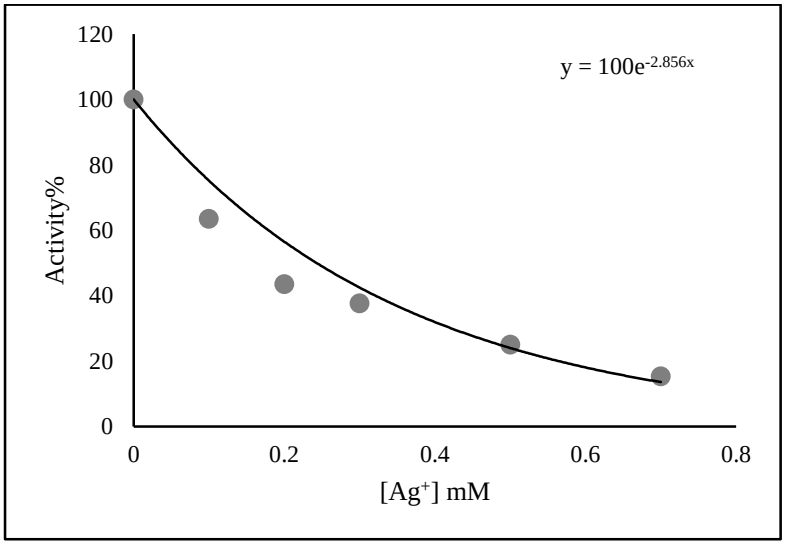

Figure 1. Activity%-[Ag^+] graph

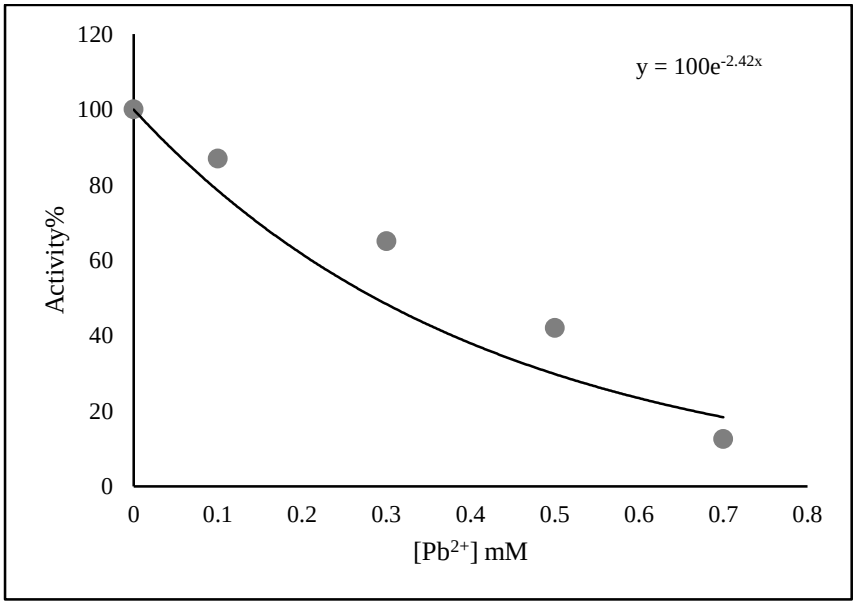

Figure 2. Activity%-[Pb^{2+}] graph

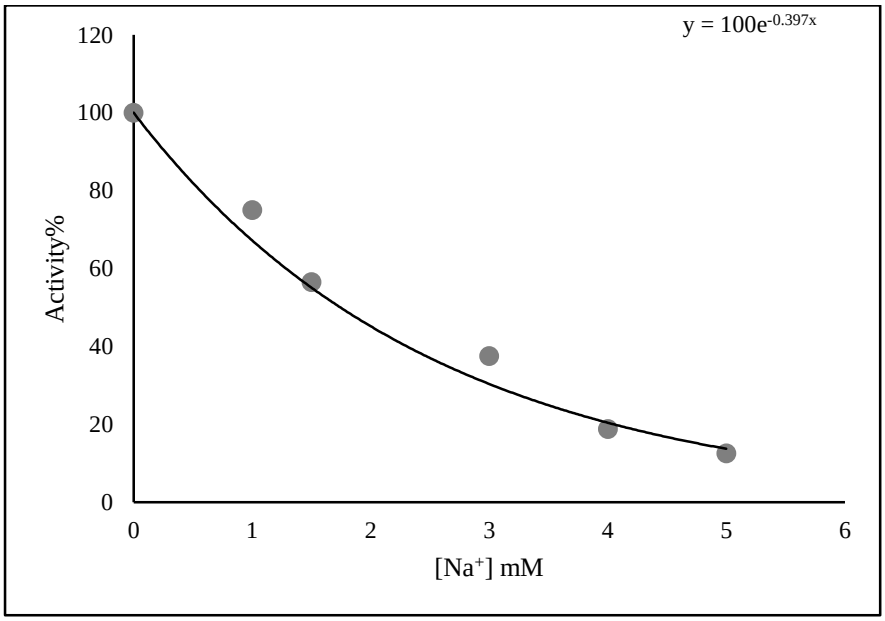

Figure 3. Activity%-[Na^{+}] graph

Table 1. Obtained IC_{50} values

Cation	**IC_{50} (mM)**
Ag^{+}	0,239
Pb^{2+}	0,283
Na^{+}	1,725

4. Conclusion

Glutathione S-transferase enzyme (GST; EC 2.5.1.18) is an important antioxidant enzyme in metabolism and takes part in reactions that provide conjugation of glutathione with many metabolites that may cause toxicity. In this study, the effects of cations such as Ag^+, Pb^{2+} and Na^+ on the enzyme were investigated. As a result of the research, it was determined that Ag^+, Pb^{2+} and Na^+ cations significantly inhibited the enzyme. Therefore, IC_{50} values were found by drawing Activity%-[I] graphs for these cations (Figures 1, 2, 3 and Table 1). According to these IC_{50} values (inhibitor concentration that reduces the enzyme activity by half), the decreasing inhibitory powers of the drugs can be listed as Ag^+, Pb^{2+} and Na^+. Because while Ag^+ with a concentration of 0.239 mM causes 50% inhibition, this value is 0.283 mM for Pb^{2+} and 1.725 mM for Na^+. According to the IC_{50} values obtained in this study, it is understood that the strongest inhibitor is Ag^+, followed by Pb^{2+} and Na^+. As a result, it will be important to conduct more detailed inhibition studies for these three cations in future studies, determine Ki constants and conduct *in vivo* studies. As a result, people exposed to heavy metals with low IC_{50} values such as Ag^+ and Pb^{2+} need to be very careful and take the necessary precautions.

References

[1] Senyuva, H.Z., and Gokmen, V. Surname N., (2005). *Food Additives and Contaminatio,* 22 (3), 204-209.

[2] Senyuva, H.Z., and Gökmen, V. (2005). *Food Additives and Contaminatio,* 22 (3), 204-209.

[1] Üçüncü, M. (2010). *Gıdaların Ambalajlanması*, Ege Üniversitesi Basım Evi, İzmir, Türkiye, 656-679.

[2] Aksoy, Y., (2002). *Antioksidan mekanizmada glutatyonun rolü*, Türkiye Klinikleri.

[3] Rebbeck, T.R. (1997). Molecıılar Epidemiology of the Human Glutathione S-Transferase Genotypes GSTM1 and GSTT1 in Cancer Susceptibility, *Cancer Epidemiology, Biomarkers &Prevention,* 6(9),733-743.

[4] Awasthi, Y. C., Dao, D. D., and Saneto, R. P. (1980). Interrelationship between anionic and cationicforms of glutathione S-transferases of human liver. *Biochem J.,* 191(1), 1-10

[5] Gyamfi, M. A., Ohtani. II., Shinno, E., and Aniya, Y. (2004). Inhibition of glutathionestransferases by thonningianin A, isolated from the African medicinal herb, Thonningia sanguinea, in vitro. Food and *Chemical Toxicology*, 42(9): 1401-1418.

[6] Bradford, M. M. (1976). A rapid and sensitive method for the quantitation of microgram quantities of protein utilizing the principle of protein-dye binding. *Analytical Biochemistry*, 72: 248-251.

[7] Habig WH, Pabst MJ, Jakoby WB (1974). Glutathione S-transferases. The first enzymatic step in mercapturic acid formation. *Journal of Biololgical Chemistry*, 249: 7130-7139.

[8] Toribio F., Martinet L.E., Pascual P., Lopez B.J., 1996. Methods for purification of glutathione peroxidase and related enzymes, *J. Chromatog. B.* 684: 77-97.

Food safety debates of salt

***Fatma BAYRAKÇEKEN NİŞANCI*[1,*], *Hüdayi ERCOSKUN*[2]**

[1] *Ataturk University, Faculty of Sciences, Department of Chemistry, Erzurum, Turkey*

[2] *Karatekin University, Faculty of Engineering, Department of Food Engineering, Çankırı, Turkey*

Abstract

Salt is the most commonly used additive for preservatives, flavor enhancers, and retention and release of water in foods. Excessive salt consumption is a factor in the formation of cardiovascular diseases, hypertension, kidney diseases, osteoporosis, stomach diseases, obesity and some other diseases. For this reason, health institutions are working to reduce salt consumption. On the other hand, salt can contain important risks such as radioactives, heavy metals, microplastics, dynamite residues and exhaust in terms of food safety. In this study, salt was evaluated in terms of food safety.

Keywords: *Salt Residue, Salt, Heavy Metal, Microplastic, Radioactivity*

1. Introduction

For thousands of years, salt has been used as a unique food preservation method. While the development and widespread use of refrigeration and freezing technologies in the last century has reduced the importance of salt in food preservation, the taste feature of salt has become even more important. In addition, with scientific and technological developments, the usage area of salt has expanded and the amount of salt used in food has dropped below 25%. Although salt is found in food raw materials, it is the most common and/or widely used additive. In addition to playing important roles in human physiology, nutrition and health, salt has very important functions such as flavor, shelf life and texture in foods. The accessibility and cheapness of salt makes its use widespread in the food industry. There is almost no food that does not contain salt (except purified and concentrated foods such as refined sugar and oil). As a natural consequence, more than 75% of the salt consumed comes from processed foods [1]. However, with the increase in fast food and ready meal consumption in recent years, salt consumption has started to increase again.

Salt is the most commonly used additive for preservatives, flavor enhancers, and retention and release of water in foods. Normally, salt does not show antimicrobial activity, but it slows down or even stops microbial growth by reducing water activity, in other words, by reducing the water available to microorganisms. Techniques used in food preservation are based on limiting and/or stopping microorganisms found in foods. Food preservation techniques; reducing water activity (drying and curing), temperature (high enough to kill microorganisms and low enough to slow down the activity of microorganisms), increasing acidity or lowering pH (by fermentation and/or addition of acids to food), chemical additives (nitrate, nitrite, sulfite), The use of salt in almost all techniques with competitive microorganisms (sucuk, yoghurt, pickles, wine) and gases in the atmosphere of food packaging (carbon dioxide, nitrogen, oxygen or vacuum) increases the microbial destruction effect [3]. Therefore, salt is more or less part of the production method in all ready-to-eat foods. Salt added to food by the final consumer constitutes approximately 25% of total salt consumption. In other words, 75% of the salt consumed by consumers is included in the content of the food when purchasing the food [4, 5].

However, excessive salt consumption paves the way for many diseases. The World Health Organization (WHO) recommends that daily salt intake should not exceed 5 grams in adults. The total amount of sodium entering the body is important in determining this amount. WHO recommends consuming less than 2 g sodium (5 g salt) per person per day. More than 95% of consumed sodium comes from salt (WHO, 2008). While per capita salt consumption is around 9-12 g in industrialized countries, it is stated to be 12 g in our country [6]. For this reason, public authorities in the world and in Turkey are working to reduce salt consumption. In this context, public awareness is increasing about hypertension, cardiovascular diseases, kidney stones, osteoporosis and some cancers caused by excessive sodium taken with salt. In Turkey, efforts to reduce salt consumption include

* Corresponding author. *e-mail address: fbayrakceken@atauni.edu.tr*

reducing the salt content of processed foods by legal means and reporting the salt content of foods on their labels [7-13]. Salt reduction strategies are implemented in more than 75 countries. Salt reduction strategies; It is done in many ways, such as ensuring less salt use in the food industry by changing the formulations in processed foods, targeting foods with high sodium content, educating consumers, including salt content and total content on labels, increasing taxes on foods containing high salt, and interventions by public institutions.

Especially in recent years, statements that ferrocyanides used as anti-crystallization or anti-caking additives in the production of refined food salt are toxic have changed the attitude of meticulous consumers towards refined salts. Food additives; Just like the active pharmaceutical ingredients, it is evaluated and permitted for use by the joint committee established by the World Health Organization and the Food and Agriculture Organization. The toxic dose of the additive is determined by toxicological tests performed first on guinea pigs and then on primates. Afterwards, the effective dose is determined for the foods to be used. Thus, it is determined that the potential food additive can be used in which food item and in what dosage. This value is usually around one percent of the toxic dose in primates. The amount of E536 (Potassium Ferrocyanide) and E538 (Calcium Ferrocyanide) that can be used in refined salts is determined by the World Health Organization and the Food and Agriculture Organization as 20mg/kg, and this value is one percent of the toxic dose. The use of ferrocyanides in food-grade salt is limited in industrial food production. For both ferrocyanides, the limit is 20 mg/kg in the European Union, Japan, and Turkey. Potassium ferrocyanide is banned and sodium ferrocyanide limited to maximum 13 mg/kg in the United States of America and both ferrocyanides are limited to 14 mg/kg for food-grade salts [14-17].

Marketing is done to encourage consumers not to consume unrefined salt and to consume raw salt, on the grounds that minerals that are essential for humans are removed through salt refining. Many sources state that some salts contain more than 80 minerals. Along with C, H, O, N, which participate in the organic structure in living organisms, Ca, P, Mg, K, Na, Cl, S, Fe, Cu, Co, Zn, Mn, Cr, Mo, F, Se, I, B The existence of elements such as , As, Br, Si, Ni, Al has been reported by various researchers. Among these, the macro minerals that the body needs more are Calcium (Ca), Sodium (Na), Potassium (K), Phosphorus (P), Magnesium (Mg); Zinc (Zn), Iodine (I), Copper (Cu), Selenium (Sl), Iron (Fe) can be given as examples of micro minerals that the body needs less. Crude salts generally contain more than 97% NaCl and more than 1% insoluble matter. Therefore, the mineral content of unprocessed salts is at most 2%. It is possible to consume 0.02 g of minerals with a maximum daily salt consumption of 5 g, which is considered appropriate for healthy individuals, but this does not make salt a mineral source. Most of the elements claimed to be minerals in unrefined salts are heavy metals or radioactive. On the other hand, while the human digestive system can absorb scientifically accepted minerals in their form bound to organic molecules, the absorption rate of inorganic ones is very low. It has been stated in many studies that in order to get even some of the daily needed minerals from salt, it is necessary to consume kilos of salt.

Health-conscious consumers have reduced their salt consumption to avoid the risk of excess salt, while also shifting their salt preferences from fine table salt to coarse salt to avoid food additives such as ferrocyanides. Salt producers also inform consumers through various channels that their salt contains essential minerals. On the other hand, the information that essential minerals are separated from salt during the salt refining process is announced to consumers in various ways. Advertising salt within the scope of reducing salt consumption is prohibited in Turkey and many other countries. Sea, lake, spring and rock salts may have different sensory properties desired by consumers, depending on the craft techniques. In recent years, there has been an increase in the consumption of natural coarse salt, which is usually sold with a spice grinder. The popularity of natural coarse salts, especially gourmet salts, is increasing. Gourmet salts are distinguished from ordinary salts by their special taste, easy dissolution, crisp texture and/or essential mineral content, as well as their salty taste. For these reasons, gourmet salts can find buyers at much higher prices than ordinary salts. Adulteration of gourmet salts can be accomplished by mixing or substituting with a cheaper table salt [18-20].

2. Results and Discussion

2.1. Food safety and Salt

Food is essential for life, so safe food is a fundamental human right. The most summary goal of food safety is; The products produced do not harm consumers or the environment we live in in terms of biological, physical and chemical aspects. Food safety is the whole of the measures taken to ensure food production without risk to human health. Food that does not harm human health if consumed is safe food. According to the Turkish Food Codex Salt Communiqué published in the Official Gazette No. 28737 on 16 August 2013, safe food production is aimed

by envisaging the production, preparation, processing, preservation, storage, transportation and marketing of salt in a technical and hygienic manner. Salt does not inherently carry microbial risks. However, chemical contamination poses major food safety risks for salts produced for food purposes. In terms of food safety, salts, heavy metals, radioactive elements, microplastics, exhaust, dynamite/explosive residues and organic residues pose risks. While direct human consumption of unprocessed raw salts is not recommended due to their impurities, on the contrary, the increase in different raw salts in the market shows that these salts are consumed with food [21,22]. Salt is one of the most common molecules on the planet. Sea, lake, river and rock salt can be produced all over the world. However, the residues contained in these salts are directly related to the pollution of the place where production takes place. Heavy metal and microplastic pollution in sea and lake salts around the world have been detected by many researchers. Radioactive elements can be found in places where radioactive experiments are conducted, nuclear leaks occur and active volcanoes exist. On the other hand, radioactivity can also be detected on the routes of nuclear ships and submarines. River salt washes underground salt mines and carries the salt to the surface. Heavy metal residues may also be found in these salts.

2.2. Microplastic Pollution in Salts

The presence of microplastics in ecology is a global environmental pollution problem. The presence of microplastics in food is a serious food safety problem. In recent years , microplastics have been detected in sea, lake, stream and rock salts; has made microplastic a food safety risk for salts. Even in refined salt samples from salt water, microplastics can contaminate the salt. On the other hand, salt can grind the packaging material in which it is placed and the packaging can contaminate the salt. For this reason, microplastics can be detected in natural and refined salts obtained from rock salts. Studies have shown that while the salt with the lowest microplastic content is rock salt, microplastic pollution in rivers, lakes and sea salts increases respectively. Microplastic analysis in salt samples is much easier than in other food samples because the salt is easily washed away. Microplastics detected in salts are physically broken down forms of the most commonly used polyethylene, polyester and polyvinyl chloride. Polyethylene, polyester and polyvinyl chloride are among the most commonly used salt packaging materials. If packaging that does not pose a threat to the environment and human health, such as cotton and glass, is used in salt produced for food purposes, microplastic contamination in rock salt can be prevented. On the other hand, microplastics can be removed from the product at the very beginning of production by adding a filtration step to the production processes of salts obtained from salt water. Especially in table grinding salt shakers used for unrefined salt, the plasticity of the grinder part can cause microplastic contamination in the salt. For this reason, porcelain and stone mills have been used in recent years [23,24].

2.3. Heavy Metal Pollution in Salts

Heavy metals are durable and common elements in nature, with high atomic weights, metallic properties, density greater than 5 g/cm3, conductors of electricity and liquids. The ever-increasing use of heavy metals in industry, agriculture and technology causes the accumulation of these metals in air, water, soil and food. Heavy metals; They are elements that can have toxic effects even at low concentrations. They are called metals or semi-metals (metalloids), which are often associated with contamination and potential toxicity or eco-toxicity. Heavy metals are taken into the organism through the mouth, breathing and skin, and most of them cannot be excreted through the body's excretory pathways (kidney, liver, intestine, lung, skin) without special support. For this reason, most of the heavy metals accumulate in biological organisms. These metals, which accumulate in living beings as a result of accumulation, can cause serious diseases (such as thyroid, neurological, autism and infertility) and even death when they reach effective doses. Hançerlioğulları and Eyüboğlu (2020) in their study on Çankırı salts; The average values of vanadium, chromium, manganese, iron, nickel, copper, zinc, molybdenum and lead concentrations are 2.7 mg/kg, 2.3 mg/kg, 12.9 mg/kg, 504.0 mg/kg, respectively. It was determined as 3.6 mg/kg, 1.9 mg/kg, 2.0 mg/kg, 0.1 mg/kg and 1.4 mg/kg. In the same study, mercury, cadmium, cobalt and tin concentrations were found below detectable values.

Heavy metal pollution in sea, lake, river and rock salts varies depending on the source. The presence of heavy metals in sea salts is a natural consequence of marine pollution. Heavy metals, which are a sign of pollution in inland waters, may also contain impurities found in the soil of the region. Heavy metals found in rock salts contain impurities found in the soil of the region. According to the research conducted by Ercoşkun (2021) on salt samples from different parts of the world; Arsenic, mercury, tin and antimony were not detected in any of the analyzed

salt samples, the highest cadmium was in Maldon salt at 5.97±0.21 ppm, the highest chromium was in Himalayan Pink, Himalayan Black, Nakhchivan, Maldon, Hawaii Black and Urmia salt samples. Nickel is found only in Himalayan Pink and Himalayan Black salt samples, the highest lead content in Himalayan Black salt samples, the highest barium amount in Çankırı and Himalayan Pink rock salts; lithium only in Guérande flake sea salt; highest aluminum in Himalayan Pink and Himalayan Black salts; The highest titanium salts are in Izmir; highest vanadium in Himalayan pink (57.10±6.46 ppb), Himalayan black (31.50±5.68 ppb) and Margherita di Savoia (20.97±2.22 ppb); cobolt is found only in Himalayan pink (624.87±7.08 ppb) and black (458.27±5.81 ppb) salts, and the highest copper content is found in Himalayan pink (486.80±13.06 ppb) and black (523.30 ppb) salts. ±10.21 ppb) salts; The highest iron content is in Himalayan black (402.67±22.12ppb) and pink (298.67±32.32 ppb) salts; The highest zinc, manganese, magnesium and calcium contents were detected in Himalayan pink and black salts.

2.4. Radioactivity in Salts

Human beings have been constantly exposed to natural radioactive rays since their existence on earth. People can be exposed to radiation from natural and artificial sources in their normal living environments in three ways; external gamma rays, inhalation of radon and other radioactive nuclides, and ingestion of radioisotopes through food and water. In particular, natural radioactivity in food comes mainly from 40K; Products of uranium and thorium can usually be found in trace amounts. Ingested or inhaled radionuclides are distributed throughout the body through the circulatory system. Analysis of salt taken with food in terms of chemical and radioactive contamination is extremely important to protect human health. Consuming contaminated food increases the amount of radioactivity and chemical contamination within the individual and therefore increases the health risks associated with radiation exposure and metal contamination. The exact effects on health depend on the type and amount of pollutants consumed. Naturally, some radioactivity results from the presence of cosmogenic and radionuclides in the earth's crust. On the other hand, artificial radioactive fallout originating from humans pose greater risks in terms of environment and food safety. The nuclear bombs dropped on Osaka and Hiroshima, the Chernobyl nuclear accident, the Fukushima nuclear accident, the nuclear bomb tests carried out especially on the Pacific islands, the authority vacuum created especially with the dissolution of the Soviets, and the nuclear wastes thrown into the seas from nuclear ships and submarines pose a food safety risk, especially for sea salts [25-27].

There are not many publications about natural and artificial radioactivity in salts. Tahir and Alaamer (2008) reported that the natural radionuclides in Himalayan salt samples obtained from the Khewra salt mine were below the effective dose. Baloch et al. (2012), in their study in the Khewra salt mine, reported that visitors and workers were directly exposed to the internal and external radiological hazards of radon and gamma rays. Hançerliogulları and Eyupoğlu (2020) investigated the natural radionuclide and potential toxic heavy metal contents of rock salt samples collected from three different salt mines in Çankırı province and found it to be 8.4 μSv, which is significantly lower than the annual average effective dose of 290 μSv received by ingesting natural radionuclides.

References

[1] MacGregor, G.A. & He, F.J. (2010). Reducing Population Salt İntake Worldwide: From Evidence to İmplementation. *Progress in Cardiovascular Diseases, 52*(5), pp. 363-382.

[2] Leistner, L. (1992). Food preservation by combined methods. *Food Research International, 25*(2), pp. 151-158.

[3] Pietinen, P., Valsta, L.M., Hirvonen, T. vd., (2008). Labelling the Salt Content in Foods: A Useful tool in Reducing Sodium Intake in Finland. *Public Health Nutrition, 11*(4), pp. 335-340.

[4] Suckling, R.J., He, F.J., MacGregor, A.G. (2010). Altered Dietary Salt Intake for Preventing and Treating Diabetic Kidney Disease. *Cochrane Database of Systematic Reviews, 12*, p. 70.

[5] Ercoşkun, H. (2022) Impurities of natural salts of the earth, *Food Additives & Contaminants: Part B, 16*(1):24-31.

[6] Kurlansky, M. (2003). Tuz- İnsanlığın Tuzlu Tarihi (Çeviren A. Çakıroğlu). İstanbul. Aykırı Yayınları.

[7] Desmond, E. (2006). Reducing Salt: A Challenge for the Meat Industry. *Meat Sci, 74*(1), pp. 188-196.

[8] Brown, I.J., Tzoulaki, I., vd., (2009). Salt Intakes Around the World: Implications for Public Health. *International Journal of Epidemiology, 38*(3), pp. 791-813.

[9] Taormina, P.J. (2010). Implications of Salt and Sodium Reduction on Microbial Food Safety. *Crit Rev Food Sci Nutr*, 50(3), pp. 209-227.

[10] Xi, B., Hao, Y., Liu, F. (2014). Salt Reduction Strategies in China. *Lancet, 383*(9923), p. 1128.
[11] Erdem, Y. (2016). Tuz Tüketimi, Vücuttaki Dağılımı ve Hipertansiyon Patogenezindeki yeri. HT Bülteni, 3(5), s. 22.
[12] Erdem, Y., Akpolat, T., Derici, Ü., Şengül, Ş., Ertürk, Ş., Ulusoy, Ş., (2017). Türkiye'de Yüksek Sodyum Alımının Diyet Kaynakları: SALTURK II. Nutrients, 9(9), s. 933.
[13] Koga A, Niino Y. 2004. Analysis of hexacyanoferrate (II) in salt. Bull Soc Sea Water Sci Japan. 58(1):24–29.
[14] Kubota H, Onishi Y, Yomota C, Tanamoto K. 2004. Analysis of ferrocyanides in food-grade salts. Japan J Food Chem. 11 (1):32–35.
[15] CODEX. 2016. Codex general standard for food additives (GSFA). http://www.fao.org/faowho-codexalimentarius/standards/gsfastandards/gsfa/en
[16] Lim H. S., Hwang, J. Y., Choi E, Lee G, Yun SS, Kim M. 2018. Assessment of ferrocyanide intake from food-grade salt in the Korean population. *LWT. 93*:620–627.
[17] Avery J. 2014. Fighting food fraud. *European Parliamentary Research Service;* p. 1–7.
[18] Wong G. 2018. Authentication of culinary salt - challenges and opportunities. Davis (CA): Office of Graduate Studies of the University California Davis.
[19] Ercoşkun, H. 2021. Salt and Food in All Aspects (77 - 106), ISBN: 978-625-433-183-1: Nobel Ankara
[20] Shariatifar N, Nejad AMS, Fathabad AE. 2017. Assessment of heavy metal content in refined and unrefined salts obtained from Urmia, Iran. *Toxin Rev. 36*(2):89–93. doi:10.1080/15569543.2016.1262875.
[21] Abdi L, Jahed-Khaniki GR, Molaee-Aghaee E, Shariatifar N, Khaneghah AM. 2021. The preliminary survey on the concentration of potentially toxic elements (PTEs) in salt samples collected from Tehran, Iran: a probabilistic health risk assessment. Environ Sci Pollut Res. 28:62651–62661.
[22] Koelmans, A. A., Redondo-Hasselerharm, P. E., Nor, NHM et al. (2022). Risk assessment of microplastic particles. *Nat Rev Mater 7*, 138–152.
[23] Gündoğdu, S. (2018) Contamination of table salts from Turkey with microplastics, Food Additives & Contaminants: Part A, 35:5, 1006-1014, DOI: 10.1080/19440049.2018.1447694
[24] Baloch et al., "A Study on Natural Radioactivity in Khewra Salt Mines, Pakistan," in Journal of Radiation Research, vol. 53, no. 3, pp. 411-421, May 2012, doi: 10.1269/jrr.11162.
[25] Caridi F, Messina M, Belvedere A, D'Agostino M, Marguccio S, Settineri L, Belmusto G. Food Salt Characterization in Terms of Radioactivity and Metals Contamination. Applied Sciences. 2019; 9(14):2882.
[26] Shabaan, DH Radioactivity measurements of different types of salt using SSNTD. *AIP Conf. Proc.* 2018, 1976, 020023.

Classification of X-ray Images of Atelectasis and Pneumonia

Mücahit Ensar ÖZTÜRK[1], ***Ebubekir BABAYİĞİT***[1], ***Mahmut BÜYÜKBAŞ***[1], ***Bekir Hakan AKSEBZECİ***[2,*]

[1]*Faculty of Engineering, Electrical-Electronics Engineering, Abdullah Gül University, Kayseri, Turkiye*

[1]*Faculty of Engineering, Electrical-Electronics Engineering, Abdullah Gül University, Kayseri, Turkiye*

[1]*Faculty of Engineering, Electrical-Electronics Engineering, Abdullah Gül University, Kayseri, Turkiye*

[2]*Faculty of Engineering, Biomedical Engineering, Abdullah Gül University, Kayseri, Turkiye*

Abstract

Atelectasis and pneumonia are serious lung diseases that can lead to serious complications, including death. The gold standard for diagnosing these diseases is X-ray imaging. This study focuses on the classification of atelectasis and pneumonia diseases through chest X-ray images. A dataset that includes 744 X-ray images was used. In this work, different image processing, feature extraction, feature selection, and classification techniques are examined to improve the performance of medical image classification. In the image processing step, resizing, Gaussian filtering and adaptive histogram equalization methods were applied to the images. Then, region of interests were detected in the segmentation step. In the feature extraction step, first-order statistical features, texture-based features, morphological features and shape-based features were extracted. Information gain, wrapper and correlation-based feature selection methods were applied in the feature selection step. In the classification part, five different machine learning algorithms such as Naive Bayes, Logistic Regression, Support Vector Machines, K-Nearest Neighbor and Decision Tree were utilized to classify X-ray images. The results of this study demonstrate that selecting the most effective feature selection and classification methods significantly improves accuracy rates.

Keywords: *Chest X-ray images, Atelectasis, Pneumonia, Image processing, Machine learning*

1. Introduction

A collapsed and non-aerated portion of the lung parenchyma is referred to as atelectasis. This condition occurs when the air sacs in that area close or deflate due to the suffocation of a certain part of the lungs. Acute lung parenchymal infection caused by a variety of microorganisms is known as pneumonia [1, 2]. Pneumonia is a disease caused by infection and inflammation in the lungs. It usually occurs when bacteria, viruses, fungi, or parasites settle in the lungs. Pneumonia is characterized by inflammation of the lung tissue and infection of the alveoli (air sacs). This condition can affect respiratory function and seriously affect respiratory system health. In addition, the symptoms of both diseases can be similar. Common symptoms include shortness of breath, cough, sputum production, chest pain, fever, fatigue, and weakness. In the diagnosis of both diseases, the signs and findings on X-ray images are of great importance. However, manually reviewing these images can be time-consuming and can lead to misdiagnosis. At this point, the use of image processing and machine learning techniques plays a crucial role.

Many studies have been conducted to identify atelectasis and pneumonia in recent years. For instance, on a study that made with 200 images for dataset, samples with atelectasis were classified correctly at a rate of 82% using Convolutional Neural Network (CNN) [3]. On another study that includes 5840 images for dataset, researchers reached 84.1% accuracy with Neural Network model in identifying pneumonia [4]. Wang et al. [5] conducted a comprehensive quantitative performance benchmarking study on eight common thoracic pathology classifications and weakly-supervised localizations using the ChestX-ray8 database. They achieved an AUC (Area-Under-Curve) of 0.7069 for atelectasis and 0.6333 for pneumonia classification with different Deep Convolutional Neural Network (DCNN) models.

** Corresponding author. *e-mail address: hakan.aksebzeci@agu.edu.tr*

In this article, the focus is on the use of X-ray images for the diagnosis of lung diseases that are atelectasis and pneumonia and the importance of image processing and machine learning techniques in classification of these images. The reason of the selecting atelectasis and pneumonia from "ChestX-ray14" dataset is their similarity on X-ray images as can be seen on Figure 1(a) and (b). They cannot easily determined even by medical experts. It can be easier to distinguish these two diseases from each other with image processing and machine learning.

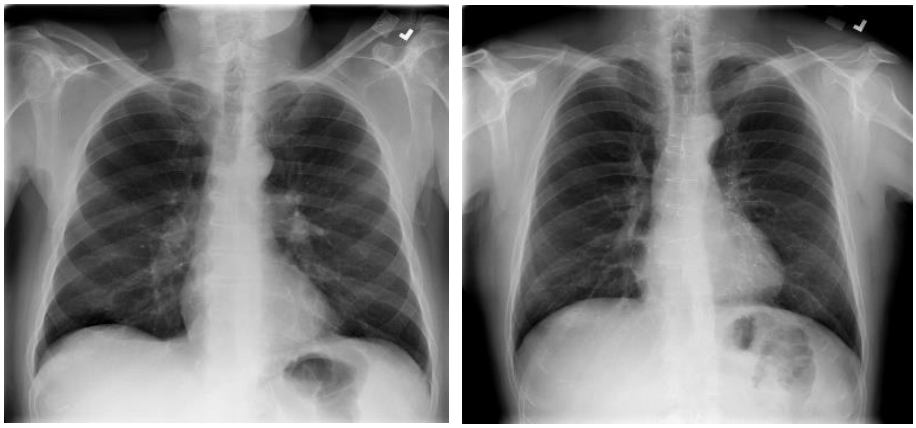

(a) (b)

Figure 1. X-ray images: (a) atelactasis, (b) pneumonia.

2. Materials and Methods

Image processing techniques play an important role in the diagnosis of lung diseases such as atelectasis and pneumonia. These techniques allow the identification of diseased regions, the extraction of features, and use for classification through the processing and analysis of X-ray images. This paper focuses on extracting features from X-ray images by applying machine learning techniques and diagnosing disease using classification algorithms. Feature extraction is used to transform raw data into numerical features. After that, feature selection is applied to find best representative features. Finally, classification algorithms are used to classify diseases that are atelectasis and pneumonia.

2.1. Dataset

The study utilized the 'ChestX-ray14 dataset, which includes 14 classes [5, 6]. However, only the atelectasis and pneumonia classes were utilized in this study due to the presence of other diseases and materials (such as pacemakers) in some images. Table 1 presents the distribution of the X-ray image dataset for the two disease classes used in this study.

Table 1. X-ray image dataset distribution by diseases.

Disease Type	Number of Images
Atelectasis	372
Pneumonia	372
Total	**744**

2.2. Image Processing

Image processing steps are important to improve the quality of the X-ray images obtained and to perform more effective analysis. After the dataset selection, image processing steps were applied in order to perform feature extraction efficiently. These steps in below were applied separately and shown in Figure 2.

1) Resizing of the X-ray images
2) Adaptive histogram equalization (AHE)
3) Contrast limited adaptive histogram equalization (CLAHE)

4) The Gaussian filtering after AHE
5) Bilateral filtering after CLAHE
6) Harmonic filtering

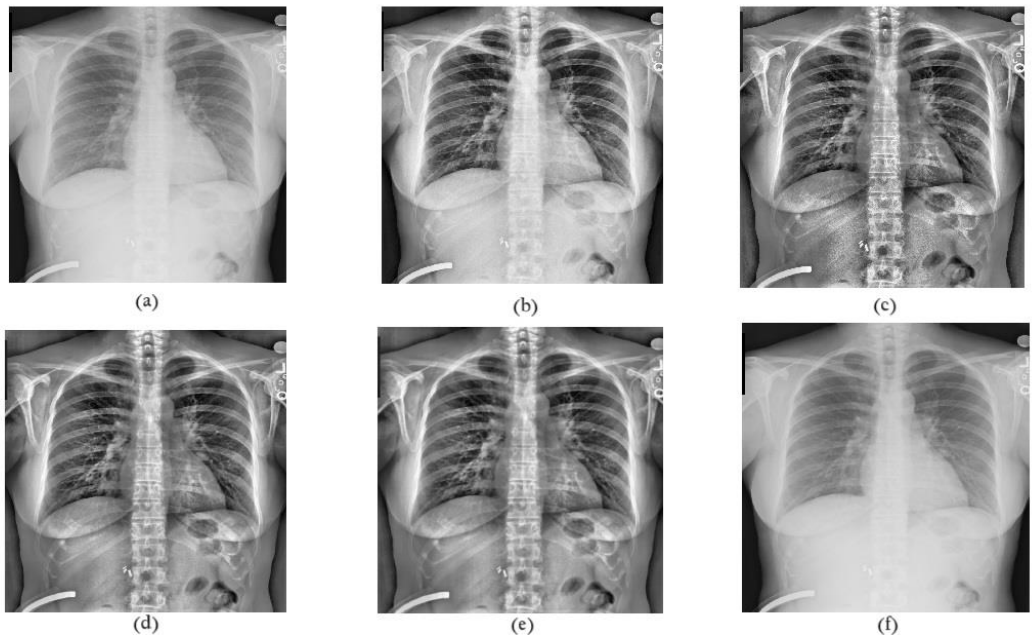

Figure 2. Image processing steps: a) original image of atelectasis, b) after AHE, c) after CLAHE, d) Gaussian filtering after AHE, e) Bilateral filtering after CLAHE, f) after harmonic filtering.

2.3. Segmentation

Segmentation is a significant step for detecting the region of interest (ROI) in images. Two different methods were used for the segmentation part. These methods are thresholding segmentation and edge-based segmentation. A certain threshold value is determined for the thresholding segmentation part. Then, the images were converted into binary masks according to this threshold value. After that, the ROIs were found by combining the resulting binary masks and original images. At the same time, the candy edge method, which is one of the edge-based segmentation methods, was applied. Edges within the image were detected and then ROIs were detected by *k*-means clustering. A sample ROI image is shown in Figure 3.

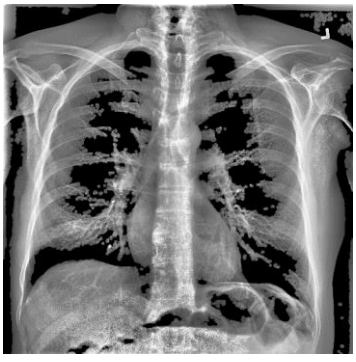

Figure 3. ROI image

2.4. Feature Extraction

According to the different features extracted from the ROIs, various information was obtained from its intensities. Extracted features and their numbers are given in Table 2. These features are given in a list below:

- First-order statistical features (Mean, median, standard deviation, minimum and maximum values, and more)
- Texture-based features (GLCM and GLSZM)
- Morphological features (Area, perimeter, compactness, stiffness, and more)
- Shape-based features (Eccentricity, Major Axis Length, Minor Axis Length, Orientation, and more)

Table 2. Distribution of the extracted features.

Features	Number of Features
First-order statistical	34
Texture-based features	150
Morphological	20
Shape-based	30
Total	**234**

2.5. Feature Selection

MATLAB has been used in the studies carried out up to this stage [7]. Three distinct feature selection strategies were chosen over Weka [8]. First, the "CfsSubsetEval" (CFS) was chosen, which is based on the correlation-based feature selection technique. Using correlation criteria, this technique finds the sequence of features by their order of importance in a dataset. Then, the information-based feature selection algorithm, "InfoGainAttributeEval" (InfoGain) was chosen. The InfoGain method seeks to choose attributes that provide a high level of information gain. InfoGain computes information gain by calculating the association of each attribute to the target class. Finally, the "WrapperSubsetEval" (Wrapper) was chosen, which is based on the learner-based feature selection technique. The performance of the classification model is used to evaluate the significance of features in this strategy.

2.6. Classification

After the feature selection part, following classification algorithms are applied. Naive Bayes computes the class probabilities of the samples. Using Bayes' theorem calculates the chance that a sample belongs to a certain class and assigns the sample to the class with the highest probability. Logistic Regression evaluates the probability that the data belong to a specified class. The model is tailored to the dataset and optimal weight values are obtained during the training phase. Support Vector Machine (SVM) strives for maximal marginal separation. In other words, it seeks the greatest disparity between classes. Kernel was selected as radial basis function for SVM classifiers in this study. K-Nearest Neighbor (KNN) is based on a measure of sample similarity. For KNN classifiers $k = 5$ was chosen in this study. Decision Tree attempts to select the best split. Splits are evaluated using metrics such as information gain, the Gini index, and the complexity criterion. The classification algorithms were applied to the dataset using the 10-fold cross validation method.

3. Results and Discussion

In this study, different image processing, feature extraction, feature selection, and classification methods are examined to improve the performance of X-ray image classification. The results in classification methods were compared according to three feature selection methods such as InfoGain, CFS and Wrapper. First of all, InfoGain method was applied for different numbers of feature selection. The results were given in Table 3. It is seen that the classification success increases when the number of features is increased. Secondly, the CFS method was tested by selecting different feature numbers. The results were given in Table 4. Choosing different numbers of features did not cause a change for the CFS method. Finally, the Wrapper method was tested on different

classification methods and all results were compared. Since the Wrapper method selects the features that give the best results, there is no need to try different numbers of feature selection.

The results obtained using different feature selection methods and classification methods are shown in Table 5. According to these results, the accuracy rates of different combinations differ from each other. For the Naive Bayes classification method, the highest accuracy rate was 81.04% using the Wrapper method. In the Logistic Regression method, the highest accuracy rate was obtained by using the Wrapper method with 83.87%. The highest accuracy rate for the SVM classification method was obtained at 84.40% with all features. The highest accuracy rate for the KNN method was obtained using the CFS method at 74.32%. In the Decision Tree classification method, the highest accuracy rate of 80.10% was obtained by using the InfoGain method.

Table 3. Classification accuracy rates (%) according to selected number of features for InfoGain method.

Classification Methods	5 Features	10 Features
Naive Bayes	75.13	78.89
Logistic Regression	77.95	79.43
SVM	75.26	79.83
KNN	70.16	73.52
Decision Tree	79.03	80.10

Table 4. Classification accuracy rates (%) according to selected number of features for CFS method.

Classification Methods	5 Features	10 Features
Naive Bayes	80.51	80.51
Logistic Regression	80.64	80.64
SVM	80.37	80.37
KNN	74.32	74.32
Decision Tree	79.03	79.03

Table 5. Classification accuracy rates (%) according to feature selection methods.

Classification Methods	InfoGain	CFS	Wrapper	No Selection
Naive Bayes	78.89	80.51	**81.04**	76.47
Logistic Regression	79.43	80.64	**83.87**	83.06
SVM	79.83	80.37	82.93	**84.40**
KNN	73.52	**74.32**	73.79	72.17
Decision Tree	**80.10**	79.03	79.43	79.43

The results show that different image processing steps and feature extraction methods have an impact on classification accuracy rates. Best accuracy rate of 84.40% was achieved by SVM using all features. This result was achieved by using resizing and cropping of images, applying CLAHE, and edge-based segmentation.

In general, variations in accuracy rates have been observed as a result of combinations using different feature selection methods and classification methods. In some cases, a particular feature selection method provided better results for a particular classification method. Therefore, choosing the right feature selection method and classification method is important in terms of increasing the accuracy rates.

4. Conclusion

In this study, medical images of atelectasis and pneumonia diseases selected from the "ChestX-ray14" dataset were studied with various image processing and machine learning algorithms. The results show that SVM and Logistic Regression algorithms stand out in terms of accuracy in binary class classifications. Additionally, this study has shown that different feature selection methods and various numbers of selected feature features significantly change the accuracy result. This situation shows the effectiveness of classification methods on the data set.

This research enhances the current understanding of detecting and classifying atelectasis and pneumonia using X-ray images. The results obtained in this study may have significant implications for physicians to accurately diagnose these diseases. In addition, changing the image processing methods, determining a more suitable dataset, and increasing the selection of different numbers of features can increase the robustness of the model.

References

[1] Peroni, D., & Boner, A. (2000b). Atelectasis: mechanisms, diagnosis and management. *Paediatric Respiratory Reviews*, *1*(3), 274–278.

[2] Mackenzie, G. (2016b). The definition and classification of pneumonia. *Pneumonia*, *8*(1).

[3] K G, S., P, S., S, S. V., V, S., S, J., Mouna M, S., & T, S. (2022). Atelectasis, Cardiomegaly and Effusion Disease Prediction using Image Processing (Convolutional Neural Networks). 2022 4th International Conference on Inventive Research in Computing Applications (ICIRCA).

[4] Yee, S. L. K., & Raymond, W. J. K. (2020b). Pneumonia Diagnosis Using Chest X-ray Images and Machine Learning. *Proceedings of the 2020 10th International Conference on Biomedical Engineering and Technology*.

[5] Wang, X., Peng, Y., Lu, L., Lu, Z., Bagheri, M., & Summers, R. M. (2017). ChestX-Ray8: Hospital-Scale Chest X-Ray Database and Benchmarks on Weakly-Supervised Classification and Localization of Common Thorax Diseases. 2017 IEEE Conference on Computer Vision and Pattern Recognition (CVPR).

[6] Papers with Code - ChestX-ray14 Dataset. (n.d.). Retrieved from https://paperswithcode.com/dataset/chestx-ray14

[7] The MathWorks Inc. (2022). MATLAB version: 9.13.0 (R2022b), Natick, Massachusetts: The MathWorks Inc. https://www.mathworks.com

[8] Frank, E., Hall, M. A., & Witten, I. H. (2016). *Data Mining: Practical Machine Learning Tools and Techniques*, Morgan Kaufmann, Fourth Edition.

The Participation of Rural Women In Decisıons Case of Karapınar District of Konya Province

Makbule TURAN [1,*], ***Aysun YENER ÖGÜR*** [2]

[1] *Selçuk University, Faculty of Agriculture, Department of Agricultural Economics, TURKEY*

[2] *Selçuk University, Faculty of Agriculture, Department of Agricultural Economics, TURKEY*

Abstract

The aim of the study is to determine the participation of women living in rural areas in decisions. The main material of the study consists of the results of the survey conducted with women in the Karapınar district of Konya. The sample size was chosen purposefully, and questionnaires were conducted face-to-face with 20 women who voluntarily participated in the survey in Karapınar. The land assets, livestock, agricultural and non-agricultural incomes of the enterprises were determined by simple percentage calculations over the averages. The roles of women living in rural areas in the family and the level of women's participation in decisions were calculated with the Likert scale. It has been determined that the spouses decide together on matters related to the house, the purchase of agricultural tools and machinery necessary for agricultural production, the type of product, and the fact that women work in a job other than agriculture. Women, on the other hand, only decide which party to vote for in the elections. Training to be given to businesses or any fair, excursion, etc. Women's participation in activities should be ensured, and their communication with the outside world should be strengthened.

Keywords: *Konya, Participation in Decisions, Rural Women*

1. Introduction

Women living in rural areas in underdeveloped and developing countries are heavily involved in agricultural production activities. However, in these countries, female farmers are eight times less likely than men to independently own agricultural land and inputs [1]. Women's labor in the agricultural sector is the unregistered, uninsured, and unpaid family workers. Women's labor is seen as a part of their natural life and causes low job perception [2]. The rate of women's participation in agricultural production varies between countries and regions. Although this difference takes shape according to culture and beliefs, other socio-economic factors are also effective [3]. Rural women differ from urban women in terms of their traditional values and the duties they undertake [4]. While women in rural areas do household chores such as cleaning, childcare, fuel supply, bread making, and feeding, they also engage in plant and animal production, handicrafts, non-agricultural work, and income-generating activities [5]. Recently, women are expected to contribute to family welfare, and this trend is increasing day by day given the rapidly increasing cost of living [6]. In rural areas, women constitute the main force of rural development [7]. The World Bank supports “community-based development" especially in low and middle-income countries. Community-Based Development programs are an approach that works with the principles of transparency, participation, demand-oriented, accountability, and local capacity building [8]. Rural development is formed by ensuring individuals' participation in development programs, the democratic participation process, and decisions that will respond to local needs. Therefore, the participation of women in decisions is very important.

In many democratic societies, important gender-related protocols are in place aimed at attracting women to decision-making roles. However, despite the implementation of these protocols, these societies face the challenge of increasing the visibility of women working in the public and other sectors in decision-making roles [9].
Women's participation in family decisions, age of women, education level, average monthly income of the family, working status of women, and having children affect decision-making. Generally, women decide on household chores, and the majority of women who decide on this are working. In order to reduce the burden on working women in order to ensure conformity with the contemporary and social family structure and to improve the democratic decision-making process in the family, the participation of men in decisions regarding housework should be ensured [10]. For this reason, the aim of the research is to determine the participation of women living in the rural areas of Konya, which has large agricultural lands, in the decisions.

2. Materials and Methods

The main material of the study consists of the results of the survey conducted with women in the Karapınar district of Konya. The main material of the research was the primary data obtained from the questionnaires made with the women in the agricultural enterprises engaged in agricultural production. The sample size was chosen purposefully, and questionnaires were conducted face-to-face with 20 women who voluntarily participated in the survey in Karapınar.

* Corresponding author. *e-mail address: aysunyener@selcuk.edu.tr*

Age, education, social security, and status of women living in rural areas in Konya Province Karapınar District were determined by simple percentage calculations over the averages. The land assets, livestock, agricultural and non-agricultural incomes of the enterprises were determined by simple percentage calculations over the averages.
The roles of women living in rural areas in the family and the level of women's participation in decisions were calculated with a Likert scale. It was interpreted by creating graphs in Excel. The Likert scale is one of the attitude measurement methods and is included in the group of graduated scales. The basic approach in the Likert scale is to give judgments about the researched subject and to rate the concentration on these judgments. For this purpose, the factor is determined first, and each factor is turned into a question in accordance with the scale conditions. Then, scale scores are created for these questions, which indicate the degree of participation of the individuals. Individuals whose attitude analysis will be made determine their own scores according to their level of participation. The scale value of the person is found with the scores calculated for the degree of participation [11]. With this value obtained, the rating of the factors that determine the attitude or attitude of the individual towards an event is made [12]. Likert scales were used as follows [11] (Likert, 1932).
1: Strongly disagree, 2: Disagree, 3: Undecided, 4: Agree, 5: Strongly agree. 1: Never, 2: A few days a year, 3: A few days a month, 4: A few days a week, 5: Every day.

3. Results and Discussion

72.10% of the population in the research region is in the 15-59 age group, 12.04% is in the 7-14 age group, 12.04% is in the 50-+ age group and 11.43% is in the 0-6 age group. 48.28% of the population is male and 51.72% is female.

Table 1. Population status in the research area (Number %)

Age	Gender	Number	Ratio of Total Population	**Ratio of Age Groups to Total Population (%)**
0-6	Male	0.10	4.76	11.43
	Female	0.15	6.67	
7--14	Male	0.25	11.90	12.04
	Female	0.30	0.13	
15-49	Male	1.50	71.43	72.10
	Female	1.50	0.67	
50-+	Male	0.25	11.90	12.04
	Female	0.30	0.13	
Total	Male	2.10	100.00	100.00
	Female	2.25	100.00	

48.19% of the population in the research region are primary school graduates, 28.92% are high school graduates, 14.46% are secondary school graduates and 8.43% are university graduates. 52.50% of primary school graduates are female and 44.19% are male. According to the results of a similar study, it has been determined that there is no clear difference between the level of education and the participation of women in the decision-making mechanism related to agricultural production [13].

Table 2. Educational status of the population in the research region (Number %)

Educational Status	Gender	Number	%
Primary school	Male	0.95	44.19
	Female	1.05	52.50
Middle school	Male	0.35	16.28
	Female	0.25	12.50
High school	Male	0.75	34.88
	Female	0.45	22.50
University	Male	0.1	4.65
	Female	0.25	12.50
Total	Male	2.15	51.81
	Female	2.00	48.19

Considering the social security status of the population in the research region, 54.55% are Bağkur and 45.45% are social insurance institutions (SSK).

Table 3. Social security status of the population in the research region (Number %)

Social Security Status	Gender	Number	%
Bağkur	Male	0.80	57.14
	Female	1.00	52.63
SSK	Male	0.60	42.86
	Female	0.90	47.37
Total	Male	1.40	100.00

	Female	1.90	100.00

Considering the ownership status of the lands in the research area, 65.48% is property land, 17.86% is rent and 16.67% is common land.

Table 4. Ownership status of lands in the research area (da,%)

	Decar	%
Property	41.25	65.48
Rent	11.25	17.86
Partner	10.50	16.67
Total	63.00	100.00

Considering the production pattern of the lands in the research area, wheat is grown at 51.98%, barley at 20.63%, corn at 10.71%, alfalfa at 10.32%, sugar beet at 4.76%, and carrot at 1.59%.

Table 5. Land production pattern in the research area (da, %)

	Decar	%
Wheat	32.75	51.98
Barley	13.00	20.63
Sweetcorn	6.75	10.71
Clover	6.50	10.32
Sugar beet	3.00	4.76
Carrot	1.00	1.59
Total	63.00	100.00

The livestock assets of the enterprises in the research area are considered cattle and small cattle. 57.14% of the bovine stock is the cow and 42.86% is the calf. All of the small cattle are sheep.

Table 6. Presence of cattle and sheep in the research area (Head %)

Cattle Assets	Head	%
Cow	2.40	57.14
Calf	1.80	42.86
Total	4.20	100.00
Small Animal Presence		
Sheep	56.25	100.00
Goat	0.00	0.00
Total	56.25	100.00

When looking at the tools and machines used in the research area, it was determined that the tractors and trailers were the most.

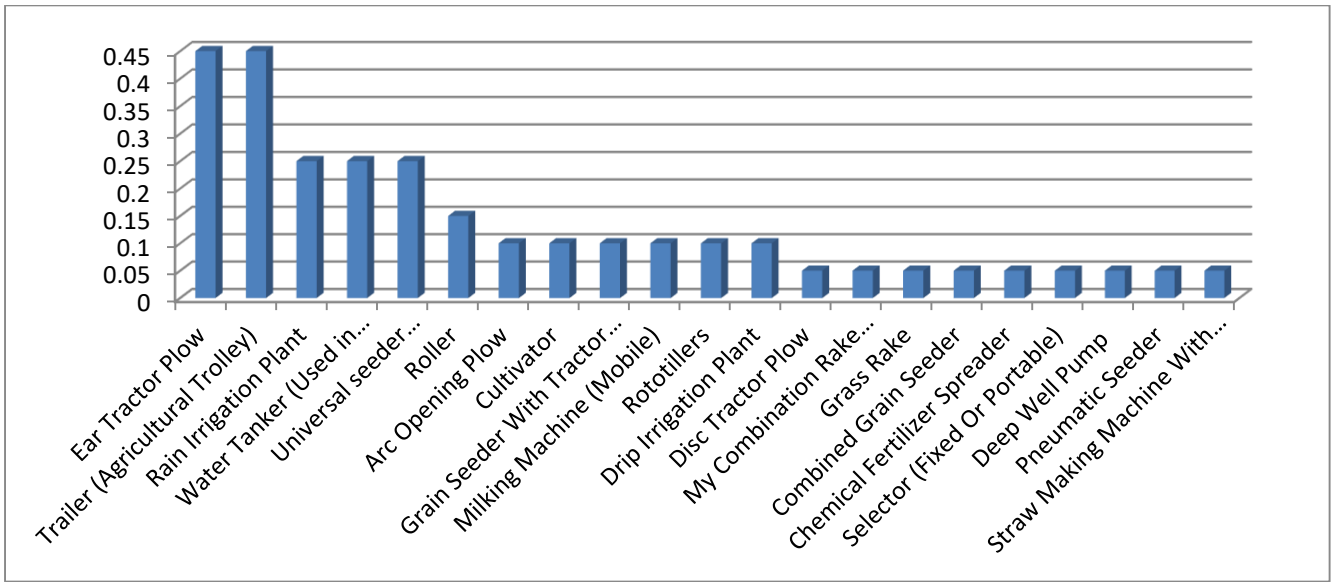

Figure1. Agricultural tools and machinery in the research area

The total annual income of the individuals in the research region is 125,126 TL. 71% of this income consists of agricultural income and 29% of non-agricultural income.

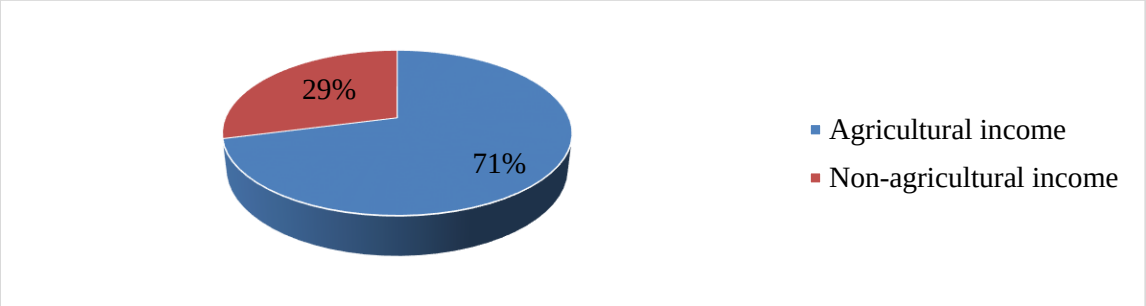

Figure 2. Agricultural and non-agricultural income (%)

It has been determined that the women in the research region do post-meal cleaning, washing dishes, purchasing food, making beds, and cleaning the house every day.

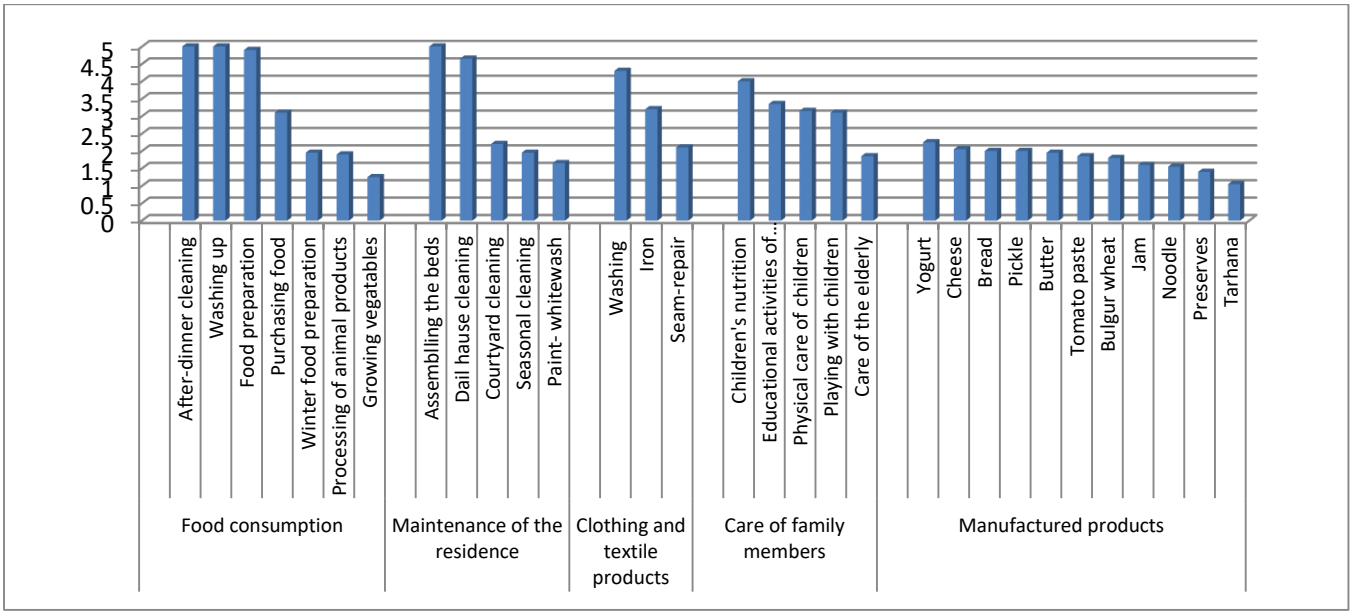

Figure 3. Jobs of women in the study area

The power to decide on any issue in the daily life of the individual is called "decision-making". Decision-making is the process of choosing among alternatives according to the values and preferences of the individual [14] (Harris, 2008). Participation of participants in the decision-making process can be affected by their perceptions of their decision-making rights [15] (Arshad et al., 2010).
Considering the situation of rural women deciding on household expenditures, it has been determined that 55% of them decide together and 45% of them are made by their spouses.

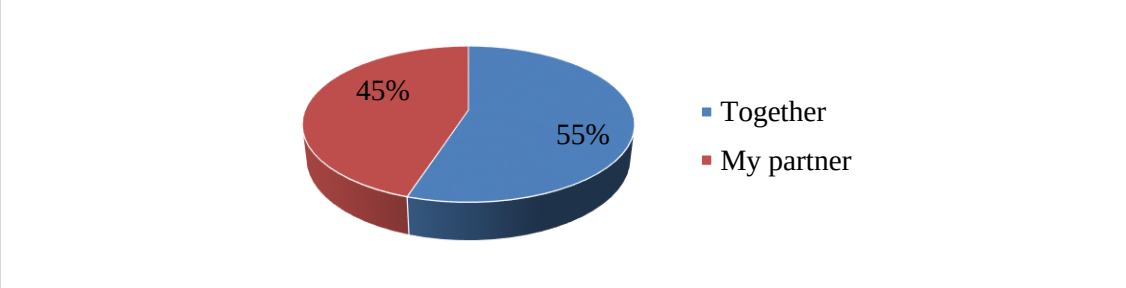

Figure 4. Decision-making on household expenses

When the participation of rural women in family decisions are examined, it has been determined that the spouses decide together to purchase clothing (3.15), household goods (3.05), the number of children desired to have (2.95), the expenditure of family income (2.80), the purchase of equipment (2.65) and the use of new technological tools (2.55). It has been determined that the man decides to buy and sell the land (2.40), work in a non-agricultural job (2.35), produce a new

agricultural product (2.2), and sell the products (2.2). It has been determined that only women decide which political party to vote for in the elections.

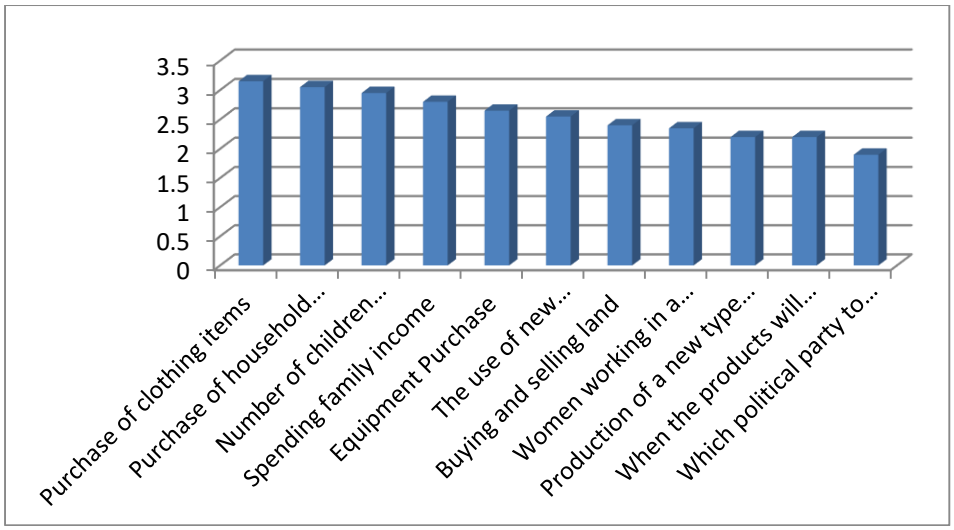

(1: Female, 2: Male, 3: Spouses together, 4: With family members)
Figure 5. Rural women's participation in family decisions

When the participation of rural women in business decisions is examined, it has been determined that they do not participate in the decisions of purchasing land (1.80), renting land (1.65), purchasing animals (1.65), and selling animals (1.65). It has been determined that they do not agree with the decisions of employing foreign workers (1.40), purchasing tools and machinery (1.40), using credit (1.40), selling products (1.40), participating in agricultural training (1.35), land processing (1.30), using fertilizers (1.25) and using pesticides (1.15).

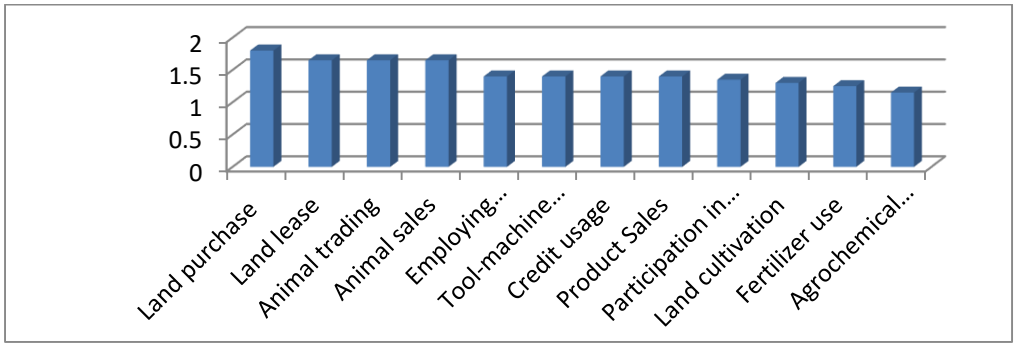

(1: Strongly Disagree, 2: Disagree, 3: Undecided, 4: Agree, 5: Strongly Agree)
Figure 6. Participation of rural women in business decisions

Looking at the information sources used by rural women, it is seen that family members (3.5) meet a few days a week, other farmers (2.2) a few days a month, agricultural engineers (1.70), dealers (1.55) and district agriculture directorate (1.5) meet several times a year. It was determined that they did not receive information from the internet (1.40), social media (1.15), printed publications (1.05), visual publications (1.05), universities (1.00), and research institutions (1.00).

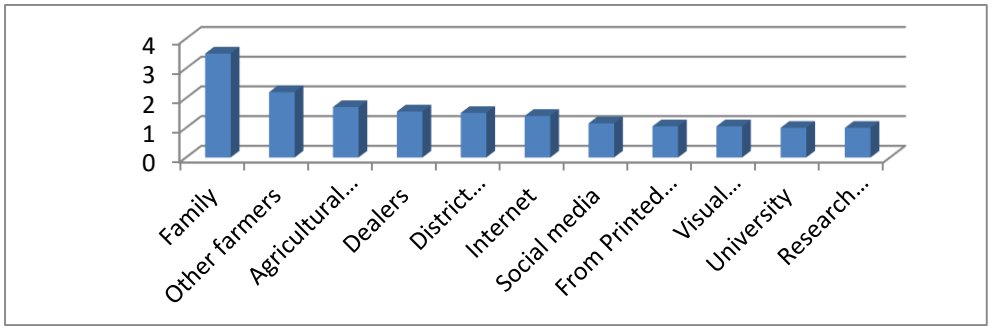

(1: Never, 2: A few days a year, 3: A few days a month, 4: A few days a week, 5: Everyday)
Figure 7. Information sources used by rural women

4. Conclusion

When the work done by women in the research area is examined, it has been determined that they frequently do housework such as cleaning after meals, washing dishes, and preparing meals, and they do not actively participate in the marketing of these products, although they also produce value-added products such as yogurt, cheese, bread, and pickles. It should be ensured that women are included in the working life by providing training on marketing, entrepreneurship, and food safety. When the participation of women in business decisions is examined, it is determined that the majority of women do not have a say in decisions, men decide, and women generally have a say in domestic affairs. In order to ensure the participation of women in business decisions, awareness training should be given to both women and men about the work women do in the business.

It has been determined that the spouses decide together on matters related to the house, the purchase of agricultural tools and machinery necessary for agricultural production, the type of product, and the fact that women work in a job other than agriculture. Women, on the other hand, only decide which party to vote for in the elections. Training to be given to businesses or any fair, excursion, etc. Women's participation in activities should be ensured, and their communication with the outside world should be strengthened.

The person who is active in the economic and social profits received in the family is usually a man. In order for women to be effective in the economic and social field, first of all, women should be registered and their participation in the activities to be carried out for the enterprise should be monitored.

In the research area, women generally carry out animal husbandry activities. Participation of women in animal husbandry training should be ensured. In addition, studies should be carried out to market the products obtained by women from both plant production and animal production by converting them into value-added products.

In order to improve women's participation in family decisions and business decisions, to improve themselves so that women can work in different business lines and have a greater say in the decisions to be taken, training and projects should be organized, extension services should be offered, women's entrepreneurship should be encouraged, and these initiatives should be supported both within the family and by the state. Women's participation and decision-making powers require a reorientation of actual agricultural and rural development programs.

References

[1] FAO/IFAD/ILO, (2010). Genderdimensions of agriculturalandruralemployment: Differentiatedpathwaysout of poverty. Rome: FAO, IFAD and ILO. [Google Scholar]

[2] Yilmaz E., Özdemir G., Oraman Y., Unakitan G. and Konyali S., (2019). Tarımsal üretimde kadınların karar alma süreçlerine katılımı ve kooperatiflerden beklentileri. *Tekirdağ Ziraat Fakültesi Dergisi*, *16*(1), 71-81.

[3] Dixon R.B., (1982). Women in agriculture: Countingthelaborforce in developingcountries. *Populationanddevelopmentreview*, 539-566.

[4] Kızılaslan N. and Otcu M., (2023). Kırsalda Kadınların Tarımsal Faaliyetlere ve Kararlara Katılımının İncelemesi: Tokat İli Merkez İlçe Örneği. *Gaziosmanpaşa Bilimsel Araştırma Dergisi*, *12*(1), 167-180.

[5] Yıldırak N., Gülçubuk B., Gün S., Olhan E. and Kılıç M., (2002). Türkiye'de Gezici ve Geçici Kadın Tarım _sçilerininÇalısma ve Yasam Kosulları ve Sorunları. *Uluslararası Çalısma Örgütü Türkiye Temsilciligi, Ankara*.

[6] Al-Nouri Q.N., (1993). Iraqiruralwomen'sparticipation in domesticdecision-making. *Journal of ComparativeFamilyStudies*, *24*(1), 81-97.

[7] Quendler E., Glatzl M. and Mayr J., (2017). Female Farmers'work Both On And Off The Farm In Austrıa. *Journal of International Scientific Publications: Agriculture&Food*, *5*(1000023), 226-237.

[8] Anonymous,(2023). https://www.sbb.gov.tr/wp-content/uploads/2020/04/KirsalKalkinmaOzelIhtisasKomisyonuRaporu.pdf(Accesseddate: 29.06.2023).

[9] Abakah E., (2018). Participationwithout a voice? Ruralwomen'sexperiencesandparticipation in localgovernanceactivities in the Abura–Asebu–Kwamankesedistrict of Ghana. *CogentSocialSciences*, *4*(1), 1549768.

[10] Arpacı F., (2014). Ailede Alınan Kararlara Kadının Katılımını Etkileyen Faktörlerin İncelenmesi. *Akademik Bakış Uluslararası Hakemli Sosyal Bilimler Dergisi*, (42).

[11] Likert R., (1932). A technique for the measurement of attitudes. *Archives of psychology*.

[12] Sezen B. and BOZ İ., (2021). Ziyaretçilerin Kırsal Turizm Faaliyetlerinden Memnuniyet Düzeyi: Cumalıkızık Köyü Örneği. *Black Sea Journal of Public and Social Science*, *4*(1), 24-33.

[13] Yavuz F., Shivan M.S., Terin M., Akay B., Güler İ.O. and Ağsu K., (2018). Gelir Getirici Faaliyetlere Karar Vermede Kırsal Kadının Rolü: Kuzeydoğu Anadolu Tra1 Bölgesi Örneği. *Uluslararası İktisadi ve İdari İncelemeler Dergisi*, 1-10.

[14] Harris R., (2008). http://www.virtualsalt.com/introduction-to-decision-making-part-1/ (Accesseddate: 19.03.2023).

[15] Arshad S., Muhammad S., Randhawa M.A., Ashraf I. and Chuadhry K.M., (2010). Ruralwomen'sinvolvement in decision-makingregardinglivestockmanagement. *Pakistan Journal of AgriculturalSciences*, *47*(2), 1-4.

The influence of pressure on the structural and elastic properties of the CuY intermetallic compound

***İlknur KARS DURUKAN*[1,*], *Yasemin ÖZTEKİN ÇİFTÇİ*[1]**

[1]*Science Faculty, Physics Department, Gazi University, Ankara, Turkey*

Abstract

Intermetallic compounds incorporating rare earth elements exhibit compelling physical and mechanical characteristics that typically surpass those of conventional metals. These properties encompass heightened strength and hardness, reduced specific gravity, enhanced corrosion resistance, and superior hot strength. Our investigation delved into the theoretical analysis of the intermetallic compound CuY. This study is purely theoretical, devoid of any reliance on experimental parameters. The compound adopts a cubic CsCl structure. We examined the impact of pressure on both the structural and electronic properties of the compound, employing the first principles method within the framework of Density Functional Theory (DFT). Given its significance as a crucial parameter, investigating materials under pressure holds merit. Exploring the deformation behavior of compounds subjected to compression is valuable, as it provides insights into alterations in their physical and chemical properties. Such research is indispensable for a comprehensive understanding of the nature of solids. The CuY compound satisfied the Born criteria, demonstrating structurally stable properties. By utilizing elastic constants, we scrutinized the impact of increasing pressure on its mechanical properties. Furthermore, upon confirming its electronic metallic properties, we delved into the examination of the compound's response to pressure

Keywords: *DFT, Elastic properties, Electronic properties*

1. Introduction

Intermetallic compounds are typically alloys formed by the combination of different metal elements in specific proportions[1]. These compounds amalgamate the characteristic properties of metal-metal bonds with traditional metallic features. These bonds involve the sharing of an electron sea among metal atoms, resulting in generally high electrical and thermal conductivity.

Moreover, intermetallic compounds often generate intricate crystal structures. These structures are pivotal factors determining the mechanical and thermal properties of materials. Additionally, with attributes such as high temperature resistance, hardness, strength, and chemical resilience, intermetallic compounds find diverse applications, particularly in industries such as aviation, energy production, and automotive[2], [3].

The distinctive properties of these compounds attract researchers and industry professionals in the fields of material engineering and material science. The exploration of intermetallic compounds establishes a crucial foundation for developing novel material designs and enhancements. Furthermore, the properties of these compounds inspire material engineers to create more effective and durable materials in various applications.

Our investigation delved into exploring the impact of pressure on the physical properties of the CuY intermetallic compound. Given the pivotal role that pressure plays, research conducted under these conditions holds significant value in unraveling the deformation behaviors exhibited by compounds. The essential alterations in the physical and chemical properties under pressure are indispensable for gaining insights into the fundamental nature of solids. Conducting studies under pressure is instrumental in providing a deeper understanding of how compounds deform and proves particularly valuable for discerning the modifications in their physical and chemical characteristics.

2. Materials and Methods

The investigation of CuY's physicochemical attributes has been conducted through the implementation of the plane-wave pseudo-potential Density Functional Theory (DFT) method, as documented in references [4], [5] utilizing the VASP software. In order to address the computational requirements, the Generalized Gradient Approximation (GGA) was employed for the exchange-correlation functional. The optimization process for

* Corresponding author. *e-mail address: ilknurdurukan.@gazi.edu.tr*

lattice parameters and atomic positions involved the utilization of a 14x14x14 Monkhorst and Pack grid of k-points for integration within the irreducible Brillouin zone. A kinetic energy cutoff of 600 eV was set for the plane-wave basis set. Elastic properties were determined through the stress-strain method [6].

3. Results and Discussion

3.1. Structural Properties

CuY represents an intermetallic compound characterized by its crystallization in the CsCl structure, specifically adopting the B2 structure, with the space group 221 (pm3m). The CsCl structure itself is composed of two intricately interlocked sub-lattices housing anions and cations. Positioned at the center of a cube within the system, an ion finds itself surrounded by eight ions. Consequently, within the unit cell, Cu and Y atoms find their designated locations at Wyckoff 1a (0,0,0) and 1b (0.5, 0.5, 0.5) respectively, as illustrated in Figure 1. Preceding any calculations, a geometric optimization was meticulously conducted to ascertain the most stable configuration of the CsCl crystal structure. The lattice constant of the compound was determined, compared with previous studies and experimental data, and presented in Table 1.

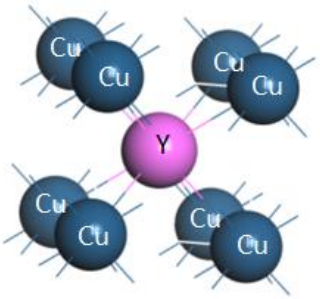

Figure 1. The unitcell of CuY.

Table 1. The calculated lattice constant, previous study, experiment

CuY, a(Å)	Present Study	Previous calculation	Experiment
[7]	3.580	3.511,3.477,3.472	3.477

3.2. Elastic Properties

The elastic constants inherent in crystals play a pivotal role in determining the stability crucial for unraveling the macroscopic mechanical characteristics of materials, making them a paramount parameter in material processing. The application of the strain-stress method facilitates the calculation of elastic constants, denoted as Cij. In the case of the cubic crystal structure of CuY, three essential elastic constants (C_{11}, C_{12}, and C_{44}) define its mechanical behavior. Specifically, C_{11} elucidates elasticity in length, while C_{44} and C_{12} delineate elasticity in shape. The evaluation of mechanical stability in the cubic crystal structure involves the application of Born elastic stability conditions [8]. Examination of Table 2 reveals that the CuY compound, with its specified Cij values, satisfies the criteria for mechanical stability.

The bulk modulus serves as a measure of a material's resistance to volume change. The shear modulus, on the other hand, quantifies a material's resistance to deformation within atomic planes. The Young's modulus, meanwhile, can be employed as an indicator of a material's resistance to elastic strain. Lower values of these moduli signify a softer character in the material. As pressure increases, the hardness of the material intensifies.

Hv is a hardness parameter, and if this value is below 10, it is known that the material is soft. As pressure increases, the hardness of the material also increases. Within the realm of materials science, plasticity refers to the phenomenon wherein a material, typically in a solid state, experiences irreversible alterations in shape when subjected to applied force. The quantification of plasticity can be achieved through the ratio B/C44. The specific plasticity values for the CuY compound have been detailed in Table 2.

Table 2. Elastic constants Cij (GPa), Bulk modulus B (GPa), shear modulus G (GPa), Young Modulus E (GPa), Hardness (GPa), Plasticity measurement B/C44 of CuY compound.

Pressure	C_{11}	C_{12}	C_{44}	B	G	E	Hv	B/C_{44}
0	115.2	46.1	36.6	69.1	35.1	91.3	3.9	1.887
5	131.7	59.9	44.4	83.8	40.7	105.0	4.5	1.887
10	145.8	73.3	51.5	97.4	44.7	116.3	4.9	1.891
15	158.4	86.4	58.0	110.4	47.9	125.5	5.3	1.903
20	169.8	99.3	64.2	122.8	50.4	133.0	5.6	1.912
25	180.3	112.1	70.1	134.8	52.4	139.1	5.8	1.922
30	189.7	124.6	75.4	146.3	53.7	143.5	5.9	1.940
35	198.2	137.1	80.2	157.4	54.4	146.3	6.0	1.962
40	206.1	149.5	84.8	168.3	54.6	147.8	6.0	1.984
45	213.7	162.0	89.1	179.2	54.4	148.2	6.0	2.011
50	220.7	174.3	93.3	189.7	53.7	147.2	5.9	2.033

The ductile or brittle nature of a material can be assessed by employing the Pugh ratio [9]. A material is characterized as ductile or brittle based on whether the Pugh ratio (G/B) is smaller or larger than 0.57, respectively. In the case of the CuY compound, the calculated Pugh ratio falls below 0.57, indicating its ductile nature, a characteristic that remains consistent even under increased pressure.

Poisson's ratio (ν) is a defining factor for the bonding forces within solids. When atomic forces in a material are centrally aligned, the ν value typically falls between 0.25 and 0.50 [10]. The obtained ν value indicates the centralization of interatomic forces in the material.

Another approach involves the use of Cauchy pressure, where the nature of the compound's structure is contingent upon whether C_{12}-C_{44} is positive or negative. A positive Cauchy pressure signifies a metallic character [11]. Given that the C_{12}-C_{44} values obtained are positive, it can be concluded that this compound exhibits metallic characteristics.

The Elastic Anisotropy Parameter A holds significant importance in engineering sciences. A solid is considered entirely isotropic when A equals 1. As pressure increases, anisotropy values persist in their anisotropic behavior.

The Debye temperature (Θ_D) holds significant relevance in elucidating various physical properties of solids, such as specific heat and melting temperature [12]. At low temperatures, vibrational excitations primarily consist of acoustic vibrations. The estimation of the Debye temperature involves the utilization of the average sound velocity (vm), derived from elastic constant data. The calculated sound velocities and Debye temperatures are also provided in Table 3. Notably, for materials categorized as hard, the Debye temperature tends to be higher, while for softer materials, it is lower. As observed in Table 3, the low Debye temperature values of CuY indicate its classification as a soft material.

Table 3. G /B ratio, C_{11}-C_{44} Cauchy pressure (GPa), Poisson's ratio (υ) and Zener Anisotropy factor (A), debye temperature (K) and sound velocities(m/s) of CuY compound

Pressure	G/B	C_{12}-C_{44}	v	A	Θ_D	V_l	V_t	V_m
0	0.516	9.5	0.279	1.059	293.2	4429	2449	2729
5	0.485	15.5	0.290	1.237	310.1	4666	2533	2826
10	0.458	21.8	0.300	1.421	322.7	4851	2588	2891
15	0.433	28.4	0.310	1.611	332.2	5003	2623	2934
20	0.410	35.1	0.319	1.821	338.9	5128	2641	2957
25	0.388	42.0	0.327	2.056	344.1	5236	2649	2970
30	0.367	49.2	0.336	2.316	347.0	5323	2642	2965
35	0.345	56.9	0.345	2.625	348.1	5345	2624	2948
40	0.324	64.7	0.353	2.996	347.7	5456	2596	2920
45	0.303	72.9	0.362	3.447	346.1	5510	2561	2884
50	0.283	81.0	0.370	4.021	343.0	5552	2516	2837

3.3. Electronic Properties

The electronic properties of materials play a pivotal role in influencing electrical conductivity, band structure, chemical bonds, and overall material quality. Fig. 2 presents the energy band structure alongside the total electronic state density, offering insights into the electronic structure and phase stability of CuY. The Fermi level is consistently set at 0 eV. The absence of a band gap near the Fermi level indicates a metallic structure for CuY, suggesting its inherent metallic properties, a characteristic that remains evident even under elevated pressure conditions.

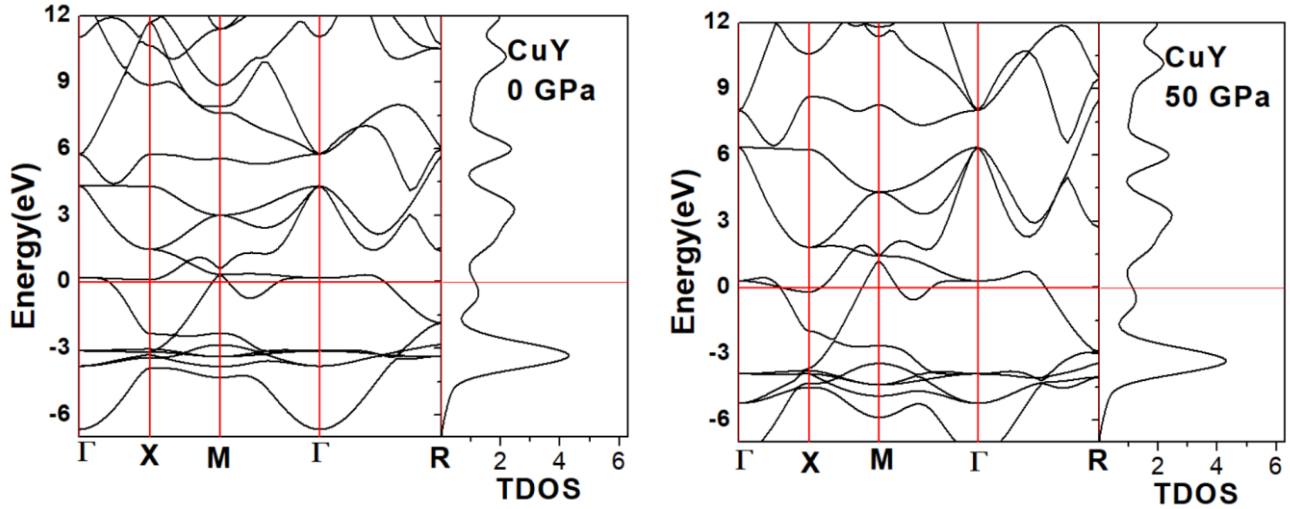

Figure 2. Electronic band structure and total density of CuY at 0, 50 GPa.

The changes in the partial DOS graphs of the CuY compound with the effect of pressure are shown in Figure 3. We can evaluate our graph as Fermi level, valence band and conduction band. The biggest contribution to the Fermi level at zero comes from the Y-d states. The largest contribution to the valence band comes from Cu-d states, while the largest contribution to the conduction band comes from Y-d states.

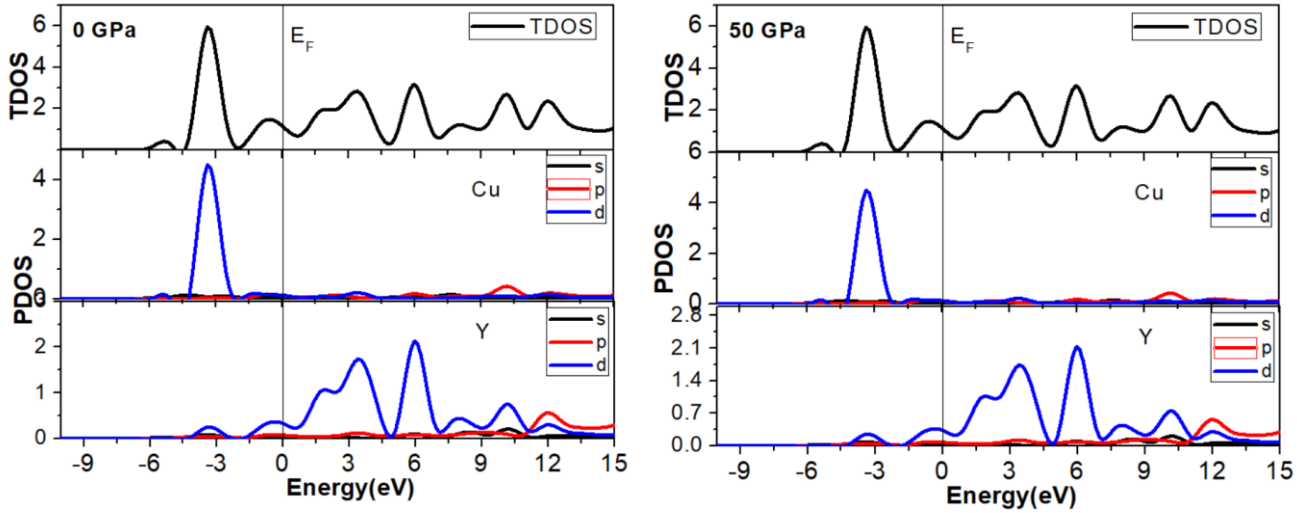

Figure 3. Electronic band structure and total density of CuY at 0, 50 GPa.

4. Conclusion

In our purely theoretical exploration, we delved into the impact of pressure on the mechanical, elastic, and electronic attributes of the CuY compound. Our findings indicate that CuY possesses characteristics of being both ductile and soft. CuY exhibiting metallic properties, also displays compressibility. Notably, the plasticity value for CuY stands at 1.887 under zero pressure. Additionally, the calculated Debye temperature, derived from elastic constants, is determined to be 293 K. Our investigation extended to examining acoustic wave velocities

in various directions, revealing a highly anisotropic elasticity for CuY. The outcomes presented in this study offer detailed insights and serve as a valuable reference for future experimental inquiries.

References

[1] Mouhat, F., & Coudert, F. X. (2014). Necessary and sufficient elastic stability conditions in various crystal systems, *Physical Review B - Condensed Matter and Materials Physics*, *90*, 4–7.

[2] Fatima, B., & Sanyal, S. P. (2018). Ab initio study of electronic structure, elasticity, bonding features and mechanical behaviour of zinc intermetallics, *Computational Condensed Matter*, *14*, 144–152.

[3] Liu, L., Chen, C., Chen, L., & Wen, Y. (2021). The elastic and thermodynamic properties of TbAl and DyAl under high pressure, *High Temperatures - High Pressures*. *50*, 133–147.

[4] Kresse, G., & Hafner, J. (1993). Ab initio molecular dynamics for liquid metals, *Physical Review B*, *47*, 558–561.

[5] Mehmood, N., Ahmad, R., & Murtaza, G. (2017). Ab Initio Investigations of Structural, Elastic, Mechanical, Electronic, Magnetic, and Optical Properties of Half-Heusler Compounds RhCrZ (Z = Si, Ge), *Journal of Superconductivity and Novel Magnetism*, *30*, 2481–2488,

[6] Ciftci, Y. O., and Evecen, M. (2018). First principle study of structural, electronic, mechanical, dynamic and optical properties of half-Heusler compound LiScSi under pressure, *Phase Transitions*, *91*, 1206–1222.

[7] Liu, L., Chen, C., Xu, G., Jiang, Y., Wen, Y., & Zeng, X. (2021). Elastic constants and thermodynamic properties of AgY and CuY compounds under pressure and temperature effects, *High Temperatures - High Pressures*, *50*, 185–195.

[8] Benmakhlouf, A., Benmakhlouf, A., Allaoui, O., & Daoud, S. (2018). Theoretical study of elastic and thermodynamic properties of CuSc intermetallic compound under high pressure, *Chinese Journal of Physics*, *57*, 179–188..

[9] Joubert, D. (1999). From ultrasoft pseudopotentials to the projector augmented-wave method, *Physical Review B - Condensed Matter and Materials Physics*, *59*, 1758–1775.

[10] Zeng, X., Peng, R., Yu, Y., Hu, Z., Wen, Y., & Song, L. (2018). Pressure effect on elastic constants and related properties of Ti3Al intermetallic compound: A first-principles study, *Materials*, *11*,114-116.

[11] Ganeshan, S., Shang, S. L., Zhang, H., Wang, Y., Mantina, M., & Liu, Z. K. (2009). Elastic constants of binary Mg compounds from first-principles calculations, *Intermetallics*, *17*, 313–318.

[12] Blanco, M. A., Francisco, E., & Luaña, V. (2004). GIBBS: Isothermal-isobaric thermodynamics of solids from energy curves using a quasi-harmonic Debye model, *Computer Physics Communications*, *158*, 57–72.

The effects of increased salinity on organisms in freshwater ecosystems: a case study of freshwater mussels

***Göktuğ GÜL*[1,*], *Pınar ARSLAN*[2], *Aysel Çağlan GÜNAL*[3]**

[1] *Medical Laboratory Programme, Health Services Vocational School, Gazi University, Ankara, Türkiye*

[2] *Department of Biology, Faculty of Science, Çankırı Karatekin University, Çankırı, Türkiye*

[3] *Department of Biology Education, Faculty of Education, Gazi University, Ankara, Türkiye*

Abstract

The melting of terrestrial glaciers, the expansion of the sea levels, and droughts due to global warming cause the increase of salinity levels in the freshwater. Notably, research on salinity in marine ecosystems is significantly higher than research in freshwater ecosystems. Freshwater mussels are an essential group of organisms that improve water quality by filtering the water body in which they are located. In addition, they are symbiotically related to other organisms in the feeding and reproduction cycle. These characteristics make freshwater mussels good model organisms. In this study, the effects of salinity increasing on total hemocyte levels (THCs) and lipid peroxidation by-product malondialdehyde (MDA) were investigated on freshwater mussels (*Unio delicatus*). After obtaining the freshwater mussels from local fishermen in Bursa (Türkiye), they were adapted to laboratory conditions for two weeks. Five freshwater mussels were placed in each aquarium and directly transferred to 12 ‰ salinity at a constant water temperature of 24 ºC for 1 hour and 24 hours in the experiment. There was also a positive control group. At the end of the exposure times, mussels were placed under ice anesthesia, and the hemolymph liquid, gill, and digestive gland tissues were taken. The THCs were investigated with the hemolymph liquid, and the levels of MDAs were calculated in gills and digestive tissues. The amount of THCs increased significantly at the end of 1 hour of salinity exposure but returned to the level of control group values at the end of 24 hours. According to the MDA results, levels in digestive and gill tissues did not change significantly within 1 hour after exposure but showed a tendency to increase during the rest of the exposure. It has been understood that mussels develop a rapid physiological and cellular response to salinity. The effects of salinity on freshwater mussels should be monitored using other parameters.

Keywords: *Salinity, Freshwater Mussel, Total Hemocyte Counts, MDA*

1. Introduction

The global warming initiated by the increased consumption of fossil fuels during the Industrial Revolution is currently perceived as one of the most critical environmental issues, posing a significant risk of ecological degradation. Global warming has given rise to climate change, with the world's average temperature increasing by 1°C during summer seasons and 2°C during winter seasons in each successive decade from the 1960s to the present. This escalation has led to the melting of glaciers, a rise in sea levels, and an expansion of marine areas, potentially resulting in the submersion of certain terrestrial regions beneath seawater. Additionally, it is anticipated that the mixing of freshwater resources with seawater may occur as a consequence of these temperature fluctuations. The intrusion of seawater or alluvium into river systems can be facilitated by various natural and anthropogenic mechanisms. In addition to seawater contamination, increases in salinity levels in freshwater sources can occur due to various factors such as salting activities on asphalt roads during winter seasons, mining operations, industrial wastewater discharge, and the mixing of groundwater with contaminated and alluvial soils. The augmentation of salinity in freshwater sources can adversely impact agriculture, livestock farming, and aquaculture [1-4].

Countries with coastlines along the Mediterranean are known to be more significantly affected by climate change. Climate change influences the flow rates of rivers, known as the world's vascular by differentiating precipitation patterns and average temperatures. Aquatic ecosystems, which host a myriad of organisms, undergo continuous changes due to natural and human-induced impacts. In recent years, an increase in salinity has been added to these ecosystem differentiations. Changes in river flow observed in rivers lead to an increase in sediment load in the waters. [2-5]. The rise in sediment load and coastal erosion in freshwater systems, resulting from seawater intrusion due to increased mixing of seawaters with inland water systems, lead to significant increases in the mineral loads of freshwater sources. The increase in mineral quantities in the waters is expressed as salinity [6].

* Corresponding author. *e-mail address: goktuggul@gazi.edu.tr*

Mussels are preferred organisms in ecological research due to their ability to inhabit various habitats. Mussels are considered model organisms in aquatic studies due to their filter-feeding behavior and symbiotic relationships with other organisms [7]. Numerous studies in the literature have investigated the population status of mussels at various salinity levels in ecosystems. However, the longevity of mussels is thought to contribute to a gradual decrease in population density. The Unionidae family, with 620 species, is the most extensive among freshwater mussels. *Unio delicatus*, belonging to this family, exhibits a wide distribution in Turkish inland water systems [7-8]. Because of this reason, this Unionid species was selected for research.

Salinity, in addition to causing reproductive and feeding disorders in freshwater mussels, can lead to variations in shell formations. Furthermore, it is known that mussels, especially non-adult and larval individuals, are sensitive to salinity. Parasitic mussel larvae in the glochidia stage lose their affinities to attach to fish gills at high salinity levels. This situation could cause significant damage to the reproduction and distribution of freshwater mussels. It is anticipated that decreases in the population numbers of freshwater mussels could lead to serious ecosystem damage [9-11].

According to the Working Group on Biological Effects of Contaminants (WGBEC), there are four different methods for investigating the responses of mussels to various pollutant groups among aquatic organisms. These include detecting tissue residue levels, identifying cellular oxidative and antioxidant responses, and detecting tissue and growth [12]. The total hemocyte count is considered an important parameter in evaluating the health status of aquatic invertebrates [13]. Malondialdehyde levels are preferred in toxicology studies to indicate cellular membrane damage in oxidative stress and antioxidant mechanisms [14].

This study examines the physiological and antioxidant mechanism responses induced by acute increases in salinity in freshwater mussels (*U. delicatus*). Changes in the total hemocyte counts (THCs) from hemolymph and lipid peroxidation byproduct malondialdehyde (MDA) levels from gill and digestive tissues were investigated in freshwater mussels.

2. Materials and Methods

2.1. Test Materials and Organisms

Freshwater mussels (n=40) were procured from local fishermen in Bursa Province and brought live to the Biology Laboratories of Gazi University Gazi Faculty of Education in aerated tanks. Mussels were selected as medium and large-sized specimens with an average weight of 34.96±6.91 g. Water from the city network was allowed to rest in aerated aquariums for one week to ensure the removal of chlorine from the water. Mussels were placed in aquariums containing 50 L of rested water and subjected to a two-week acclimation process; during the process, they were fed with commercial spirulina once a day.

For the experiment, 4 aquariums containing 10 L of rested water each were used, and sea salt was added to achieve a salinity of ‰12. Aquarium water parameters were measured daily and maintained at a constant level (pH: 7.6±0.1; 24±1.3 ^{o}C; Salinity= ‰12±0.01). Five mussels were introduced into each aquarium. The experiment was conducted with a control group (Salinity=0.01 ppm) for 1 and 24 hours of exposure, with two replicates each.

2.2. Total Haemocyte Counts

Following exposure, mussels were anesthetized under ice, and hemolymph was taken, entering from the adductor muscle using 2.5 mL syringes. From the hemolymph, 1 mL was transferred to Eppendorf tubes and fixed with 4% formaldehyde at a ratio of (1:1). Hemocytes were counted using Thoma slides under a light microscope. The total hemocyte counts (THCs) were determined as cell/mL by analyzing according to the Yavuzcan and Benli method [15].

2.3. Lipid Peroxidation

Under ice anesthesia, gill and digestive tissues were dissected, quickly packaged in aluminum foil, and placed in liquid nitrogen. Lipid peroxidation analyses were conducted according to the method described by Mihara and Uchiyama. Gill and digestive tissues were homogenized in 1.15% KCl buffer in a cold environment, treated with thiobarbituric acid, and read at 535 nm using a spectrophotometer. The results were expressed in nM/mg tissue [16].

2.4. Statical Analysis

Total hemocyte counts (THCs) and malondialdehyde (MDA) results were calculated using Microsoft Excel, and the data were expressed as mean ± standard error. Graphs representing the data were also created using Microsoft Excel.

3. Results and Discussion

In recent years, the increase in salinity in freshwater has begun to raise concerns within the scientific community. Organisms exhibiting filter-feeding characteristics, such as mussels, tend to accumulate aquatic contaminants. Moreover, variations occurring in aquatic habitats lead to disruptions in various cellular, physiological, and antioxidant mechanisms [17-19]. Although there are predictions about the association of salinity impact mechanisms with hardness, information on this topic is very limited [1]. This study investigated responses induced acutely by marine salinity levels in freshwater mussels, focusing on total hemocyte counts (THCs) and the lipid peroxidation byproduct malondialdehyde (MDA) levels. No deaths occurred in the control and experimental groups during acute exposure.

3.1. Total Haemocyte Counts

Total hemocyte counts (THCs) were conducted on hemolymph tissues obtained from mussels at the end of the experiment. The results are presented in Figure 1. Following a 1-hour exposure in the experiment, THCs increased approximately 6-times compared to the control groups. After a 24-hour exposure, despite a subsequent decrease, THCs were found to be 1.5 times higher than the levels in the control group ($p<0.05$).

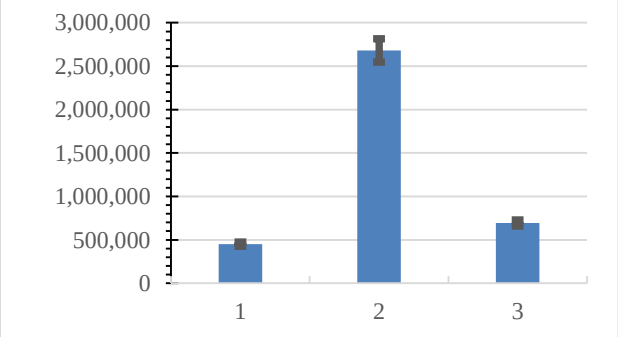

Figure 1. Total Haemocyte Counts (THCs) (Mean±SEM) of freshwater mussels

The responses exhibited by mussels to environmental influences occur both at the cellular and extracellular levels. Any alteration in ecosystems will trigger mussels' immune systems and homeostatic mechanisms, resulting in abrupt fluctuations in the hemocyte counts within their circulatory systems. Therefore, total hemocyte counts (THCs) are a crucial parameter employed in immunological studies [20]. Responses developed against environmental stress factors have been examined in various studies. In the case of *Mytilus galloprovincialis* collected from an area where environmental conditions were disrupted, differences in THCs between stations have been reported [21]. Several studies have reported fluctuations, both increases and decreases, in THC counts in response to various environmental influences [22-24].

In a study investigating the combined effects of salinity and various contaminating pollutants, it was reported that salinity variations did not have a direct impact on THCs. Still, other humoral factors were directly influenced by salinity [25]. A study exploring the effect of water quality on THCs in ship oysters (*Barbatia decussate*) in the Iranian Basra Gulf indicated a relationship between salinity increase and THC [27]. A study examining the effects of hypoxic elevations in the diel cycle on the Hong Kong oyster (*Crassostrea hongkongensis*) reported an inverse relationship between salinity increases and THC levels [28]. Within the scope of this study, the 1-hour exposure appears to trigger the immune system, causing an acute increase in THC levels, followed by the intervention of homeostatic mechanisms to restore hemocyte counts to their original levels.

3.2. Lipid Peroxidation Byproduct Malondialdehyde Level

MDA levels were determined in gill and digestive system tissues at control, 1, and 24-hour intervals. While MDA levels showed no significant difference between control and 1-hour salinity exposures, they exhibited an

approximately 2-times increase in gill tissue and an approximately 3-times increase in digestive canal tissue after 24 hours (Figure 2).

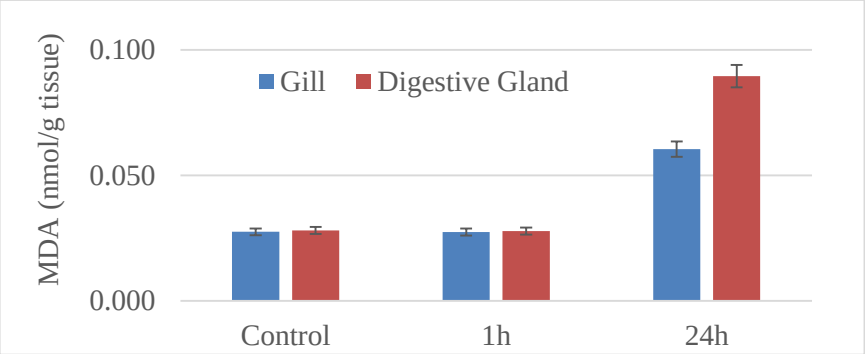

Figure 2. Changing of MDA levels in gill and digestive gland tissues in freshwater mussels

Organisms exposed to environmental stressors rapidly activate their immune systems, and the antioxidant defense system impedes cellular activities [29]. In ecotoxicology studies, lipid peroxidation is the most commonly utilized antioxidant mechanism [30]. When reviewing the literature, it has been established that malondialdehyde (MDA), a byproduct of lipid peroxidation, is used as a robust biomarker [31-32]. In this study, a significant difference was observed in both gill and digestive canal tissues of freshwater mussels exposed to 24 hours of salinity stress, particularly in comparison to the control and 1-hour groups. In *Unio ravoisieri* freshwater mussels exposed to different salinity levels for one week, it was reported that gill MDA levels increased from 0.55 to 5.35 µmol/mg, and digestive canal tissue levels increased from 1.7 to 3.6 µmol/mg [33].

A study involving Mediterranean mussels (*M. galloprovincialis*) found higher MDA levels at low salinity levels (‰14) due to cellular damage. Lower MDA levels were detected at high salinity levels (‰28-35) [34]. Another study on oysters (*Crassostrea gigas*) exposed them to salinity levels of 9-15-25-35 ppt for 10 and 17 days. In the 10-day exposure, MDA levels in oysters were similar at 9 and 35 ppt but significantly higher at 15 and 25 ppt. Additionally, in the 17-day exposure, MDA values were relatively close across all salinity levels [35].

4. Conclusion

This study demonstrated the sensitivity of *U. delicatus* to salinity. The results indicated that U. delicatus significantly affected the activities of THCs and MDA. THCs showed a significant increase in the 1-hour exposure, also referred to as the shock effect. It is believed that after 24 hours, homeostasis comes into play, balancing the immune system. While no significant change was observed in the MDA values related to cellular damage in gill and digestive tissues during the initial 1-hour exposure, MDA levels showed 2-3 times increase after 24 hours. It is speculated that the rapid increase in salinity levels to ‰12 could lead to cellular damage. This study highlights the need to investigate further the interaction between physiological biomarkers of organisms living in freshwater environments and salinity.

References

[1] Wang, N., Ivey, C.D., Dorman, R.A., Ingersoll, C.G., Steevens, J., Hammer, E. J., Bauer, C.R. & Mount, D.R. (2018). Acute toxicity of sodium chloride and potassium chloride to a unionid mussel (*Lampsilis siliquoidea*) in water exposures. *Environmental toxicology and chemistry*, *37*(12), 3041-3049.

[2] Karataş, E.C. *Economic policy of the effect of global warming on available water resources: The case of Turkey-Germany*. PhD. Thesis, Istanbul University, Institute of Social Sciences, Department of European Union, 2022, 370p., Istanbul.

[3] Sağlam, N.E., Düzgüneş, E., & Balık, İ. (2008). Küresel Isınma ve İklim Değişikliği. *Ege Journal of Fisheries and Aquatic Sciences*, *25*(1), 89-94.

[4] Uzan, H.K. (2023). Sürdürülebilir Kalkınma Çerçevesinde İklim Değişikliğinin Kırsal Kalkınmaya Etkisi. *Fiscaoeconomia*, *7*(3), 2250-2272.

[5] Benson, J.A., Close, P.G., Stewart, B.A., & Lymbery, A.J. (2019). Freshwater tributaries provide refuge and recolonization opportunities for mussels following salinity reversal. *Science of the Total Environment*, *683*, 231-239.

[6] Beatty, S.J., Morgan, D.L., Rashnavadi, M., Lymbery, A.J., 2011. Salinity tolerances of endemic freshwater fishes of south-western Australia: implications for conservation in a biodiversity hotspot. Marine Freshw. Res. 62, 91–100.
[7] Arslan, P., & Günal, A.Ç. (2023). Does Fipronil Affect on Aquatic Organisms? Physiological, Biochemical, and Histopathological Alterations of Non-Target Freshwater Mussel Species. *Water*, *15*(2), 334.
[8] Ferreira-Rodríguez, N., Akiyama, Y.B., Aksenova, O.V., Araujo, R., Barnhart, M.C., Bespalaya, Y.V., Bogan A.E., Bolotov, I.N., Budha, P.B., Clavijo, C., Clearwater, S.J., Darrigran, G., Do, V.T., Douda, K., Froufe, E., Gumpinger, C., Henrikson, L., Humprey, C.L., Johnson, N.A., Klishko, O., & Vaughn, C.C. (2019). Research priorities for freshwater mussel conservation assessment. *Biological Conservation*, *231*, 77-87.
[9] Akkuş, M., Sarı, M., & Arabacı, M. (2019). Sarımehmet Barajı'nda (VAN) İlk Zebra Midye Kaydı ve Zebra Midye Popülasyonunun Bölge Balıkçılığına Olası Etkileri. *Commagene Journal of Biology*, *3*(2), 97-102.
[10] Todd, A. K., & Kaltenecker, M. G. (2012). Warm season chloride concentrations in stream habitats of freshwater mussel species at risk. *Environmental pollution*, *171*, 199-206.
[11] Beggel, S., & Geist, J. (2015). Acute effects of salinity exposure on glochidia viability and host infection of the freshwater mussel Anodonta anatina (Linnaeus, 1758). *Science of the Total Environment*, *502*, 659-665.
[12] Yancheva, V., Velcheva, I., Georgieva, E., Stoyanova, S., Todorova, B., Antal, L., & Nyeste, K. J. (2023). Are Mytilus species suitable bioindicators for assessing aquatic pollution along the Black Sea Coast? A review. *Ecologia Balkanica*, *15*(1), 49-76.
[13] Günal, A.Ç., Tunca, S.K., Arslan, P., Gül, G., Dinçel, A.S. (2021). How does sublethal permethrin effect non-target aquatic organisms? *Environmental Science and Pollution Research. 28*(37):52405–52417.
[14] Köprücü. K., Yonar, S.M., Şeker, E. (2010). Effects of cypermethrin on antioxidant status, oxidative stress biomarkers, behavior, and mortality in the freshwater mussel *Unio elongatulus eucirrus. Fisheries Science. 76*(6):1007–1013
[15] Yavuzcan, H.Y., & Benli, A.Ç.K. (2004). Nitrite toxicity to crayfish, Astacus leptodactylus, the effects of sublethal nitrite exposure on hemolymph nitrite, total hemocyte counts, and hemolymph glucose. *Ecotoxicology and Environmental Safety. 59*, 370–375.
[16] Mihara, M., & Uchiyama, M. (1978). Determination of malonaldehyde precursor in tissues by thiobarbituric acid test. *Analytical Biochemistry 86*(1):271–278.
[17] Afsa, S., De Marco, G., Giannetto, A., Parrino, V., Cappello, T., ben Mansour, H., & Maisano, M. (2022). Histological endpoints and oxidative stress transcriptional responses in the Mediterranean mussel *Mytilus galloprovincialis* exposed to realistic doses of salicylic acid. *Environmental Toxicology and Pharmacology*, *92*, 103855.
[18] Khudhur, S. M., Shekha, Y. A., & Ahmed Shekha, Y. (2019). Histopathological and biochemical biomarker response of mussel, *Unio pictorum*, to carbamate pesticide carbaryl: A laboratory study. *Indian Journal of Animal Researches*, *1157*, 1-5.
[19] Arslan, P. (2022). How Does Cyphenothrin Affect the Freshwater Mussel as In Vitro and In Vivo Models?. *Water, Air, & Soil Pollution*, *233*(9), 386.
[20] Qyli, M., Aliko, V., & Faggio, C. (2020). Physiological and biochemical responses of Mediterranean green crab, *Carcinus aestuarii*, to different environmental stressors: Evaluation of hemocyte toxicity and its possible effects on immune response. *Comparative Biochemistry and Physiology Part C: Toxicology & Pharmacology*, *231*, 108739.
[21] Ayhan, M. M., Katalay, S., & Günal, A. Ç. (2021). How pollution effects the immune systems of invertebrate organisms (*Mytilus galloprovincialis* Lamark, 1819). *Marine Pollution Bulletin*, *172*, 112750.
[22] Suresh, K., & Mohandas, A. (1990). Effect of sublethal concentrations of copper on hemocyte number in bivalves. *Journal of Invertebrate Pathology*, *55*(3), 325-331.
[23] Hossain, M. A., Sarker, T. R., Sutradhar, L., Hussain, M., & Iqbal, M. M. (2023). Toxic effects of chlorpyrifos on the growth, hemocytes counts, and vital organ's histopathology of freshwater mussel, *Lamellidens marginalis*. *Journal of King Saud University-Science*, *35*(2), 102482.
[24] Arslan, P., Gül, G., & Günal, A.Ç. (2023). How do biocidals affect the non-target marine organisms: the short-term effects of antifouling agent sodium pyrithione on Mediterranean mussels (*Mytilus galloprovincialis*, Lamark 1819). *Environmental Science and Pollution Research*, 1-9.
[25] Perrigault, M., Dahl, S. F., Espinosa, E. P., & Allam, B. (2012). Effects of salinity on hard clam (*Mercenaria mercenaria*) defense parameters and QPX disease dynamics. *Journal of invertebrate pathology*, *110*(1), 73-82.

[26] Höher, N., Köhler, A., Strand, J., & Broeg, K. (2012). Effects of various pollutant mixtures on immune responses of the blue mussel (*Mytilus edulis*) collected at a salinity gradient in Danish coastal waters. *Marine environmental research*, *75*, 35-44.
[27] Khoei, A.J. (2022). Seasonal heavy metal accumulations in the bivalve *Barbatia decussate* and their relationships with water quality and the metal-induced biochemical biomarkers. *Environmental Science and Pollution Research*, 1-10.
[28] Xie, Z., Wei, S., Dong, H., Chen, H., Zhang, Q., Liu, W., Peng, J., Sokolova, I.M., Hu, M., & Wang, Y. (2021). Hemocyte responses of the oyster *Crassostrea hongkongensis* exposed to diel-cycling hypoxia and salinity change. *Frontiers in Marine Science*, *8*, 749623.
[29] Boaventura, T.P., Souza, C.F., Ferreira, A.L., Favero, G.C., Baldissera, M.D., Heinzmann, B.M., & Luz, R.K. (2021). The use of *Ocimum gratissimum* L. essential oil during the transport of Lophiosilurus alexandri: Water quality, hematology, blood biochemistry and oxidative stress. *Aquaculture*, *531*, 735964.
[30] Cordeiro, L., Müller, L., Manske Nunes, S., Kist, L. W., Bogo, M. R., Ruas, C. P., & Ventura-Lima, J. (2021). Co-exposure to nTiO2 impairs arsenic metabolism and affects antioxidant capacity in the marine shrimp *Litopenaeus vannamei*. *Drug and Chemical Toxicology*, *44*(1), 30-38.
[31] Fuat Gulhan, M., Duran, A., Selamoglu Talas, Z., Kakoolaki, S., & Mansouri, S. M. (2012). Effects of propolis on microbiologic and biochemical parameters of rainbow trout (*Oncorhynchus mykiss*) after exposure to the pesticide. *Iranian Journal of Fisheries Sciences*, *11*(3), 490-503.
[32] Serdar, O. (2019). The effect of dimethoate pesticide on some biochemical biomarkers in *Gammarus pulex*. *Environmental Science and Pollution Research*, *26*(21), 21905-21914.
[33] Lassoued, A., Khalloufi, N., Saidani, W., Khazri, A., Ghanem-Boughanmi, N., Bouayed, J., & Ben-Attia, M. (2023). Effects of increased salinity on oxidative stress status in the freshwater mussel *Unio ravoisieri*. *Chemistry and Ecology*, *39*(3), 256-267.
[34] Freitas, R., De Marchi, L., Bastos, M., Moreira, A., Velez, C., Chiesa, S., & Soares, A.M. (2017). Effects of seawater acidification and salinity alterations on metabolic, osmoregulation and oxidative stress markers in *Mytilus galloprovincialis*. *Ecological Indicators*, *79*, 54-62.
[35] Zanette, J., de Almeida, E. A., da Silva, A. Z., Guzenski, J., Ferreira, J. F., Di Mascio, P., & Bainy, A. C. D. (2011). Salinity influences glutathione S-transferase activity and lipid peroxidation responses in the Crassostrea gigas oyster exposed to diesel oil. *Science of the total environment*, *409*(10), 1976-1983.

Investigation of Methylene Blue Adsorption from Aqueous Solutions by Dried Leaves

Tiba SALEH GHANI AL-OKAIDAT [1], ***Volkan EYUPOGLU*** [2] ***M. Bora AKIN*** [1*]

[1] *Department of Chemical Engineering, Çankırı Karatekin University, Çankırı, Turkiye*

[2] *Department of Chemistry, Çankırı Karatekin University, Çankırı, Turkiye*

Abstract

With the arrival of autumn each year, the leaves of trees dry up and consequently fall off. The fallen leaves are beneficial for preserving declining wildlife populations. They cover the tree/shrub and plant root systems, maintain soil moisture, prevent weeds, and suppress other plants. They gradually decompose, returning essential nutrients to the plants. However, in landscaped gardens created through landscaping, especially in October, fallen leaves are collected. If not collected, they can cause discoloration in the lawn area and promote fungal growth. These leaves are considered waste and are sometimes disposed of by burning or sent to landfills. In recent years, research has been conducted on the utilization of fallen leaves from various trees. Some of these studies explore various applications such as using leaves as a feed supplement [1] and in paper manufacturing [2]. In this study, the adsorption of methylene blue dye from aqueous solutions by dried *Acer platanoides* leaves was investigated. The parameters studied in the study include temperature, adsorbent dose, and concentration, and the removal of methylene blue over time has also been investigated at a dye concentration of 200 mg/L. In experiments conducted at 25°C, the q_e value of dried *Acer platanoides* leaves used at 0.5 g/L was found to be 0.3395 mol/kg.

Keywords: *Adsorption, Wastewater, Methylene Blue, Acer platanoides leaves, Adsorbent*

1. Introduction

In many industries such as dyes, textile, paper, plastic, leather and food, wastewater generated during processes is an important environmental problem. The resulting wastewater contains toxic and carcinogenic substances. These substances pose serious risks to human health and the environment [3]. Adsorption can be defined as the adhesion of liquid or gaseous substances to the surface of a solid substance. Adsorption is used to clean wastewater by retaining pollutants on adsorbents. Various adsorbents are used for the adsorption of dyestuffs in wastewater [4,5]. These adsorbents can be listed as activated carbon, clay minerals, biomasses, industrial by-products and synthetic polymers. In the selection of the adsorbent, its advantages and limitations are taken into account. Activated carbon is widely used due to its high surface area and adsorption capacity. Obtaining it from different sources is also a reason for preference [4]. The reasons why "clays" are preferred are their low cost and easy availability. They are effective in the adsorption of dyes, but their general adsorption capacity is low [6]. The fact that the structures of polymers can be planned during their production enables high adsorption capacities to be obtained, but their environmental effects and high costs limit their use [7,8]. Polymers are used effectively in the adsorption of dyestuffs from wastewater [9]. At this point, biomass-based adsorbents are an alternative due to their environmental friendliness and low production costs. Agricultural wastes, seaweed and various microorganisms appear as biomass-based adsorbents. The increase in the number of publications on adsorbents produced from biomass in recent years is evidence of the interest of researchers. There are many studies on the adsorption of different dyestuffs by adsorbents obtained from various biomass sources [4]. A study shows that sumac leaves have an effect on methylene blue adsorption [10]. Thanks to adsorbents produced from biomass, it is also possible to provide economic and environmental benefits by reusing waste materials [11-15].

Various factors are effective in the adsorption of dyes, such as pH, temperature, adsorbent dosage, initial dye concentration, particle size and mixing speed. The efficiency of the adsorption process depends on these factors and therefore laboratory research is carried out to determine these optimum conditions [16]. Various adsorption isotherm models (such as Langmuir and Freundlich) and kinetic models are used critically in understanding this process [4]. In recent years, some new approaches to the adsorption of dyes have been developed. These appear

* Corresponding author. *e-mail address: mbakin@karatekin.edu.tr*

as magnetic adsorbents, nanomaterials and hybrid systems. Various surface modifications and reuse of adsorbents are being studied to increase adsorbent efficiency [17].

Adsorption of dyestuffs in aqueous media plays a vital role in wastewater treatment and contributes greatly to environmental sustainability. Research in this field makes significant contributions to a cleaner and healthier environment. In this study, dried leaves of the Acer platanoides plant, obtained from Çankırı Karatekin University campus, were used for the adsorption of methylene blue in the aqueous environment. During the study, temperature, adsorbent dosage and initial dye concentration were examined as parameters. Additionally, adsorption behaviors against time using 0.5 mg/L adsorbent and 200 mg/L dyestuff concentration are given in the study.

2. Materials and Methods

Methylene blue was obtained from Sigma Aldrich. Leaves of Acer platanoides were collected from trees on the Uluyazı Campus of Çankırı Karatekin University. Leaves that fell in October were gathered (Figure 1), and after removing their stems, they were crushed to reduce their size. A magnetic stirrer (IKA) and a UV spectrophotometer (Shimadzu) were used in the dye adsorption experiments.

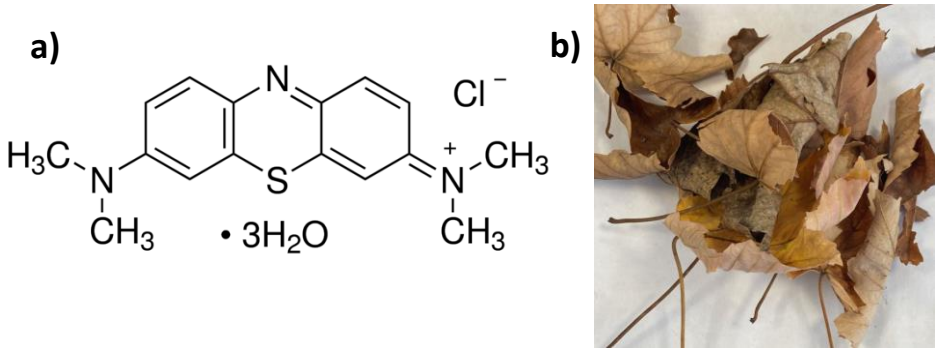

Figure 1. The chemical structure of methylene blue (a), and the leaves of *Acer platanoides* (b)

A stock solution of methylene blue was prepared at 1 g/L in 1000 mL. This stock solution was diluted to different concentrations to create a calibration graph for use in measurements. The wavelength λ in the UV spectrophotometer was selected as 665 nm for methylene blue. In the experiments conducted to determine adsorption capacity, the initial concentrations of methylene blue were chosen as 10 mg/L, 25 mg/L, 50 mg/L, 100 mg/L, 200 mg/L, 300 mg/L, 400 mg/L, 500 mg/L, 750 mg/L, and 1000 mg/L, respectively. Experiments at 25 °C were conducted with leaves used as the adsorbent (0.5 mg/L) in prepared 100 mL solutions. In time-dependent experiments, a concentration of 200 mg/L methylene blue was used, and samples were taken at 0 min, 2 min, 5 min, 10 min, 20 min, 30 min, 45 min, 60 min, 90 min, 180 min, 240 min, 300 min, 360 min, 420 min, and 1440 min during the removal process. The taken samples were measured with a UV spectrophotometer. Experiments investigating the effect of temperature on the adsorbent used temperatures of 5 °C, 25 °C, and 40 °C. In experiments examining the adsorbent dose, leaf amounts of 0.3 mg/L, 0.5 mg/L, 1 mg/L, and 2.5 mg/L were selected. Table 1 summarizes the parameters used in the experiments and the selected values for the parameters.

Table 1. Parameters and their levels used in the experiments.

Parameters	Temp. (°C)	Adsorbent Dose (mg/L)	Conc. of methylene blue (mg/L)	Time (min)
Levels	5, 25, 40	0.3 0.5, 1, 2.5	10, 25, 50, 100, 200, 300, 400, 500, 750,1000	0, 2, 5, 10, 20, 30, 45, 60, 90, 180, 240, 300, 360, 420,1440

3. Results and Discussion

3.1. Effect of Initial Dye Concentration

In the conducted study, the adsorption capacities (q_e) were examined using leaves at a concentration of 0.5 mg/L for different concentrations. The q_e values obtained against the concentrations studied are presented in Figure 2. The highest adsorption capacity within the initial concentrations was obtained at 750 mg/L with 0.5848 mol/kg.

A rapid increase in the q_e value is observed up to an initial concentration of 100 mg/L. Since the rate of increase in the q_e value decreases after 200 mg/L, 200 mg/L has been selected as the limit for the initial concentration value, and this concentration has been used in the examination of other parameters.

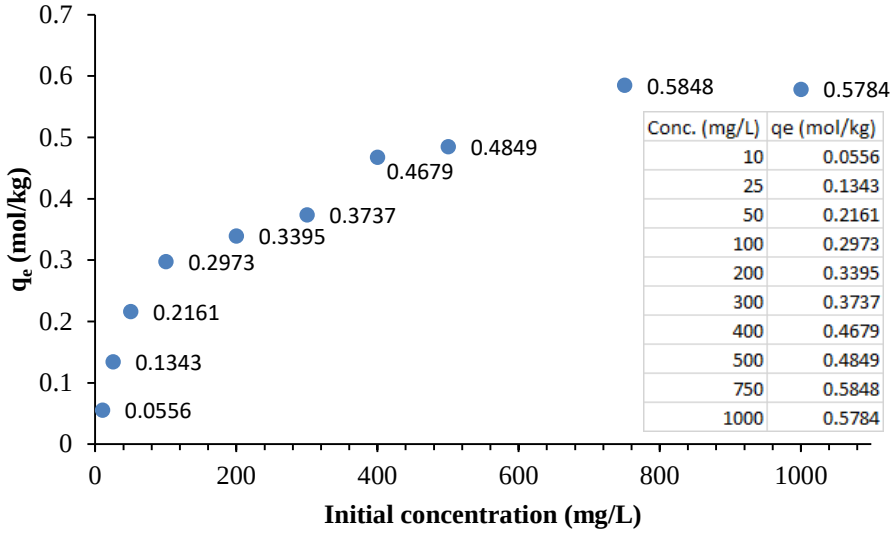

Figure 2. The effect of initial dye concentrations on adsorption capacity.

3.2. Effect of Time

For the experiment examining the effect of time on qe, an initial concentration of 200 mg/L was selected. To determine the q_e value at the selected concentration, samples taken at specific times were measured to find the concentration values. When Figure 3a is examined, it is understood that the concentration decreases over time, indicating that the adsorbent is functioning. After 1440 minutes, the dye concentration drops to 157.97 mg/L. Calculations made using these concentrations show the change in the qe value over time (Figure 3b). After 1440 minutes, at an initial dye concentration of 200 mg/L, the q_e value is 0.3395 mol/kg.

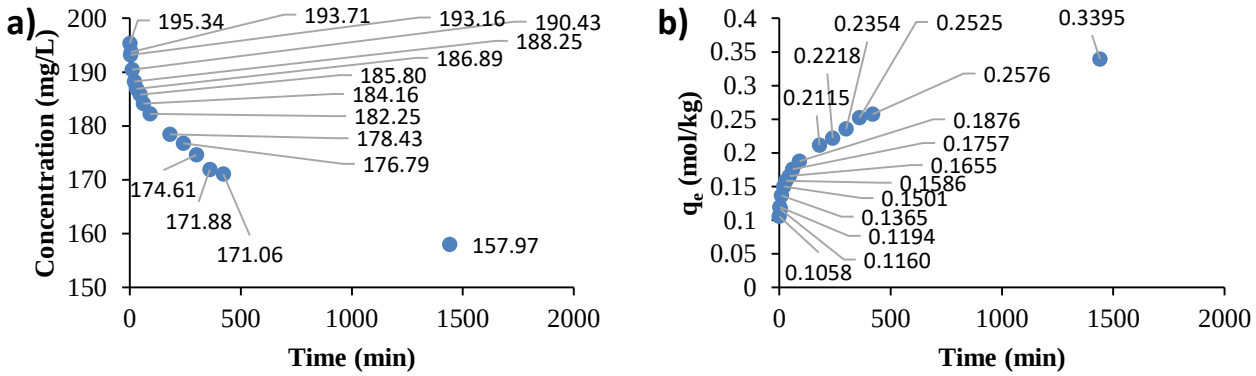

Figure 3. The effect of 0.5 mg/L adsorbent at a 200 mg/L initial dye concentration: a) concentration of dye solution, and b) adsorbent capacity

3.3. Effect of Adsorbent Amount

With the increase in the amount of adsorbent, the q_e value remains unchanged up to 1 mg/L, but decreases beyond this point. While the q_e value is 0.3395 at 1 mg/L of adsorbent, it drops to 0.2262 at 2.5 mg/L of adsorbent (Figure 4a). Additionally, it is observed that the adsorption percentage is 51% with the use of 1 mg/L adsorbent, and it increases to 85% with the use of 2.5 mg/L adsorbent (Figure 4b).

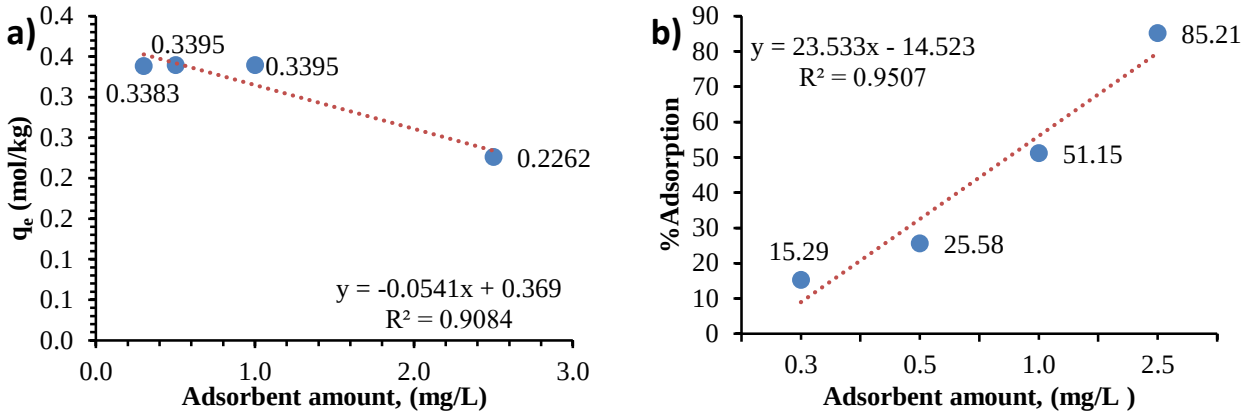

Figure 4. The effect of the amount of adsorbent a) adsorption capacity, and b) adsorption percentage

3.4. Effect of Temperature

Experiments investigating the effect of temperature on the q_e value were conducted at temperatures of 5 °C, 25 °C, and 40 °C. The q_e values were 0.5441 mol/kg at 5 °C, 0.3395 mol/kg at 25 °C, and 0.1201 mol/kg at 40 °C, respectively. According to the obtained data, the q_e value decreases with the increase in temperature (Figure 5).

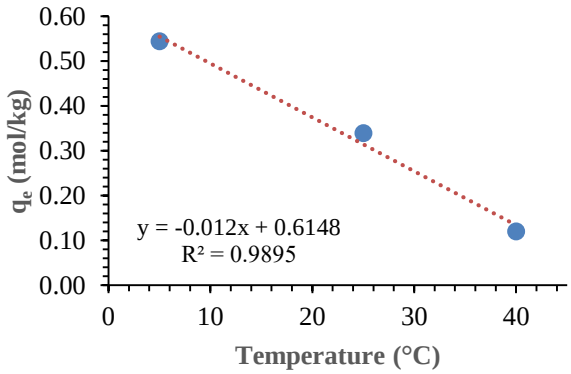

Figure 5. Effect of temperature on adsorbtion capacity

4. Conclusion

The conducted study has revealed that the adsorption of dye from Methylene Blue solutions is possible using *Acer platanoides* leaves. It has been observed that the q_e value increases with the rising initial dye concentration, but the rate of increase slows down after 200 mg/L. A q_e value of 0.3395 mol/kg has been achieved using 0.5 mg/L of leaves at a 200 mg/L starting concentration. With the increase in the amount of leaves used as adsorbent to 2.5 mg/L, the adsorption efficiency increases, reaching 81%, with a q_e value of 0.2262 mol/kg. Additionally, the obtained data indicate that the adsorption capacity decreases with rising temperature. At 40 °C, the q_e value has been determined to be 0.1201 mol/kg.

Acknowledgement

All experimental work was conducted in the Chemical Engineering Department Laboratory at Çankırı Karatekin University. The authors would like to thank the Chemical Engineering Department.

References

[1] Boğa, M., Avcı, B. C., Kılıç, H. N., & CivanerR, A. G. (2022). Bazı Baklagil Ağaç Yapraklarının Alternatif Yem Kaynağı Olarak Besin Madde İçerikleri ve Sindirilebilirliklerinin Belirlenmesi. Kahramanmaraş Sütçü

İmam Üniversitesi Tarım ve Doğa Dergisi, 25(5), 1191–1197. https://doi.org/10.18016/ksutarimdoga.vi.993655.

[2] Sibaly, S., & Jeetah, P. (2017). Production of paper from pineapple leaves. Journal of Environmental Chemical Engineering, 5(6), 5978–5986. https://doi.org/10.1016/j.jece.2017.11.026.

[3] Al-Tohamy, R., Ali, S. S., Li, F., Okasha, K. M., Mahmoud, Y. A. G., Elsamahy, T., Jiao, H., Fu, Y., & Sun, J. (2022). A critical review on the treatment of dye-containing wastewater: Ecotoxicological and health concerns of textile dyes and possible remediation approaches for environmental safety. Ecotoxicology and Environmental Safety, 231, 113160. https://doi.org/10.1016/j.ecoenv.2021.113160.

[4] Aragaw, T. A., & Bogale, F. M. (2021). Biomass-Based Adsorbents for Removal of Dyes From Wastewater: A Review. Frontiers in Environmental Science, 9(December). https://doi.org/10.3389/fenvs.2021.764958.

[5] Wong, S., Ghafar, N. A., Ngadi, N., Razmi, F. A., Inuwa, I. M., Mat, R., & Amin, N. A. S. (2020). Effective removal of anionic textile dyes using adsorbent synthesized from coffee waste. Scientific Reports, 10(1), 1–13. https://doi.org/10.1038/s41598-020-60021-6.

[6] Alshameri, A., Wei, X., Wang, H., Fuguo, Y., Chen, X., He, H., Yan, C., & Xu, F. (2019). A Review of the Role of Natural Clay Minerals as Effective Adsorbents and an Alternative Source of Minerals. In K. S. Essa (Ed.), Minerals. IntechOpen. https://doi.org/10.5772/intechopen.87260.

[7] Zeng, H., Qu, X., Xu, D., & Luo, Y. (2022). Porous Adsorption Materials for Carbon Dioxide Capture in Industrial Flue Gas. Frontiers in Chemistry, 10(June), 1–18. https://doi.org/10.3389/fchem.2022.939701.

[8] Saenz Cavazos, P. A., Hunter-Sellars, E., Iacomi, P., McIntyre, S. R., Danaci, D., & Williams, D. R. 2023. Evaluating solid sorbents for CO2 capture: linking material properties and process efficiency via adsorption performance. Frontiers in Energy Research, 11(July), 1–22. https://doi.org/10.3389/fenrg.2023.1167043.

[9] Dutta, S., Gupta, B., Srivastava, S. K., & Gupta, A. K. (2021). Recent advances on the removal of dyes from wastewater using various adsorbents: A critical review. Materials Advances, 2(14), 4497–4531. https://doi.org/10.1039/d1ma00354b.

[10] Gülen, J., Akın, B., & Özgür, M. (2016). Ultrasonic-assisted adsorption of methylene blue on sumac leaves. Desalination and Water Treatment, 57(20), 9286–9295. https://doi.org/10.1080/19443994.2015.1029002.

[11] Angelova, R., Baldikova, E., Pospiskova, K., Maderova, Z., Safarikova, M., & Safarik, I. (2016). Magnetically modified Sargassum horneri biomass as an adsorbent for organic dye removal. Journal of Cleaner Production, 137, 189–194. https://doi.org/10.1016/j.jclepro.2016.07.068.

[12] Benito-González, I., López-Rubio, A., Gómez-Mascaraque, L. G., & Martínez-Sanz, M. (2020). PLA coating improves the performance of renewable adsorbent pads based on cellulosic aerogels from aquatic waste biomass. Chemical Engineering Journal, 390(February), 124607. https://doi.org/10.1016/j.cej.2020.124607.

[13] Daneshvar, E., Sohrabi, M. S., Kousha, M., Bhatnagar, A., Aliakbarian, B., Converti, A., & Norrström, A. C. (2014). Shrimp shell as an efficient bioadsorbent for Acid Blue 25 dye removal from aqueous solution. Journal of the Taiwan Institute of Chemical Engineers, 45(6), 2926–2934. https://doi.org/10.1016/j.jtice.2014.09.019.

[14] Mullerova, S., Baldikova, E., Prochazkova, J., Pospiskova, K., & Safarik, I. (2019). Magnetically modified macroalgae Cymopolia barbata biomass as an adsorbent for safranin O removal. Materials Chemistry and Physics, 225(September 2018), 174–180. https://doi.org/10.1016/j.matchemphys.2018.12.074.

[15] Son, E. B., Poo, K. M., Mohamed, H. O., Choi, Y. J., Cho, W. C., & Chae, K. J. (2018). A novel approach to developing a reusable marine macro-algae adsorbent with chitosan and ferric oxide for simultaneous efficient heavy metal removal and easy magnetic separation. Bioresource Technology, 259(December 2017), 381–387. https://doi.org/10.1016/j.biortech.2018.03.077.

[16] Rápó, E., & Tonk, S. (2021). Factors affecting synthetic dye adsorption; desorption studies: A review of results from the last five years (2017–2021). Molecules, 26(17). https://doi.org/10.3390/molecules26175419.

[17] Khodakarami, M., & Bagheri, M. (2021). Recent advances in synthesis and application of polymer nanocomposites for water and wastewater treatment. Journal of Cleaner Production, 296, 126404. https://doi.org/10.1016/j.jclepro.2021.126404.

Computational Investigation on the Complexes between Aza-Cryptands and Transition Metals

***Abdurrahman Atalay*[1,*], *Emel Ekinci*[2], *Harun Çiftçi*[3,4]**

[1] *Avrasya University, Department Of Nutrition And Dietetics, Trabzon, Turkey*

[2] *Çankırı Karatekin University, Department of Chemistry, Çankırı, Turkey*

[3] *Kırşehir Ahi Evran University, Department of Medical Biochemistry, Kırşehir, Turkey*

[4] *Çankırı Karatekin University, Institute of Science, Department of Chemistry, Çankırı, Turkey*

Abstract

Cryptands are useful in a variety of fields such as organic chemistry, biochemistry, and material science because of their ability to selectively interact with metal ions. In this study, we have performed a computational study to elucidate the structures and energetics of the complexes formed by transition metals, such as Cr^{2+}, Mn^{2+}, Fe^{2+}, Co^{2+}, Ni^{2+}, Cu^{2+} and Zn^{2+}, with aza-cryptand 3^6adamanzane using DFT method. At their optimized geometries of complexes studied, all complexes possess the S_4 symmetry except the 3^6adz−Cr^{2+} and 3^6adz−Cu^{2+} complex (C_1 symmetry). The computed interaction energies of all 3^6adz−M^{2+} complexes studied were given with and without relativistic energy corrections at the CAM-B3LYP/6-311++G(d,p) level. The 3^6adz−Ni^{2+} complex possesses a highest IE value (−438.6 kcal mol^{-1}) including relativistic energy corrections than the other complexes.

Keywords: *Cryptands, Transition Metal Complexes, DFT, Noncovalent Interactions*

1. Introduction

The three-dimensional counterparts of crown ethers, known as cryptands, were first synthesized in 1987 by Lehn and coworkers [1]. They are helpful in several fields, including organic chemistry, biology, and material science, because of their ability to modify the size of the metal ion cavity and interact with metal ions selectively [2-5]. Furthermore, cryptands have the unique ability to combine with alkali metals to create stable complexes [2-5]. A cryptant and a metal ion interact electrostatically in a host-guest type interaction. A great deal of research has been done on the complexes of cryptands with heavy metals and alkali cations [2-6]. Among these cryptand-metal complexes, especially those with transition metals are quite interesting [2,3,6]. Dehghani and coworkers reported the structures and energetics of complexes formed by Cryptand[2.2.2] and Mn^{2+}, Fe^{2+}, Co^{2+}, Ni^{2+}, Cu^{2+}, and Zn^{2+} cations utilizing DFT methods and and stated that those formed by respective cryptand with Cu^{2+} and Co^{2+} were the most and the least stable systems, respectively [7]. Behjatmanesh–Ardakani et al. reported the binding energies of complexes formed by benzocryptand [222B] with alkali metals, Li^+, Na^+, K^+, and alkaline earth metal Ca^{2+} using DFT methods [8].

A crucial class of chemical molecules is amine-containing cryptands, aza-cryptands [9-11]. These compounds can also form complexes with different transition and main-group metal ions [9-11]. Based on the aforementioned properties of the cryptands, the structure and energetics of the complexes formed by the 3^6adamanzane (3^6adz) aza-cryptand (Figure 1) with transition metal (M) cations (M: Cr^{2+}, Mn^{2+}, Fe^{2+}, Co^{2+}, Ni^{2+}, Cu^{2+}, and Zn^{2+}) were computationally investigated using DFT methods.

2. Materials and Methods

Geometry optimization and harmonic vibrational frequency computations were performed by employing the density functional theory (DFT) and the CAM-B3LYP functional [12,13] for the complexes formed by 3^6adz with M cations such as Cr^{2+}, Mn^{2+}, Fe^{2+}, Co^{2+}, Ni^{2+}, Cu^{2+}, and Zn^{2+}. In this regard, the 6-31+G(d,p) basis set [14,15] was utilized for all complexes. To determine the structures with the lowest energy for 3^6adz−M^{2+}

* Corresponding author. *e-mail address: atalay.abdurrahman@yahoo.com*

complexes, doublet, quartet, and sextet spin states of 3^6adz−Co^{2+}, 3^6adz−Cu^{2+}, and 3^6adz−Mn^{2+} complexes, and singlet, triplet, quintet, and septet spin states of 3^6adz−Cr^{2+}, 3^6adz−Fe^{2+}, 3^6adz−Ni^{2+}, and 3^6adz−Zn^{2+} complexes were optimized at the CAM-B3LYP/6-31+G(d,p) level. All interaction energies for all complexes studied were computed with the counterpoise procedure [16] at the CAM-B3LYP/6-311++G(d,p) level. In addition, the Douglas-Kroll-Hess (DKH) approximation was used to account for scalar relativistic effects on the complexes considered [17,18].

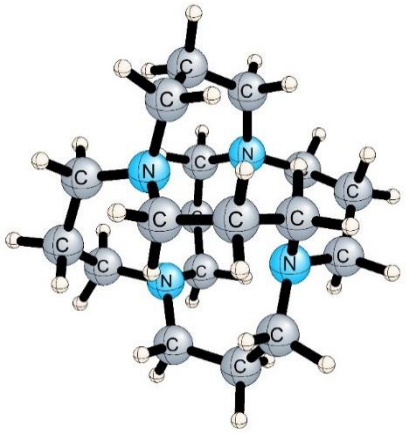

Figure 1. Optimized Structure of 3^6adz Aza-Cryptand at the CAM-B3LYP/6-31+G(d, p) level.

3. Results and Discussion

The optimized geometries of all complexes studied at the CAM-B3LYP/6-31+G(d, p) level is illustrated in Figure 2. The structures with the lowest energy are quintet for 3^6adz−Cr^{2+} and 3^6adz−Fe^{2+}, sextet for 3^6adz−Mn^{2+}, quartet for 3^6adz−Co^{2+}, triplet for 3^6adz−Ni^{2+}, doublet 3^6adz−Cu^{2+}, and singlet state 3^6adz−Zn^{2+} complexes at the CAM-B3LYP/6-31+G(d,p) level. The 3^6adz is an S_4-symmetric structure containing the four lone pairs of the N atom oriented toward the center of the cage. The M^{2+}−N1 and M^{2+}−N2 distances are 2.049−2.059, 2.057−2.057, 2.022−2.022, 1.993−1.993, 1.985−1.985, 1.982−1.992, and 1.994−1.994 Å for the 3^6adz−M^{2+} (M: Cr^{2+}, Mn^{2+}, Fe^{2+}, Co^{2+}, Ni^{2+}, Cu^{2+}, and Zn^{2+}) complexes at their optimized geometries, respectively. This clearly shows that in the 3^6adz−Mn^{2+}, Fe^{2+}, Co^{2+}, Ni^{2+}, and Zn^{2+} complexes studied the metal cations were symmetrically placed to the center of the 3^6adz to which they are attached, while in the 3^6adz−Cr^{2+} and Cu^{2+} complexes metal cations were not symmetrically placed to it. The critical structural parameters for all 3^6adz−M^{2+} complexes are shown in Table 1. As seen in Figure 2, the 3^6adz−Mn^{2+}, Fe^{2+}, Co^{2+}, Ni^{2+}, and Zn^{2+} complexes maintain the S_4 symmetry of 3^6adz, whereas the 3^6adz−Cr^{2+} and Cu^{2+} complexes is lowered to C_1.

Table 1. $M^{2+}\cdots$N1/N2 Distances (in Å) at the CAM-B3LYP/6-31+G(d, p) Level, Nonrelativistic Interaction Energies and Interaction Energies Including Relativistic Corrections (in kcal mol^{-1}) at the CAM-B3LYP/6-311++G(d,p) Level for the 3^6adz−M^{2+} (M: Cr, Mn, Fe, Co, Ni, Cu and Zn) Complexes Considered.

Complexes	M···N1 Distance	M···N2 Distance	Non-relativistic IEs	IEs Including Relativistic Corrections
3^6adz−Cr^{2+}	2.049	2.059	−339.7	−342.8
3^6adz−Mn^{2+}	2.057	2.057	−330.9	−334.9
3^6adz−Fe^{2+}	2.022	2.022	−363.1	−367.8
3^6adz−Co^{2+}	1.993	1.993	−400.0	−405.2
3^6adz−Ni^{2+}	1.985	1.985	−432.7	−438.6
3^6adz−Cu^{2+}	1.982	1.992	−420.7	−427.0
3^6adz−Zn^{2+}	1.994	1.994	−404.1	−413.1

Table 1 shows the computed nonrelativistic interaction energies (IE) for the 3^6adz−M^{2+} complexes considered at the CAM-B3LYP/6-311++G(d,p) level. The computed nonrelativistic IE values for the 3^6adz−M^{2+} complexes are −339.7 for 3^6adz−Cr^{2+}, −330.9 for 3^6adz−Mn^{2+}, −363.1 for 3^6adz−Fe^{2+}, −400.0 for 3^6adz−Co^{2+}, −432.7 for

3^6adz−Ni^{2+}, −420.7 for 3^6adz−Cu^{2+} and −404.1 kcal mol^{-1} for 3^6adz−Zn^{2+} at the CAM-B3LYP/6-311++G(d,p) level.

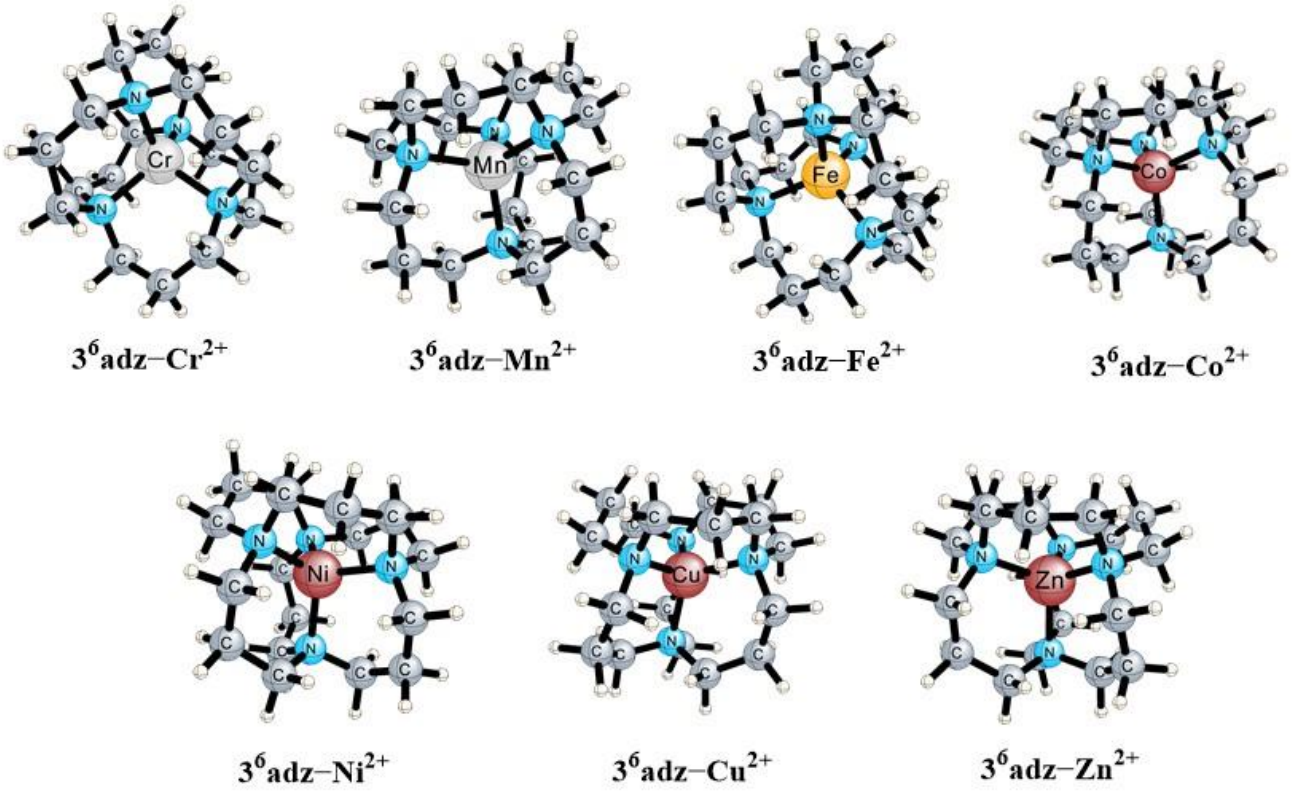

Figure 2. The optimized geometries of the 3^6adz−M^{2+} (M: Cr, Mn, Fe, Co, Ni, Cu and Zn) complexes at the CAM-B3LYP/6-31+G(d,p) level.

The computed IE values with relativistic corrections for the 3^6adz−M^{2+} complexes at the CAM-B3LYP/6-311++G(d,p) level are reported in Table 1. The computed relativistic energy correction for interaction energy is −3.1 for 3^6adz−Cr^{2+}, −4.0 for 3^6adz−Mn^{2+}, −4.6 for 3^6adz−Fe^{2+}, −5.3 for 3^6adz−Co^{2+}, −5.9 for 3^6adz−Ni^{2+}, −6.3 for 3^6adz−Cu^{2+} and −9.0 kcal mol^{-1} for 3^6adz−Zn^{2+}complex at the CAM-B3LYP/6-311++G(d,p) level, indicating that these energy correction values are not negligible for an accurate description of interaction energies of the corresponding 3^6adz−M^{2+} complexes.

The computed IE values including relativistic energy correction for the 3^6adz−M^{2+} complexes are −342.8 for 3^6adz−Cr^{2+}, −334.9 for 3^6adz−Mn^{2+}, −367.8 for 3^6adz−Fe^{2+}, −405.2 for 3^6adz−Co^{2+}, −438.6 for 3^6adz−Ni^{2+}, −427.0 for 3^6adz−Cu^{2+} and −413.1 kcal mol^{-1} for 3^6adz−Zn^{2+}at the CAM-B3LYP/6-311++G(d,p) level. The highest negative value for the 3^6adz−Ni^{2+} complex indicates that it is more stable than the other complexes because it fits into the cage cavity more easily.

4. Conclusion

In recent study, we have performed an computational study to elucidate the structures and interaction energies of the complexes formed by transition metals, such as Cr^{2+}, Mn^{2+}, Fe^{2+}, Co^{2+}, Ni^{2+}, Cu^{2+} and Zn^{2+}, with 3^6adamanzane using DFT method and CAM-B3LYP functional. At their optimized geometries of complexes studied, the 3^6adz−Mn^{2+}, Fe^{2+}, Co^{2+}, Ni^{2+}, and Zn^{2+} complexes maintain the S_4 symmetry of 3^6adz, whereas the 3^6adz−Cr^{2+} and Cu^{2+} complexes is lowered to C_1. The computed relativistic energy correction for interaction energy is −3.1, −4.0, −4.6, −5.3, −5.9, −6.3, and −9.0 kcal mol^{-1} for 3^6adz−Cr^{2+}, Mn^{2+}, Fe^{2+}, Co^{2+}, Ni^{2+}, Cu^{2+} and Zn^{2+} complexes, respectively, at the CAM-B3LYP/6-311++G(d,p) level, indicating that these energy correction values are not negligible for all complexes. The computed IE values including relativistic energy correction for the 3^6adz−M^{2+} complexes are −342.8 for 3^6adz−Cr^{2+}, −334.9 for 3^6adz−Mn^{2+}, −367.8 for 3^6adz−Fe^{2+}, −405.2 for 3^6adz−Co^{2+}, −438.6 for 3^6adz−Ni^{2+}, −427.0 for 3^6adz−Cu^{2+} and −413.1 kcal mol^{-1} for 3^6adz−Zn^{2+} at the CAM-B3LYP/6-311++G(d,p) level.

References

[1] Dietrich, B., J. M. Lehn, ve J. P. Sauvage. 1969. "Diaza-polyoxa-macrocycles et macrobicycles". *Tetrahedron Letters* 10(34):2885-88. doi: 10.1016/S0040-4039(01)88299-X.

[2] Beer, Paul D., Andrew R. Cowley, John C. Jeffery, Rowena L. Paul, ve Wallace W. H. Wong. 2003. "Self-assembled xanthate-transition metal polyether macrocycles and cryptands". *Polyhedron* 22(5):795-801. doi: 10.1016/S0277-5387(02)01412-2.

[3] Buschmann, H. J., E. Cleve, ve E. Schollmeyer. 1997. "Complex Formation Between Heavy Metal Cations and Diaza Crown Ethers and Cryptands in Aqueous Solution". *Journal of Coordination Chemistry* 42(1-2):127-30. doi: 10.1080/00958979708045285.

[4] Sarkar, Bijay, Pritam Mukhopadhyay, ve Parimal K. Bharadwaj. 2003. "Laterally non-symmetric aza-cryptands: synthesis, catalysis and derivatization to new receptors". *Coordination Chemistry Reviews* 236(1):1-13. doi: 10.1016/S0010-8545(02)00058-9.

[5] Sesta, Blanca, ve Alessandro D'Aprano. 1998. "Ionic transport across lipid bilayers activated by cryptands and alkyl-cryptands". *Colloids and Surfaces A: Physicochemical and Engineering Aspects* 140(1):119-26. doi: 10.1016/S0927-7757(98)00231-3.

[6] Sun, Wei-Ming, Xin Cheng, Wen-Lu Wang, ve Xiang-Hui Li. 2022. "Designing Magnetic Superalkalis with Extremely Large Nonlinear Optical Responses". *Organometallics* 41(17):2406-14. doi: 10.1021/acs.organomet.2c00193.

[7] Dehghani, Nasibeh, Bahram Ghalami-Choobar, Masoud Arabieh, ve Hamid Dezhampanah. 2019. "Theoretical Insight to the Complexation of Some Transition Metals with Cryptand". *Structural Chemistry* 30(4):1437-50. doi: 10.1007/s11224-018-1268-0.

[8] Behjatmanesh-Ardakani, Reza, Motahare Arab, Zahrabatoul Mosapour Kotena, ve Saharuddin Bin Mohamad. 2016. "NBO- NEDA and AIM studies on the interactions between benzocryptand [222B] and Li+, Na+, K+ and Ca2+". *Int J Pharml Sci Rev Res* 39:45-53.

[9] Bharadwaj, Parimal K. 2017. "Metal Ion Binding by Laterally Non-Symmetric Macrobicyclic Oxa–Aza Cryptands". *Dalton Transactions* 46(18):5742-75. doi: 10.1039/C7DT00722A.

[10] Gupta, Mayank, Kapil Tomar, Sarvesh K. Pandey, ve Parimal K. Bharadwaj. 2019. "Weak and Reversible Binding of Alkali Metal Ions (Na+/K+) by an Aza-Oxa Cryptand". *ChemistrySelect* 4(5):1785-88. doi: 10.1002/slct.201803353.

[11] Taschner, Ian S., Tia L. Walker, Sharath Chandra M, Briana R. Schrage, Christopher J. Ziegler, Xinfeng Gao, ve Steven E. Wheeler. 2020. "Topomeric Aza/Thia Cryptands: Synthesis and Theoretical Aspects of in/out Isomerism Using n-Alkyl Bridging". *Organic Chemistry Frontiers* 7(9):1164-76. doi: 10.1039/D0QO00123F.

[12] Tawada, Yoshihiro, Takao Tsuneda, Susumu Yanagisawa, Takeshi Yanai, ve Kimihiko Hirao. 2004. "A long-range-corrected time-dependent density functional theory". *The Journal of Chemical Physics* 120(18):8425-33. doi: 10.1063/1.1688752.

[13] Yanai, Takeshi, David P. Tew, ve Nicholas C. Handy. 2004. "A new hybrid exchange–correlation functional using the Coulomb-attenuating method (CAM-B3LYP)". *Chemical Physics Letters* 393(1):51-57. doi: 10.1016/j.cplett.2004.06.011.

[14] Ditchfield, R., W. J. Hehre, ve J. A. Pople. 2003. "Self-Consistent Molecular-Orbital Methods. IX. An Extended Gaussian-Type Basis for Molecular-Orbital Studies of Organic Molecules". *The Journal of Chemical Physics* 54(2):724-28. doi: 10.1063/1.1674902.

[15] Hehre, W. J., R. Ditchfield, ve J. A. Pople. 2003. "Self—Consistent Molecular Orbital Methods. XII. Further Extensions of Gaussian—Type Basis Sets for Use in Molecular Orbital Studies of Organic Molecules". *The Journal of Chemical Physics* 56(5):2257-61. doi: 10.1063/1.1677527.

[16] Boys, S. F., ve F. Bernardi. 1970. "The calculation of small molecular interactions by the differences of separate total energies. Some procedures with reduced errors". *Molecular Physics* 19(4):553-66. doi: 10.1080/00268977000101561.

[17] Douglas, Marvin, ve Norman M. Kroll. 1974. "Quantum Electrodynamical Corrections to the Fine Structure of Helium". *Annals of Physics* 82(1):89-155. doi: 10.1016/0003-4916(74)90333-9.

[18] Jansen, Georg, ve Bernd A. Hess. 1989. "Revision of the Douglas-Kroll transformation". *Physical Review A* 39(11):6016-17. doi: 10.1103/PhysRevA.39.6016.

Effect of Initial Reactant Concentration on the Calcium Sulfate Size Distribution

Ghassan MUTTAR JASSEM JASSEM [1], ***Muhammed Bora AKIN*** [2*]

[1] *The Ministry of Industry and Minerals, General Company for Engineering Industries, Nassiryh, Iraq*

[2] *Faculty of Engineering, Department of Chemical Engineering, Çankırı Karatekin University, Çankırı, Turkiye*

Abstract

In ancient Egypt and medieval Europe, gypsum, known as alabaster, was used for wall decorations and reliefs (Jeong et al., 2019). Gypsum, a mineral abundant in nature, consists of calcium sulfate ($CaSO_4$). In parallel with developing technology, traditional practices have also become widespread. The ability to control the size distribution during crystallization in synthesis has enabled its use in various fields. [1,2].

This study investigates the effect of initial concentrations of reactants on the size distribution of $CaSO_4$ crystals that precipitate at low temperatures through the reaction of calcium chloride ($CaCl_2$) and sodium sulfate (Na_2SO_4) spontaneously. The sizes of the resulting crystals were measured via SEM analysis to determine their size distribution. (This study was prepared from the student's master's thesis.)

Keywords: *Concentration, $CaSO_4$, Calcium sulfate, Size distribution, Crystallization, Bassanite*

1. Introduction

Calcium sulfate is a naturally occurring mineral and is commonly found in gypsum and anhydrite forms. This compound, whose chemical formula is $CaSO_4$, consists of calcium and sulfate ions. It is used in many different areas due to its form that can be shaped with water and its resistance to heat [3]. Plaster was used in wall decorations and reliefs in ancient Egypt. In medieval Europe, plaster emerged as an important material in the construction of buildings and the restoration of works of art.

It is widely used in the construction industry, especially in the production of drywall and plaster [5]. Its hydrated form ($CaSO_4 \cdot 2H_2O$) loses its water when exposed to heat and becomes Plaster of Paris. This form, which hardens after drying, is preferred in many areas such as wall correction, ceiling and wall decoration. Calcium sulfate is used as a soil conditioner in agriculture. It is preferred to meet the calcium and sulfate needs in the soil, to improve the structure of heavy soils and to regulate soil acidity. It is also a source of nutrients for plants [7]. CaSO4, also known as E516, is widely used as an additive in the food industry and is applied as a coagulant in cheese making and as a stabilizer in bread and other bakery products. For this reason, it is found in many processed foods and beverages as an additive [8,9].

CaSO4 is obtained especially through mining activities. These ores contain large amounts of calcium sulfate dihydrate ($CaSO_4 \cdot 2H_2O$). This material is then processed and used in various forms [10]. Apart from this, $CaSO_4$ is sometimes produced synthetically in industrial processes, especially as a byproduct of phosphoric acid production. This creates an opportunity for situations and regions where there is no mineral production [11]. In these processes, formation occurs by crystallization. Crystallization is the process by which ions in a solution combine to form a solid structure. This process varies with factors such as temperature, concentration of the solution and pH. The size and shape of the crystal structure also varies depending on these factors and the speed of the crystallization process [12]. The crystal structure and size of calcium sulfate are also important depending on the area of use. The crystal structure of the plaster used in the construction industry affects the hardness and durability of the material. In the food industry, homogeneity and purity of the crystal structure are important [13]. For this reason, it will be preferred to work with crystals with different structures. Recovery of calcium sulfate from industrial waste is important in waste management and sustainable production practices. Calcium sulfate formed during the production of phosphoric acid also finds a place in various applications [14].

* Corresponding author. *e-mail address: mbakin@karatekin.edu.tr*

This material finds its place in more areas with developing technology and innovative applications. Research on calcium sulfate-based implants and bone grafts shows that they also have uses in medicine [15]. In addition, the use of filling material $CaSO_4$ in the production of light and durable composite materials may find interest especially in the automotive and aviation industries [2]. In 3D printing technologies, calcium sulfate has been seen as an option for the production of biocompatible materials and objects with complex geometries [16]. Technological progress and applications involving environmentally focused innovations will expand the use of this material [17,18].

In this study, the effect of the initial concentration of the reactant on the size distribution of $CaSO_4$ crystals precipitated as a result of the reaction using $CaCl_2$ and Na_2SO_4 is revealed. The sizes of the obtained crystals in SEM photographs were measured and a statistical study was conducted to obtain information about their sizes.. Changes in crystal size distribution were observed with varying initial reactant concentrations.

2. Materials and Methods

A mechanical stirrer (IKA Eurostar 20) and a circulation-cooled water bath (Polyscience) were used in the experiments. $CaCl_2 \cdot 2H_2O$ (ACS reagent > 99%) and Na_2SO_4 (ACS reagent > 99.5%) used in the experiments were obtained from Sigma. In the experiments, the reactants were equimolar and the reactions were carried out spontaneously at 0.04 M, 0.05 M, 0.06 M, 0.07 M, and 0.08 M concentrations. Experiments were carried out in a 1 L capacity jacketed glass reactor. The temperature was set at 30°C and the stirring speed set at 300 rpm also. The precipitate obtained as a result of the reaction was dried in a vacuum oven at 80 °C for approximately 12 hours. XRD and SEM analyzes were performed on the resulting powder. The examination of the powder materials was carried out using X-ray diffraction with a Bruker D8 Discover device. The analyses were performed using a Carl Zeiss Sigma 300 VP field emission scanning electron microscope [19].

In a previous study, XRD analyses showed that the materials produced in all experiments consisted of monoclinic calcium sulfate in the Bassanite form. Table summarizes the Bassanite forms identified in the XRD analyses and their properties. [19].

Table 1. Properties of the Sythesized Bassanite Crystals [19]

Reference Code	Chemical Name	Chemical Formula	Calculated Density (g/cm^3)	Volume of Cell (10^6 pm^3)
98-001-1607	Calcium Sulfate(VI) 0.67-hydrate - Alpha	$Ca(SO_4)$ $(H_2O)_{0.67}$	2.80	1055.96
98-003-4677	Calcium Sulfate Hemihydrate	$Ca(SO_4)$ $(H_2O)_{0.5}$	2.73	1058.07
98-002-8108	Calcium Sulfate Hydrate (1/1/0.6)	$Ca(SO_4)$ $(H_2O)_{0.6}$	2.76	529.88

3. Results and Discussion

While preparing the width and length distributions of the crystals, at least 97 measurements were made for each size shown in the SEM photographs. These measurements were then statistically analyzed and represented in graph form. The average length of the material synthesized with a 0.04 M concentration was 23.86 ± 15.85 µm. Under the same conditions, the minimum crystal length was 2.79 µm, and the maximum crystal size was 96.98 µm. Similarly, the average width was 5.70 ± 3.96 µm (Figure 1).

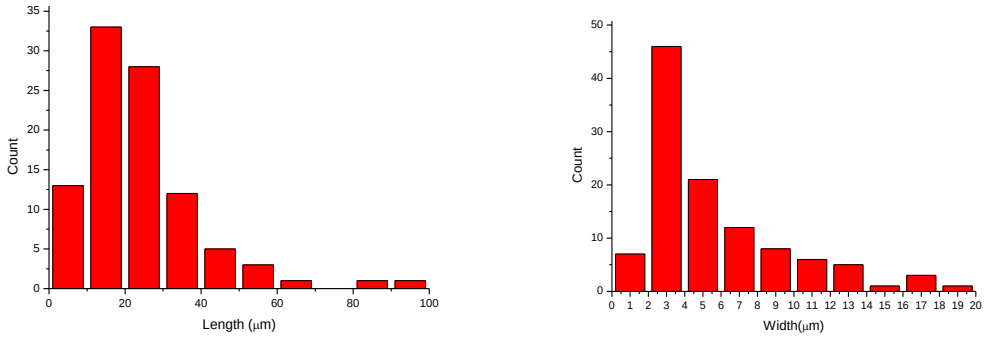

Figure 1. Size distributions of synthesized material with equimolar reactant concentration of 0.04 M

Figure 2 shows the size distributions generated from the size measurements taken from the SEM image of materials produced using a 0.05 M starting concentration. According to these results, the average height was 25.21 ±19.63 μm, and the average width was 5.11 ±3.64 μm.

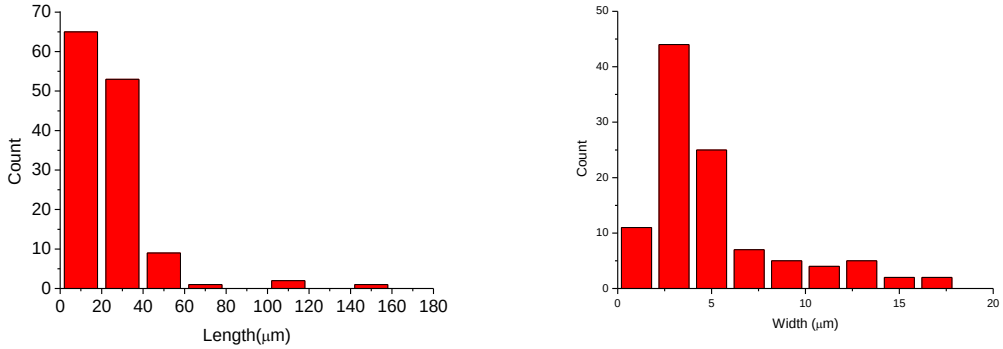

Figure 2. Size distributions of synthesized material with equimolar reactant concentration of 0.05 M

Figure 3 shows the size distributions of the material obtained using a 0.06 M starting concentration, determined through size analysis using the same method. The data indicate that the average length of the material was 26.51 ±12.17 μm, and the average width was 5.57 ±4.70 μm.

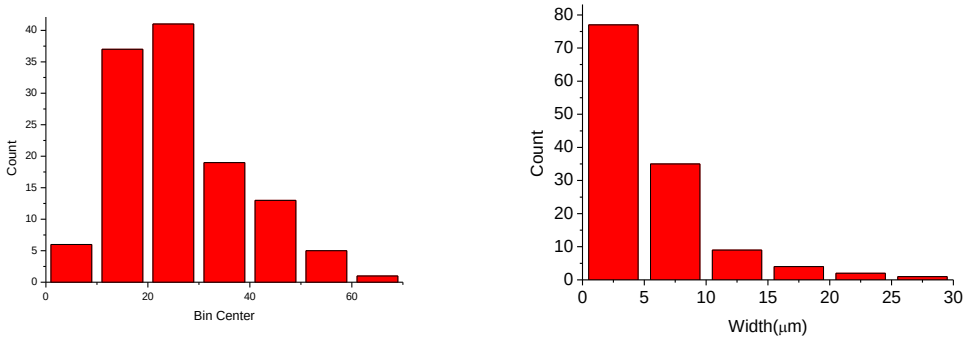

Figure 3. Size distributions of synthesized material with equimolar reactant concentration of 0.06 M

The size distributions of the material prepared using a 0.07 M starting concentration are shown in Figure 4. The statistical processing of this material yielded an average length of 26.55 ±13.00 μm and an average width of 4.17 ±2.17 μm.

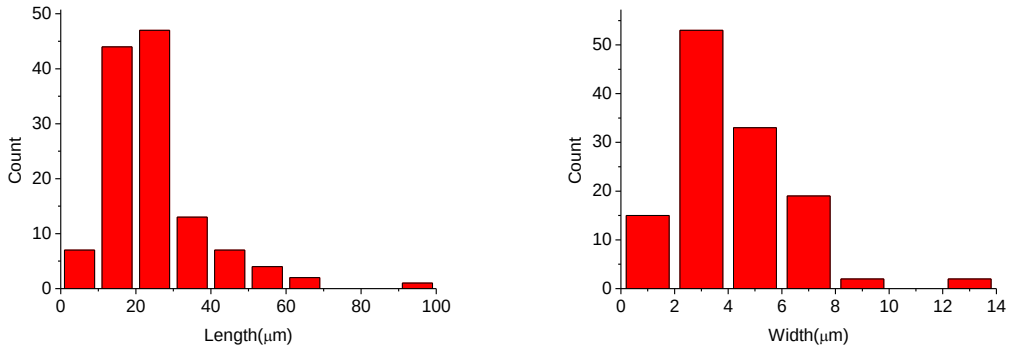

Figure 4. Size distributions of synthesized material with equimolar reactant concentration of 0.07 M

Figure 5 presents the size distributions of the material produced with a 0.08 M starting concentration. According to the statistical data based on size measurements, the average length was 32.30 ±14.36 μm, and the average width was 4.12 ±2.58 μm. The maximum measured length of the crystals was 83.84 μm, and the maximum width was 21.46 μm. The same measurements found the minimum length to be 7.84 μm, and the minimum width to be 1.17 μm (Table 2).

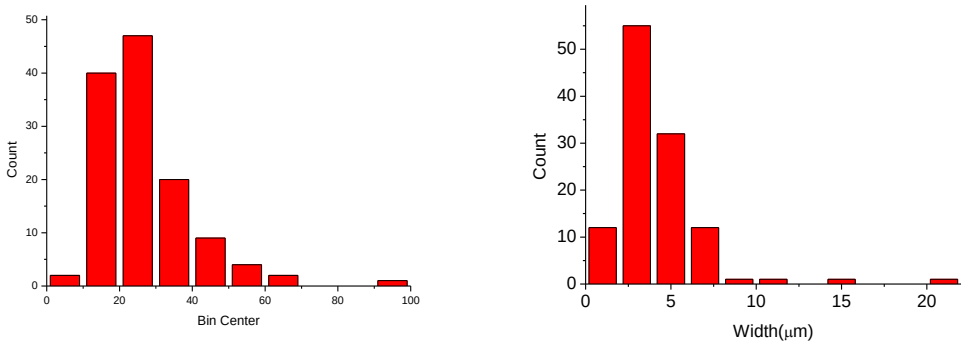

Figure 5. Size distributions of synthesized material with equimolar reactant concentration of 0.08 M

Table 2 summarizes the data on standard deviation, median, minimum, and maximum values related to the calculated average length and width values, based on the measurements.

Table 2. Effect of reactant initial concentration on dimensions

Initial Conc., M	Dimension	N total	Mean, μm	Sum	Minimum, μm	Median, μm	Maximum, μm
0.04	Length	97	23.86 ± 15.85	2314.54	2.79	21.18	96.98
	Width	110	5.57 ± 3.96	612.68	1.05	4.168	19.22
0.05	Length	131	25.21 ± 19.63	3302.92	6.60	20.00	158.99
	Width	105	5.12 ± 3.64	537.08	1.38	3.89	17.22
0.06	Length	122	26.51 ± 12.17	3234.58	1.02	24.33	61.21
	Width	128	5.57 ± 4.70	712.97	0.86	4.03	28.77
0.07	Length	125	26.55 ± 13.00	3319.31	9.39	22.91	90.81
	Width	124	4.17 ± 2.17	517.49	1.06	3.80	13.49
0.08	Length	121	32.31 ± 14.36	3909.15	7.84	30.04	83.84
	Width	115	4.12 ± 2.58	474.26	1.17	3.69	21.46

4. Conclusion

In this study, micron-sized calcium sulfate crystals were synthesized through spontaneous reactions using $CaCl_2$ and Na_2SO_4 solutions, and the synthesized crystals were identified as bassanite via XRD analysis. Measurements taken from SEM photographs were then statistically analyzed to obtain size distributions. It was observed that the average length value increased with the rise in the reactant starting concentration in the experiments. While the increasing starting concentration did not significantly affect the maximum value, a decrease in this value was noted. An increase in the starting concentration value resulted in a rise in the median value.

Acknowledgement

All experimental work was conducted in the Chemical Engineering Department Laboratory at Çankırı Karatekin University. The authors would like to thank the Chemical Engineering Department.

References

[1] Gong, S., Li, X., Song, F., Lu, D., Chen, Q. (2020). Preparation and Application in HDPE of Nano-CaSO4 from Phosphogypsum. ACS Sustain Chem Eng, 8: 4511–4520. https://doi.org/10.1021/acssuschemeng.9b07632.

[2] Wang, Y., Li, Y., Yuan, A., Yuan, B., Lei, X., Ma, Q., et al. (2014). Preparation of calcium sulfate whiskers by carbide slag through hydrothermal method. Cryst Res Technol, 49: 800–807. https://doi.org/10.1002/crat.201400155.

[3] Van Driessche, A.E.S., Stawski, T.M., Kellermeier, M. (2019). Calcium sulfate precipitation pathways in natural and engineered environments. Chem Geol, 530: 119274. https://doi.org/10.1016/j.chemgeo.2019.119274.

[4] Jeong, Y., Hargis, C.W., Kang, H., Chun, S.C., Moon, J. (2019). The effect of elevated curing temperatures on high ye'elimite calcium sulfoaluminate cement mortars. Materials (Basel), 12: 10–2. https://doi.org/10.3390/ma12071072.

[5] Zhang, J., Guan, X., Wang, X., Ma, X., Li, Z., Xu, Z., et al. (2020). Microstructure and Properties of Sulfoaluminate Cement-Based Grouting Materials: Effect of Calcium Sulfate Variety. Adv Mater Sci Eng. https://doi.org/10.1155/2020/7564108.

[6] Malin Nilsson, M.H.Z., Tägil, M. (2013). The composite of hydroxyapatite and calcium sulphate: a review of preclinical evaluation and clinical applications. Expert Rev Med Devices, 10: 675–684. https://doi.org/10.1586/17434440.2013.827529.

[7] Peters, C.L., Hines, J.L., Bachus, K.N., Craig, M.A., Bloebaum, R.D. (2006). Biological effects of calcium sulfate as a bone graft substitute in ovine metaphyseal defects. J Biomed Mater Res - Part A, 76: 456–462. https://doi.org/10.1002/jbm.a.30569.

[8] Feng, Y., Guo, R., Lin, Z. (2021). Effect of Aluminum Sulfate and Succinic Acid on the Growth Law of α - Calcium Sulfate Hemihydrate under Microwave Irradiation. Adv Mater Sci Eng, 2021. https://doi.org/10.1155/2021/6630638.

[9] Thomas, M.V., Puleo, D.A. (2009). Calcium sulfate: Properties and clinical applications. J Biomed Mater Res - Part B Appl Biomater, 88 :597–610. https://doi.org/10.1002/jbm.b.31269.

[10] Orsini, G., Ricci, J., Scarano, A., Pecora, G., Petrone, G., Iezzi, G., et al. (2004). Bone-Defect Healing with Calcium-Sulfate Particles and Cement: An Experimental Study in Rabbit. J Biomed Mater Res - Part B Appl Biomater, 68: 199–208. https://doi.org/10.1002/jbm.b.20012.

[11] Asadi-Eydivand, M., Solati-Hashjin, M., Farzad, A., Abu Osman, N.A. (2016). Effect of technical parameters on porous structure and strength of 3D printed calcium sulfate prototypes. Robot Comput Integr Manuf, 37: 57–67. https://doi.org/10.1016/j.rcim.2015.06.005.

[12] Liu, D., Cui, C., Chen, W., Shi, J., Li, B., Chen, S.. (2023). Biodegradable Cements for Bone Regeneration. J Funct Biomater, 14. https://doi.org/10.3390/jfb14030134.

[13] Chiang, C.Y., Chang, W.C., Chang, W.M., Shih, Y.C., Lin, F.H., Wu, C.C., et al. (2023). An assessment of physical properties and the viability of osteoblast-like cells of cefazolin-impregnated calcium sulfate bone-void filler. J Biomed Mater Res - Part B Appl Biomater, 111: 382–391. https://doi.org/10.1002/jbm.b.35157.

[14] Moradinezhad, F., Ghesmati, M., Khayyat, M. (2020). Postharvest Calcium Salt Treatment of Fresh Jujube Fruit and its Effects on Biochemical Characteristics and Quality after Cold Storage. J Hortic Res, 27: 39–46. https://doi.org/10.2478/johr-2019-0009.
[15] Asadi-Eydivand, M., Solati-Hashjin, M., Shafiei, S.S., Mohammadi, S., Hafezi, M., Osman, N.A.A. (2016). Structure, properties, and in vitro behavior of heat-treated calcium sulfate scaffolds fabricated by 3D printing. PLoS One, 11: 1–29. https://doi.org/10.1371/journal.pone.0151216.
[16] Kennedy, C.D., Kleinman, P.J.A., DeMoranville, C.J., Elkin, K.R., Bryant, R.B., Buda, A.R. (2017). Managing Surface Water Inputs to Reduce Phosphorus Loss from Cranberry Farms. J Environ Qual, 46: 1472–1479. https://doi.org/10.2134/jeq2017.04.0134.
[17] Hesaraki, S., Moztarzadeh, F., Nemati, R., Nezafati, N. (2009). Preparation and characterization of calcium sulfate-biomimetic apatite nanocomposites for controlled release of antibiotics. J Biomed Mater Res - Part B Appl Biomater, 91: 651–661. https://doi.org/10.1002/jbm.b.31441.
[18] Hesaraki, S., Nemati, R., Nazarian, H. (2009). Physico-chemical and in vitro biological study of zinc-doped calcium sulfate bone substitute. J Biomed Mater Res - Part B Appl Biomater, 91: 37–45. https://doi.org/10.1002/jbm.b.31371.
[19] Muttar Jassem Jassem, G., Akın M.B. (2022). Effect of Parameters on the Calcium Sulfate Crystallization, 1st International Karatekin Science and Technology Conference (IKSTC1st), p. 317–320, Cankiri, Turkiye.

Investigation of the Antienzyme and Antimicrobial Properties of the Fruit Extracts of the Oleaster (*Elaeagnus angustifolia L.*) Under *In Vitro* Conditions

Şule Azime YENİÇERİ*[*1], ***Merve BALABAN***[2], ***Bülent HALLAÇ***[3] ***Ebru AKKEMİK***[3]

[1]*Technical Services Vocational High School, Food Technology Department, Siirt University, Siirt, Türkiye*

[2] *Science and Technology Application and Research Center, Siirt University, Siirt, Türkiye*

[3]*Engineering Faculty, Food Engineering, Siirt University, Siirt, Türkiye*

Abstract

Oleaster fruit, which is a rich source of nutrients, is also an important source of antioxidants. Not only the fruit but also all parts of the plant such as roots, bark, flowers and leaves have medicinal properties. For this reason, this plant is utilized in many sectors such as food, medicine and perfumery. PPO, an enzyme commonly found in fruits and vegetables, causes enzymatic browning, resulting in loss of color, odor, taste, nutritional and economic value of foods. At the same time, it is of great importance to prevent microbiological spoilage that causes food spoilage. In this study, the inhibition effect of the oleaster fruit against the PPO enzyme and its antimicrobial effect against 4 pathogenic bacteria and one yeast cell were investigated by well diffusion technique. At the end of the study, it was observed that there was no inhibition effect and antimicrobial effect of oleaster fruit. As a result, it was determined that the extraction and inhibition method changes the inhibition depending on the enzyme and the effect on the enzyme in anti-enzyme studies. In addition, in antimicrobial studies, it was observed that the extraction method, especially the strain used, affected the antimicrobial study result.

Keywords: *Elaeagnus angustifolia L., PPO inhibition, Antibacterial, Antifungal*

1. Introduction

The Latin name *Elaeagnus angustifolia L.* is also known as Russian Olive (1). This thorny plant in tree or shrub form is a perennial plant that can reach a length of seven meters with leaves covered with silver scales, single-seeded, brown fruit (2). The inside of the oleaster fruit, which has a similar appearance to dates, is dry, white and has a sweet taste (1). Oleaster, which is distributed in Asia (central and western regions), the Gobi Desert, the Alps, around the Mediterranean and in our country (Black Sea, Marmara, Southern Anatolia and Southeastern Anatolia), can be found naturally and can also be cultivated (3). The production of oleaster, which is a tree growing in temperate regions, is around 6000 tons in our country (1). The fruit is a rich source of nutrients, chemical compounds, minerals and antioxidants (4).

This plant, which has a high health value, can grow even in arid environments, salty and calcareous soils, can improve soil conditions by binding the free nitrogen of the air with nodules in its roots (3), and has important environmental effects such as erosion control and wind stopping (1). Decoctions and infusions of fruits, flowers, leaves and bark are traditionally used in the treatment of various diseases. Raw or boiled fruit is consumed to treat some diseases (5). Since all parts of the plant such as root, bark, flower, leaf and fruit have medicinal properties, this plant is also utilized in the food, medicine and perfumery industry (6). In Iranian folk medicine, oleaster fruit is used as a painkiller, and recent pharmacological studies have determined that it has anti-inflammatory and antioxidant properties (5). In addition, many antimicrobial and antienzyme studies have been conducted to determine the pharmacological properties of *Elaeagnus angustifolia L.* (7; 8). It has been reported that fruit and leaf extracts of oleaster showed inhibition effect on AChE, BChE, Tyrosinase, α-Amylase and α-Glucosidase enzyme activities depending on the extraction method (7). In different studies, it was stated that the oleaster leaf extract had an inhibition effect on α-Amylase and α-Glucosidase enzyme activities (9). In another study, it was reported that the components isolated from *Elaeagnus angustifolia L.* generally did not show inhibition effect on α-Amylase and α-Glucosidase enzyme activity (10). As can be understood from the literature, polyphenol oxidase enzyme, which has pharmacological potential, is also an important enzyme in the food enzyme industry. This enzyme, which is widely found in fruits and vegetables, causes enzymatic browning by catalyzing the oxidation of phenolic compounds to quinones that produce brown pigments (11). Some substances show the ability to reduce o-quinones that cause color change to phenolic forms. Thus, the browning reaction stops and the color does not deteriorate (12). In recent studies, the PPO enzyme inhibitory effects of various plant extracts such as damson

* Corresponding author. *e-mail address: sulezengin@siirt.edu.tr*

plum bark extract (12), rosehip fruit extract (13) were investigated and it was determined that they had inhibitory effects on PPO.

Within the scope of our study, the inhibitory effect of methanol extract of oleaster fruit on PPO enzyme activity and antimicrobial effects against various pathogenic bacteria (*Bacillus subtilis* ATCC 6633, *Staphylococcus aureus* ATCC 29213, *Enterococcus faecalis* ATCC 29242, *Escherichia coli* ATCC 25922) and yeast (*Candida albicans* ATCC 10231) cells were also investigated. Thus, it was tried to find a solution to the problem caused by PPO enzyme, which causes economic losses as well as color, odor, taste and nutritional values of foods.

2. Materials and Methods

Samples of the oleaster to be used in the study were obtained commercially from local markets. After separating the fruit from the core, methanol extract was prepared and this extract constituted the sample of the inhibition and antimicrobial study.

Preparation of methanol extract: 5 grams of oleaster fruits were weighed and homogenized with 50 mL of methanol. For this purpose, it was kept in a shaker incubator (200 rpm, room temperature) overnight in the dark. Then it was filtered with filter paper and placed in tared flasks and the solvent was removed by evaporation. The extract concentration was prepared as 1 mg/mL by dissolving in 10% DMSO. Dilutions during the study were carried out with distilled water. The whole study was carried out at 4^{o}C.

2.1. Enzyme extraction

Jang and Moon's method was modified and used in enzyme extraction (14). The banana discs were homogenised (Velp, Scientifica, OV5/ Europe) in a ten fold amount of chilled 50 mM K-phosphate buffer (pH 7.5) for 2 min using a homogenizer. The homogenate was filtered through whatman filter paper and the filtrate was centrifuged (Thermo Scientific Heraeus Megafuge 16 R, Germany) at 6700 rpm for 60 min at 4^{o}C. The supernatant solution was used in experiments.

2.2. Determination of Polyphenoloxidase (PPO) Enzyme Activity

For this purpose, the method used by Sakiroglu (1994) (15) and Kim and Kim (2011) (16) was utilized. 50 mM pH 7.5 phosphate buffer, 0.1 M catechol solution (1,2 dihydroxy benzene), 10 µL PPO were used and the enzyme activity at 420 nm wavelength for 1 min was determined in a spectrophotometer (VWR-UV-6300 PC, Double Beam Spectrophotometer). Within the scope of the inhibition study, enzyme activity was examined at at least five different inhibitor concentrations. Reaction medium without inhibitor was considered as control. Inhibition effect was determined by plotting %Activity versus [I] (17).

2.2. Determination of Antimicrobial Effect

Well agar diffusion method was used to determine the antimicrobial effect (*Bacillus subtilis* ATCC 6633, *Staphylococcus aureus* ATCC 29213, *Enterococcus faecalis* ATCC 29242, *Escherichia coli* ATCC 25922, *Candida albicans* ATCC 10231) (18). Bacterial strains used for this purpose were activated in Tryptic Soy Broth and fungi in Sabouraud Dextrose broth medium at 37°C for 18-24 hours and their concentrations were adjusted according to 0.5 McFarland standard. Then, each bacterial strain was inoculated separately into Mueller-Hinton medium, and after the absorption of the bacterial solution into the medium, 0.6 cm diameter wells were made on the medium with at least 2 cm between each well. 30 µL of each sample was transferred to the wells, the amikacin antibiotic disk was placed on the petri surface and allowed to be absorbed into the medium for approximately 20 minutes. On the other hand, similar procedures were applied to determine the antifungal effect of the dilutions using Sabouraud Dextrose agar medium and the antifungal agent nystatin. The petri dishes were then inverted and incubated at 37°C for 18-24 hours under aerobic conditions. At the end of incubation, the diameters of the transparent zones were measured with a digital caliper and the severity of antimicrobial effect was determined.

3. Results and Discussion

As a result of the study, it was determined that there was no inhibition effect of oleaster fruit against PPO enzyme (Figure 1). In a study, the correlation between the chemical composition and high antioxidant potential of leaf extracts compared to fruit extracts in terms of phenolic and pigment content of oleaster was confirmed and all extracts showed a promising effect against tyrosinase (7). Tyrosinase enzyme used in the study in question is another synonym of PPO enzyme, but the enzyme activity method and inhibition technique of the enzyme used differ from our study. Therefore, the results obtained in both studies are not similar. Similarly, in a different study, the fact that the components obtained from the leaf extract of oleaster leaf did not show inhibition effect on α-Amylase and α-Glucosidase enzyme activities confirms our study (10). Therefore, it can be said that the inhibition effect and dosage depend on the extract and inhibition method as well as the extracted parts of the plant.

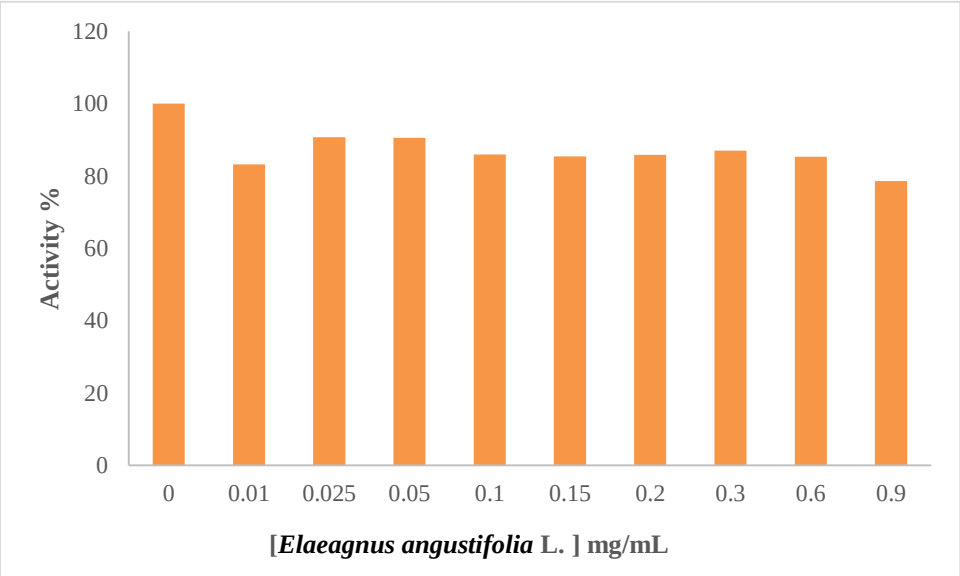

Figure 1. Effect of *Elaeagnus angustifolia L.* fruit extract on PPO enzyme activity

Similarly, it was observed that oleaster fruit had no antimicrobial effect against the pathogenic bacteria and yeast cells examined (Figure 2). In another study, it was observed that methanol extract of oleaster leaves did not form inhibition zone against *Escherichia coli* ATCC 1122 and *Candida albicans* RSKK 02029. In the same study, 9 mm inhibition zone was formed against *Bacillus subtilis* RSKK 245, *Staphylococcus aureus* RSKK 2392, while 10 mm inhibition zone was formed against *Enterococcus faecalis* ATCC 8093 (19). In another study, it was determined that oleaster ethyl extract formed an inhibition zone of 15 mm for *E. coli*, 14 mm for *S. aureus* and 10 mm for *B. cereus*. Fruit hexane extract showed no effect against *E. coli*, while fruit methanol extract showed no antibacterial effect against *B. cereus*. It was observed that the type of extract was also effective on the antimicrobial effect (20). When the literatures are examined, it is seen that the antimicrobial effect varies depending on the strain used, extraction method and raw material composition.

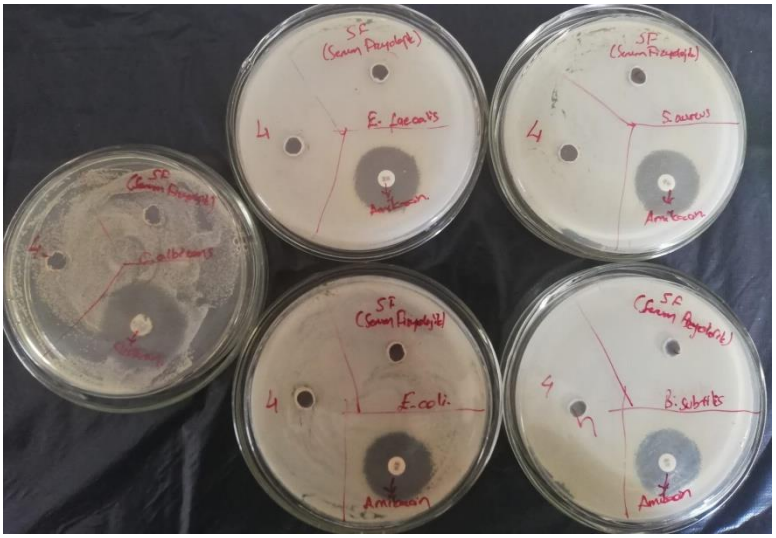

Figure 2. Antimicrobial analysis result of *Elaeagnus angustifolia L.* fruit extract

4. Conclusion

Although it is seen that the methanol extract of the fruit of the needle has no enzyme inhibitor and antimicrobial effect, it is thought that the extracts to be prepared with different solvents may give positive results. However, it is thought that it would not be appropriate to use the methanol extract for the studied bacteria and enzyme.

References

[1] Durmaz, E., (2012). Microwave Extraction of Phenolic Compounds from Caper and Oleaster. Yüksek Lisans Tezi, Fen Bilimleri Enstitüsü, Orta Doğu Teknik Üniversitesi, Ankara.

[2] Meşe, A., (2023). Mardin Bölgesinde Yetişen İğde (*Elaeagnus Angustıfolıa*) Bitkisinin Kimyasal Kompozisyonu Ve Biyolojik Uygulamalarının Araştırılması. Mardin Artuklu Üniversitesi, Lisansüstü Eğitim Enstitüsü, Kimya Anabilim Dalı, Yüksek Lisans Tezi, 46s.

[3] Yalçın, G., (2012). İğde (*Elaeagnus angustifolia L.*) Bitkisinin Çeşitli Kısımlarının Kimyasal Bileşenlerinin farklı yöntemler kullanılarak antioksidan kapasitesinin incelenmesi. Ege Üniversitesi, Sağlık Bilimleri Enstitüsü, Analitik Kimya (Eczacılık) Programı, Doktora Tezi, 244s.

[4] Hassanzadeh, Z., & Hassanpour, H. (2018). Evaluation of physicochemical characteristics and antioxidant properties of *Elaeagnus angustifolia L*. *Scientia Horticulturae*, 238, 83-90.

[5] Hamidpour, R., Hamidpour, S., & Doostmohamadi, P. (2019). Chemistry, pharmacology and medicinal property of Russian olive (*Elaeagnus angustifolia L.*). *Cancer Science Research*, 6 (1), 1-7.

[6] Berktaş, S., & Çam, M., (2020). İğde (*Elaeagnus angustifolia L.*) meyve ve yapraklarının antioksidan ve antidiyabetik özellikleri. *Akademik Gıda*, 18(3), 270-278.

[7] Carradori, S., Cairone, F., Garzoli, S., Fabrizi, G., Iazzetti, A., Giusti, A.M., Menghini, L., Uysal, S., Ak, G., Zengin, G., & Cesa, S., (2020). Phytocomplex Characterization and Biological Evaluation of Powdered Fruits and Leaves from *Elaeagnus angustifolia*. *Molecules*, 25, 1-19.

[8] Dehghan, M.H., Soltani, J., Kalantar, E.; Farnad, M., Kamalinejad, M., Khodaii, Z., Hatami, S., & Natanzi, M.M. (2014). Characterization of an antimicrobial extract from *Elaeagnus angustifolia*. *International Journal of Enteric Pathogens*, 2(3), e20157, 1-4.

[9] Saltan, F. Z., Okutucu, B., Canbay, H. S., & Özel, D. (2017). In vitro α-Glucosidase and α-amylase enzyme inhibitory effects in *Elaeagnus angustifolia* Leaves Extracts. *Eurasian Journal of Analytical Chemistry*, 12(2):117-126.

[10] Yuca, H., Özbek, H., Demirezer, L. Ö., Kasil, H. G., & Güvenalp, Z. (2021). trans-Tiliroside: A potent α-glucosidase inhibitor from the leaves of *Elaeagnus angustifolia L*. Phytochemistry, 188, 112795, 1-15.

[11] Yılmaz, L., & Elmacı, Y. (2018). Polifenol oksidaz enzimi ve inaktivasyon yöntemleri. *Türk Tarım- Gıda bilimi ve teknoloji dergisi*, 6(3), 333-345.

[12] Sahin, Z., & Sonmez, F. (2023). Mürdüm eriği (*Prunus domestica subsp. Insititia*) Kabuk Ekstraktının PPO Enzim İnhibisyonu. AS-Proceedings, 2 nd International Conference on Frontiers in Academic Research, 348-351.
[13] Sahin, Z., & Sonmez, F. (2023). Kuşburnu Meyve Ekstraktının Elma Dilimleri Üzerine Uygulanması ile Enzimatik Esmerleşemeye Etkisinin ve PPO İnhibisyonun Belirlenmesi. AS-Proceedings, 4 th International Conference on Engineering and Applied Natural Sciences, 164-168.
[14] Jang, J. H., & Moon, K. D. (2011). Inhibition of polyphenol oxidase and peroxidase activities on fresh-cut apple by simultaneous treatment of ultrasound and ascorbic acid. *Food chemistry*, 124(2), 444-449.
[15] Şakiroğlu, H. (1994). Kuşburnu meyvasından izole edilen polifenol oksidaz enziminin kinetik ve elektroforetik özelliklerinin incelenmesi. Atatürk Üniversitesi, Fen Bilimleri Enstitüsü, Kimya Ana Bilim Dalı, Doktora Tezi, 121s.
[16] Kim JJ and Kim WY (2013) Purification and characterization of polyphenol oxidase from fresh ginseng. *Journal of Ginseng Research*, 37(1):117-123. doi: 10.5142/jgr.2013.37.117. PMID: 23717165, PMCID: PMC3659630.
[17] Akkemik, E., Aybek, A., & Felek, I. (2019). Effects of Cefan melon (*Cucumis melo L.*) seed extracts on human erythrocyte carbonic anhydrase I-II enzymes. *Applied Ecology and Environmental Research*, 17(6), 14699-14713.
[18] Temiz, A. (2010). Genel Mikrobiyoloji Uygulama Teknikleri (5. Baskı). Ankara, Türkiye: Hatiboğlu Yayınevi.
[19] Okmen, G., and Turkcan, O. (2014). A study on antimicrobial, antioxidant and antimutagenic activities of *Elaeagnus angustifolia L*. leaves. *African Journal of Traditional*, Complementary and Alternative Medicines, 11(1), 116-120.
[20] Alev, I., Vatansever, C., & Servi, H., (2019). The Antibacterial Activity of *Elaeagnus angustıfolıa L*. Fruit And Leaf Extracts. Mesmap-5 Proceedings Book, 129.

Automated Detection of Solar Panel Defects Using Deep Learning

Bahaa ALBUARAB [1*], ***Hakan KUTUCU*** [2]

[1]*Computer Engineering, Karabuk University, Karabuk, Turkey*

[2]*Software Engineering, Karabuk University, Karabuk, Turkey*

Abstract

High temperature differentials and external pressures pose significant challenges in the production of photovoltaic (PV) cells for the solar energy sector. These flaws are often evaluated manually, which can lead to issues such as human error, fatigue, and increased costs. To address this challenge, our research focuses on using deep learning methods for the automatic identification of defects in PV modules. We designed and analyzed two distinct models: a custom-built Convolutional Neural Network (CNN) and an adapted, pre-trained InceptionV3 model. To distinguish between healthy and unhealthy PV cells, we conducted an experiment with a dataset of 2,624 electroluminescence (EL) images, performing a binary classification task. While the custom CNN achieved an impressive accuracy of 89.47%, it was slightly outperformed by the InceptionV3 model, which reached an accuracy of 90.88%. These results highlight the potential of both custom-designed and pre-trained deep learning models for defect detection in PV modules, depending on resource availability, computational capacity, and the requirements of the specific application. This study underscores the growing importance of machine learning software in the advancement of renewable energy systems.

Keywords: *CNN, Photovoltaic (PV), InceptionV3, Electroluminescence (EL), Defect detection*

1. Introduction

Renewable energy sources and solar power in particular, have emerged as key players in the fight against climate change and carbon emissions [2]. Photovoltaic (PV) cells, which turn sunlight into electricity, are at the center of this movement. However, surface flaws such as micro-cracks can arise in PV cells due to the complexity of the manufacturing process [1]. These flaws can have a major effect on solar panels' efficiency, reducing electricity production and shortening their lifespan [5]. Manual inspections have traditionally been used to spot these flaws, but they are time-consuming, inconsistent, and fraught with human error [3].

Due to technological progress, automated approaches for flaw identification in PV cells are being investigated. The goal of these techniques is to improve upon manual inspections by offering more precise, trustworthy, and time-efficient means of finding flaws [4]. The use of electroluminescence (EL) photography has been a noteworthy step forward in this area, enabling the detection of flaws that are not immediately apparent by the human eye [6, 7, 8]. However, improvements are needed before this technology can fully realize its potential in the area of fault identification.

In this regard, deep learning—and in particular the application of Convolutional Neural Networks (CNNs)—has emerged as a useful technique. In recent years, convolutional neural networks (CNNs) have been extensively used to evaluate EL pictures of PV cells [9, 10, 11] because to their efficacy in image identification and classification tasks. CNNs are ideally suited for detecting small flaws in PV modules due to their capacity to learn complicated patterns and characteristics from data. To improve defect identification in PV cells, scientists have experimented with a wide range of deep learning architectures, from custom-built models to modifications of established frameworks like InceptionV3 [12, 13, 14]. These models have demonstrated potential in boosting the accuracy and efficiency of fault identification, consequently adding to the overall dependability of solar power systems.

We want to add to these previous successes by designing and contrasting a novel CNN model with a modified version of the InceptionV3 model for PV module fault detection. Our method entails using a dataset including pictures of solar panels with different kinds of defects to train and evaluate these models. Through this comparison research, we want to evaluate the usefulness of these models in automating the defect detection process, hence enhancing the accuracy, reducing the labor costs, and overcoming the limits associated with human inspections.

A- Dataset

* Corresponding author. *e-mail address: bahaqq645@gmail.com*

In this study, we employed a database including 2,624 high-resolution EL images of monocrystalline and polycrystalline PV modules. One of 44 different PV modules was used to capture each of the 300 pixel short images. With such a wide range of options, you may rest assured that you'll find something to suit your preferred PV system.

Buerhop-Lutz et al. [6] used their knowledge to divide the dataset into two categories: pictures with no flaws ('None Defected'; 1,508 images) and images with defects ('Defected'; 715 images). Due to the importance of distinguishing between healthy and unhealthy PV cells, we have posed this task as a binary classification problem. Figure 1 shows Typical (A) and deficient (B) photovoltaic (PV) cell surfaces.

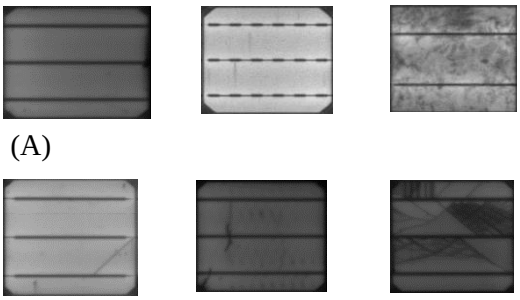

(A)

(B)

Figure 1. Photovoltaic (PV) cells with normal (A) and flawed (B) surfaces

2. Literature Review

Transparent solar panels are gaining popularity as a viable renewable energy option because of their decreasing prices. Large-scale solar power plant efficiency may be maintained with the use of defect detection methods, such as the detection of micro-cracks in photovoltaic modules. To prove that UV fluorescence can detect faults in solar panels on residential rooftops in Boulder, Colorado, Gabor et al. [19] used a pole-mounted UV flash camera system. This technique worked quite well for a wide range of panel types and ages. Together with a UAV fitted with a thermal camera and GPS, Han et al. [20] presented a deep learning strategy based on an improved YOLOv3-tiny model. This system outperformed the industry-standard YOLOv3-tiny model in defect identification with an accuracy of 96.45%.

By analyzing RGB photos, Espinosa et al. [21] showed that CNNs can automatically diagnose physical problems in PV plants, with an average accuracy of 75% for two classes and 70% for four classes. Attaining 90% AUC on benchmark EL image datasets, Acharya et al. [13] proposed a deep Siamese CNN for defect classification in solar cells. Using models like Inception-v3 and ResNet50-v3, Rahman et al. [23] were able to identify micro-cracks in EL pictures of PV modules with an accuracy of over 96%. The CNN-based architecture used by Akram et al. [9] achieved 99.23% accuracy, however this may not be applicable outside of their small dataset.

Mathias et al. [24] analyzed 2000 EL photos using perspective modification and textural analysis, reaching good accuracies with both SVM and neural networks. Replicating this model yielded impressive results for Winston et al. [25], including an F1-score of 94.6%. Last but not least, Xue et al. [27] employed fuzzy c-means clustering in conjunction with AlexNet CNN to accurately detect concealed cracks [28].

These advancements in deep learning for fault identification in PV modules constitute a significant milestone for solar energy technology. They not only address the solar industry's immediate demands, but also provide the groundwork for advances in automated problem identification in the future, highlighting solar power's vital role in the world's most promising energy sources.

3. Methodology

In this study, we set out to develop robust computational models for PV cell characterization and defect diagnosis. Our models were developed with excellent accuracy and efficiency in mind, taking into account the large number of PV cells used in real-world applications. A Custom Convolutional Neural Network (CNN) and the InceptionV3 model are two examples of the types of computational models covered in detail by the technique. Through the use of various tools and techniques, such as data purification, architectural design, training methodologies, and assessment benchmarks, we take a scientific approach to the process, beginning with the collection of raw EL

pictures and ending with the evaluation of the produced models. This strategy is based on the most cutting-edge findings and established practices in the fields of deep learning and image analysis.Figure 2 shows General flow chart of the proposed models.

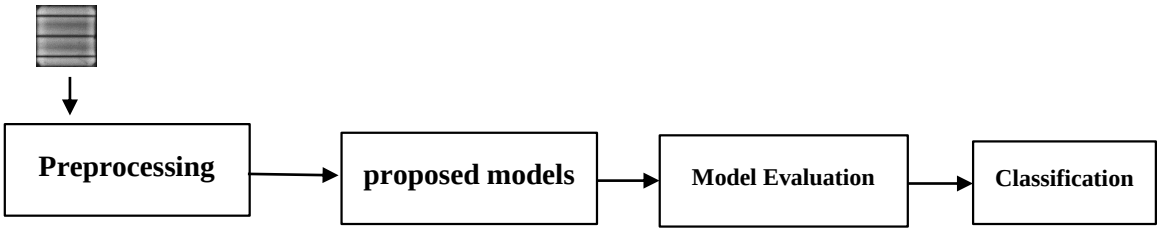

Figure 2. General flow chart of the proposed models

3.1 Preprocessing Techniques:

The ELVP database included the collection of grayscale photos of photovoltaic (PV) modules with varied degrees of deterioration. A multi-stage picture preparation pipeline, including the following steps, was designed to improve the characteristics of interest and reduce noise: The Preprocessing Stage Flowchart is depicted in Figure 3.

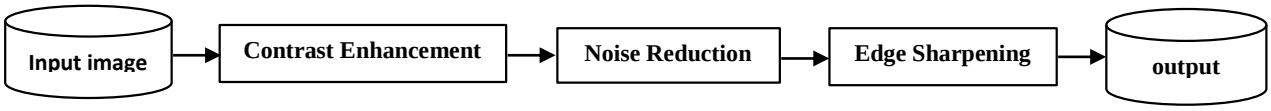

Figure 3 : Flowchart of the Preprocessing Stage.

Because of its improved edge detail retention, Contrast Limited Adaptive Histogram Equalization (CLAHE) was employed to improve photos of PV modules subjected to varying lighting and texturing. Image clarity was further improved by removing random noise with a Gaussian Blur filter (5x5 pixel kernel). A 3x3 kernel-sharpening filter was used to boost the high-frequency edge components and so improve the perceived sharpness of the edges. The calibrated preprocessing processes greatly enhanced feature visibility and noise reduction, allowing machine-learning algorithms to detect defects with higher precision.

Data augmentation techniques were used to deal with the handful of flawed photos present in the collection. Modifying contrast, brightness, saturation, and picture orientation were among the methods used to avoid model overfitting and improve generalizability. Contrast enhancements mimicked different lighting situations to bring out previously hidden elements. With an increase from 715 to 1,668 flawed photos, the dataset now provides a bigger and more diverse training pool. Similar augmentation techniques, such as rotation, axis flip, Gaussian blur, and contrast enhancement, were also used to the small training set of the ELPV dataset. These techniques increased the variety of defect manifestations, which is critical for improving the models' generalizability and avoiding overfitting.

3.2 Custom CNN Model architecture

High-resolution electroluminescence imaging of photovoltaic cells is the focus of the study, which uses a Custom CNN Model architecture developed especially for this purpose. Convolutional layers with 3x3 filters of sizes 32, 64, 128, and'same' padding to maintain spatial dimensions follow the Image Input Layer for 300x300x3. Incorporating non-linearity and improving feature extraction, batch normalization and ReLU activation are provided. To lessen the need for storage space and processing power, we implement Max pooling layers with a pool size of 2 x 2 and a stride of 2. The design closes with a fully connected layer for binary classification, a softmax layer for class probability, and a classification layer for choices. This setup strikes a good compromise between complexity and efficiency, making it useful for applications like flaw detection in PV cells.

Tuning the learning rate, number of epochs, and batch size during training and compilation of the CNN improves its effectiveness. The effectiveness of feature extraction is directly affected by the architecture's layers and filters. Activation functions like ReLU, sigmoid, or tanh add non-linearity, allowing the model to capture complicated patterns. Minimization of the loss function is affected by the selection of optimizer, such as Adam or SGD. These tweaks are essential to assure the model's efficacy for certain tasks, balancing learning efficiency with prediction accuracy. Table 1 contains the specifics of these options.

Table 1. Settings for Training and Compilation

Parameter	Value
Optimizer	Adam
Loss Function	Categorical Cross-Entropy
Performance Metric	Accuracy
Batch Size	32
Number of Epochs	30
Validation Split	Typically 0.2 (20% for validation)

3.3 InceptionV3 model architecture

The study uses the InceptionV3 architecture, which has 23.8 million parameters and strikes a good balance between complexity and layer count. The scale and intricacy of patterns are improved by the use of varying filter sizes within the same layer. In comparison to AlexNet and VGG, this model has fewer parameters while providing a more comprehensive representation of features. Including three sets of Inception layers and two grid-thinning components, its 350 connections make it stand out.

The final result is the result of extracting various functional levels via a fully connected (FC) layer, which is the result of global average pooling. The input layer handles 299x299x3 pictures, and there are 94 convolution layers with varied filter sizes. Particularly, a scaling layer is ideally positioned after the input layer, which results in a first convolution layer with a weight matrix of 149x149x32 dimensions.

The InceptionV3 model's complete training and compilation parameters are presented in Table 2. This architecture shines in complex machine learning applications that need in-depth picture analysis.

Table 2. Training and Compilation Parameters

Parameter	Typical Value/Setting
Batch Size	32
Optimizer	Adam
Learning Rate	0.001
Loss Function	Cross-entropy
Epochs	30
Metric(s) for Evaluation	Accuracy, Precision, Recall, F1 Scor.
Validation Split	Typically 0.2 (20% for validation)

4. Results and Discussion

Two deep learning models, the Custom CNN and InceptionV3, were evaluated and compared in this work, with both having been trained using data from photovoltaic cells. Accuracy, F1-Score, Precision, and Recall all hovered around 89.5%, demonstrating the Custom CNN's all-around excellence. This harmony indicates a model with somewhat superior precision, with a little more weight placed on the precision of positive predictions. Figure 5(A) displays the confusion matrix, which confirms this model's efficacy, especially in detecting faulty cells, which is essential in quality control settings.

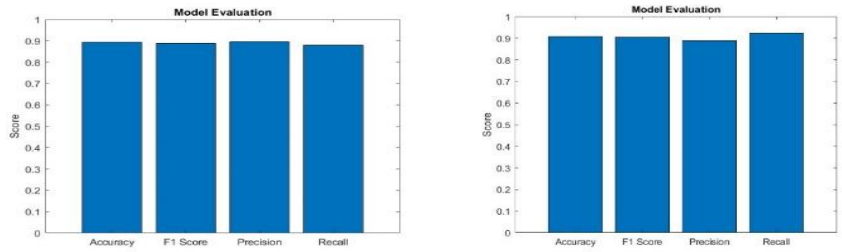

(a) Custom CNN Performance (b) InceptionV3 Performance

Figure 4. Custom CNN and InceptionV3 Performance

While both the Accuracy and F1-Score of the InceptionV3 model were over 90%, the Recall was significantly higher at 92.38%, demonstrating the model's remarkable ability to generalize and accurately identify new data. According to the metrics presented in Table 3, InceptionV3 excels at detecting the positive class (defective cells) while avoiding false-positive results. This is essential for preserving the dependability of solar systems by preventing the accidental overlooking of damaged cells.

Figure 4(b) further underscored the strong performance of the InceptionV3 model, with high Recall and F1-Score indicating a well-tuned balance between sensitivity (true positive rate) and specificity (true negative rate). The confusion matrix in

Figure 5(b) visually reinforced these findings, showing the model's effectiveness in correctly identifying defective cells, which is paramount in preventing the deployment of faulty PV modules.

Table 3. Performance Metrics

Model	Accuracy	Precision	Recall	F1-Score
Custom CNN	89.47%	90.72%	89.38%	90.04%
InceptionV3	90.88%	88.85%	92.38%	90.58%

In conclusion, while both models perform admirably, the InceptionV3 model demonstrates a slight edge, particularly in Recall, which could make it the preferred choice in applications where the cost of false negatives is high. The study's results suggest that advanced architectures like InceptionV3 can significantly benefit photovoltaic cell analysis and defect detection, which is a vital step in the quality assurance process.

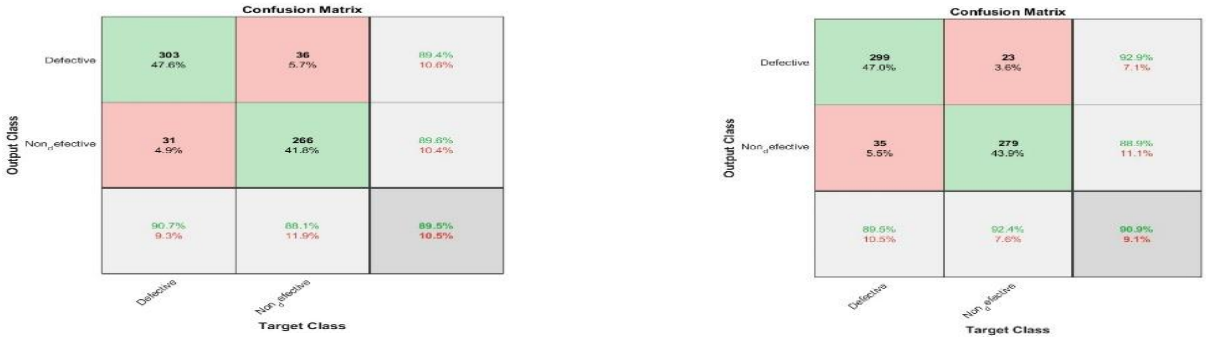

(a) Custem CNN (b) InceptionV3

Figure 5. Confusion matrix

4.1 Comparison with Previous Works

Using the same dataset as in our study, we conducted a comparative analysis of our results with those of recently developed approaches in the field of defective PV module cell classification. The outcomes, as presented in Table 4, reveal that our proposed models achieved an accuracy of 89.47% for the Custom CNN and 90.88% for the InceptionV3 model. This comparison with prior studies highlights the advancements and effectiveness of our models:

Table 4. Comparison with Previous Works

References	**Method**	**Dataset**	**ACC**
[7]	SVM	solar cell	82.44
[7]	CNN	solar cell	88.42
[13]	CNN	solar cell	74.75
[14]	L-CNN	solar cell	89.33
[14]	DFB-SVM	solar cell	94.52
This study	Custom CNN model	same as used	89.47
This study	InceptionV3 model	same as used	90.88

5. Conclusions

Our study explored the use of artificial intelligence in the renewable energy sector, focusing on the inspection of photovoltaic (PV) cells for defects, which is critical for maintaining their efficiency. We addressed the limitations of traditional manual inspections by developing and comparing two machine learning models: a custom-built Convolutional Neural Network (CNN) and an adapted InceptionV3 model. Both models were trained on electroluminescence images of PV cells and performed binary classification tasks. The custom CNN model achieved an accuracy of 89.47%, while the more complex InceptionV3 model achieved slightly higher accuracy at 90.88%. This comparison demonstrates the potential of both custom-designed and pre-trained deep learning models in automating PV cell inspection, enhancing precision, and reducing costs. Our findings support the further integration of AI in renewable energy, indicating a future where sustainable energy is improved through computational intelligence.

References

[1] Hussain, M.; Al-Aqrabi, H.; Hill, R. PV-CrackNet Architecture for Filter Induced Augmentation and Micro-Cracks Detection within a Photovoltaic Manufacturing Facility. Energies 2022, 15, 8667.

[2] CO2 Emissions in 2022–Analysis-IEA. Available online: https://www.iea.org/reports/co2-emissions-in-2022 (accessed on 11 April 2023).

[3] Padmavathi, N.; Chilambuchelvan, A. Fault detection and identification of solar panels using Bluetooth. In Proceedings of the 2017 International Conference on Energy, Communication, Data Analytics and Soft Computing, ICECDS 2017, Chennai, India, 1–2 August 2017; pp. 3420–3426.

[4] Dhimish, M.; Mather, P. Development of Novel Solar Cell Micro Crack Detection Technique. IEEE Trans. Semicond. Manuf. 2019, 32, 277–285.

[5] Dhimish, M.; Holmes, V.; Dales, M.; Mehrdadi, B. Effect of micro cracks on photovoltaic output power: Case study based on real time long term data measurements; Effect of micro cracks on photovoltaic output power: Case study based on real time long term data measurements. Micro Nano Lett. 2017, 12, 803–807.

[6] Buerhop-Lutz, C., Deitsch, S., Maier, A., Gallwitz, F., & Brabec, C. J. (2018). A Benchmark for Visual Identification of Defective Solar Cells in Electroluminescence Imagery. 35th European PV Solar Energy Conference and Exhibition, 1287–1289.

[7] Deitsch, S., Christlein, V., Berger, S., Buerhop-Lutz, C., Maier, A., Gallwitz, F., & Riess, C. (2019). Automatic classification of defective photovoltaic module cells in electroluminescence images. Solar Energy, 185(February), 455–468.

[8] Deitsch, S., Buerhop-Lutz, C., Sovetkin, E., Steland, A., Maier, A., Gallwitz, F., & Riess, C. (2021). Segmentation of photovoltaic module cells in uncalibrated electroluminescence images. Machine Vision and Applications, 32(4). DOI: 10.1007/s00138-021-01191-9

[9] Akram, M. W., Li, G., Jin, Y., Chen, X., Zhu, C., Zhao, X., & Ahmad, A. (2019). CNN based automatic detection of photovoltaic cell defects in electroluminescence images. Energy, 189. https://doi.org/10.1016/j.energy.2019.116319

[10] Tang, W., Yang, Q., Xiong, K., & Yan, W. (2020). Deep learning based automatic defect identification of photovoltaic module using electroluminescence images. Solar Energy, 201(November 2019), 453–460. 10.1016/j.solener.2020.03.049.

[11] Tang Wuqin, Quiang Yang, W. Y. (2019). Deep Learning Based Models For Defect Detection of Mono Cr. PV Modules with EL Images Using Data Augmentation. In 2019 IEEE PES Asia-Pacific Power and Energy Engineering Conference (APPEEC), Macao, Macao. (pp. 1–5).

[12] Luo, Z., Cheng, S. Y., & Zheng, Q. Y. (2019). Corrigendum: GAN-Based Augmentation for Improving CNN Performance of Classification of Defective Photovoltaic Module Cells in Electroluminescence Images (IOP Conf. Ser.: Earth Environ. Sci. 354 012106). IOP Conference Series: Earth and Environmental Science, 354, 012132. 10.1088/1755- 1315/354/1/012132.

[13] Acharya AK, Sahu PK, Jena SR. 2019. Deep neural network based approach for detection of defective solar cell. Materials Today: Proceedings 39(5):2009–2014 DOI 10.1016/j.matpr.2020.09.048.

[14] Demirci MY, Beşli N, Gümüşçü A. 2021. Efficient deep feature extraction and classification for identifying defective photovoltaic module cells in Electroluminescence images. Expert Systems with Applications 175(2):114810 DOI 10.1016/j.eswa.2021.114810.

[15] Wang Y, Li L, Sun Y, Xu J, Jia Y, Hong J, Hu X, Weng G, Luo X, Chen S, Zhu Z, Chu J, Akiyama H. 2021. Adaptive automatic solar cell defect detection and classification based on absolute electroluminescence imaging. Energy 229:120606

[16] S.Amarnadh, P. P. Reddy, and N. Murthy, ―FreeHand Sketch-based Authenticated Security System using Convolutional Neural Network,‖ Int. J. Eng. Adv. Technol. ISSN, pp. 2249–8958.

[17] X. Xu, J. Wu, J. Wang, Q. Qu, Z. Tan, and M. Luo, ―Materials Identification of Polarized Pulse Laser Detection Based on Sparse Autoencoder and Softmax Classifier Framework,‖ IEEE Trans. Instrum. Meas., vol. 71, pp. 1–9, 2022.

[18] Xie, X., Lai, G., You, M., Liang, J., & Leng, B. (2022). Effective transfer learning of defect detection for photovoltaic module cells in electroluminescence images. Solar Energy. https://doi.org/10.1016/j.solener.2022.10.055Title

[19] Gabor, A.M.; Knodle, P. UV Fluorescence for Defect Detection in Residential Solar Panel Systems. In Proceedings of the Conference Record of the IEEE Photovoltaic Specialists Conference, Fort Lauderdale, FL, USA, 20–25 June 2021; pp. 2575–2579.

[20] Han, S.H.; Rahim, T.; Shin, S.Y. Detection of faults in solar panels using deep learning. In Proceedings of the 2021 International Conference on Electronics, Information, and Communication, ICEIC 2021, Jeju, Republic of Korea, 31 January–3 February 2021.

[21] Espinosa, A.R.; Bressan, M.; Giraldo, L.F. Failure signature classification in solar photovoltaic plants using RGB images and convolutional neural networks. Renew. Energy 2020, 162, 249–256.

[22] Rahman, M.R.; Tabassum, S.; Haque, E.; Nishat, M.M.; Faisal, F.; Hossain, E. CNN-based Deep Learning Approach for Micro-crack Detection of Solar Panels. In Proceedings of the 2021 3rd International Conference on Sustainable Technologies for Industry 4.0, STI 2021, Dhaka, Bangladesh, 18–19 December 2021.

[23] Zhang, N.; Shan, S.; Wei, H.; Zhang, K. Micro-cracks Detection of Polycrystalline Solar Cells with Transfer Learning. J. Phys. Conf. Ser. 2020, 1651, 012118.

[24] Mathias, N.; Shaikh, F.; Thakur, C.; Shetty, S.; Dumane, P.; Chavan, D.S. Detection of Micro-Cracks in Electroluminescence Images of Photovoltaic Modules. In Proceedings of the 3rd International Conference on Advances in Science & Technology (ICAST), Padang, Indonesia, 24–25 October 2020.

[25] Winston, D.P.; Murugan, M.S.; Elavarasan, R.M.; Pugazhendhi, R.; Singh, O.J.; Murugesan, P.; Gurudhachanamoorthy, M.; Hossain, E. Solar PV's Micro Crack and Hotspots Detection Technique Using NN and SVM. IEEE Access 2021, 9, 127259–127269.

[26] Singh, O.D.; Gupta, S.; Dora, S. Segmentation technique for the detection of Micro cracks in solar cell using support vector machine. Multimed Tools Appl. 2023, 1–26.

[27] Xue, B.; Li, F.; Song, M.; Shang, X.; Cui, D.; Chu, J.; Dai, S. Crack Extraction for Polycrystalline Solar Panels. Energies 2021, 14, 374.

[28] Chen, H.; Zhao, H.; Han, D.; Liu, K. Accurate and robust crack detection using steerable evidence filtering in electroluminescence images of solar cells. Opt. Lasers Eng. 2019, 118, 22–33.

[29] Zyout, I.; Qatawneh, A. Detection of PV Solar Panel Surface Defects using Transfer Learning of the Deep Convolutional Neural Networks; Detection of PV Solar Panel Surface Defects using Transfer Learning of the Deep Convolutional Neural Networks. In Proceedings of the 2020 Advances in Science and Engineering Technology International Conferences (ASET), Dubai, United Arab Emirates, 4 February–9 April 2020.

[30] Alaa S. , Ibrahim DA, Zebari DA, Hammadi S, Mohammed H, Mohammed MA, Damaševičius R . Identifying defective solar cells in electroluminescence images using deep feature representations: DOI 10.7717/peerj-cs.992

Effect of Gliding Arc Discharge on Reducing The Microbial Load of Black Table Olives

Melike CANBOLAT, ***Baran ÖNAL ULUSOY***[1,*]

[1] *Food Engineering, Çankırı Karatekin University, Çankırı, Turkey*

Abstract

In this study, it was aimed to investigate the potential of Gliding Arc Discharge (GAD) plasma, one of the non-thermal cold plasma types, for reducing the natural microbial load in Gemlik type black olives obtained from İzmir province. The GAD plasma conditions were optimized using the Box-Behnken experimental design with black olives, harvested in 2020 and then stored at +4 °C for natural microorganism growth. Olives were treated with the GAD plasma at optimum plasma condition of 0.7 mL/min gas flow rate, 0.5 cm distance between electrodes, 5 min time with dry air (99.9%). Changes in microbiological (mold-yeast and lactic acid bacteria count) of olives with and without plasma treatment were determined. After plasma treatment, 5.4% reduction in mold-yeast count and 10.7% reduction in lactic acid bacteria count were detected. The results showed that air-GAD plasma is a promising method for the pre-decontamination of fruits that are sensitive to heat and have high moisture content.

Keywords: *Gliding arc discharge plasma, Black table olives, Mold-yeast, Lactic acid bacteria, Decontamination*

1. Introduction

Olive fruit (Olea europaea L.), cultivated in Mediterranean countries and widely consumed worldwide, stands as a valuable product. Turkey is one of the key countries with intense olive production. Olives have an important value not only due to their nutritional value but also in terms of their contribution to the economy, culturally and environmentally [4].

In addition to its nutritional and health-benefiting properties, olive fruit is one of the foods where microbiological spoilage is frequently encountered. Proper hygiene conditions during harvesting and storage are essential, and hygiene and quality conditions must also be maintained during olive processing. Otherwise, mold formation, a common type of spoilage, could occur in olives. Mold floras in olives are primarily composed of molds belonging to the Penicillium and Aspergillus genera [3].

Certain pre-processing steps such as salting and/or pickling process and caustic application are applied to olives to preserve their nutritional value, reduce microbiological load, minimize microbial growth during storage, and enhance stability. Non-thermal (cold) plasma technology is one of these pre-processing steps. Plasma is generated by applying electrical or electromagnetic fields to or within a gas with a high electrical potential difference between two electrodes. The reactive compounds in plasma typically include reactive oxygen species (O, O2, ozone (O3), and OH), reactive nitrogen species (NO, NO2, and NOx), ultraviolet radiation (UV), free radicals, and charged particles [6]. These compounds possess the necessary energy for decontamination. Parameters such as the type of gas used, electrodes, and production system in plasma generation lead to diversity in reactive species and variations in decontamination effectiveness [10]. Additionally, parameters like the distance to the target, application time, and direct vs. indirect application might influence decontamination efficacy.

In recent years, plasma application for sterilization and disinfection purposes has become widespread in the food industry. Plasma treatment does not elevate the temperature of the food to levels that would adversely affect on its nutritional value and not cause significant changes in the composition and physical properties of the food while providing effective antimicrobial protection [1]. Among plasma treatments, GAD is preferred due to its low equipment and operating costs, as well as its high efficiency in the inactivation of various microorganisms and its operation at atmospheric pressure with low gas flow rates [2-8]. In a study using dry air GAD plasma, reductions of 3.4 and 3.7 log CFU/ml were observed in *E. coli* O157:H7 and *Salmonella* Stanley strains on agar medium and Golden Delicious apples, respectively [7]. Khalili et al. (2018) achieved complete decontamination of *E. coli* strains in almonds with air GAD-plasma treatment for 5 min [5].

* Corresponding author. *e-mail address: baran@karatekin.edu.tr*

There are limited studies on GAD plasma but not on olives. The aims of this study is to explore the efficacy of cold air-GAD plasma treatment in reducing the microbial load of Gemlik-type black olives. The objectives of this study involve applying GAD plasma to Gemlik-type black olives that naturally develop mold after one year of storage at +4°C. Future research will focus on evaluating the impact of optimized plasma conditions, determined through statistical analysis, on the physicochemical, microbiological quality, and storage stability of black olives.

2. Materials and Methods

2.1 Samples and Chemicals

Gemlik type black olives, harvested in 2020 with hand picking, were suppplied from the Aliağa district of İzmir province and stored at +4°C until plasma treatment. Sodium chloride (NaCl), methanol, and other chemicals were obtained from Sigma-Aldrich (Munich, Germany). Potato Dextrose Agar (PDA), Man Rogosa Sharp (MRS) and other chemicals of analytical quality were purchased from Merck (Darmstadt, Germany). The high-purity (99.9%) dry air used in plasma generation was purchased from Ankara Gaz (Ankara, Turkey).

2.2 GAD Plasma System Setup and Optimization of Treatment Parameters

GAD plasma system[8] with constant the electrical power is generated between copper electrodes (10.4 cm length, 1.5 mm thickness) at atmospheric pressure using high-purity air, with a discharge frequency of 20 kHz and an applied voltage of 15 kV. For the optimization of treatment conditions, a flow control mechanism (Bronkhorst, Netherlands) was used to adjust the gas flow at 0.3, 0.5 and 0.7 mL/min. As shown in Table 1, while the gas type used in this study (high-purity dry air) was kept constant, the electrode gap was set to 0.5, 0.7 and 0.9 cm. Plasma characteristics were examined by applying plasma for 1, 3, and 5 min to enhance the efficiency of plasma. The gas flow, adjusted by the flow controller, was applied to the top parts of olives stalk where visible mold formation was concentrated, from a fixed distance of 0.5 cm. The images of the plasma application are shown in Figure 1.

To determine the optimum process parameters, the Box-Behnken method under the Design of Expert menu in Minitab 17 statistical software was used.

Table 1. Air-GAD Plasma Experimental Design

Gas Flow Rate (mL/min)	Electrode Gap (cm)	Treatment time (min)
0.3	0.5	1
0.5	0.7	3
0.7	0.9	5

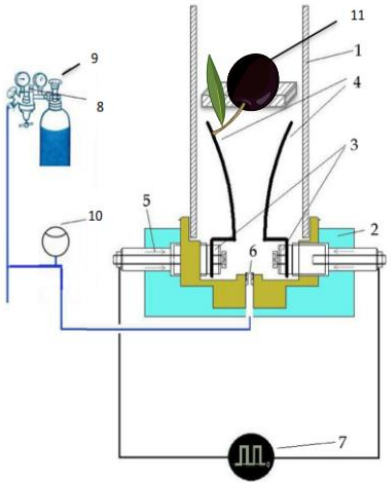

Figure 1. Laboratory stand with mini GAD plasma reactor (1: discharge chamber, 2: case, 3: connectors for working electrodes, 4: electrodes, 5: power cord connectors, 6: nozzle, 7: power supply, 8: pressure gauge, 9: gas, 10: flow rate controller, 11: sample)

2.3 Microbiological Analyses

Microbiological analyses were conducted both before and after plasma treatment. Olive samples, separated from 5 g of the core within a sterile cabinet, were diluted at a ratio of 1:10 (10-1) with 45 mL of sterile physiological saline solution (0.85%). Subsequently, microbial counts of total mesophilic aerobic bacteria, yeast-mold, lactic acid bacteria, and coliform were performed by inoculating different dilutions (10-2, 10-3, 10-4, and 10-5) of samples onto various agar media.

The results of mold-yeast and lactic acid bacteria counts were considered in determining the optimum treatment conditions of plasma because total mesophilic aerobic bacteria and coliform bacteria were not detected in our numerous attempts to modify inoculation procedure.

For counting total yeast and mold, PDA was prepared, sterilized, and adjusted its pH to ~3.4 by adding a 10% sterile lactic acid solution. Inoculation was performed using the spread plate method and the petri dishes were incubated at 30°C for 72 hours. The microbiological results were expressed as log CFU/g [9]. For the enumeration of lactic acid bacteria (LAB), dilutions were inoculated on MRS, using the spread plate method. After 48 hours of incubation at 30°C, the petri dishes were taken for colony counting. Throughout incubation, the petri dishes were wrapped in a refrigerator bag to create an anaerobic environment. The results were expressed as log CFU/g [9].

3. Results and Discussion

3.1 GAD plasma treatment optimization

The initial mold-yeast count was found to be 6.25 log CFU/g, while lactic acid bacteria were found to be 6.33 log CFU/g. Plasma was applied to olive samples under 15 different conditions according to the Box-Behnken experimental design. The maximum reduction in mold-yeast count, 8%, was observed at 0.7 mL/min gas flow rate, 0.7 cm electrode distance, and 5 min duration and this condition resulted in an 8% reduction in count of lactic acid bacteria. The highest reduction of 11% in lactic acid bacteria was determined after plasma treatment at 0.7 mL/min gas flow rate, 0.5 cm electrode distance, and 3 min. The post-plasma treatment temperatures of the samples were ranged from 24.46 to 30.68°C and indicated that air-GAD plasma as a cold process in food production.

Microbiological analysis results were analyzed using the Minitab 17.0 program and the "Select optimal design" menu to determine the conditions where the mold-yeast quantity was minimized while lactic acid bacteria and temperature were not optimized. Accordingly, the optimum plasma conditions were determined as 0.7 mL/min gas flow rate, 0.5 cm electrode distance, and 5 min treatment time (Table 2).

Table 2. The data for optimum plasma treatment conditions generated with "Select Optimum Design" menu

Gas Flow Rate (mL/min)	Electrode Gap (cm)	Treatment Time(min)	Log CFU/g		Logarithmic Reduction (%)	
			Mold-yeast	Lactic acid bacteria	Mold-yeast	Lactic acid bacteria
0.7	0.5	5	5.44	5.65	13	11

Note: log CFU/g denotes logarithm of Colony Forming Units per gram. The percentages are calculated based on the reduction in microbial counts compared to the initial counts.

The impact of plasma application on microorganisms is complex and influenced by various factors. The high-energy ions, electrons, and radicals generated as a result of plasma induce damage to the cell membrane, DNA, and RNA structures of microorganisms. This can reduce or eliminate the reproductive capabilities of microorganisms. Simultaneously, free radicals can create oxidative stress within cells, potentially leading to cellular death.

4. Conclusion

The results showed that decontamination of Gemlik type black olives using air GAD plasma could be achieved without rising of temperature up 50 °C which would adversely affect food quality. Cold air GAD plasma treatment is a new food processing technology for pre-decontamination of foods either alone or in combination with other preservation methods.

Acknowledgement

In this study, the financial supports were provided by The Scientific and Technological Research Council of Turkey (TUBITAK), Project No. 122O860 and Çankırı Karatekin University Scientific Research Projects Unit, Project No. MF 210621L14. All experimental study were conducted in Çankırı Karatekin University Food Engineering Dept. Research Laboratories.

References

[1] Ashtiani, S. H. M., Rafiee, M., Morad, M. M., Khojastehpour, M., Khani, M. R., Rohani, A., Shokri, B. & Martynenko, A. (2020). Impact of gliding arc plasma pretreatment on drying efficiency and physicochemical properties of grape. *Innovative Food Science and Emerging Technologies, 63*, 102-381.

[2] Dasan, B. G., Onal-Ulusoy, B., Pawlat, J., Diatczyk, J., Sen, Y., & Mutlu, M. (2017). A new and simple approach for decontamination of food contact surfaces with gliding arc discharge atmospheric non-thermal plasma. *Food and Bioprocess Technology, 10(4)*, 650-661.

[3] El Adlouni, C., Tozlovanu, M., Naman, F., Faid, M., & Pfohl-Leszkowicz, A. (2006). Preliminary data on the presence of mycotoxins (ochratoxin A, citrinin and aflatoxin B1) in black table olives "Greek style" of Moroccan origin. *Molecular Nutrition and Food Research, 50(6)*, 507-512.

[4] Franzetti, L., Scarpellini, M., Vecchio, A., & Planeta, D. (2011). Microbiological and safety evaluation of green table olives marketed in Italy. *Annals of Microbiology, 61(4)*, 843-851.

[5] Khalili, F., Shokri, B., Khani, M. R., Hasani, M., Zandi, F., & Aliahmadi, A. (2018). A study of the effect of gliding arc non-thermal plasma on almonds decontamination. *AIP Advances, 8(10)*, 105024.

[6] Laroque, D. A., Seó, S. T., Valencia, G. A., Laurindo, J. B., & Carciofi, B. A. M. (2022). Cold plasma in food processing: Design, mechanisms, and application. *Journal of Food Engineering, 312*, 110748.

[7] Niemira, B. A., & Sites, J. (2008). Cold plasma inactivates Salmonella Stanley and Escherichia coli O157: H7 inoculated on golden delicious apples. *Journal of Food Protection, 71(7)*, 1357-1365.

[8] Onal-Ulusoy, B. (2021). Effects of Cold Atmospheric Gliding Arc Discharge Plasma, Non-thermal Ultrasound, and Low-Temperature Oven Treatments on Quality Parameters of Turkish Blossom Honey. *Food and Bioprocess Technology, 14(9)*, 1763-1771.

[9] Panagou, E.Z. (2006). Greek dry-salted olives: Monitoring the dry-salting process and subsequent physico-chemical and microbiological profile during storage under different packing conditions at 4 and 20 °C. *LWT, 39*, 322–329.

[10] Sen, Y., Onal-Ulusoy, B., & Mutlu, M. (2019). Aspergillus decontamination in hazelnuts: Evaluation of atmospheric and low-pressure plasma technology. *Innovative Food Science and Emerging Technologies, 54*, 235-242.

Effect of microwave heating on technological properties of aquafaba

Saif Jamal Mahdy MAHDY, ***Sezin TUTA ŞİMŞEK****

Faculty of Engineering, Food Engineering Department, Cankiri Karatekin University, Cankiri, Turkiye

Abstract

The production of plant-based food additives for food formulations instead of animal-based proteins gains importance due to change in eating habits, climate change and sustainability. Aquafaba is a plant-based product which is obtained by cooking or canning chickpeas in water and draining chickpea seeds. Functional properties, foaming, emulsifying and gelling, lead to the use of aquafaba as an egg replacer. However, those properties need to improve since the effect of microwave heating on functional properties of aquafaba was investigated in this study. Firstly, aquafaba samples were heated by microwave at 350 W and 600 W and no heated samples were named as control. The foaming expansion, foaming capacity and emulsifying activity index were analysed. To understand the effect of microwave heating on chemical composition, FTIR and XRD analyzes were carried out and SEM analyzes were conducted for morphological analyses. The effect of microwave heating on foaming properties was statistically insignificant ($p>0.05$), which of statistically significant for the emulsifying activity index after 72h ($p<0.05$). FTIR and XRD results showed that saponin structure may have changed after microwave heating. This study showed that promising results can be obtained about the emulsifying properties of aquafaba using moderate microwave heating.

Keywords: *Aquafaba, Microwave, Emulsion*

1. Introduction

Plant-based proteins have received increasing attention to replace animal-based proteins in recent years. Legumes can be compared with animal proteins due to their functional properties. Fat binding, water holding capacity, solubility, gelation, foaming and emulsifying properties lead to replacing animal-based proteins with legume-based proteins. Moreover, sustainability, low price and high production capacity with low allergenicity and high nutrition content support industrial usage of legumes and legume-based proteins [1]. Canning or cooking of legume seeds results in the formation of a solution by draining legume seeds which can be used as a plant-based rheological additive for formulations. This remaining solution, aquafaba, has become a popular food ingredient [2].

Chickpea is the oldest and most used legume in the world and is an important food source in developing countries. Chickpea production was 14.8 million tons in 2017 and this amount is expected to increase to 21 million tons in 2024. Chickpea is one of the most used legumes for aquafaba production. Chickpea is processed in two steps: soaking and blanching (boiling or cooking under pressure). The remaining water which is a waste of frozen chickpea production or canning is an important aquafaba source. Recent studies showed that aquafaba obtained from chickpeas has foaming, emulsifying and gelling properties which means it is a potential egg replacer. However, the foam stability, foam expansion and emulsion activity index of aquafaba are weaker than egg white [3]. This leads to focusing the studies on the improvement of the functional properties of aquafaba using novel technologies. Heat treatment causes a change in functional properties due to secondary structure change with protein denaturation which affects the protein structures of legumes [4]. Ultrasound application to the aquafaba was reported to increase foam expansion, and foam stability and improve the emulsion activity index with better colour and textural properties as stated by Meurer et al. [3]. Alsalman and Ramaswamy [4] reported the effect of high pressure on the carbohydrate quality of aquafaba. Using high pressure strengthened the gel structure, and increased starch digestibility, and starch crystallinity significantly.

Microwaves are one of the novel technologies and electromagnetic waves with wavelengths ranging from 300 MHz to 300 GHz. In the food industry, microwaves are used for drying, sterilization, thawing, defrosting or reheating mostly. In general, domestic and industrial microwave ovens operate at 2450 MHz and 915 MHz, respectively. The direct interaction between electromagnetic waves and food provides faster and volumetric heating [5]. Heating aquafaba by microwave has not been studied or found in the literature. In the present study, the effect of microwave heating on functional, chemical and morphological properties of aquafaba was

* Corresponding author. *e-mail address: sezintuta@karatekin.edu.tr*

investigated. The effect of microwave heating on the functional properties of aquafaba will be important information to be used in industrial applications.

2. Materials and Methods

Aquafaba was obtained by draining chickpeas from commercial canned chickpeas (Tamek, Turkiye). Aquafaba samples of 100 mL were transferred to glass beakers. Microwave heating was conducted at 350 W (MW350) and 600 W (MW600) microwave power for 2 min in a household microwave oven. Untreated aquafaba samples were called as control. The initial temperature of aquafaba samples was 22°C. The final temperatures of aquafaba samples after 2 min microwave heating at 350 W and 600 W were 66.3±0.6°C and 85.7±1.5°C, respectively.

2.1. Foaming expansion and capacity of aquafaba samples

The foaming expansion and capacity of control and mw-treated aquafaba samples were determined according to Meurer et al. [3] with some modifications. Aquafaba samples of 20 mL were transferred to falcon tubes and homogenized by homogenizator (IKA T25, Ultraturrax, China) for 2 min. Foaming expansion was calculated using Eq. 1.

$$Foaming\ expansion\ (\%) = \left(\frac{V_f}{V_i}\right) * 100 \quad (1)$$

where V_f was foam volume (mL) and V_i was initial aquafaba volume (mL). Homogenized aquafaba samples were kept for 10 min and 20 min to determine foaming stability and it was calculated using Eq. 2.

$$Foaming\ stability\ (\%) = \left(\frac{V_i - V_t}{V_i - V_0}\right) * 100 \quad (2)$$

where V_0 was liquid volume of aquafaba at t=0 and V_t was liquid volume after 10 min and 20 min.

2.2. Emulsion stability of aquafaba samples

Control and mw-treated aquafaba samples (20 mL) and sunflower oil (30 mL) were homogenized using homogenizator (IKA T25, Ultraturrax, China) for 2 min at 5 rpm to prepare oil in water emulsions. Emulsions were transferred to the graduated cylinder and kept for 1 h, 24h and 72h [3]. The emulsion activity index was calculated using Eq. 3.

$$Emulsion\ activity\ index\ (\%) = \left(\frac{V_i}{V_t}\right) * 100 \quad (3)$$

where V_i was initial emulsion volume (mL) and V_t was emulsion volume after 1h, 24h and 72h.

2.3. FTIR analysis

FTIR analyses were conducted to determine the chemical structure change of control and mw-treated aquafaba samples. Analyses were conducted between 400 cm^{-1} to 4000 cm^{-1} spectral regions by FTIR (ATR-FTIR, Bruker, Tensor 2 Bruker Optic, Germany).

2.4. XRD analysis

The crystal structures of control and mw-treated aquafaba samples were analyzed using X-Ray diffraction (Bruker, AXS, D8 Advance, USA). Freeze-dried aquafaba samples were compressed 1-2 mm thickness and 13 mm diameter and analyses were conducted at room temperature.

2.5. SEM analysis

The morphological structure of freeze-dried control and microwave-heated aquafaba samples was examined by SEM analysis. The samples, to which a special adhesive was applied to the surface, were analyzed after being coated with gold. Images were obtained at x1000 and x3000 magnifications.

2.6. Statistical analysis

The statistical differences between the foaming properties and emulsion activity index of control and microwave-heated aquafaba were analyzed with the Tukey test ($p = 0.95$).

3. Results and Discussion

3.1. Functional properties of aquafaba samples

Aquafaba contains proteins (0.95 g/100g), carbohydrates (3.61 g/100g), saponins (4.5 mg/100g) and phenolic components which are responsible functional properties of aquafaba [6]. Aquafaba foams due to its albumin,

polysaccharide and saponin content. Foaming occurs thanks to the protein content, remains stable thanks to its carbohydrate content and saponins lead to form air bubbles due to its amphiphilic nature [7]. Foaming expansion and foaming stability of control, MW350 and MW600 aquafaba samples are shown in Figure 1. The differences in foaming expansion and foaming stability of control and microwave-treated aquafaba samples were statistically insignificant ($p>0.05$). The increase in foaming expansion of MW600 was higher than that of control and MW350 (Figure 1-a). The highest foaming stability was observed for MW350 aquafaba samples (Figure 1-b).

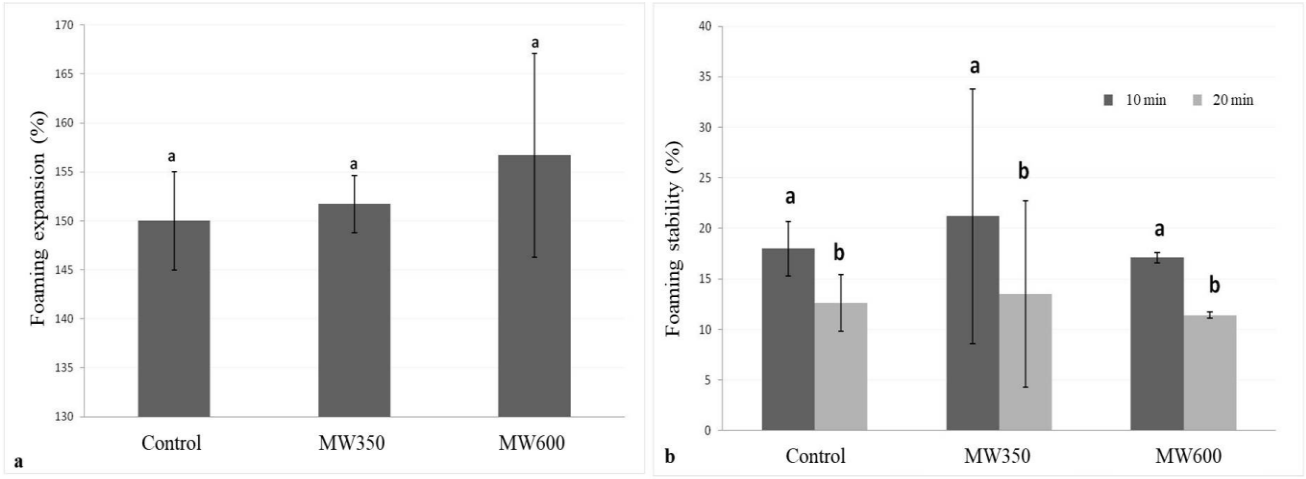

Figure 1. Foaming expansion (a) and foaming stability (b) of control, MW350 and MW600 aquafaba samples.

The emulsion activity index of control, MW350 and MW600 aquafaba samples are shown in Figure 2. No change was observed for the emulsion activity index of control and microwave-heated samples after 1h from emulsion preparation. Statistically significant differences were observed between MW600 and control- MW350 for emulsion activity index after 24h ($p<0.05$). The highest emulsion activity index was observed for MW350 and the lowest was MW600 after 24h. The emulsion activity index decreased over time for all samples. The difference between the emulsion activity index of control and MW350 was statistically insignificant ($p>0.05$). The lowest emulsion activity index was observed in MW600 at the end of 72 hours, the difference between MW350 and MW600 was statistically significant ($p<0.05$). Although statistically insignificant, moderate microwave heating at 350W led to an improvement in emulsifying properties as observed after 24 h and 72h. This may be related to partial denaturation due to temperature increase. The emulsion activity index of aquafaba is the lowest at 600W after 24 and 72 hours. The emulsion activity index decreased with the increase in microwave power. Studies have reported that emulsification and foaming capacity can increase due to improved surface properties of amphiphilic biopolymers by controlled heating of proteins and polysaccharides [8]. The temperature of aquafaba increased to approximately 85°C at 600 W while it was 66°C at 350 W. The greater temperature increment at 600 W may have increased protein denaturation rate, changes in saponins and decreased emulsion activity.

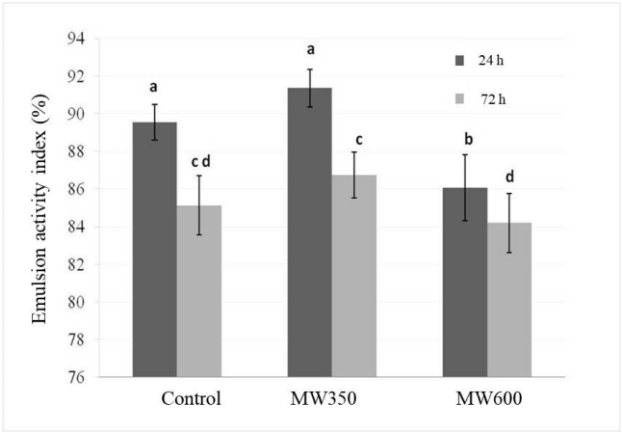

Figure 2. Emulsion activity index of control, MW350 and MW600 aquafaba samples.

3.2. FTIR

The chemical composition of aquafaba was analyzed using FTIR spectrums depicted in Figure 3. In the FTIR spectrum, peaks at ≈1600 cm^{-1}, ≈1500 cm^{-1}, ≈1200 cm^{-1} informed about Amid 1, Amid 2 and Amid 3 protein bands; and peaks at ≈3300 cm^{-1} and ≈3100 cm^{-1} were Amid A and Amid B protein bands [9]. These peaks for control and microwave-heated aquafaba samples were observed at ≈3273 cm^{-1}, ≈2929 cm^{-1} for Amid A, Amid B bands and ≈1642 cm^{-1}, ≈1551 cm^{-1}, ≈1242 cm^{-1} for Amid 1, Amid 2 and Amid 3 protein bands. The intensity of these peaks changed according to aquafaba samples as seen in Figure 3 and the lowest peak density was observed for control and that of the highest for MW350. Amid A and Amid B bands could be related to the water content of samples because hydrogen bonds vibrate in this region and peaks form according to the strength of hydrogen bonds. Ertuğrul et al. [9] reported that heating the pea protein and sugar mixture by microwave led to stronger hydrogen bonds. This may be why the lowest band intensity was observed in Amid A and Amid B regions in the spectrum of unheated aquafaba samples.

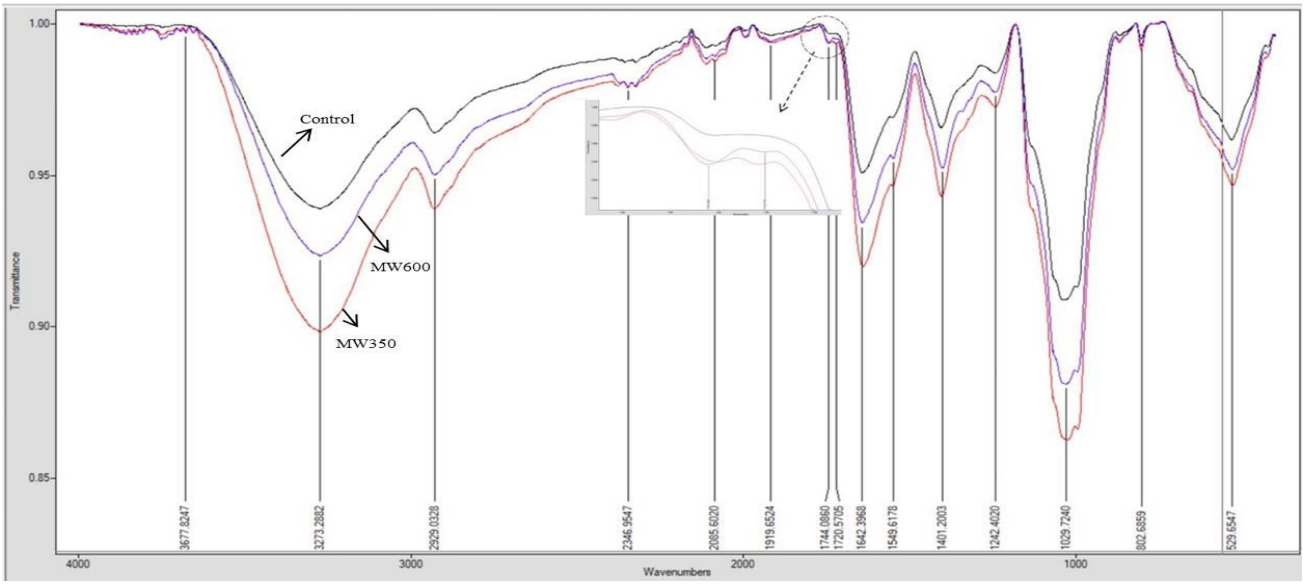

Figure 3. FTIR spectrum of control, MW350 and MW600 aquafaba samples.

Saponins are bioorganic compounds naturally found in plants and contain at least one glycosidic bond between the sapogenin and the sugar chain. Saponins are amphiphilic glycosides that contain lipophilic (steroid, triterpenoid or alkaloid) and one or more hydrophilic oligosaccharides (pentose, hexose, uronic acid), therefore they have surfactant properties [10]. Terpenoid saponins are characteristically observed at 3429 -3316 cm^{-1} (-OH), 2922-2929 cm^{-1} (C-H), 1619-1651 cm^{-1} (C=C) and 1740-1736 cm^{-1} (C=O), 1072-1034 cm^{-1} (C-O-C) in the FTIR spectrum [11]. The differences in IR bands were observed at 1740 cm^{-1} for control and microwave-heated samples as seen in the circled region in Figure 3. The other characteristic saponin peaks may have overlapped in the IR spectrum, but the peaks at 1740 and 1240 cm^{-1} provide information about the aliphatic acetyl group and the acetylation of saponins. The absence of characteristic saponin peaks may have been about acetylation as reported in Amarowicz et al. [12].

3.3. XRD

XRD spectrums of freeze-dried control and microwave-heated aquafaba samples are shown in Figure 4. The spectrums between 0-40° and 15-30° are Figure 4-a and 4-b, respectively. Peaks for control were observed at 27.43°, 31.72°, 45.41°and those of at 27.49°, 28.46°, 31.80°, 45.51° for MW350 and at 27.45°, 28.48°, 31.78°, 45.52° for MW600 as seen in Figure 4-a. Peaks at ≈20° were observed for control and MW600 and peaks at ≈28° split into two for microwave-treated samples in Figure 4-b. Bai et al. [13] associated the peak formation at ≈20° with the crystal region of water-soluble polysaccharides of raw and heat-treated chickpea samples. El Barky and Mohamed [14] extracted and characterized triterpenoid saponins in sea cucumber and examined extracted saponins and standard saponin solution by XRD analysis. Accordingly, they obtained sharp peaks at 31.94° and 45.7° in the extracted saponin. As seen in Figure 4.6-a, the peaks at ≈31° and ≈45° may have informed about the amount of saponin in all three samples. The peak heights observed, especially at ≈31°, are higher in microwave-treated samples. Shi et al. [15] reported that the intensity of the peaks 31° and 45° tended to increase with the increment of NaCl in native potato starch and NaCl mixture. According to this information, the diffraction peaks

at 31° and 45° can also be correlated with the NaCl content of aquafaba due to using NaCl for industrial canning chickpeas. To clearly understand the effect of microwave heating on saponin, a detailed analysis should be carried out additionally.

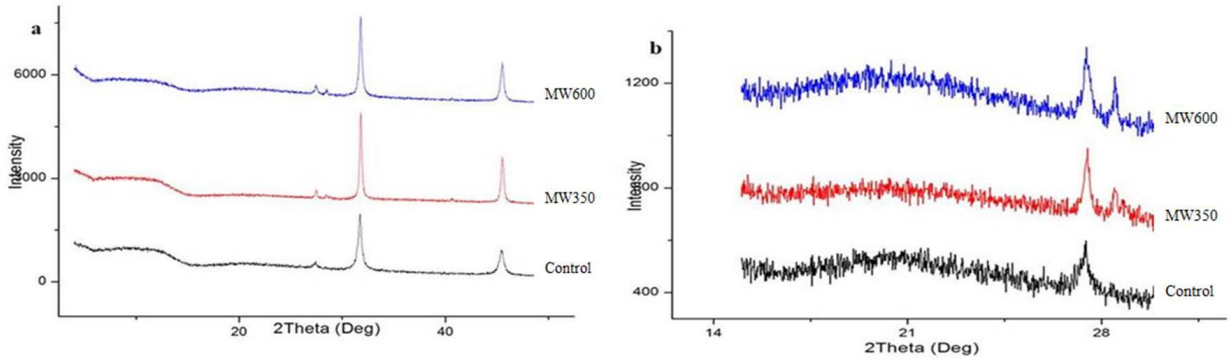

Figure 4. XRD spectrums of control, MW350 and MW600 freeze-dried aquafaba samples.

3.4. SEM

SEM images of freeze-dried control and microwave-heated aquafaba samples with x3000 and x1000 magnifications are shown in Figure 5. The control had a more compact structure and microwave heating deteriorated this compact structure and an increase in microwave power pronounced this deterioration.

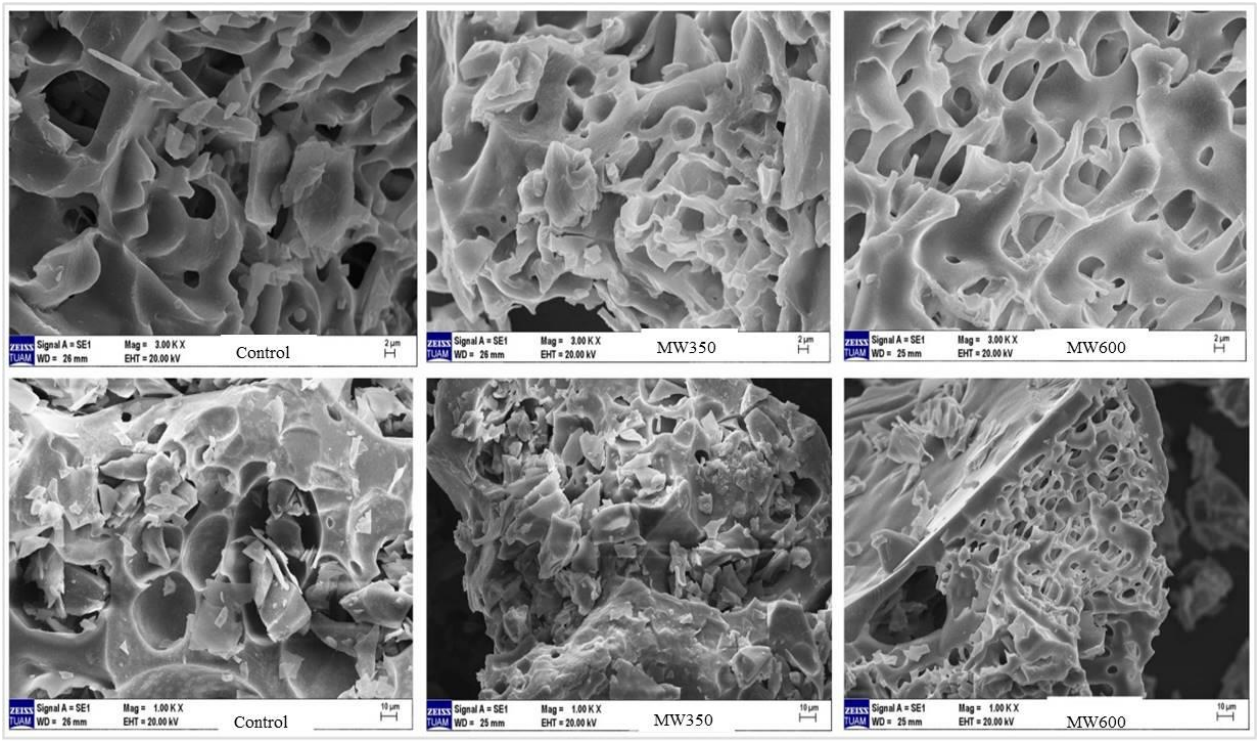

Figure 5. SEM images of freeze-dried aquafaba samples at x3000 (top) and x1000(bottom) magnifications.

4. Conclusion

In this study, the effect of microwave heating on the functional (foaming and emulsification), chemical (FTIR and XRD analysis), and morphological properties (SEM analysis) of aquafaba was evaluated. Microwave heating was observed not to affect the foaming properties of aquafaba at two power levels. The emulsifying properties of aquafaba can be improved by microwave heating. Microwave heating was seen as a potential processing method to improve emulsifying properties, especially at moderate microwave powers. Further studies need to understand microwave heating's effect on the saponin, protein and carbohydrate content of aquafaba.

References

[1] Buhl, T. F., Christensen, C. H., & Hammershøj, M. (2019). Aquafaba as an egg white substitute in food foams and emulsions: Protein composition and functional behavior. *Food Hydrocolloids*, *96*, 354-364.

[2] He, Y., Meda, V., Reaney, M. J., & Mustafa, R. (2021). Aquafaba, a new plant-based rheological additive for food applications. *Trends in Food Science & Technology*.

[3] Meurer, M. C., de Souza, D., Ferreira-Marczak, L. D. (2020). Effects of ultrasound on technological properties of chickpea cooking water (Aquafaba). *Journal of Food Engineering*, 265, 109688.

[4] Alsalman, F. B., & Ramaswamy, H. S. (2021). Evaluation of changes in protein quality of high-pressure treated aqueous aquafaba. *Molecules*, *26*(1), 234.

[5] Tuta, S., & Palazoğlu, T. K. (2016). Finite element modeling of continuous-flow microwave heating of fluid foods and experimental validation. *Journal of Food Engineering*, *192*, 79-92.

[6] Begliyev, H., Yavuz, N., & Ok, S. (2023). Effects of high-pressure homogenization on the rheological properties of spray-dried aquafaba powder. *Journal of Food Process Engineering*, *46*(8), e14389.

[7] Stasiak, J., Stasiak, D. M., & Libera, J. (2023). The potential of aquafaba as a structure-shaping additive in plant-derived food technology. *Applied Sciences*, *13*(7), 4122.

[8] Mustafa, R. & Reaney, M. J. T. (2020). Aquafaba, from food waste to a value-added product. In: Food wastes and by products: Nutraceutical and health potential, R. Campos-Vega, Oomah, B. D., Vergara-Castañeda, H. A. (eds.), pp 93 – 126. New York, Wiley.

[9] Ertuğrul, U., Namli, S., Tas, O., Kocadagli, T., Gokmen, V., Sumnu, S. G. & Oztop, M. H. (2021). Pea protein properties are altered following glycation by microwave heating. *LWT*, 150, 111939.

[10] Das, G., Sharma, A. & Sarkar, P. K. 2022. Conventional and emerging processing techniques for the post-harvest reduction of antinutrients in edible legumes. *Applied Food Research*, 100112.

[11] Ahn, M. S., Jie, E. Y., Song, S. Y., Kim, H. S., Kim, I. J. & Kim, S. W. (2016). Simultaneous estimation of saponin contents from soybean seed using Fourier transform infrared spectroscopy and high-performance liquid chromatography analysis. *Plant Biotechnology Reports*, 10(6), 403-414.

[12] Amarowicz, R., Yoshiki, Y., Pegg, R. B. & Okubo, K. (1997). Presence of two saponins in faba bean (Vicia faba L.) seeds. *Food/Nahrung*, 41(6), 352-354.

[13] Bai, Y. P., Zhou, H. M., Zhu, K. R. & Li, Q. (2022). Impact of thermally induced wall breakage on the structural properties of water-soluble polysaccharides in chickpeas. *International Journal of Biological Macromolecules*, 208, 869-882.

[14] El Barky, A. R. & Mohamed, T. M. (2020). Isolation, Characterization and the Biological Activity of Some Natural Components of Marine Sea Cucumber and Orange Peel. *Biomedical Journal of Scientific and Technical Research*, 27(2), 20554-20565.

[15] Shi, M., Zhang, M., Yang, L., Li, D., Yan, Y., Huang, X., & Liu, Y. (2019). Effect of sodium chloride on the structure and properties of fried starch. *Starch - Stärke*, *71*(9-10), 1900014.

Molecular Docking Study against Human Lactate Dehydrogenase A Enzyme of Some Phenoxy Chalcones

Mohamed Ab. Khalifa IBRAHIM [1,*], ***Zeyad Adil Hameed HAMEED*** [2], ***Şevki ADEM*** [3]

[1] *Department of Chemistry Sciences, School of Natural and Applied Sciences, Çankiri Karatekin University, Libya*

[2] *Department of Chemistry Sciences, School of Natural and Applied Sciences, Çankiri Karatekin University, Iraq*

[3] *Department of Chemistry Sciences, School of Natural and Applied Sciences, Çankiri Karatekin University, Turkey*

Abstract

Human lactate dehydrogenase A (hLDHA), aglycolytic enzyme responsible for the conversion of pyruvate to lactate coupled with oxidation of NADH to NAD+ , plays a crucial role in the promotion of glycolysis in invasive tumorcells. Recently, hLDHA has been considered a vital therapeutic target for invasive cancers. Selective inhibition of hLDHA using small molecules holds potential prospects for the treatment of cancer and associated diseases. Consequently, significant progress has been made in the discovery of selective smallmolecule hLDHA inhibitors displaying remarkable inhibitory potencies. Molecular docking studies using Molegro Virtual Docker (MVD) provided insights into the binding affinity and interactions of the selected compounds with the Human Lactate Dehydrogenase A enzyme. Results and discussions revealed that several Phenoxy Chalcones, including 5a, 5e, 5f, 5d, 5c, 5g, 5b, 4e, 4g, 4d, 4c, 4f, 4a , and 4b, demonstrated significant affinity potantials on Human Lactate Dehydrogenase A enzyme activity. In this study Molecular docking analysis of designed molecules with hLDHA (PDB ID: 4AJP) demonstrates that VAL30, THR 247 , GLN 99 , TYR 82 , GLY 31, ARG98 , ASN 137 , ARG 105 , and VAL 52 possessed strong interaction with the compounds. Notably, compounds 5a, 5e, 5f, 5d, exhibited strong binding affinity with key amino acids, inhibiting the enzyme's activity. In this study contributes to the understanding of the Phenoxy Chalcones potential, benefits of specific in modulating Human Lactate Dehydrogenase Aenzyme activity .The inhibitory effects of the selected compounds suggest their potential as valuable therapeutic agents for conditions associated with Human Lactate Dehydrogenase A deficiency.

Keywords: *Lactate dehydrogenase A, Phenoxy chalcones, Docking study*

1. Introduction

Cancer cells rely on an enhanced rate of glycolysis, which ferments glucose into lactate, even under aerobic conditions. Otto Warburg observed the metabolic switch from oxidative phosphorylation (OXPHOS) toward aerobic glycolysis, which was initially thought to be caused by a mitochondrial defect [1] . Cancer cells present largely different bioenergetics than normal cells and are dependent on an enhanced rate of tumor glycolysis [2] . Cancer cell metabolism, specifically tumor glycolysis, has emerged as a unique cancer phenotype due to higher consumption of glucose resulting in higher lactate production in cancer cells than in normal cells even under normoxic conditions. Consequently, tumor glycolysis creates acidosis in the extracellular matrix, which facilitates tumor initiation, progression, invasion, and metastasis [3] . Enhanced rate of tumor glycolysis in cancer cells ensures their high energy and metabolite demand, resulting in excess lactate and H+ ion production, which is then transported outside the cell by MCT enzymes and establishes the lactate flux[4−6]. A very close association between cancer cell metabolism and cancer stemness was also established [7]. Cancer cells represent common characteristic features such as an enhanced rate of aerobic glycolysis, a higher rate of glucose consumption and lactate production, and an increased rate of extracellular acidosis, which can be exploited for drug development [8−11]. Therefore, tumor glycolysis is considered a novel target in search of better cancer treatment options.

2. Materials and Methods

Computational chemistry or as known as molecular modeling is a fascinating branch of chemistry. It uses modeling and virtual simulations to help solve chemistry modern problems. Lately, virtual screening of compound libraries has become a standard technology in modern drug discovery pipelines. In our study, to perform in-silico specific site docking, we used a powerful bioinformatics tool; Docking. In order to visualize the data, we utilized Molegro Virtual Docker

* Corresponding author. *e-mail address: Ma.Kik@yahoo.com*

2.1-Molecular docking

X-ray crystal structures of proteins were obtained from ProteinDataBank for docking studies. Crystal structures with ID number 4AJP for Human lactate dehydrogenase A (hLDHA) were selected. Using the protein preparation tool of the Molegro Virtual Docker software, crystalline water molecules were taken, and missing amino acid residues were modified. The 3D conformations of the ligands to be docked were prepared and optimized on the MarvinSketch, and imported to docking software using import molecules tool. The coordinates of the ligand in the crystalline structure were chosen as the centers of the regions to interact with the molecules. Before docking, redocking was done with a crystalline ligand. The protocol with an RMSD value below two was selected for docking. The center coordinates of binding site were determined as X:4.95, Y:9.46, Z:17.94 for hLDHA. Ten docking runs were enforced for each ligand, and the best pose results were taken to evaluate the interaction diagrams. This protocol was used in subsequent docking studies. The docking results with the best scores were determined and their 2D interaction details were shown with the Discovery Studio 2021 Client software.

3. Results and Discussion

In this part, the most compounds were selected with Human Lactate Dehydrogenase A Enzyme , and we can see Human Lactate Dehydrogenase A Enzyme in the Figure 1. These complexes can be seen in the Table 1 and figure 2, and we will learn about them in detail in the next steps.

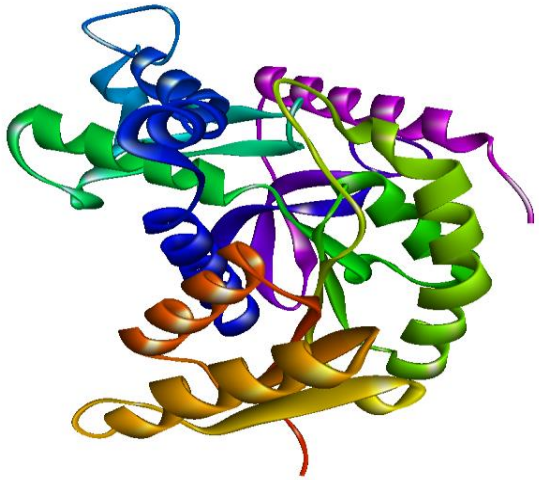

Figure 1. Human Lactate Dehydrogenase A structure

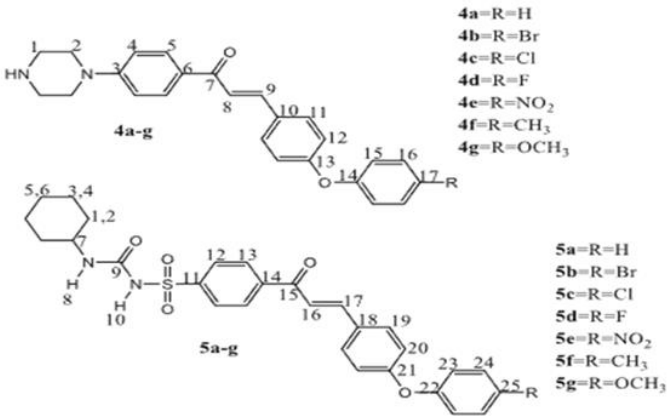

Figure 2. Synthetic pathway of phenoxy chalcones (4a-4g) and (5a-5g)

Table 1. Presentation of findings and concluding remarks

Ligand name	Ligand Codes	MolDockScore	HBond
(E)-N-(cyclohexylcarbamoyl)-4-(3-(4-phenoxyphenyl)acryloyl)benzenesulfonamide	5a	-197.781	-10.5125
(E)-N-(cyclohexylcarbamoyl)-4-(3-(4-(4-nitrophenoxy)phenyl)acryloyl) benzenesulfonamide	5e	-192.888	-10.9774
E)-N-(cyclohexylcarbamoyl)-4-(3-(4-(p-tolyloxy)phenyl)acryloyl)benzenesulfonamide	5f	-189.746	-8.30703
(E)-N-(cyclohexylcarbamoyl)-4-(3-(4-(4-fluorophenoxy)phenyl)acryloyl)benzenesulfonamide (5	5d	-183.627	-6.76428
(E)-4-(3-(4-(4-chlorophenoxy)phenyl)acryloyl)-N(cyclohexylcarbamoyl)benzensulfonami	5c	-180.661	-4.66241
(E)-N-(cyclohexylcarbamoyl)-4-(3-(4-(4-methoxyphenoxy)phenyl) acryloyl)benzenesulfonamide	5g	-179.495	-9.46268
(E)-4-(3-(4-(4-bromophenoxy)phenyl)acryloyl)-N(cyclohexylcarbamoyl)benzensulfonamide	5b	-169.868	-1.72758
(E)-3-(4-(4-nitrophenoxy)phenyl)-1-(4-(piperazin-1-yl)phenyl)prop2-en-1-one	4e	-159.996	-4.62272
(E)-3-(4-(4-methoxyphenoxy)phenyl)-1-(4-(piperazin-1-yl)phenyl) prop-2-en-1-one	4g	-155.908	-3.84334
(E)-3-(4-(4-fluorophenoxy)phenyl)-1-(4-(piperazin-1-yl)phenyl)prop2-en-1-one	4d	-148.138	-5.967
(E)-3-(4-(4-chlorophenoxy)phenyl)-1-(4-(piperazin-1-yl)phenyl)prop2-en-1-one	4c	-145.004	-3.0607
(E)-1-(4-(piperazin-1-yl)phenyl)-3-(4-(p-tolyloxy)phenyl)prop-2-en1-one	4f	-144.613	-2.98174
(E)-3-(4-phenoxyphenyl)-1-(4-(piperazin-1-yl)phenyl)prop-2-en1-one	4a	-143.227	-5.09298
(E)-3-(4-(4-bromophenoxy)phenyl)-1-(4-(piperazin-1-yl)phenyl)prop2-en-1-one	4b	-139.964	-2.263

Docking studies were conducted to investigate the inhibitory mechanism, revealing a robust binding affinity (MolDock score: -197.781) between the compound 5a and the Human Lactate Dehydrogenase A enzyme. Figure 3 depicts a 2D interaction map, elucidating the specific interactions between 5a and the enzyme's amino acids. Notably, hydrogen bond interactions emerged as vital contributors to the binding process, facilitated by, VAL30, GLY31, THR 247, ARG 98, and GLN 99 And it interact with van der waals with ARG105, ILE 241, LEU108 ALA97, SER 136, ASN 112, ALA237, VAL135, THR 94, GLY28, VAL 27, ILE 115, GLY 26, TYR82, VAL25, VAL50, ASP51. also interact with carbon hydrogen bond with ALA29, GLY96. and pi-alkyl with ILE119, ALA95, VAL52 amino acids. These interactions stabilize the binding and intensify the inhibitory effects. Additionally, the presence of red separating interactions suggests the displacement of water molecules from the enzyme's active site. Consequently, this leads to a conformational change and disruption of the catalytic activity of the enzyme. Hence, 5a obstructs the normal functioning of the Human Lactate Dehydrogenase A enzyme by binding to its active site. The potent inhibitory effects of 5a on Human Lactate Dehydrogenase A enzyme are attributed to its high binding affinity, with hydrogen bond interactions and the displacement of water molecules playing pivotal roles. These findings offer valuable insights for the development and design of potential therapeutic agents aimed at addressing diseases associated with Human Lactate Dehydrogenase A enzyme deficiency.

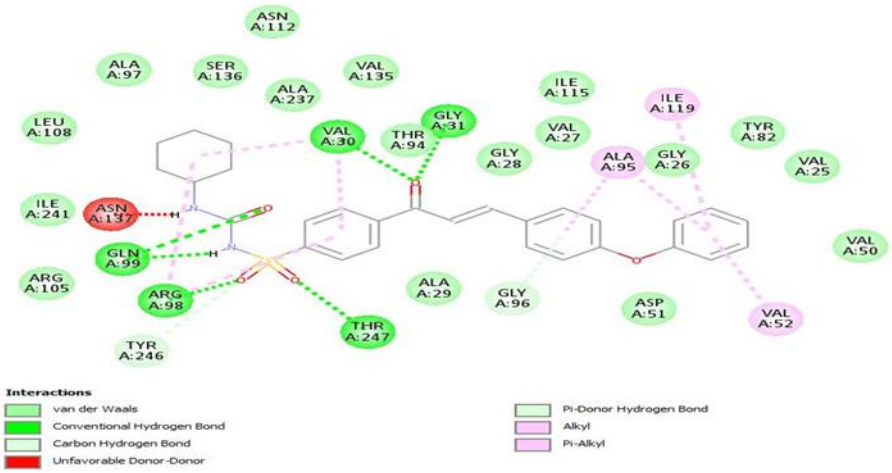

Figure 3. Two-dimensional structures in the 5a compound have been investigated

Docking studies were conducted to investigate the inhibitory mechanism, revealing a robust binding affinity (MolDock score: -192.888) between the compound 5e and the Human Lactate Dehydrogenase A enzyme. Figure 4 depicts a 2D interaction map, elucidating the specific interactions between 5e and the enzyme's amino acids. Notably, hydrogen bond interactions emerged as vital contributors to the binding process, facilitated by TYR 82, GLY 31, VAL30, ARG98, ASN 137 And THR 247, And it interact with van der waals with LEU164, ARG168, ALA29, THR 94, GLY25, VAL25, PHE118, ILE119, ILE115, ILE 241, GLN99, ARG105, ARG168, LEU164. also interact with carbon hydrogen bond with TYR246, GLY28 , GLY96 . and pi-alkyl with ILE251, ALA95, VAL52, HIS192, ALA237. And interact with pi-Anion with ASI 51. amino acids. These interactions stabilize the binding and intensify the inhibitory effects. Additionally, the presence of red separating interactions suggests the displacement of water molecules from the enzyme's active site. Consequently, this leads to a conformational change and disruption of the catalytic activity of the enzyme. Hence, 5e obstructs the normal functioning of the Human Lactate Dehydrogenase A enzyme by binding to its active site. The potent inhibitory effects of 5e on Human Lactate Dehydrogenase A enzyme are attributed to its high binding affinity, with hydrogen bond interactions and the displacement of water molecules playing pivotal roles. These findings offer valuable insights for the development and design of potential therapeutic agents aimed at addressing diseases associated with Human Lactate Dehydrogenase A enzyme deficiency.

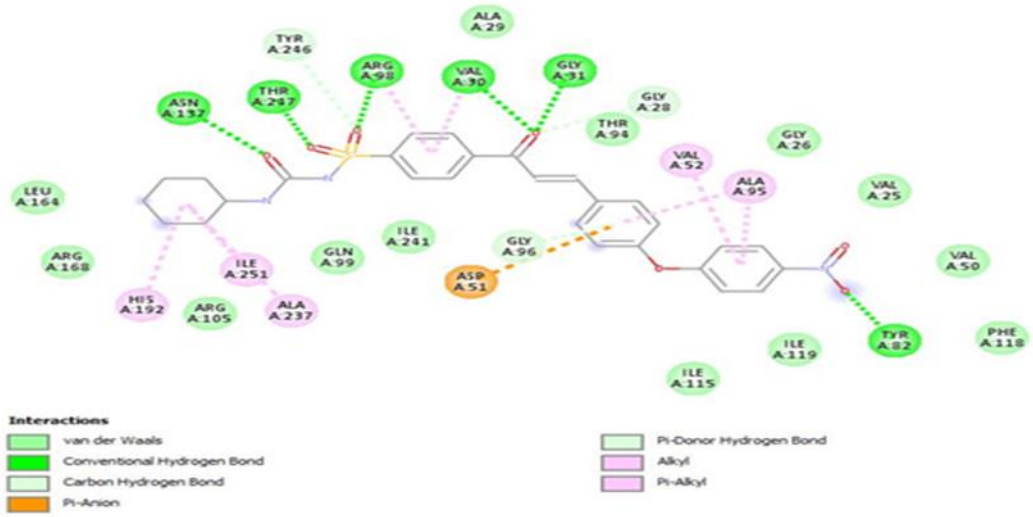

Figure 4. Two-dimensional structures in the 5e compound have been investigated

Docking studies were conducted to investigate the inhibitory mechanism, revealing a robust binding affinity (MolDock score: -189.746) between the compound 5f and the Human Lactate Dehydrogenase A Enzyme. Figure 5 depicts a 2D interaction map, elucidating the specific interactions between 5f and the enzyme's amino acids. Notably, hydrogen bond interactions emerged as vital contributors to the binding process, facilitated by ARG

105, GLN99, ASN137 and THR 247. And it interact with van der waals with ILE53, ILE119, GLY31, GLY 28, THR94V, ARG168, ALA29, ILE241, ALA237, ILE251, VAL135, LEU164, ASN112, ALA97 , GLY96, VAL27, GLY26. also interact with carbon hydrogen bond with SER136. and pi-alkyl with ARG 98, VAL30, ALA95, VAL52. And interact with pi-Anion with ASI 51, HIS 192. amino acids. These interactions stabilize the binding and intensify the inhibitory effects. Additionally, the presence of red separating interactions suggests the displacement of water molecules from the enzyme's active site. Consequently, this leads to a conformational change and disruption of the catalytic activity of the enzyme. Hence, 5f obstructs the normal functioning of the Human Lactate Dehydrogenase A Enzyme by binding to its active site. The potent inhibitory effects of 5f on Human Lactate Dehydrogenase A Enzyme are attributed to its high binding affinity, with hydrogen bond interactions and the displacement of water molecules playing pivotal roles. These findings offer valuable insights for the development and design of potential therapeutic agents aimed at addressing diseases associated with Human Lactate Dehydrogenase A Enzyme deficiency.

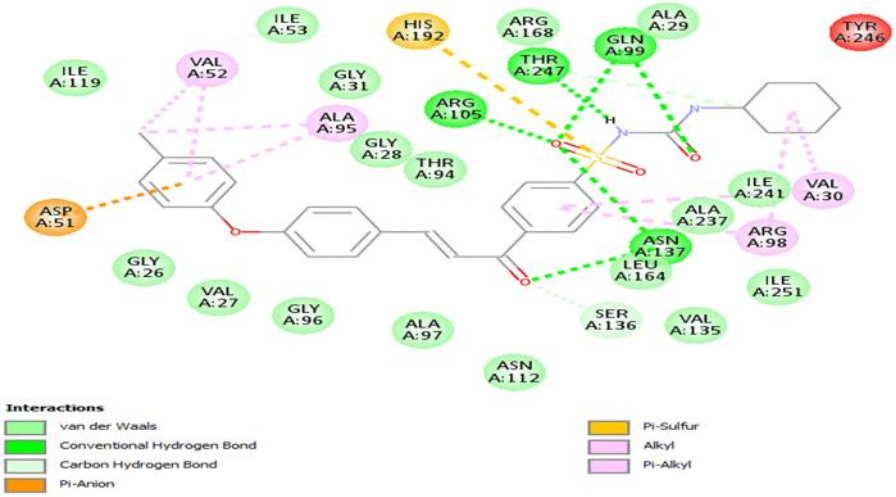

Figure 5. Two-dimensional structures in the 5e compound have been investigated

Docking studies were conducted to investigate the inhibitory mechanism, revealing a robust binding affinity (MolDock score: -183.627) between the compound 5d and the Human Lactate Dehydrogenase A Enzyme. Figure 6 depicts a 2D interaction map, elucidating the specific interactions between 5d and the enzyme's amino acids. Notably, hydrogen bond interactions emerged as vital contributors to the binding process, facilitated by VAL 52, ASN137 and THR 247 and it interact with van der waals with TYR246, GLN99, ARG105, VAL135, ALA29, THR94, GLY26, VAL 27, ILE 251 . also interact with carbon hydrogen bond with GLY28, SER136, ILE251, TYR82, PHE118. and pi-alkyl with ILE119, ALA95, VAL30, ARG98, ILE241. And interact with pi-donerhydrogen bond ASP51, GLY96. in additon it react with halogen(flouorine) with ILE115, amino acids. These interactions stabilize the binding and intensify the inhibitory effects. Additionally, the presence of red separating interactions suggests the displacement of water molecules from the enzyme's active site. Consequently, this leads to a conformational change and disruption of the catalytic activity of the enzyme. Hence, 5d obstructs the normal functioning of the Human Lactate Dehydrogenase A Enzyme by binding to its active site. The potent inhibitory effects of 5d on Human Lactate Dehydrogenase A Enzyme are attributed to its high binding affinity, with hydrogen bond interactions and the displacement of water molecules playing pivotal roles. These findings offer valuable insights for the development and design of potential therapeutic agents aimed at addressing diseases associated with Human Lactate Dehydrogenase A Enzyme.

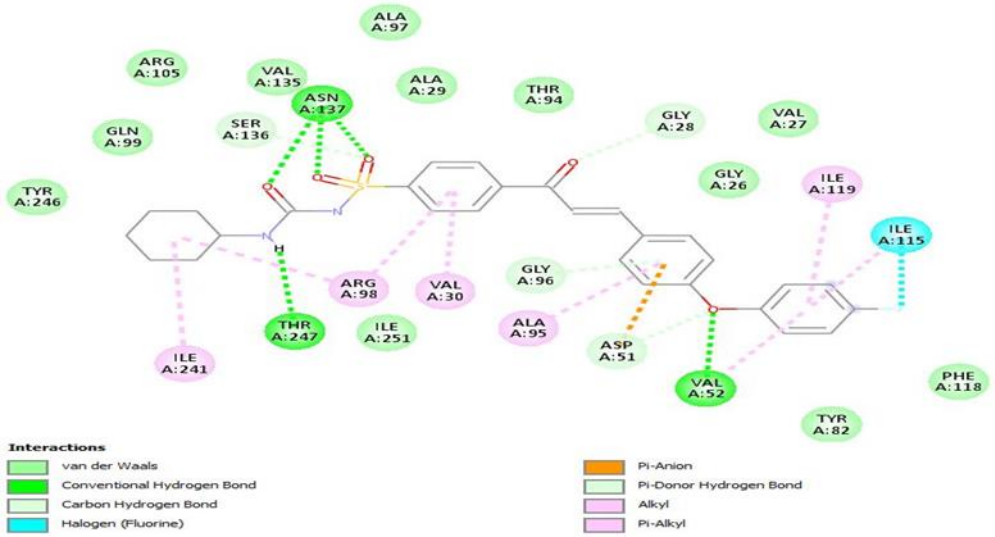

Figure 6. Two-dimensional structures in the 5d compound have been investigated.

4. Conclusion

In normal cells, pyruvate is converted into lactate by LDHA, which is overexpressed in most cancer cells and stem cells. This enzyme is strongly correlated with cancer initiation, development, invasion, angiogenesis, and metastasis. LDHA has shown therapeutic potential in preclinical studies, with its inhibition resulting in significant anti-proliferative effects in several cancer cells, including breast, prostate, and pancreatic cancer. A new series of Phenoxy Chalcones central scaffold based small molecules 5a, 5e, 5f, 5d, 5c, 5g, 5b, 4e, 4g, 4d, 4c, 4f, 4a , and 4b were synthesized and screened for hLDHA inhibitory activities. In silico binding affinity of these compounds was calculated against the hLDHA enzyme.The hLDHA inhibitory activities showed that compounds 85a, 5e, 5f, and 5d, have adequate inhibitory activities, which are consistent with an in silico study. Molecular docking studies depicted that the VAL30, THR 247 , GLN 99 , TYR 82 , GLY 31, ARG98 , ASN 137 , ARG 105 , and VAL 52 , amino acids of hLDHA strongly interacted with compounds through hydrogen bonding and electrostatic and hydrophobic interaction, which might play important roles in inhibitory activities.

References

[1] Warburg, O. On the origin of cancer cells. Science 1956, 123, 309−314.
[2] Hanahan, D.; Weinberg, R. A. Hallmarks of cancer: The next generation. Cell 2011, 144, 646−674.
[3] Martinez-Outschoorn, U. E.; Peiris-Pagés, M.; Pestell, R. G.; Sotgia, F.; Lisanti, M. P. Cancer metabolism: A therapeutic perspective. Nat. Rev. Clin. Oncol. 2017, 14, 11−31.
[4] Kumar, V.; Rani, R. Lactate dehydrogenase enzyme: An old enzyme but new viable target offers new hope in cancer therapeutics. Lactate Dehydrogenase (LDH): Biochemistry, Function and Clinical Significance 1.
[5] Sharma, D.; Singh, M.; Rani, R. Role of LDH in tumor glycolysis: Regulation of LDHA by small molecules for cancer therapeutics. Semin. Cancer Biol. 2022, 87, 184−195.
[6] Sharma, D.; Singh, M.; Gupta, R.; Kumar, V.; Kumar, V.; Rani, R. Intervention on lactate in cancer: A promising approach for the development of cancer therapeutics. Adv. Cancer Biol.: Metastasis 2022, 5, 100058.
[7] Intlekofer, A. M.; Finley, L. W. S. Metabolic signatures of cancer cells and stem cells. Nat. Metab. 2019, 1, 177−188.
[8] Menendez, J. A.; Alarcón, T. Metabostemness: A new cancer hallmark. Front. Oncol. 2014, 4, 262.
[9] Jagust, P.; De Luxán-Delgado, B.; Parejo-Alonso, B.; Sancho, P. Metabolism-based therapeutic strategies targeting cancer stem cells. Front. Pharmacol. 2019, 10, 203.
[10] Kumar, V.; Rani, R. Selective inhibitors of human lactate dehydrogenase A to fight against metabolic cancer: a patent landscape. Pharm. Pat. Anal. 2020, 9, 155−157.
[11] Singh, M.; Afonso, J.; Sharma, D.; Gupta, R.; Kumar, V.; Rani, R.; Baltazar, F.; Kumar, V. Targeting Monocarboxylate Transporters (MCTs) in cancer: How close are we to the clinics? Semin. Cancer Biol. 2023, 90, 1−14.
[12] Morris GM, Huey R, Lindstrom W, et al. AutoDock4 and AutoDockTools4: automated docking with selective receptor flexibility.J Comput Chem. 2009;30:2785-2791.

Tyrosinase Inhibitors: Uncovering Tyrosinase Inhibitors In Vitro for Skin Hyperpigmentation Management

Zeyad Adil Hameed HAMEED [1,*], ***Bedriye Seda KURŞUN AKTAR*** [2], ***Şevki ADEM*** [3]

[1] *Department of Chemistry Sciences, School of Natural and Applied Sciences, Çankiri Karatekin University, Iraq*

[2] *Department of Hair Care and Beauty Services, Yesilyurt Vocational School, Malatya Turgut Özal University, Malatya, Turkey*

[3] *Department of Chemistry Sciences, School of Natural and Applied Sciences, Çankiri Karatekin University, Turkey*

Abstract

Tyrosinase has attracted a lot of interest as a potential inhibitor target since it is an enzyme that plays an important role in human melanogenesis as well as in the enzymatic browning of fruits and fungi. Complex chemical and enzymatically catalysed events are involved in melanogenesis, the process that leads to melanin synthesis. The purpose of this research is to find tyrosinase inhibitors in both natural and manmade compounds. Also discussed are the possible medicinal uses of these inhibitors in avoiding fruit enzymatic browning and skin hyperpigmentation, two undesirable results. Synthetic compounds (5d, 5e, 5f, and 5g) were tested for their inhibitory effect on mushroom tyrosinase using a microtiter plate reader. Compounds 5d, 5e, 5f, and 5g exhibited inhibitory effects on tyrosinase activity, and the results showed that the inhibition was concentration dependent. Additional information on the binding sites of these synthetic compounds with the tyrosinase active site was gleaned from molecular docking experiments. The inhibitory effects of compound 5d were highlighted using enzyme activity testing and visual depictions, indicating its potential as a tyrosinase inhibitor. To highlight the inhibitory mechanism, a two-dimensional interaction map was used to demonstrate critical hydrogen bond interactions with certain amino acids. There was a concentration-dependent reduction in tyrosinase activity when compounds 5e, 5f, and 5g were tested. Important hydrogen bond interactions were highlighted in the interaction maps, suggesting that the chemicals may be able to stabilise binding and increase inhibitory effects. Our research adds to the growing body of knowledge on potential new tyrosinase inhibitors for use in skin lightening and antibrowning foods. The research highlights the need of studying the molecular interactions between tyrosinase and synthetic inhibitors in order to create anti-hyperpigmentation medicines that work. To confirm these chemicals' medicinal potential, further study may include in vivo tests and clinical trials.

Keywords: *Skin hyperpigmentation, Tyrosinase, Activity enzyme*

1. Introduction

Because tyrosinase is essential for both human melanogenesis and the enzymatic browning of fruits or fungi, tyrosinase inhibitors have occupied much attention over the last few decades. The term "melanogenesis" refers to the series of events that culminate in the creation of melanin, a kind of dark macromolecular pigment. Chemical and enzymatically catalysed processes work together to produce melanin [3] and [4] have recently updated the biosynthetic route for melanin synthesis in numerous living forms, which was first revealed by [1] and [2]. Tyrosinase catalyses the first stage of tyrosine oxidation to dopaquinone, which initiates melanogenesis. Melanin production is limited by this first step since, at physiological pH values, the rest of the reaction cascade may continue spontaneously [5]. The auto-oxidation process transforms the following dopaquinone into dopa and dopachrome. Tyrosinase may oxidise dopa to dopaquinone, which is another substrate of the enzyme. The final result of the dopachrome synthesis, eumelanin, is generated via a sequence of oxidation reactions involving dihydroxyindole (DHI) and dihydroxyindole-2-carboxylic acid (DHICA). The presence of glutathione or cysteine causes dopaquinone to be transformed to glutathionyldopa or cysteinyldopa, respectively. After that, pheomelanin is created. Allomelanin is the name given to "melanin" that does not include tyrosine but does contain phenolic monomers, such as eumelanin or pheomelanin. In a similar vein to melanogenesis, oxidative polymerization is often associated with the browning process in fungi and fruits. Allomelanin differs primarily in that it is built on various quinoid building blocks rather than dopaquinone-derived motifs, which are the major monomers in its structure. An essential function of melanin is to shield the skin from the sun's damaging ultraviolet (UV) rays. Our phenotypic look is also determined by melanin. While melanin primarily serves as a sun protection factor for human skin, an excess of melanin in certain areas, leading to darker patches, might be considered an aesthetic issue. Furthermore, it is not desired for fresh fruits, drinks, veggies, and mushrooms to undergo enzymatic

* Corresponding author. *e-mail address: zeyad95adil@gmail.com*

browning [6]. After harvest, browning happens to many crops, including mushrooms, lowering their market value. Enzymatic browning of fruits and hyperpigmentation of human skin are both undesirable outcomes. These findings have prompted scientists to look for novel, highly effective tyrosinase inhibitors for application in food antibrowning and skin lightening products. While previous reviews have addressed certain tyrosinase inhibitors [7-9], this article provides a summary of recently identified tyrosinase inhibitors derived from both natural and synthetic sources. Conversely, there has been tremendous advancement in our understanding of melanocyte biology and the mechanisms behind melanin formation in recent years, which has led to new opportunities in the pharmacologic treatment of skin hyperpigmentation. There are various ways to treat hyperpigmentation, such as blocking tyrosinase catalytic activity, tyrosinase mRNA transcription, tyrosinase glycosylation, maturation, degradation, transfer, and inflammation-induced melanogenic response, skin turnover, and interference with melanosome maturation and transfer. In light of this, several studies have thoroughly examined a plethora of depigmenting or whitening chemicals created using these different methods [10–16]. Therefore, these directed methods for treating hyperpigmentation are not included in this study.

2. Materials and Methods

According to earlier reports, we used a microtiter plate reader to detect the inhibitory activity of the mushroom tyrosinase enzyme at 492 nm [18]. Enzyme activity test reaction medium (250 mL) included 100 mL of various chemical concentrations in addition to 0.5 mM L-DOPA in 50 mM phosphate buffer (PH 6.8). The reaction was carried out for 7 minutes at a temperature of 37 °C. The chemicals were diluted to the appropriate concentration after dissolving in 1 mg/mL DMSO. Every time, we ran the controls without inhibitors but with DMSO in the reaction medium. The IC50 values, which represent the doses at which an inhibitory effect on tyrosinase activity was seen, were used to express the compounds' inhibitory effects. A molecular docking investigation was conducted using the Molegro Virtual Docker programme to try to understand the likely binding positions of the synthetic chemicals with the tyrosinase active site [19]. Access to the X-ray crystal structure of tropolone-cocrystallized tyrosinase from Agaricus bisporus (2Y9X)[17] was made possible via the RCSB Protein Data Bank. The MarvinSketch programme was used to build the 3D models of compounds 5d, 5f, 5e, and 5g. After importing the protein into Molegro Virtual Docker, the crystal structure was water-extracted and optimised to fill in any amino acid gaps in preparation for docking. By calculating all of the coordinates to tropolone, the binding site for tiny compounds might be characterised. For each molecule, ten docking experiments were run. Then, the conformations that scored the highest were chosen to investigate the interaction details in the Discovery Studio 2021 Client.

3. Results and Discussion

The symbols used in this study and the findings for these samples are shown in Table 1.

Table 1. Discloses the signals used and the outcomes of the sample

Compounds	Results μM
5d	76.170
5e	36.290
5f	203.867
5g	36.674

In theory, 5d may be utilised to treat pathological disorders like obesity that are associated with tyrosinase enzyme activity, as it has been shown to inhibit tyrosinase enzyme activity. Visualising the relationship between enzyme activity % and 5b concentration, Figure 1 provides a thorough explanation of the activity. The graph clearly shows that the enzyme tyrosinase's activity diminishes as the amount of 5d rises. Figure 2 shows a two-dimensional interaction map that shows the particular interactions of 5d with the amino acids of the enzyme. Amino acids MET 257 all played important roles in hydrogen bond interactions, which are essential for binding. These interactions stabilise the binding and enhance the inhibitory effects. Also, when you see red separation contacts, it means that water molecules have left the enzyme's active site. The enzyme undergoes a conformational shift and subsequently ceases to catalyse processes. For that reason, 5d inhibits tyrosinase activity.

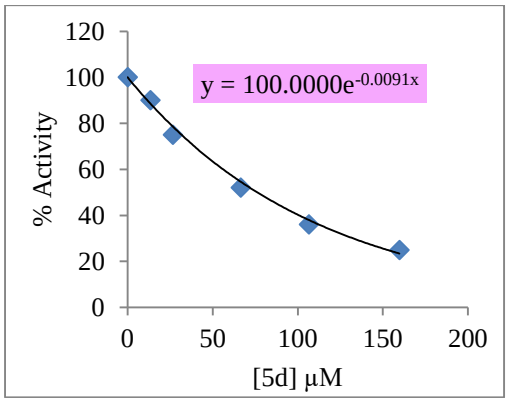

Figure 1. Minimise 5d tyrosinase enzyme activity

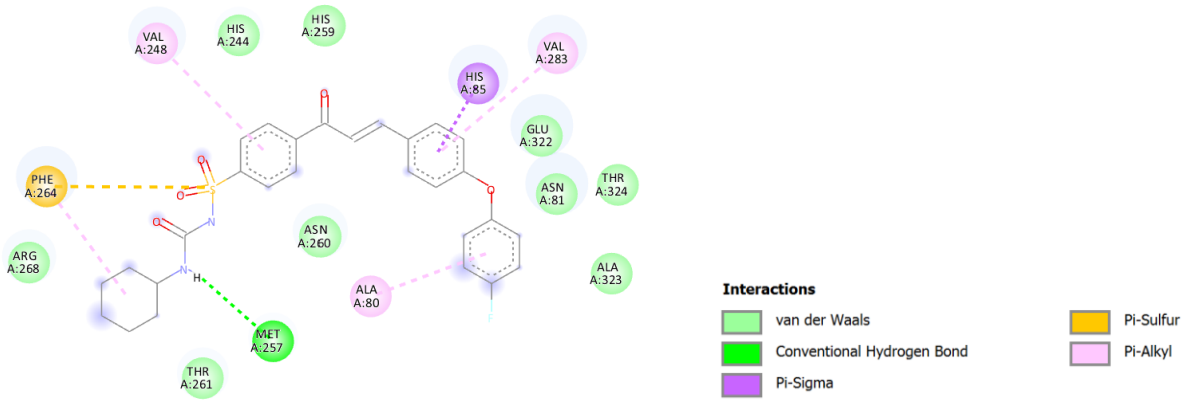

Figure 2. The tyrosinase enzyme and the 5d molecule's two-dimensional structures

In theory, 5e may be utilised to treat pathological disorders like obesity that are associated with tyrosinase enzyme activity, as it has been shown to inhibit tyrosinase enzyme activity. Visualising the relationship between enzyme activity % and 5e concentration, Figure 3 provides a thorough explanation of the activity. The graph clearly shows that the enzyme tyrosinase's activity diminishes as the amount of 5e rises. Figure 4 shows a two-dimensional interaction map that shows the particular interactions of 5e with the amino acids of the enzyme. Amino acids ARG 268, HIS 85 and GLU 322 all played important roles in hydrogen bond interactions, which are essential for binding. These interactions stabilise the binding and enhance the inhibitory effects. Also, when you see red separation contacts, it means that water molecules have left the enzyme's active site. The enzyme undergoes a conformational shift and subsequently ceases to catalyse processes. For that reason, 5e inhibits tyrosinase activity.

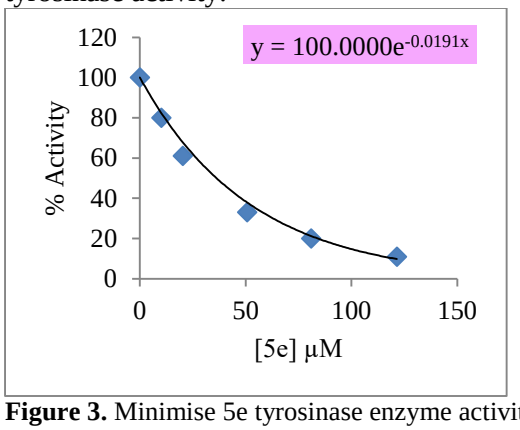

Figure 3. Minimise 5e tyrosinase enzyme activity

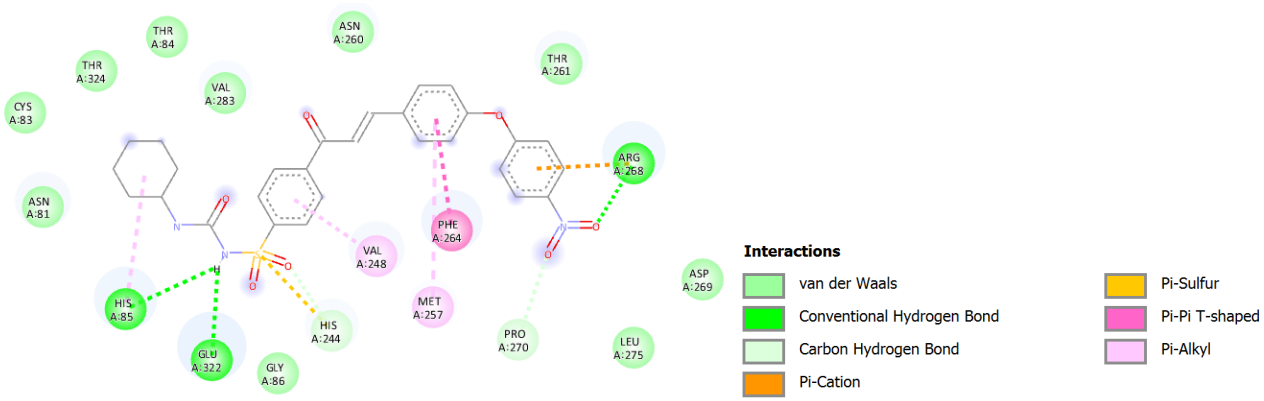

Figure 4. The tyrosinase enzyme and the 5e molecule's two-dimensional structures

In theory, 5f may be utilised to treat pathological disorders like obesity that are associated with tyrosinase enzyme activity, as it has been shown to inhibit tyrosinase enzyme activity. Visualising the relationship between enzyme activity % and 5f concentration, Figure 5 provides a thorough explanation of the activity. The graph clearly shows that the enzyme tyrosinase's activity diminishes as the amount of 5f rises. Figure 6 shows a two-dimensional interaction map that shows the particular interactions of 5f with the amino acids of the enzyme. Amino acids ARG 268 all played important roles in hydrogen bond interactions, which are essential for binding. These interactions stabilise the binding and enhance the inhibitory effects. Also, when you see red separation contacts, it means that water molecules have left the enzyme's active site. The enzyme undergoes a conformational shift and subsequently ceases to catalyse processes. For that reason, 5f inhibits tyrosinase activity.

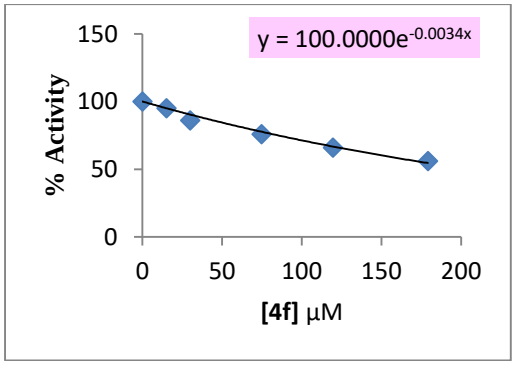

Figure 5. Minimise 5f tyrosinase enzyme activity

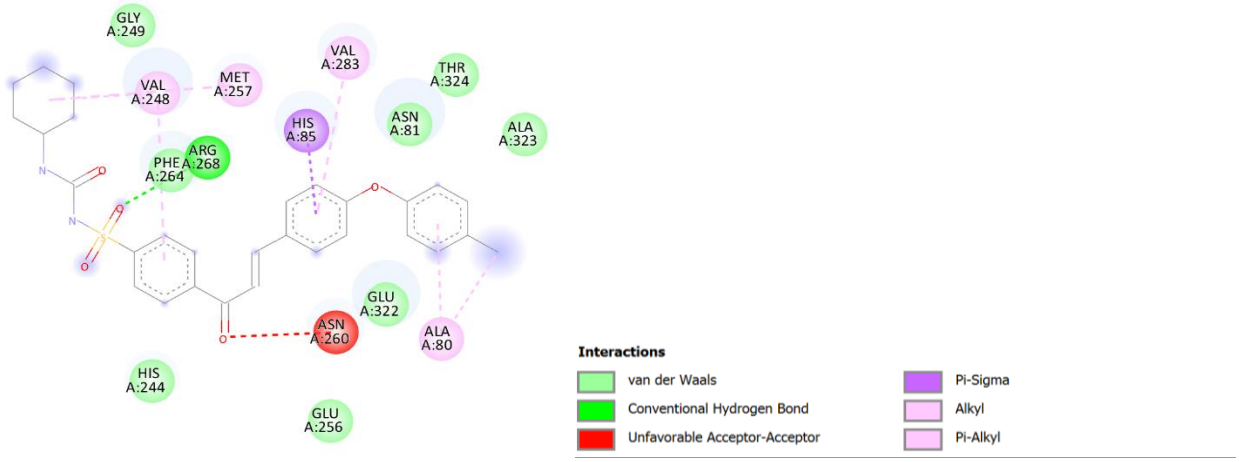

Figure 6. The tyrosinase enzyme and the 5f molecule's two-dimensional structures

In theory, 5g may be utilised to treat pathological disorders like obesity that are associated with tyrosinase enzyme activity, as it has been shown to inhibit tyrosinase enzyme activity. Visualising the relationship between enzyme activity % and 5g concentration, Figure 7 provides a thorough explanation of the activity. The graph clearly shows that the enzyme tyrosinase's activity diminishes as the amount of 5g rises. Figure 8 shows a two-

dimensional interaction map that shows the particular interactions of 5g with the amino acids of the enzyme. Amino acids ARG 268 all played important roles in hydrogen bond interactions, which are essential for binding. These interactions stabilise the binding and enhance the inhibitory effects. Also, when you see red separation contacts, it means that water molecules have left the enzyme's active site. The enzyme undergoes a conformational shift and subsequently ceases to catalyse processes. For that reason, 5g inhibits tyrosinase activity.

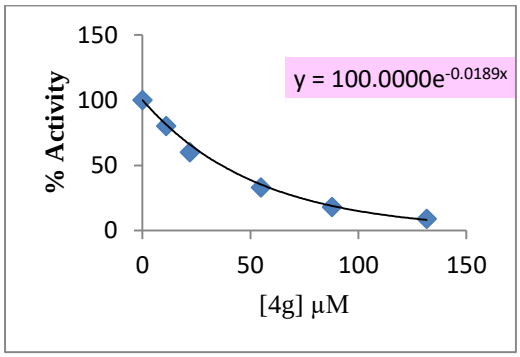

Figure 7. Minimise 5g tyrosinase enzyme activity

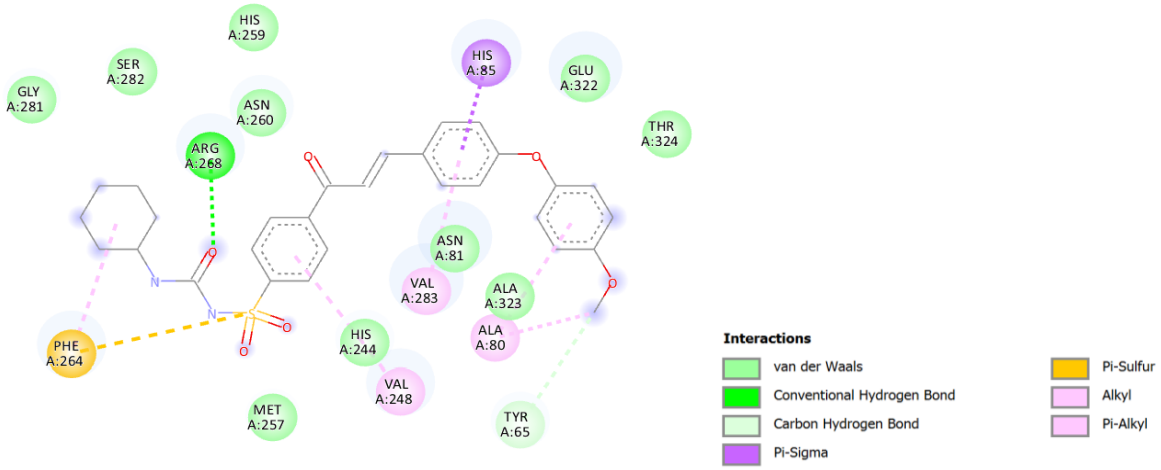

Figure 8. The tyrosinase enzyme and the 5g molecule's two-dimensional structures

4. Conclusion

Pursuing remedies for skin hyperpigmentation and fruit browning has found tyrosinase, an enzymatic browning enzyme and essential enzyme in melanin formation, to be an enthralling target. This research investigated the possibility of four synthetic chemicals (5d, 5e, 5f, and 5g) acting as tyrosinase inhibitors; the findings showed promise for use in food and cosmetics. The potential effectiveness of these four compounds as tyrosinase inhibitors was suggested by their concentration-dependent suppression of activity. To further understand where these chemicals attach to the active site of tyrosinase, molecular docking studies were conducted. Enzyme activity assays and visual renderings indicated compound 5d's powerful inhibitory effects. Its significant inhibitory activity may be based on the hydrogen bond interactions shown by a two-dimensional interaction map with certain amino acids. Even though it was less pronounced than in 5d, compounds 5e, 5f, and 5g showed tyrosinase inhibition. Hydrogen bond interactions were highlighted in their interaction maps as a possible optimisation target for improved inhibition. Potential tyrosinase inhibitors for skin whitening and antibrowning uses have been greatly enhanced by this study. The results highlight the need for further research into the molecular interactions between tyrosinase and synthetic inhibitors in order to develop more efficient therapies for hyperpigmentation. These findings hold great promise, but to confirm the chemicals' medical potential and guarantee their safety and effectiveness, more study is essential. This research should include in vivo tests and clinical trials. This work opens up new possibilities for the creation of tyrosinase inhibitors, which might lead to better skin whitening products and ways to reduce food browning caused by enzymes.

References

[1] Raper, H. S. (1928). The aerobic oxidases. *Physiological Reviews*, *8*(2), 245-282.

[2] Mason, H. S. (1948). The chemistry of melanin: III. Mechanism of the oxidation of dihydroxyphenylalanine by tyrosinase. *Journal of Biological Chemistry*, *172*(1), 83-99.

[3] Cooksey, C. J., Garratt, P. J., Land, E. J., Pavel, S., Ramsden, C. A., Riley, P. A., & Smit, N. P. (1997). Evidence of the indirect formation of the catecholic intermediate substrate responsible for the autoactivation kinetics of tyrosinase. *Journal of Biological Chemistry*, *272*(42), 26226-26235.

[4] Schallreuter, K. U., Kothari, S., Chavan, B., & Spencer, J. D. (2008). Regulation of melanogenesis–controversies and new concepts. *Experimental dermatology*, *17*(5), 395-404.

[5] Halaban, R., Patton, R. S., Cheng, E., Svedine, S., Trombetta, E. S., Wahl, M. L., ... & Hebert, D. N. (2002). Abnormal acidification of melanoma cells induces tyrosinase retention in the early secretory pathway. *Journal of Biological Chemistry*, *277*(17), 14821-14828.

[6] Artés, F., Castaner, M., & Gil, M. I. (1998). Enzymatic browning in minimally processed fruit and vegetables. *Food Science and Technology International*, *4*(6), 377-389.

[7] Rescigno, A., Sollai, F., Pisu, B., Rinaldi, A., & Sanjust, E. (2002). Tyrosinase inhibition: general and applied aspects. *Journal of Enzyme Inhibition and Medicinal Chemistry*, *17*(4), 207-218.

[8] Kim, Y. J., & Uyama, H. (2005). Tyrosinase inhibitors from natural and synthetic sources: structure, inhibition mechanism and perspective for the future. *Cellular and molecular life sciences CMLS*, *62*, 1707-1723.

[9] Parvez, S., Kang, M., Chung, H. S., & Bae, H. (2007). Naturally occurring tyrosinase inhibitors: mechanism and applications in skin health, cosmetics and agriculture industries. *Phytotherapy Research: An International Journal Devoted to Pharmacological and Toxicological Evaluation of Natural Product Derivatives*, *21*(9), 805-816.

[10] Briganti, S., Camera, E., & Picardo, M. (2003). Chemical and instrumental approaches to treat hyperpigmentation. *Pigment cell research*, *16*(2), 101-110.

[11] Rendon, M. I., & Gaviria, J. I. (2005). Review of skin-lightening agents. *Dermatologic surgery*, *31*, 886-890.

[12] Draelos, Z. D. (2007). Skin lightening preparations and the hydroquinone controversy. *Dermatologic therapy*, *20*(5), 308-313.

[13] Parvez, S., Kang, M., Chung, H. S., Cho, C., Hong, M. C., Shin, M. K., & Bae, H. (2006). Survey and mechanism of skin depigmenting and lightening agents. *Phytotherapy Research: An International Journal Devoted to Pharmacological and Toxicological Evaluation of Natural Product Derivatives*, *20*(11), 921-934.

[14] Solano, F., Briganti, S., Picardo, M., & Ghanem, G. (2006). Hypopigmenting agents: an updated review on biological, chemical and clinical aspects. *Pigment cell research*, *19*(6), 550-571.

[15] Ando, H., Kondoh, H., Ichihashi, M., & Hearing, V. J. (2007). Approaches to identify inhibitors of melanin biosynthesis via the quality control of tyrosinase. *Journal of Investigative Dermatology*, *127*(4), 751-761.

[16] Zhu, W., & Gao, J. (2008, April). The use of botanical extracts as topical skin-lightening agents for the improvement of skin pigmentation disorders. In *Journal of Investigative Dermatology Symposium Proceedings* (Vol. 13, No. 1, pp. 20-24). Elsevier.

[17] Ismaya, W. T., Rozeboom, H. J., Weijn, A., Mes, J. J., Fusetti, F., Wichers, H. J., & Dijkstra, B. W. (2011). Crystal structure of Agaricus bisporus mushroom tyrosinase: identity of the tetramer subunits and interaction with tropolone. *Biochemistry*, *50*(24), 5477-5486.

[18] Yırtıcı, Ü., Ergene, A., Atalar, M. N., & Adem, Ş. (2022). Phytochemical composition, antioxidant, enzyme inhibition, antimicrobial effects, and molecular docking studies of Centaurea sivasica. *South African Journal of Botany*, *144*, 58-71.

[19] Thomsen, R., & Christensen, M. H. (2006). MolDock: a new technique for high-accuracy molecular docking. *Journal of medicinal chemistry*, *49*(11), 3315-3321.

New Methods and Materials Used in Soil–Related Road Deterioration in the Uluyazı (Çankırı) Campus, Türkiye

Muharrem TIRIN [1*], ***Ender SARIFAKIOĞLU*** [2]

[1]*Department of Construction and Technical Affairs, Çankırı Karatekin University, Çankırı, Türkiye*

[2]*Faculty of Engineering, Department of Civil Engineering, Çankırı Karatekin University, Çankırı, Türkiye*

Abstract

While the world is experiencing the age of technology at full speed, Turkey is also taking steps to implement innovations by following these technological developments. These technological and industrial innovations have become rapidly widespread in the construction industry. The rapid population growth of countries, which is seen as a problem of the developing world, increases the need for new settlement areas and new roads. With population growth and the slow development of widespread railway networks in public transportation services due to their costs, the vehicle load on the roads also increases and old roads and traditional methods lose their effectiveness in the long term. Therefore, these vehicle loads cause permanent problems on the roads. The main reasons for deterioration in road structures are the same applications in regions with different weather conditions, errors during application, errors in the selection of methods, as well as deformations caused by the type of ground on which the application will be made. Problems that may occur as a result of ground effect are observed as cracks and deformations on the coating surface. The lithological characteristics of the ground of the new road line in the Çankırı Karatekin University, Uluyazı Campus especially the melting–collapse at gypsum levels, the deformations caused by these and the areas with landslide risk were examined. For the improvements that can be made on the new road line and landslide risk area, the contributions of a number of new applications and materials (geosynthetics) suitable for the lithological characteristics of the region have been examined. (This study derived from Muharrem TIRIN's master thesis)

Keywords: *Çankırı, Gypsum, Landslide Prevention, New Road Construction Method, Geosynthetics*

1. Introduction

Along with innovations in the field of engineering, the materials used in the manufacturing and construction phases of a job have also developed rapidly. Thanks to the developments in the construction sector, they have increased their quality in production, saved time by shortening work completion times thanks to practical conveniences, and provided advantages in costs with the increase in access opportunities. Geotextiles, which have been used for many years in leading countries in technological development but have become widespread in Turkey in the 21st century, have shown a rapid rise by taking part in many areas in the construction industry. Thanks to the strength parameters of geotextiles increasing in line with technology, their usage area in road construction has rapidly expanded.

The dominant lithological units in the Çankırı basin are gypsum, rock salt, sandstone, mudstone, claystone and limestone, which are frequently encountered in the Central Anatolia region. The most important factor that causes deformation, especially in gypsum levels, is melting when groundwater and surface water come into contact. The magnitude of the deformations caused by the dissolution of gypsum minerals is related to the gypsum layer thickness, the lithology of the other rock units with which it is intercalated (such as mudstone, sandstone), the chemical content of the gypsum and the geological structure of the region (such as folds, faults). Such minerals found in the ground cause structural deformations in buildings and road pavements.

The main reasons for the collapses, slides and cracks in the road superstructure that occurred over time on the ring road built during the construction of the Çankırı Karatekin University, Uluyazı Campus were determined as;

- The campus is on loose ground that is not resistant to abrasion,
- Groundwater and rainwater form a natural bed in the region,
- The slope on the road line, which is at risk of landslide, cannot maintain its stability in this situation.

1.1. Study Area

The study area is within the borders of the central district of the Çankırı province (Figure 1). The altitude of Çankırı City Center is 720 meters above the sea level, and the altitude of Uluyazı Hill is 900 meters above the sea level.

* Corresponding author. *e-mail address: m.tirin@karatekin.edu.tr*

Figure 1. Study area layout information [6].

1.2. Regional Geology

Around the Çankırı city, from oldest to the youngest unit belonging to the Tertiary period, the İncik, Bayındır, Kızılırmak, Bozkır, Değim formations and Quaternary alluviums and terraces are observed [1–4–5]. The Oligo-Miocene aged İncik formation consists of red-coloured, thick–very thick layered conglomerates and creamy light brown-coloured sandstones and mudstones. The Middle Miocene aged Bayındır formation includes sandstone, mudstone levels and gypsum interlayers (Figure 2a, b). The Bozkır formation consists of mudstone and gypsum levels. The mudstone layers, which are light greenish and light gray in color, are thinner than gypsum layers and generally contain gypsum crystals. The Bozkır formation represents a deposit in a lacustrine evaporative environment.

Figure 2. a) The Bayındır (ByF), Kızılırmak (KF), Bozkır (BzF) formations and Acı creek alluviums exposed on the Çankırı–Ankara highway. **b)** Sandstone–conglomerate intercalated levels belonging to the İncik Formation exposed around the Çankırı Castle. **c)** Gypsum (Gyp) levels and fine-grained, loose sandstone (St) alternations in the Uluyazı Campus area.

2. Material and Methods

2.1. Field Studies

In this section, the studies carried out in the field to identify the geological units cropping out in the Uluyazı campus, to determine the lateral and vertical changes of the detected units, and to determine the groundwater level are mentioned under 3 headings:

- Determination of Surface Movements
- Landslide Area Drilling Works
- Situation Analysis of the Landslide Area
- New Road Route Drilling Works

2.1.1. Determination of surface movements

It has been observed that the slope in an area close to the campus road route line cannot ensure its stability. The movement of the sliding mass in the landslide area was determined by processing the data obtained from the guides placed in order to observe the displacements occurring on the ground surface (Figure 3).

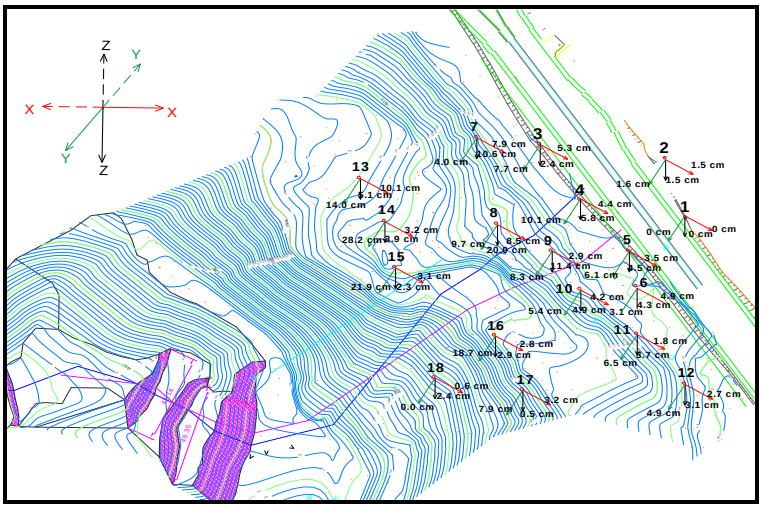

Figure 3. Reference points and displacement amounts [6].

The readings made from the placed reference points were repeated with GPS measurements approximately 40 days later and the amounts of surface movement during the elapsed time were determined. In the elapsed time period, displacements of 28 cm in the horizontal direction and 20 cm in the vertical direction were determined between the first and last readings.

2.1.2. Landslide area drilling works

Total of 13 basic drillings and 3 observation wells were opened in the landslide area at the border of the campus ring road. When the drilling data and field observations were evaluated, it was determined that the lowest hard layer in the study area contained claystone, sandstone and conglomerate, and the upper levels of this layer consisted of gypsum silty clay, clayey silt and clay layers, and there was filling material at the upper levels (Table 1).

Table 1. Drilling Well Data [6].

Well No	Depth (m)	Lithology
DW–1	24	
DW–2	18	
DW–3	39.7	
DW–4	6.4	
DW–5	8.3	Clay between 0–2.50 m., clay–mudstone–gypsum between
DW–6	4.5	2.50–7.50 m., mudstone–gypsum between 7.5–15 m., 15–30
DW–7	21.9	m. mudstone–gypsum, sandstone in places, conglomerate
DW–8	22.1	alternation. The lowest layer is sandstone, conglomerate
DW–9	22	intercalation.
DW–10	13	
DW–11	38	
DW–12	11.85	
DW–13	6.2	

2.1.3. Situation analysis of the landslide area

Using the data obtained from the field investigations and the Slide 2018 software, a comparative analysis was made of the static situation of the landslide area and the risk assessments in the earthquake zone of the region (Figure 4). In the analysis, deformations (mass strength loss) caused by dynamic stresses in the slope under earthquake loads were determined. Deterioration of slope stability due to deterioration in the stress-strain behavior of the material and loss of strength under dynamic loads was examined.

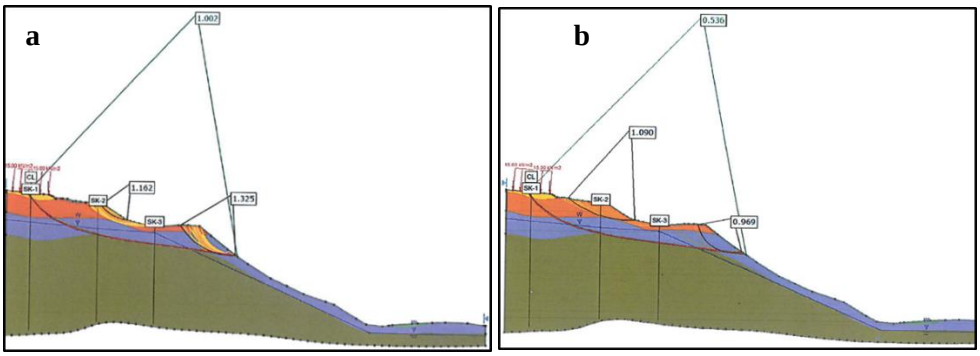

Figure 4. a) Analysis model showing the current situation screenshot (static situation). **b)** Analysis model showing the current situation screenshot (earthquake situation).

As can be seen from the software analysis, while the safety number of the slope area approaches 1 in static condition, it drops below 1 under dynamic earthquake loads. For this reason, it is seen that permanent deformations will occur with the deterioration of stability (Factor of Safety / F.S. is calculated according to Eurocode 7 and BS 8006 standards) (Figure 5).

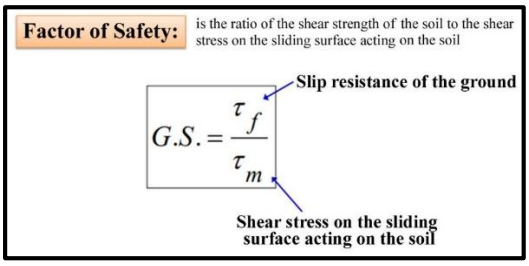

Figure 5. Factor of Safety formula of the foundation [2–3].

2.1.4. New road route drilling works

The old road route in the study area was changed due to being in a landslide risk area and dissolution due to ground lithology. It was decided to carry out drilling between the starting and ending points of the road, approximately 100 m apart, parallel to the axis of the planned new road route. The aim of the studies is to determine the lithological characteristics of the ground on the road route and to determine the areas where groundwater is concentrated by determining the groundwater level. Drilling studies were carried out at an average depth of 35 m and samples were taken every 1 m (Figure 6).

Figure 6. a) Drilling wells, **b)** Samples obtained from drilling studies [6].

2.2. Evaluation of Field Data

- As a result of drilling observations carried out in the campus area, it was observed that groundwater formed a bed near the landslide area.
- As a result of drilling core samples, it was determined that the study area was formed by gypsum–mudstone alternation.
- Due to the dissolution and decomposition of the gypsum unit seen in the field under the influence of underground and surface waters, it created a sensitivity problem on the slopes by digging a deep valley.
- Additionally, the faults around the Çankırı province are seismically active. The active earthquake danger is too high to be ignored.

2.3. Improvement Practices

Improvement works carried out on the road route and on slopes at risk of landslides are examined under this section.

2.3.1. Controlling the groundwater level

In order to determine the groundwater level in the landslide area and the road route to be constructed, drill wells with a depth of 30–40 m. were opened. In the borehole investigations, it was determined that the underground water level next to the landslide area was 6–7 m. As a result of the observation wells opened, it was determined that groundwater flows by forming a bed near the landslide area. Electric water evacuation pumps were placed in these wells to keep the water level at 35 m. Groundwater discharged from the wells is connected to rainwater lines through surface drainage channels (Figure 7).

Figure 7. Studies on the detection and discharge of groundwater [6].

2.3.2. Strengthening road infrastructure

Lithologically, the intercalation of gypsum with clay or mudstone negatively affects the road infrastructure and coating. When gypsum comes into contact with water, dissolution in these areas causes collapse. Another negative aspect of the gypsum mineral is that it creates a landslide risk as a result of its intercalation with clay layers. As a result of these data and evaluations, it was considered appropriate to replace the natural ground with durable (basalt) filling material before starting the road construction. The natural soil with gypsum along the road route was excavated for an average of 1 m and replaced with coarse-grained filling material by compaction (Figure 8).

Figure 8. Excavation of the gypsum soil and its replacement with compressed fill [6].

The most important task expected from a highway is to avoid deformations in the asphalt layer exposed to dynamic loads. The soft filled soil on the new road line at the Çankırı Karatekin University, Uluyazı campus is one of the biggest problems and exhibits weak behavior under tensile stresses. For this reason, after the road infrastructure works, the stage of strengthening the foundation ground was started and for this purpose, the infrastructure was supported with geosynthetic products. The contribution of geosynthetics in construction areas with their properties such as filtration, reinforcement and separation has been revealed [7]. The most important reason for using geosynthetics in road construction is that the ground behaves in a reinforced manner. Geosynthetic products, geomembrane and geocell, were used together in campus road construction (Figure 9).

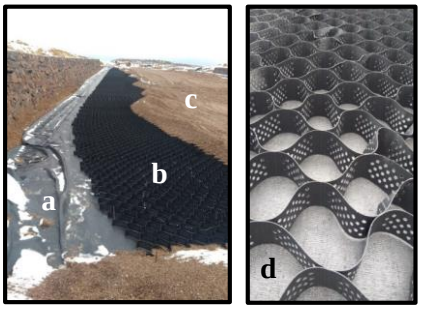

Figure 9. a) Geomembrane, **b)** Geocell, **c)** Filtration aggregate, **d)** Detailed view of Geocell [6].

2.3.3. Carrying Out Remediation Studies on Slopes with Landslide Risk

Although many methods are used to remediate landslides, this study aims to ensure slope stability with cellular filling of the landslide area. As improvement studies, reducing the slope, changing the slope fill soil, strengthening with geocell and afforestation were implemented (Figure 10). Firstly, the inclination of the slope was reduced by filling the road infrastructure with compressed soil. In addition, the negative effects of gypsum–clay alternations on plant growth in the Uluyazı region were eliminated by covering the gypsum land cover with filling material. The cellular filling system to be used with the new filling material will contribute to landslide prevention by increasing vertical rooting by holding plant roots more firmly to the slope. As an additional precaution to these practices, the lines of the drainage discharge water flowing into the landslide area have been changed.

Figure 10. Views from improvement studies of the landslide area [6].

3. Discussion and Conclusion

Expected results from field observations, laboratory experiments, tectonic activity data in the region and the applications made as a result of these observations–analyses are as follows;

1. Cellular filling system (Geocells) prevents the formation of collapses and cracks in the upper layer of the road route exposed to vertical moving loads,
2. Thanks to its distinctive feature, the geomembrane minimizes the deformations in the upper layer by preventing the passage of groundwater between the asphalt base layer and the route ground,
3. By laying compressed ground fill on the gypsum ground, foundation fill is created and the road is placed on a more solid ground,
4. Keeping water away from the ground as much as possible with underground drainage water pumps and aboveground drainage lines,
5. Slope reduction works are carried out with fillers in the landslide area, and cellular filler is applied to the slope surface with geocells to increase the stability of the slope and reduce the speed of the landslide.
6. Elimination of irregular loads by preventing uncontrolled filling in the landslide area during campus works, these studies aimed to create a safer campus road route and to prevent accidents and loss of life in the landslide area.

Acknowledgements

This study is derived from Muharrem Tırın's MSc Thesis. We would like to thank to the Department of Construction and Technical Affairs of the Çankırı Karatekin University, for the opportunities provided and our colleagues working within the scope of the project for their support.

References

[1] Akyürek, B., Bilginer, E., Çatal, E., Dağer, Z., Soysal, Y. and Sunu, O. 1980. Eldivan–Şabanözü (Çankırı), Hasayaz–Çandır (Kalecik–Ankara) dolayının jeolojisi. MTA Report No: 6741

[2] British Standard, BS8006–1, 1995. Code of Practice for Strengthened/Reinforced Soils and Other Fills.

[3] EN 1997–1. 2004. Eurocode 7: Geotechnical design – part 1: General rules. European Committee for Standardization, Brussels.

[4] Hakyemez, Y., Barkurt, M.Y., Bilginer, E., Pehlivan, Ş., Can, B., Dağer, Z. and Sözeri, B. 1986. Yapraklı–Ilgaz–Çankırı–Çandır dolayının jeolojisi. MTA Report No. 7966

[5] Sarıfakıoğlu, E., Sevin, M., Esirtgen, E., Bilgiç, T. Duran, S., Parlak, O., Karabalık, N. N., Alemdar, S., Dilek, Y. and Uysal. İ. 2011. Çankırı–Çorum havzasını çevreleyen ofiyolitik kayaçların jeolojisi: Petrojenezi, tektoniği ve cevher içerikleri. Maden Tetkik ve Arama Genel Müdürlüğü, Report No: 11449, Ankara

[6] Tırın, M. 2023. Uluyazı (Çankırı) Kampüsünde Zemin Kaynaklı Yol Bozulmalarında Uygulanan Yeni Metotlar ve Kullanılan Malzemeler. MSc Thesis. Çankırı Karatekin Üniversitesi, Fen Bilimleri Enstitüsü 74 p., Çankırı.

[7] Adams, M. and Collin, J. 1997. Large model spread footing load tests on geosynthetic reinforced soil foundations. J. Geotech. Geoenviron. Eng., 123(1), 66–72.

Numerical study of flow and heat transfer in a straight duct containing a circular region with a pair of fins

***Selma AKÇAY*[1,*] *Nasser ABDOUL-HALIM ISMAEL*[2]**

[1*] *Çankırı Karatekin University, Engineering Faculty, Department of Mechanical Engineering, Çankırı, Türkiye*

[2] *Çankırı Karatekin University, Undergraduate Student of Mechanical Engineering, Çankırı, Türkiye*

Abstract

This study numerically investigates flow and heat transfer characteristics in a straight duct containing a circular region with a pair of fins. Analyzes are carried out with ANSYS Fluent solver. The pressure-velocity connection is handled with the SIMPLE algorithm. There are adiabatic straight sections at the inlet and outlet of the duct. The duct structure contains a circular region near the inlet of the duct, and a pair of fins are installed within the circular region. The walls of the duct before and after the circular region are flat. The circular region and subsequent channel surfaces are kept at a constant temperature of T_s=350K. Nusselt number (Nu), thermal enhancement factor (TEF), pressure drop (ΔP), friction factor (f), and performance factor (PF) are calculated for different Reynolds numbers ($100 \leq Re \leq 800$). The results of the study are given as a function of dimensionless numbers. The numerical study is compared with previous study results. To observe the effects of the circular region and the pair of fins on the flow and temperature fields, velocity and temperature contours are obtained, and the results are discussed. In addition, the study results are compared to the duct without fins and the straight duct. Numerical results show that the fins in the circular region increased the Nusselt number. However, the presence of fins causes a slight increase in pressure drop.

Keywords: *Circular region, Fins, Straight duct, Heat transfer, Laminar flow, Thermal enhancement*

1. Introduction

Passive heat transfer enhancement methods are widely used in many heat transfer devices, especially heat exchangers [1, 2]. Wavy/corrugated channels are among the most used passive methods. These channels enhance the heat transfer performance by increasing the heat transfer surface area [3, 4]. To date, flow and heat transfer performance in wavy/corrugated channels with different wave profiles have been examined through numerical and experimental studies. The results of these studies have denoted that thermal performance and pressure drop in wavy/corrugated channels are higher than in straight channels [5-7]. Choudhary et al. [8] compared the flow and heat transfer of wavy and straight channels in a heat exchanger and declared that the heat transfer and pressure drop were higher in wavy channels than in straight channels. Ahmad et al. [9] numerically studied the heat transfer in triangular, sinusoidal, and rectangular corrugated mini ducts with different wave amplitudes, and they found that the heat transfer in the rectangular duct was improved by 22.19% at an amplitude ratio of 0.12. Ajeel et al. [10] experimentally and numerically investigated the flow and heat transfer in the circular and trapezoidal corrugated ducts and stated that the heat transfer increased by 3.1 times in the trapezoidal wave profile.

Another passive method is the addition of baffles, fins, and winglets into the duct. These modifications change the flow structure by directing the flow to certain regions. The addition of fins/winglets in different configurations into the duct enhances the flow and heat transfer [1, 7]. Akcay [5] numerically studied the nanofluid flow and heat transfer in a zigzag wavy channel with winglets and reported that the winglets added to the channel increased the heat transfer and the best thermohydraulic performance was found to be 2.12 at Re=400. Sun et al. [11] experimentally and numerically examined the heat transfer of multiple rectangular wings in a circular heat exchanger. Li and Gao [12] numerically examined the effects of delta-shaped baffles on heat transfer for different apex angles in a triangular wavy bottom wall. They showed that if the appropriate parameters are selected, the Nu can increase by 2.1 and 4.3 times. Naderifar et al. [13] numerically investigated the effects of wave number and fin height on the flow and heat transfer in a rectangular wavy duct with fins. They found that when the wave number is 2 and the fin height is 7.5, the best thermal improvement was achieved compared to the straight channel. Promvonge et al. [14] experimentally and numerically studied the flow and heat transfer of V-type wings. They reported that the wings can increase the heat transfer up to 3.8 times if appropriate parameters are

* Corresponding author. *e-mail address: selmaakcay@karatekin.edu.tr*

used. Akcay and Akdag [15] numerically examined heat transfer in a circular channel with different baffle angles (θ=30º, 90º, 180º). They declared that the highest heat transfer and pressure drop were obtained at the 90º baffle angle. Feng et al. [16] numerically examined the flow and heat transfer in the triangular wavy duct with trapezoidal baffles declared that the heat transfer enhanced by 1.7 times compared to the straight duct, while the pressure drop increased by 3.5 times.

In this numerical study, more than one passive method was used together to further increase heat transfer. In the study, to reduce pressure loss, a large circular region was placed near the inlet of the duct; in this way, the number of waves was minimized, and the other walls of the duct were kept straight. The purpose of using fins is to direct the fluid to circular surfaces. In the study, the flow and thermal characteristics of the laminar steady flow were examined for different Reynolds numbers ($100 \leq Re \leq 800$) in a straight channel containing a circular region with a pair of fins. The results were compared with the straight duct.

2. Materials and Methods

2.1. Numerical model

Figure 1 shows the geometry and mesh structure of the numerical model used in this study. The duct contains adiabatic straight sections with a length of L_1 = 50 mm at the inlet and outlet. The height of the duct is H_1 = 10 mm. At the duct inlet after the adiabatic section, there is a circular region with a length of L_2 = 20 mm. After the circular region, there is a heated straight section with a length of L_3 = 80 mm, which extends to the beginning of the adiabatic section at the duct outlet.

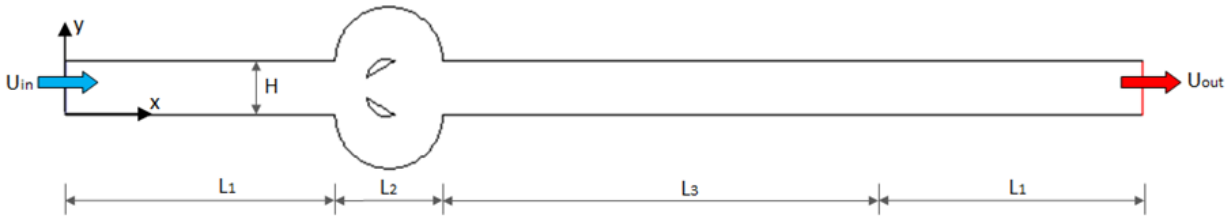

(a) Numerical model

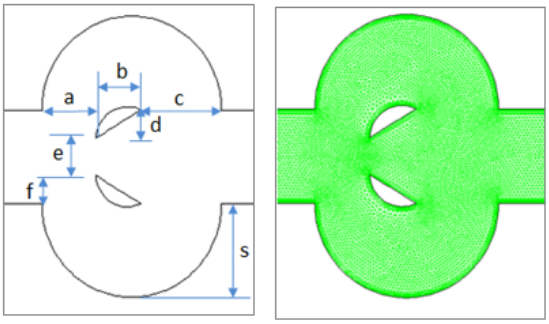

Parameter	Value
a	5 mm
b	6 mm
c	9 mm
d	3 mm
e	6 mm
f	3 mm
s	10 mm

(b) Details of the numerical model and mesh structure

Figure 1. Geometry and mesh structure of the numerical model

2.2. Governing equations

In the numerical study, the fluid is considered single-phase, incompressible and Newtonian type. The flow field is 2d. The fluid flows in laminar and steady flow conditions. Viscous terms are neglected. Fluid properties are assumed to be constant. The effect of gravity and radiation are not taken into account. According to the these assumptions, governing equations are given below:

$$\frac{\partial u_i}{\partial t} + \nabla(\rho u) = 0 \quad (1)$$

$$\frac{\partial u_i}{\partial t} + \frac{\partial (u_i u_j)}{\partial x_i} = \frac{\partial P}{\partial x_i} + \frac{1}{Re}\nabla^2 u_j \quad (2)$$

$$\frac{\partial T}{\partial t} + u_i \frac{\partial T}{\partial x_i} = \frac{1}{RePr} + \nabla^2 T \quad (3)$$

2.3. Numerical method and boundary conditions

The numerical study was carried out using the ANSYS Fluent solver. The laminar model was used as the flow model. Governing equations were discretized with the finite volume approach and the velocity-pressure relationship was solved with the SIMPLE algorithm. A value of 10^{-7} was set for all equations as the convergence criterion. For the mesh independence testing, Nusselt numbers were calculated for different element numbers. As a result of this calculations, it was decided that 41560, and 42660 element numbers are sufficient for the duct without fins, and the duct with fins, respectively.

Water was used as the working fluid. The fluid enters the duct at a uniform velocity (U_{in}) and temperature (T_o=300 K). In the study, Reynolds number varied in the range of 100≤Re≤800. The heated duct surfaces (L_2 and L_3) were kept constant at T_w=350 K. The non-slip wall condition was defined for the all surfaces. Straight sections at the inlet and outlet of the duct are adiabatic. The fins were assumed to be adiabatic and non-slip conditions.

2.4. Data Reduction

The Reynolds number (Re) is calculated by Equation (4):

$$\mathrm{Re} = \frac{\rho U D_h}{\mu} \quad (4)$$

where, D_h is the hydraulic diameter, ρ is the density, μ is the dynamic viscosity, and U is the velocity.

The average Nusselt number (Nu) is obtained by Equation (5):

$$\mathrm{Nu} = \frac{h D_h}{k_f} \quad (5)$$

where, k_f and h are thermal conductivity coefficient and convective heat transfer coefficient, respectively.

The thermal enhancement factor (TEF) is described with Equation (6).

$$\mathrm{TEF} = \frac{\mathrm{Nu}_f}{\mathrm{Nu}_o} \quad (6)$$

where, Nu_f and Nu_o represent the Nusselt numbers obtained in the duct with and the without fins, respectively.

The friction factor (f) is calculated in the duct is given by Equation (7):

$$\mathrm{f} = \frac{2\Delta P D_h}{\rho U^2 L} \quad (7)$$

Relative friction factor (f_f/f_o) is obtained by Equation (8):

$$\mathrm{f_{rel}} = \frac{f_f}{f_o} \quad (8)$$

where, f_f and f_o are the average friction factors obtained in the channel with and without fins, respectively.

The performance factor (PF) is obtained by Equation (9):

$$\mathrm{PF} = (\mathrm{Nu_f}/\mathrm{Nu_o})(f_f/f_o)^{-1/3} \quad (9)$$

3. Results and Discussion

3.1. Validation of the numerical results

Numerical results obtained in this study were compared with the results of previous studies. Wang et al. [17] experimentally investigated flow and heat transfer behavior of the water in a straight channel. Figure 2 indicated the comparison of the results of numerical study with the results of Wang et al. [17].

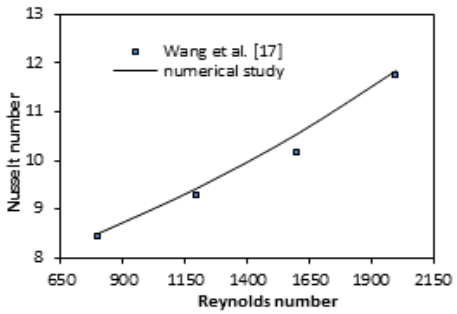

Figure 2. Validation of the numerical study [17]

In numerical study, velocity and temperature contours were obtained to demonstrate the effects of duct geometry, fins, and Reynolds number on flow and heat transfer. In Figure 3a, velocity contours are indicated in ducts with and without fins for Re=100 and Re=800. Re and fins appear to affect the flow structure. The fins divided the flow into three main branches. The flow passing around the fins is directed towards the circular cavities and is provides better contact with the circular walls. Increasing the flow velocity increases the mass flow rate and inertia forces. Therefore, increasing the Reynolds number ensures a significant contribution to heat transfer. In Figure 3b, the temperature contours are exhibited in ducts with and without fins for Re=100 and Re=800. Reynolds number and fins affect the temperature contours. Increasing Reynolds number reduces the wall temperature in the duct. It is observed that the wall temperatures in the duct with fins are lower than in the duct without fins at Re=800.

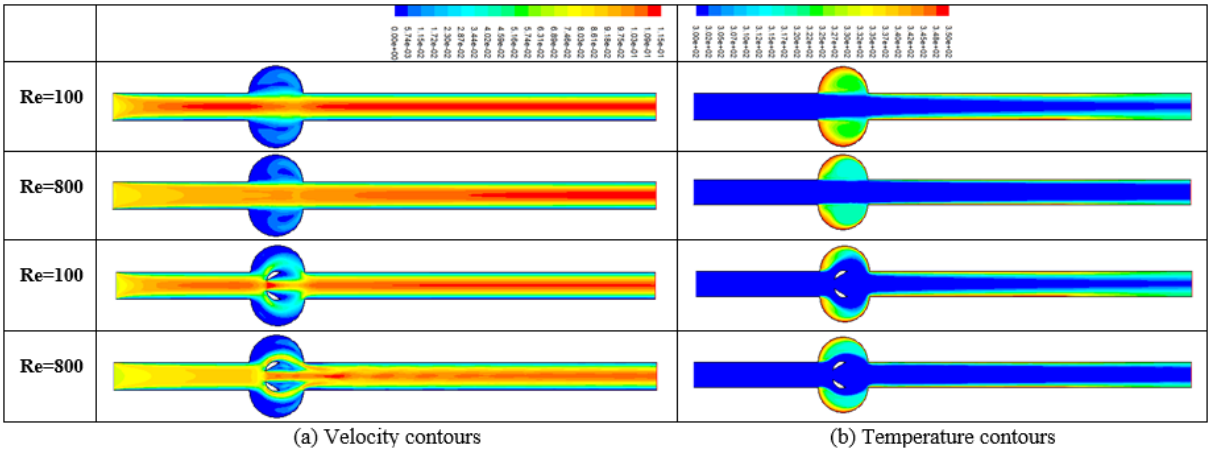

Figure 3. Velocity contours (a) and temperature contours (b) for Re=100 and Re=800

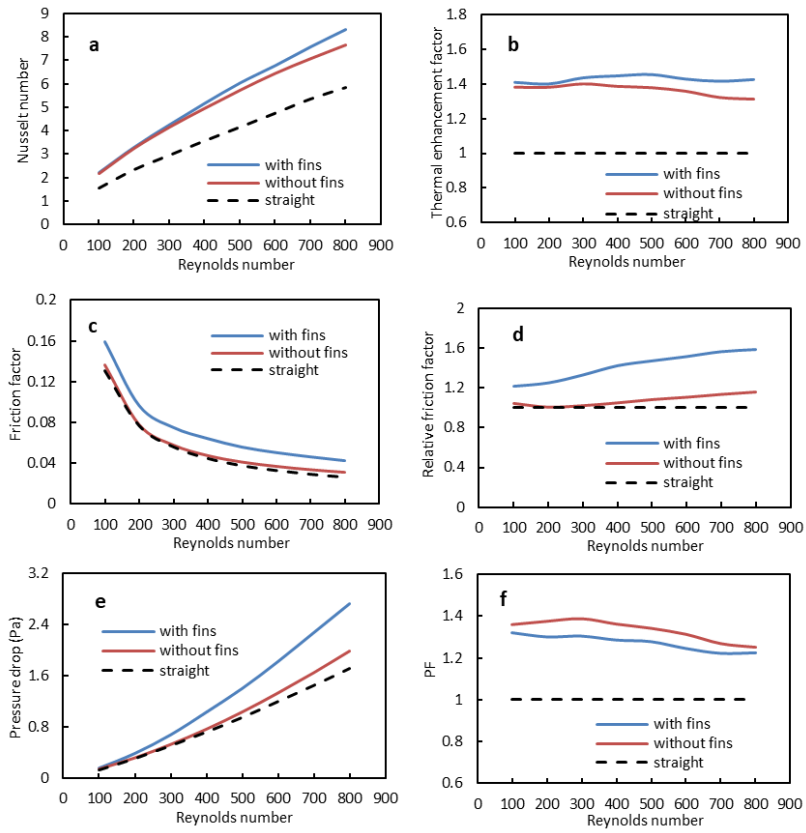

Figure 4. a-Nusselt number, b- Thermal enhancement, c- Friction factor, d- Relative friction factor, e-Pressure drop, f-Performance factor with Reynolds number

Figure 4 shows the Nusselt number (a), thermal enhancement factor (b), friction factor (c), relative friction factor (d), pressure drop (Pa) (e), and performance factor (f) with Reynold number for all duct flows. In Figure 4a, the Nusselt number increases as the Reynolds number increases. The highest Nusselt number was obtained to be 8.30 at Re=800 in the duct with fins. In Figure 4b, thermal enhancement factor in the duct with and without fins was obtained to be higher than in the straight duct. The highest TEF was found to be 1.45 at Re=500 in the duct with fins. In Figure 4c, as the Reynolds number increases, the friction factor decreases for all duct flows. Friction factors in straight duct and duct without fins were found very close to each other. The friction factor in the duct with fins was found to be higher than in other ducts. In the duct without fins, the relative friction factor increased slightly with the Reynolds number, while the highest relative friction factor was obtained to be 1.58 at Re=800 in the duct with fins (Fig. 4d). The pressure drop increased with Reynolds number in all flow cases. The highest pressure loss was found to be 2.72 Pa in the duct with fins at Re = 800 (Fig. 4e). It was observed that the performance factors of the duct without and with fins were higher than the straight duct at all Reynolds numbers (Fig. 4f). The highest performance factor was obtained in the duct without fins. Because the pressure drop obtained in the duct without fins was found to be very close to the straight duct. The highest performance factor was obtained to be 1.39 at Re=300 in the duct without fins.

4. Conclusion

In this study were numerically analyzed flow and heat transfer in a straight duct containing a circular region with a pair of fins. Nusselt number (Nu), thermal enhancement factor (TEF), friction factor (f) and performance factor (PF) were calculated for different Reynolds numbers. To observe the effects of the circular region and fins on the flow and temperature fields, velocity and temperature contours in the duct were obtained at different Reynolds numbers. In addition, the study results were compared with the duct without fins and the straight channel. The important findings of the numerical study are given below:

- The fins in the circular region increased the heat transfer. However, the presence of fins causes a slight increase in pressure drop.

- The highest Nusselt number was obtained to be 8.30 at Re=800 in the duct with fins.
- The highest TEF was obtained to be 1.45 at Re=500 in the duct with fins.
- Friction factors in straight duct and duct without fins were obtained very close to each other.
- The friction factor in the duct with fins was found to be higher than in other flow cases.
- The highest relative friction factor was obtained to be 1.58 at Re=800 in the duct with fins.
- The highest pressure drop was found to be 2.72 Pa at Re=800 in the duct with fins.
- The highest PF was obtained to be 1.39 at Re=300 in the duct without fins.

References

[1] Ajarostaghi SSM, Zaboli M, Javadi H, Badenes B, & Urchueguia JF. (2022). A review of recent passive heat transfer enhancement methods. *Energies*, 15, 986.

[2] Alam T, & Kim MH. (2018). A comprehensive review on single phase heat transfer enhancement techniques in heat exchanger applications. *Renewable and Sustainable Energy Reviews*, 81, 813-839.

[3] Kurtulmus N, & Sahin B. (2019). A review of hydrodynamics and heat transfer through corrugated channels. *International Communications in Heat and Mass Transfer*, 108, 104307.

[4] Modi, AJ., & MK. Rathod. (2019). Comparative study of heat transfer enhancement and pressure drop for fin-and-circular tube compact heat exchangers with sinusoidal wavy and elliptical curved rectangular winglet vortex. *International Journal of Heat and Mass Transfer*, 141, 310-326.

[5] Akçay S. (2023). Numerical analysis of hydraulic and thermal performance of Al_2O_3-water nanofluid in a zigzag channel with central winglets. *Gazi University Journal of Science*, 36 (1), 383-397.

[6] Wang G, Qia C, Liu M, Li C, Yan Yu, & Liang L. (2019). Effect of corrugation pitch on thermo-hydraulic performance of nanofluids in corrugated tubes of heat exchanger system based on exergy efficiency. *Energy Conversion and Management*, 186, 51–65.

[7] Nitturi LK, Kapu VK, Gugulothu R, Kaleru A, Vuyyuri V, & Farid A. (2023). Augmentation of heat transfer through passive techniques. *Heat Transfer*, https://doi.org/10.1002/htj.22877

[8] Choudhary T, Sahu MK, Shende V, & Kumar A. (2022). Computational analysis of a heat transfer characteristic of a wavy and corrugated channel. *Material Today: Proceedings*, 56, 263-273.

[9] Ahmad F, Mahmud S, Ehsan MM, & Salehin M. (2023). Numerical assessment of nanofluids in corrugated minichannels: Flow phenomenon and advanced thermo-hydrodynamic analysis. *Int. J. Thermofluids*, https://doi.org/10.1016/j.ijft.2023.100449.

[10] Ajeel RK, Salim WI, Sopian K, Yusoff MZ, Hasnan K, Ibrahim A, & Al- Waeli AH. (2019). Turbulent convective heat transfer of silica oxide nanofluid through corrugated channels: an experimental and numerical study. *Int. J. Heat Mass Transf.*, 145, 118806.

[11] Sun Z, Zhang K, Li W, Chen Q, & Zheng N. (2020). Investigations of the turbulent thermal-hydraulic performance in circular heat exchanger tubes with multiple rectangular winglet vortex generators. *Applied Thermal Engineering*, 168, 114838.

[12] Li Z, & Gao Y. (2022). Numerical study of turbulent flow and heat transfer in cross-corrugated triangular ducts with delta-shaped baffles. *International Journal of Heat and Mass Transfer*, 108, 658-670.

[13] Naderifar A, Nikian M, Javaherdeh K, & Borji M. (2022). Numerical investigation of the effect of fins on heat transfer enhancement of a laminar non-newtonian nanofluid flow through a corrugated channel. *J. Thermal Analysis and Calorimetry*, 147, 9779-9791.

[14] Promvonge P, Promthaisong P, & Skullong S. (2020). Experimental and numerical heat transfer study of turbulent tube flow through discrete V-winglets. *International Journal of Heat and Mass Transfer*, 151, 119351.

[15] Akcay S, & Akdag U, (2022). Effect of baffle angles on flow and heat transfer in a circular duct with nanofluids. *International Advanced Researches and Engineering Journal*, 6 (3), 176-185.

[16] Feng C-N, Liang C-H, & Li Z-X. (2022). Friction factor and heat transfer evaluation of cross-corrugated triangular flow channels with trapezoidal baffles. *Energy & Buildings*, 257, 111816.

[17] Wang G, Qia C, Liu M, Li C, Yan Yu, & Liang L. (2019). Effect of corrugation pitch on thermo-hydraulic performance of nanofluids in corrugated tubes of heat exchanger system based on exergy efficiency. *Energy Conversion and Management*, 186, 51–65.

Mathematical modelling of ultrasound pretreated kumquat (*Citrus japonica var. margarita*) in freeze dryer

Dilek Otal SENOL [1,*], ***Zehra Ozden OZYALCIN*** [1], ***Azmi Seyhun KIPCAK*** [1]

[1] *Chemical Metallurgical Faculty, Chemical Engineering Department, Yıldız Technical University, Istanbul, Turkiye*

Abstract

Kumquat (*Citrus japonica var. margarita*) is a citrus fruit that resembles a tiny orange and is rich in flavonoids. Kumquat, which can be consumed raw and processed, was dried in a freeze dryer with ultrasonic pre-treatment and its mathematical modelling were investigated in this study. Ultrasound pretreatment was applied for 30 and 60 seconds and the drying process was proceeded at -68.6 C and 0.9 Pa for control and pretreated samples. The experimental drying data is fitted into Hendersen & Pabis, Jena & Das, Lewis, and Two-Term Exponential drying models, and the data-model compatibilities were compared. The most suitable model was determined as Jena & Das model with the highest R^2, and the lowest χ^2, and *RMSE*. It was observed that the R^2 values of all the models applied varied between 0.994740 and 0.998673.

Keywords: *Kumquats, Exotic fruits, Lyophilisation, Ultrasonication*

1. Introduction

Fruits are a food group rich in vitamins and minerals, but also contain high amounts of water. In this case, fruit is one of the food products most prone to spoilage due to its high enzymatic and microbiological activity. Increasing the shelf life of a fruit product is possible by stopping this microbiological activity. Drying is the most popular method for preserving fruits. The main features of this method are to extend shelf life, reduce weight for transportation, minimize storage space, and reduce water activity. With the freeze-drying method, the highest quality product can be obtained compared to other drying methods. When water is added again to the freeze-dried material, it quickly absorbs water in its structure (rehydration) thanks to its wrinkle-free and porous structure and reaches a structure very close to its structure before drying. Another advantage of freeze-dried foods and biological materials is that they experience little loss of taste and aroma during the drying process [1]. There is less antioxidant loss in freeze-dried products than in products dried with other drying methods [2]. In studies conducted for exotic fruits, it has been stated that freeze drying preserves physical properties, minimizes shrinkage, and preserves vitamin C and phenolic content more than other methods [3, 4]. Kumquat is a small, elliptical-shaped fruit which contains high amounts of antioxidant substances. They are used as traditional folk medicine to manage inflammation of the respiratory tract. The flavonoid compositions of kumquats are very different from those of other citrus species [5-7].

In the literature, there are studies on freeze drying of citrus fruits and the effects of ultrasonic pretreatment for many fruits and vegetables. Izli et al. (2018) determined optimal drying conditions for Kumquat in an oven dryer at 70°C [8]. Igual et al. (2019) focused on freeze-drying grapefruit with high molecular weight solutes. The study included a microwave drying pretreatment, revealing Midilli-Küçük and Page models as suitable for different formulations (F1, F2, F3) with corresponding freeze-drying times. Nutrition and antioxidant capacity were evaluated, showing a protective effect of gum arabic and bamboo fiber [9]. Silva-Espinoza et al. (2021) explored freeze-dried orange snacks, considering freezing rate, shelf temperature, and working pressure. Sensory factors influenced optimal freeze-drying conditions [10]. Dziki (2020) investigated various pretreatment methods on freeze-dried food, highlighting the reduction in drying time for fruits with ultrasound (US) pretreatment. US also enhanced antioxidant properties but caused reduced hardness and shrinkage in quince fruit [11]. Tüfekci et al. (2017) studied ultrasonic pre-treatment on carrot slices before hot air drying, finding increased drying speed and reduced time with longer pre-treatment. Page and Modified Page models explained drying kinetics, and SEM images showed tissue damage with higher amplitude [12]. Turgut (2021) compared freeze drying and hot air drying (50°C, 60°C, 70°C, 1 m/s) effects on Kumquat slices. Freeze-dried slices exhibited superior properties in terms of color, total phenolic, total flavonoid, and ascorbic acid content. The study suggests freeze drying as an alternative for bioactive-rich fruits like kumquat [13].

* Corresponding author. *e-mail address: dilek.otal@std.yildiz.edu.tr*

Despite numerous freeze-drying modeling studies on other citrus fruits, research on kumquat has focused solely on quality characteristics. Furthermore, while ultrasound (US) pretreatment is commonly applied to various fruits before freeze drying, there is a lack of studies on kumquat. Hence, this study aims to develop mathematical models for the freeze-drying process of kumquat slices with ultrasonic pre-treatment.

2. Materials and Methods

2.1. Sample Preparation and the Drying Experiments

Kumquats were obtained from a retail market in Turkiye/Istanbul in September 2023. Kumquat samples was prepared for the study by cutting it in half, each piece weighing approximately 5.0 ± 0.5 g using a Radwag AS 220.R2 Digital Balance (Radwag, Radom, Poland) with an accuracy of 0.0001 g. Ultrasonic pre-treatment (US) was applied to Kumquat samples for 30 and 60 seconds in Isolab Water Bath with 1°C sensitivity and 120 W ultrasonic power (Isolab, Germany). Initial weighing of all samples was taken, and their moisture contents were determined at 105°C for 4 hours using a KH-45 hot air-drying oven (Kenton, Guangzhou, China). The samples were dried in a freeze dryer under conditions of -68.6 ºC and 0.9 Pa. Every 60 minutes, the system's vacuum was switched off to allow for the removal of the samples, which took less than two minutes to weigh and record. Then, the vacuum was activated, and the products were put back into the freeze drier. When the samples' moisture content reached 5%, the drying process was stopped, and the samples were vacuum-packed.

2.2. Modeling Analyses

The mass diffusion equation for drying edible products with a falling-rate period is represented by Fick's second law of diffusion. It is observed that the moisture content of the sample is decreased while the drying process continues. To investigate this process moisture content, and the moisture ratio calculations are performed with the following equations (1), (2), and (3).

$$M = {}^{m_w}/_{m_d} \tag{1}$$

where moisture content (*M*) is calculated by the ratio of water content in the material (kg) to the dry matter content (kg).

$$MR = \frac{M_t - M_e}{M_i - M_e} \tag{2}$$

where M_t is the moisture content at a specific time, M_e is the moisture content at equilibrium, and M_i is the moisture content of the material initially. Since M_e value is rather small compared to M_t and M_i the simplified equation, equation (3) is used for moisture rate calculations [14,15].

$$MR = \frac{M_t}{M_i} \tag{3}$$

In this research mathematical modeling of Kumquat is done using different models as shown in Table.

Table 1. Drying models and equations**

Model	Equation	
Hendersen & Pabis	$MR = aexp(-kt)$	[16]
Jena & Das	$MR = aexp(-kt + bt^{1/2}) + c$	[17]
Lewis	$MR = exp(-kt)$	[18]
Two-Term Exponential	$MR = aexp(-kt) + (1-a)exp(-kat)$	[19]

**In Table 1, a, b and c are the drying exponent coefficients that are defined for each equation separately: k is the drying coefficient that are defined equations separately and the t stands for time.

To find the best suitable model coefficient of determination (R^2), root-mean-square error (*RMSE*), and reduced chi-squared statistic (χ^2) are used. Required parameters for given models are estimated using the non-linear

regression method with Statistica (Statistica, 2016). Equations for these methods are given below in equations (4), (5), and (6) respectively as follows.

$$R^2 = 1 - \frac{\sum_{i=1}^{n}\left(MR_{exp.i} - MR_{pre.i}\right)^2}{\sum_{i=1}^{n}\left(MR_{exp.i} - \left(\frac{1}{n}\right)MR_{exp.i}\right)^2} \quad (4)$$

$$RMSE = \left(\frac{1}{n}\sum_{i=1}^{n}\left(MR_{exp.i} - MR_{pre.i}\right)^2\right)^{1/2} \quad (5)$$

$$\chi^2 = \frac{\sum_{i=1}^{n}\left(MR_{exp.i} - MR_{pre.i}\right)^2}{n-z} \quad (6)$$

where MR_{exp} is the experimental moisture ratio values, MR_{pre} is the predicted moisture ratio values, n is the total number of the experiments, and z is the number of the constants in the given model. In the selection of best fitted model R^2 values are expected to be closer to 1. On the other hand, *RMSE* and χ^2 values are expected to be closer to 0 [14,15].

3. Results and Discussion

3.1. Drying Experiments' Results

In the moisture determination study carried out before freeze drying, the moisture contents were determined as 80.10% on wet basis in the control sample, 83.49% on wet basis in 30 seconds US pretreatment, and 81.65% on wet basis in 60 seconds s US pretreatment. Drying of control and pretreated samples was completed at 480 minutes. Kumquats before and after freeze drying are shown in Figure 1.

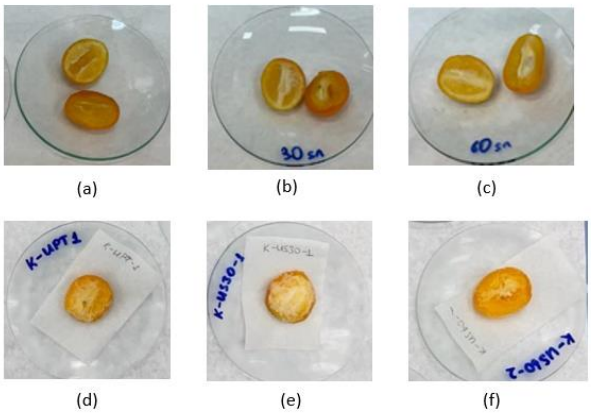

Figure 1. Control (a), 30 s US (b), and 60 s US (c) samples before drying and control (d), 30 s US (e), and 60 s US (f) samples after drying

3.2. Modeling Analyses Results

The most suitable model was chosen with non-linear regression by Statistica software. Experimental moisture ratios with respect to drying time were fitted into Hendersen & Pabis, Jena & Das, Lewis, and Two-Term Exponential drying models. Statistical results of drying process at different parameters are given in Table 2. Comparison between the results showed that the lowest R^2 average is seen in Lewis model as 0.994854, 0.996505, and 0.996888 for control, 30 second US, 60 seconds US samples, respectively. Whereas the highest R^2 average is seen in Jena & Das model as 0.997620, 0.997944, and 0.998673 for control, 30 second US, 60 seconds US samples, respectively. In support of these results, the lowest values of χ^2 0.000802, 0.000638 and 0.000411 and the lowest values of *RMSE* as 0.021106, 0.018820 and 0.015119 are obtained with Jena & Das model for drying of control, 30 second US, 60 seconds US samples, respectively. From the statistical methods, it can be seen that

all the drying models are sufficient to define the relation between moisture ratio and the drying time, but Jena & Das model was chosen as the most fitted model.

Table 2. Mathematical and statistical parameters for drying models**

Model	Parameter	Unpretreated	30 sec - US	60 sec - US
Hendersen & Pabis	*a*	1.026427	1.017758	1.020772
	k	0.004783	0.004353	0.004334
	R^2	0.995460	0.996810	0.997306
	χ^2	0.001091	0.000706	0.000596
	RMSE	0.029133	0.023437	0.021531
Jena & Das	*a*	15.966409	1.616275	3.166849
	k	0.005854	0.005038	0.005086
	b	0.018107	0.012023	0.013184
	c	-2.776722	-0.485897	-1.157761
	R^2	0.997620	0.997944	0.998673
	χ^2	0.000802	0.000638	0.000411
	RMSE	0.021106	0.018820	0.015119
Lewis	*k*	0.004657	0.004271	0.004238
	R^2	0.994854	0.996505	0.996888
	χ^2	0.001082	0.000677	0.000602
	RMSE	0.031011	0.024530	0.023140
Two-Term Exponential	*a*	0.002413	0.001987	0.002735
	k	1.921299	2.141615	1.541651
	R^2	0.994740	0.996434	0.996773
	χ^2	0.001264	0.000789	0.000714
	RMSE	0.031353	0.024778	0.023564

**In Table 2, *a*, *b* and *c* are the drying exponent coefficients that are defined for each equation separately: *k* is the drying coefficient that are defined equations separately and the t stands for time.

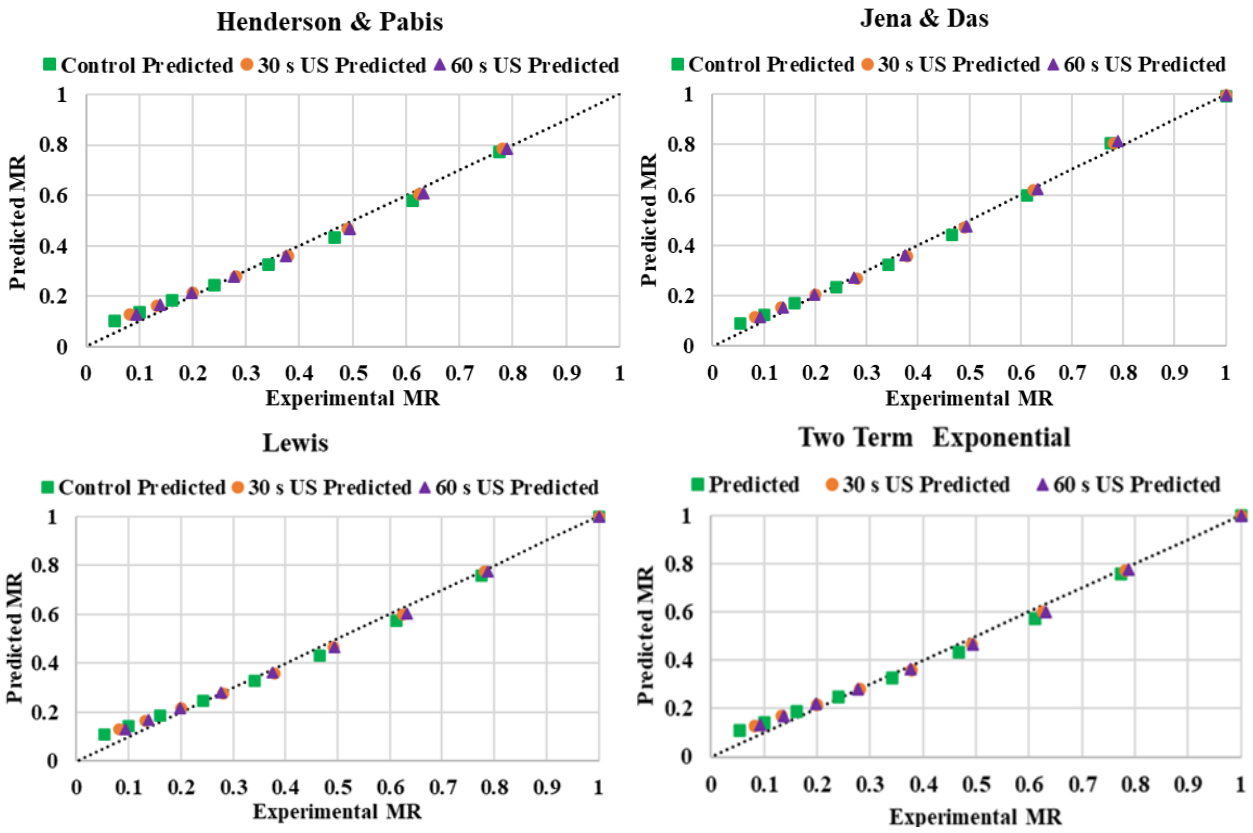

Figure 1. Graphs of mathematical drying models overlapping with data

4. Conclusion

This study was carried out to investigate the freeze-drying kinetics and mathematical modeling of Kumquat. The pretreatment was carried out for two different times, but the drying times for the control and pretreated samples were found to be the same. Different mathematical drying models were applied and Jena & Das drying model was selected as the most appropriate model for all samples considering R^2, *RMSE* and χ^2. The experimental and predicted moisture content graphs of the applied models were drawn and data distributions were observed. Accordingly, it was concluded that the US pretreatment showed similar results with the control sample within the applied times and measured parameters.

Acknowledgement

This work has been supported by Yildiz Technical University Scientific Research Projects Coordination Unit under project number FHD-2023-5569.

References

[1] Öz Ö., *Production of Soluble Tea by Freeze Drying*, Master of Science Thesis, Gebze Higher Institute of Technology, Chemical Engineering Department, 2019, 94, Kocaeli.
[2] Gümüşay Ö.A., Borazan A.A., Ercal N. & Demirkol O. (2014). Drying Effects on The Antioxidant Properties of Tomatoes and Ginger, *Food Chemistry, 173(2015)*, 156-162.
[3] Chong C.H., Law C.H. (2010). Drying of Exotic Fruits, *Vegetables and Fruit, Vol 2*, 1-42.
[4] Marques, L.G., Ferreira, M.C. & Freire, J.T. (2007). Freeze-drying of acerola (Malpighia glabra L.), *Chemical Engineering and Processing, 46*, 451-457.
[5] Barreca D., Bellocco E., Caristi C., Leuzzi U. & Gattuso G. (2010). Kumquat (Fortunella japonica Swingle) juice: Flavonoid distribution andantioxidant properties, *Food Research International, 44*, 2190–2197.
[6] Chaverri J., Rodríguez N.C., Ibarra M.O. & Rojas J.M.P (2008). Medicinal properties of mangosteen (Garcinia mangostana), *Food and Chemical Toxicology, 46*, 3227–3239.
[7] Chaovanalikit, A., Mingmuang, A., Kitbunluewit, T., Choldumrongkool, N., Sondee, J. & Chupratum, S. (2012). Anthocyanin and total phenolics content of mangosteen and effect of processing on the quality of mangosteen products, *International Food Research Journal 19, 3*, 1047-1053.
[8] Izlı, G., Izlı, N., Taskin, O. & Yildiz. G. (2018). Convective drying of kumquat slices: comparison of different drying temperatures on drying kinetics, colour, total phenolic content and antioxidant capacity, *Latin American Applied Research, 48*, 37-42.
[9] Igual M., Cebadra L., Cámara R.M., Agudelo C., Navarrete N.M. & Cámara M. (2019). Novel Ingredients Based on Grapefruit Freeze-Dried Formulations: Nutritional and Bioactive Value, *Foods 2019, 8*, 506-520.
[10] Silva-Espinoza, M. A.; Salvador, A., Camacho, M. D. M. & Martínez-Navarrete, N. (2021). Impact of Freeze-Drying Conditions on the Sensory Perception of a Freeze-Dried Orange Snack. *J. Sci. Food Agric. 2021, 101*, 4585–4590.
[11] Dziki D. (2020). Recent Trends in Pretreatment of Food before Freeze-Drying, *Processes 2020, 8*, 1661-1679.
[12] Tüfekçi S. & Özkal S.G. (2018). Ultrases Ön İşleminin Havuç Dilimlerinin Kuruma Karakteristikleri Üzerine Etkisi, *Akademik Gıda,16(1),*11-19.
[13] Yıldız T.D. (2021). Some Quality Properties of Kumquat Slices Dried by Freeze Drying And Hot Air Drying Methods, *Bahçe 51,1*,11-19.
[14] Doymaz, İ., Kipcak, A. S., & Piskin, S. (2015). Characteristics of thin-layer infrared drying of green bean, *Czech Journal of Food Sciences, 33(1)*, 83–90.
[15] Kipcak, A. S. (2017). Microwave drying kinetics of mussels (Mytilus edulis), *Research on Chemical Intermediates, 43(3)*, 1429-1445.
[16] Jena S. & Das H. (2007). Modelling for vacuum drying characteristics of coconut presscake, *Journal of Food Engineering, 79(1)*, 92-99.
[17] İsmail O., Kipçak A.S., Doymaz İ. & Pişkin S. (2017). Thin-layer drying kinetics of nectarine slices using IR, MW and hybrid methods, *Bulgarian Chemical Communications, 49*, 92-100.
[18] Acar B., Sadikoglu H. & Doymaz I. (2013). Freeze-Drying Kinetics and Diffusion Modeling of Saffron (Crocus Sativus L.), *Journal of Food Processing and Preservation*, 1-8.

[19] Kıpçak A.S., Derun E.M., Tuğrul N. & Doymaz İ. (2021). Drying Characteristics of Blue Mussels by Tradıtıonal Methods, *Chem. Ind. Chem. Eng. Q., 27 (3),* 279−288

How to determine the extent of the gas-solid reactions via effluent gas analysis

Elaf Abdulameer Taher ALSALIHI [1], ***Nesibe DİLMAÇ*** [2,*]

[1] *Engineering Faculty, Chemical Engineering Department, Çankırı Karatekin University, Çankırı, Türkiye*

[2] *Engineering Faculty, Chemical Engineering Department, Çankırı Karatekin University, Çankırı, Türkiye*

Abstract

This study describes the method used for converting the effluent gas composition data into the extent of the gas-solid reaction. Specifically, the "direct reduction" reaction between the H_2 gas and iron ore (which contains mainly Fe_2O_3) was considered. As the first step, the reactive gas (H_2) whose flow rate and composition were adjusted by a mass flow controller, was sent to the empty fluidized bed reactor in the absence of the solid reactant, and the composition of the effluent was recorded with a simultaneous gas analyzer. In this way, a constant "base concentration" line that showed the effluent concentration values in no reaction conditions was determined. Afterward, the procedure was repeated with the same H_2 concentration for 5 g of iron ore in the reactor, and the composition of the effluent gas was recorded. In this way, a time-dependent concentration curve was obtained. The points constituted that curve corresponded to the "instantaneous unconsumed H_2 " values. By subtracting the unconsumed values from the base values via Microsoft Excel®, the "instantaneous H_2 consumption" curve of the reaction was obtained. Inserting the laboratory temperature, pressure, and the volumetric rate of gas flow rate into the ideal gas law, the curve was rearranged to show the molar amount of the instantly consumed H_2. As the last step, taking into account the reaction stochiometry between Fe_2O_3 and H_2, the instantaneous molar amount of the oxygen removed from the ore was calculated. As the extent of the direct reduction reaction is mostly defined as the ratio of the oxygen removed from the ore to the total amount of removable oxygen in the ore, the instantaneous reaction extent was calculated considering the oxygen content of the 5 g iron ore. By summing all the calculated instantaneous values, the final reduction degree was determined.

Keywords: *Effluent gas analysis, Direct reduction, Gas-solid reactions, Iron ore, Hematite*

1. Introduction

Direct reduction of iron ores is an important issue since the world's stainless-steel requirement increases daily. The traditional blast furnace (BF) method is the major producer of the iron and steel industry [1]. However, high-grade iron ore and metallurgical coke reserves which are convenient for the pyrometallurgical BF method are depleting. Moreover, the first investment costs for the integrated BF-basic oxygen furnace (BOF) facilities may be unaffordable for many countries. All these facts make direct reduction (DR) processes an attractive alternative for metallic iron production. The basic concept of gaseous DR processes depends on removing the lattice oxygen of the iron ore (preferably hematite, limonite, or goethite) in the solid state via a reducing gas that contains various blends of CH_4, CO, and H_2. Since the melting of the ore is avoided in this production route, it is more energy-efficient and affordable compared to the BF method. Furthermore, low-grade ores which are inconvenient for the BF method can also be utilized and converted into metallic iron in these processes. Thanks to all the abovementioned facts, the share of the DR processes in metallic iron production increased constantly since the 1960s. Thus, understanding and analyzing the kinetics of the DR reactions became a requirement for more precise process design and optimization studies. In this context, determining and tracing the extent of the iron ore reduction with high accuracy is of vital importance [2].

The direct reduction of hematite (Fe_2O_3) with H_2 is a multistage reaction system given in Eq.1 to Eq.3. As 11% of the lattice oxygen is removed from hematite, the material transforms into magnetite (Fe_3O_4), while a further 22% (33% in total) removal results in the formation of wustite (FeO). In the last step, the remaining 67% moves away from the material, leaving behind the metallic iron [3].

$$3Fe_2O_3 + H_2 \rightarrow 2Fe_3O_4 + H_2O \quad (1)$$

$$2Fe_3O_4 + 2\,H_2 \rightarrow 6FeO + 2\,H_2O \quad (2)$$

$$6FeO + 6\,H_2 \rightarrow 6Fe + 6\,H_2O \quad (3)$$

* Corresponding author. *e-mail address: ndilmac@karatekin.edu.tr*

The conversion of the iron ore during these reactions can be stated with Eq.4, where "m_t, m_o, and m_r" are the instantaneous, fully oxidized, and fully reduced weights of the iron ore.

$$\alpha = \frac{m_o - m_t}{m_o - m_r} \tag{4}$$

In traditional studies, the conversion of the ore used to be calculated by interrupting the reduction run at several stages, taking a piece of solid sample from the reactor, and analyzing the content of the said sample via various methods such as titration, spectroscopy, etc. to determine oxygen loss.This is costly, time-consuming, and labor-intensive. For this reason, in the current study, we offer a faster and easier method that depends on tracing the effluent gas composition during the experiment. In this method, the amount of oxygen removed from the ore is calculated depending on the enrichment of the effluent gas in respect of oxygen.

2. Materials and Methods

2.1 Set-up

Fig.1 shows the experimental set-up in which the DR tests are performed. It consists of gas cylinders, gas lines, mass flow controllers, a programmable logic control unit, a vertical furnace, a quartz fluidized bed reactor, and an online simultaneous gas analyzer (ABB EL 3020).

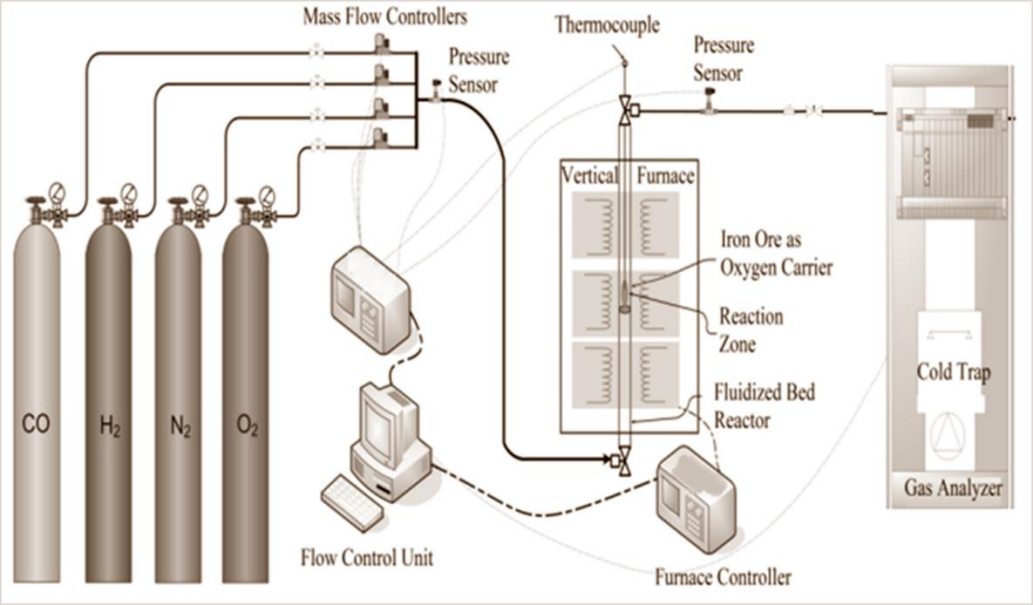

Figure 1. The experimental set-up

2.2 Method

As the first step, the reactive gas (H_2) whose flow rate and composition were adjusted by a mass flow controller, was sent to the empty fluidized bed reactor in the absence of the solid reactant, and the composition of the effluent was recorded with the simultaneous gas analyzer. In this way, a constant "base concentration" line that showed the effluent concentration in no reaction condition was determined.

Afterward, the procedure was repeated with the same H_2 concentration for 5 g of iron ore in the reactor, and the composition of the effluent gas was recorded. In this way, a time-dependent concentration curve which can be referred as the "experiment curve" was obtained. An example illustration is given in Fig.2 for a test performed with a 25% H_2-containing gas stream. As can be seen in Fig.2, while the baseline has a constant 25% value from the beginning to the end, the beginning parts of the experiment curve have low concentration values due to the consumption of H_2 in the reactor. As the reduction progresses, the effluent concentration values increase gradually depending on the reaction kinetics, and finally, they reach to the inlet concentration since the H_2-consuming reaction is almost completed. The points constituted that curve correspond to the "instantaneous unconsumed H_2 " values.

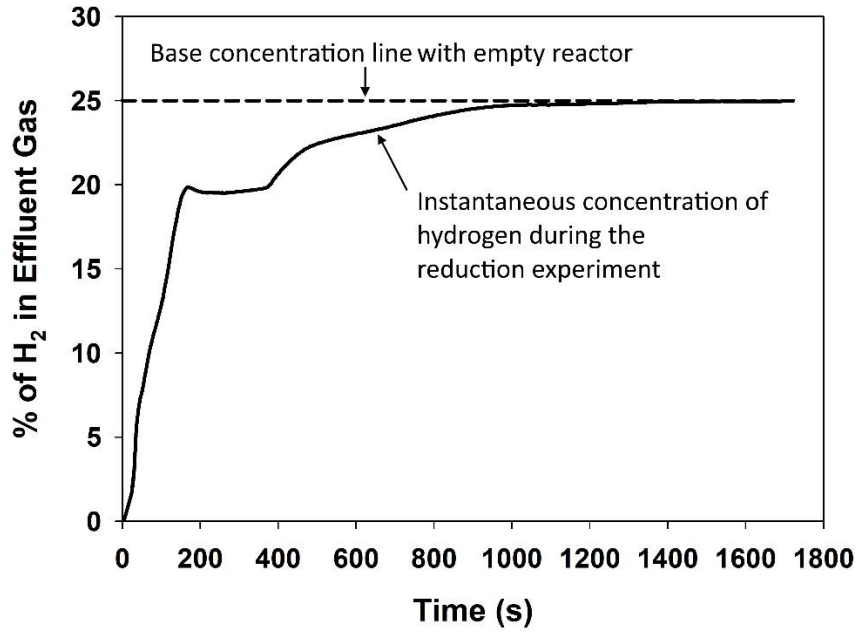

Figure 2. "Base concentration line" and "experiment curve" for a DR test performed with 25% H_2

By subtracting the unconsumed values from the base values via Microsoft Excel®, the "instantaneous H_2 consumption" curve of the reaction can be obtained. Inserting the laboratory temperature, pressure, and the volumetric rate of gas flow rate into the ideal gas law, the curve can be rearranged to show the molar amount of the instantly consumed H_2 as seen in Fig.3 [4,5]. It is worth to emphasize that the curve in Fig.3 has high values at beginning due to the fast consumption of H_2, while by the end of the test, the instantaneous consumption of the gas reactant nearly stops.

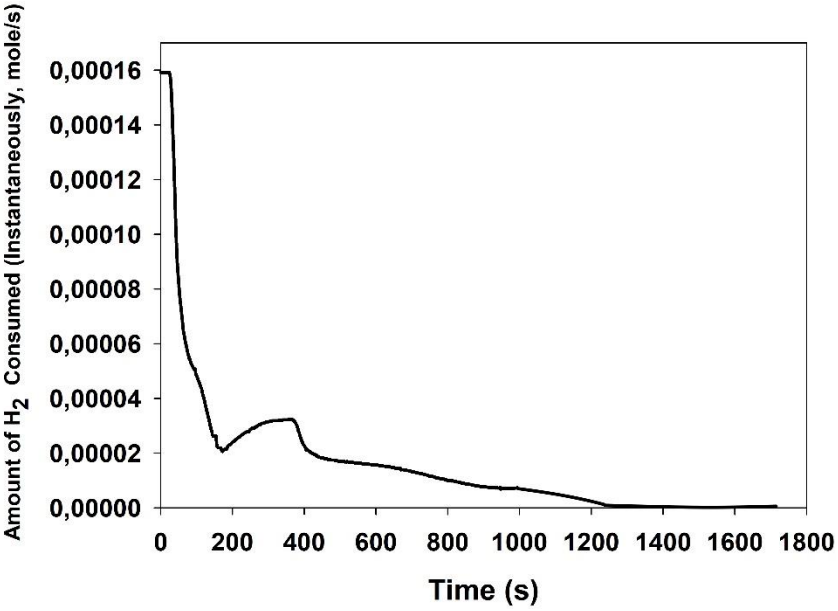

Figure 3. "Instantaneously consumed H_2" curve for a DR test performed with 25% H_2

As is known, the area under the curve in Fig.3 is equal to the total amount of consumed H_2. Summing all the instantaneous values means integration of the curve seen in Fig.3. Since Microsoft Excell has no specific tool for integrating a given data set, the "midpoint rule" can be applied to the data and the "total consumed H_2" curve given in Fig.4 can be obtained [6]. After obtaining the total amount of consumed H_2, instantaneous molar amount of the oxygen removed from the ore can be calculated by taking into account the reaction stochiometries given in Eq.1 to Eq.3.

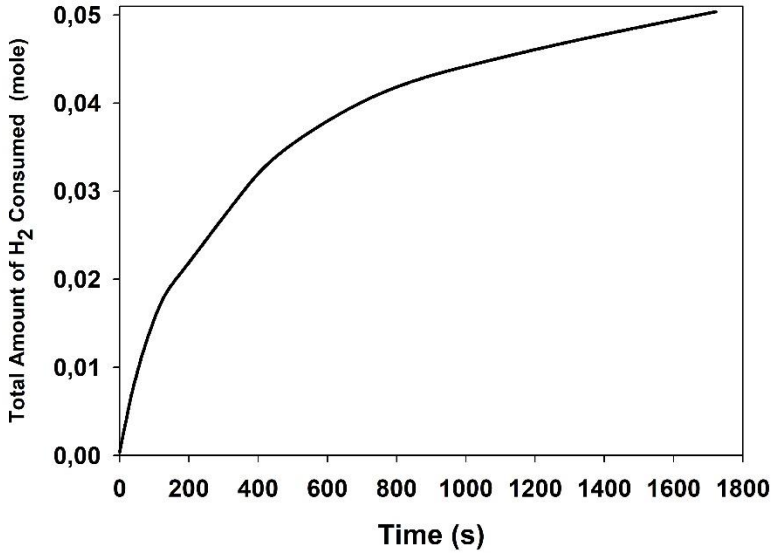

Figure 4. "Total consumed H_2" curve for a DR test performed with 25% H_2

As the extent of the direct reduction reaction is mostly defined as the ratio of the oxygen removed from the ore to the total amount of removable oxygen in the ore (Eq.5), the reaction extent can be calculated considering the oxygen content of the 5 g iron ore, and the obtained values can be graphed as seen in Fig.5.

$$Reduction\ Degree\ (R) = \frac{Amount\ of\ total\ removed\ oxygen\ during\ test}{Amount\ of\ total\ oxygen\ bounded\ to\ iron\ in\ 5\ g\ iron\ ore} \times 100 \qquad (5)$$

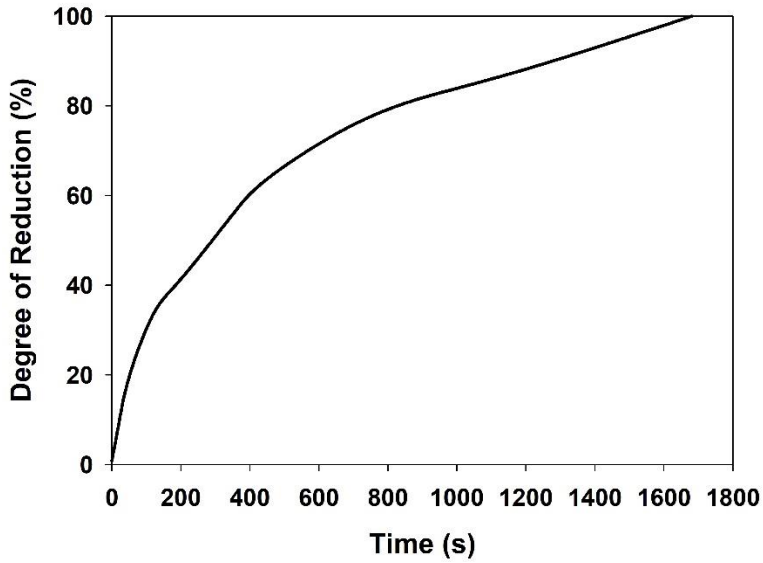

Figure 5. "t-R%" curve for a DR test performed with 25% H_2 (R=100×α)

3. Conclusion

In this study, the extent of a gas-solid reaction was determined by tracing the effluent gas concentration. The obtained results were in high accordance with the ones determined by volumetric titration [7]. Thus, it can be concluded that, using online gas analysing technique is easier and faster than traditional methods that depend on interrupting the test for taking the solid sample out of the reaction zone. In other words, reaserchers focus on the changes of the gaseous media as a result of the reaction instead of the changes occurred in the solid reactant.

Acknowledgement

This study was financially supported by Çankırı Karatekin University Scientific Researches Council (ÇAKÜ BAP Birimi) under Grant Number MF080120B19. The authors thank all supporters due to their precious contributions.

References

[1] Hammam, A., Li, Y., Nie, H., Zan, L., Ding, W., Ge, Y., Li, M., Omran, M., & Yu, Y. (2021). Isothermal and non-isothermal reduction behaviors of iron ore compacts in pure hydrogen atmosphere and kinetic analysis. *Mining Metall. Explor., 38*: 81-93.

[2] Bohn, C. D., Cleeton, J. P., Muller, C. R., Davidson, J. F., Hayhurst, A. N., Scott, S. A., & Dennis, J. S. (2010). The kinetics of the reduction of iron oxide by carbon monoxide mixed with carbon dioxide. *AIChE J., 56 (4)*: 1016-1029.

[3] Chen, H., Zheng, Z., Chen, Z., Yu, W., & Yue, J. (2017). Multistep reduction kinetics of fine iron ore with carbon monoxide in a micro fluidized bed reaction analyzer. *Metall. Mater. Trans. B-Process. Metall. Mater. Process. Sci., 48 (2)*: 841-852.

[4] Dilmaç, N., Yörük, S., & Gülaboğlu, M.Ş. (2012). Determination of reduction degree of direct reduced iron via FT-IR spectroscopy, *Vibrational Spectroscopy, 61*: 25-29.

[5] Chen, H., Zheng, Z., Chen, Z., & Bi, X.T. (2017). Reduction of hematite (Fe_2O_3) to metallic iron (Fe) by CO in a micro fluidized bed reaction analyzer: A multistep kinetics study, *Powder Technology, 316*: 410-420.

[6] Web site. https://www.youtube.com/watch?v=R8g3B2iySA4. Date of access: 22.12.2023.

[7] Alsalihi E., Menteş yöresi hematit cevherinin akışkan yatak reaktörde indirgenme kinetiğinin belirlenmesi, MSc Thesis, Çankırı Karatekin University, Graduate School of Natural and Applied Sciences, 2022, 52 pages, Çankırı.

The result on fixed points in Δ-symmetric quasi-metric spaces through θ-contraction

Gonca DURMAZ GÜNGÖR [1,*], *Ishak ALTUN* [2]

[1]*Department of Mathematics, Faculty of Science, Çankırı Karatekin University, 18100 Çankırı, Turkey*

[2]*Department of Mathematics, Faculty of Science and Arts, Kirikkale University, 71450 Yahsihan, Kirikkale, Turkey*

Abstract

In this study, we present a fixed point theorems for single-valued mappings considering a new type contraction on some kind of complete Δ-symmetric quasi-metric spaces, which has a comprehensive structure space and has a more application on computer science and semantics. On the other hand, an attracted generalization of the Banach contraction principle given by Jleli and Samet, introduced a new type of contractive condition, we shall call it as θ-contraction. In this work, by considering the Jleli and Samet's technique for contractions on metric space, we give a new concept for single-valued mappings on Δ-symmetric quasi metric spaces.

Keywords: *Quasi metric space, θ-contraction, fixed point, Δ-symmetric quasi metric*

1 Introduction and preliminaries

After the introduction of the Banach contraction principle [5], fixed point theory, a renowned tool in nonlinear analysis, gained prominence in research endeavors. Owing to its utility in addressing nonlinear integro-differential equations, nonlinear Volterra integral equations, game theory, and more, the existence of fixed points for contraction-type mappings in metric spaces has been explored by numerous researchers.

In addition to these developments, as documented by Jleli and Samet in their work [9], they have introduced a novel category of contractive mappings termed θ-contractions. This concept represents a compelling generalization within the field. Mappings satisfying the θ-contraction condition have been the subject of extensive investigation in the literature (see [3, 8]). Liu et al., in their publication [14], proposed an alternative condition (θ_3) as a means to define a distinct class of functions. To gain a deeper insight into these methodologies, let's delve into some key concepts and relevant findings pertaining to the θ-contraction, as defined in [9] and [14].

Eligible the function $\theta: (0,\infty) \to (1,\infty)$ can be called by the set Θ satisfies conditions $(\theta_1, \theta_2, \theta_3)$, and let it be called by the set Π if it satisfies conditions $(\theta_1, \theta_2, \theta_3^*)$.

(θ_1) θ is nondecreasing;

(θ_2) Considering every sequence $\{\varkappa_n\} \subset (0,+\infty)$, $\lim_{n\to\infty}\varkappa_n = 0^+$ if, and only if, $\lim_{n\to+\infty}\theta(\varkappa_n) = 1$;

(θ_3) There exists $0 < p < 1$ and $\beta \in (0,+\infty]$ such that $\lim_{\varkappa\to 0^+}\frac{\theta(\varkappa)-1}{\varkappa^p} = \beta$;

(θ_3^*) θ is continuous on $(0,+\infty)$.

Let $\theta_1(\varkappa) = e^{\varkappa}$, $\theta_2(\varkappa) = \varkappa + e^{\varkappa}$, $\theta_3(\varkappa) = 1 + \sinh\varkappa$ and $\theta_4(\varkappa) = \cosh\varkappa$ be functions belonging to the class Π. Furthermore, when $(\varkappa) = e^{\varkappa}$, the conditions $(\theta_1), (\theta_2)$ and (θ_3^*) are satisfied, but the condition for (θ_3) is not satisfied, thus it can be observed that it belongs to $\Pi \nsubseteq \Theta$. Similarly, if $\theta(\varkappa) = \begin{cases} e^{\sqrt{\varkappa}}, & \varkappa \le 1 \\ 9, & \varkappa > 1 \end{cases}$, then the conditions $(\theta_1), (\theta_2)$ and (θ_3) are satisfied, but the condition for (θ_3^*) is not satisfied, thus it can be

* Corresponding author. *e-mail address: gncmatematik@hotmail.com.*

observed that it belongs to $\Theta \nsubseteq \Pi$. Additionally, if we consider $\theta(\varkappa) = e^{\sqrt{\varkappa}}$, then $\theta \in \Theta \cap \Pi$, and thus we can infer that the set $\Theta \cap \Pi$ is different from the empty set.

Let $\theta \in \Theta$(resp. $\theta \in \Pi$) and (Λ, ρ) be a metric space, then $\Upsilon: \Lambda \to \Lambda$ is said to be a θ(resp. θ^*)-contraction if there exists $0 < \delta < 1$ such that

$$\theta(\rho(\Upsilon\omega, \Upsilon\gamma)) \leq [\theta(\rho(\omega, \gamma))]^{\delta} \quad (1)$$

for each $\omega, \gamma \in \Lambda$ with $\rho(\Upsilon\omega, \Upsilon\gamma) > 0$.

If a mapping Υ is the Banach contraction, then it satisfies (1). After these categorizations, Jleli and Samet [9] and Liu et al. [14] have represented every θ (θ^*)-contraction on complete metric space has a unique fixed point in their theorems, which are a generalized variant of Banach contraction mapping principle. These results provide a valuable insight into the uniqueness and existence of fixed points for a wide range of contractive mappings.

But owing to the strict conditions of the metric space and the specific properties imposed, the need to work with topological structures that have more flexible conditions than the metric space has emerged.Therefore, many generalizations of the Banach fixed point theorem have been obtained in this space by defining the quasi-metric space. Furthermore, quasi-metric spaces are useful in numerous topics of mathematics, like optimization, functional analysis and computer science. They provide a more general framework for studying approachs related to distances and convergence, allowing for more flexible and adaptable notions of proximity (see [1, 12]). Now, let's review the definitions and notations related to quasi-metric space:

$\Lambda \neq \emptyset$ and ρ are a function $\rho: \Lambda \times \Lambda \to \mathbb{R}$ such that for each $\omega, \gamma, \eta \in \Lambda$:

- $\rho(\omega, \omega) = 0$,
- $\rho(\omega, \gamma) \leq \rho(\omega, \eta) + \rho(\eta, \gamma)$ (triangle inequality),
- $\rho(\omega, \gamma) = \rho(\gamma, \omega) = 0$ implies $\omega = \gamma$ (asymmetry),
- $\rho(\omega, \gamma) = 0$ implies $\omega = \gamma$.

If (i) and (ii) conditions are satisfied, then ρ is called a quasi-pseudo metric (shortly qpm); if (i), (ii) and (iii) conditions are satisfied, then ρ is called quasi metric (shortly qm); in addition, if a qm ρ satisfies (iv), then ρ is called T_1-qm.

Let (Λ, ρ) be a qms, $\{\omega_n\}$ be a sequence and $\omega \in \Lambda$. If $\lim_{n\to\infty} \rho(\omega_n, \omega) = \lim_{n\to\infty} \rho(\omega, \omega_n) = 0$ holds, then $\{\omega_n\}$ is said to converges to ω. A more detailed explanation of some essential metric properties can be found in [7, 10].

In a qms,the limit for a convergent sequence (in the sense above) is unique. If the sequence $\{\omega_n\}$ converges to ω, we have for all η in Λ

$$\lim_{n\to\infty} \rho(\omega_n, \eta) = \rho(\omega, \eta) \quad \text{and} \lim_{n\to\infty} \rho(\eta, \omega_n) = \rho(\eta, \omega).$$

Also, a sequence $\{\omega_n\}$ in Λ is called left (resp. right) K-Cauchy if for every $\varepsilon > 0$, there exists $n_0 \in N$ such that for all n, k in $\mathbb{N}$ with $n \geq k \geq n_0$ (resp. $k \geq n \geq n_0$), $\rho(\omega_k, \omega_n) < \varepsilon$ (resp. $\rho(\omega_k, \omega_n) < \varepsilon$). In addition that a sequence $\{\omega_n\}$ in Λ is called Cauchy if for every $\varepsilon > 0$,there exists $n_0 \in N$ such that for all n, k in $\mathbb{N}$, $n, k \geq n_0$, $\rho(\omega_k, \omega_n) < \varepsilon$. Furthermore, it is clear that a sequence $\{\omega_n\}$ is Cauchy iff it is left K-Cauchy and right K-Cauchy in a qms.

To find the fixed point, the most important part is to use the completeness of the metric space. But since there is no symmetry conditions in a qms, there are many definitions of completeness in these spaces in the literature (see [4, 13, 6]). Furthermore, every convergent sequence is indeed a Cauchy sequence, but since this may not hold true in qms.

[[11]] Let (Λ, ρ) be a qms. Then (Λ, ρ) is said to be if every left (right) K -Cauchy sequence is convergent, then left (right) K-complete. Furthermore, it is clear that (Λ, ρ) is said to be if every Cauchy sequence is convergent, then complete.

[[11]] Let Λ be a nonempty set, ρ qm on Λ and $\Upsilon: \Lambda \to \Lambda$ be a mapping. Then Υ is said to be continuous at ω in Λ, if for all sequence $\{\omega_n\}$ in Λ such that

$$\lim_{n\to\infty}\rho(\Upsilon\omega_n,\Upsilon\omega)=\lim_{n\to\infty}\rho(\Upsilon\omega,\Upsilon\omega_n)=0.$$

In this paper, considering the above explanations, we introduce the concept of θ_ρ-contraction mappings on qms and then we present a fixed-point result for such mappings.

2. The result

Our basic results are based on a novel approach that we have developed.

Let (Λ,ρ) be a qms, $\Upsilon:\Lambda\to\Lambda$ be given a mapping and we will consider $\Upsilon_\rho=\{(\omega,\gamma)\in\Lambda\times\Lambda:\rho(\Upsilon\omega,\Upsilon\gamma)>0\}$.Let (Λ,ρ) be a qms and $\Upsilon:\Lambda\to\Lambda$ be a mapping satisfying

$$\rho(\omega,\gamma)=0 \text{ implies } \rho(\Upsilon\omega,\Upsilon\gamma)=0. \tag{2}$$

$\theta\in\Pi$ be a function and if there exists constant $0<\delta<1$ such that $\theta(\rho(\Upsilon\omega,\Upsilon\gamma))\le[\theta(\rho(\omega,\gamma)]^\delta$ for each $(\omega,\gamma)\in\Upsilon_\rho$, then we say that Υ is a θ_ρ-contraction.

This situation is apparent to if (Λ,ρ) is a T_1-qms, then every mapping $\Upsilon:\Lambda\to\Lambda$ satisfies the condition (2).

Recently, a novel extension in the realm of qualitative mapping structures (qms) has been introduced, introducing Δ-symmetric qms in [2] and [11]. This conceptualization can be articulated as follows:

If a pair (Λ,ρ) satisfies $\rho(\omega,\gamma)\le\Delta\rho(\gamma,\omega)$ for all ω,γ in Λ, where Δ is a positive real number, then the pair (Λ,ρ) can also be referred to as a Δ-symmetric quasi-metric space (Δ-symmetric qms).

If Λ consists of more than one point, we can find distinct elements ω,γ in Λ such that the distance $\rho(\omega,\gamma)$ between them is positive. Therefore, we have the inequality

$$0<\rho(\omega,\gamma)\le\Delta\rho(\omega,\gamma)\le\Delta^2\rho(\omega,\gamma).$$

From this, it follows that Δ must be greater than or equal to 1.

Let $(\mathbb{R},d)$ be a metric space and a function $\rho:\mathbb{R}\times\mathbb{R}\to\mathbb{R}^+$, where

$$\rho(\omega,\gamma)=\begin{cases}4d(\omega,\gamma), & \text{if}\ \omega\ge\gamma\\ d(\omega,\gamma), & \text{otherwise.}\end{cases}$$

Then, $(\mathbb{R},\rho)$ is a 4- symmetric qms, but it is not a metric space.

Below, we will outline several key characteristics of a Δ-symmetric qms.

[see [11]] Let (Λ,ρ) be a Δ-symmetric qms, $\{\omega_n\}$ be a sequence in Λ and ω in Λ. Then,

- $\{\omega_n\}$ is right Cauchy implies $\{\omega_n\}$ is left Cauchy implies $\{\omega_n\}$ is Cauchy
- if $\{\omega_n\}$ and $\{\gamma_n\}$ are two sequences in Λ and $\rho(\omega_n,\gamma_n)\to0$ then $\rho(\gamma_n,\omega_n)\to0$.

By utilizing the approach of a θ_ρ-contraction, we will now present the following theorem.

Let (Λ,ρ) be a complete Δ-symmetric T_1-qms and $\Upsilon:\Lambda\to\Lambda$ be a θ_ρ-contraction. Then Υ has a fixed point in Λ given that one of the following conditions is satisfied:

- (Λ,ρ) is Hausdorff space and Υ is continuous,
- (Λ,ρ) is $Smyth$ complete.

Proof. Let $\omega_0\in\Lambda$. Define a sequence $\{\omega_n\}$ in Λ by $\omega_n=\Upsilon\omega_{n-1}$ for each n in $\mathbb{N}$. If there exists $k\in\mathbb{N}$ with $\omega_k=\omega_{k+1}$, then $\omega_{k+1}=\Upsilon\omega_k=\omega_k$, then ω_k is a fixed point of Υ, since ρ is T_1 qms. Presume $\omega_n\neq\omega_{n+1}$ and then $\rho(\omega_n,\Upsilon\omega_n)>0$ for each n in $\mathbb{N}$. In this case, the pair $(\omega_n,\omega_{n+1})\in\Upsilon_\rho$. Since Υ is a θ_ρ-contraction and (θ_1), we obtain

$$\theta(\rho(\omega_n,\omega_{n+1}))=\theta(\rho(\Upsilon\omega_{n-1},\Upsilon\omega_n))\le[\theta(\rho(\omega_{n-1},\omega_n)]^\delta. \tag{3}$$

Denote $z_n=\rho(\omega_n,\omega_{n+1})$ for n in $\mathbb{N}$, then $z_n>0$ for each n in $\mathbb{N}$ and repeating this process by using and from (3), we have

$$\theta(z_n)\le[\theta(z_0)]^{\delta^n},$$

i.e.

$$1 < \theta(z_n) \leq [\theta(z_0)]^{s^{n-1}} \tag{4}$$

for each n in $\mathbb{N}$. When taking the limit as $n \to +\infty$ in (4), we obtain

$$\lim_{n\to\infty} \theta(z_n) = 1. \tag{5}$$

Using (θ_2), we can deduce that

$$\lim_{n\to\infty} f_n = 0^+. \tag{6}$$

Conversely, considering $\zeta_n = \rho(\omega_{n+1}, \omega_n)$ and taking into account its Δ-symmetry, we can establish the existence of $\Delta > 0$ such that

$$\frac{1}{z_n} \leq \zeta_n \leq \Delta z_n.$$

As $n \to +\infty$, utilizing the "Squeeze Theorem" and considering the convergence of the sequence $\{\omega_n\}$ to 0, we obtain the limit

$$\lim_{n\to+\infty} \zeta_n = \lim_{n\to+\infty} \rho(\omega_{n+1}, \omega_n) = 0^+. \tag{7}$$

We hereby state that $\{\omega_n\}$ is a Cauchy sequence, exhibiting properties of both left Cauchy and right Cauchy sequences within the qms (Λ, ρ). Arguing by contradiction, we assume that there exist $\varepsilon > 0$ and sequences $\{k(n)\}$ and $\{l(n)\}$ of natural numbers such that

$$k(n) > l(n) > n, \rho(\omega_{k(n)}, \omega_{l(n)}) \geq \varepsilon, \rho(\omega_{k(n)-1}, \omega_{l(n)}) < \varepsilon \tag{8}$$

for all n in $\mathbb{N}$. Thus, we have

$$\begin{aligned} &\varepsilon \leq \rho(\omega_{k(n)}, \omega_{l(n)}) \\ &\leq \rho(\omega_{k(n)}, \omega_{k(n)-1}) + \rho(\omega_{k(n)-1}, \omega_{l(n)}) \\ &\leq \rho(\omega_{k(n)}, \omega_{k(n)-1}) + \varepsilon, \end{aligned}$$

or, we denote $\sigma_n = \rho(\omega_{k(n)}, \omega_{l(n)})$,

$$\varepsilon \leq \sigma_n \leq \zeta_n + \varepsilon. \tag{9}$$

Since $\zeta_n \to 0$, taking $n \to +\infty$ in (9), we obtain

$$\varepsilon \leq \lim_{n\to+\infty} \sigma_n \leq \varepsilon$$

so, $\lim_{n\to+\infty}\sigma_n = \lim_{n\to+\infty}\rho(\omega_{k(n)}, \omega_{l(n)}) = \varepsilon$. On the other hand from (6), there exists N_1 in $\mathbb{N}$ such that

$$\rho(\omega_{k(n)}, \omega_{k(n)+1}) < \frac{\varepsilon}{3}, \rho(\omega_{l(n)}, \omega_{l(n)+1}) < \frac{\varepsilon}{3} \tag{10}$$

for all $n \geq N_1$. Next, we claim that

$$\rho(\Upsilon\omega_{k(n)}, \Upsilon\omega_{l(n)}) = \rho(\omega_{k(n)+1}, \omega_{l(n)+1}) > 0 \tag{11}$$

for all $n \geq N_1$. Arguing by contradiction, there exists $m \geq N_1$ such that

$$\rho(\omega_{k(m)+1}, \omega_{l(m)+1}) = 0. \tag{12}$$

It follows from (8), (10) and (12) that

$$\begin{aligned} &\varepsilon \leq \rho(\omega_{k(m)}, \omega_{l(m)}) \\ &\leq \rho(\omega_{k(m)}, \omega_{k(m)+1}) + \rho(\omega_{k(m)+1}, \omega_{l(m)+1}) + \rho(\omega_{l(m)+1}, \omega_{l(m)}) \\ &< \frac{\varepsilon}{3} + 0 + \frac{\varepsilon}{3} \\ &= \frac{2\varepsilon}{3}. \end{aligned}$$

This contradiction establishes the relation (11). Also, from from (6) and $\lim_{n\to+\infty}\sigma_n = \varepsilon$, we can choose a positive integer N in $\mathbb{N}$ such that

$$\frac{1}{2}\rho(\omega_{k(n)}, \Upsilon\omega_{k(n)}) < \frac{1}{2}\varepsilon < \rho(\omega_{k(n)}, \omega_{l(n)})$$

for all $n \geq N$. So, we get, for all $n \geq \max\{N, N_1\}$

$$\begin{aligned} &\theta(\rho(\omega_{k(n)+1}, \omega_{l(n)+1})) = \theta(\rho(\Upsilon\omega_{k(n)}, \Upsilon\omega_{l(n)})) \\ &\leq [\theta(\rho(\omega_{k(n)}, \omega_{l(n)}))]^{\delta}. \end{aligned} \tag{13}$$

Then, by taking limit as $n \to +\infty$ and using (θ_3^*) and (13), we get

$$\theta(\varepsilon) \leq \theta(\varepsilon)]^{\delta} \leq \theta(\varepsilon),$$

which is a contradiction. This contradictions show that $\{\omega_n\}$ is a left Cauchy sequence in the qms. (Λ, ρ). Analogously, it can be shown that $\{\omega_n\}$ is right Cauchy and we can conclude that$\{\omega_n\}$ is a Cauchy sequence in the complete Δ symmetric qms (Λ, ρ). This implies that the sequence $\{\omega_n\}$ converges to some point η, that is $\rho(\eta, \omega_n) \to 0$ and $\rho(\omega_n, \eta) \to 0$ as $n \to +\infty$.

We will now establish that η is a fixed point of Λ.

First, assume that (i) is satisfied. So, we get $\rho(\Upsilon\eta, \Upsilon\omega_n) \to 0$ and $\rho(\Upsilon\omega_n, \Upsilon\eta) \to 0$ as $n \to +\infty$. Since Λ is Hausdorff, we get $\Upsilon\eta = \eta$.

Second, assume that (ii) is satisfied. Since Λ is left Smyth complete, then $\rho^s(\omega_n, \omega) \to 0$ and $\rho^s(\omega, \omega_n) \to 0$ as $n \to +\infty$. On the other hand, from (θ_2), by (2) and for all (ω, γ) in Υ_α, we obtain

$$\rho(\Upsilon\omega, \Upsilon\gamma) \leq \rho(\omega, \gamma). \tag{14}$$

Furthermore, by (2), we have

$$\begin{aligned}\rho(\eta, \Upsilon\eta) &\leq \rho(\eta, \omega_{n+1}) + \rho(\Upsilon\omega_n, \Upsilon\eta)\\ &\leq \rho(\eta, \omega_{n+1}) + \rho(\omega_n, \eta) \to +\infty,\end{aligned}$$

we have $\eta = \Upsilon\eta$.

References

[1] C. Alegre, J. Marin, S. Romaguera, A fixed point theorem for generalized contractions involving w-distances on complete quasi metric spaces, Fixed Point Theory Appl., 2014 (2014), 8 pages.

[2] B. Alqahtani, A. Fulga, E. Karapinar, Fixed Point Results On D-Symmetric Quasi-Metric Space Via Simulation Function With An Application To Ulam Stability, Mathematics 2018, 6, 208.

[3] I. Altun, H. A. Hançer, G. Mınak, On a general class of weakly Picard operators, Miskolc Math. Notes, 16 (1) (2015), 25-32.

[4] I. Altun, G. Mınak, M. Olgun, Classification of completeness of quasi metric space and some new fixed point results, Nonlinear Functional Analysis and Applications, (2017), 371-384.

[5] Banach S., Sur les operations dans les ensembles abstraits et leurs applications aux equations integrales. Fund. Math.1922,3, 133–181.

[6] S. Cobzaş, Completeness in quasi-metric spaces and Ekeland variational principle, Topol. Appl., 158 (2011), 1073-1084.

[7] N. V. Dung, Remarks on quasi-metric spaces, Miskolc Math. Notes, 1 (2014), 401-422.

[8] M. Jleli, E. Karapinar, B. Samet, Further generalizations of the Banach contraction principle, J. Inequal. Appl. 2014, 2014:439, 9 pp.

[9] M. Jleli, B. Samet, A new generalization of the Banach contraction principle, J. Inequal. Appl. 2014, 2014:38, 8 pp..

[10] E. Karapinar, S. Romaguera, On the weak form of Ekeland's Variational Principle in quasi-metric spaces, Topol. Appl., 184 (2015), 54-60.

[11] E. Karapinar, A. F. Roldan-Lopez-de-Hierro, B. Samet, Matkowski theorems in the context of quasi-metric spaces and consequences on G-metric spaces, Analele Stiintifice Ale Univ. Ovidius-Constanta-Ser. Mat., 24 (2016), 309-333.

[12] J. Marın, S. Romaguera, P. Tirado, Weakly contractive multivalued maps and w-distances on complete quasimetric spaces, Fixed Point Theory Appl., 2011 (2011), 9 pages.

[13] S. Romaguera, Left K-completeness in quasi-metric spaces, Math. Nachr., 157 (1992), 15-23.

[14] X.-D. Liu, S.-S. Chang, Y. Xiao, L.-C. Zhao, Some fixed point theorems concerning (ψ,ϕ)-type contraction in complete metric spaces, J. Nonlinear Sci. Appl., 9 (6) (2016), 4127-4136.

Optimization of Machining Parameters in Terms of Thrust Force and Chip Formation of E-Glass/Epoxy-Carbon Nanotube Composites

***Sakine KIRATLI*[1,*], *Hüseyin GÖKÇE*[2], *Mohammed Mudhafar Hussein Hussein*[3]**

[1,2,3]*Faculty of Engineering, Mechanical Engineering, Çankırı Karatekin University, Çankırı, Turkiye*

Abstract

In this study, the drilling performances of laminated composites containing multi-walled carbon nanotubes at different weight ratios were optimized with the Taguchi method in terms of thrust forces, which is a quality characteristic. Analysis of variance (ANOVA) was performed to determine significance levels. Material, drill bit, cutting speed and feed rate for each five levels were selected as control factors and an L25 vertical array experimental design was designed accordingly. A clamping mold was manufactured for the test samples with dimensions of 150 mm × 25 mm, and the samples placed in this clamping mold were connected to the bench table with a force gauge. Chip formation was examined by means of a digital microscope. It was determined that the carbon nanotube ratio was the most effective factor on the thrust forces with 69.03%, and as the carbon nanotube ratio increased, the thrust forces increased. The effectiveness rates were found to be 21.23% in feed rate, 2.17% in drill tip and 2.12% in cutting speed, respectively. It has been observed that chip formation is mostly affected by changes in feed amount and cutting speed. Although discrete chip formation is frequently observed, it has been observed that chips form in powder form, especially at low feed rate and high cutting speeds. Verification experiments were carried out under optimum conditions determined as a result of optimization. The results measured from these experiments were compared with the results calculated by the mathematical model. It was observed that the model could be used safely with a correlation value of 94.55%.

Keywords: *Laminated composite, Taguchi method, drilling, thrust force, chip formation.*

1. Introduction

Composite materials find a place in almost every field of production, especially aviation, marine industry, wind turbines, automotive, construction, and aerospace [1]. Polymer matrix composites, which are included in the composite material class, have become interesting in industrial applications due to their light weight, superior mechanical properties, and functionalities such as versatile processing techniques [2, 3]. During the production of these polymer composites, significant increases are observed in the mechanical properties of the material with reinforcement elements added to the matrix structure [4]. In recent years, various nano- or micro-sized fillers have been added to matrices in order to improve the existing properties of composites [5–8].

In some usage areas, composite materials need to be assembled either to each other or to other components that make up the structure. In the majority of these assemblies, riveted or bolted connections are used. These joints are widely used, especially in aircraft fuselages [9]. In this type of joint, it is inevitable to drill holes in the relevant materials. High hole quality has a significant impact on ease of assembly and the life of the material. In addition, the forces that will occur during the drilling process are also an important criterion in the selection of drill bits and machine tools.

We looked at thrust forces and chip shapes during the drilling process of polymer matrix composites that had carbon nanotubes in them at different weight ratios and without any other additives. The experimental design was made using a Taguchi L25 orthogonal array. Optimization was made in terms of thrust forces, control factors (material, drill bit, cutting speed, and feed amount), and levels. Additionally, an analysis of variance was performed to determine the importance of control factors.

* Corresponding author. *e-mail address: skiratli@karatekin.edu.tr*

2. Materials and Methods

In this study, E-glass fiber and epoxy matrix were used. Two different multi-walled carbon nanotubes were added to the epoxy at rates of 0.1 and 0.5 wt.%. The carbon nanotube coded with 1 has an outer diameter of 10-20 nm, an inner diameter of 5-10 nm, and a length of 0.5–2 µm, and a carbon nanotube coded with 2 has an outer diameter of 30-50 nm, an inner diameter of 5-12 nm, and a length of 10–20 µm. Hand lay-up and vacuum bagging techniques were used in the manufacturing of composite materials. The cutting tools used in the experiments are uncoated drill bits produced from high-speed steel (HSS) material in different geometries, which is frequently preferred in industrial operations. HSS drill bits are frequently preferred for drilling composites due to their low cost and widespread use [10–12]. The drill bits used in the experiments, their geometries, and some basic dimensions are given in Table 1.

Table 1. Drill bits and basic dimensions used in experiments

Test code	Technical specifications	Drill bit images
1	β_1: 135º - β_2: 90º β_0: 30º - L: 80 mm L_1: 47 mm - z: 2	Ø5 mm step HSS - without coating 
2	β: 140º - β_0: 30º L: 100 mm L_1: 60 mm - z: 2	Ø5 mm wood HSS - without coating 
3	β: 90º - β_0: 30º L: 80 mm L_1: 40 mm - z: 2	Ø5 mm 90° HSS - without coating 
4	β: 140º - β_0: 30º L: 80 mm L_1: 50 mm - z: 2	Ø5 mm 140° HSS - without coating 
β: Tip angle, β_0; Helical angle, K: Coating, L: Drill tip length, L_1: Helical channel length, z: Number of helical channels		

The experiments were carried out on the Arion IMM-600 CNC vertical machining center. The test pieces were connected to a force meter mounted on the bench table with a clamping mold. Thrust forces were measured with a force meter based on a load cell. The chips formed as a result of the drilling experiments carried out under dry conditions were imaged with a 5-megapixel digital microscope with a resolution of 2592×1944.

In order to reach a more economical and faster solution, a Taguchi L16 orthogonal array was used in the experimental design. Control factors and levels for the relevant materials were determined as a result of similar studies and preliminary experiments in the literature. The control factors and levels used in the experiments are given in Table 2.

Table 2. Control factors and their levels used in experiments

L25 orthogonal array						
		Level				
Control factors	**Code**	1	2	3	4	5
Materials	A	1-0.1	1-0.5	2-0.1	2-0.5	0 - Pure
Drill bits	B	Step HSS	HSS wood	90° HSS	140° HSS	140° WC
Cutting speed (m/min)	C	30	60	90	120	150
Feed rate (mm/rev)	D	0.04	0.08	0.12	0.16	0.20

In the experiments, thrust force was determined as the quality characteristic, and experiments were carried out to optimize the control factors. It is desirable that the thrust force values be low to determine the optimum levels of control factors. For this purpose, the "smallest is best" objective function given in Equation 1 was used to

calculate the signal-to-noise (S/N) ratio. In this equation, n is the total number of experiments, i is the experimental order, and Y is the measurement result.

$$S/_N = -10\log\left(1/n\sum_{i=1}^{n} Y_i^2\right) \quad (1)$$

An analysis of variance (ANOVA) was applied to the experimental results at a 95% confidence interval to determine the effect of control factors on thrust force values. The Taguchi method and variance analysis were performed with the Minitab program.

3. Results and Discussion

The thrust force values occurring in drilling composite materials and the S/N ratios obtained with the "smallest is the best" objective function are given in Table 3. The main effect graphs for S/N ratios are shown in Figure 1. At the same time, the distribution of the average S/N ratios calculated for the thrust forces according to the control factors is given in Table 4.

Table 3. Thrust forces measured as a result of the experiments and calculated S/N ratios

Test no	Material	A	Drill bit	B	Vc (m/min)	C	f (mm/rev)	D	Thrust force (N)
1	1-0.1		1		30		0.04		63.9
2	1-0.1		2		60		0.08		62.2
3	1-0.1		3		90		0.12		63.3
4	1-0.1		4		120		0.16		64.7
5	1-0.1		5		150		0.2		66.9
6	1-0.5		1		60		0.12		66.8
7	1-0.5		2		90		0.16		66.4
8	1-0.5		3		120		0.2		67.4
9	1-0.5		4		150		0.04		62.6
10	1-0.5		5		30		0.08		66.7
11	2-0.1		1		90		0.2		70.8
12	2-0.1		2		120		0.04		66.4
13	2-0.1		3		150		0.08		67.1
14	2-0.1		4		30		0.12		68.5
15	2-0.1		5		60		0.16		69.9
16	2-0.5		1		120		0.08		68.9
17	2-0.5		2		150		0.12		70.1
18	2-0.5		3		30		0.16		73.2
19	2-0.5		4		60		0.2		79.4
20	2-0.5		5		90		0.04		69.8
21	0 - Pure		1		150		0.16		62.1
22	0 - Pure		2		30		0.2		65.1
23	0 - Pure		3		60		0.04		56.7
24	0 - Pure		4		90		0.08		61.1
25	0 - Pure		5		120		0.12		62.5

According to the main effect graphs in Figure 1 and the highest and lowest points of the S/N ratios in Table 4, it can be seen that the material is the most important control factor affecting the thrust forces. When Table 4 is examined, it can be seen that the control factors affecting the thrust forces are, in order of importance, material,

feed rate, drill tip, and cutting speed. It can be seen that the thrust force (Fz) values measured in the drilling of pure layered composite materials are relatively low compared to additive composite materials. The increase in material strength values with the addition and amount of additive can explain this situation [13]. However, this will result in increased forces required for the drilling process. As the chip cross-sectional area increases as the feed rate increases, more power is needed to remove the chip. Therefore, it is expected that the cutting force values will increase as the feed rate increases [14].

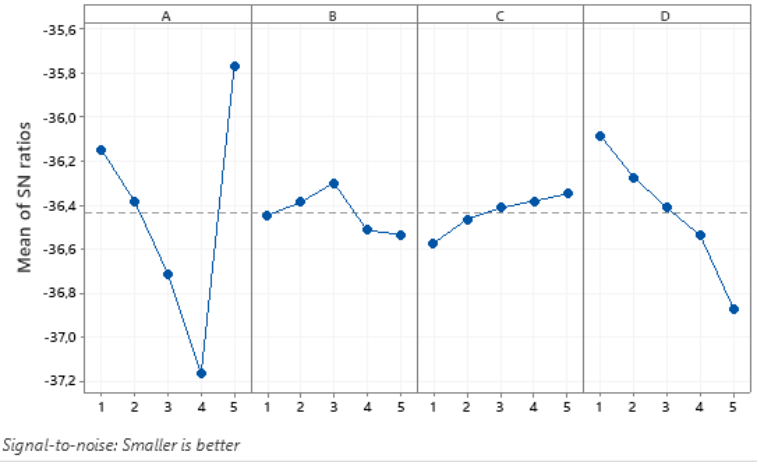

Figure 1. Main effect plots for S/N ratios of thrust forces

Tablo 4. Order of importance of control factors for average S/N ratios of thrust forces

Level	Material - A	Drill bit - B	Cutting speed - C	Feed rate - D
1	-36.15	-36.45	-36.57	-36.09
2	-36.39	-36.39	-36.47	-36.28
3	-36.71	-36.30	-36.41	-36.41
4	-37.17	-36.52	-36.38	-36.54
5	-35.77	-36.54	-36.35	-36.87
Delta	1.40	0.23	0.22	0.78
Rank	1	3	4	2

ANOVA was performed to determine the effect levels of control factors on thrust forces, and the results are given in Table 5. In this table, degrees of freedom (DF), sum of squares (Adj SS), mean of squares (Adj MS), F value, P value indicating the significance level of control factors on Fc, and percentage contribution rates are given. According to the ANOVA results, the P value being less than 0.05 indicates that the effect of the control factors on the thrust forces is statistically significant. Accordingly, it is seen that the most important control factor on thrust force is material, with 69.03%.

Table 5. Analysis of variance for thrust forces

Source	DF	Adj SS	Adj MS	F-Value	P-Value	PCR
Material	4	339.34	84.836	25.36	0.000	69.03
Drill bit	4	10.68	2.670	0.80	0.559	2.17
Cutting speed	4	10.41	2.602	0.78	0.570	2.12
Feed rate	4	104.35	26.088	7.80	0.007	21.23
Error	8	26.77	3.346			5.45
Total	24	491.55				

After determining the levels of control factors that will give optimum results, the next stage is to conduct verification experiments to test the accuracy of the optimization. The best levels for thrust forces were found to be A5-B3-C5-D1 for pure molybdenum based on S/N ratios (Figure 1). The estimated thrust force that can be achieved according to these levels was calculated with the regression equation (Equation 2). In addition, verification experiments were carried out for optimum levels and compared with the calculated values. There is

a difference of approximately 3% between the validation experiments and the calculated values. Additionally, a high correlation of 94.55% was found (Table 6). These two results reveal the accuracy of the optimization.

$$\text{Thrust force} = 62.59 + 0.086\,\text{M} + 0.252\,\text{D} - 0.0149\,\text{Vc} + 35.3\,\text{f} \quad (2)$$

Table 6. Validation experiments and comparison of predicted values

	Predistion Mean	**Verification experiment Mean**	**Variation** *(%)*	**R-sq** *(%)*
Thrust force (N)	57.2017	58.3	≈3	94.55

Examining the chip forms produced during the drilling experiments reveals that the cutting speed and feed rate have the greatest impact on the chip form. It has been observed that decreasing the feed value at high cutting speeds causes the resulting chips to become very thin or even powder. In the opposite case (low cutting speed and high feed rate), it has been observed that the chips thicken, the chips are more resistant to breaking, and relatively long chips are formed. The material change did not change the chip forms, but darker-colored chips were formed depending on the ratio of the additive material. Figure 2a shows the chips formed at 30 m/min cutting speed and 0.2 mm/rev feed rate, and Figure 2b shows the chips formed at 150 m/min cutting speed and 0.04 mm/rev feed rate.

(a) (b)

Figure 2. Chips formed depending on cutting speed and feed rate

4. Conclusion

- It was found that the most important control factor for thrust force depends on material selection (≈69%). This is followed by the amount of progress, with a rate of ≈21%.
- Thrust forces increased with the increasing amount of advance. Thrust forces are relatively reduced with high-speed steel drill bits with a 90° tip angle.
- The chip geometries formed in the experiments were not affected by the additive material (carbon nanotube) or its ratio to the composite material.
- Especially cutting speed and feed rates affect chip formation.

Acknowledgement

In this study, the financial support was provided by Çankırı Karatekin University Scientific Research Projects Coordination Unit, Project No. MF210621B20. All experimental works were conducted in Çankırı Karatekin University Research Laboratory. The author would like to thanks to all supporters due to their precious contributions.

References

[1] Gay, D. (2022). *Composite Materials: Design and Applications*. CRC press.

[2] Das, T.K., Ghosh, P., & Das, N.C. (2019). Preparation, development, outcomes, and application versatility of carbon fiber-based polymer composites: a review. *Advanced Composites and Hybrid Materials*, *2*, 214-233.
[3] Singh, B., Kumar, R., & Chohan, J.S. (2020). Polymer matrix composites in 3D printing: A state of art review. *Materials Today: Proceedings*, *33*, 1562-1567.
[4] Kiratli, S., & Aslan, Z. (2022). Influence of multi-walled carbon nanotubes with different diameters and lengths on the tension, shear and bending performance of glass/epoxy laminates. *Polymer Bulletin*, *79*(7), 4801-4826.
[5] Jain, V., Jaiswal, S., Dasgupta, K., & Lahiri, D. (2022). Influence of carbon nanotube on interfacial and mechanical behavior of carbon fiber reinforced epoxy laminated composites. *Polymer Composites*, 43(9), 6344-6354.
[6] Huang, K., Guo, H., Qin, Z., Cao, S., & Chen, Y. (2020). Flutter analysis of laminated composite quadrilateral plates reinforced with graphene nanoplatelets using the element-free IMLS-Ritz method. *Aerospace Science and Technology*, 103, 105915.
[7] Ramezani, H., Kazemirad, S., Shokrieh, M.M., & Mardanshahi, A. (2021). Effects of adding carbon nanofibers on the reduction of matrix cracking in laminated composites: Experimental and analytical approaches. *Polymer Testing*, 94, 106988.
[8] Ebrahimnezhad-Khaljiri, H., Eslami-Farsani, R., & Talebi, S. (2020). Investigating the high velocity impact behavior of the laminated composites of aluminum/jute fibers-epoxy containing nanoclay particles. *Fibers and Polymers*, 21, 2607-2613.
[9] Rao, Y.S., Mohan, N.S., Shetty, N., & Shivamurthy, B. (2019). Drilling and structural property study of multi-layered fiber and fabric reinforced polymer composite-a review. *Materials and Manufacturing Processes*, 34(14), 1549-1579.
[10] Nassar, M.M., Arunachalam, R., & Alzebdeh, K.I. (2017). Machinability of natural fiber reinforced composites: a review. *The International Journal of Advanced Manufacturing Technology*, *88*, 2985-3004.
[11] Sheikh-Ahmad, J.Y. (2009). *Machining of polymer composites* (Vol. 387355391). New York: Springer.
[12] Gökçe, H., Yavuz, M., & Çiftçi, İ. (2020). An investigation into the performance of HSS drills when drilling commercially pure molybdenum. *Sigma Journal of Engineering and Natural Sciences*, *38*(1), 61-70.
[13] Kiratli, S., & Aslan, Z. (2023). Investigation of mechanical properties of nanoclay modified E-glass/epoxy composites. *Journal of Composite Materials*, *57*(16), 2501-2512.
[14] Çiftçi, İ., & Gökçe, H. (2019). Molibden alaşımlarının işlenmesinde kesici takım ve kesme parametrelerinin Taguchi Metodu ile optimizasyonu. *Gazi Üniversitesi Mühendislik Mimarlık Fakültesi Dergisi*, *34*(1), 201-214.

Optimization of Laser Cutting Parameters of Composite Materials Modified with Boron Nitride

Hüseyin GÖKÇE [1,*], *Sakine KIRATLI* [2], *Mehmet GÜNEŞ* [3], *Mohamed Babiker Ibrahem ABDALLA* [4]

[1,2,4] *Faculty of Engineering, Mechanical Engineering, Çankırı Karatekin University, Çankırı, Turkiye*

[3] *Vocational School, Materials and Material Processing Technologies, Çankırı Karatekin University, Çankırı, Turkiye*

Abstract

In this study, five different continuous fiber-reinforced composite materials, one pure and four with boron nitride modified at different weight ratios, were cut using the laser cutting method, and the changes in dimensions after cutting were observed. Laser cutting parameters (control factors) were determined as cutting speed, laser power, and laser focusing distance. 10, 14, 18 mm/s, 50%, 60%, 70%, and 5, 6, 7 mm were used for cutting speed, laser power, and focal length, respectively. Experiments were performed using a Taguchi L9 orthogonal array for each material. Using the Taguchi method, control factors were optimized in terms of changes in dimensions (quality characteristics), and their importance levels were determined. Even though the impact rates vary for each material group, cutting speed was found to be the most important control factor. This was followed by laser power and focal length. Optimum results were observed at cutting parameters of 50% power value and 10 mm/s cutting speed. With the help of the experimental results, regression analysis was performed, and mathematical models were developed for measurement changes. Mathematical models have been tested with verification experiments, and it has been seen that the models can be used safely.

Keywords: *Boron nitride, laser cutting, laminated composite, Taguchi method.*

1. Introduction

Fiber-reinforced polymer matrix composites attract much attention in industrial applications due to their superior mechanical, physical, and thermal properties [1, 2]. It has a very important place in the aviation industry, especially in the defense industry. One of the main reasons for this is that it is very light as well as having high strength [3, 4]. Applications for glass fiber-reinforced polymer composites are particularly found in sports, aviation, electronics, transportation, and related industries [5]. When these polymer matrix composites are made, the material's different mechanical properties get a lot better when reinforcement elements are added to the matrix structure [6]. In recent years, nano- or micro-sized fillers have been added to matrices in order to improve the existing properties of composites [7, 8]. In recent years, research has been conducted by incorporating processed boron minerals into polymers [9, 10].

The word laser was coined by Gordon Gould in 1957 and joined the scientific world. It means light is amplified by stimulated radiation. Its English name is LASER, and it is a word consisting of the initials of the definition "Light Amplification by Stimulated Emission of Radiation." The foundation of the laser was Albert Einstein's theory of stimulated radiation, which he proposed in 1916. According to Einstein's theory, an atom at the excited radiation energy level should emit photons when it drops to a lower energy level. The emitted photons produce a monochromatic, polarized light beam with the same direction and the same strength. As a result, energy is released [11-14].

In laser generation, the reaction takes place in an optically transparent laser tube. The laser tube, which is filled with a solid, liquid, or gaseous substance, has a fully reflective mirror at one end and a partially reflective mirror at the other end. Energy is supplied to the laser tube from outside, and this energy is transmitted to the atoms in the environment. External energy delivery in the laser tube can be achieved by passing an electric current through the environment, by chemical means, or by excitation with external light. Some of the atoms absorb this energy,

* Corresponding author. *e-mail address: huseyingokce@karatekin.edu.tr*

and the excess energy makes the photon unstable. As a result of photons striking unstable and excited atoms, these atoms emit photons and try to become stable. These emitted photons are reflected from the mirrors inside the tube and rotate, accelerating the reaction. Meanwhile, the number of photons in the environment increases as a result of stimulation and excitation. When the majority of atoms emit photons, the light becomes stronger, and this strengthened light goes out from the partially reflective mirror end [15, 16].

The Taguchi method is one of the experimental design methods most commonly used by scientists in the literature. The Taguchi method enables the control of variability resulting from uncontrollable factors that traditional experimental design does not take into account. It converts objective function values into a signal-to-noise ratio (S/N) to measure the performance characteristics of the levels of control factors against these factors. The S/N ratio is defined as the desired signal ratio for the unwanted random noise value and indicates the quality characteristics of the experimental data. Three different functions are basically used: "smallest is best," "largest is best," and "target value is best," which is known as the objective function and is also expressed as the S/N ratio [17]. Additionally, Analysis of Variance (ANOVA) is applied to determine the statistical significance of the cutting parameters. The optimum combination of cutting parameters is determined with the help of ANOVA and the S/N ratio. Finally, a verification experiment is performed using the optimum processing parameters found by the Taguchi method, and the validity of the optimization is tested.

2. Materials and Methods

In this research, E-glass fiber, epoxy, and boron nitride were used. Boron nitride was examined at 0.2 and 0.4% by weight at 65–75 and 790 nm dimensions. The production of pure and boron nitride-added composites was done using hand lay-up and vacuum bagging techniques. In this study, a total of five different composite materials (Table 1), one without additives and four with different amounts of boron nitride additives, were cut using the laser cutting method, and the changes in dimensions (quality characteristics) after cutting were observed. The thickness of the test materials is 3 mm, and cuts with dimensions of 15×15 mm must be made. Dimensional changes were measured using a digital caliper.

Table 1. Materials and additive ratios used in experiments

Material size (nm)	Contribution rate to boron nitride (wt.%)
Pure	0
65-75	0.4
65-75	0.2
790	0.4
790	0.2

Experiments were carried out using the LazerFix LF9013 laser cutting machine. The machine has 120W laser power, 500 mm/s speed, and a carbon dioxide glass tube. Dimensional changes were measured using a digital caliper. Cutting speed, laser power, and laser focusing distance were determined as laser cutting parameters (control factors). The levels of 10, 14, 18 mm/s for cutting speed (CS), 50%, 60%, 70% for laser power (P), and 5, 6, 7 mm for focal length (FL) were used.

Table 2. Control factors and their levels used in experiments

Control factors	Code	Level		
		1	2	3
Cutting speed (mm/s)	CS	10	14	18
Power (%)	P	50	60	70
Focal length (mm)	FL	5	6	7

In the experiments, dimensional change was determined as a quality characteristic, and experiments were carried out to optimize the control factors. In order to determine the optimum levels of control factors, dimensional change values are desired to be low. For this purpose, the "smallest is best" objective function given in Equation 1 was used to calculate the Signal/Noise (S/N) ratio. In the equation, n is the total number of experiments, i is the order of experiments, and Y is the measurement result. Analysis of Variance (ANOVA) was applied to the experimental results with a 95% confidence interval to determine the effect of control factors on dimensional change values. The Taguchi method and variance analysis were performed with the Minitab program.

$$S/_N = -10\log\left(1/n\sum_{i=1}^{n} Y_i{}^2\right) \quad (1)$$

3. Results and Discussion

Laser cutting experiments were carried out in accordance with the Taguchi L9 orthogonal experimental design. Relative error values were calculated with Equation 2, according to the measured values after cutting and the desired values (actual value, 15 mm). Experimental design and relative error rates are presented in Table 3.

$$Relative\ error\ (\%) = (Real\ value - Measured\ value)/(Real\ value) \times 100 \quad (2)$$

Table 3. Experimental design and relative error rates calculated as a result of experiments

Cutting speed (CS) (mm/s)	Power (P) (%)	Focal length (FL) (mm)	Pure	65-75 nm 0.4 wt.%	65-75 nm 0.2 wt.%	790 nm 0.4 wt.%	790 nm 0.2 wt.%
10	50	5	0.19	0.32	0.28	0.22	0.18
10	60	6	0.24	0.34	0.29	0.28	0.26
10	70	7	0.35	0.39	0.37	0.31	0.28
14	50	6	0.34	0.40	0.41	0.32	0.33
14	60	7	0.60	0.44	0.46	0.33	0.39
14	70	5	0.71	0.45	0.49	0.33	0.41
18	50	7	0.61	0.45	0.58	0.42	0.47
18	60	5	0.69	0.47	0.63	0.45	0.52
18	70	6	0.78	0.51	0.96	0.52	0.63

The highest and lowest points of the S/N ratios in Table 4 and the related main effect graphs show that the cutting speed (CS) is the most important control factor for the relative error for the pure composite material. This is followed by power (P) and then focal length (FL). When the graph and table are examined together, it is seen that the optimum experimental parameters are 10 mm/s for CS, 50% for P, and 6 mm for FL. Similarly, in 65-75 nm 0.4 wt.% composite material, 10 mm/s for S, 50% for P, and 6 mm for FL; in 65-75 nm 0.2 wt.% composite material, 10 mm/s for S, 50% for P, and 5 mm for FL. For 790 nm 0.4 wt.% composite material, 10 mm/s for S, 50% for P, and 5 mm for FL; and for 790 nm 0.4 wt.% composite material, 10 mm/s for S, 50% for P, and 5 mm for FL.

ANOVA was conducted to determine the effect levels of control factors on relative error, and the results are given in Table 9. In this table, degrees of freedom (DF), sum of squares (Adj SS), mean of squares (Adj MS), F value, and P value indicating the significance level of control factors on the error and percentage contribution rates are given. According to the ANOVA results, the P value being less than 0.05 indicates that the effect of control factors on the relative error is statistically significant. Accordingly, the ratios of the most important control factors to relative error are:

For pure, 71.76%; for 65-75 nm (0.4 wt.%), 78.94%; for 65-75 nm (0.2 wt.%), 71.23%; for 790 nm (0.4 wt.%), 81.49%; for 790 nm (0.2 wt.%), and 85.54%.

Table 4. Order of importance of control factors and main effect graphs for relative error S/N ratios

		Level	CS	P	FL	Main effect graphs
(a)	**Pure**	1	11.980	9.363	6.874	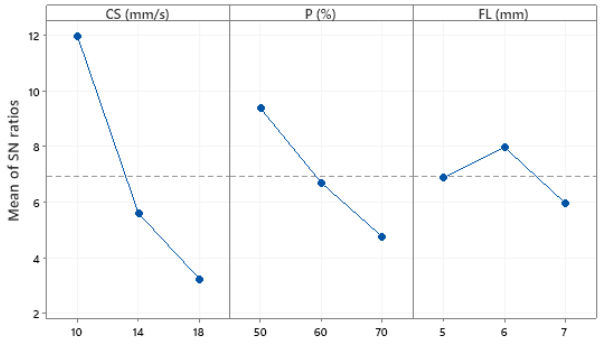
		2	5.594	6.685	7.975	
		3	3.225	4.751	5.950	
		Delta	8.755	4.612	2.025	
		Rank	1	2	3	
(b)	**65-75 nm 0.4 wt.%**	1	9.149	8.264	7.797	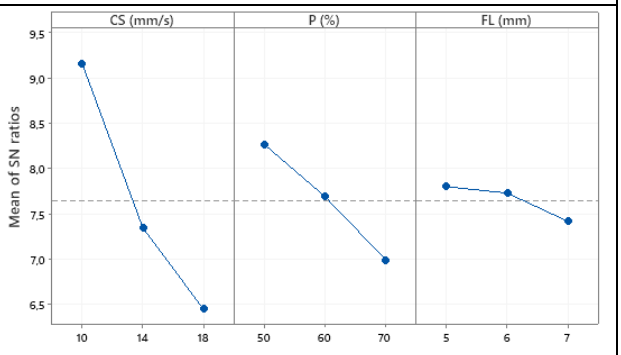
		2	7.342	7.686	7.726	
		3	6.447	6.988	7.415	
		Delta	2.701	1.276	0.382	
		Rank	1	2	3	
(c)	**65-75 nm 0.2 wt.%**	1	10.148	7.844	7.089	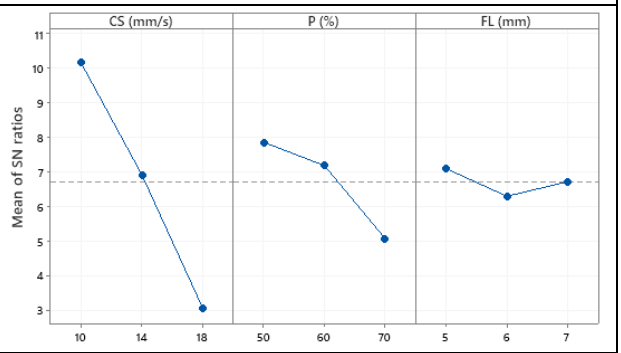
		2	6.895	7.170	6.284	
		3	3.033	5.062	6.704	
		Delta	7.115	2.782	0.805	
		Rank	1	2	3	
(d)	**790 nm 0.4 wt.%**	1	11.460	10.195	9.906	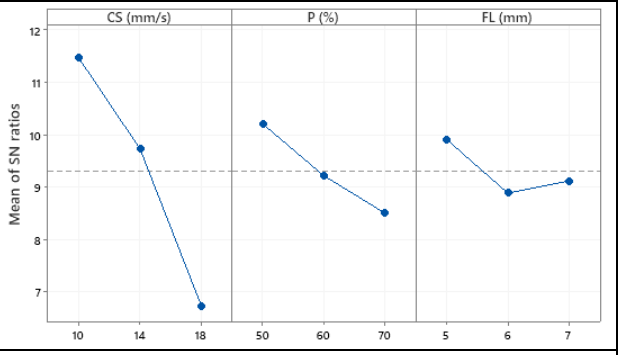
		2	9.719	9.207	8.878	
		3	6.717	8.494	9.113	
		Delta	4.743	1.700	1.028	
		Rank	1	2	3	
(e)	**790 nm 0.2 wt.%**	1	12.551	10.361	9.440	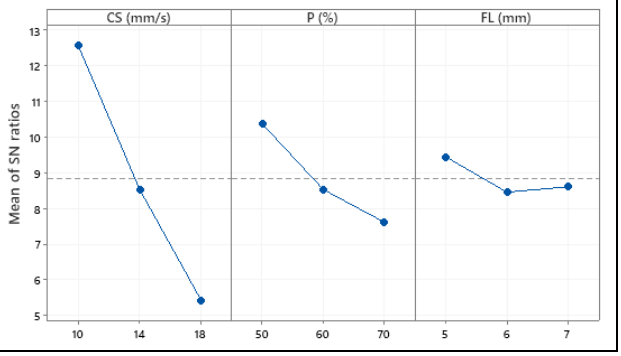
		2	8.518	8.520	8.448	
		3	5.417	7.605	8.598	
		Delta	7.134	2.756	0.992	
		Rank	1	2	3	

Table 5. Variance analysis for relative error values

	Source	DF	Adj SS	Adj MS	F-Value	P-Value	PCR
Pure	Cutting speed	1	0.281667	0.281667	48.55	0.001	**71.76**
	Power	1	0.081667	0.081667	14.08	0.013	20.81
	Focal length	1	0.000150	0.000150	0.03	0.879	0.04
	Error	5	0.029006	0.005801			7.39
	Total	8	0.392489				100.00
65-75 nm 0.4 wt.%	Cutting speed	1	0.024067	0.024067	159.26	0.000	**78.94**
	Power	1	0.005400	0.005400	35.74	0.002	17.71
	Focal length	1	0.000267	0.000267	1.76	0.241	0.88
	Error	5	0.000756	0.000151			2.48
	Total	8	0.030489				100.00
65-75 nm 0.2wt.%	Cutting speed	1	0.252150	0.252150	24.52	0.004	**71.23**
	Power	1	0.050417	0.050417	4.90	0.078	14.24
	Focal length	1	0.000017	0.000017	0.00	0.969	0.00
	Error	5	0.051417	0.010283			14.52
	Total	8	0.354000				100.00
790 nm 0.4 wt.%	Cutting speed	1	0.056067	0.056067	51.28	0.001	**81.49**
	Power	1	0.006667	0.006667	6.10	0.057	9.69
	Focal length	1	0.000600	0.000600	0.55	0.492	0.87
	Error	5	0.005467	0.001093			7.95
	Total	8	0.068800				100.00
790 nm 0.2 wt.%	Cutting speed	1	0.135000	0.135000	198.21	0.000	**85.54**
	Power	1	0.019267	0.019267	28.29	0.003	12.21
	Focal length	1	0.000150	0.000150	0.22	0.659	0.10
	Error	5	0.003406	0.000681			2.16
	Total	8	0.157822				100.00

After the levels of control factors are determined, verification experiments are carried out to test the accuracy of the optimization. Optimum levels were determined for minimum relative error values (E) according to S/N ratios. The predictive relative error values that can be obtained according to these levels are calculated with regression equations (Equations 3, 4, 5, 6, and 7). In addition, verification experiments were carried out for optimum levels and compared with the calculated values. There is a difference of approximately 3% between the validation experiments and the calculated values. Additionally, a high correlation of 94.55% was found (Table 6). These two results reveal the accuracy of the optimization.

$$E_{\text{pure}} = -0.927 + 0.05417\,\text{CS} + 0.01167\,\text{P} - 0.0050\,\text{FL} \quad (3)$$

$$E_{65-75\text{ nm }0.4\text{ wt.\%}} = -0.0228 + 0.01583\,\text{CS} + 0.003000\,\text{P} + 0.00667\,\text{FL} \quad (4)$$

$$E_{65-75\text{ nm }0.2\text{ wt.\%}} = -0.781 + 0.0512\,\text{CS} + 0.00917\,\text{P} + 0.0017\,\text{FL} \quad (5)$$

$$E_{790\text{ nm }0.4\text{ wt.\%}} = -0.245 + 0.02417\,\text{CS} + 0.00333\,\text{P} + 0.0100\,\text{FL} \quad (6)$$

$$E_{790\text{ nm }0.2\text{ wt.\%}} = -0.5094 + 0.03750\,\text{CS} + 0.00567\,\text{P} + 0.0050\,\text{FL} \quad (7)$$

Table 6. Comparison of validation experiments and predicted values

	Prediction mean	Verification experiment mean	Variation *(%)*	R-sq *(%)*
Pure	0,091	0,09	≈6	92.61
65-75 nm 0.4 wt.%	0,326	0,35	≈7	97.52
65-75 nm 0.2 wt.%	0,210	0,22	≈6	85.48
790 nm 0.4 wt.%	0,217	0,23	≈7	92.05
790 nm 0.2 wt.%	0,166	0,17	≈7	97.84

Confirmation experiments were carried out for optimum levels and compared with the calculated values. There is a difference of 5%–7% between verification experiments and calculated values. Additionally, a high correlation of 94.55% was found (Table 10). These two results reveal the accuracy of the optimization.

4. Conclusion

- The dimensional change in laser cutting of boron nitride-added composite materials was optimized using the Taguchi method.
- Although the contribution rates of the materials are different, it has been found that the most important control factor in each material group is the cutting speed (CS), followed by laser power (P) and focal length (FL).
- The high correlation values of the mathematical models and verification test results obtained by regression analysis showed that the optimization was valid and could be used safely.

Acknowledgement

In this study, the financial support was provided by Çankırı Karatekin University Scientific Research Projects Coordination Unit, Project No. MF210621B20. All experimental works were conducted in Çankırı Karatekin University Research Laboratory. The author would like to thanks to all supporters due to their precious contributions.

References

[1] Mittal, G., Rhee, K.Y., Mišković-Stanković, V., & Hui, D. (2018). Reinforcements in multi-scale polymer composites: Processing, properties, and applications. *Composites Part B: Engineering*, *138*, 122-139.

[2] Maiti, S., Islam, M.R., Uddin, M.A., Afroj, S., Eichhorn, S.J., & Karim, N. (2022). Sustainable fiber-reinforced composites: A Review. *Advanced Sustainable Systems*, *6*(11), 2200258.

[3] Clyne, T.W., & Hull, D. (2019). *An introduction to composite materials*. Cambridge University Press.

[4] Gibson, R.F. (2010). A review of recent research on mechanics of multifunctional composite materials and structures. *Composite Structures*, *92*(12), 2793-2810.

[5] Rajak, D.K., Wagh, P.H., & Linul, E. (2021). Manufacturing technologies of carbon/glass fiber-reinforced polymer composites and their properties: A review. *Polymers*, *13*(21), 3721.

[6] Kiratli, S., & Aslan, Z. (2022). Influence of multi-walled carbon nanotubes with different diameters and lengths on the tension, shear and bending performance of glass/epoxy laminates. *Polymer Bulletin*, *79*(7), 4801-4826.

[7] Manjunath, M., Renukappa, N.M., & Suresha, B. (2016). Influence of micro and nanofillers on mechanical roperties of pultruded unidirectional glass fiber reinforced epoxy composite systems. *Journal of Composite Materials*, *50*(8), 1109-1121.

[8] Megahed, M., Fathy, A., Morsy, D., & Shehata, F. (2021). Mechanical performance of glass/epoxy composites enhanced by micro-and nanosized aluminum particles. *Journal of Industrial Textiles*, *51*(1), 68-92.

[9] Zhou, T., Smith, M.K., Berenguer, J.P., Quill, T.J., Cola, B.A., Kalaitzidou, K., & Bougher, T.L. (2020). The impact of polymer matrix blends on thermal and mechanical properties of boron nitride composites. *Journal of Applied Polymer Science*, *137*(19), 48661.

[10] Chen, J., Liu, X., Zeng, X.L., Ye, H.Y., & Zhang, G.Q. (2022). A facile method to prepare oriented boron nitride-based polymer composite with enhanced thermal conductivity and mechanical properties. *Composites Communications*, *29*, 101038.

[11] Asyalı M.H., Kara S. & Yılmaz B. (2014). *Biyomedikal Mühendisliğinin Temelleri*, Ankara, Türkiye, Seçkin Yayıncılık.

[12] Naqavi I.Z., *Conduction and Non-Conduction Limited Laser Heating Process Mathematical Simulation*, MSc Thesis, King Fahd University of Petroleum and Minerals, College of Graduate Studies, 2001, Dhahran, Saudi Arabia.

[13] Dahotre, N.B. (Ed.). (1998). *Lasers in surface engineering* (Vol. 1). ASM international.

[14] Tunç M., *CO_2 Lazer Kesim Tezgâhlarında Kesme Parametrelerinin Yüzey Pürüzlülüğüne Etkilerinin İncelenmesi*, MSc Thesis, Karabük Üniversitesi, Fen Bilimleri Enstitüsü, 2015, Karabük.

[15] Türkmen M., *Cam Elyaf Takviyeli Polimerik Kompozit Malzemelerde Lazerli Kesme ve Delme Parametrelerinin Belirlenmesi*, MSc Thesis, Kocaeli Üniversitesi, Fen Bilimleri Enstitüsü, 2018, Kocaeli.

[16] Tekin S., *Osilator Sel Sisteminde Optik Kavite Yapıları Ve Lazer Kazanç Mekanizmaları,* MSc Thesis, Ankara Üniversitesi, Fen Bilimleri Enstitüsü, 2008, Ankara.

[17] Çiftçi, İ., & Gökçe, H. (2019). Molibden alaşımlarının işlenmesinde kesici takım ve kesme parametrelerinin Taguchi Metodu ile optimizasyonu. *Gazi Üniversitesi Mühendislik Mimarlık Fakültesi Dergisi*, *34*(1), 201-214.

Periodic solutions of some higher order difference equations

Melih GÖCEN *

Faculty of Science, Department of Mathematics, Zonguldak Bülent Ecevit University, Zonguldak, Turkey

Abstract

In this work, we deal with the general form of the solutions and the periodicity of some higher order difference equations

$$x_{n+1}=\frac{\prod_{k=0}^{r}x_{n-2k}}{\prod_{k=0}^{r-1}x_{n-(2k+1)}\left(-1\pm\prod_{k=0}^{r}x_{n-2k}\right)},\qquad n,k\in\mathbb{N}_0,r\in\mathbb{N}$$

where the initial values are nonnegative real numbers such that the denominator is always nonzero. Moreover, some numerical examples are presented to verify our theoretical results.

Keywords: *Periodicity, Higher order difference equations, Form of the solutions.*

1. Introduction

The study of difference equations is an extensive research field and difference equations have been used in mathematical models describing real life situations in population biology, information system, medicine, engineering, physiology, physics and so forth. There have been many recent investigations and interest in nonlinear difference equations by several authors, see [2, 3, 4, 7]. On the other hand, nonlinear difference equations of order greater than one are of great importance in applications. Obviously, higher order rational difference equations have become a research hot spot in mathematical modelling and have also been widely studied but still have many aspects to be investigated, see [6, 10, 11]. T. F. Ibrahim [8] investigated the solutions of the difference equation

$$x_{n+1}=\frac{x_nx_{n-2}}{x_{n-1}(a+bx_nx_{n-2})}.$$

Then they found that every solution of the following difference equation

$$x_{n+1}=\frac{x_nx_{n-2}}{x_{n-1}(a+bx_nx_{n-2})}$$

is periodic with period four. E. M. Elsayed and T. F. Ibrahim [5] obtained the form of the solutions of the rational difference equation

$$x_{n+1}=\frac{x_nx_{n-2}x_{n-4}}{x_{n-1}x_{n-3}(\pm1\pm x_nx_{n-2}x_{n-4})}$$

Motivated by above studies, we deal with the following higher order rational difference equations

$$x_{n+1}=\frac{\prod_{k=0}^{r}x_{n-2k}}{\prod_{k=0}^{r-1}x_{n-(2k+1)}\left(-1+\prod_{k=0}^{r}x_{n-2k}\right)},\qquad n,k\in\mathbb{N}_0,r\in\mathbb{N}$$

which is the general form of the difference equations given in [5,8] and the initial conditions are nonnegative real numbers. Throughout this work, we will assume that solutions are well-defined, that is, the denominator is always nonzero. We begin by introducing some basic definitions and some theorems needed in the sequel. For details, see [1].

Let I be some interval of real numbers and let $f: I^{k+1}\to I$ be a continuously differentiable function. A difference equation of order $(k+1)$ is an equation of the form

$$x_{n+1}=f(x_n,x_{n-1},\dots,x_{n-k}),\qquad n=0,1,\cdots. \tag{1.1}$$

A solution of Eq.(1.1) is a sequence $\{x_n\}_{n=-k}^{\infty}$ that satisfies Eq.(1.1) for all $n\geq -k$.

* Corresponding author. *e-mail address: gocenm@hotmail.com*

Definition 1.1. A solution of Eq.(1.1) that is constant for all $n \geq -k$ is called an equilibrium solution of Eq.(1.1).If $x_n = \bar{x}, \quad for\ all\ n \geq -k$

is an equilibrium solution of Eq.(1.1) then $\bar{x}$ is called an equilibrium point, or simply an equilibrium of Eq.(1.1).

Definition 1.2. (Stability) Let $\bar{x}$ an equilibrium point of Eq.(1.1).

(a) An equilibrium point $\bar{x}$ of Eq.(1.1) is called locally stable if, for every ε > 0; there exists δ> 0 such that if $\{x_n\}_{n=-k}^{\infty}$ is a solution of Eq.(1.1) with$|x_k - \bar{x}| + |x_{1-k} - \bar{x}| + \cdots + |x_0 - \bar{x}| < \delta$, then

$|x_n - \bar{x}| < \varepsilon, for\ all\ n \geq -k.$

(b) An equilibrium point $\bar{x}$ of Eq.(1.1) is called locally asymptotically stable if, it is locally stable, and if in addition there exists $\gamma > 0$ such that if $\{x_n\}_{n=-k}^{\infty}$ is a solution of Eq.(1.1) with $|x_k - \bar{x}| + |x_{1-k} - \bar{x}| + \cdots + |x_0 - \bar{x}| < \delta$, then we have

$\lim_{n\to\infty} x_n = \bar{x}.$

(c) An equilibrium point $\bar{x}$ of Eq.(1.1) is called a global attractor if,every solution $\{x_n\}_{n=-k}^{\infty}$ of Eq.(1.1), we have

$\lim_{n\to\infty} x_n = \bar{x}.$

(d) An equilibrium point $\bar{x}$ of Eq.(1.1) is called globally asymptotically stable if it is locally stable and a global attractor.

(e) An equilibrium point $\bar{x}$ of Eq.(1.1) is called unstable if it is not locally stable.

Suppose that the function *f* is continuously differentiable in some open neighborhood of an equilibrium point $\bar{x}$. Let

$q_i = \frac{\partial f}{\partial u_i}(\bar{x}, \bar{x}, \dots, \bar{x}), \quad for\ i = 0,1, \dots, k$

denote the partial derivative of $f(u_0, u_1, \dots, u_k)$ with respect to u_i evaluated at the equilibrium point $\bar{x}$ of Eq.(1.1).

Definition 1.3. The equation

$z_{n+1} = q_0 z_n + q_1 z_{n-1} + \cdots + q_k z_{n-k}, \quad n = 0,1, \dots,$ (1.2)

is called the linearized equation of Eq.(1.1) about the equilibrium point $\bar{x}$, and the equation

$\lambda^{k+1} - q_0\lambda^k - \cdots - q_{k-1}\lambda - q_k = 0$ (1.3) is called the characteristic equation of Eq.(1.2) about $\bar{x}$.

Definition 1.4. (Hyperbolic) An equilibrium point $\bar{x}$ of Eq.(1.1) is called hyperbolic if no root of Eq.(1.3) has absolute value equal to one. If there exists a root of Eq.(1.3) with absolute value equal to one then the equilibrium point $\bar{x}$ is called nonhyperbolic.

Definition 1.5. (Periodicity) A sequence $\{x_n\}_{n=-m}^{\infty}$ is said to periodic with periodic *p* if

$x_{n+p} = x_n \ \ for\ all\ n \geq -m.$

2. The Difference Equation

In this section, firstly, we investigate the form of the solutions and the periodicity of the following rational difference equations

$x_{n+1} = \frac{\prod_{k=0}^{r} x_{n-2k}}{\prod_{k=0}^{r-1} x_{n-(2k+1)}(-1 \pm \prod_{k=0}^{r} x_{n-2k})}, \quad n, k \in \mathbb{N}_0, r \in \mathbb{N}$ (2.1)

where the initial conditions are nonnegative real numbers such that the denominator is always nonzero.

Theorem 2.1. *Let* $\{x_n\}_{n=-(2k+1)}^{\infty}$ be solutions of system (2.1). Then the following results holds:

(a) $\{x_n\}_{n=-(2k+1)}^{\infty}$ are periodic with period $2(r+1)$ for $n \geq -(2k+1)$.

(b) We have

$$x_{2(r+1)n+i} = \begin{cases} \frac{\prod_{j=0}^{r} x_{-2j}}{\prod_{j=0}^{r-1} x_{-(2j+1)}(-1\pm\prod_{j=0}^{r} x_{-2j})}, & i = 1, \\ x_{i-2(r+1)}, & 2 \le i \le 2r+2. \end{cases}$$

Proof. It follows from Eq.(2.1) and after making some necessary calculations we have

(a) $x_1 = \frac{\prod_{k=0}^{r} x_{-2k}}{\prod_{k=0}^{r-1} x_{-(2k+1)}(-1\pm\prod_{k=0}^{r} x_{-2k})} = \frac{A}{B(-1\pm A)}$

$$x_2 = \frac{\prod_{k=0}^{r} x_{1-2k}}{\prod_{k=0}^{r-1} x_{-2k}\,(-1 \pm \prod_{k=0}^{r} x_{1-2k})} = \frac{Bx_1}{\frac{A}{x_{-2r}}(-1 \pm Bx_1)} = x_{-2r}$$

$$x_3 = \frac{\prod_{k=0}^{r} x_{2-2k}}{\prod_{k=0}^{r-1} x_{1-2k}\,(-1 \pm \prod_{k=0}^{r} x_{2-2k})} = \frac{x_2\frac{A}{x_{-2r}}}{x_1\frac{B}{x_{1-2r}}\left(-1 \pm x_2\frac{A}{x_{-2r}}\right)} = x_{1-2r}$$

$$x_{2r+1} = \frac{\prod_{k=0}^{r} x_{2r-2k}}{\prod_{k=0}^{r-1} x_{2r-1-2k}\,(-1 \pm \prod_{k=0}^{r} x_{2r-2k})}$$

$$= \frac{x_{2r}x_{2r-2}\cdots x_2\frac{A}{x_{-2}x_{-4}x_{-2r}}}{x_{2r-1}x_{2r-3}\cdots x_1\left(-1\pm x_{2r}x_{2r-2}\cdots x_2\frac{A}{x_{-2}x_{-4}x_{-2r}}\right)} = \frac{A}{x_1\frac{B}{x_{-1}}(-1\pm A)} = x_{-1}$$

$$x_{2r+2} = \frac{\prod_{k=0}^{r} x_{2r+1-2k}}{\prod_{k=0}^{r-1} x_{2r-2k}(-1\pm\prod_{k=0}^{r} x_{2r+1-2k})} = \frac{x_{2r+1}x_{2r-1}x_{2r-3}\cdots x_3x_1}{x_{2r}x_{2r-2}x_{2r-4}\cdots x_2(-1\pm x_{2r+1}x_{2r-1}x_{2r-3}\cdots x_3x_1)} = \frac{Bx_1}{\frac{A}{x_0}(-1\pm Bx_1)} = x_0\,,$$

where $A = \prod_{k=0}^{r} x_{-2k}$ and $B = \prod_{k=0}^{r-1} x_{-(2k+1)}$.

Thus $x_{n+(2r+2)} = x_n$.

Hence, it is easy to see that $\{x_n\}_{n=-(2k+1)}^{\infty}$ solutions are periodic with period $2(r+1)$ for $n \ge -(2k+1)$.

(b) For $i = 1$, the equality can be seen obviously. From Eq.(2.1), for $2 \le i \le 2r+2$, we obtain that

$$x_{n+1} = \frac{\prod_{k=0}^{r} x_{n-2k}}{\prod_{k=0}^{r-1} x_{n-(2k+1)}\,(-1 \pm \prod_{k=0}^{r} x_{n-2k})} = \frac{x_n x_{n-2}x_{n-4}\cdots x_{n-2r}}{x_{n-1}x_{n-3}x_{n-5}\cdots x_{n-(2r-1)}(-1 \pm x_n x_{n-2}x_{n-4}\cdots x_{n-2r})}$$

$$= \frac{\frac{x_{n-1}x_{n-3}x_{n-5}\cdots x_{n-(2r+1)}}{x_{n-2}x_{n-4}x_{n-6}\cdots x_{n-2r}(-1\pm x_{n-1}x_{n-3}x_{n-5}\cdots x_{n-(2r+1)})}x_{n-2}x_{n-4}\cdots x_{n-2r}}{x_{n-1}x_{n-3}x_{n-5}\cdots x_{n-(2r-1)}\left(-1 \pm \frac{x_{n-1}x_{n-3}x_{n-5}\cdots x_{n-(2r+1)}}{x_{n-2}x_{n-4}x_{n-6}\cdots x_{n-2r}(-1\pm x_{n-1}x_{n-3}x_{n-5}\cdots x_{n-(2r+1)})}x_{n-2}x_{n-4}\cdots x_{n-2r}\right)}$$

$$= x_{n-(2r+1)}.$$

In the following example, we show the periodicity of the solutions for special cases of Eq. (2.1).

Example 1. *Consider the Eq.(2.1) with* $r = 1$ *and the initial conditions* $x_{-2} = 0.3$, $x_{-1} = 0.2$, $x_0 = 0.4$ *to verify our theoretical results.*

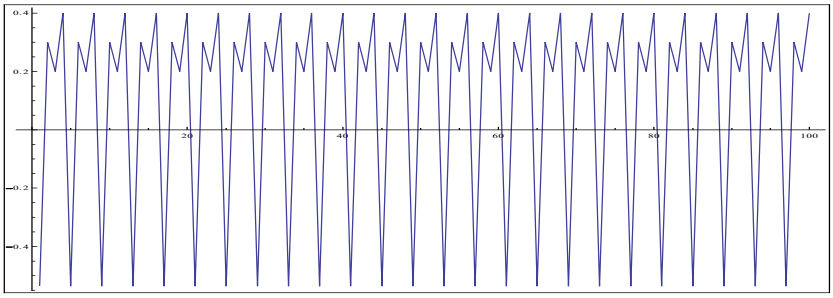

Figure 1. Plot of $x_{n+1} = \frac{x_n x_{n-2}}{x_{n-1}(-1-x_n x_{n-2})}$.

The periodic solutions are, {-0.535714, 0.3, 0.2, 0.4, -0.535714, 0.3, 0.2, 0.4, -0.535714, 0.3, 0.2, 0.4, -0.535714, 0.3, 0.2, 0.4,...}.

Example 2. *Consider the Eq.(2.1) with* $r = 2$ *and the initial conditions* $x_{-4} = 0.2$, $x_{-3} = 9$, $x_{-2} = 5$, $x_{-1} = 7$, $x_0 = 2$ *to verify our theoretical results.*

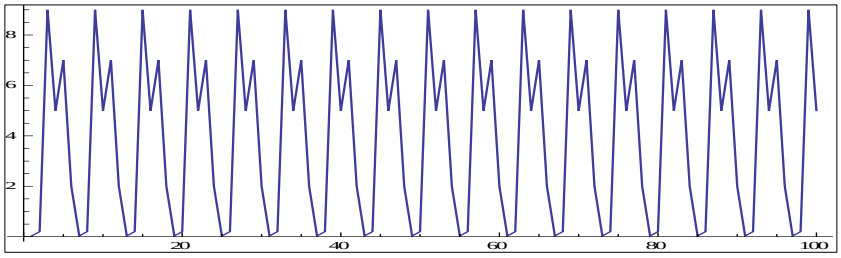

Figure 2. Plot of $x_{n+1} = \frac{x_n x_{n-2} x_{n-4}}{x_{n-1} x_{n-3}(-1+x_n x_{n-2} x_{n-4})}$.

The periodic solutions are,

{0.031746, 0.2, 9, 5, 7, 2, 0.031746,0.2, 9, 5, 7, 2, 0.031746, 0.2, 9, 5, 7, 2, 0.031746, 0.2, 9, 5, 7, 2,...}.

2.1 Local Stability of the Equilibrium Points of Eq.(2.1).

Now, we deal with the local stability of the solutions of Eq.(2.1). We first give the equilibrium points of Eq.(2.1).

Lemma 2.2. The equilibrium points of the Eq.(2.1) are $0, \sqrt[r+1]{\pm 2}$ and the equilibrium points $x = \sqrt[r+1]{\pm 2}$ are nonhyberpolic.

Proof.

$$\bar{x} = \frac{\bar{x}^{r+1}}{\bar{x}^{r}(-1 \pm \bar{x}^{r+1})}$$

$$\bar{x}^{r+1}(-1 \pm \bar{x}^{r+1}) = \bar{x}^{r+1}$$

$$\bar{x}^{r+1}(\pm\bar{x}^{r+1} - 2) = 0.$$

Thus, the equilibrium points of the Eq.(2.1) are $0, \sqrt[r+1]{\pm 2}$. Let $f: (0,\infty)^{2r+1} \to (0,\infty)$ be a function defined by

$$f(u_1, u_2, \dots, u_{2r+1}) = \frac{u_1 u_3 \dots u_{2r+1}}{u_2 u_4 \dots u_{2r}(-1 \pm u_1 u_3 \dots u_{2r+1})}.$$

Hence, it follows that

$$f_{u_1}(u_1, u_2, \dots, u_{2r+1}) = -\frac{u_3 \dots u_{2r+1}}{u_2 u_4 \dots u_{2r}(-1 \pm u_1 u_3 \dots u_{2r+1})^2},$$

$$f_{u_2}(u_1, u_2, \dots, u_{2r+1}) = -\frac{u_1 u_3 \dots u_{2r+1}}{{u_2}^2 u_4 \dots u_{2r}(-1 \pm u_1 u_3 \dots u_{2r+1})},$$

$$f_{u_3}(u_1, u_2, \dots, u_{2r+1}) = -\frac{u_1 u_5 \dots u_{2r+1}}{u_2 u_4 \dots u_{2r}(-1 \pm u_1 u_3 \dots u_{2r+1})^2},$$

$$\vdots$$

$$f_{u_{2r}}(u_1, u_2, \dots, u_{2r+1}) = -\frac{u_1 u_3 \dots u_{2r+1}}{u_2 u_4 \dots {u_{2r}}^2(-1 \pm u_1 u_3 \dots u_{2r+1})},$$

$$f_{u_{2r+1}}(u_1, u_2, \dots, u_{2r+1}) = -\frac{u_1 u_3 \dots u_{2r-1}}{u_2 u_4 \dots u_{2r}(-1 \pm u_1 u_3 \dots u_{2r+1})^2}.$$

Since we have two different types of equations, we investigate the local stability of these equations separately.

Case I : We consider the following difference equation

$$x_{n+1} = \frac{\prod_{k=0}^{r} x_{n-2k}}{\prod_{k=0}^{r-1} x_{n-(2k+1)}(-1+\prod_{k=0}^{r} x_{n-2k})}. \tag{2.2}$$

Now, we will show that the equilibrium points $x = \sqrt[r+1]{2}$ is nonhyberpolic. Since

$f_{u_1}(\bar{x}, \bar{x}, \dots, \bar{x}) = -1,\ f_{u_2}(\bar{x}, \bar{x}, \dots, \bar{x}) = -1,\ f_{u_3}(\bar{x}, \bar{x}, \dots, \bar{x}) = -1, \cdots,$

$f_{u_{2r}}(\bar{x}, \bar{x}, \dots, \bar{x}) = -1,\ f_{u_{2r+1}}(\bar{x}, \bar{x}, \dots, \bar{x}) = -1,$

the characteristic equation about the equilibrium point $\sqrt[r+1]{2}$ is

$$\lambda^{2r+1} + \lambda^{2r} + \lambda^{2r-1} + \cdots + \lambda^4 + \lambda^3 + \lambda^2 + \lambda + 1 = 0. \tag{2.3}$$

We can easily see that $\lambda = -1$ is one of the root of Eq.(2.3), therefore the equilibrium point $x = \sqrt[r+1]{2}$ is nonhyperbolic.

Case II : We consider the following difference equation

$$x_{n+1} = \frac{\prod_{k=0}^{r} x_{n-2k}}{\prod_{k=0}^{r-1} x_{n-(2k+1)}(-1-\prod_{k=0}^{r} x_{n-2k})}, \tag{2.4}$$

where *r* is even number. Similarly, the characteristic equation about the equilibrium point $x = \sqrt[r+1]{-2}$ is

$$\lambda^{2r+1} + \lambda^{2r} + \lambda^{2r-1} + \cdots + \lambda^4 + \lambda^3 + \lambda^2 + \lambda + 1 = 0. \tag{2.5}$$

It follows that $\lambda = -1$ is one of the root of Eq.(2.5), so the equilibrium point $x = \sqrt[r+1]{-2}$ is nonhyperbolic.

References

[1] Elaydi, S. (1996). *An Introduction to Difference Equations*, Springer-Verlag, New York, Inc.

[2] El-Metwally H., & Elsayed, E. M. (2012). Qualitative Study of Solutions of Some Difference Equations, *Abstract and Applied Analysis*, Article ID 248291, 16 pages.

[3] Elsayed, E. M. (2016). Expression and behavior of the solutions of some rational recursive sequences, *Mathematical Methods in the Applied Sciences*, 39(18) 5682-5694.
[4] Elsayed, E. M. (2011). On the solution of some difference equations, *European Journal of Pure and Applied Mathematics*, 4(3) 287-303.
[5] Elsayed, E. M., & Ibrahim, T.F. (2015). Solutions and periodicity of a rational recursive sequences of order five, *Bulletin of the Malaysian Mathematical Sciences*, 38 95–112.
[6] Göcen, M., & Cebeci, A. (2018). On the periodic solutions of some systems of higher order difference equations, *Rocky Mountain J. Math*., 48(3) 845-858.
[7] Göcen, M., & Güneysu, M. (2018). The global attractivity of some rational difference equations, *Journal of Computational Analysis and Applications*, 25(7) 1233-1243.
[8] Ibrahim, T.F. (2009). On the Third Order Rational Difference Equation $x_{n+1} = \frac{x_n x_{n-2}}{x_{n-1}(a+bx_n x_{n-2})}$. *Int. J. Contemp. Math. Sciences*, 4(27) 1321-1334.
[9] Ibrahim, T.F. (2009). Dynamics of a rational recursive sequence of order two. *International Journal of Mathematics and Computation*, 5(9) 98-105.
[10] Göcen, M., & Cebeci, A. (2022). Form of the periodic solutions of some systems of higher order difference equations. *Asian-European Journal of Mathematics*, 15(2), Doi: 10.1142/S1793557122500292.
[11] Folly-Gbetoula , M., Göcen, M., & Güneysu, M. (2022). General form of the solutions of some difference equations via Lie symmetry analysis. *Journal of Analysis and Applications*, 20(2), 105-122.

In Vitro Effects of Some Chemotherapy Drugs on Glucose-6-Phosphate Dehydrogenase Enzyme Purified from Sheep Spleen

Çiğdem ÇOBAN [1], ***Mehmet ÇİFTCİ*** [2,*]

[1]*Bingol University, Solhan Health Services Vocational School, Bingol, Türkiye*

[2]*Bingol University, Faculty of Veterinary Science, Bingol, Türkiye*

Abstract

In this study, the inhibition effects of some important drugs used in chemotherapy on glucose-6-phosphate dehydrogenase, a $NADP^+$-dependent enzyme obtained from sheep spleen tissue, were examined in vitro. Sheep spleen glucose-6-phosphate dehydrogenase enzyme (D-glucose-6-phosphate: NADP+ oxidoreductase, EC 1.1.1.49, G6PD) was first purified by 2', 5'-ADP Sepharose 4B affinity chromatography. Enzyme activity was determined spectrophotometrically at 340 nm by the Beutler method. This method was applied in all kinetic studies. Carboplatin, cisplatin, oxaloplatin, fluorouracil, cyclophosphamide and ibandronic acid were used as drugs. In vitro studies showed that oxaloplatin, carboplatin and cyclophosphamide drugs had inhibitory effects on the enzyme in question. It was observed that other drugs did not affect the enzyme much. IC_{50} values were found by drawing % Activity-[I] graphs for drugs showing inhibitory effects. The IC_{50} values obtained for oxaloplatin, carboplatin and cyclophosphamide drugs were 3.22 mM, 7.26 mM, and 34.5 mM, respectively.

Keywords: *Glucose-6-phosphate dehydrogenase, Kemoterapi drugs, Inhibiton*

1. Introduction

Glucose 6-phosphate dehydrogenase (G6PD) (E.C. 1.1.1.49) catalyzes the first reaction of the pentose phosphate metabolic pathway. The only source for NADPH formation in erythrocytes is the pentose phosphate metabolic pathway, and NADPH is significantly reduced in G6PD deficiency. The most important role of NADPH in erythrocytes is to reduce oxidized glutathione (GSH). This reaction is catalyzed by glutathione reductase. The reduced form of glutathione (GSSH) is a tripeptide containing a free thiol group. The free thiol group acts as a sulfhydryl buffer, keeping hemoglobin and erythrocyte proteins in a reduced state; It also takes part in detoxification events by reacting with hydrogen peroxide and organic peroxides. For this reason, G6PD can be defined as an indirect antioxidant enzyme. As a result, this enzyme is for living things; It is very important in growth, development and protection against oxidative stress. NADPH is also a coenzyme involved in the synthesis of biomolecules such as fatty acids, steroids and some amino acids. Many drugs such as anti-inflammatory antibiotics and anesthetics are used in the medical treatment of animal diseases. However, little information is available about the effects of drugs on different enzymes. For example, the in vivo and in vitro inhibition effects of metamizole, amikacin sulfate, sodium ampicillin, and netilmicin sulfate drugs on G6PD enzyme activity obtained from rat erythrocytes were examined. In this study, the purification of G6PD enzyme from sheep spleen tissue and the effects of drugs such as carboplatin, cisplatin, oxaloplatin, fluorouracil, cyclophosphamide and ibandronic acid on this enzyme activity were investigated [1-3].

2. Materials and Methods

2.1. Preparation of Hemogenate

The spleen tissue, obtained from the Bingöl Provincial Combined Meat and Milk Institution in accordance with the cold chain rules, was first divided into certain pieces in the laboratory and stored at -20°C. During the experiment, 15 g of spleen tissue was taken, chopped into small pieces, and suspended in 45 mL of 50 mM KH_2PO_4 (pH 7.5) buffer. Then, homogenate was formed by centrifuging at 13,000xg for 1 hour and removing the precipitate [4-6].

* Corresponding author. *e-mail address: mciftci@bingol.edu.tr*

2.2. 2', 5'-ADP Sepharose 4B Affinity Chromatography

The dialyzed enzyme solution was loaded into the column and the flow rate was set to 20 mL/hour. Then, the column was injected successively with 25 mL 0.1 M K-acetate + 0.1 M K-phosphate, (pH: 6.0) and 25 mL 0.1 M KCl + 0.1 M K-phosphate (pH: 7, 85) was washed with. Washing with 0.1 M KCl + 0.1 M K-phosphate (pH: 7.85) was continued until the absorbance difference became 0.05 at 280 nm. Finally, the enzyme was eluted with a solution of 80 mM K-phosphate + 80 mM KCl + 0.5 mM NADP + + 10 mM EDTA (pH: 7.85). Enzyme activities were measured in the fractions. Tubes showing activity were pooled together. Protein determination was made in the final solution. The temperature was kept at +4 ^{o}C throughout all procedures [4,7].

2.3. Activity Determination

Activity determination was made according to the Beutler method. An enzyme unit was defined as the amount of enzyme that converts 1 mol $NADP^{+}$ into NADPH in 1 minute [4,8].

2.4. Protein Determination

Quantitative protein determination was performed spectrophotometrically at 595 nm according to the Bradford method, using bovine serum albumin as the standard [9].

2.5. Kinetic Studies

The effects of drugs such as carboplatin, cisplatin, oxaloplatin, fluorouracil, cyclophosphamide and ibandronic acid on G6PD were examined. The tube containing no drug was used as a control and its activity was accepted as 100%. For each drug that inhibits the enzyme, a Activity%-[Drug] graph was drawn at different inhibitor concentrations. IC_{50} values were calculated through these graphs.

3. Results

Activity%-[Drug] graphs drawn for drugs showing inhibitory effects on sheep spleen G6PD enzyme are shown in Figures 1, 2, and 3. The IC_{50} values obtained for the drugs oxaloplatin, carboplatin and cyclophosphamide, which have an inhibitory effect on the enzyme, were 3.22, 7.26, and 34.50 mM, respectively, and are shown in Table 1.

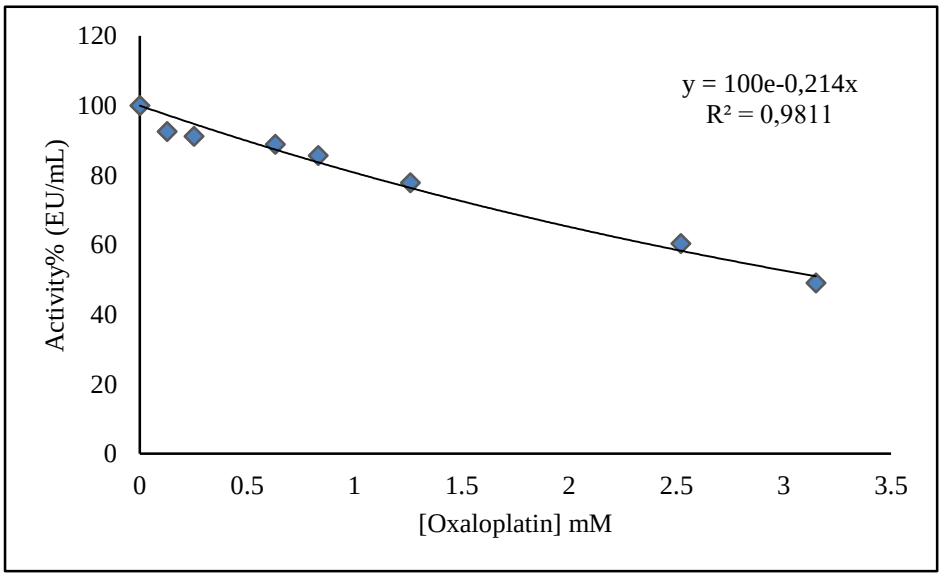

Figure 1. Activity%-[I] graph obtained for oxaloplatin

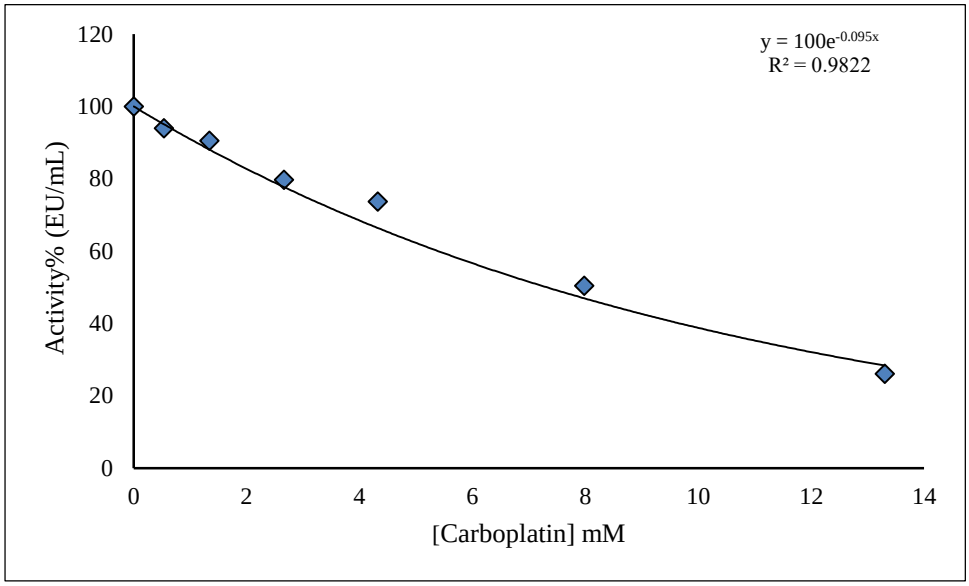

Figure 2. Activity%-[I] graph obtained for carboplatin

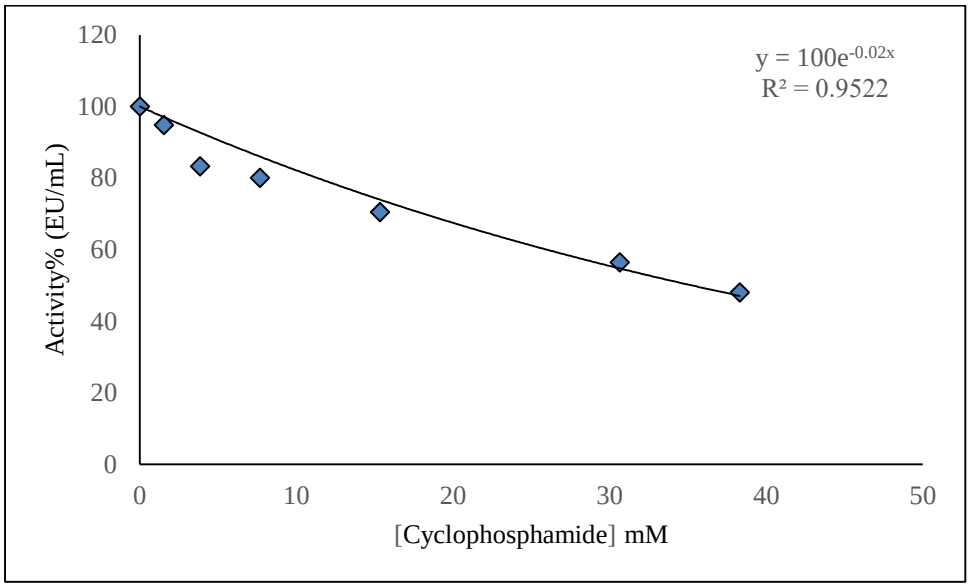

Figure 3. Activity%-[I] graph obtained for cyclophosphamide

Table 1. Obtained IC_{50} values

Drugs	**IC_{50} (mM)**
Oxaliplatin	3,22
Carboplatin	7,26
Cyclophosphamide	34,5

4. Conclusion

Because of its important functions in the pentose phosphate pathway, the G6PD enzyme has been purified and characterized from many human, animal and plant tissues. Especially recently, the effects of many medical drugs

and different chemicals on enzyme activity have been investigated. Inhibition of G6PD is of vital importance, especially in patients with G6PD deficiency. In this study, the effects of drugs such as carboplatin, cisplatin, oxaloplatin, fluorouracil, cyclophosphamide and ibandronic acid on the enzyme were investigated. As a result of the research, although the drugs cisplatin, fluorouracil and ibandronic acid did not have significant effects on the enzyme, it was determined that oxaloplatin, carboplatin and cyclophosphamide drugs inhibited the enzyme to a significant extent, and %Activity-[Drug] graphs were drawn for these drugs (Figures 1, 2, 3).) IC_{50} values were found (Table 1). According to these IC_{50} values (inhibitor concentration that reduces the enzyme activity by half), the decreasing inhibitory powers of the drugs can be listed as oxaloplatin, carboplatin and cyclophosphamide. Because while oxaloplatin with a concentration of 3.22 mM causes 50% inhibition, this value is 7.26 mM for carboplatin and 34.5 mM for cyclophosphamide. According to the IC_{50} values obtained in this study, it is understood that the strongest inhibitor is oxaloplatin, followed by carboplatin and cyclophosphamide.

As a result, it will be important to conduct more detailed inhibition studies for these three drugs in future studies, determine Ki constants and conduct *in vivo* studies. In addition, it will be important for body metabolism to take these IC_{50} values into consideration when adjusting the dosages of these drugs used in treatment.

References

[1] Lehninger, AL., Nelson, DL., Cox, MM. (1993) *Principles of Biochemistry*, 2nd edn. New York: Worth Publishers Inc, 436-437.

[2] Kanji, MI., Toews, ML., Carpar, WR. (1976) A kinetic study of glucose-6-phosphate dehydrogenase. *J Biol Chem*, 25, 2258-2262.

[3] Yuregir, GT., Aksoy, K., Arpaci, A., Unlukurt, I., Tuli, A. (1994) Studies on red cell glucose-6-phosphate dehydrogenase, evaluation of reference values. *Ann Clin Biochem*, 31, 50-55.

[4] Ninfali, P., Orsenigo, T., Barociani, L., Rapa, S. (1990) Rapid purification of glucose-6-phosphate dehydrogenase from mammal's erythrocytes. *Prep Biochem*, 20, 297-309.

[5] Delgado, C., Tejedor, C., Luquue, J. (1990) Partial purification of glucose-6-phosphate dehydrogenase and phosphofructokinase from rat erythrocyte haemolysate by partitioning in aqueous two-phase systems. *J Chromatographi*, 498, 159-168.

[6] Shreve, DS., Levy, HR. (1977) On the molecular weight of human glucose-6-phosphate dehydrogenase. *Biochem Biophy Res Com*, 78, 1369-1375.

[7] Morelli, A., Benatti, U., Gaetani, GF., De Flora, A. (1979) Biochemical mechanisms of glucose-6-phosphate dehydrogenase deficiency. *Proc Natl Acad Sci*, 75, 1979-1983.

[8] Beutler, E. (1971) *Red Cell Metabolism Manual of Biochemical Methods*. London: Academic Press, 68-70.

[9] Bradford MM. (1976) A rapid and sensitive method for the quantition of microgram quantities of protein utilizing the principle of protein-dye binding. *Anal Biochem*, 72, 248-251

Oxidative stress and antioxidant in pregnancy women conceived by In Vitro fertilization and Intrauterine Insemination

Zainab Y. EJAM [1*], Şevki ADEM [2], Asmaa KADHIM GATEA [3]

[1] *College of Pharmacy, Department of Pharmacutical chemistry, University of Babylon, Hilla, Iraq*

[2] *Faculty of Sciences, Department of Chemistry, Cankiri Karatekin University, Cankiri, 18100, Turkey*

[3] *College of Medicine, Department of Obstetrics and Gynecology, University of Babylon, Hilla, Iraq*

Abstract

One of the most widely used methods of assisted reproduction is in vitro fertilization (IVF). This approach is a most used infertility curative and frequently represents the sole chance for the infertile couples to become parents. The Intrauterine Insemination (IUI) is a straightforward, affordable, non-invasive, and secure therapy option for the management of infertility. Oxidative stress (OS) is the outcome of significant reactive oxygen species (ROS) causing oocyte senility and many reproductive problems in females, while antioxidant can balance out the increased levels of ROS that cause a high state of OS, they have long been used in the treatment of subfertility. This study was to detect the serum of superoxide dismutase, catalase, glutathione, reactive oxygen species, and Malondialdehyde levels of pregnant with different types of assisted reproductive techniques in relation with the age group, body mass index (BMI). Enzyme-linked immune sorbent assay (ELISA) based on for the detection of SOD,CAT, ROS levels in the serum of pregnant women in the first trimester of pregnancy, while GSH measured by using amino acid analyzer. The present study showed that the serum SOD, CAT, and GSH showed a significant decrease in IVF, IUI, SP pregnant groups in comparison with NP. While ROS and MDA significant increase. There were a non- significant difference present between the different pregnant groups (IVF, IUI, and SP) also in ages and BMI groups. There is significant decreases in serum GSH, CAT, and SOD during pregnancy corresponding significant increases in serum of ROS and MDA because pregnant women were more capable to oxidative damage than the non-pregnant as show by the decreased antioxidants. There is no significant effect among the groups of pregnant (IVF, IUI, and SP), perhaps because they are similar in age and BMI.

Keywords: *Superoxide dismutase, Catalase, Glutathione, Reactive oxygen species, Malondialdehyde*

1. Introduction

One of the most widely used methods of assisted reproduction is in vitro fertilization (IVF). This approach is a widely used infertility medication and frequently represents the sole way for infertile couples to become parents. IVF may be beneficial for patients with a history of endometriosis who have undergone unsuccessful medical or surgical treatment as well as those whose conservative reproductive treatments have failed or who have unexplained infertility [1]. The two forms of antioxidants that can be found in the body normally are enzymatic antioxidants and non-enzymatic antioxidants. Catalase (CAT), the glutathione peroxidase (GSH-Px), the glutathione reductase (GSH-R), and the superoxide dismutase (SOD), are the most prominent enzymatic antioxidants. Because glutathione shields eggs from oxidative stress during folliculogenesis, it is essential for egg quality. The oocytes with higher intracellular glutathione levels create embryos that are more robust and healthy. Oxidative stress clarify to be one of the main causes of IVF failure, among other factors [2].

2. Patients and Methods

The case study include 150 pregnant women in the first trimester of the pregnancy these women divided in to three types a. women that pregnant by IVF technique, b. women that pregnant by IUI technique, and c. women that pregnant spontaneously. The study take 50 apparently healthy women without pregnant considered as a control groups. Sample collection and work carried out in Taiba Center for Infertility Treatment, in Babylon province/Iraq For the period from March 2022 to January 2023. The study was confirmed by the University of Babylon/College of the Medicine Ethical Committee. Informed of admission was obtained from all women that

3. Results

The present study showed that the serum SOD, CAT, and GSH showed a significant decrease in IVF, IUI, SP pregnant groups in comparison with NP. There were a non- significant that difference present between the

* *Corresponding author. e-mail address: ejamzainab@gmail.com*

different pregnant groups ($p<0.05$) regarding the serum level of SOD, CAT, and GSH as shown in the (Table 1). Statistical analysis also showed a non- significant difference present between the different age and BMI groups regarding the serum levels of all studied SOD, CAT, and GSH (Table 2) and (Table 3). Statistical analysis show there is a significant increase in serum of reactive oxygen species and Malondialdehyde in groups of SP, IUI, and IVF comparison to non-pregnant ($p<0.05$), while a non- significant the difference present between the different pregnant groups (Table 4). There is increase but not significant in serum of ROS in SP and IVF groups. While MDA increase and not significant in SP group only, there is no statistical effect in IVF and IUI groups. (Table 5). In BMI groups, there is no significant analyses in serum of ROS and MDA in all groups of pregnant as show on in (Table 6).

Table 1. The relation of serum levels of SOD, CAT, and GSH between different groups.

Group	SOD Mean±SD	P value	CAT Mean±SD	P value	GSH Mean±SD	P value
IVF	58.202±8.502	0.991	42.095±4.451	0.557	4.780±0.20	0.667
IUI	57.365±7.317		42.842±8.737		4.665±0.85	
IVF	58.202±8.502	0.717	42.095±4.451	0.546	4.780±0.20	0.345
SP	58.227±9.176		41.456±6.022		4.635±0.59	
IVF	58.202±8.502	0.048*	42.095±4.451	0.047*	4.780±0.20	0.018*
NP	62.105±9.665		44.234±7.615		4.808±0.58	
IUI	57.365±7.317	0.705	42.842±8.737	0.836	4.665±0.85	0.640
SP	58.227±9.176		41.456±6.022		4.635±0.59	
IUI	57.365±7.317	0.034*	42.842±8.737	0.012*	4.665±0.85	0.030*
NP	62.105±9.665		44.234±7.615		4.808±0.58	
SP	58.227±9.176	0.025*	41.456±6.022	0.024*	4.635±0.59	0.015*
NP	62.105±9.665		44.234±7.615		4.808±0.58	

p > 0.05: Non-Significant; * p<0.05 Significant; **p<0.01: Highly Significant

Table 2. Means ±SD of serum levels of SOD, CAT, and GSH in the different pregnant groups according to the age.

Biochemical Test	Age group (Year)	(SP) Mean ±SD	P value	(IUI) Mean ±SD	P Value	(IVF) Mean ±SD	P value
SOD	18-25	60.291±8.11	0.627	60.63±7.194	0.626	62.337±8.275	0.286
	26-33	58.80±10.31		60.146±7.823		59.922±8.863	
	Above 34	57.134±9.725		58.219±6.94		57.213±7.981	
CAT	18-25	43.807±7.907	0.175	42.063±3.332	0.667	44.042±4.139	0.250
	26-33	40.081±2.758		42.887±2.870		43.365±5.130	
	Above 34	42.457±4.878		42.169±2.876		41.417±3.408	
GSH	18-25	4.992±0.73	0.02*	4.917±0.29	0.10	4.843±0.17	0.16
	26-33	4.545±0.49		4.861±0.68		4.850±0.24	
	Above 34	4.506±0.37		4.553±0.28		4.730±0.14	

Table 3. Means ±SD of serum levels of SOD, CAT, and GSH in the different pregnant groups according to the BMI.

Biochemical Test	BMI	(SP) Mean ±SD	P Value	(IUI) Mean ±SD	P value	IVF Mean ±SD	P value
SOD	Normal weight	60.634±6.88	0.591	58.959±6.95	0.743	61.781±8.172	0.166
	Overweight	59.091±9.98		60.539±7.54		61.401±9.778	
	Obese	56.884±10.1		58.869±7.77		56.961±7.233	
CAT	Normal weight	44.893±9.28	0.062	42.811±2.96	0.771	43.501±4.869	0.280
	Overweight	42.261±3.83		42.463±3.12		43.956±4.499	
	Obese	39.475±2.31		41.984±2.79		41.732±4.071	
GSH	Normal weight	4.952±0.65	0.132	5.012±0.71	0.076	4.837±0.31	0.443
	Overweight	4.719±0.68		4.695±0.40		4.739±.031	
	Obese	4.463±0.28		4.610±0.26		4.713±0.21	

Table 4. The relation of serum levels of ROS and MDA between different groups.

Group	ROS Mean±SD	P value	MDA Mean±SD	P value
IVF	323.209±49.07	0.853	1.67±0.95	0.314
IUI	321.35±42.29		1.73±0.41	
IVF	323.209±49.07	0.873	1.67±0.95	0.348
SP	312.05±34.27		1.65±0.51	
IVF	323.209±49.07	0.048*	1.67±0.95	0.041*
NP	282.70±65.45		1.47±0.37	
IUI	321.35±42.29	0.965	1.73±0.41	0.967
SP	312.05±34.27		1.65±0.51	
IUI	321.35±42.29	0.026*	1.73±0.41	0.018*
NP	282.70±65.45		1.47±0.37	
SP	312.05±34.27	0.021*	1.65±0.51	0.049*
NP	282.70±65.45		1.47±0.37	

Table 5. Means ±SD of serum levels of ROS and MDA in the different pregnant groups according to the age.

Biochemical Test	Age group (Year)	(SP) Mean ±SD	P value	(IUI) Mean ±SD	P Value	(IVF) Mean ±SD	P value
ROS	18-25	314.07±25.63	0.702	323.04±38.51	0.973	320.17±50.25	0.584
	26-33	319.90±39.17		319.84±39.18		309.31±54.00	
	Above 34	325.18±33.91		319.54±50.97		328.34±41.92	
MDA	18-25	1.53±0.41	0.435	1.67±0.27	0.804	1.90±1.31	0.630
	26-33	1.62±0.40		1.61±0.27		1.64±0.25	
	Above 34	1.73±0.4		1.63±0.26		1.68±0.26	

Table 6. Means ±SD of serum levels of SOD, CAT, and GSH in the different pregnant groups according to the BMI.

Biochemical Test	BMI	(SP) Mean ±SD	P Value	(IUI) Mean ±SD	P value	IVF Mean ±SD	P value
ROS	Normal weight	325.57±41.44	0.420	323.39±38.77	0.397	321.51±43.49	0.508
	Overweight	314.40±33.40		326.30±45.15		307.18±52.08	
	Obese	330.06±35.33		306.06±41.44		326.02±50.61	
MDA	Normal weight	1.43±0.25	0.916	1.65±0.27	0.681	2.11±1.65	0.252
	Overweight	1.70±0.42		1.59±0.28		1.66±0.29	
	Obese	1.72±0.43		1.67±0.24		1.63±0.23	

4. Discussion

In the current research, it was found that there were significant decreases in serum GSH, CAT, and SOD in pregnant women when compared to non-pregnant women ($P < 0.05$). These results come in agreement with other research; they found that the GSH and CAT levels underwent slight but significant decreases in the healthy pregnant women when compared with that of healthy non-pregnant women [3]. Bassi found a highly significant decrease in SOD in pregnant in the first trimester than that of non- pregnant [4]. In addition, Singh found a significant decrease in CAT during pregnancy period [5]. The present research showed a significant increase of in serum MDA in healthy pregnant women when compared with that of healthy non-pregnant women. According to some studies reported that the MDA was increased during normal pregnancy [6]. During normal pregnancy, it was found that a little increase in the oxidative stress could occur, even in the presence of the antioxidant systems [7]. According to the findings, there was a statistically significant difference in the MDA levels between women who underwent IVF and those who did not become pregnant. MDA levels were significantly higher in IVF pregnant women than in non-pregnant ones, which may be related to the weak positive correlation between MDA and the quantity of grade A embryos and fertilization rate, two key indicators of successful IVF outcomes. These findings concur with those of Pasqualotto, who discovered that lipid peroxidation levels were higher in pregnant women [8]. The present research showed a non-significant increase of serum ROS in healthy pregnant women in the first trimester when compared with that of healthy non-pregnant women. During the time of pregnancy, the numerous physiological and the metabolic changes that occur in the mother's body which help the production of ROS, particular in the second half of the pregnancy. The primary causes of this are an increase in basic metabolism and oxygen "consumption" as well as the predominant use of fatty acids as an energy source by the majority of maternal retro placental tissues. Pregnancy's third trimester is a unique time when insulin resistance, fat catabolism, and the release of free fatty acids all increase. The third trimester of the pregnancy is a special time when free fatty acid release, fat catabolism, and insulin resistance all rise. The level of oxidative stress was slightly significantly in women with IUI pregnant comparison to NP its maybe increase endometrial content of ROS [9]. The present study show increase in serum of ROS in IVF pregnant women some data indicate that an increase in ROS linked to rising maternal age may have an impact on oocyte quality, where it found ROS demonstrated to negatively affect oocyte maturation, but they also play a critical function in cellular signaling for the activation of meiosis in the oocyte [10].

References

[1] Iketubosin, F. (2018). In vitro fertilization embryo transfer processes and pathway: a review from practice perspective. Tropical Journal of Obstetrics and Gynaecology, 35(3), 227-232.

[2] Patil, S. B., Kodliwadmath, M. V., & Kodliwadmath, S. M. (2007). Study of oxidative stress and enzymatic antioxidants in normal pregnancy. Indian Journal of clinical biochemistry, 22, 135-137.

[3] Hassan, I. S., & Laylani, L. A. A. S. S. (2017). Oxidative stress state during pregnancy period. Iraqi Journal of Science, 58(2C), 984-987.

[4] Singh, S. P., Sharma, P., Kumar, P., & Sharma, R. (2020). Estimation of malondialdehyde and catalase in pregnant & non-prenant women.

[5] Poston, L., & Raijmakers, M. T. M. (2004). Trophoblast oxidative stress, antioxidants and pregnancy outcome—a review. Placenta, 25, S72-S78.

[6] Tiwari, D., Akhtar, S., Garg, R., Manger, P. T., & Khan, M. M. (2016). A comparative study of oxidative status in pregnant and non-pregnant women.

[7] Pasqualotto, E. B., Agarwal, A., Sharma, R. K., Izzo, V. M., Pinotti, J. A., Joshi, N. J., & Rose, B. I. (2004). Effect of oxidative stress in follicular fluid on the outcome of assisted reproductive procedures. Fertility and sterility, 81(4), 973-976.

[8] Duhig, K., Chappell, L. C., & Shennan, A. H. (2016). Oxidative stress in pregnancy and reproduction. Obstetric medicine, 9(3), 113-116.
[9] Demir, B., Dilbaz, B., Cinar, O., Karadag, B., Tasci, Y. A. S. E. M. İ. N., Kocak, M., ... & Goktolga, U. (2011). Factors affecting pregnancy outcome of intrauterine insemination cycles in couples with favourable female characteristics. Journal of Obstetrics and Gynaecology, 31(5), 420-423.
[10] Carbone, M. C., Tatone, C., Monache, S. D., Marci, R., Caserta, D., Colonna, R., & Amicarelli, F. (2003). Antioxidant enzymatic defences in human follicular fluid: characterization and age-dependent changes. MHR: Basic science of reproductive medicine, 9(11), 639-643.

Retrospective Analysis of the Diagnostic Dilemma in Malignant and Benign Lesions of the Maxillofacial Region Review

Zuhal Ovuz*

[1] *Faculty of Dentistry, Department of Maxillofacial Radiology, Çankırı Karatekin University, Çankırı, Turkiye*

Abstract

There are different types of gingival enlargements. It varies according to etiological and pathological factors. Definitive diagnosis of the enlargement is important, as some gingival enlargements may indicate malignant lesions that extensive morbidity and even death. Oral cancers, especially squamous cell carcinomas, differ in the affected areas. Detailed medical history, clinical examination, and radiographic evaluation will help identify the lesion and biopsy will aid in definitive diagnosis. Malignant-benign lesions of the maxillofacial region published as case reports in the last 10 years were scanned in the Pubmed database. 6790 articles were found. Titles and abstracts were reviewed, 127 case reports that were confused as pyogenic granuloma or metastasis in the maxillofacial region were identified. Articles older than 10 years were excluded, 30 case reports (19 men, 11 women) were reviewed. The age range of females and males was 1-78 (49,18). 22 pyogenic granuloma cases with a prediagnosis and 8 metastasis cases with a prediagnosis were determined. The region of lesions, age, gender, habits Statistical analysis was performed with IBM SPSS Statistics 25 program. It should be considered that a newly diagnosed malignancy in the maxillofacial region may metastasize from distant sites and may present signs and symptoms before the primary tumor. The clinical manifestations of oral cancers are similar to benign lesions. Histopathological evaluation is important for early diagnosis. The aim of this study is to evaluate the current literature on misconceptions in the diagnosis of malignant-benign lesions in the maxillofacial region.

Keywords: *Benign, Malign, Metastasis, Pyogenic Granuloma*

1. Introduction

Metastatic tumours of the maxillofacial region are uncommon and account for approximately 1-4% of all oral malignancies [1]. Oral metastases can occur in the oral soft tissues. These malignancies are likely to exhibit non-specific symptoms and may clinically mimic benign lesions, thus making it difficult for practitioners to diagnose [2]. The lungs, kidney, breast, and bone comprise the majority of primary sites that metastasize to the oral cavity [3]. Pyogenic granuloma is a non-neoplastic inflammatory hyperplasia that responds to various stimuli such as oral hygiene, chronic local irritation, trauma, hormonal changes, and reactions to grafts [4]. It presents as a localised, exophytic, peduculated, or an ulcerative, painless growth of mucousa [5]. The most common intraoral site is the gingiva (nearly 75%), but it also affects the lips, mucosa, and tongue [6].

2. Materials and Methods

Malignant-benign lesions of the maxillofacial region published as case reports in the last 10 years were scanned in the Pubmed database. 6790 articles were found. Titles and abstracts were reviewed, 127 case reports that were confused as pyogenic granuloma or metastasis in the maxillofacial region were identified. Articles older than 10 years were excluded, 30 case reports (19 men, 11 women) were reviewed. The region of lesions, age, gender, habits and prediagnosis- diagnosis were analysed statistical analysis with IBM SPSS Statistics 25 program (SPSS Inc., Chicago, IL, USA).

3. Results

As a result of the evaluations, 22 of the 30 cases were sent for pathological evaluation with the preliminary diagnosis of pyogenic granuloma and a definitive diagnosis of metastasis was made. 8 of them were diagnosed as metastasis, but were reported to be pyogenic granuloma (Table 1). It was determined that 30 cases were more prevalent among males (n = 19/% 63,3) than females (n = 11/36,6 %). The age range of the women was 1-78 (mean 49.18 - median 58 - sd 22.973). The age range of men was found to be 20 - 75 (mean 46-median 46 sd 13,888). Table 5 shows relation of gender and age. When the habits of the cases were examined, it was learned

* Corresponding author. *e-mail address: zuhalovuz@karatekin.edu.tr*

that the number of smokers was 9 (30%) and 21 cases were non-smokers (70%). It was learned that the number of alchol was 8 (26,70%) yes and 22 cases were no (73,30%) (Table 2). Regarding the anatomical location in soft tissues, lesions in gingiva (*n* = 21/70%), were more prevalent, lips, buccal mucosa and tongue on each (n=1/3.30%), It was found that there were (n=6/20%) cases in the palate (Table 4). Table 4. shows the symptoms seen in the lesions, ulceration was determined as (n=25/83.30%), bleeding as (n=20/66.70%), swelling as (n=28/93.30%), pain as (n=13/43.30%).

Table 1. Diagnosis and prediognosis frequance analysis

		Count	Column N %
Diagnosis	Piyogenic Granulama	8	26,70%
	Metastasis	22	73,30%
	Total	30	100,00%
Prediagnosis	Piyogenic granuloma	22	73,30%
	Metastasis	8	26,70%
	Total	30	100,00%

Table 2. Analysis of habits

		Count	Column N %
Smoking	yes	9	30,00%
	no	21	70,00%
	Total	30	100,00%
Alchol	yes	8	26,70%
	no	22	73,30%
	Total	30	100,00%
Tobacco	yes	0	0,00%
	no	30	100,00%
	Total	30	100,00%

Table 3. Symptoms

		Count	Column N %
Ulceration	yes	25	83,30%
	no	5	16,70%
	Total	30	100,00%
Bleeding	Yes	20	66,70%
	No	10	33,30%
	Total	30	100,00%
Swelling	Yes	28	93,30%
	No	2	6,70%
	Total	30	100,00%
Pain	Yes	13	43,30%
	No	17	56,70%
	Total	30	100,00%

Table 4. Anatomical Location

Region	Count	Column N %
Gingiva	21	70,00%
Lip	1	3,30%
Buccal mucosa	1	3,30%
Tongue	1	3,30%
Palate	6	20,00%
Total	30	100,00%

Table 5. Relation between gender and age

Gender	N	Age Mean	Median	Std. Deviation	Maximum	Minimum
Female	11	49,18	58	22,973	78	1
Male	19	46	46	13,888	75	20
Total	30	47,17	48	17,44	78	1

4. Discussion

Distant metastasis to the maxillofacial region is a rare, accounts only 1% of all oral malignancies [7]. The clinical diagnosis of oral metastasis is a challenge. Therefore, these lesions are usually misdiagnosed as pyogenic granuloma, hyperplastic gingival inflammation, peripheral giant cell granuloma, or other benign tumours [8].
The definiteve diagnosis can be done after histopathological evaluation. In this study, we reviewed cases with metastasis after incisional biopsy and mimicking pyogenic granuloma. Histopathological evaulation is very important for the final diagnosis of the oral metastatic lesions. In some cases oral metastasis occured as a first sign of the primary carcinomas. In this case, immunohistochemical stains may be needed to characterize the primary tumour or confirm the metastasis [9].

Metastatic tumors may appear in the oral soft tissues, jaw bones or both. In this study, 21 cases were detected in the gingiva, 1 case in each of the lips, cheeks and tongue, and 6 cases in the palate. According to some meta-analysis about oral metastases, the gender distribution is either predominantly male or nearly equal. In this study male cases were the majority (% 63,3 male, % 36,6 female). The overall average age of the cases was 47,17 years, the mean age of female was 49,18 years and the men was 46 years. This finding is consistent with the results of previous studies that reported that oral metastatic tumors were diagnosed between the fifth and seventh decades [10]. In the literature, it has been reported that multiple signs and symptoms such as pain, swelling, bleeding, paresthesia, and tooth mobility are seen [11]. Similarly, the most common signs and symptoms in our study were swelling (93,30%), pain (43,30%), bleeding (66,70%), and ulcer (83,30%).

Tobacco and alcohol consumption are well-recognized risk factors for cancers of the oral cavity and pharynx [12]. Comparatively few studies have investigated the role of tobacco and alcohol in relation to malign lesions risk. In the literature, smoking and alcohol use are known as risk factors for malignant lesions of the oral region [13]. In this review, it was noticed that there were cases of smokers (30%) and alchol drinkers (26,70 %).

5. Conclusion

Maxillary metastases of HCC are rare and may mimic benign lesions; hence, awareness and meticulous clinical and histopathological examinations play an important role in ensuring proper treatment.

References

[1] Doğan M, Kankaya D, Büyükçelik A, Karataş F, Utkan G, Şencan O, et al. 2009. Gingival Metastasis in Large Celi Lung Carcinoma. Acta Oncologica Turcica. 42(1):30–2.

[2] Ramirez JR, Seoane J, Montero J, Esparza Gómez GC, Cerero R. 2003 Oct. Isolated gingival metastasis from hepatocellular carcinoma mimicking a pyogenic granuloma. J Clin Periodontol. 31;30(10):926–9.
[3] Bilgiç Küçükgüven M, Aktaş A, Ateş Özdemir D. 2019. A Rare Case Of Maxıllary Hepatocellular Carcinoma Metastasis Mimicking Pyogenic Granuloma In A Gerıatrıc Patıent. Turkısh Journal Of Gerıatrıcs-Turk Gerıatrı Dergısı. 22(1):112–6.

Antibiotic Removal from Wastewater by Adsorption

Mohammed Thabit Shihab SHİHAB [1], ***Bengi ÖZKAHRAMAN*** [2], ***Zehra ÖZBAŞ*** [1*]

[1] *Institute of Natural Sciences, Faculty of Engineering, Department of Chemical Engineering, Çankırı Karatekin University, Çankırı, Türkiye*

[2] *Institute of Graduate Education, Faculty of Engineering, Department of Polymer Materials Engineering, Hitit University, Çorum, Türkiye*

Abstract

Antibiotics, are chemicals that reduce or inhibit the proliferation and growth of microorganisms, and are useful in the treatment of human infectious diseases, the livestock industry, and aquaculture. After administration, antibiotics are only partially metabolized in the body, while the remaining antibiotics are excreted. The sewage treatment plants of municipal systems and pharmaceutical businesses are not efficient enough to remove these antimicrobials [1, 2]. Among the existing processes for the treatment of antibiotic-containing wastewater, the adsorption process is accepted as an effective and efficient method [3]. In the present study, epichlorhydrin cross-linked chitosan particles were kept in carboxymethyl cellulose solution before cross-linked with citric acid. Ampicillin (AMP) adsorption studies were carried out with the obtained particles. The physical and morphological characterization of the prepared adsorbent before and after adsorption was revealed by FTIR (Fourier-transform infrared), BET (Brunner-Emmett-Teller surface area) and SEM/EDX (Scanning electron microscopy-energy dispersive X-ray) analyses. The recommended contact time under application conditions is determined as 28 hours. Kinetic studies have shown that the process is more compatible with the pseudo-second-order kinetic model. According to the experimental data obtained, it was determined that the equilibrium adsorption obeyed the Langmuir isotherm. These results demonstrate the feasibility of the process and the application potential of the chitosan- carboxymethyl cellulose adsorbent in the treatment of AMP-containing waters such as hospital wastewater and pharmaceutical industrial wastewater.

Keywords: *Antibiotics, Adsorption, Ampicillin, Chitosan, Carboxymethyl cellulose*

1. Introduction

Antibiotics are chemotherapeutic agents that are widely used in the treatment of diseases in animals and humans, as well as in the field of food to increase the growth rates of animals [1]. Due to their chemical structure, antibiotics are resistant to many chemicals, oxidizing agents and heat, and they are not biodegradable. Therefore, once released into the aquatic environment, antibiotics are difficult to remove from wastewater [1, 2]. There are many methods for removing contaminants from water. The most important of these methods are reverse osmosis, ion exchange, precipitation and adsorption [1, 3].

In the study, crosslinked chitosan particles were kept in carboxymethyl cellulose solution and then re-crosslinked with citric acid to be used in ampicillin adsorption. Characterization of these prepared particles was carried out by FTIR, BET and SEM/EDX analyses, and ampicillin adsorption kinetics and isotherms were examined.

2. Materials and Methods

Materials Used in Adsorbent Synthesis: CS (chitosan), CH_3COOH (acetic acid), NaOH (sodium hydroxide), EPC (epichlorohydrin), CMC (carboxymethyl cellulose), CA (citric acid), AMP (ampicillin), and HCl (hydrogen chloride) used in this study were Sigma-Aldrich products. Distilled water was used in the purification process while preparing the adsorbent.

Polymeric Adsorbent Preparation Method: After 1 g of CS was dissolved in 30 mL of 5% (v/v) CH_3COOH at 40°C, it was dropped into 0.5 M NaOH solution with a syringe and the formation of instant gelled particles was observed. The resulting CS particles were left in NaOH solution for 24 hours and then washed with distilled water. The obtained CS particles were kept in 0.01 M EPC solution at 60°C for 3 hours for cross-linking to occur. At the end of the period, the particles were washed with distilled water until the solution became neutral. Separately, 1 g of CMC was dissolved in 50 mL of water at 50°C. Then, the CS particles washed with water were

* Corresponding author. *e-mail address:zehraozbas@karatekin.edu.tr*

kept in the prepared CMC solution for 24 hours for complex formation. At the end of the period, 0.2 g CA was added to the solution containing CS particles and mixed for 2 hours at 80°C for cross-linking. The final product obtained, the adsorbent, was named CS-CMC. Removal experiments of AMP with CS-CMC from solutions by adsorption were carried out in a batch system. The maximum absorbance wavelength of AMP (260 nm) was determined with a UV–vis spectrometer and all the absorbance measurements were made with a UV–vis spectrometer (Shimadzu UV-1800).

3. Results and Discussion

3.1. Characterization Studies

Figure 1(a) shows the FTIR spectrum of the complex particle formed by crosslinked CS with crosslinked CMC. In the spectrum, except for the peaks belonging to the crosslinked CS, the peak at 1723 cm^{-1} was attributed to the carbonyl band of the free carboxylic acid groups and the carbonyl groups of the ester structure formed during the crosslinking process. Figure 1(b) shows the FTIR spectrum of AMP adsorbed CS-CMC adsorbent. In the spectrum, apart from the characteristic peaks observed in the spectrum of the CS-CMC adsorbent, there were peaks belonging to AMP, but these peaks were not obvious because they interfered with each other.

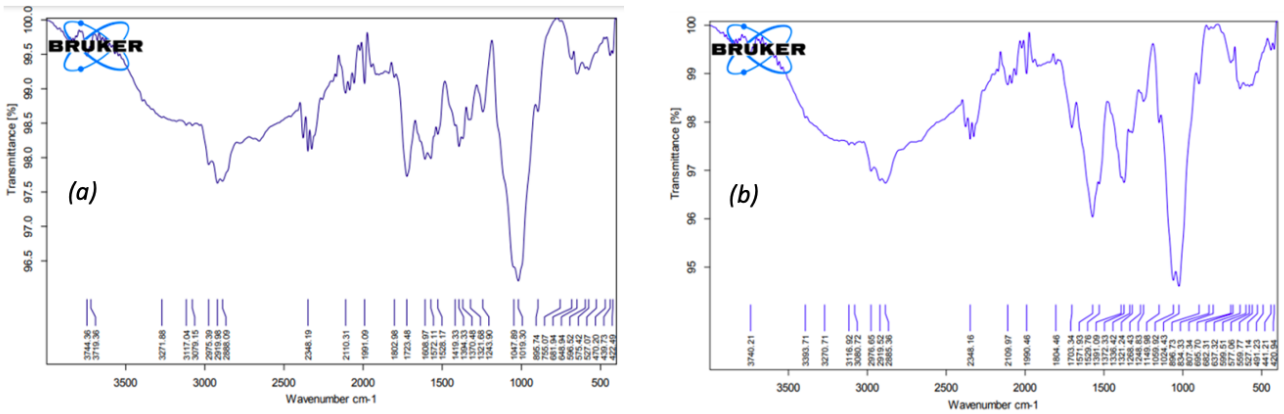

Figure 1. FTIR spectra of CS-CMC before (a) and after (b) adsorption.

According to the results of BET analysis, the specific surface area of the complex adsorbent CS-CMC was 7.30 m^2/g before adsorption and 22.72 m^2/g after adsorption. SEM images of the prepared CS-CMC adsorbent before and after adsorption were presented in Figure 2 (a) and (b) and Figure 3 (a) and (b). When the images were evaluated, it was determined that the CS-CMC sample before adsorption had a non-porous, slightly rough surface morphology, while the surface layer thickened after adsorption. EDX analysis results of the samples before and after adsorption were presented in Figure 2 (c) and Figure 3 (c). According to the analysis, % weight values before adsorption: 42.95 % carbon, 6.97 % nitrogen and 50.08 % oxygen, while the % weight values after adsorption changed to 47.70 % carbon, 6.41 % nitrogen, 41.76 % oxygen and 4.13 % sulfur due to the sulfur in the structure of adsorbed AMP.

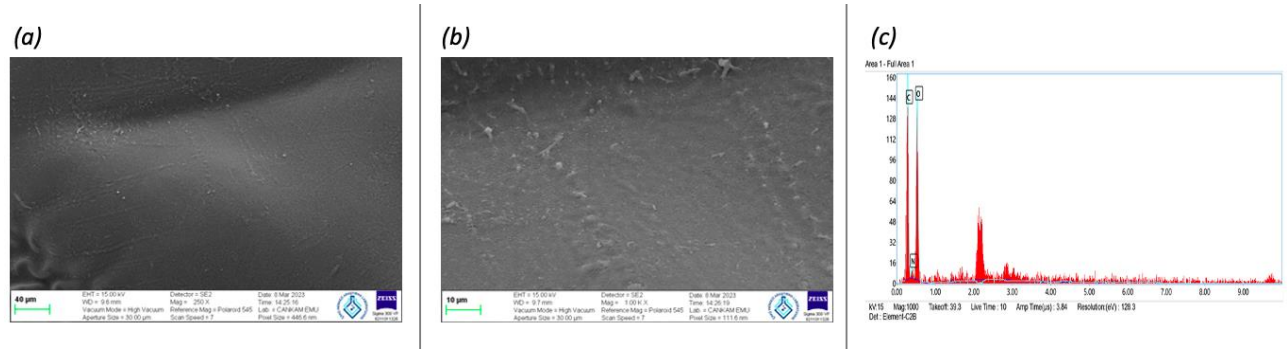

Figure 2. SEM/EDX analysis of CS-CMC before adsorption.

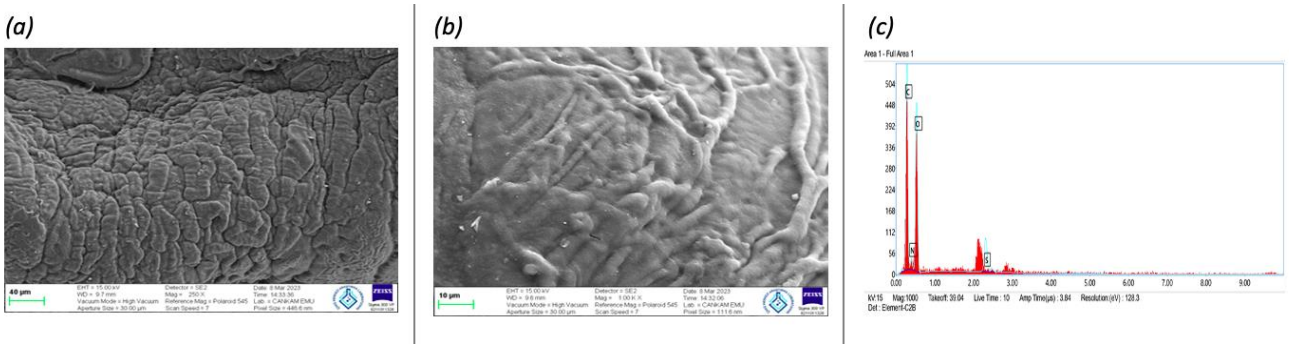

Figure 3. SEM/EDX analysis of CS-CMC after adsorption.

3.2. Adsorption Studies

To study the adsorption kinetics, approximately 10 mg of CS-CMC adsorbent was kept at 25°C in a 250 ppm solution with a pH of 7 until equilibrium was reached. According to the result obtained, the process did not show any capacity increase after the 28th hour and reached equilibrium, and the adsorption capacity at this hour was found to be 231.41 mg/g. The kinetic parameters were presented in Table 1.

Table 1. The linear equations, plots and the calculated values for pseudo-first-order and pseudo-second-order kinetic models.

Kinetic models	Linear equations*	Plots	Calculated parameters
Pseudo-first-order [4]	$\ln(q_e - q_t) = \ln q_e - k_1 t$	$\ln(q_e-q_t)$ vs t	k_1= 0.1313 h^{-1} q_e= 153.88 $mg.g^{-1}$ r^2= 0.9514
Pseudo-second-order [4]	${}^{t}/_{q_t} = {}^{1}/_{k_2 q_e^2} + {}^{t}/_{q_e}$	t/q_t vs t	k_2= 1.24×10^{-3} $g.mg^{-1}.h^{-1}$ q_e= 256.41 $mg.g^{-1}$ r^2= 0.9966

*q_t: adsorbent capacity at time t, q_e: adsorbent capacity at equilibrium, $k_{1,2}$: rate constants

In order to study the adsorption isotherm, experimental studies were carried out for AMP adsorption at 25°C in solutions with initial solution concentrations of 50, 100, 150, 200 and 250 ppm, using pH 7 and approximately 10 mg CS-CMC adsorbent. According to the result, q_e values increased with increasing initial solution concentration. The calculated isotherm parameters were presented in Table 2.

Table 2. The linear equations, the plots and the calculated parameters for Langmuir and Freundlich isotherms.

Models	Equations and plots*	Calculated parameters	
Langmuir [4]	${}^{C_e}/_{q_e} = {}^{1}/_{b.q_{max}} + {}^{C_e}/_{q_{max}}$ Plot: C_e/q_e vs C_e	b ($L.mg^{-1}$) q_{max} ($mg.g^{-1}$) R_L r^2	0.0063 416.67 0.387 0.9977
Freundlich [4]	$\ln q_e = \ln K_F + {}^{1}/_{n} \ln C_e$ Plot: In q_e vs In C_e	K_F ($(mg.g^{-1}).(L.mg^{-1})^{1/n}$) 1/n r^2	9.83 0.5981 0.9769

*b: Langmuir constant, q_{max}: monolayer capacity of the adsorbent, K_F: Freundlich constant, n: Freundlich exponent

4. Conclusion

In the study, AMP adsorption was carried out with complex adsorbent particles prepared with cross-linked CS and CMC from aqueous solutions. The physical and morphological characterization of the prepared adsorbent before and after adsorption was revealed by FTIR, BET and SEM/EDX analyses. The recommended contact time under application conditions was determined as 28 hours. According to the results, the process was more compatible with the pseudo-second-order kinetic model, and it was determined that the equilibrium adsorption obeyed the Langmuir isotherm. These results demonstrate the feasibility of the process and the application potential of the CS-CMC adsorbent in the treatment of AMP-containing waters such as hospital wastewater and pharmaceutical industrial wastewater.

References

[1] Balarak, D., Khatibi, A. D., & Chandrika, K. 2020. Antibiotics Removal from Aqueous Solution and Pharmaceutical Wastewater by Adsorption Process: A Review. *International Journal of Pharmaceutical Investigation, 10(2),* 106-111.

[2] Dutta, J., & Mala, A. A. 2020. Removal of antibiotic from the water environment by the adsorption technologies: A review. *Water Science and Technology, 82(3),* 401-426.

[3] Homem, V., & Santos, L. 2011. Degradation and removal methods of antibiotics from aqueous matrices–a review. *Journal of Environmental Management, 92(10),* 2304-2347.

[4] Özkahraman, B. & Özbaş, Z. 2020. Removal of Al(III) ions using gellan gum-acrylic acid double network hydrogel. *Journal of Polymers and the Environment, 28,* 689-698.

The Performance of Waste Banana Peels in the Removal of Congo Red in Wastewater

Tiba SALEH GHANI AL-OKAIDAT [1], ***Saqer A.K. ALLOH*** [1]

M. Bora AKIN [1*]

[1] *Department of Chemical Engineering, Çankırı Karatekin University, Çankırı, Turkiye*

Abstract

Various studies demonstrate the potential of banana peels as a biodegradable and low-cost biosorbent. Banana peels have a multilayered porous structure, which increases the chance of success in its use as an adsorbent. When the literature is examined, it can be seen that banana peels are used to remove lead (II), mercury and also various pollutants from water. In this study, the adsorption of Congo Red dye in wastewater with banana peel was investigated. The aim of the study is to examine the effects of variables such as time, initial dye concentration, adsorbent amount and temperature on adsorption during the removal of Congo Red from water with banana peel.

Keywords: *Wastewater, Adsorption, Congo Red, Banana peel, Adsorbent*

1. Introduction

Banana peels have potential as a biodegradable and low-cost bioadsorbent. Since banana peels have a high calcium carbonate ($CaCO_3$) content, they can be converted into high-value products [1]. Especially materials such as banana peel and wood ash have high adsorption percentages and a porous structure [2]. Since banana peel is a stable, inexpensive and multilayered porous structure, it can serve as a good adsorbent [3]. In addition, it is known that the powder obtained from calcined banana is an adsorbent with a sufficiently porous structure [4]. In the study, banana peel was used to remove metals such as lead (II) [4] and mercury [6] in water. Apart from this, in another study, banana peel is also used to remove pollutants such as sulfadiazine, sulfamethazine and sulfachloropyridazine [5].

These findings demonstrate the potential of banana peels as an effective bioadsorbent in removing various pollutants. The biodegradability and low cost of banana peels highlight their use as an effective adsorbent for dyes..

In this study, banana peels without pretreatment were dried and used for the adsorption of Congo Red in wastewater. The effects on adsorption capacity were examined by changing the parameters of time, temperature, adsorbent dose and initial dye concentration. The parameters of the study were chosen as time, temperature, adsorbent dose and initial dye concentration.

2. Materials and Methods

Congo Red dyestuff was purchased from Sigma Aldrich. Banana peels were dried at 80 °C using a vacuum oven. After drying, the size reduction process was applied by grinding. A magnetic stirrer (IKA) and UV spectrophotometer (Shimadzu) were used in Congo Red adsorption experiments.

In this study, a calibration chart was created by diluting Congo Red adsorption experiments using 1000 mL stock solution to obtain different concentrations. While a UV spectrophotometer was used to measure Congo Red absorbance values, the wavelength was set to 497 nm for intensity measurements. In experiments where adsorption capacity was determined, initial concentrations were prepared as 10, 25, 50, 100, 200, 300, 400, 500, 750 and 1000 mg/L, respectively. Experiments were carried out at 25 °C using 0.5 mg/L adsorbent in 100 mL solution. In time-dependent experiments, measurements were recorded at 0, 2, 5, 10, 20, 30, 45, 60, 90, 180, 240,

* Corresponding author. *e-mail address: mbakin@karatekin.edu.tr*

300, 360, 420 and 1440 minutes using a dye concentration of 200 mg/L. Then, concentration values were calculated using the calibration chart. To examine the temperature effect on the adsorption process, experiments were carried out at temperatures of 5 °C, 25 °C and 40 °C. For the adsorbent dose effect, 0.3, 0.5, 1 and 2.5 mg/L adsorbent was used. Adsorption capacity was calculated from the following equation:

$$q_e = \frac{(C_0 - C_e)}{m} \cdot V \quad (1)$$

Here, q_e is the capacity of the adsorbent (mg/g), C_0 is the initial concentration of the adsorbate (mg/L), C_e is the equilibrium concentration of the adsorbate (mg/L), V (mL) is the solution volume and m is the weight of the adsorbent used (g).

3. Results and Discussion

3.1. Effect of Initial Dye Concentration

In the study, adsorption capacities (q_e) were examined using adsorbent with 0.5 mg/L for different concentrations. The q_e values obtained for the concentrations examined in the study are given in Figure 1. Among the initial concentrations, the highest adsorption capacity was obtained at 750 mg/L with $2.6 \cdot 10^{-4}$ mol/kg. An increase in the q_e value is observed up to the initial concentration of 750 mg/L. 200 mg/L was chosen as the working concentration and this concentration was used to examine other parameters.

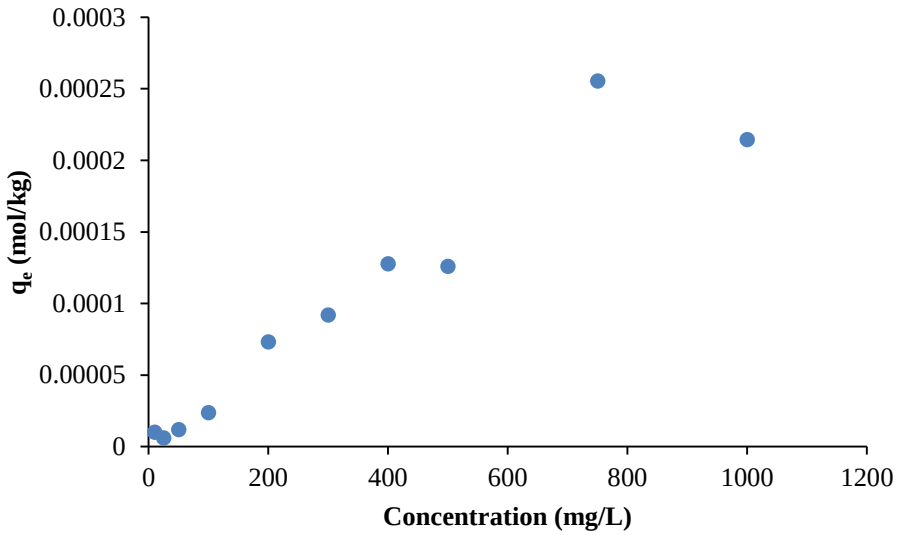

Figure 1. Boyarmadde başlangıç konsantrasyonlarının adsorbsiyon kapasitesine etkisi.

3.2. Effect of Time

For the experiment in which the effect of time on q_e was examined, 200 mg/L was chosen as the initial concentration. To find the q_e value at the selected concentration, concentration values were found by measuring samples taken at certain times. When Figure 2a is examined, it is understood that the concentration decreases over time, meaning that the adsorbent does its job. At the end of 1440 minutes, the dye concentration decreases to 174.75 mg/L. The calculation made using concentrations shows the change of q_e value with time (Figure 2b). At the end of 1440 minutes, the q_e value is $8.7 \cdot 10^{-5}$ mol/kg at an initial dye concentration of 200 mg/L.

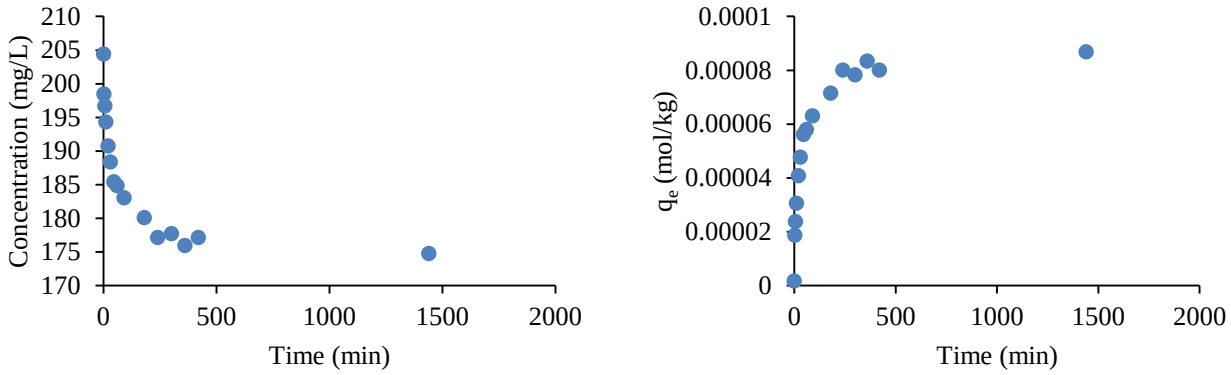

Figure 2. Effect of 0.5 mg/L adsorbent at 200 mg/L initial dye concentration: a) Concentration and b) adsorbent capacity

3.3. Effect of Adsorbent Amount

As the amount of adsorbent increases, the q_e value becomes $9.1 \cdot 10^{-5}$ at 0.3 mg/L and $8.7 \cdot 10^{-5}$ mol/kg at 0.5 mg/L. While the q_e value is $7 \cdot 10^{-5}$ mol/kg at 1 mg/L adsorbent amount, this value decreases to $1.8 \cdot 10^{-5}$ mol/kg at 2.5 mg/L adsorbent amount (Figure 3a). The decrease in q_e appears to be linear. The regression coefficient was obtained as 0.9986. It is seen that the highest adsorption percentage is 23.72% with the use of 1 mg/L adsorbent, and the closest value to this value is 15.6% with the use of 2.5 mg/L adsorbent (Figure 3b).

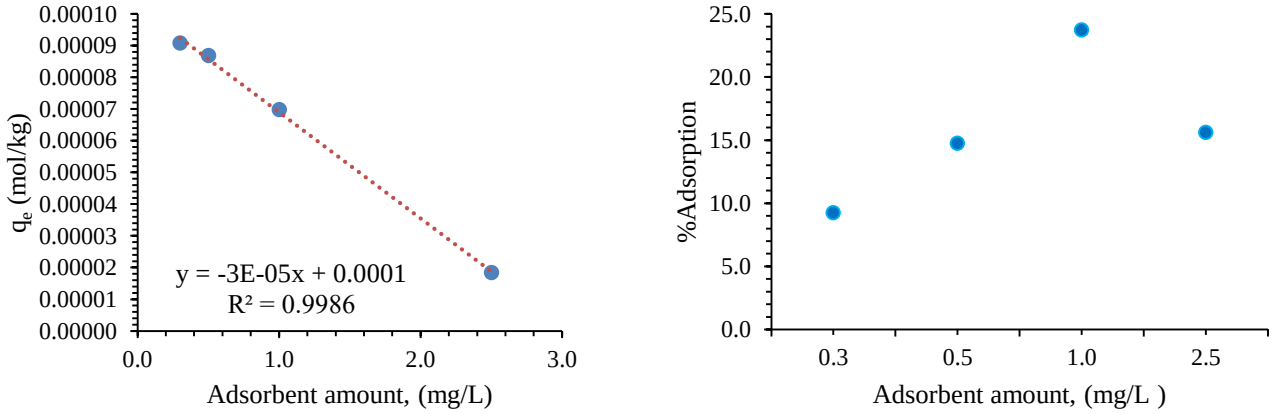

Figure 3. Effect of adsorbent amount a) adsorption capacity, b) Adsorption percentage

3.4. Effect of Temperature

In experiments conducted at 5 °C, 25 °C and 40 °C, where the effect of temperature on adsorption capacity was examined, q_e values were $12 \cdot 10^{-5}$ mol/kg at 5 °C and 9·10-5 mol/kg at 25 °C, respectively. and at 40 °C it was $5 \cdot 10^{-5}$ mol/kg. According to the data obtained, the q_e value decreases as the temperature increases (Figure 4).

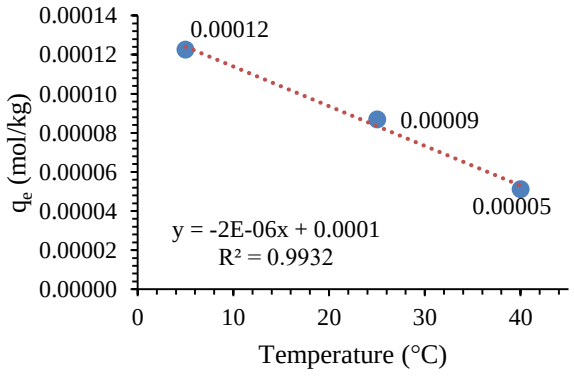

Figure 4. Effect of temperature on adsorption capacity

4. Conclusion

The data obtained in the study show that it is possible to use dried banana peels in the adsorption of Congo Red. It was observed that the q_e value increased with increasing initial dye concentration. The highest q_e value was obtained at a dye concentration of 750 mg/L and $2.6 \cdot 10^{-4}$ mol/kg. By using 0.5 mg/L adsorbent at an initial concentration of 200 mg/L, the q_e value was obtained as $8.7 \cdot 10^{-5}$ mol/kg. As the amount of adsorbent used as adsorbent increases to 1 mg/L, the adsorption efficiency increases and reaches 23.7%. At this yield, the q_e value is $7 \cdot 10^{-5}$ mol/kg. The q_e value was obtained as $5 \cdot 10^{-5}$ mol/kg at 40 °C. The q_e value was found to be $12 \cdot 10^{-5}$ mol/kg at 5 °C. Adsorption capacity decreases with increasing temperature.

Acknowledgement

All experimental work was conducted in the Chemical Engineering Department Laboratory at Çankırı Karatekin University. The authors would like to thank the Chemical Engineering Department.

References

[1] Ma, X., Tao, S., Fu, S., Yang, H., Lin, B., Lou, Y., et al. (2023). Adsorption of Pyrethroids in Water by Calcined Shell Powder: Preparation, Characterization, and Mechanistic Analysis. Materials (Basel). https://doi.org/10.3390/ma16072802.

[2] Wang, Q., Jiang, F., Ouyang, X., Yang, L-Y., Wang, Y.. (2021). Adsorption of Pb(II) From Aqueous Solution by Mussel Shell-Based Adsorbent: Preparation, Characterization, and Adsorption Performance. Materials (Basel). https://doi.org/10.3390/ma14040741.

[3] Gigante, V., Cinelli, P., Righetti, M.C., Sandroni, M., Tognotti, L., Seggiani, M., et al. (2020). Evaluation of Mussel Shells Powder as Reinforcement for PLA-Based Biocomposites. Int J Mol Sci. https://doi.org/10.3390/ijms21155364.

[4] Cela-Dablanca, R., Nebot, C., López, L.R., Fernández-Calviño, D., Arias-Estévez, M., Núñez-Delgado, A., et al. (2021). Efficacy of Different Waste and by-Products From Forest and Food Industries in the Removal/Retention of the Antibiotic Cefuroxime. Processes. https://doi.org/10.3390/pr9071151.

[5] Conde-Cid, M., Cela-Dablanca, R., Ferreira-Coelho, G., Fernández-Calviño, D., Núñez-Delgado, A., Fernández-Sanjurjo, M.J., et al. (2021). Sulfadiazine, Sulfamethazine and Sulfachloropyridazine Removal Using Three Different Porous Materials: Pine Bark, “Oak Ash” and Mussel Shell. Environ Res. https://doi.org/10.1016/j.envres.2021.110814.

[6] Nameni, M., Alavi Moghadam, M.R., Arami, M.. (2008). Adsorption of Hexavalent Chromium From Aqueous Solutions by Wheat Bran. Int J Environ Sci Technol. https://doi.org/10.1007/bf03326009.

Performance Evaluation of Graphene Oxide Synthesis from Graphite by Hummers Method

Haluk KORUCU [1], ***Esra YILMAZ MERTSOY*** [1], ***Mohammad Ruhul Amin BHUIYAN*** [2], ***Enes BEKTAŞ*** [1], ***Ahmet YARTAŞI*** [1], ***Aboubakar Ibrahim MOHAMED*** [1*], ***Tabarek Salam MAJEED*** [1], ***Mahdi Mohamed DAHER*** [1], ***Mahad Ousleyeh ALI*** [1]

[1] *Department of Chemical Engineering, Faculty of Engineering, Çankırı Karatekin University, Uluyazı, Çankırı 18100, Turkey*

[2] *Department of Electrical and Electronic Engineering, Islamic University, Kushtia 7003, Bangladesh*

Abstract

The purpose of this study was to evaluate how well the use of acetic and propionic acids performed in the Hummers technique of graphene oxide production in place of phosphoric acid. Three trials were conducted using the Hummers method to ascertain the effects under the same conditions and using just phosphoric acid, acetic acid, and propionic acid. Particle size distribution analyses, Zeta Potential, surface area measurement with BET, and structure characterisation with FTIR were all used to characterize the effects. Explosions occasionally occurred during the propionic acid experiment due to the fast and exothermic reaction mechanism, which had an adverse effect on the oxidation mechanism. The effective synthesis of graphene oxide was achieved through controlled oxidation in the presence of phosphoric and acetic acids. Using phosphoric acid and the traditional Hummers TOUR method, the best outcome was achieved between these two compounds. Using the graphite sample as a reference, the recovery rates for surface area, particle size, and zeta potential were found to be -19.72%, 39.95%, and 61.50%, respectively. The FTIR measurements showed that the synthesis of graphene oxide using acetic acid and propionic acid was successful, whereas the synthesis using propionic acid was not successful.

Keywords: *Graphene Oxide, Hummers TOUR Method, Acetic Acid, Propionic Acid, Phosporic Acid*

1. Introduction

Graphene-based materials have become a focal point of significant interest among scientists in recent years. This is primarily due to graphene's exceptional properties such as high surface-to-volume ratio, superior conductivity, and high mechanical strength. These remarkable attributes make graphene-based materials versatile in various fields, including biosensors [1], fuel cells, energy storage devices, protective coatings, integrated circuits (ICs), biomedical applications such as drug/gene delivery systems, and wastewater management [2]. Graphene oxide (GO) synthesis involves adding graphite to concentrated acid in the presence of an oxidizing agent. While there are several methods for GO synthesis, some of these methods have disadvantages. Although the mechanical exfoliation method is attractive for producing high-quality GO, its feasibility for large-scale production poses a drawback [3]. Thermal exfoliation and chemical vapor deposition (CVD) methods[4] are considered other GO production methods, but chemical oxidation, particularly methods like Brodie, Staudenmaier, Hummers, Modified Hummers, and Tour, stands out as the most popular GO production method [5] Among chemical oxidation methods, various approaches such as Brodie, Staudenmaier, Hummers, Modified Hummers, and Tour have been developed. In 1958, Hummers and Offeman introduced a synthesis method based on the reaction of graphite with potassium permanganate ($KMnO_4$) and concentrated sulfuric acid (H_2SO_4). In their studies, Marcano and colleagues replaced $NaNO_3$, which causes toxic gases in the Hummers method, with H_3PO_4, doubling the amount of $KMnO_4$ used [6]. Hummers method is a widely recognized approach for the synthesis of graphene oxide (GO), a crucial precursor in the production of graphene-based materials. In this method, phosphoric acid (H_3PO_4), acetic acid (CH_3COOH), and propionic acid (C_2H_5COOH) play vital roles in the oxidation and exfoliation processes. The use of phosphoric acid aids in the intercalation of graphite layers, facilitating subsequent exfoliation. Acetic acid, with its oxidizing properties, contributes to the formation of functional groups on the graphene surface, promoting the hydrophilicity of GO. Propionic acid, being a carboxylic acid, participates in the oxidation of graphite and assists in achieving the desired functionalization. Phosphoric acid, as a strong dehydrating agent, facilitates the removal of water molecules during the reaction, preventing the re-stacking of graphene layers.

* Corresponding author. *e-mail address: aboubakeribrahim18@gmail.com*

Acetic acid serves as a carbon source, contributing to the functionalization of graphene by introducing carboxylic groups. Propionic acid, with its longer carbon chain, adds complexity to the functional groups on the graphene oxide surface. The synergistic action of these acids in the Hummers method results in a well-defined graphene oxide structure, making it a versatile material for various applications in nanotechnology, electronics, and biomedical fields. Overall, the strategic use of phosphoric, acetic, and propionic acids in the Hummers method ensures the successful synthesis of graphene oxide with tailored properties for specific applications. In this study, graphene oxide synthesis using the Hummers method in the presence of phosphoric acid, acetic acid and propionic acid were performed. The reduced graphene oxide samples were analyzed by different characterization techniques such as zeta potential measurement and particle size distribution analysis, FTIR analysis, surface area measurement.

2. Materials and Methods

The purpose of this study was to assess how well propionic acid, acetic acid, and phosphoric acid performed in the Hummers technique of graphene oxide synthesis. The performance of phosphoric acid, acetic acid, and propionic acid in the synthesis of graphene oxide was assessed in three separate tests that were conducted for this purpose, all of which were conducted under identical conditions. This study aimed to assess the efficacy of propionic acid and acetic acid using the Hummers Tour method's phosphoric acid reference experiment. sing the Hummers method, the temperature was maintained at 5°C in a double-walled glass reactor using a circulated water bath for all three experiments. Two grams of graphite sample, 50 milliliters of H_2SO_4, and 20 milliliters each of phosphoric, acetic, and propionic acids were added, and the mixture was mixed for sixteen hours. Subsequently, the mixes were combined for six hours at 95°C while 50 milliliters of distilled water was added. The mixture was allowed to cool after the time, and 5 ml of H_2O_2 and 5 ml of HCl acid were added to them to stop the process. Every test solution was transferred to five-liter containers and cleaned using the decantation method until the pH reached three. After being centrifuged, cleaned, and baked at 60°C, the samples were dried. Structure characterization using FTIR, surface area measurements using BET, dimensional analysis with dispersion property, and Particle Size Distribution with Zeta Potential were carried out to assess the performance of the generated graphene oxide samples. Table 1 lists the quality standards that were established for the graphene oxide characterization process.

Table 1. Quality criteria of Graphene Oxide Synthesis by Hummers Method

Quality Criteria	Symbol	Explanation	Information	The goal for GO
1	FTIR	Characatarizaton of the structure	Functional groups	
2	PB	Particle Size	Feature improvement	Larger is better
3	ZP	Zeta Potential	Stable distribution	Smaller is better
4	BET	Surface Area	Degree of porosity	Larger is better

3. Results and Discussion

The graphite Hummers method yields FTIR graphs of graphene oxide samples, as shown in Figure 1. The results showed that the vibration peak C=O at 1721 cm^{-1}, the vibration and deformation peaks of the O-H groups at 3391 cm^{-1} and 1410 cm^{-1}, the stress peak C-O at 1221 cm^{-1}, the stress peak C-O at 1046 cm^{-1}, and the stress peak C=C at 1680 cm^{-1} were observed at 1620 cm^{-1} in graphene oxide samples synthesized with phosphoric acid and acetic acid in the FTIR-ATR analysis pattern. The graphene oxide structure in the propionic acid experiment showed almost the same peaks as the graphite structure, which was not observed. The presence of oxygen-containing functional groups suggests that graphene oxide synthesis is successful for phosphoric and acetic acids but failed for propionic acid, according to the results of FTIR research.

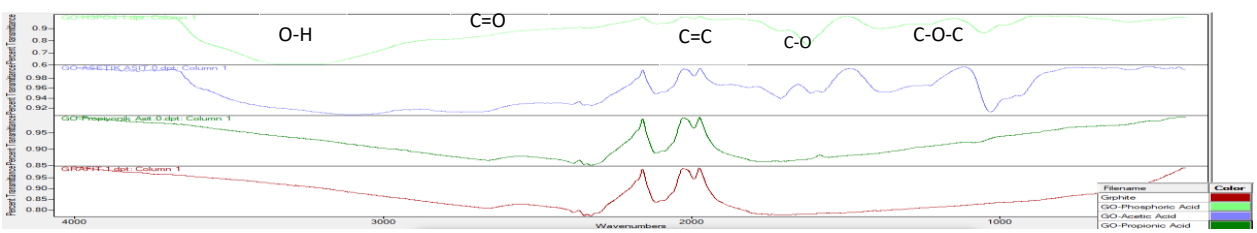

Figure 1. FTIR images of graphite and graphene oxide samples

BET surface area measurements of produced graphene oxide and graphite samples are shown in Figure 2. In the process of synthesizing graphene oxide from graphite, there has been a decrease in surface area, when a rise is anticipated. The reason for the huge surface area is the creation of a porous structure; in graphene oxide samples, a component that plugs their pores may have caused a drop in surface area.

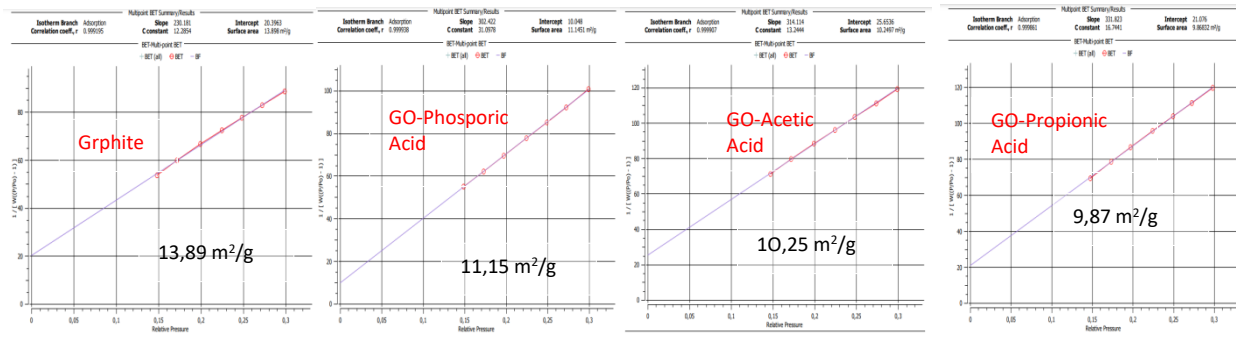

Figure 2. BET images of graphite and graphene oxide samples

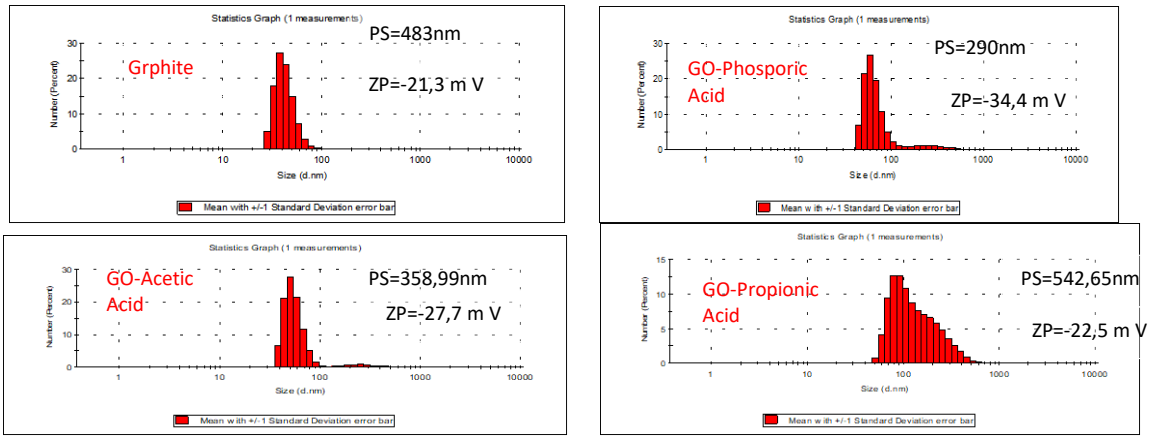

Figure 3. Zeta Sizer and Particle Size Results of Graphite and Graphene oxide Samples

Figure 3 displays the findings of the particle size and Zeta Potential analyses. Propionic acid synthesis showed a negative effect on the particle size value, whereas phosphoric acid and acetic acid synthesis showed an improvement in the values with the creation of graphene oxide. Figure 3 displays the findings of the particle size and Zeta Potential analyses. In the synthesis of phosphoric acid and acetic acid, the values improved with the generation of graphene oxide; however, in the synthesis of propionic acid, there was a negative effect on the particle size value.

Table 2. Recovery ratios reference-concrete between Reduced graphene oxide-concrete

Answers	Ref[a] Grphite	GO-Phosporic Acid	GO-Acetic Acid	GO-Propionic Acid	Recovery Rate GO-Phosporic Acid (%)	Recovery Rate GO-Acetic Acid (%)	Recovery Rate GO-Propionic Acid (%)
BET (SA-m^2/g)	13,89	11,15	10,25	9,87	**-19,72**	-35,51	-28,94
ZP (ZP-mV)	-21,3	-34,4	-27,7	-22,5	**61,50**	23,10	**5,63**
ZP (PS-nm)	483	290	359	543	39.95[b]	25,67	**-12,42**

Calculation of the % recovery rate of the experiment performed reference graphite

[b] *((11,15-13,89) / 13,89)*100 =-19,72 (Negative Value means a decrease)*

According to the findings from this investigation, the synthesis using propionic acid was unsuccessful because the exothermic reaction in the propionic acid experiment was uncontrolled and oxidation was not possible due to

intermittent explosions. The production of acetic acid was successful and the experiment was completed without any problems. Acetic acid has behaved similarly to phosphoric acid in the manufacture of graphene oxide. Since acetic acid is more cost-effective and environmentally friendly than phosphoric acid, it can be used in the processing of graphene oxide instead of phosphoric acid.

Acknowledgement

This research was carried out with the support of the Scientific Research Project (MF081123B33) funded by Çankırı Karatekin University. Author thank to Çankırı Karatekin University, Scientific Research Project Management Unit (ÇAKÜ-BAP).

References

[1] Y. Bai, T. Xu, and X. Zhang, "Graphene-based biosensors for detection of biomarkers," *Micromachines*, vol. 11, no. 1, 2020, doi: 10.3390/mi11010060.

[2] K. Thakur and B. Kandasubramanian, "Graphene and Graphene Oxide-Based Composites for Removal of Organic Pollutants: A Review," *J. Chem. Eng. Data*, vol. 64, no. 3, pp. 833–867, 2019, doi: 10.1021/acs.jced.8b01057.

[3] S. Some *et al.*, "High-quality reduced graphene oxide by a dual-function chemical reduction and healing process," *Sci. Rep.*, vol. 3, no. Figure 1, pp. 1–5, 2013, doi: 10.1038/srep01929.

[4] Palomba, M., Carotenuto, G., & Longo, A. (2022). A Brief Review: The Use of L-Ascorbic Acid as a Green Reducing Agent of Graphene Oxide. Materials, 15(18), 6456..

[5] Darabi, R., Karimi-Maleh, H., Akin, M., Arikan, K., Zhang, Z., Bayat, R., ... & Sen, F. (2023). Simultaneous determination of ascorbic acid, dopamine, and uric acid with a highly selective and sensitive reduced graphene oxide/polypyrrole-platinum nanocomposite modified electrochemical sensor. Electrochimica Acta, 457, 142402..

[6] V. Agarwal and P. B. Zetterlund, "Strategies for reduction of graphene oxide – A comprehensive review," *Chem. Eng. J.*, vol. 405, no. September 2020, p. 127018, 2021, doi: 10.1016/j.cej.2020.127018.